AN ABSTRACT OF THE THESIS OF

Kaj Johannes Wåg for the degree of Doctor of Philosophy in Chemical Engineering presented on October 3, 1996. Title: Characterization and Modeling of Black Liquor Char Combustion Processes.

Abstract approved:

Redacted for Privacy

W.J.Frederick

An investigation of the physical properties and the combustion and gasification behavior of kraft black liquor char at conditions relevant to kraft recovery furnaces was undertaken. Pyrolysis experiments were conducted in a laminar entrained-flow reactor to produce black liquor char samples. The highly porous char was characterized using the following techniques: SEM, TEM, EMPA, and X-ray diffraction. The char appears as a honeycomb structure with embedded crystalline whiskers that were high in sodium and oxygen. The graphite-like char matrix was amorphous.

Total and active surface area measurements were carried out using N_2, CO_2, and O_2 as probe molecules. The char was meso- and microporous and the total surface area measured was lower than for activated carbon. The experimental isotherms showed hysteresis. The specific surface area, pore volume, and heat of adsorption increased at higher carbon conversions indicating an increasing reactivity from phenolic zig-zag edges.

Char burning experiments were conducted using a convective flow semi-batch reactor was coupled to a molecular beam mass spectrometer. CO was the main gas

released during black liquor char gasification at 1100°C. Three rate models were developed to predict the release of carbon in 5% O_2, 10% CO_2, and 5% O_2 + 10% CO_2.

Char burning experiments were also conducted using an atmospheric thermobalance coupled to a molecular beam mass spectrometer. The experiments showed that CO was the main gas released but not CO_2. CO_2 was consumed at ~750°C when heating the thermobalance at a constant rate of 10°C per min to 1000°C in a gas mixture of CO_2 and CO. A char burning mechanism was proposed suggesting that catalyzed carbon gasification, carbonate and sulfate reduction are coupled processes.

An assessment of available data on black liquor char gasification showed that the rate of carbon release may be additive with respect to CO_2 and water vapor at atmospheric pressure but definitely not at higher. Strong CO_2 adsorption probably accounted for why most of the carbon release in the presence of water vapor was due to carbon dioxide. Rate constants were evaluated for a mechanistic model for black liquor char data in mixtures of CO_2, $H_2O(g)$, CO, and H_2 at 750°C. The variation of the rate constants obtained, implied that the amount of oxidized phenolate groups increased with conversion. The number of total sites went through a maximum being consistent with known rate behavior and surface area data. An assessment of the water gas shift reaction showed that this reaction is probably at equilibrium in typical black liquor combustion conditions.

A computer program was developed for predicting the mass distribution and heat of pyrolysis during devolatilization of black liquor. Another computer program was developed to predict char burning times, sulfate and carbonate reduction, swelling, the release of carbon, sodium, sulfur, potassium, and chloride, accounting for transport limitations. Laboratory data showed that the release of fume increased at higher temperatures except for sulfur. The release of fume increased with decreasing particle size. The predictions using the computer program agreed well with laboratory data.

Characterization and Modeling of Black Liquor Char Combustion Processes

by

Kaj J. Wåg

A THESIS

submitted to

Oregon State University

in partial fulfillment of
the requirements for the
degree of

Doctor of Philosophy

Presented October 3, 1996
Commencement June 1997

Doctor of Philosophy thesis of Kaj Johannes Wåg presented on October 3, 1996

APPROVED:

Redacted for Privacy

Major Professor, representing Chemical Engineering

Redacted for Privacy

Head of Department of Chemical Engineering

Redacted for Privacy

Dean of Graduate School

I understand that my thesis will become part of the permanent collecton of Oregon State University libraries. My signature below authorizes release of my thesis to any reader upon request.

Kaj Johannes Wåg, Author

ACKNOWLEDGMENT

This research was supported by the U.S. Department of Energy through the Office of Industrial Technology, the National Renewable Energy Laboratory through the Associated Western Universities Inc., and the Niemi foundation at Oregon State University.

Professor W.J.Frederick is acknowledged for arranging thesis related research work at The Institute of Paper Science and Technology in 1992, The Combustion Chemistry Research Group at Åbo Akademi U. in the summer of 1993, and The National Renewable Energy Laboratory in 1995 and 1996. The opportunity to attend conferences in Seattle, Sydney, Irvine, Yosemite, San Francisco, Toronto, Dallas and Chicago is also acknowledged. Mr. Stanley Sobczynski, formerly with the U.S. Department of Energy, provided the major funding for this project. Dr. Tom Grace is acknowledged for help in developing the overall char burning model and "the spreadsheet program". Dr. Kimura played an important role in directing my work in the morphology chapter. Dr. Jovanovic was always available to help in research and classwork related problems. Dr. Koretsky is acknowledged for input in thermo related problems. Dr. Rorrer is acknowledged for giving me responsibility for the surface area analyzer.

Drs. Dave Dayton and Steve Kelley, as well as Mr. Joe Patrick are recognized for advice and guidance at NREL. Dr. Carlos Leon with the Quantachrome Corporation is acknowledged for the chemisorption results. Dr. Cindy Dogan with the U.S. Bureau of Mines is acknowledged for SEM, TEM and EDAX results. Dr. Roger Nielsen at OSU:s Oceanography Department is acknowledged for providing microprobe analysis and elemental mapping data. Mr. Dean Hanson with OSU:s Central Analytical Laboratory supervised the carbonate titration experiments. Mr. Al Soeldner at OSU:s Department of Botany & Plant Pathology provided many of the SEM photos. Dr. Larry Baxter approved complementing SEM characterization experiments at Sandia National Laboratories in Livermore, California. Nick Wannenmacher is recognized for assistance during computer and other technical problems. Lastly, I would like to express my appreciation to the graduate students in my class for an outstanding spirit of comradeship.

TABLE OF CONTENTS

TABLE OF CONTENTS (CONTINUED)

TABLE OF CONTENTS (CONTINUED)

TABLE OF CONTENTS (CONTINUED)

Page

TABLE OF CONTENTS (CONTINUED)

TABLE OF CONTENTS (CONTINUED)

Page

TABLE OF CONTENTS (CONTINUED)

Page

TABLE OF CONTENTS (CONTINUED)

Page

TABLE OF CONTENTS (CONTINUED)

TABLE OF CONTENTS (CONTINUED)

LIST OF FIGURES

LIST OF FIGURES (CONTINUED)

LIST OF FIGURES (CONTINUED)

LIST OF FIGURES (CONTINUED)

LIST OF FIGURES (CONTINUED)

LIST OF FIGURES (CONTINUED)

LIST OF FIGURES (CONTINUED)

LIST OF TABLES

LIST OF TABLES (CONTINUED)

LIST OF TABLES (CONTINUED)

LIST OF APPENDICES

LIST OF APPENDICES (CONTINUED)

LIST OF APPENDICES (CONTINUED)

LIST OF APPENDIX FIGURES

LIST OF APPENDIX FIGURES (CONTINUED)

LIST OF APPENDIX FIGURES (CONTINUED)

LIST OF APPENDIX FIGURES (CONTINUED)

LIST OF APPENDIX TABLES

LIST OF APPENDIX TABLES (CONTINUED)

DEDICATION

This thesis is dedicated to my parents, my brother Peter, and the fellow students at Oregon State during the years 1992-1996.

PREFACE

"Men stumble over the truth from time to time, but most pick themselves up and hurry off as if nothing happened."

- Sir Winston Churchill

Characterization and Modeling of Black Liquor Char Combustion Processes

Chapter 1

Introduction and Objectives

Black liquor is a fuel of high industrial importance. It is the sixth most important fuel in the world today, and it is the largest single volume organic product manufactured by industry apart from agricultural products [1]. Black liquor is the residue produced from the chemical conversion of wood to papermaking fiber. It is a mixture of water, organic matter and inorganic compounds. During combustion the water is evaporated, the organic matter undergoes thermal decomposition and subsequent gasification, and the inorganic compounds interact with the solid and gas phases. The inorganic materials used in the pulping process are comparable to major chemical products such as salt, sulfuric acid, nitric acid, caustic soda, potash, and fertilizers.

The kraft pulping process is the most common pulping method today. A series of processes and pieces of equipment are used to transform spent pulping liquor, weak black liquor, into regenerated pulping liquor, white liquor. The main task of the kraft recovery process is to recycle the chemicals used during pulping of wood fiber as well as to generate steam and power from the residual organic matter. These two goals are achieved by combusting black liquor in the Tomlinson recovery boiler. Black liquor is sprayed into a furnace cavity with special droplet forming nozzles. The walls of the furnace are lined with water filled tubes into which heat is transferred. The steam generated in the tubes is further used to obtain power with steam turbines. The tubes are kept cool to form a layer of smelt. The liquor will fall to the bottom of the furnace and accumulate in the char bed.

---

[1] Reeve, D.W., The Kraft Recovery Cycle, Kraft Recovery Operations Short Course, p.1-16, 1992

Air is added at several levels in such a way that the char bed operates under reducing conditions and the upper part of the furnace under oxidizing conditions.

The black liquor droplets burn in four partially overlapping stages: drying, devolatilization, char burning, and smelt reactions. During drying and devolatilization the droplets swell significantly to form popcorn like particles. As char burning proceeds, the particle decreases in size leaving only the inorganic components in a smelt form. The smelt is reduced in the char bed by the action of carbon, and it is tapped from the furnace through smelt spouts. The pulping chemicals are then regenerated by further processing the tapped smelt.

The scope of this thesis is to improve the understanding of black liquor combustion by characterizing the important physical and chemical phenomena during char burning. Furthermore, this thesis aims at accomplishing the capability to accurately predict the release of key elements during black liquor char combustion. This work is of special interest for boiler manufacturers as well as for the pulp and paper industry in a continuous effort to improve the design and operation of recovery boilers by computational fluid dynamic methods. The presented submodels are developed from extensive experimental data, that also provide a basis for the development of new recovery technologies where a rigorous understanding of the basic combustion phenomena of black liquor is vital.

The specific objectives of this thesis are listed as follows:

1. To characterize the morphology of black liquor char by identifying its structure, different phases, the elemental concentration and dispersion. Scanning electron microscopy, transmission electron microscopy, X-ray diffraction, and electron microprobe analysis were used.
2. To characterize the specific surface area, porosity, and the average pore size of black liquor char. Nitrogen physisorption was used to obtain the total surface area. CO_2 and O_2 chemisorption analyses were employed to obtain the active surface area.
3. To characterize the gasification behavior of black liquor char using thermal analysis methods such as thermogravimetry and differential scanning calorimetry.
4. To obtain a basic understanding of the product gases released from black liquor char in a convective flow reactor coupled to a molecular beam mass spectrometer.

5. To identify the chemical reactions during the release of key elements during combustion and gasification of black liquor char.
6. To derive simple engineering models for predicting the release of carbon, sodium, potassium, sulfur, and chloride during char burning.
7. To validate the models by existing data and by obtaining new experimental data.
8. To develop a computer program for predicting char burning times and the degree of sulfate reduction for different types of liquors at typical combustion conditions.
9. To develop a computer program for estimating the heat of pyrolysis and the element distribution during devolatilization of black liquor.
10. To propose specific issues in black liquor combustion where further research is relevant.

Several unresolved issues in the relevant literature are being addressed, e.g.:

- Why do not impregnated alkali ions enhance the gasification reactivity as much as for black liquor char?
- What is the heat of adsorption of CO_2 on black liquor char?
- What are the active and total surface areas of black liquor char as a function of carbon conversion and pyrolysis temperature?
- Is simultaneous gasification with CO_2 and O_2 an additive process?
- Is simultaneous gasification with CO_2 and $H_2O(g)$ always an additive process?
- Why are gasification and oxidation mutually exclusive?
- To what extent is sodium carbonate reduction reversible in black liquor char?
- Why is there mixed data on the inhibiting effects of CO_2 on the sodium carbonate reduction reaction?
- Why is the release of sodium enhanced at high oxygen concentrations?

An attempt is made to address these questions, but many issues were not possible to include because they would increase the scope of this work well beyond the time and resources available. Such topics include how the fractal dimensions change on black liquor char surfaces as a function of carbon conversion and pyrolysis temperature? The heterogeneous interaction of H_2 and CO is still an evolving field in the literature. How

does the chemisorption behavior of CO_2 and O_2 change for the complete set of char samples? Limitations on addressing these questions were imposed by high experimental costs.

This thesis is organized into 13 chapters. Chapters 1 and 2 give the introduction, objectives and a literature survey. Black liquor char is characterized in Chapters 3, 4, 5, and 6. An improved carbonate reduction model is given in Chapter 6. Chapter 7 gives an empirical method of estimating the heat of pyrolysis and establishing the initial conditions for char burning. The modeling work is reported in Chapters 8, 9, and 10. These chapters have been presented in various conferences. Chapter 6 has also been accepted for presentation in a conference at the time of completion of this thesis. Chapters 3 and 4 will constitute the basis for another paper. Conclusions and recommendations are given in Chapter 11. Chapter 12 summarizes the references. The computer program for simulation of black liquor combustion and a detailed documentation of this computer program are given in Appendix 13. The laminar entrained-flow reactor used to obtain the char samples studied in this dissertation is also described in Appendix 13. This thesis comes with a disk containing the combustion simulation program as well as the devolatilization program developed in Chapter 7. Other spreadsheets reported in this thesis are given in the same disk. A README.TXT-file describes all the files contained in the disk.

Chapter 2
Overview of Black Liquor Research

A lot of work has been done in studying combustion and gasification of black liquor in the 1990s. During the past three years, 9 master's theses regarding black liquor combustion have been defended at Oregon State University (OSU) alone. Elsewhere, research is being or has been conducted to a significant degree particularly at the following institutions: Åbo Akademi University (ÅAU), the Technical Research Center of Finland (VTT), McGill University and University of New Brunswick in Canada, the Institute of Paper Science and Technology (IPST) in Atlanta, Georgia, Sandia National Laboratories in Livermore, California, and most recently the National Renewable Energy Laboratory (NREL) in Golden, Colorado (1).

At OSU, advances have been made in many topics such NO_X formation and depletion via various mechanisms (2,3,4), and NO_X modeling is now under way (5). The release of inorganic elements such as potassium and chloride are now better understood (6). Progress has been made in understanding the sulfur release and transformation processes (7). Sintering of recovery boiler fume deposits (8) and their effect on the oxidation of ammonia have been most recently addressed (9). Aerosol deposition models are being developed in cooperation with Sandia National Laboratories. Advanced experimental equipment are being used at the National Renewable Energy Laboratory to improve the understanding of black liquor combustion and gasification. Some of these results are presented in this thesis. Further work includes the measurement of the radiative properties of black liquor fume using FTIR (10).

In Europe, ÅAU may be the leader in black liquor research. ÅAU was the first to propose the four partially overlapping combustion stages that are widely accepted today (11). In the early 1990s, a lot of work was done at ÅAU in the field of pressurized gasification of black liquor char (12) and the release of sodium and sulfur (13). Since then, the focus has been geared to investigate the effects of liquor type, and the synthetic

generation of black liquor (14). At VTT there are many research programs concerning all aspects of black liquor combustion. Pyrolysis studies have been performed using a heated grid reactor to characterize the release of carbon, sodium and sulfur (15). VTT has expanded its research to include pressurized thermogravimetry (16). A special research group is fully devoted to studying aerosol processes. Some modeling work has been done at Tampere University of Technology (TUT) (17). Cooperatively, TUT, ÅAU, and OSU have published the first surface temperature measurements of burning black liquor droplets using pyrometry (18). In Sweden, the Swedish Pulp and Paper Research Institute (STFI) in conjunction with the Royal Institute of Technology as well as Chalmers University of Technology have done some modeling work (19).

In Canada a great deal of pivotal investigations have been conducted to characterize and comprehend the reaction mechanisms during black liquor char combustion and gasification (20,21). Especially valuable have been the kinetic data that were obtained using atmospheric thermobalances at McGill University (22,23). These data are the basis for the principal kinetic models still in use today. Some characterization of black liquor char using SEM and energy dispersive spectroscopy was performed at McGill (22). PAPRICAN has done some valuable work in the field of sulfur and sodium emission during char gasification (24,25). The University of British Columbia is focusing on flow field simulations of recovery boilers and do not conduct any experimental work (26). At the University of Toronto, the field of concentration is fume formation and deposition (27) but some modeling work is being done there also.

In the United States, IPST has been a cornerstone in black liquor research with consistent research programs over many years. Sulfate reduction was first discovered at IPST (28,29), and so was the first gasification study of black liquor char (30). Pioneering work has been performed to understand inorganic aerosol formation (31). The impact of liquor composition on nitrogen release has been addressed (32). NO_X issues have also been addressed (33). Several dissertations on comprehensive recovery boiler combustion models have been released (34,35,36,37). A spectroscopic evaluation of the gas phase above a burning char bed has been performed (38). Attempts to study CO_2 gasification have also been made (39). Early work on sulfur release (40), fume deposition (41),

swelling of black liquor (42) and droplet drying (43) was done at IPST. IPST has also done contract research work for the US Department of Energy concerning black liquor combustion (44,45). Many other distinguished pulp & paper schools in the United States have not published articles regarding black liquor combustion in recent years.

At Sandia, novel techniques are being developed to diagnose and measure the deposition characteristics of black liquor fume (46). NREL may be the first laboratory in the world to use mass spectrometry in studying black liquor combustion (1). At Oak Ridge National Laboratory (ORNL) parallel computing methods are implemented to speed up the convergence times in CFD modeling of recovery boilers (47). ORNL develops techniques to validate comprehensive recovery boiler models with different techniques (48).

Many private organizations, such as Babcock & Wilcox, Champion International, Manufacturing and Technology Conversion International Inc., Ahlström, Tampella, Chemrec/Kvaerner, and Götaverken are showing continuous interest in novel gasification technologies. Intensive research has been done on a pilot scale, and progress has been made in applying this technology into practice particularly at the Frövifors mill in Sweden. Atmospheric and pressurized gasification processes could substantially improve the operation and economy of black liquor conversion into green liquor. Research interest into this important industrial field is not expected to diminish in strength in the near future. With ever stricter environmental regulations, the question is not whether the conventional Thomlinson recovery boilers will be substituted with more advanced technologies, but when in the 21st century this will occur?

BIBLIOGRAPHY

1. Dayton, D.C., Frederick, W.J., Direct Observation of Alkali Release during Biomass Combustion and Gasification. 2. Black Liquor Combustion at 1100°C, Energy & Fuels, Vol.10, No.2, p.284-292, 1996

2. Carangal, A., M.S. thesis, Oregon State University, 1995

3. Pianpucktr, R., M.S. thesis, Oregon State University, 1996

4. Wu, S.-L., M.S. thesis, Oregon State University, 1995

5. Rompho, N., M.S. thesis, Oregon State University, in progress

6. Reis, V., M.S. thesis, Oregon State University, 1995

7. Sricharoenchaikul, V., M.S. thesis, Oregon State University, 1995

8. Techakijkajorn, U., M.S. thesis, Oregon State University, 1996

9. Tanganpanyapinit, V., M.S. thesis, Oregon State University, 1996

10. Samretvanich, A., M.S. thesis, Oregon State University, in progress

11. Hupa, M., Solin, Hyöty, P., Combustion Behavior of Black Liquor Droplets, JPPS, 13(2):J67-72, 1987

12. Wåg, K.J., M.Sc. thesis, Åbo Akademi University, 1991

13. Forssén, M., M.Sc. thesis, Åbo Akademi University, 1991

14. Whitty, K.J., Backman, R., Forssén, M., Hupa, M., Rainio, J., Sorvari, V., Liquor to liquor Differences in Combustion and Gasification Processes: Pyrolysis Behavior and Char Reactivity, International Chemical Recovery Conference, April 24-27, p.A245, 1995

15. McKeough, P.J., Kurkela, M., Arpiainen, V., Mikkanen, P., Kauppinen, E., Jokiniemi, J., The Release of Carbon, Sodium and Sulfur During Rapid Pyrolysis of Black Liquor, International Chemical Recovery Conference, April 24-27, p.A217, 1995

16. Saviharju, K., Moilanen, A., van Heiningen, A.R.P., New High Pressure Gasification Rate Data on Fast Pyrolysis of Black Liquor Char, International Chemical Recovery Conference, April 24-27, p.A237, 1995

17. Karvinen, R., Recovery Boiler Modeling, Yosemite Colloquium on Recovery Boiler Modeling, Yosemite Marriot, California, September 25-28, 1994

18. Frederick, W.J., Hupa, M., Stenberg, J., Hernberg, R., Optical Pyrometric Measurements of Surface Temperatures During Black Liquor Char Burning and Gasification, FUEL, Vol.73, No.12, p.1889, 1994

19. Thunman, H., M.Sc. thesis, Chalmers University of Technology, 1994

20. Li, J., van Heiningen, A.R.P., Mass Transfer Limitations in the Gasification of Black Liquor Char by CO_2, JPPS, Vol.12, No.5, p.J146-J151, September 1986

21. Li, J., van Heiningen, A.R.P., Reaction Kinetics of Gasification of Black Liquor Char, Canadian J. Chem. Eng., Vol.67, p.693-697, August 1989

22. Li, J., van Heiningen, A.R.P., Kinetics of CO_2 Gasification of Fast Pyrolysis Black Liquor Char, Ind.Eng.Chem.Res., Vol.29, No.9, p.1776, 1990

23. Li, J., van Heiningen, A.R.P., Kinetics of Gasification of Black Liquor Char by Steam, Ind.Eng.Chem.Res., Vol.30, No.7, p.1594, 1991

24. Li, J., van Heiningen, A.R.P., Sodium Emission During Pyrolysis and Gasification of Black Liquor Char, TAPPI J., p.213, December 1990

25. Li, J., van Heiningen, A.R.P., Sulfur Emission During Slow Pyrolysis of Kraft Black Liquor, TAPPI J., p.237, March 1991

26. Nowak, P., Matys, P., Sabhapathy, P., Abdullah, Z., Salcudean, M., Numerical Study of a Kraft Recovery Furnace, International Chemical Recovery Conference, April 24-27, p.A149, 1995

27. Tavares, A., Tran, H., Barham, D., Rouilard, P., Adams, B., Fume Chemistry, Morphology and Deposition in a Kraft Recovery Boiler, International Chemical Recovery Conference, April 24-27, p.A87, 1995

28. Cameron, J.H., Grace, T.M., Kinetic Study of Sulfate Reduction with Carbon, Ind.Eng.Chem.Fundam., Vol.22, No.4, 1983

29. Grace, T.M., Cameron, J.H., Clay, D.T., Role of the sulfate-sulfide Cycle in Char Burning: Experimental Results and Implications, TAPPI J., October 1986

30. Goereg, K.A., Cameron, J.H., A Kinetic Study of Kraft Char Gasification with CO_2, Proc. AIChE Summer National Meeting, Boston, p.E7-E12, August 1986

31. Verrill, C.L., PhD thesis, The Institute of Paper Science and Technology, 1994

32. Martin, D.M., PhD thesis, The Institute of Paper Science and Technology, 1995

33. Thompson, L., PhD thesis, The Institute of Paper Science and Technology, 1995

34. Jones, A.K., PhD thesis, The Institute of Paper Science and Technology, 1989

35. Walsh, A.R., PhD thesis, The Institute of Paper Science and Technology, 1989

36. Sumnicht, D.W., PhD thesis, The Institute of Paper Science and Technology, 1989

37. Kulas, K.A., PhD thesis, The Institute of Paper Science and Technology, 1990

38. Medvecz, P., PhD thesis, The Institute of Paper Science and Technology, 1991

39. Lee, S.R., PhD thesis, The Institute of Paper Science and Technology, 1993

40. Harper, F.D., PhD thesis, The Institute of Paper Science and Technology, 1989

41. Georg, K.A., PhD thesis, The Institute of Paper Science and Technology, 1989

42. Miller, P.T., PhD thesis, The Institute of Paper Science and Technology, 1986

43. Robinson, M.L., PhD thesis, The Institute of Paper Science and Technology, 1987

44. Frederick, W.J., Combustion Processes in Black Liquor Recovery, US DOE Report DOE/CE/40637-T8 (DE90012712), March, 1990

45. Clay, D.T., Lien, S.J., Grace, T.M., Brown, C.A., Empie, H.L., Macek, A., Amin, N., Rao Charangundla, S., US DOE Report DOE/CE/40637-T9 (DE91018580), March, 1990

46. Sinquefield, S., Sandia National Laboratories, in progress, 1996

47. Aggarwal, R., Zaccharia, T., Parallel Computing, Yosemite Colloquium on Recovery Boiler Modeling, Yosemite Marriot, California, September 25-28, 1994

48. Hylton, J.O., Information for Validation of Combustion Models, Yosemite Colloquium on Recovery Boiler Modeling, Yosemite Marriot, California, September 25-28, 1994

Chapter 3

Characterization of the Morphology of Black Liquor Char

INTRODUCTION

The characterization of solids and the elucidation of its morphology is a major concern in many industrial activities. The development of powerful investigation methods for the characterization of solids and catalysts has been a major advance in recent years. Present research on catalyst containing fuels, such as black liquor, involves the cooperation of people of quite different backgrounds: chemists, physicists, and engineers, who may feel overwhelmed by the abundance of techniques available today. The aim of this chapter is to clarify ideas in this respect, and to apply some of these methods for describing the morphology and structural nature of black liquor char.

The first feature that should be known about a solid is the nature of the basic building units constituting the solid, i.e. the average atomic composition. Then comes the arrangement of these basic building units, i.e. the architecture of the catalyst. The determination of this architecture should logically go from the most macroscopic features toward the most microscopic. Figure 3.1 is an attempt to summarize some paths along which this study should proceed.

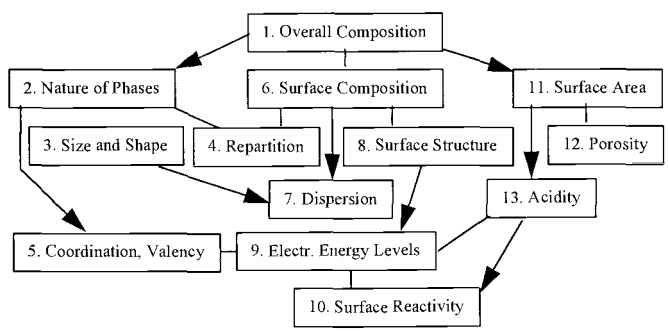

Figure 3.1. General scheme of the characterization of catalysts (1).

Path A concerns with the nature of the bulk of the solid. The individual atoms are grouped and often organized to form a limited number of phases, amorphous or crystalline, which can be characterized macroscopically by features such as crystal structure or reactivity. Knowing the overall composition of the solid (box 1), the first step is to discover the nature of these phases (box 2). The investigation may then proceed both toward the description of the size and shape (box 3) as well as the study of the mutual position of the phases within the solid (box 4). This is called repartition or distribution in space. Measurement of repartition includes the determination of the atomic composition, especially when no separate phase can be distinguished. Path A may also proceed toward a more microscopic description of the chemical state of the individual atoms such as coordination, valency, and electron energy levels (boxes 5 and 9). Obviously, the coordination of an individual atom is directly related to the nature of the phase to which it belongs. As the chemical state of the atom is determined largely by its environment, these two features are strongly interrelated.

Path B deals with the nature of the surface of the solid. The first step is the measurement of the atomic composition of the surface (box 6). It is also desirable to get information on the repartition of this surface composition. Obviously, the surface repartition is related to the repartition of the bulk composition (box 4). The knowledge of both bulk and surface compositions allows the measurement of the dispersion of the various phases constituting the catalyst (box 7). In some favorable cases, dispersion may also be determined from the size and shape of the particles belonging to the various phases. Path B may also proceed toward the study of long range atomic arrangements, i.e. the crystal structure at the surface (box 8), and of the more local arrangement (coordination) and chemical state of the surface atoms (box 9).

Presently, the properties of surfaces are often most easily determined by studying their interaction with selected molecules. The last step along path B is the study of the reactivity of the surfaces. This includes selective adsorption and surface chemical transformations. The reactivity of a surface is a direct consequence of the macroscopic and microscopic features, but its characterization requires specific investigation methods (box 10).

Path C concerns a series of characteristics which are usually considered separately, although they are not completely independent of those already considered. The first step is the measurement of the surface area (box 11). The study of the shape and distribution of the pores follows logically (box 12). A further step is the study of the surface acidic and basic sites. Clearly, the coordination, chemical state, and reactivity of surfaces have a strong bearing on the existence and nature of such surface sites.

One should remember that the scheme presented in Figure 3.1 is merely a general framework, the details of which cannot correspond to all practical situations. For example, the study of coordination may, in some cases, lead to the discovery of a macroscopic phase which could otherwise not be detected. The numerous interconnections drawn in Figure 3.1 illustrate how tightly the various characteristics of the architecture of the catalysts are related. This stresses the need for an approach involving many techniques, each complementing each other. Although every technique is likely to bring its own insight, one can hardly imagine that the researcher would characterize the same factor by using all available techniques. Thus, the final selection is much a matter of personal appreciation.

OBJECTIVES

The objective is to gain a general understanding of the characterization techniques employed for porous solids in modern laboratories. Another objective is to gain a feel for basic strategies on how to characterize a solid, what the questions are and how to answer them. Specifically it was the aim to characterize black liquor char with standard techniques used for investigating catalysts and carbon surfaces. Such techniques include scanning electron microscopy and electron microprobe analysis. Transmission electron microscopy was also used.

TECHNIQUES FOR CATALYST CHARACTERIZATION

Three main classes have been distinguished to classify the characterization techniques according to the phenomena studied: (a) chemical techniques, (b) static physicochemical techniques, and (c) spectroscopy and related methods.

Chemical techniques

There are two main categories of chemical techniques: gas adsorption experiments and measurement of reactivity of solids.

Gas adsorption experiments are based on the interpretation of the physisorption isotherm of an inert gas for determining the surface area. The most common method is that developed by Brunauer, Emmett, and Teller (BET). Another technique is the chemisorption of a reactive gas for measuring the acidity of the surface. The amount of a gaseous base, such as ammonia or pyridine, adsorbed as a function of temperature is a superior measure of acid strength. Adsorption of a gaseous acid is used to measure the amount of basic sites. Examples are carbon dioxide, nitric oxide, and phenol.

The measurements of the reactivity of solids can be obtained by thermal analysis comprising several different methods. Thermogravimetry (TG) and differential scanning calorimetry (DSC) are perhaps the most common ones. TG is based on the measurement of weight loss or gain as a function of temperature and time. DSC consists of measuring heat evolution or absorption as a function of increasing/decreasing temperature. Thermal analysis is discussed in more detail in chapter 6. Temperature programmed desorption (TPD) or reduction (TPR) are measurements that allow the study of the reactivity of a reactive solid. It involves the adsorption of gases into a solid surface in a controlled atmosphere and temperature after which the solid is outgassed. After outgassing, the solid is subjected to a set temperature program under which the evolved gases are monitored.

Static physicochemical techniques

These techniques consist of measuring the response of the solid when submitted to a static field of forces. There are two main forces involved: (a) mechanical forces, and (b) electromagnetic forces.

Mechanical forces can be applied with mercury porosimetry that measures the distribution of the pore sizes by forcing mercury to penetrate into the porous volume. Mercury porosimetry was applied to the material studied in this thesis (black liquor char), but the solid structure was too fragile making the measurement impossible. Electromagnetic forces are used to measure properties such as electrical and thermal conductivity, surface potentials, and to show atomic arrangements. These properties are important in metallic catalysts but not for black liquor char.

Spectroscopy and related techniques

These techniques involve measuring the response of a solid when submitted to radiation, either an electromagnetic wave or particles such as electrons. This response may be merely the scattering or absorption of the induced radiation. The response may also involve absorption followed by emission of another type of radiation. The techniques can be classified according to the nature of the incident radiation versus the nature of the response. Table 3.1 classifies the most common techniques according to the following combination: nature of excitation and the response to it.

Table 3.1. The classification of techniques used in this study.

Excitation	Response			
	Photons	Electrons	X-rays	Neutrals
Photons	NMR*	not used	not used	na
Electrons	not used	SEM, TEM	EMPA, EDAX	na
Ions	not used	not used	not used	na
X-rays	na	na	X-ray diffraction	na
Neutrals	na	na	na	not used

na = not applicable, * = non-published data

Table 3.1 shows that the techniques employed in characterization of solids are organized according to the type of excitation and response obtained. Only the methods used in this study are covered.

Incident radiation: photons / Response: photons

Nuclear magnetic resonance (NMR) is a technique based on a property of many nuclei that when placed in a magnetic field, absorb characteristic energies from a radio frequency field superimposed upon them. The interaction of the nuclear spins with the external magnetic field causes a splitting of the corresponding energy levels. For nuclei having a magnetic moment, transitions between these levels occur when this splitting corresponds to the energy of the incident wave. This phenomenon allows the study of the nuclei, their motion and orientation within the solid.

Incident radiation: electrons / Response: electrons

Scanning electron microscopy (SEM) is a technique that allows the imaging of the topography of a solid surface with a resolution of better than 5 nm. The surface is swept in a raster pattern with a finely focused beam of electrons. The electron beam is swept across the surface in a straight line, returned to its starting position, and shifted by a standard increment. This procedure is repeated until a desired area has been scanned. Several types of signals are produced when it is scanned with an energetic beam of electrons. These signals include backscattered electrons, secondary electrons, Auger electrons, X-ray fluoresence and other photons of various energies. Backscattered and secondary electrons are the basis of scanning electron microscopy, and X-ray fluoresence (photons) are used in electron microprobe analyses.

SEM consists of an electron optical column, a vacuum system and electronics. There are three lenses to focus the electrons into a fine spot onto the specimen with no lenses below the specimen. When the primary beam strikes the specimen, the electrons produced are turned into an electrical signal that can be monitored. The specimen is scanned in a rectangular raster pattern with the primary beam. The whole trajectory from source to screen is under vacuum.

The operation principle is almost the same for Transmission electron microscopy (TEM) except that the electrons pass through the specimen. Therefore, the specimen has to be very thin to allow the electrons to penetrate it. TEM involves a variety of imaging techniques: bright field, dark field, or high resolution. It allows the determination of the microtexture or microstructure of electron transparent samples with a resolution better than 0.5 nm. The method of irradiation of the sample distinguishes conventional transmission electron microscopy (CTEM) from scanning transmission electron microscopy (STEM). Figure 3.2 illustrates the operation principles of SEM and TEM.

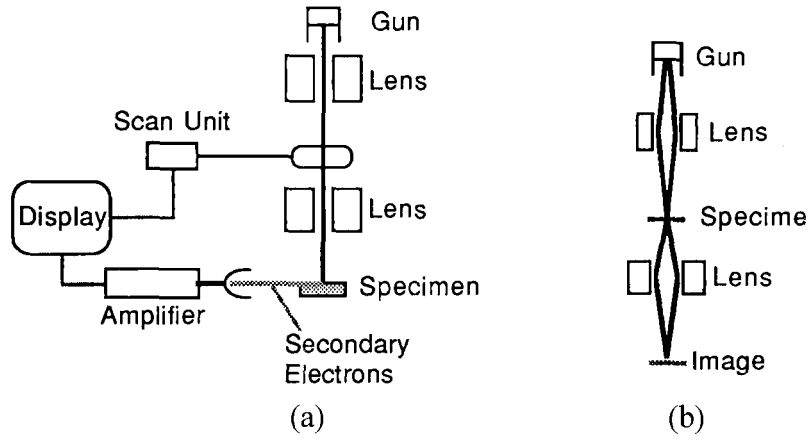

Figure 3.2. Schematic of (a) SEM and (b) TEM (2). The specimen is under electron bombardment, and the scattered electrons are detected either by an e-detector or an X-ray detector.

Incident radiation: electrons / Response: X-ray

Electron microprobe analysis (EMPA) and energy-dispersive X-ray microanalysis (EDAX) are methods that allow the quantitative measurement of the composition of solids with a spatial resolution in the order of 1 μm. The deexcitation of atoms ionized upon the impact of high energy electrons brings about the emission of characteristic X-ray photons having energies equal to the energy level separation of the ionized atoms (E_2-E_1).

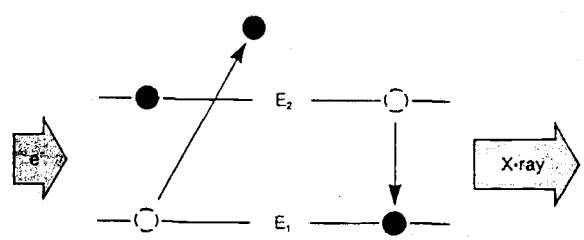

Figure 3.3. When an electron is dislodged from a shell of low energy (E_1), an electron from a shell of higher energy (E_2) fills the vacancy by emitting X-rays (3,4).

Incident radiation: X-ray / Response: X-ray

In X-ray diffraction a beam of X-rays of a known wavelength is directed at a sample, and the angles and intensities of the diffracted beams are measured. If the sample is crystalline, a diffraction pattern can be observed. If the the sample is amorphous, the atoms are arranged in an irregular jumble, and no diffraction pattern is formed.

MATERIAL STUDIED

The char sample studied was obtained by feeding dry black liquor particles into a laminar-entrained flow-reactor (LEFR) at Oregon State University with a residence time of 0.67 sec at 900°C. A detailed description of this device and the experimental procedure can be found in Appendix 13. The char sample was generated by pyrolyzing black liquor solids with diameters between 90-125 μm. Figure 3.4 shows that black liquor solids (BLS) looks like a cactus.

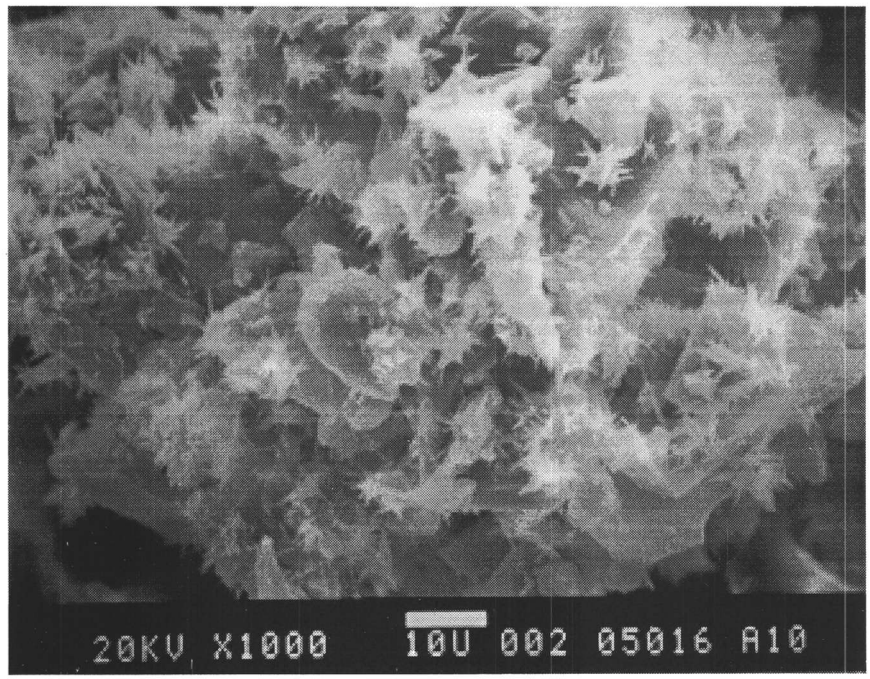

Figure 3.4. BLS looks like a cactus with a high population of whiskers on what apperas to be a graphitic bulk structure. Magnification: 1000×, Scale: 10 μm.

The BLS was transformed to a char that was swollen three times with respect to its initial diameter. The composition of the char studied is given in Table 3.2. Figure 3.5 shows that a typical char particle is highly porous after pyrolysis.

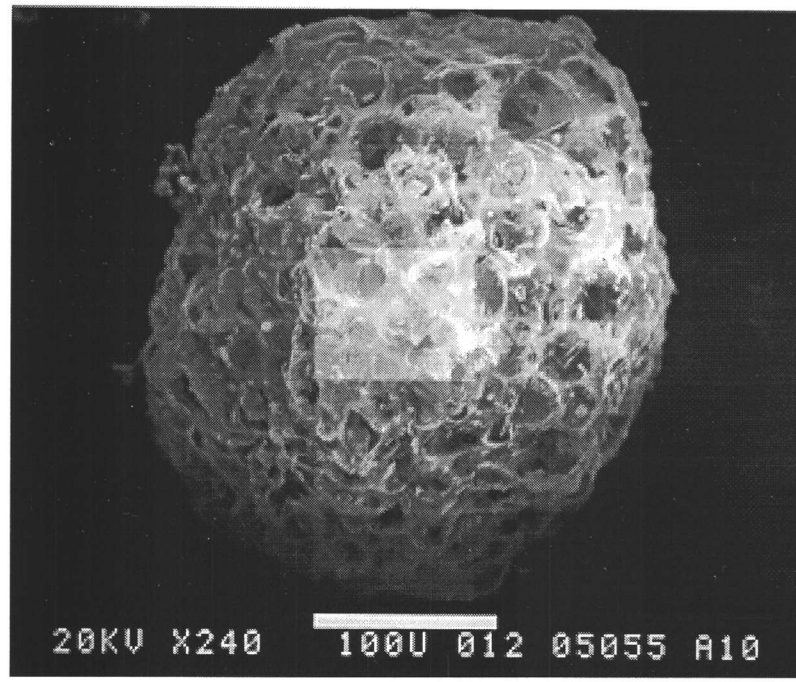

Figure 3.5. The resulting char particle after pyrolysis has swollen and is therefore porous. Magnification: 240×, Scale: 100 μm.

Figure 3.5 shows that a fairly spherical popcorn like particle that resembles a beehive is obtained during pyrolysis. By studying different chars with higher magnification, one can observe that the resulting char from the LEFR is different depending on the residence time and temperature. This is shown in Appendix 3.1.

Comparison with previous results

The work of Li et al. (5) concluded from their work with energy dispersive spectroscopy (EDS) that sodium is uniformly dispersed within black liquor char causing very high reactivity. They studied BLC and impregnated activated carbon (IAC) by SEM-EDS using a JSM-T300 from JEOL. However, they obtained the char by pyrolysing in a tube reactor for 20 min under nitrogen with 10% CO at 580°C. The char used in the

current study was produced using a LEFR that more closely resembles the devolatilization process in a real recovery boiler. What exactly is ment with an "extrimely fine catalyst dispersion" is not clearly defined from a molecular viewpoint. Their conclusion is mainly based on Figure A.3.1.1 in Appendix 3.1 without taking into account that most of the spots may be caused by an uneven surface of the char. Superior equipment used in this study will show no "extrimely fine catalyst dispersion" causing a high reactivty.

CHARACTERIZATION STRATEGY

The characterization strategy followed is based on the steps shown in Figure 3.1.

Bulk composition

The water soluble fraction of the char sample was extracted with deionized water. Capillary electrophoresis was used to quantify the concentrations of sodium, potassium, chloride ions, and sulfur containing ions such as sulfate. Carbon analysis was performed using a Carlo Erba elemental analyzer at a commercial laboratory (6). The oxygen content was obtained by difference. The elemental composition of the studied char #77 (see Table A.4.6.1 in Chapter 4) is given in Table 3.2.

Table 3.2. The elemental composition of char studied. The units are in weight-%.

C (%)	Na (%)	K (%)	S (%)	Cl (%)	O (%) *
31.7	18.8	0.1	0.72	0.7	47.98

* by difference

Nature of phases

Energy dispersive X-ray microanalysis (EDAX) was used to identify any crystalline and amorphous phases.

Size and Shape

SEM was used in this study to determine the particle size and shape. For sufficiently large scale features (>100 nm), SEM is more usable than TEM, as it does not require the preparation of electron transparent specimens. Analytical electron microscopy would allow the study of the size and shape of particles down to about 0.5 nm. Black liquor char was not suitable for particle size analyzers available. It is too soluble and light to be suspended in water or other solvents, as is necessary to obtain a satisfactory dispersion in a liquid during size measurement.

Repartition

There are two scales at which the repartition of a phase must be studied: macroscopic and microscopic. The distribution of composition across a catalyst pellet is a typical large-scale characteristic. A few microanalytical techniques are available for measuring this distribution that provide a resolution of 1 μm. Elemental line scanning was employed due to the fact that this method allows the best quantitative precision. This method is a variation of electron microprobe analysis (EMPA). It was used to address the issue of to what extent the catalyst was dispersed in BL char.

Coordination, valency, and electron-energy levels

There exists no universal method allowing the characterization of the structure of the outer electronic shells and of the immediate environment of the atoms of all elements. Therefore, one has to resort to a variety of techniques, each of which are adapted to a particular case or gives only partial insight.

NMR is a highly sensitive technique for studying the arrangement of specific individual atoms. NMR is suitable for atoms having a nuclear magnetic moment. Black liquor char has recently been studied with this method. However, these results are still unpublished (7).

Surface composition

Electron microprobe analysis (EMPA) was used to characterize the surface composition. This issue is discussed later in this chapter.

Dispersion

Dispersion may be defined as the fraction of potentially active atoms which are effectively on the surface of the solid, i.e. exposed to the gas. Therefore, it is clearly the most important property of a catalyst. Its characterization is essential for researchers involved in the study of reaction kinetics. It is well known that using largely empirical experimental recipes, the dispersion of some metals can be measured by chemisorption methods. This is discussed in chapter 4.

Surface structure

An interpretation of the SEM pictures was made to assess the morphology of the char surface. No method is presently available for determining the long-range two-dimensional arrangement of the atoms, i.e. the crystal structure.

Coordination and chemical state at the surface

X-ray photoelectron spectroscopy is the only technique allowing a selective study of the valency of near surface atoms. This was not stated as a research objective in this study.

Surface reactivity

The study of the reactivity of the solid was investigated using thermogravimetry and differential scanning calorimetry (chapter 6). Temperature programmed desorption (TPD) is a convenient tool which can reveal the presence of different surface phases. Temperature-programmed reduction (TPR) exhibits a good sensitivity for the detection of small transformations of the solid. TPD and TPR were not employed in this study.

Surface area

Surface areas were determined by the measurement of the amount of N_2 adsorbed. Other probe gases such as CO_2 and O_2 were used in this work as well. Adsorption of N_2 is physical in nature, but CO_2 and O_2 are chemical.

Porosity

The porosity or void fraction can be obtained when the total pore volume per unit mass is known. The average pore radius is obtained from the pore size distribution. This information was deduced from the surface area data. This is covered in chapter 4.

Acidity

The acid strength of a solid may be determined by its ability to change the adsorbed neutral organic base into its conjugate acid form. The acid strength is expressed by the Hammett acidity function, H_0, which typically can be measured over the range of +4 (weak) to about -8 (strong). H_0 values can be thought of as relative quantities used to provide an acidity scale. The acid strength decreases with decreasing catalytic activity.

The pH of aqeous extracts of black liquor char samples was measured to be around 9 and 10 indicating that the sites in BL char are basic. The amount of basic sites on the surface of a catalyst can be measured by titration with benzoic acid using color indicators in a manner analogous to that used with an amine for acid catalysts. A titration method has been developed to characterize the acid-base strength distribution of a water-insoluble solid using a common H_0 scale. Previous research shows that the specific activity of basic sites increases in the order Li < Na < K < Rb < Cs (1). No attempt was made to measure the amount of basic sites, because the sample would fully disintegrate when exposed to water.

EXPERIMENTAL RESULTS

SEM and EDAX results

SEM pictures show that black liquor char has two phases: a carbonaceous phase and a phase of whiskers that are connected to each other. The whiskers are the most abundant in the original black liquor solids. The amount of dendritic clusters decreased after pyrolysis as shown in Appendix 3.1. The shape of the whiskers appears as acicular needles and tapered columns. The variation in whisker shape with increasing pyrolysis temperature and pyrolysis time was scattered. However, it can be concluded with certainty that the whiskers were transformed to micron size aerosol particles at a pyrolysis temperature of 1100°C and a long pyrolysis time. EDAX spectra showed that the whiskers contained mainly sodium, oxygen, and carbon. However, some of the carbon in the spectrum may be from the support film on which the whiskers were mounted. Minor quantities of aluminum, silicon, sulfur, chlorine, and potassium were detected. Table 3.3 shows the results in weight-% from three EDAX spectra, two whiskers and for the bulk structure. Appendix 3.2 gives the analysis reports for Table 3.3.

Table 3.3. The composition of whiskers using energy-dispersive X-ray microanalysis.

	C (%)	O (%)	Na (%)	K (%)	S (%)	Cl (%)	Al (%)	Si (%)
whisker #1	4.05	5.31	89.58	0.16	0.22	0.40	0.05	0.22
whisker #2	2.06	2.37	78.22	3.50	6.69	1.23	5.94	-
bulk structure	10.3	5.8	77.8	1.16	0.81	0.65	3.46	-

Table 3.3 shows that the whiskers contain mainly sodium, oxygen, sulfur, and carbon. This is an indication that sodium carbonate, sulfate, and sulfide may be localized within the whiskers. The apparent high sodium content in the bulk structure could be due

to an inorganic coating on the char surface as appears in Figure 3.6 and Figures A.3.1.2 and A.3.1.3 in Appendix 3.1. This coating could originate from the whiskers during pyrolysis as the temperature rises above the melting point of the inorganics. Therefore, the inorganic coating may have essentially the same composition as the whiskers.

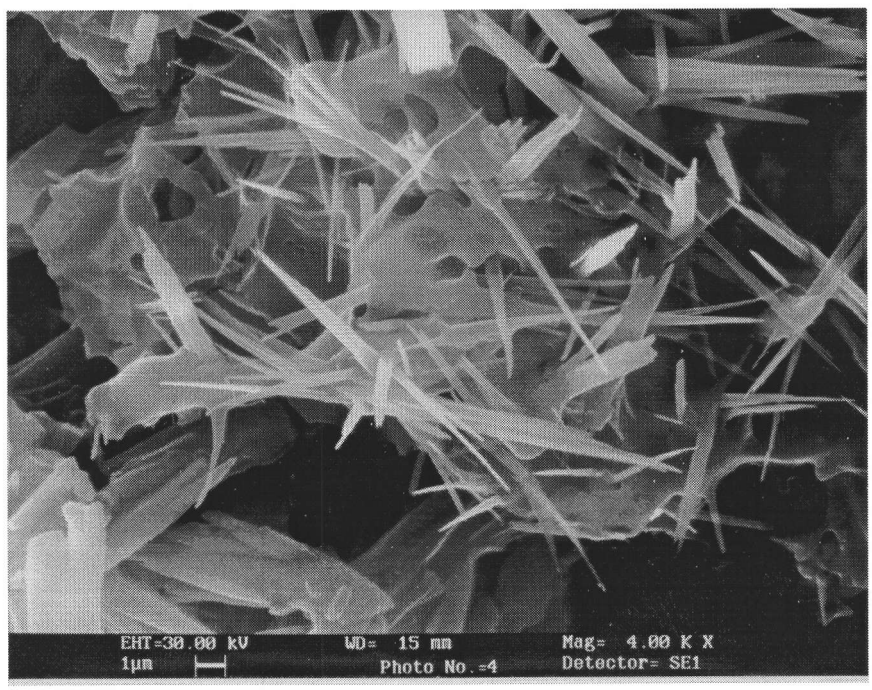

Figure 3.6. Black liquor char consists of an amorphous carbon structure with embedded crystalline whiskers. A typical structure of BL char shown at 900°C and an LEFR pyrolysis time of 0.67 s.

Figure 3.6 shows the presence of whiskers embedded in a porous bulk structure. The whiskers were determined to be crystalline as shown in Figure A.3.1.4 in Appendix 3.1. Because of the small size of the whiskers and their tendency to volatilize rapidly under the electron beam, it was not possible to identify them as sodium carbonate, sulfate, or sulfide. Work beyond the scope of the objectives may have provided a verification to this. However, it is known from the literature that sodium carbonate, sulfide, and sulfate form no ternary compound (8). Thus, if the whiskers and the coating are the same

material, then they can be described by any of the following three phases (8): (a) a solid mixture containing Na_2CO_3 and Na_2SO_4, (b) a hot liquid consisting of Na_2CO_3, Na_2S, and Na_2SO_4 and (c) the pure solid Na_2S. Phases (a) and (b) are the most likely ones. The bulk structure was confirmed to be amorphous carbon by the absence of the spots in the diffraction pattern. This is evidence of the presence of two phases: amorphous and crystalline. At higher temperatures the whiskers are transformed into micron shize sphere like particles as shown in Figure 3.7.

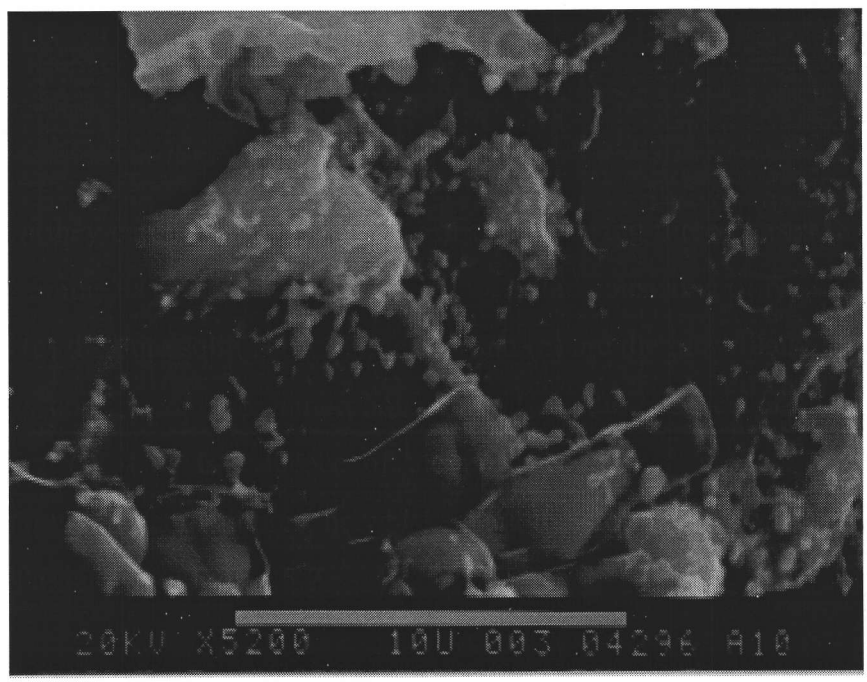

Figure 3.7. At extreme conditions the whiskers have formed into micron size particles that look like small spheres. Sample #: 81, LEFR res. time = 1.32 s, T = 1100°C, Magnif.: 5200×, Scale: 10μm.

Electron microprobe results

A special sample preparation procedure had to be conducted prior to the analysis using the electron microprobe analyzer. Black liquor char was immersed in 5 parts of

resin with 1 part hardener and placed in a vacuum chamber for 20 minutes. The resin contains 4,4' isopropylidenediphenol epichlorohydrin, alkyl clycidyl ether, and poly-acrylate ether. The hardener contains diethylenetriamine. The sample and epoxy were poured into a mold, and allowed to harden over night. The next day, a hole was drilled into the hardened plug. A mixture of epoxy and char grains was poured into this hole. This was done to ensure that the char particles were adequately coated with epoxy and would not pluck out during polishing. When everything was sufficiently hardened, the plug was ground on a wheel in order to expose interior portions of the char grains. The plug was then polished to 0.05 μm. The polished plug was placed in the vacuum chamber of the EMPA, and scanned from left to right, across the cross section of the 30 μm particle shown in Figure 3.8.

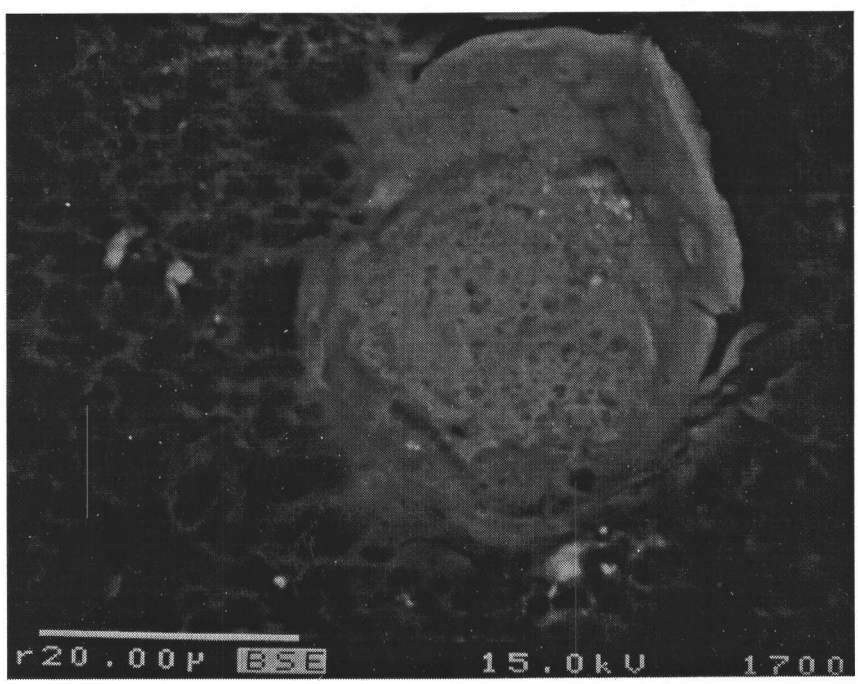

Figure 3.8. The cross section of a black liquor char grain. No whiskers can be observed inside the char particle.

The cross section in Figure 3.8 shows that BL char is porous and that there is no clear whisker population inside the char particle. The results of the EMPA scans are given in Figures 3.9 and 3.10. The beam width was 2 μm and depth 5 μm.

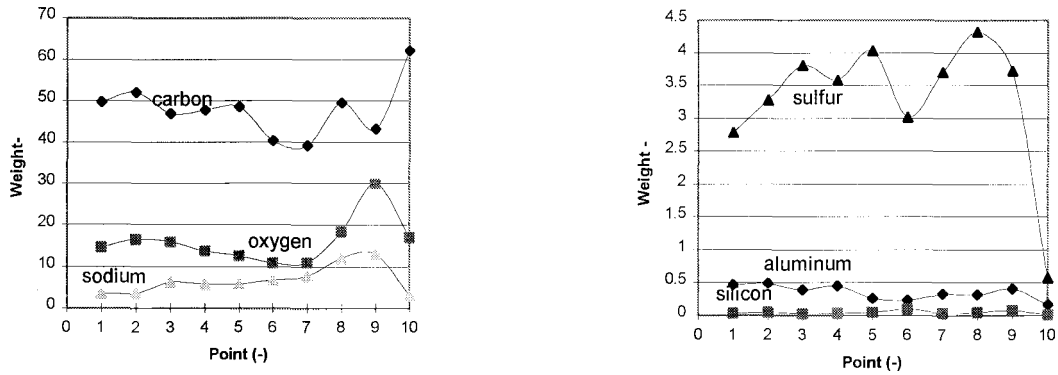

(a) (b)

Figure 3.9. The elemental distribution of (a) carbon, sodium, oxygen; (b) sulfur, aluminum, and silicon across a cross-section of a black liquor char grain.

Figure 3.9 shows that the carbon concentration is fairly constant at 50 weight-% on the left half of the particle but varies from less than 40% to more than 60% on the right half of the particle. Comparing this to the overall carbon content of ~32% raises immediately the question why there is such a big difference. One explanation could be that the sodium present is not dispersed to that extent as has been asserted in the literature (8). Another question is why the carbon content is so high compared to the EDAX results where the carbon content was 10.3%. The most probable explanation is the way the sample has been prepared. The cross section of the EMPA sample does not contain whiskers and no inorganic coating is visible even though possible. The high oxygen content confirms the high population of basic sites. The content of oxygen, sodium, and sulfur appear to go through a maximum near the right edge of the particle. This is likely

due to the whiskers near the particle surface. The mass balance closure for Figure 3.8 is given in Table 3.4.

Table 3.4. The sum of the elements measured was between 61 and 91%.

	1	2	3	4	5	6	7	8	9	10
Sum (w-%)	71.2	75.9	73.5	71.5	71.3	61.4	62.1	84.7	90.6	83.1

To improve the mass balance closure, the electron beam width was increased from 2 to 10 μm to decrease the local sodium vaporization. After the beam width increase, the mass balance closure increased to the 71-98% range (Table 3.5). The variation of the composition for different particles and locations within the same particle is given in Figures 3.9-11.

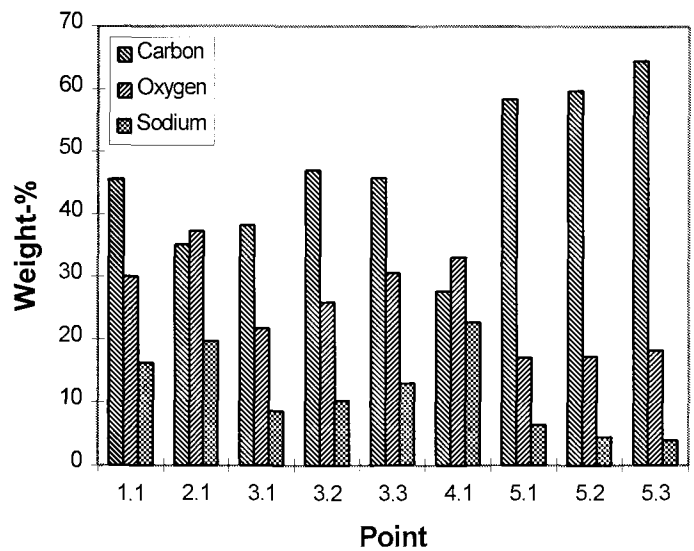

Figure 3.10. The variation in the elemental composition can be observed for different particles and locations within the same particle. The first digit signifies a discrete particle, and the second digit signifies a different location within that particle.

Figure 3.10 infers that the surface composition is very non-uniform. The carbon concentration can vary from below 30% to above 60% for different particles of the same char. Within the same particle, the difference in carbon concentration was 10% or less at different locations. Sodium varied from 5 to 25%. Oxygen was between 18 and 38%. Sulfur varied between 0.5 and 5.5%. Aluminum and silicon were present only in trace amounts and could originate from sample preparation. Figure 3.11 shows the variation of sulfur, silicon, and aluminum.

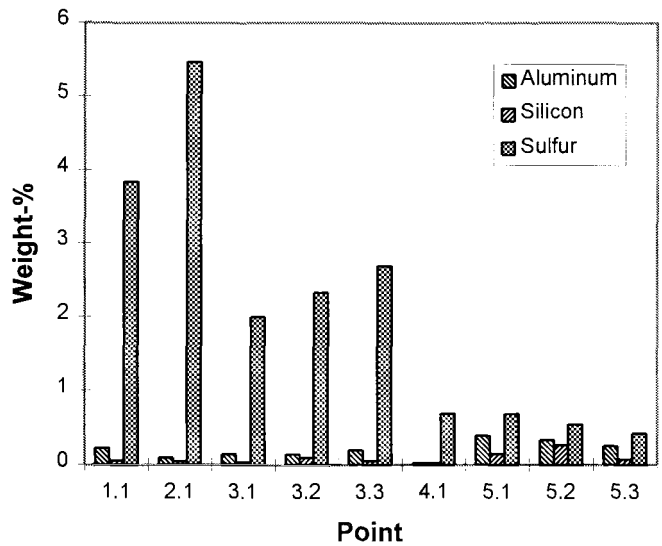

Figure 3.11. The variation in the elemental composition can be observed for different particles and locations within the same particle. The first digit signifies a discrete particle, and the second digit signifies a different location within that particle.

The mass balance closure for Figures 3.10 and 3.11 is shown in Table 3.5.

Table 3.5. The sum of measured elements was between 71 and 98% for Figures 3.10-11.

Sample	1.1	2.1	3.1	3.2	3.3	4.1	5.1	5.2	5.3
Sum (w-%)	96.0	97.9	70.7	85.9	92.3	84.4	83.3	82.6	87.4

After increasing the electron beam width, the mass balance closure for the EMPA improved the closure of the sum of elements. The raw data from the EMPA and the standards used during quantification are given in Appendix 3.3.

Elemental Mapping

Microprobe scans were made to obtain maps showing the distribution of C, Na, S. The resolution is 1 to 2 μm. These scans are for the same particle as in Figure 3.8. The green ridge in the upper right hand corner corresponds to the slightly vertical ridge in Figure 3.8. Figure 3.12 shows the concentration of carbon in dark blue color.

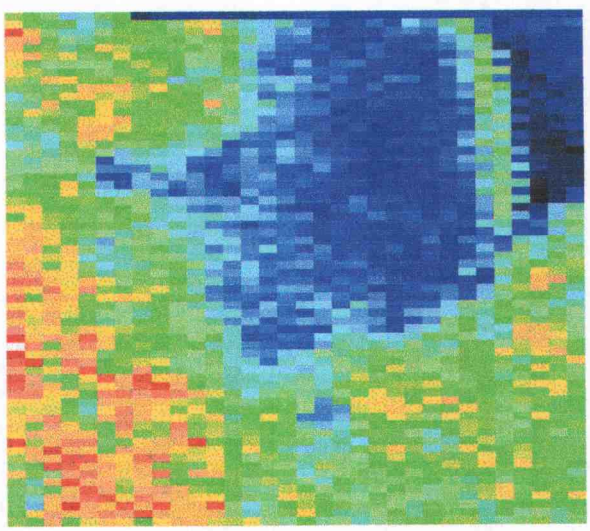

Figure 3.12. Carbon is the blue and dark area. The other areas are from carbon in the resin.

Figure 3.12 indicates that the amorphous carbon may be separate from the inorganic phase which is in line with the electron diffraction patterns. Figure 3.12 confirms that sodium is localized to clusters. This sodium is different from the whiskers embedded on the char surface, and it is probably molten whiskers that have resolidified. It is not known why some inorganic matter would resolidify as whiskers but some would remain as a coating on the pore surface. Figure 3.13 shows that the sulfur is concentrated adjacent to the sodium clusters. This is in harmony with the known fact that the inorganic matter consists mostly of Na_2S and Na_2SO_4.

Red: ~ 10%
Yellow: ~ 7%
Green: ~ 5%
Blue: ~ 1-2%

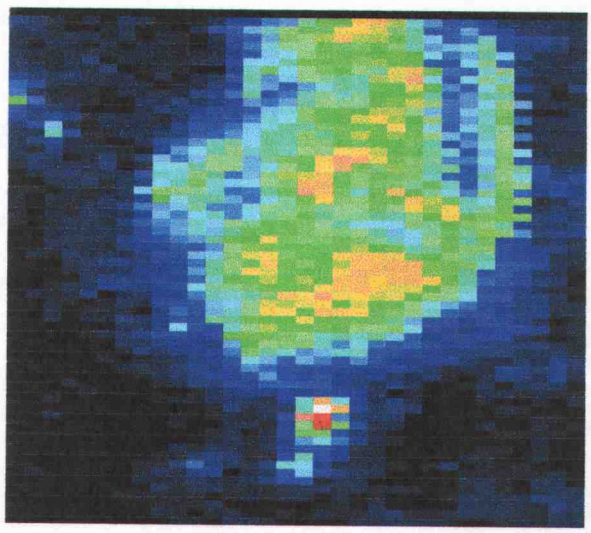

Figure 3.13. Sodium is concentrated in the yellow and brown areas. The red dot in the bottom has the highest sodium content.

Red: ~ 10%
Yellow: ~ 7%
Green: ~ 5%
Blue: ~ 1-2%

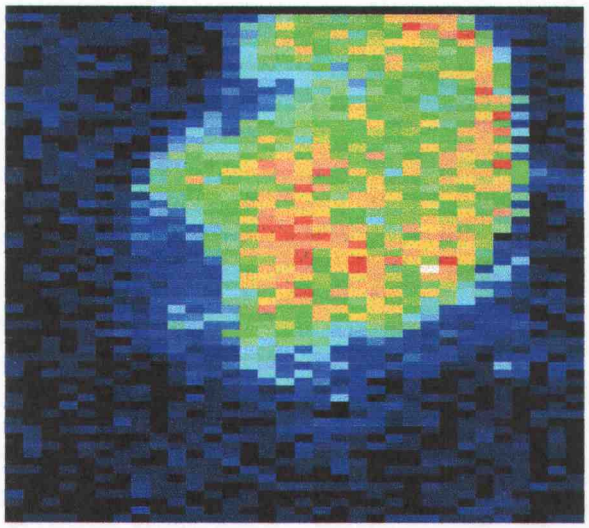

Figure 3.14. Sulfur is concentrated in the red, brown and yellow areas.

Summary of EMPA Results

EMPA shows that the elemental composition of BL char is heterogeneous with large variations within the same particle and between particles of the same char. Elemental mapping indicates that there are distinct areas where carbon, sodium, and sulfur are located. This would confirm the indication of the SEM pictures and the EDAX spectra that the whiskers including the inorganic coating on the char surface should be considered as a separate phase. However, this alone is not sufficient to fully address the question to what extent there is sodium dispersed in the amorphous carbon. NMR is more suitable to address this question.

TEM results

TEM was used to study the porous structure of black liquor char. Figures 3.15-17 show results from this analysis method. Figure 3.15 shows the general morphology of black liquor char.

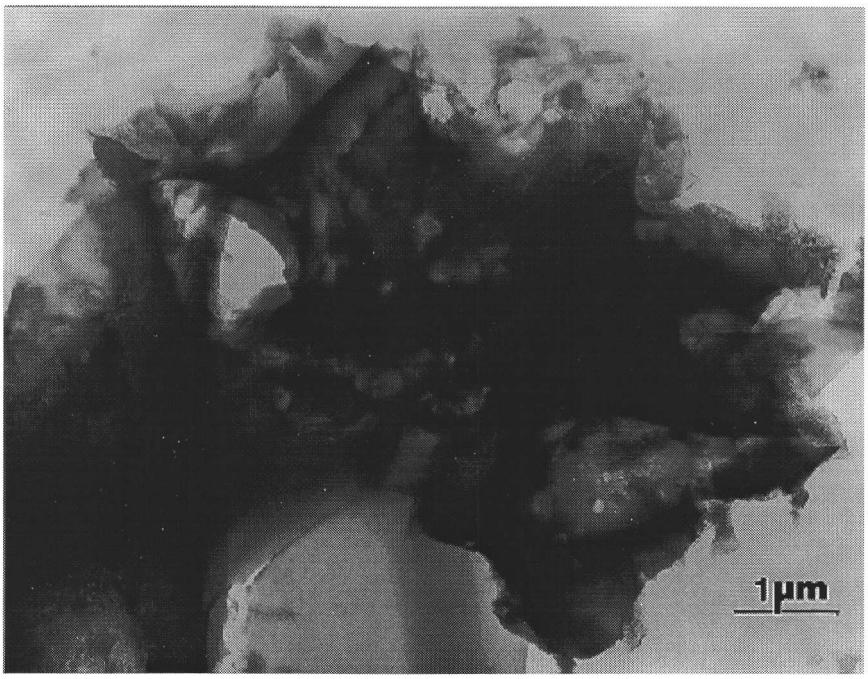

Figure 3.15. The general morphology of BL char appears different using TEM compared to SEM.

Figure 3.16 shows the presence of whiskers and macro pores within a graphite like structure. The dark area what appears to be a three edged star is a fragment of a whisker.

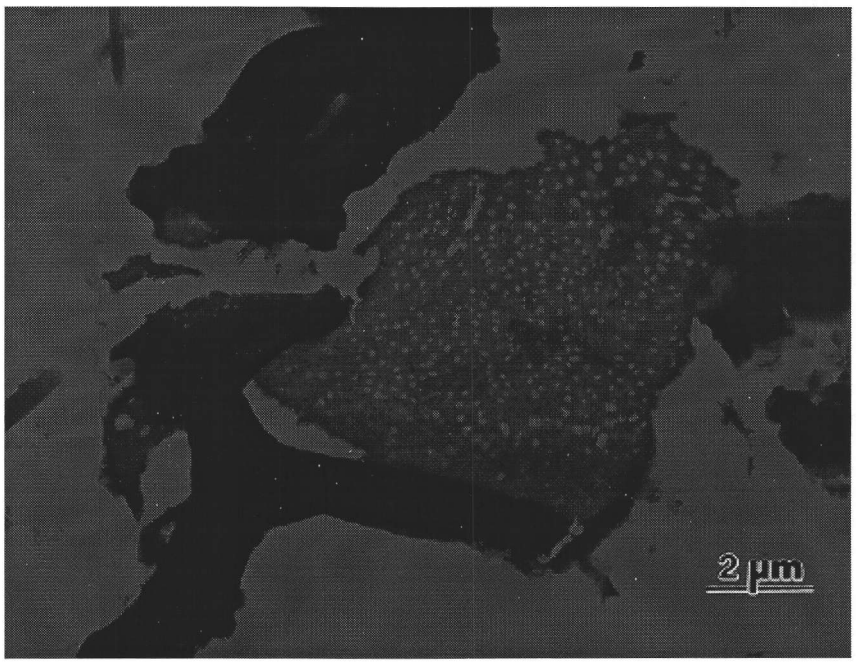

Figure 3.16. BL char contains inorganic whiskers and a porous organic phase.

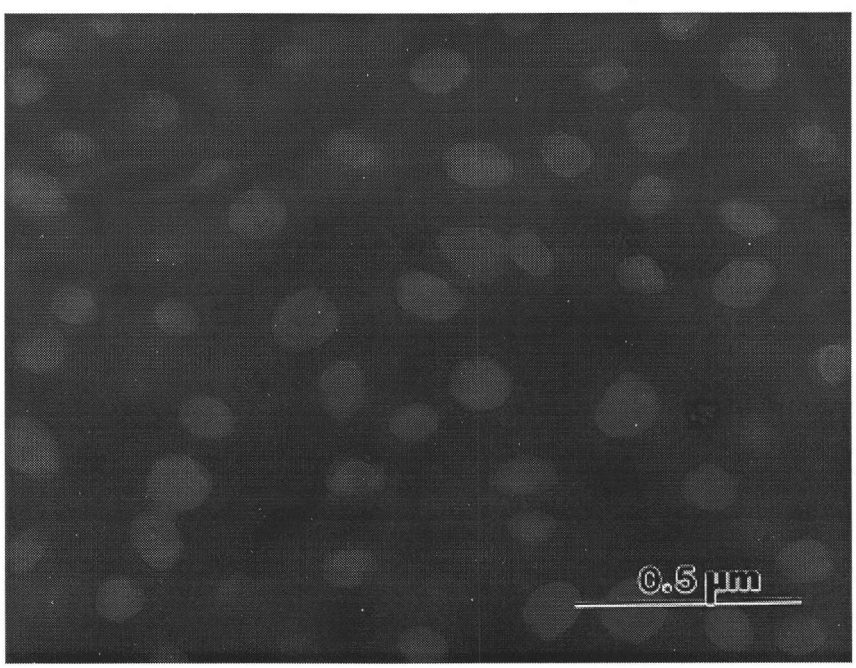

Figure 3.17. The macropores are about 140-240 nm in diameter.

An assessment of Figure 3.17 shows that the average diameter of the macropores is approximately 140-240 nm. These macropores are actually openings to the inner parts of the char. The data in chapter 4 shows that the majority of pores are mesopores, and that the average pore-size is much less than 200 nm. In fact, it is between one tenth or even one hundredth of the size of the visible macro pores. The reason why the macro pores are nearly uniform in diameter is a subject of further study. A discussion of the possible atomic arrangements surrounding the pores is given in Chapter 4.

CONCLUSIONS AND RECOMMENDATIONS

SEM, TEM, EDAX, EMPA and X-ray diffraction techniques were used to characterize the morphology of black liquor char. The results show that:

1. The active sites in black liquor char are basic.
2. Black liquor char is comprised of two phases: amorphous and crystalline. The former is dominating and the latter is the minor one. The amorphous phase is a porous graphite like carbon structure with some sodium present on the pore surfaces. The crystalline phase is composed of whiskers and an inorganic coating on the surface of the amorphous carbon structure. The inorganic phase was high in sodium, carbon, oxygen, and sulfur. These elements are in the form of sodium carbonate and sulfate.
3. The number of whiskers decreases with increasing pyrolysis temperature. At a high pyrolysis temperature and pyrolysis time, the whiskers appeared as micron size spheres. This may be due to increased fume formation at higher temperatures.
4. The data presented here indicate that the inorganic matter is not dispersed homogeneously. In fact, the data show that BL char is heterogeneous in composition. However, more data are needed to fully address the question to what extent sodium is dispersed in the amorphous phase.

It is recommended that other techniques be used such as Scanning tunneling microscopy and Auger spectroscopy to better understand why the macropores are uniform in diameter. It would be useful to characterize BL char samples obtained at other conditions more typical in recovery boilers, i.e. mixtures of water vapor, CO_2 and oxygen. Complete NMR results would have significantly increased the contribution to knowledge in this chapter.

ACKNOWLEDGMENT

Dr. Cindy Dogan with the U.S. Bureau of Mines (Albany, OR) is acknowledged for providing the SEM, TEM, X-ray diffraction and EDAX results. Dr.Roger Nielsen at the Oceanography department is acknowledged for the microprobe analysis results. Mr. Al Soeldner is acknowledged for part of the SEM work. Dr. Larry Baxter approved a set of complementing SEM experiments to be done at Sandia National Laboratories.

REFERENCES

1. Delannay, F., Characterization of Heterogeneous Catalysts, Chemical Industries, Vol.15, Marcel Dekker, Inc., New York, NY, 1984

2. Marsh, H., Introduction to Carbon Science, Butterworths & Co., 1989

3. Reed, S.J.B., Electron Microprobe Analysis, 2nd ed., Cambridge U. Press, 1993

4. Energy-Dispersive X-ray Microanalysis, An Introduction, Kevex Corporation, Foster City, CA, handout from Dr. Cindy Dogan, U.S. Bureau of Mines, Albany, OR, 1996

5. Li, J., van Heiningen, A.R.P., Kinetics of CO_2 Gasification of Fast Pyrolysis Black Liquor Char , Ind.Eng.Chem.Res., Vol. 29, No. 9, p.1776-1785, 1990

6. Weyerheuser Analytical & Testing Services, Federal Way, WA, September 20, 1994

7. Davis, M., Wåg, K., unpublished results, National Renewable Energy Laboratory, Golden, CO, April, 1996

8. Backman, R., Sodium and Sulfur Chemistry in Combustion Gases, Academic Dissertation, Åbo Akademi U., paper VI, p.8, May 12, 1989

9. Dogan, C., U.S. Bureau of Mines, Albany, OR, personal correspondence, April 30, 1996

APPENDICES

APPENDIX 3.1

EDS, SEM and Electron Diffraction Data

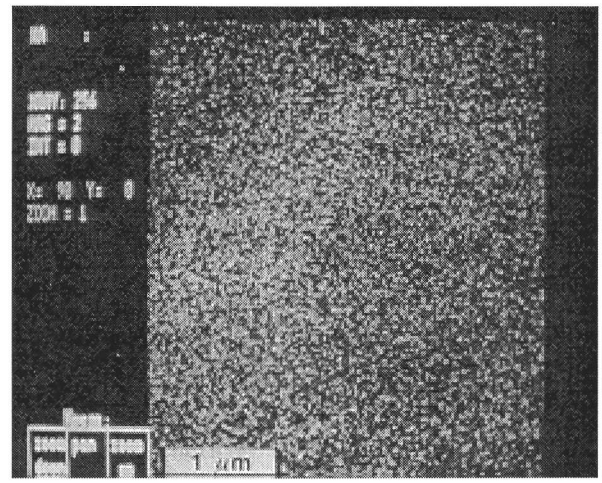

Figure A.3.1.1. EDS indicates the catalyst being finely distributed according to Li et al. (5). However, this could be caused by the roughness of the BLC surface.

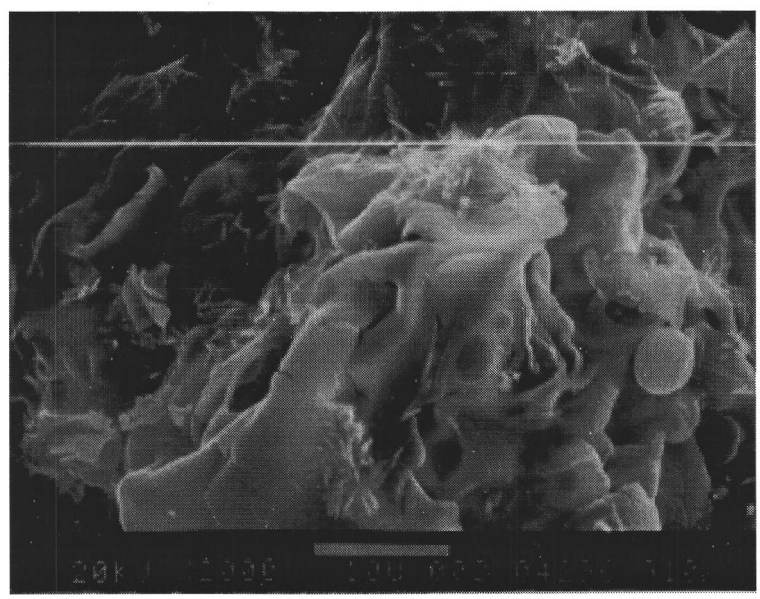

Figure A.3.1.2. There is plenty of whiskers left after pyrolysis at 700°C in LEFR. Sample #: 62, LEFR Res. time = 1.49s, T = 700°C, Magnif.: 2000×, Scale: 10µm.

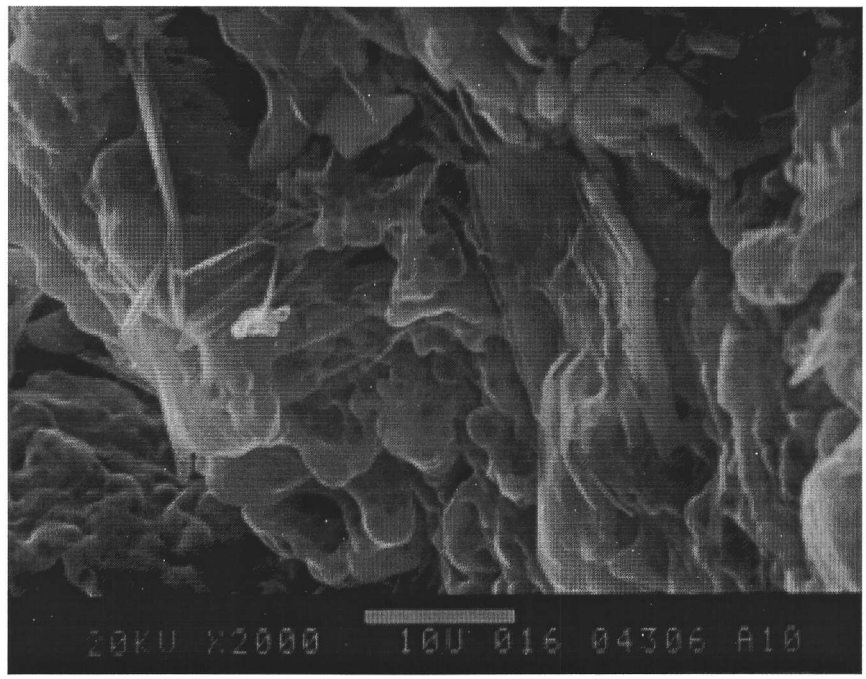

Figure A.3.1.3. The whiskers have partially molten to form a coating on the bulk structure at 1100°C in the LEFR. Sample #: 91, LEFR Res. time = 0.31s, T = 1100°C, Magnif.: 2000×, Scale: 10μm.

Figure A.3.1.4. The whiskers are crystalline which is shown by the spot pattern from electron diffraction. No spot pattern was observed for the bulk structure.

APPENDIX 3.2

Raw Data For EDAX Results

The EDAX analysis was a semiquantitative, standardless analysis, where the true composition depends on the elements that are present. For heavier elements with $Z > 14$, e.g. sodium, the error is probably not more than 5%. For lighter elements, such as carbon, the error could be as much as 25%. The reasons are as follows (9). First, light elements have a low X-ray excitation efficiency and rather give off an Auger electron. Second, low energy X-rays are easily absorbed by heavier elements. Third, the X-ray detector is not efficient in detecting low energy X-rays. Compounding the problem is the volatility of the sodium in the char sample. The sodium content was decreasing with exposure time in the microscope.

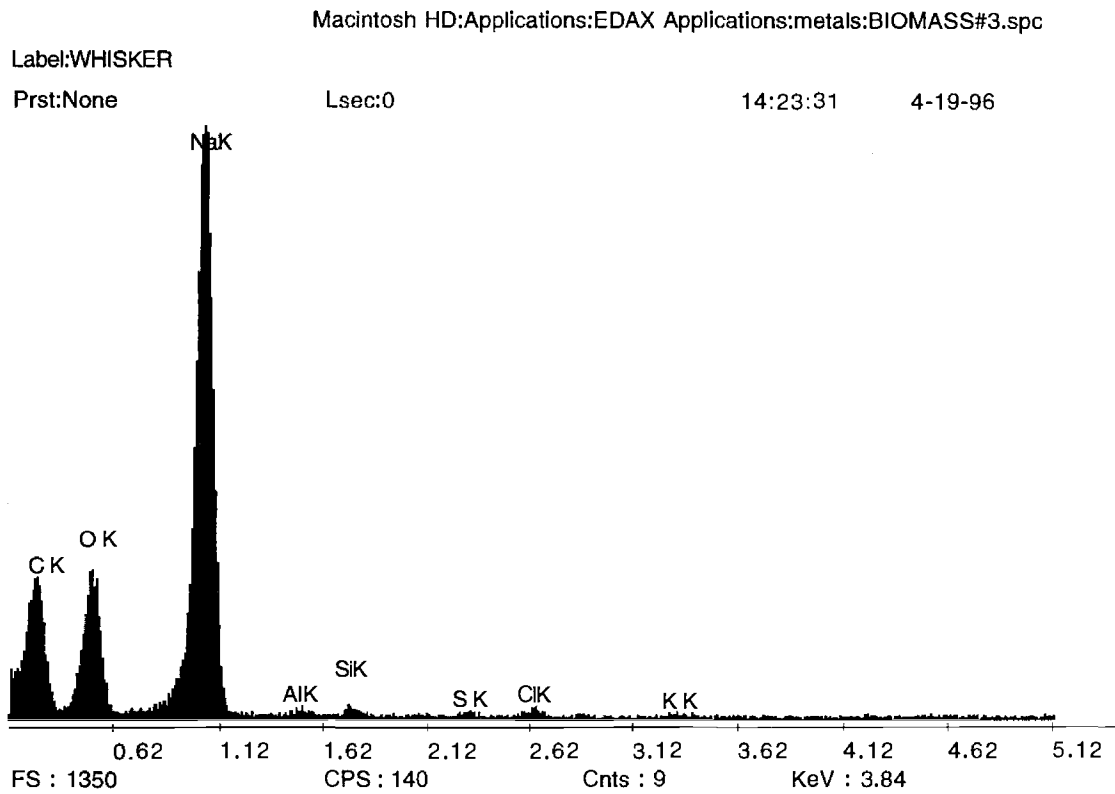

Macintosh HD:Applications:EDAX Applications:metals:BIOMASS#3.spc

Label : WHISKER
Time : 14:23:00 Date : 4-19-96

Thin Apx
User KAB Table, Elements

Element	Weight %	Atomic %
C K	4.051	7.336
O K	5.313	7.222
NaK	89.584	84.746
AlK	0.046	0.037
SiK	0.223	0.173
S K	0.224	0.152
ClK	0.401	0.246
K K	0.157	0.088
Total	100.000	100.000

Figure A.3.2.1. Whiskers contain mainly sodium according to EDAX.

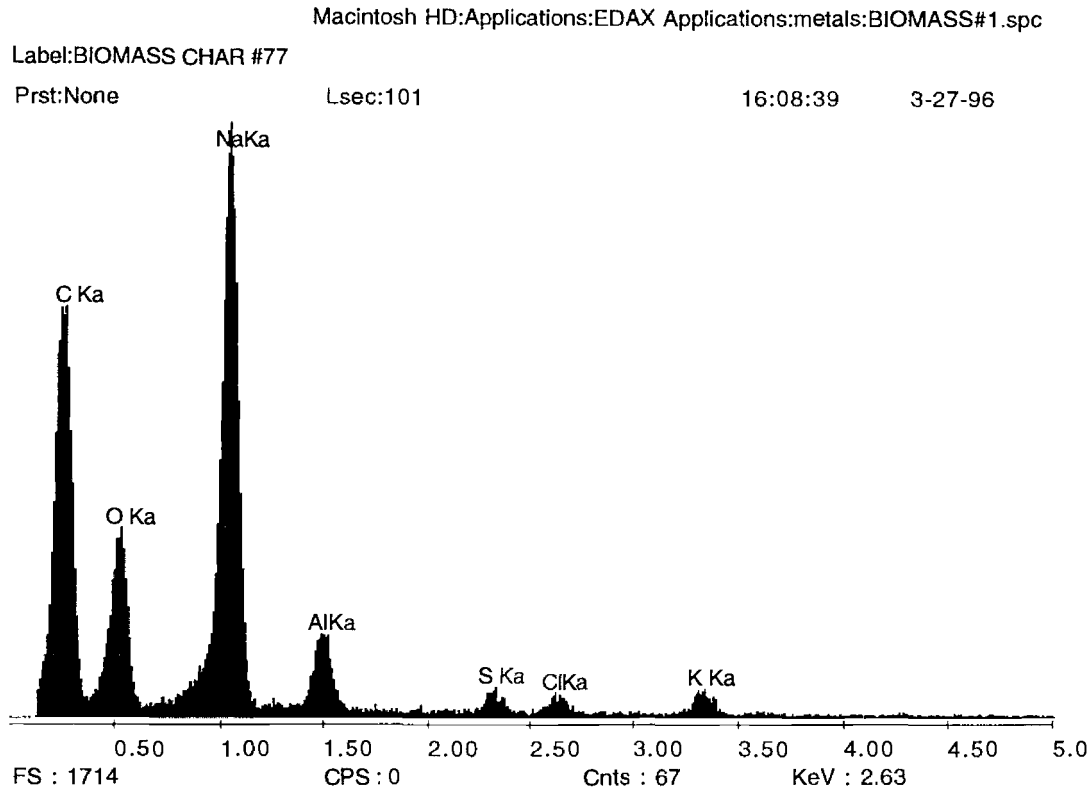

Macintosh HD:Applications:EDAX Applications:metals:BIOMASS#1.spc

Label : BIOMASS CHAR #77
Time : 16:08:00 Date : 3-27-96

Thin Apx
User KAB Table, Elements

Element	Weight %	Atomic %
C K	10.336	17.902
O K	5.758	7.487
NaK	77.816	70.412
AlK	3.464	2.671
S K	0.813	0.527
ClK	0.654	0.384
K K	1.159	0.617
Total	100.000	100.000

Figure A.3.2.2. The bulk structure contains much more carbon than the whiskers.

APPENDIX 3.3

EMPA Standards and Data Tables

Standards used in EMPA:
Carbon: graphite with PCI crystal
Oxygen: quartz
Sodium: sodium aluminum silicate
Sulfur: $FeCuS_2$ (chalcopyrite)
Aluminum: corundum
Silicon: quartz

The data file from 16/04/96 was obtained with an electron beam width of 2 μm.
The data file from 17/04/96 was obtained with an electron beam width of 10 μm.
Data points with a mass balance closure less than 60% were considered erroneous.
Label signifies a different location, No is the experiment number, X and Y the coordinates under the EMPA analyzer sample holder, and W the weight-% of respective species.

Table A.3.3.1. EMPA data for a beam width of 2 μm.

User Name :	Roger Nielsen	Company :	Oregon State
File :	NAC.ANA		
Last Saved :	16/04/96 11:04		
Beam Current :	50		
Acc. Voltage :	15.1		
Take Off Angle :	40		
Tilt Angle :	0		
Azimut Angle :	0		

Label	No	X	Y	W% (C)	W% (O)	W% (Na)	W% (Al)	W% (Si)	W% (S)
A.pn 1.1_1	1	-19691	2604	49.58	14.78	3.53	0.465	0.028	2.79
A.pn 1.1_2	2	-19688	2603	51.93	16.63	3.53	0.489	0.043	3.28
A.pn 1.1_3	3	-19684	2603	46.88	16.00	6.34	0.392	0.024	3.82
A.pn 1.1_4	4	-19681	2602	47.69	13.83	5.87	0.449	0.032	3.59
A.pn 1.1_5	5	-19678	2601	48.47	12.66	5.85	0.262	0.044	4.03
A.pn 1.1_6	6	-19674	2601	40.34	10.94	6.76	0.226	0.097	3.02
A.pn 1.1_7	7	-19671	2600	39.20	11.11	7.74	0.325	0.032	3.71
A.pn 1.1_8	8	-19668	2599	49.47	18.44	12.07	0.309	0.042	4.33
A.pn 1.1_9	9	-19664	2599	43.19	30.03	13.18	0.408	0.075	3.73
A.pn 1.1_10	10	-19661	2598	62.22	17.08	3.06	0.165	0.009	0.58
A.ph 2.1_1	11	-20458	2836	48.96	15.24	9.61	0.110	0.056	6.91
A.ph 2.1_2	12	-20456	2840	45.96	13.12	6.69	0.113	0.036	8.00
A.ph 2.1_4	14	-20453	2847	35.50	16.28	8.28	0.111	0.054	6.29
A.ph 2.1_5	15	-20452	2851	35.60	19.71	8.32	0.139	0.030	5.67
A.ph 2.1_6	16	-20450	2855	47.95	20.63	3.82	0.103	0.037	3.30
A.ph 2.1_7	17	-20449	2859	49.73	19.93	3.95	0.107	0.042	4.86
A.ph 2.1_8	18	-20447	2862	48.54	25.15	5.34	0.095	0.061	5.08
A.ph 2.1_9	19	-20446	2866	32.62	23.33	10.98	0.079	0.029	4.22
A.ph 2.1_10	20	-20444	2870	20.62	10.02	1.04	0.145	0.002	0.35
A.ph 2.1_11	21	-20443	2874	56.48	15.95	2.36	0.418	0.085	4.34
A.ph 2.1_12	22	-20441	2877	47.40	13.82	2.74	0.549	0.077	5.25
A.ph 2.1_13	23	-20440	2881	34.76	22.69	7.46	0.483	0.071	5.30
A.ph 2.1_14	24	-20438	2885	42.22	17.65	5.69	0.344	0.124	6.77
C.ph1.1_3	27	-13529	-7569	31.16	14.77	10.12	0.168	0.085	2.59
C.ph1.1_4	28	-13533	-7567	22.36	18.14	7.66	0.105	0.049	2.02
C.ph1.1_5	29	-13538	-7566	40.72	22.30	9.71	0.123	0.061	2.41
C.ph1.1_6	30	-13542	-7564	69.24	25.23	7.78	0.149	0.048	2.23
C.ph1.1_7	31	-13546	-7563	78.24	21.08	0.26	0.040	0.008	0.14
C.ph1.1_8	32	-13550	-7561	80.68	25.08	0.08	0.016	0.003	0.12
C.ph1.2_1	33	-13614	-7650	50.86	30.51	0.65	0.212	0.898	0.95
C.ph1.2_2	34	-13611	-7652	60.56	24.11	7.62	0.211	0.820	5.86
C.ph1.2_3	35	-13607	-7655	49.88	23.21	1.04	1.640	2.196	0.11
C.ph1.2_4	36	-13604	-7657	45.13	30.02	0.29	0.162	0.539	0.06
C.ph1.2_5	37	-13601	-7659	39.80	34.13	0.28	0.308	0.654	0.06
C.ph1.2_6	38	-13597	-7662	33.94	12.13	0.25	0.150	0.482	0.06
C.ph1.2_7	39	-13594	-7664	49.07	21.71	0.14	0.197	0.496	0.07
C.ph1.2_8	40	-13590	-7667	51.98	15.01	0.13	0.167	0.514	0.10
C.ph1.2_10	42	-13584	-7671	55.04	24.48	1.18	1.118	0.647	0.68
C.ph1.2_11	43	-13580	-7674	53.16	26.09	1.24	0.370	0.649	0.14
C.ph1.2_12	44	-13577	-7676	49.09	20.05	1.44	0.567	1.145	0.14

Table A.3.3.2. EMPA data for a beam width of 10 μm.

User Name :	Roger Nielsen	Company :	Oregon State
File :	NAC.ANA		
Last Saved :	17/04/96 10:24		
Beam Current :	30.3		
Acc. Voltage :	15.1		
Take Off Angle :	40		
Tilt Angle :	0		
Azimut Angle :	0		

Label	No	X	Y	W% (C)	W% (O)	W% (Na)	W% (Al)	W% (Si)	W% (S)
A.ph 1.1	1	-19822	2374	45.55	30.02	16.32	0.221	0.060	3.840
A.ph 2.1	2	-20605	2590	35.14	37.30	19.84	0.094	0.050	5.465
A.ph 3.1	3	-18670	2442	38.22	21.74	8.54	0.138	0.040	2.004
A.ph 3.2	4	-18809	2331	47.00	26.01	10.27	0.144	0.094	2.331
A.ph 3.3	5	-18815	2333	45.82	30.56	12.97	0.194	0.056	2.691
A.ph 4.1	6	-18399	1440	27.68	33.09	22.82	0.028	0.031	0.689
A.ph 4.2	7	-18389	1440	13.20	4.48	35.87	0.028	0.032	0.668
A.ph 5.1	8	-18061	1797	58.46	17.19	6.43	0.394	0.154	0.689
A.ph 5.2	9	-18080	1737	59.78	17.24	4.48	0.335	0.266	0.547
A.ph 5.3	10	-18110	1736	64.51	18.24	3.94	0.254	0.079	0.423
C.ph 1.1	11	-13165	-7477	35.48	44.84	20.56	0.161	0.100	4.736
C.ph 1.2	12	-13250	-7561	55.27	30.63	1.90	0.198	0.579	0.863
C.ph 1.3	13	-13172	-7432	54.82	8.40	2.67	0.160	0.420	0.580
C.ph 1.4	14	-13107	-7475	39.77	42.53	29.11	0.038	0.071	8.624
C.ph 2.1	15	-11870	-7228	57.63	16.53	6.26	0.286	0.061	2.693
C.ph 2.2	16	-11862	-7221	52.56	24.48	10.29	0.168	0.039	5.234
C.ph 3.1	17	-13832	-6849	49.16	22.87	8.78	0.105	0.062	2.148
C.ph 3.2	18	-13832	-6955	34.51	17.60	4.24	0.165	0.293	1.558
C.ph 4.1	19	-13907	-6295	52.00	32.80	16.01	0.036	0.057	7.045
C.ph 4.2	20	-13917	-6282	38.96	26.63	9.35	0.024	0.028	1.200
C.ph 4.3	21	-13844	-6241	22.59	42.03	0.11	0.164	18.577	0.038

Chapter 4

Porosity and Surface Area of Black Liquor Char

INTRODUCTION

Porous carbons have been used by humans for thousands of years. Their application in water purification can be traced back to 2000 BC when the ancient Egyptians used charcoal to purify water for medical purposes. Advanced research on carbons began during WW1 when granular activated carbon was manufactured for use in gas masks. In the last 50 years the understanding of porosity in synthetic carbons and graphites has advanced substantially. Today, the applications developed are numerous. About 300,000 tons of high porosity (activated) carbon is manufactured annually worldwide for gas- and liquid-phase adsorption processes (1). Low porosity graphite is being manufactured for the nuclear power industry. Massive graphite electrodes are used in the steel industry to carry large electrical currents at high thermal stresses. Carbon electrodes are used in aluminum production in the electrochemical process. High strength carbon fibers are obtained by subjecting carbon to high stress during carbonization. Diamond-like films have been developed to obtain abrasion resistant coatings. The degree and type of porosity can be controlled from virtually zero porosity to any desired characteristic.

Carbons produced from parent materials such as wood and coal are essentially microporous. Microporosity gives the ability to adsorb relatively large quantities of diverse harmful molecules, which makes it useful for purification and separation processes. If the carbonization process is conducted using an oxidizing agent or the carbon structure is influenced by a chemical agent, then the microporous structure is enhanced considerably. Chemical activation is usually limited to cellulosic precursors. This process involves carbonizing the parent material after impregnation with e.g. alkali metal carbonates, chlorides, or sulfides. The common feature of these compounds is their ability to act as dehydrating agents affecting the pyrolytic decomposition and tar

formation. The temperature range for chemical activation is 400-800°C. Physical activation is the development of porosity by gasification with an oxidizing gas at 700-1100°C. Commonly used gases include steam, CO_2, and air, in combination or individually. Steam is the preferred activation gas because the water molecule has smaller dimensions than the CO_2 molecule. Consequently this leads to a faster diffusion into the porous carbon matrix, easier access into the micropores, and, thus, a faster reaction rate. However, the steam reaction is product inhibited due to adsorption of hydrogen molecules into the active sites.

The reaction of CO_2 with solid carbon is known as the Boudouard reaction, which has been studied extensively. Activation with CO_2 is inhibited by CO by decreasing the forward reaction rate [$C + CO_2 \Leftrightarrow CO + C(O)$]. The literature shows (1) that the addition of CO to the reacting gas resulted in the development of a better microporous structure besides decreasing the rate of gasification. CO_2 activation requires higher temperatures than steam activation. Although pore development is dependent on temperature and concentration of reactant gas, the origin of the carbon precursor affects the characteristics of the activated carbon produced and the nature of porosity evolved. The type of reactor used also has an effect on the properties of the porous carbon generated.

The gasification of black liquor char has been characterized by measuring the kinetics in CO_2 and steam (2,3). The high reactivity of black liquor char has been explained by the degree of dispersion of catalytically active sodium in the char (2). The gasification rate has been found to correlate with the surface area and the sodium/carbon molar ratio (4). However, no attempt has been made to systematically study the evolution of porosity and surface area as a function of pyrolysis temperature and carbon conversion.

OBJECTIVES

The objective of this chapter is to gain a basic understanding of the porosity and surface area of carbons in general and black liquor char in particular. These properties of interest include the following:

- pore diameter, pore volume, and porosity,
- pore-size distribution,
- the shapes of the pores,
- total and active surface areas,
- the interaction of the black liquor char surface and the primary gasification molecules,
- the effect of pyrolysis temperature and carbon conversion on porosity and surface area.

The specific aim is to characterize black liquor char by obtaining adsorption and desorption isotherms using the following probe molecule: N_2, CO_2, O_2. It was also the aim to review relevant literature concerning adsorption processes and porous carbons, and to compare the results obtained for black liquor char with other carbons.

STRUCTURE OF POROUS CARBONS

Porous carbons are a non-graphitic form of carbon, characterized by internal surface areas ranging from typically 500 to 3000 $m^2\ g^{-1}$. Black liquor char has typically an average surface area an order of magnitude less. X-ray studies show that the structure of porous carbons is carbon atoms in arrangements that are roughly aligned in layered structures (1). Some of these layers are stacked approximately parallel to each other over distances over a few nanometers. This is usually interpreted as a hypothetical crystallite. However, the crystallite structure does not exist as such in porous carbons, and it is, therefore, not useful in explaining the processes of pyrolysis, carbonization, and sorption. The concept of surface area in porous solids gives a more practical understanding of these structure related processes.

Carbon has the electron configuration $1s^2 2s^2 2p^2$ with valencies of 2, 3, and 4. It has the ability to bond to itself via sp^3 and sp^2 hybridization. The sp^2 hybrid has three outer electrons in equal bonding orbitals which are directed in a plane at 120° to each other. The fourth electron in the p-orbital is capable of forming π-bonds with neighboring atoms giving the hard crystalline diamond structure. Elemental carbon exists in two crystallographic forms. There is diamond with its tetragonal bonding, which has no relevance here. Attention is directed to the other form, graphite, which has a lamellar structure in which each lamella is composed of carbon atoms in six-membered ring systems. Within the rings, the adjacent carbon-carbon distance is 2.46 Å. In the hexagonal form of graphite the lamellae are arranged relative to each other with an ABAB stacking sequence in which all atoms in lamellae A lie above each other and likewise for lamellae B. The interlamellar distance is 3.35 Å. In the less stable rhombohedral form, the lamellae are arranged relative to each other in an ABCABC sequence. Figure 4.1 shows the arrangement of the two principal structures of graphite. The recently discovered fullerenes are essentially a derivative of graphite because the base unit is the graphitic lamella. Five membered rings within six-membered systems adopt spherical shapes with about 70 carbon atoms per sphere. Cylindrical fullerene-type structures also exist.

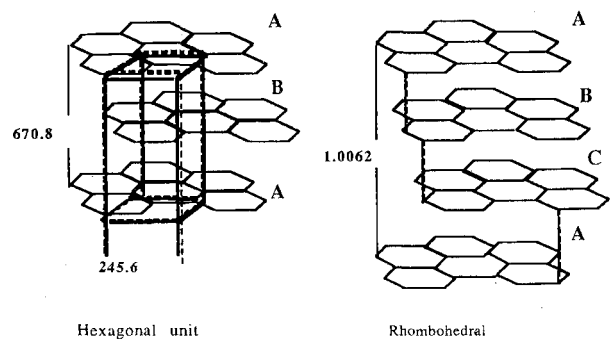

Figure 4.1. Models of (A) hexagonal and (B) rhombohedral structures of graphite (1). The adjacent carbon-carbon distance is 245 pm. The interlamellar distance is 335 pm.

Perfect graphite is a rare form of carbon, and the majority of carbons are found in less ordered structures which are chemically heterogeneous, such as coals, cokes, and chars. These types of carbons are described as graphitic or non-graphitic depending on the degree of crystallographic ordering. Graphitic carbons possess three-dimensional symmetry and non-graphitic carbons do not. The non-graphitic carbons are further divided into two categories, the graphitizable and the non-graphitizable carbons. Figure 4.2 shows the classification of carbon materials.

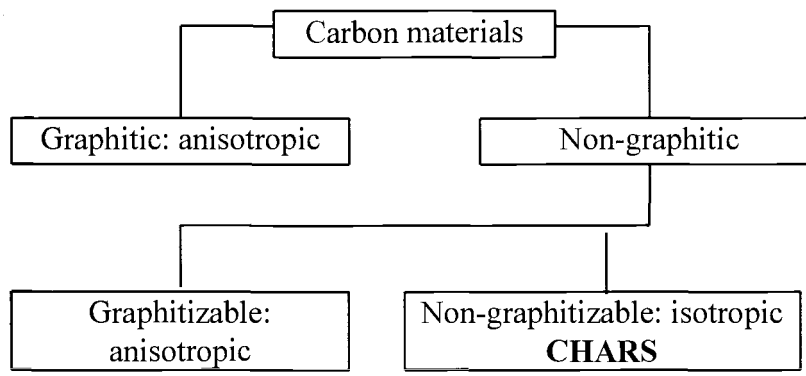

Figure 4.2. Black liquor char is non-graphitizable and isotropic according to the classification of carbon materials.

Graphitizable carbons are non-graphitic carbons which can be converted into graphitic carbon by heat treatment. The degree of graphitization depends on the heat treatment and the time allowed at a set temperature to affect the structure. The graphitizable carbons, called cokes, are formed commercially by the pyrolysis of aromatic petroleum and coal-tar pitches. Figure 4.3 shows a structural model of graphitizable carbon at different temperatures.

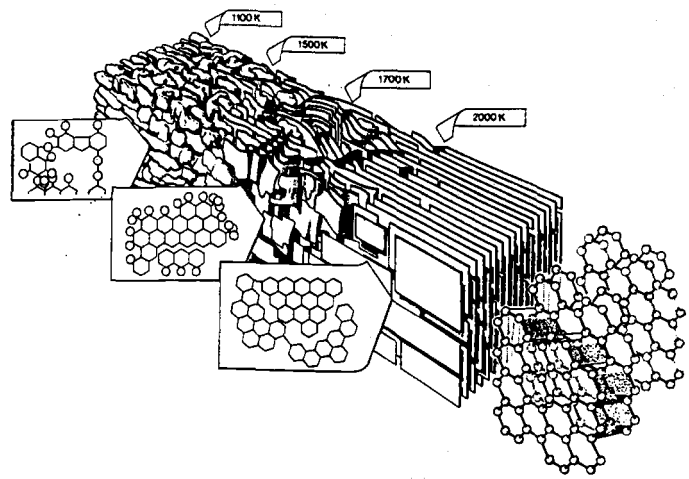

Figure 4.3. A structural model of graphitizable carbon to demonstrate parallel stacking of imperfect graphite-like lamellae (1).

A non-graphitizable carbon is a non-graphitic carbon which cannot be transformed into a graphitic carbon by heat treatment under inert conditions at atmospheric and lower pressures. The non-graphitizable carbons, called chars, constitute carbonization products from wood, activated carbons, brown coals, lignites, highly volatile bituminous coals, black liquor and others. Such parent materials do not pass through a fluid phase during pyrolysis and carbonization. Chars have a short-range structural order, < 100 Å, roughly layered, and isotropic in all properties. Figure 4.4 shows the location of carbon atoms in three dimensions for a non-graphitized carbon.

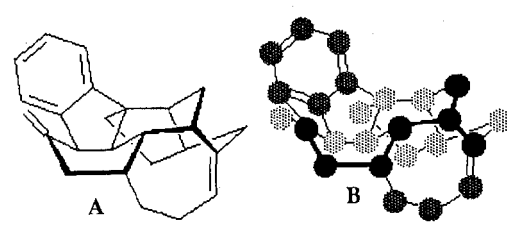

Figure 4.4. A structural model of non-graphitizable carbon to illustrate (A) the defective nature of the solid matrix, and (B) to show the location of carbon atoms in three dimensions (1).

Definition of porosity

The word pore is derived from the Greek, meaning a passage distinguishing it from an isolated void. In this paper, porosity is defined as the empty space in solid materials where there is a discontinuity in the array of atoms and molecules, i.e. where the electron density falls to zero (1). Porosity in solids is classified into three groups by the International Union of Pure and Applied Chemistry (IUPAC) (5):

- micropores: diameter less than 20 Å
- mesopores: diameter between 20 and 500 Å
- macropores: diameter greater than 500 Å

Micropores are considered as being about the size of adsorbate species, and they can accommodate one, two, or perhaps three molecules. Mesopores or transitional pores are wider, and are typically characterized by the hysteresis effect with respect to gas adsorption and desorption. A more detailed discussion about mesopores is given later in this chapter. Macropores are transport pores to the interior of the solid matrix and are typically of little interest. The pores (micro, meso, macro) constitute the adsorbent and the adsorbing gases, the adsorbates, as shown in Figure 4.5.

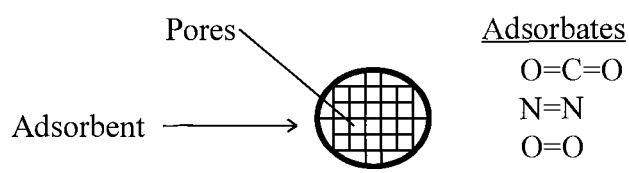

Figure 4.5. Adsorbent and adsorbates for porous carbons.

Table 4.1 lists the porosities of common carbons.

Table 4.1. Porosity in different carbons.

Carbon	Porosity (%)	Bulk density (kg/m^3)	Avg. pore diameter (Å)	Surface area (m^2/g)	Source
Shell-based	60	450-550	20	800-1600	(6)
Wood-based	80	250-300	not listed	800-1800	(6)
Petroleum-based	80	450-550	20	900-1300	(6)
Peat-based	55	300-500	10-40	800-1600	(6)
Lignite-based	70-85	400-700	30	400-700	(6)
Bituminous-coal	60-80	400-600	20-40	900-1200	(6)
Black liquor char	10-35*	200-300	40-200	10-330	this work

* = measured data low due to sample preparation

Formation of porosity

A detailed look at the process of pyrolysis and carbonization illustrates the complexity of the formation of an isotropic porous char from a parent material having a different structure (e.g. black liquor char). This material consists of a three-dimensional polymeric or macromolecular network, composed of cellulose and lignin associated with any other additional compounds (black liquor contains significant amounts of inorganic substances originating from the pulping chemicals). Coals have their own aromatic, macromolecular structural networks that are coal-rank related. As such, they exhibit low internal surface areas. During pyrolysis a process of decomposition of the parent polymeric network is initiated as shown in Figure 4.6. Free radicals are formed and considerable strain energy is introduced into the lattice. Major changes takes place in the molecular structure and the development of aromatic carbon occurs (carbonization).

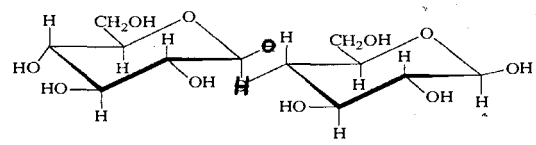

A cellulosic-type precursor (A).

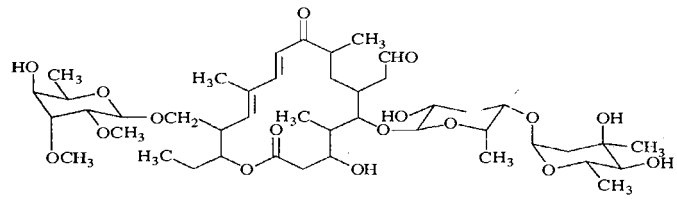

A possible structure intermediate between cellulose and an aromatic carbon (B).

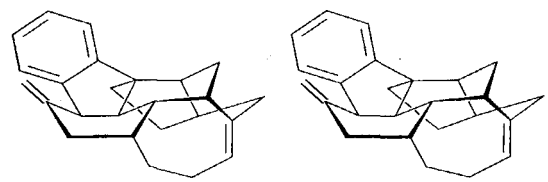

Possible, highly defective carbonaceous structures which, when interconnected, create microporosity (C).

Figure 4.6. Formation of porosity from a cellulosic type precursor (A), via an intermediate (B) to a porous aromatic carbon matrix (C) (1).

During pyrolysis, the cellulosic structure loses small molecules as volatiles such as water and CO_2 together with a wide range of aliphatic acids, carbonyls, alcohols, etc.. These evolutions do not occur at a single decomposition temperature, but over a range of temperatures. As small molecules are removed from the original macromolecular network, the resulting chemically reactive lattice tends to close the vacancies created by loss of the volatiles. Consequently, a new lattice is continuously created with a composition of higher C/H and C/O ratios due to preferential loss of hydrogen and oxygen. The newly created carbon rich lattice possesses considerable strain energy and is not in thermodynamic equilibrium, because the more stable state is the graphite-like lamellar constituent molecules. Hence, with increasing heat treatment temperature into the carbonization range, the unstable network becomes more carbonaceous and more aromatic as the carbon atoms readjust their positions to the six-membered ring systems.

Further increases in temperature cause additional removal of hydrogen oxygen, nitrogen, and sulfur, leaving clusters of defective ring systems. The random bonding of these clusters ensures an apparent density of the char formed (1 g cm^{-3} for coal char; 0.4 g cm^{-3} for black liquor char) that is considerably less than that of a single crystal graphite (2.2 g cm^{-3}). It is the spaces between these clusters that constitute the microporosity of the solid matrix. Meso- and macroporosity are created by swelling during pyrolysis and by shrinkage during carbonization.

Models of porosity

Because of the differences in size of the clusters of the six-atom ring systems and the modes of attachment to each other, the sizes and shapes of the spaces trapped between the clusters also differ. In fact, it is unlikely that any two shapes are similar. In the literature, these spaces are described as cylindrical tubes (1). For engineering calculations this approximation may be warranted, but it is a misconception that the pores actually are a series of interconnecting tubes. No mechanism exists for the creation of a tubular system during pyrolysis and carbonization. The evidence from scanning and transmission electron microscopy reveals no such structures (1).

A more realistic concept considers that the carbon atoms of solid porous carbon form a covalently bonded three-dimensional network with imperfect lamellar-type arrangements. The volume elements with no electron density determines microporosity. As these volume elements exist between the carbon atoms, they have the sizes of atoms and molecules. Therefore, the carbon atom network and microporosity are intimately related. The interconnections between micropores are of various sizes, and the interconnections themselves are part of the microporous system. This means that all sizes of pores form both part of the adsorption system as well as the transportation system. In other words, one micropore could be both an adsorption site and part of a passage.

A satisfactory model of the adsorption process is the filling of individual adsorption sites (volume elements) that have as nearest neighbors about six other sites of different

size and shape. Perhaps the best way to envisage microporosity is a series of interconnecting volume elements, where each volume element is of a different size and shape, and connected in three dimensions in a random way, without pattern. Such a model, as opposed to the tube model, is a logical consequence from analyses of formation mechanisms of micropores and also from the molecular sieve characteristics of carbons (1). Microporous carbons adsorb molecules with a range of different sizes. As the size of the adsorbate molecules increases, so the extent of adsorption decreases as pores of smaller size are excluded from access. Figure 4.7 illustrates this exclusion.

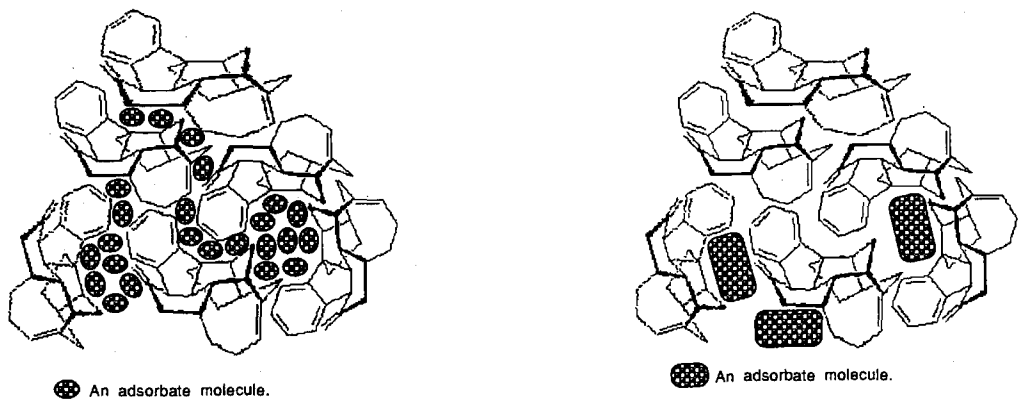

Figure 4.7. Model for clusters of six-membered ring systems that create porosity. Small molecules can get to pores where larger molecules cannot (1).

Microporosity within a carbon changes with temperature. The covalent carbon matrix is not thermally stable. At temperatures above 700°C, carbon atom displacement and relocation occurs to form a more stable graphite-like lamellar structure, thus, changing the microporosity. Between 600-800°C the adsorption capacity changes little. Published results show that the adsorption capacity is reduced to zero at 1000°C for carbons from polyfurfuryl alcohol (1). Cellulose carbons maintain adsorption capacity to 1200°C, and polyvinylidene chloride to 1600°C. These differences reflect variations in cross-link densities within the carbon network.

METHODS FOR MEASURING POROSITY AND SURFACE AREA

A range of techniques is available for estimating porosity and surface area. This section is not, however, an attempt to review all methods available, but rather to review the procedures adopted in this work for studying black liquor char. Two methods were employed: gas adsorption using the BET, Dubinin-Astakhov, and Dubinin-Raduschkevich theories, and mercury porosimetry. A review of physical and chemical adsorption is given in Appendix 4.1.

Langmuir and BET theories

To quantify the adsorption process, the degree of adsorption is related to the equilibrium partial pressure P/P_0 at constant temperature which is defined as the isotherm. Adsorption isotherms are studied to obtain information about the following:

- surface area,
- pore volume,
- surface chemistry of the adsorbent,
- nature of the adsorbed phase.

Interpretation of isotherms is not straightforward, and this has caused debate among surface chemists. Adsorption processes in micropores are the most difficult to describe accurately. The adsorption processes in mesopores is more easily understood, and of main focus here. Macroporosity behaves in the same way as an open surface to adsorption, and accounts for <1% of the adsorption processes within microporous carbons. Figure 4.8 lays out the six major classes of isotherm shapes that are obtained from adsorption experiments.

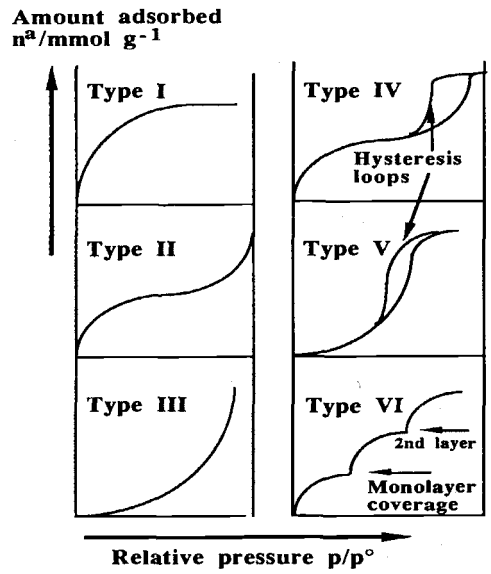

Figure 4.8. Classification of isotherm shapes into six principal classes (1).

A knowledge of adsorption mechanisms in different sizes of pores is necessary to explain the isotherm shapes. Type I isotherms are typical for microporous solids. Micropore filling occurs at relatively low partial pressures, $<0.1P/P_0$, and the adsorption process is complete at $0.5P/P_0$. Type II isotherms describe physical adsorption of gases by non-porous solids. Monolayer coverage is succeeded by multilayer adsorption at higher p/p_0 values. Type II isotherms can also be obtained from carbons with mixed micro- and mesoporosity. Type III and V isotherms are convex towards the x-axis. These isotherms are typical for weak gas-solid interactions. Type III isotherms originate from non-porous and microporous solids. Type V isotherms originate from microporous and mesoporous solids. The weakness of the adsorbent-adsorbate interactions causes the uptakes at low pressures to be small. However, once a molecule has become adsorbed at a primary site, the adsorbate-adsorbate forces promote further adsorption in a cooperative way described by the cluster theory (1). An example is the adsorption of water vapor on oxides of carbon molecules. Types IV and V isotherms possess a hysteresis loop, the shape of which varies from one adsorption system to another. Hysteresis loops are associated with

mesoporous solids. The type VI isotherm represents the formation of successive monomolecular layers. The stepwise isotherm arise from extremely homogeneous, non-porous surfaces and the step height corresponds to monolayer capacity.

A significant literature exists describing models to interpret the shapes of isotherms obtained from porous solids. Usually these models ignore structural features of the adsorbent, except in a few general ways, e.g. distribution of adsorption energy (microporosity) and pore width (mesoporosity). Information concerning the effective surface areas, pore-size distributions, micropore volumes, etc., is incorporated within the isotherm. How to extract this information is a matter of debate since direct experimental evidence is limited.

The term surface area does not describe a carbon unequivocally. Carbons with similar effective surface areas can be very different structurally. Results obtained using one adsorbate can differ when other adsorbates are used, especially at another temperature. When an adsorbate molecule is strongly bound and localized to one adsorption site, surface areas can be obtained for type I isotherms using the Langmuir equation (1):

$$\frac{V}{V_m} = \frac{bP}{1+bP} \qquad (4\text{-}1)$$

where V is the amount of gas adsorbed at equilibrium, V_m, the amount of gas required for monolayer coverage, and, "b", a constant describing the energetics of the surface.

At sufficiently low pressures, $bP \ll 1$, the Langmuir equation becomes:

$$\frac{V}{V_m} = bP \qquad (4\text{-}2)$$

This region of the isotherm is the Henry's law region, where the uptake is directly proportional to the pressure. At high pressures, $bP \gg 1$, the Langmuir equation becomes: $V = V_m$.

Surface areas are obtained using the following relationship (1):

$$S = V_m N_A \sigma \tag{4-3}$$

where N_A is Avogadro's number, and σ the projected area of the adsorbate molecule.

The Langmuir equation is based on the following assumptions:

- only monolayer adsorption can occur,
- no adsorbate-adsorbate interactions exist,
- the adsorbent has a homogeneous surface (uniform energy).

The Brunauer, Emmett and Teller (BET) equation was derived to improve the Langmuir model to account for unrestricted multilayer adsorption. The first layer contains sites for molecules in the second layer etc., and the rate of adsorption and desorption for each layer is at steady state. On the basis of these modified assumptions, the well known BET equation is obtained by summation over all the layers (1):

$$\frac{P}{V(P_0 - P)} = \frac{1}{V_m c} + \frac{c-1}{V_m c} \cdot \frac{P}{P_0} \tag{4-4}$$

where c is related exponentially to the heat of adsorption of the first monolayer:

$$c = e^{\left(\frac{\Delta H_A - \Delta H_L}{RT}\right)} \tag{4-5}$$

The BET equation is widely used to interpret isotherms obtained using nitrogen at 77K. Over the past 50 years, this equation has remained the most widely used model for determining the surface area of porous materials. Despite the fact that the assumptions made are not strictly valid, the BET equation is useful and applicable to many isotherms.

Dubinin-Astakhov and Dubinin-Raduschkevich theories

The Dubinin-Astakhov (DA) and Dubinin-Raduschkevich (DR) theories are based on energies of adsorption rather than physical adsorption. This is particularly useful for reactive probe molecules such as CO_2 and O_2. Such processes can be described by the Dubinin-Astakhov equation (1):

$$W = W_0 e^{\left[-\left(\frac{A}{\beta E_0}\right)^n\right]} \tag{4-6}$$

where W represents the volume filled at temperature T and relative pressure P/P_0, W_0 is the total volume of the micropores, $A = RT\ln(P/P_0)$, and n, E_0, and β are parameters of the system. E_0 is called the characteristic energy. β is the so-called affinity coefficient with the reference benzene = 1. Dubinin found empirically that adsorption data of microporous carbons could often be linearized. This corresponds to the Dubinin-Radushkevich equation with the exponent n = 2 (1):

$$W = W_0 e^{\left[-B\left(\frac{T}{\beta}\right)^2 \log^2\left(\frac{P}{P_0}\right)\right]} \tag{4-7}$$

where the structural constant B is related to the characteristic energy according to equation 4-8.

$$E_0 = \frac{0.01914}{\sqrt{B}} \tag{4-8}$$

where E_0 corresponds to the heat of adsorption.

Mercury porosimetry

Mercury porosimetry is used to investigate meso- and macropores. This method involves the evacuation of all gas from a porous sample. Mercury is then penetrated into the sample pores under vacuum. Pressure is applied to force the mercury to the interparticle and intraparticle voids. The Washburn equation is used to calculate pore radii using mercury intrusion data (7).

$$r = \frac{2\gamma \cos\alpha}{\Delta P} \qquad (4\text{-}9)$$

where r is the pore radius, γ, the surface tension, α, the contact angle, ΔP, the pressure required to force mercury into the pores. The pores are assumed to be non-intersecting cylinders. Surface area and pore size distribution data using mercury porosimetry are in good agreement with the data using the BET method. However, mercury porosimetry is not suitable for micropore analysis, nor can it be used to measure mesoporosity in friable materials, because the high pressures required can damage the pore structure. This was the case with black liquor char. Therefore, pore radii were calculated from desorption pore volume data according to the method outlined in Appendix 4.4.

CHARS STUDIED

The black liquor char samples studied were obtained by feeding dry black liquor particles into the laminar entrained flow-reactor (LEFR) at Oregon State. A description of this device and the experimental procedures can be found in Appendix 13. Residence times were varied between 0.3 and 1.6 seconds at 700, 900, 1000, and 1100°C. 24 char samples were generated by pyrolyzing black liquor solids with a diameter of 90-125 μm with a heating rate of ~10000°C/s. The char samples obtained were all basic (pH ~ 9) indicating that the active sites were rich in oxygen containing complexes relative to hydrogen. Prior to the surface area measurement, a further degassing procedure was

performed. Char samples prepared at 700°C contained a lot of unremoved volatile organic matter especially at low residence times. Since a high volatile content sample could be harmful for the degassing device, only the high residence time char samples pyrolyzed at 700°C were investigated. Tables 4.2 shows the major elemental constituents and the degree of carbon conversion for the chars used in the chemisorptioin experiments.

Table 4.2. Specifications of chars used in chemisorption experiments.

	Run 54	Run 64
T (°C)	900	1000
Res.time (s)	0.64	1.52
Xc (%)	57.0	67.1
C (%)	28.6	26.8
Na (%)	18.9	20.9
K (%)	0.5	0.03
Cl (%)	0.69	0.82
$S^{=}$ (%)	1.04	2.24

The carbon analysis was done at a commercial laboratory (8). Sodium, potassium, and chloride data were obtained using a capillary electrophoresis analyzer at OSU. Sulfur data was taken from (9). X_C has units (g carbon reacted away) ÷ (g carbon in the BL solids). Appendix 4.2 shows how X_C was calculated. Appendix 4.7 lists all chars used in the physisorption experiments.

CHARACTERIZATION OF POROSITY AND SURFACE AREA

The porosity of BL char was assessed by observation of SEM pictures. Figure 4.9 shows the pore structure in BL char, and that the tortuosity is high.

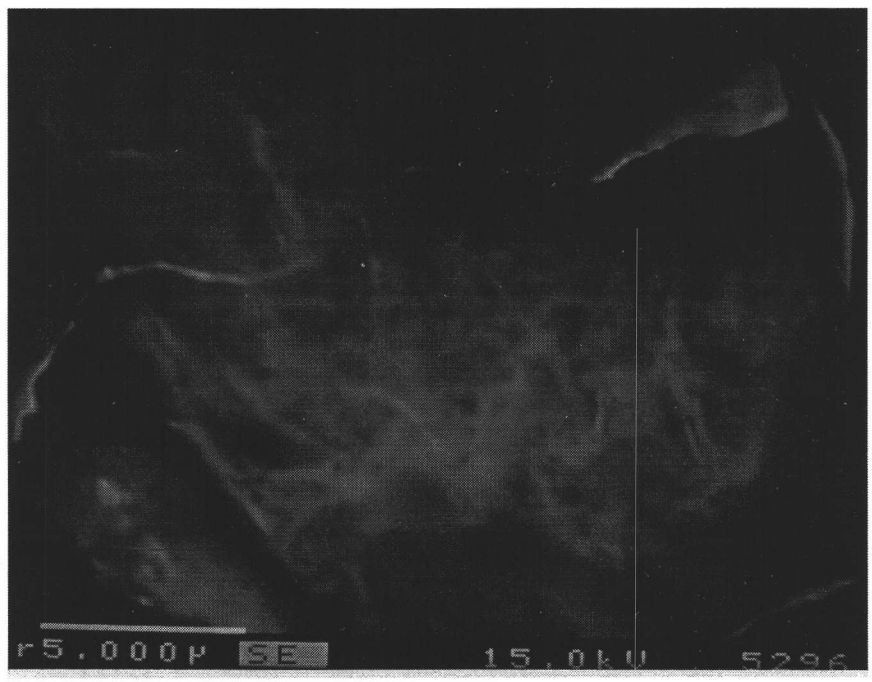

Figure 4.9. The macropore structure of BL char is tortuous.

Figure 4.9 shows that dry black liquor solids consists of a graphite like bulk structure with tortuous macropores and a high a void fraction. It was not possible to visually study the geometry and shape of the mesopores with the equipment available. The surface areas were determined by obtaining adsorption and desorption isotherms using a Micromeritics ASAP 2000 instrument. Details on the experimental procedures can be found in the literature (12). Figure 4.10 shows three typical isotherms for black liquor char measured with nitrogen at 77K.

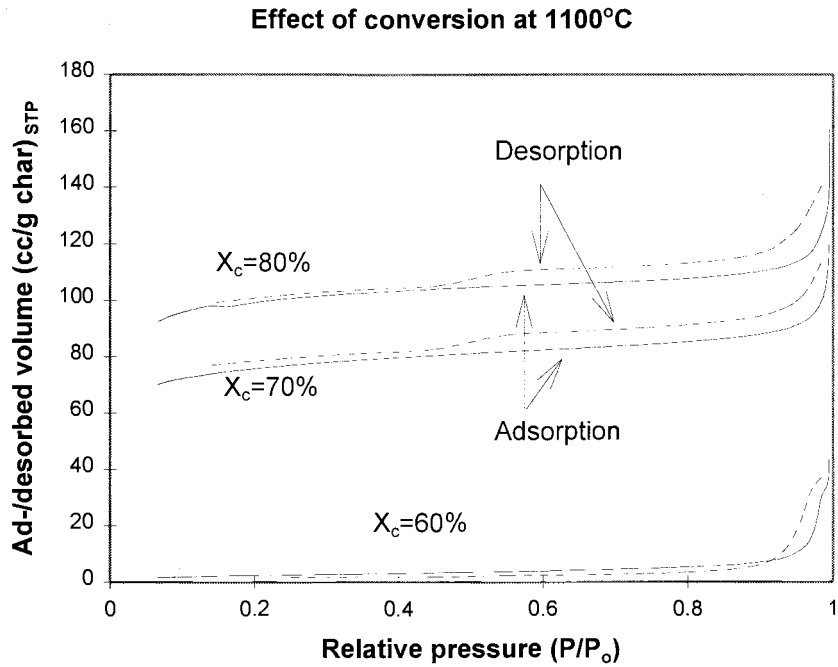

Figure 4.10. Type V isotherms with the hysteresis effect can be observed for three different carbon conversions in nitrogen at 77K.

At lower temperatures, the isotherms were all at the same level for all conversions. At 1000°C a similar trend could be seen for the samples that had rapid increase in N_2 surface area. Figure 4.10 shows that there are two relative pressures corresponding to a given quantity adsorbed with the lower pressure residing on the desorption isotherm, also known as the hysteresis effect. This is a reflection of the difference of the state of the adsorbate during adsorption and that during desorption. The hysteresis effect comes from the fact that $P_{des} < P_{ads}$ or $\Delta G_{des} < \Delta G_{ads}$. $\Delta G_{ads,des}$ are given by equation 4-10 (7).

$$\Delta G_{ads,des} = RT \ln \frac{P_{ads,des}}{P_0} \qquad (4\text{-}10)$$

Hysteresis isotherms can be divided into five subtypes according to de Boer (7) and are discussed further in Appendix 4.3.

Total surface area results

The surface area can be obtained assuming the BET theory applies, even though other theories are available. The adsorption isotherm gives the volume adsorbed versus relative pressure. By plotting the left hand side of the BET equation (equation 4-4) versus relative pressure, one can calculate the slope and intercept as shown in Figure 4.11. From the slope and the intercept, the unknown parameters in equation 4-4 are defined and the amount of gas adsorbed, V_m, can be evaluated. The surface area can then be obtained by equation 4-3. Figure 4.11 shows a characteristic BET plot for black liquor char.

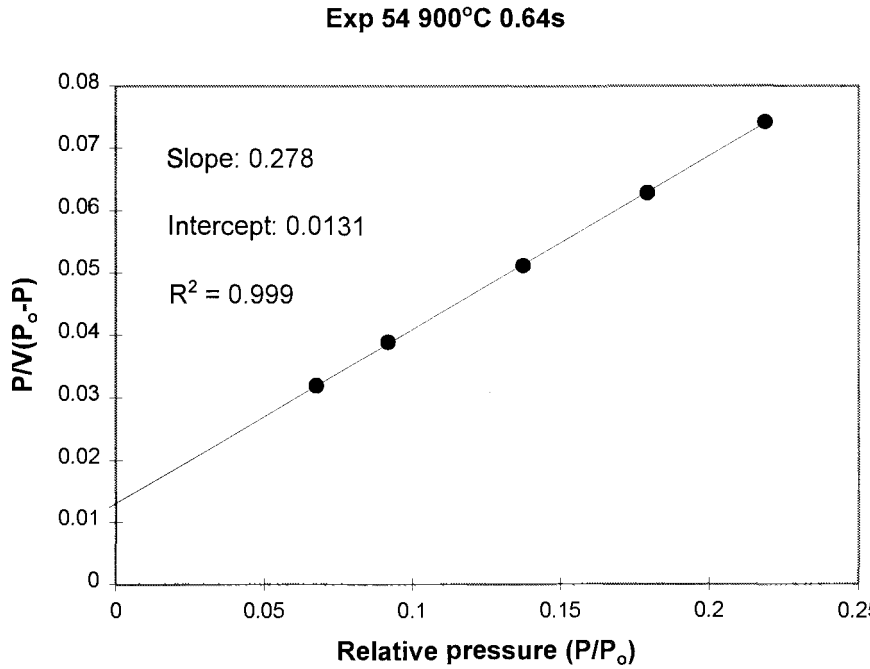

Figure 4.11. The BET plot gives the slope and intercept needed to calculate the surface area.

Figure 4.12 illustrates the variation of the specific surface area with carbon conversion and LEFR temperature. It also shows the effect of the fraction carbon that has

reacted away. This is a reflection of the enlargement of microporosity. These values agree well with the data reported by van Heiningen et al. (4): 10 - 250 m^2/g depending on liquor type. However, these surface area measurements were geared to examine the effect of liquor type. Here, one kraft liquor was examined systematically as a function of temperature and carbon conversion. Experiments were made in argon as well, but the adsorption isotherms obtained were not acceptable. Therefore, these results are not presented here. Appendix 4.2 contains the data for Figure 4.12.

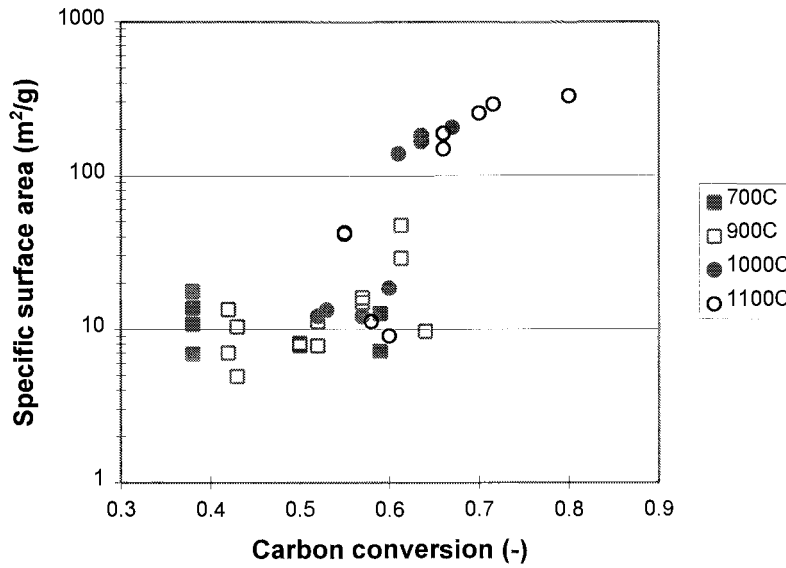

Figure 4.12. The specific surface area increases with carbon conversion and LEFR temperature. Data is in Appendix 4.2.

Active surface area results

The total surface area is not the most appropriate measure for amount of active sites. Surface areas measured with CO_2 and O_2 will attach only to the active gasification sites, which is therefore a more realistic measure of the active surface area. Two samples were tested: #54 and #64. The former sample was obtained using the LEFR in 0.64 s at

900°C and the latter in 1.52 s at 1000°C. Hence, were a comparison is made between a low carbon conversion and low temperature char versus a high carbon conversion and high temperature char. The differences in active surface area, pore sizes and pore volumes for respective probe molecule are given in Table 4.3. The data given in Appendix 4.6 were taken at a commercial laboratory (11).

Table 4.3. Summary of the total and active surface areas, and crystallite sizes for chars 54 and 64. The CO_2, O_2 and crystallite data given in Appendix 4.6 were taken at a commercial laboratory (11).

Parameter	Char #54	Char #64
BET-N_2 S.A. (m^2/g char)	15.6	206
DR-CO_2 S.A. (m^2/g char)	14.3	178
ASA-O_2 (m^2/g char)	67*	97
Crystallite size of carbon (Å)	420	290

* = overestimation due to "oxygen spillover", adsorption of O_2 in catalyst, and possibly CO formation

Table 4.3 shows that the CO_2 surface area is about 92% of the total surface area for the low carbon conversion, low temperature char. However, for the high conversion, high temperature char, substantial differences in surface area were obtained depending on the probe molecule used. The CO_2 surface area is 84% of the total surface area, and the O_2 surface is only 47% of the total. The question now rises why there is such a significant difference in surface area between the chars. One explanation could be differences in the cluster sizes. The crystallite size was about 31% smaller for the high conversion, higher temperature char. This would expose more of the char structure making the surface areas one order of magnitude higher than for the other char. Another question is why the difference between total and active surface area is much larger for the high conversion, high temperature char. One plausible explanation could be that there is a lower active site population since there is relatively less carbon left.

Heat of chemisorption results

One of the objectives was to study the interaction between black liquor char and the primary gasification molecules of interest, namely CO_2, H_2O and O_2. The heat of adsorption is usually obtained from the pressure versus temperature relationship (isostere) at a constant degree of coverage, and then employing the Clausius-Clapeyron equation (12). However, in this work the heat of adsorption was obtained from the CO_2 isotherms using the Dubinin-Radushkevich theory.

The heat of chemisorption is exothermic due to loss of internal degrees of freedom during surface reaction. The results from a commercial laboratory (11) show that the heat of chemisorption is 24.5 kJ/mol for char #54 and 32.4 for char #64 (Appendix 4.6). This means that more heat is evolved for the high conversion, high temperature char compared to the low when CO_2 is adsorbed to the surface. There is a noticeable trend for the heats of adsorption to decrease as one moves moves from left to right across the periodic table, but this trend is overwhelmed by the variation of ΔH_{ads} with the atomic structure of the surface (12). From this it can be concluded that different structural forms are dominating for the two chars in question. It can also be perceived as an increase in reactivity when the chemisorption energy is higher. A high reactivity in turn is caused by more edge carbon atoms than basal plane atoms. There are two types of edge atoms: zig-zag and arm-char as shown in Figure 4.13. The literature shows that the zig-zag edges are more reactive than the arm-chair edges (5). Hence, the conclusion is that the high conversion, high temperature char has more zig-zag edge atoms. An additional factor that supports this conclusion is that higher reactivity is caused by more structural defects (5). A high conversion, high pyrolysis temperature char has definetely more structural defects than a low conversion, low temperature char.

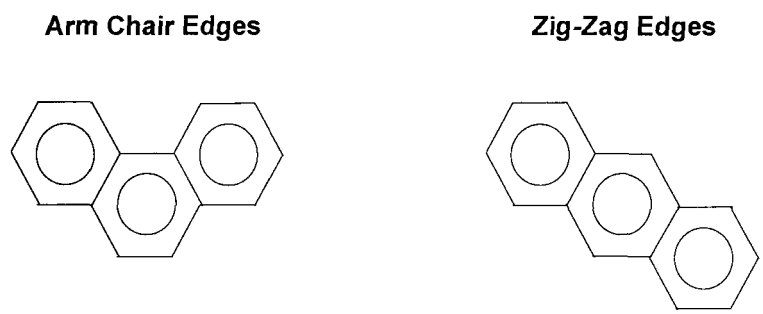

Figure 4.13. The zig-zag edges are dominating for the high conversion, high temperature char, and vice versa for the other char.

Pore-size and pore volume results

From the desorption pore volume curve the average pore diameters were evaluated using a modified Kelvin equation as outlined in Appendix 4.4. Figure 4.14 shows the pore diameters obtained for each char studied. Figure 4.15 shows the total pore volume for the same chars. Desorption pore volume plots are shown Figures 4.16 and 4.17.

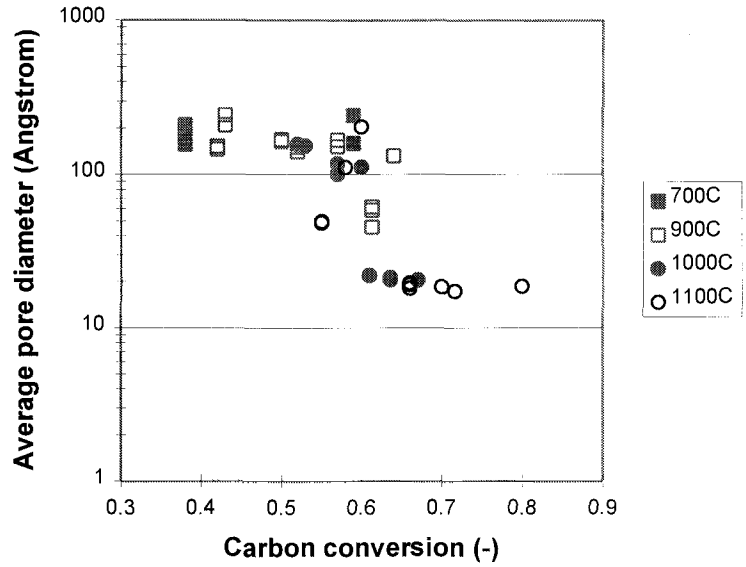

Figure 4.14. The average pore diameter decreases with carbon conversion at high pyrolysis temperatures. The lower the pyrolysis temperatures, the smaller this effect is.

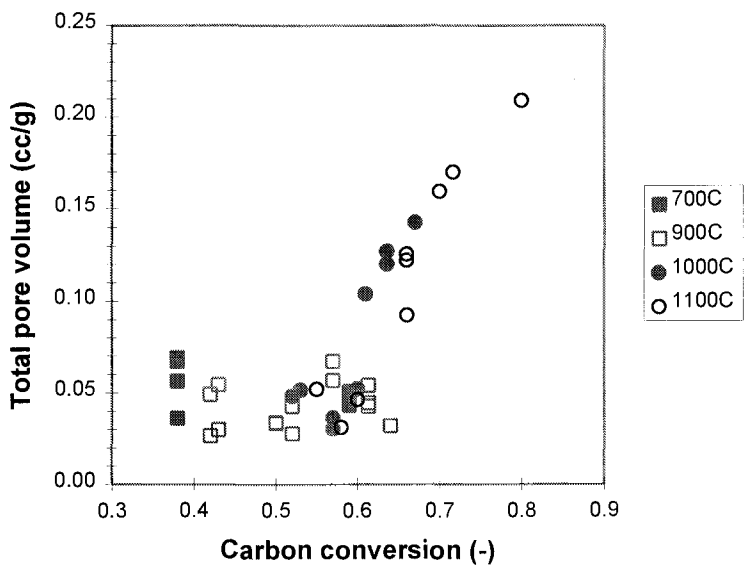

Figure 4.15. The total pore volume increases linearly with carbon conversion at high pyrolysis temperatures. At low pyrolysis temperatures the total pore volume is independent of carbon conversion.

Figures 4.14 and 4.15 show a correlation between pore-size and pore volume on one hand and carbon conversion and pyrolysis temperature on the other. The decrease in pore diameter and increase in pore volume indicates an increase in porosity. Void fraction data was calculated assuming a true density of 2.2 g/cc which resulted in porosities varying between 10 and 35%. Values above 90% were expected, but since the char samples had probably contracted and lost their original shape during sample preparation, lower porosities were obtained.

CO_2 and O_2 data

Pore size data with CO_2 and O_2 were obtained allowing a comparison with nitrogen data. Table 4.4 summarizes the results using different probe molecules.

Table 4.4. Summary of pore size and pore volume data for chars 54 and 64.

Parameter	Char #54	Char #64
BET-N_2 pore vol. (cm^3/g)	0.062	0.143
DR-CO_2 pore vol. (cm^3/g)	0.00475	0.0592
BET-N_2 pore size (Å)	160	20.5
DR-CO_2 pore size (Å)	10.6	8.0
DA-CO_2 pore size (Å)	11.8	12.0

The larger DA-CO_2 value for char #64 suggests that it has a wider pore size distribution than char #54. The desorption pore volume data shown in Figures 4.16 and 4.17 illustrate that this is in fact true. Appendix 4.5 contains a complete listing of pore volume and pore diameter data for N_2. The data for CO_2 and O_2 in Table 4.4 are given in Appendix 4.6.

Changes in pore-size distribution

Figures 4.16 and 4.17 show characteristic plots of the adsorbed and desorbed pore volume versus pore diameter for black liquor char.

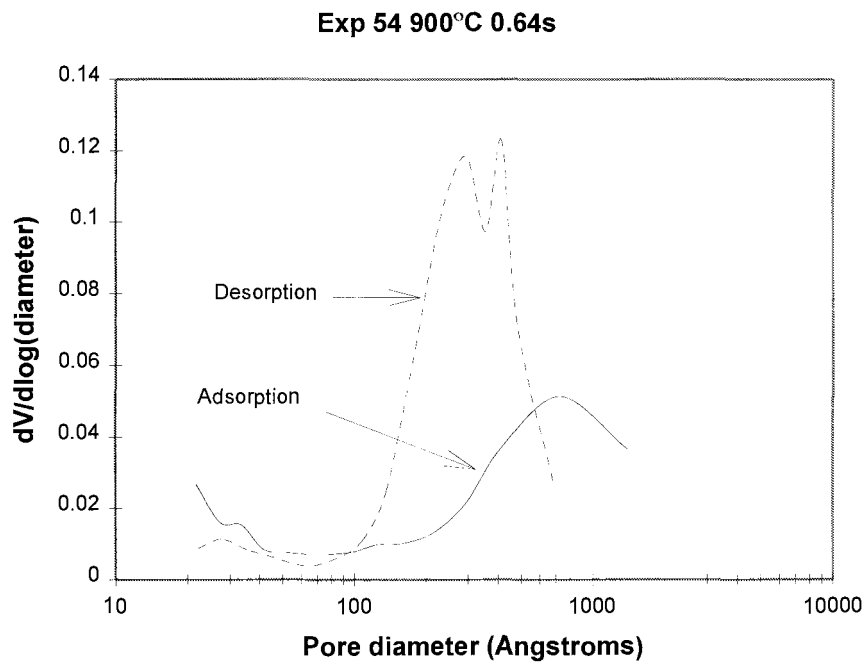

Figure 4.16. At 900°C and below the desorption pore volume curve peaks between 150 and 200 Å.

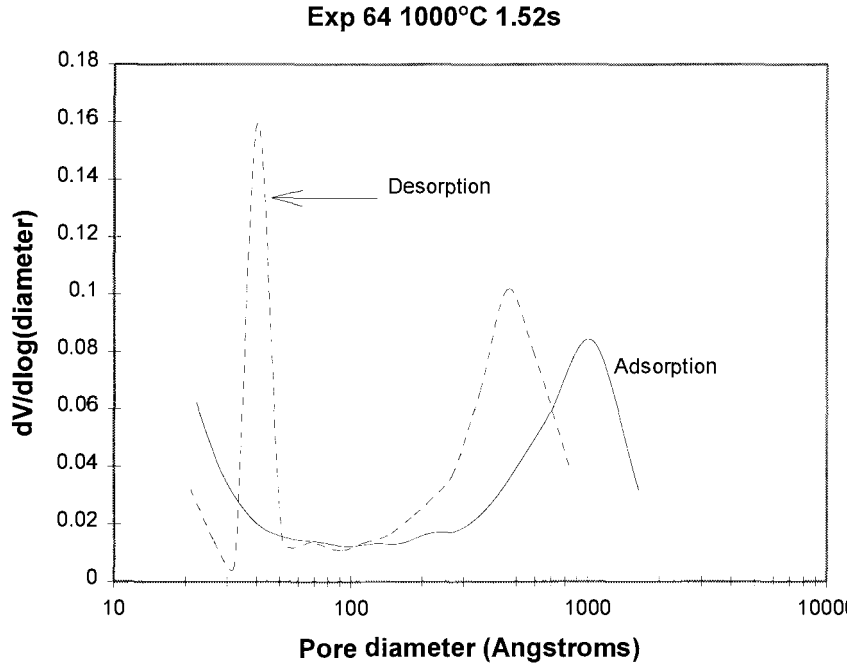

Figure 4.17. At 1000°C the desorption pore volume curve is bimodal.

Figure 4.16 shows a desorption peak at around 200 Å. Figure 4.17 is bimodal with peaks at around 20 and 200 Å. At 1000 and 1100°C there is a transition from a right bimode to a left bimode with increasing carbon conversion. This means that the average pore diameters decrease in size with conversion. Since there are more small pores than large pores, the total pore volume increases with conversion.

CONCLUSIONS AND RECOMMENDATIONS

Black liquor char is an isotropic and non-graphitizable carbon with mesopores being the dominating pore type. Strictly, the pores are not cylindrical tubes, but it is the best approximation for calculating pore diameters. The chemisorption isotherms with CO_2 were of type I. Some hysteresis could be observed for the CO_2 isotherms, but it

could not be classified in any category. The physisorption isotherms were of type V with hysteresis of types C and D. This shows that the energy of desorption is lower than adsorption. This is also an indication that the pores are a mixture of tapered and wedge shaped pores with either open ends or with narrow necks at one or both open ends.

The total surface areas were constant for 700 and 900°C chars, and, thus, independent of carbon conversion. At 1000 and 1100°C, the average surface area increased rapidly at higher degrees of carbon conversion. The average pore diameter was around 150 Å for 700 and 900°C chars. For the 1000 and 1100°C chars, the pore diameter decreased rapidly with conversion to around 20 Å as the surface area increased one order of magnitude. The pore volume increased with conversion due to the increased amount of small pores. Thus, the porosity increased with conversion and pyrolysis temperature.

The active surface area with O_2 increased with pyrolysis temperature and carbon conversion. The heat of chemisorption for CO_2 behaved the same way, but the cluster size decreased. This shows different structural forms prevailing depending on the conversion and temperature. The presence of more structural defects in a high conversion, high pyrolysis temperature char enhances the reactivity. Reactivity is higher with higher chemisorption energies. A high reactivity in turn is caused by more edge carbon atoms than basal plane atoms. Of the edge atom structures, the zig-zag edges are more reactive than the arm-chair edges. Hence, the conclusion is that a high conversion, high temperature char has more zig-zag edge atoms.

Pore size distribution measurements using mercury porosimetry were not successful because the studied char samples were too fragile and small. Another method, e.g. immersion calorimetry, may give better results. Infrared spectroscopy is recommended in studying the chemical transformations in black liquor char. IR spectra could verify the structural changes during pyrolysis and carbonization, e.g. the formation of aromatic structures from aliphatic structures.

ACKNOWLEDGMENT

Dr. Carlos Leon y Leon D. with the Quantachrome Corporation is acknowledged for the chemisorption data. The time and money he spent was not covered by the regular analysis fees. Mr. Hirofumi Honda is acknowledged for the mercury porosimetry experiment at the laboratories of Fuji Silysia Chemical Ltd. in Kasugai, Japan. Dr. Rorrer is acknowledged for giving me the responsibility for the BET analyzer. Mr. Nick Wannenmacher is acknowledged for soldering the dewar elevator motor and repairing the vacuum pump in the BET analyzer.

NOMENCLATURE

Symbol	Description, dimension
A	Dubinin-Astakhov parameter, J/mol
b	constant describing the energetics of the surface, dimensionless
c	constant in BET equation, dimensionless
E_0	characteristic energy, J/mol
ΔG	change in Gibbs' free energy, J
ΔH	change in enthalpy, J
ΔH_{ads}	heat of adorption, kJ/mol
ΔH_A	activation energy for chemisorption, kJ/mol
ΔH_C	heat of chemisorption, kJ/mol
ΔH_D	heat of dissociation, kJ/mol
ΔH_L	heat of condensation, kJ/mol
ΔH_P	heat of physisorption, kJ/mol
N_A	Avogadro's number, 6.022137×10^{23} mol^{-1}
n	Dubinin-Astakhov parameter, dimensionless
P	absolute pressure, atm
ΔP	pressure required to force mercury into the pores, MPa

r_K Kelvin pore radius, μm

r_P actual pore radius, μm

R gas constant, 8.314 J/molK

ΔS change in entropy, J/K

S surface area, $m^2 g^{-1}$

t adsorbed film thickness, Å

T absolute temperature, K

V amount of gas adsorbed at equilibrium per unit mass of adsorbent, mmol g^{-1}

V_m amount of gas required for monolayer coverage of adsorbent, mmol g^{-1}

$\overline{V}$ molar volume of condensed gas, $m^3 mol^{-1}$

W volume of pores filled, $cm^3 g^{-1}$

W_t total volume of micropores, $cm^3 g^{-1}$

X_C fractional conversion of carbon, g C reacted away ÷ g C initially in BL**S**

Greek Symbols

α contact angle, °

β affinity coefficient, dimensionless (C_6H_6=1)

γ surface tension, N m^{-1}

θ degree of coverage, not applicable

σ projected area of adsorbate, m^2 $molecule^{-1}$

(data from (6): N_2: 16.2, O_2: 14.1, CO_2: 19.5 $Å^2$)

Subscripts

m monolayer complete

0 ambient

REFERENCES

1. Patrick, J.W., editor, Porosity in Carbons: Characterization and Applications, Halsted Press, 1995

2. Li, J., van Heiningen, A.R.P., Kinetics of CO_2 Gasification of Fast Pyrolysis Black Liquor Char, Ind.Eng.Chem.Res., Vol.29, No.9, p.1776-1785, 1990

3. Li, J., van Heiningen, A.R.P., Kinetics of Gasification of Black Liquor Char by Steam, Ind.Eng.Chem.Res., Vol.30, No.7, p.1594-1601, 1991

4. van Heiningen, A.R.P., Arpiainen, V.T., Alén, R., Effect of Liquor Type and Pyrolysis Rate on the Steam Gasification Reactivities of Black Liquors, 1992 International Chemical Recovery Conference, Seattle, WA, June, 1992

5. Marsh, H., editor, Introduction to Carbon Science, Butterworth & Co., chapter 4 by H. Marsh and K. Kuo, 1989

6. Levenspiel, O., Chemical Reaction Engineering, 2nd ed., John Wiley & Sons, p.470, 1972

7. Lowell, S., Shields, J.E., Powder Surface Area and Porosity, 3rd edition, Chapman & Hall, 1991

8. Weyerheuser Analytical & Testing Services, Federal Way, WA, September 20, 1994

9. Sricharoenchaikul, V., M.S. thesis, Oregon State University, 1995

10. Lourvanij, K., Academic Dissertation, Appendix B, Oregon State University, 1995

11. Quantachrome Corp., report 8-29-96 from Dr. C.A. Leon y Leon D., Boynton Beach, FL, 1996

11. Quantachrome Corp., report 8-29-96 from Dr. C.A. Leon y Leon D., Boynton Beach, FL, 1996

12. Somorjai, G., Introduction to Surface Chemistry and Catalysis, John Wiley and Sons, 1994

APPENDICES

APPENDIX 4.1

Review of Physical and Chemical Adsorption

All adsorption processes can be divided into two categories: chemical and physical adsorption. Chemical adsorption is also called irreversible adsorption or chemisorption. It is characterized by large interaction potentials leading to high heats of adsorption which often approach the values of chemical bonds. This fact, and results of other experimental observations, confirms that chemisorption involves true chemical bonding of the gas with the surface. Because chemisorption occurs through chemical bonding, it is associated with evolved heat, the heat of adsorption. The temperature rise from the evolved heat can be measured using calorimetric methods with an accuracy on the order of 10^{-3} K (12). As is true for most chemical reactions, chemisorption is usually associated with an activation energy. In addition, chemisorption is restricted to a single layer of adsorbate molecules that are not free to migrate on the surface. This enables e.g. the number of catalyst sites to be determined by simply measuring the quantity of chemisorbed gas.

The second category, physical, reversible adsorption or physisorption, exhibits characteristics that make it suitable for surface area measurements. Physical adsorption is accompanied by low heats of adsorption with no disruptive structural changes occurring to the surface. Unlike chemisorption, physical adsorption may lead to surface coverage by more than one layer of adsorbate. Thus, the pores can be filled for pore volume measurements. Physical adsorption equilibrium is achieved rapidly since no activation energy must be overcome as is generally true in chemisorption. Physical adsorption is fully reversible, and adsorbed molecules are not restricted to specific sites. For this reason, surface areas rather than numbers of sites can be measured.

Upon adsorption, the entropy change of the adsorbate is necessarily negative since the condensed state is more ordered than the gaseous state because of the loss of at least one degree of translational freedom. A reasonable assumption for physisorption is that the entropy of the adsorbent remains essentially constant and definitely does not increase

more than the adsorbate's entropy decreases. Therefore, the entropy for the entire system is necessarily negative. The spontaneity of the adsorption process requires that the Gibbs' free energy also be negative. Based upon the entropy and free energy changes, the enthalpy change accompanying physisorption is always negative, indicating an exothermic process according to equation A.4.1-1.

$$\Delta H = \Delta G + T\Delta S \qquad \text{(A.4.1-1)}$$

An important interaction at the gas-solid interface is due to dispersion forces. These forces are present regardless of the nature of other interactions and often account for the major part of the adsorbate-adsorbent potential. The electron motion in a molecule leads to a rapidly oscillating dipole moment. At any instant, the lack of symmetry of the electron distribution about the nuclei results in a transient dipole moment to another molecule, which vanishes when averaged over a longer time interval. When in close proximity, the rapidly oscillating dipoles of neighboring molecules couple into phase with each other leading to a net attracting potential. Among adsorbate-adsorbent interactions contributing to adsorption are:

1. ion-dipole interactions
2. ion-induced dipole interactions
3. dipole-dipole interaction
4. quadrupole interactions

It is evident from above that adsorption forces are similar in nature and origin to forces that lead to condensation of vapors and that the same intermolecular interactions are responsible for both phenomena. Thus, vapors with high boiling points, and, therefore, strong intermolecular interactions will be strongly adsorbed. Above the critical temperature, the thermal energy possessed by gas molecules is sufficient to overcome the forces leading to liquefaction. Because of the similarity of condensation and adsorption, the critical temperature can be used as an estimate of the maximum temperature at which measurable amounts of physical adsorption can occur.

Often an attempt is made to distinguish physisorption and chemisorption on the basis of the heat of adsorption. However, this is not entirely a satisfactory procedure. The smallest physical heat of adsorption will be slightly greater than the heat of condensation of the adsorbate. Were this not true, the vapor would condense and not be adsorbed. The upper limit for physical adsorption may be higher than 80 kJ mol^{-1} for adsorption in narrow pores. The heats of chemisorption range from over 400 to about 40 kJ mol^{-1}. Therefore, only very high or very low heats of adsorption can be used as criteria for the type of adsorption process. A more definitive criterion as to whether a particular interaction is physical or chemical is to search for reaction products. Elaborate techniques exist that can be used to establish a detailed description of the adsorbate-adsorbent interaction. Figure A.4.1.1 illustrates some of the essential differences between chemical and physical adsorption.

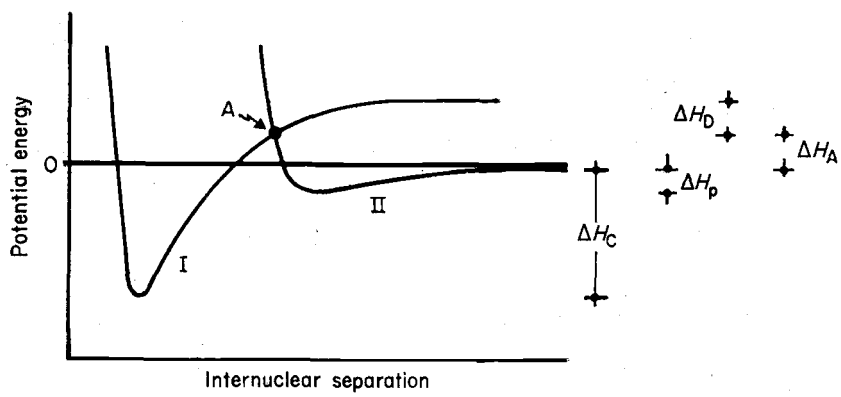

Figure A.4.1.1.Potential energy curves for (I) chemical and (II) physical adsorption. ΔH_A = activation energy for chemisorption, ΔH_C = heat of chemisorption , ΔH_D = heat of dissociation , ΔH_P = heat of physisorption (7).

Curves I and II represent potential energy plots for chemical and physical adsorption, respectively. The zero of potential energy is taken at finite separation of the reacting species. The minimum in curve I, below zero potential energy, is equal to the

heat of chemisorption, ΔH_C . The minimum of curve II is equal to the heat of physical adsorption, ΔH_P. The fact that curve I lies above zero potential energy at large internuclear separations implies that the chemisorbed gas is in an activated state or has undergone dissociation. The term ΔH_D , then, is the heat of dissociation. If dissociation does not occur, then curve I would approach zero potential energy asymptotically, similar to curve II. The minimum of curve I occurs at a smaller internuclear separation than that of curve II because chemical bonding, involving orbital overlap, will bring nuclei closer together than the less energetic physical adsorption forces can.

The transition from physical adsorption to chemisorption occurs at point A. The potential energy at A is in excess of that for the adsorbate and the adsorbent when separated. This represents the activation energy required for chemisorption, ΔH_A . If curve I resided more to the right or curve II more to the left, then the transition from physical to chemical adsorption would occur with no activation energy since the crossover point would reside beneath zero potential energy.

Figure A.4.1 is difficult to obtain experimentally for the interaction between black liquor char and the primary gasification molecules of interest, namely CO_2 and H_2O. Ab initio simulations (molecular orbital modeling) would have to be employed to generate figure A.4.1, which was beyond the scope of the defined objectives. However, it is possible to determine the heat of chemisorption using the pressure versus temperature relationship (isostere) at a constant degree of coverage using equation A.4.1-2, the Clausius-Clapeyron formula (12).

$$\left(\frac{d\ln P}{dT}\right)_{\theta=const} = -\frac{\Delta H_{ads}}{RT^2} \qquad \text{(A.4.1-2)}$$

There are two other types of adsorption data: the isotherm and the isobar. The isotherm gives the amount of molecules adsorbed as a function of pressure. The principal types of isotherms are shown in figure 4.10 in the main text. The isobar will give the amount adsorbed as a function of temperature. Typically, the amount of adsorbed molecules varies with temperature as illustrated in figure A.4.1.2.

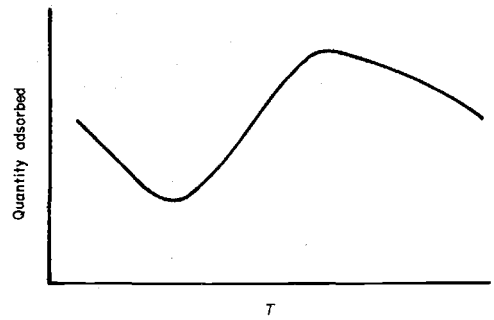

Figure A.4.1.2. Variation in quantity of adsorbed molecules with temperature (7).

The initial decrease in the quantity adsorbed is due to thermal desorption of the physically adsorbed gas. Subsequently, the quantity adsorbed increases with increasing temperature due to initiation of enhanced chemisorption. Finally, the curve slopes down when a sufficiently high temperature is reached to desorb the chemisorbed molecules. The measurement of the equilibrium between the gaseous and the chemisorbed state is frequently difficult because of the very low equilibrium pressures required to saturate the surface.

APPENDIX 4.2

Calculation Procedure for X_C

The following data is known:

A: The carbon in the char (g C in char / grams char)

B: The char yield after pyrolysis (g char / g BLS)

C: Carbon content in BL solids (g C in BLS / g BLS)

X_C can now be calculated as:

$$X_C(\%) = 100 - 100 \times \frac{\left(\frac{\text{g C in char}}{\text{g char}}\right)\left(\frac{\text{g char}}{\text{g BLS}}\right)}{\left(\frac{\text{g C in BLS}}{\text{g BLS}}\right)}$$

Table A.4.2.1 Summary of carbon in char data.

Exp no.	T (°C)	Res.time	A	B	C	X_C (%)
EXP71	700	0.88	0.310	0.695	0.350	38.5
EXP76	700	1.25	0.317	0.683	0.350	38.1
EXP61	700	1.71	0.288	0.493	0.350	59.4
EXP93	900	0.39	0.317	0.656	0.350	40.6
EXP54	900	0.64	0.286	0.522	0.350	57.4
EXP77	900	0.67	0.317	0.627	0.350	43.2
EXP75	900	1.12	0.310	0.546	0.350	51.6
EXP85	900	1.32	0.299	0.584	0.350	50.1
EXP60	900	1.59	0.274	0.459	0.350	64.1
EXP66	900	1.68	0.273	0.497	0.350	61.3
EXP92	1000	0.31	0.300	0.558	0.350	52.2
EXP88	1000	0.50	0.303	0.546	0.350	52.8
EXP68	1000	0.72	0.302	0.503	0.350	56.6
EXP56	1000	0.92	0.278	0.509	0.350	59.5
EXP84	1000	1.15	0.291	0.438	0.350	63.6
EXP83	1000	1.34	0.289	0.474	0.350	60.8
EXP64	1000	1.52	0.268	0.430	0.350	67.1
EXP91	1100	0.31	0.300	0.468	0.350	59.9
EXP86	1100	0.51	0.292	0.544	0.350	54.6
EXP69	1100	0.72	0.294	0.502	0.350	57.8
EXP74	1100	0.96	0.308	0.385	0.350	66.1
EXP80	1100	1.17	0.306	0.339	0.350	70.4
EXP81	1100	1.32	0.312	0.318	0.350	71.6
EXP65	1100	1.53	0.285	0.246	0.350	79.9

APPENDIX 4.3

Classification of Hysteresis Effect

Hysteresis isotherms can be divided into five subtypes according to de Boer (7). Each of the isotherms have a different explanation, but none of them are universally accepted.

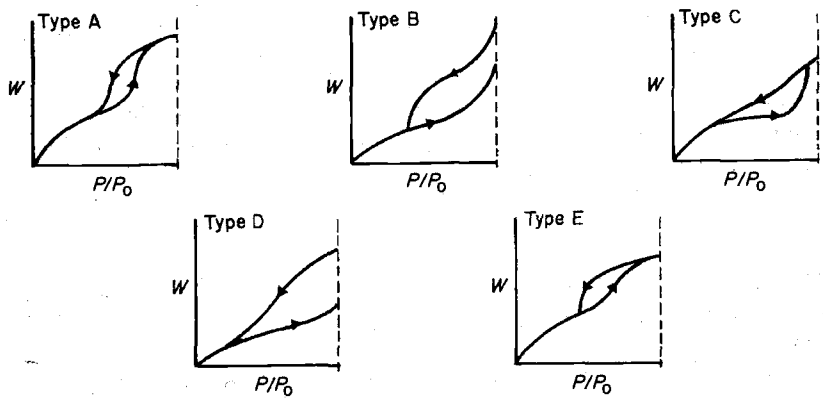

Figure A.4.3.1. Classification of the hysteresis effect according to de Boer (7).

Type A hysteresis is due to condensation producing a cylindrical meniscus with one radius of the curvature equal to the pore radius, and the other radius is the length of the pore. During desorption the meniscus is viewed hemispherical. Assuming the Kelvin equation applies, equation A.4.3-1 can be obtained and the hysteresis can be explained (7):

$$\left(\frac{P}{P_0}\right)_{ads} = \left(\frac{P}{P_0}\right)_{des} \qquad \text{(A.4.3-1)}$$

Equation A.4.3-1 predicts that pores of approximately cylindrical geometry with a given radius will fill at a higher relative pressure than they will empty. Type B hysteresis is associated with slit-shaped pores or the space between parallel plates. Type C hysteresis comes from pores with tapered or wedge-shaped pores with open ends. Type D curves are also from tapered or wedge-shaped pores but with narrow necks at one or both ends. Type E hysteresis result from bottle neck pores. BL char is a combination of type C and D hysteresis.

APPENDIX 4.4

Review of Estimating Average Pore Diameter

The average pore diameters were evaluated from the desorption pore volume curve using the Kelvin equation. The adsorption pore volume curve is generally used only for type E hysteresis, bottle-neck pores (see appendix 4.3). The Kelvin equation is given by equation A.4.4-1 (7).

$$\ln\frac{P}{P_0} = -\frac{2\gamma \overline{V}}{rRT}\cos\theta \qquad \text{(A.4.4-1)}$$

where P is the equilibrium vapor pressure of the condensed gas contained in a narrow pore of radius r, and P_0 is the equilibrium pressure of the same condensed gas exhibiting on a plane surface. The terms γ and $\overline{V}$ are the surface tension and molar volume of the condensed gas, respectively. α is the contact angle of the condensed gas and the pore wall as shown in figure A.4.4.1.

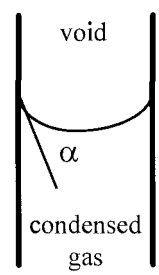

Figure A.4.4.1. Wetting angle during physisorption of a condensable gas such as N_2.

When it is assumed that the pores are cylindrical with zero wetting angle, the Kelvin equation can be simplified (7):

$$\ln\frac{P}{P_0} = \frac{-2\gamma \overline{V}}{rRT} \qquad \text{(A.4.4-2)}$$

This equation is the working equation for pore size analysis by adsorption methods, if no information is available about the pore geometry and the wetting angle. It relates the equilibrium vapor pressure of a curved surface, such as that of a liquid in a capillary or pore, to the equilibrium pressure of the same liquid on a plane surface.

For nitrogen at its normal boiling point at 77K, the Kelvin equation can be rewritten as (7):

$$r_K = \frac{4.15}{\log\frac{P}{P_0}}(\text{Å}) \qquad \text{(A.4.4-3)}$$

The term r_K indicates the radius into which condensation occurs at the required relative pressure. This radius, the Kelvin radius, is not the actual pore radius since some adsorption has already occurred on the pore wall prior to condensation. The actual pore radius is then given by (7):

$$r_P = r_K + t \qquad \text{(A.4.4-4)}$$

where t is the depth of the adsorbed film. It is given by the Halsey equation (7) assuming that the adsorbed film depth in a pore is the same as on a plane surface:

$$t = 3.54\left(\frac{5}{2.303\log\frac{P}{P_0}}\right)^{0.333} \qquad \text{(A.4.4-5)}$$

APPENDIX 4.5

Summary of BET Data

Table A.4.5.1. Summary of surface area, pore volume, and pore diameter data.

Char #	Data file #	T (°C)	Res.time (s)	X_C (-)	S.A. (m^2/g)	PoreVol. (cm^3/g)	PoreDia. (Å)	Spl.W. (g)
71	191	700	0.88	0.38	17.6	0.0691	157.2	0.0660
71	198	700	0.88	0.38	10.8	0.0563	209.2	0.3070
76	190	700	1.25	0.38	13.8	0.0670	194.2	0.0870
76	199	700	1.25	0.38	6.9	0.0361	208.2	0.5754
61	188	700	1.71	0.59	12.7	0.0506	159.7	0.0701
61	200	700	1.71	0.59	7.2	0.0433	241.6	0.5163
93	162	900	0.39	0.42	7.0	0.0265	152.3	0.1790
93	197	900	0.39	0.42	13.5	0.0492	145.9	0.1469
54	193	900	0.64	0.57	15.0	0.0569	152.1	0.0535
54	195	900	0.64	0.57	16.1	0.0673	167.6	0.0466
77	166	900	0.67	0.43	4.9	0.0299	243.1	0.1771
77	192	900	0.67	0.43	10.4	0.0543	209.4	0.1630
75	167	900	1.12	0.52	7.9	0.0277	141.2	0.1441
75	196	900	1.12	0.52	11.3	0.0428	151.9	0.1020
85	224	900	1.32	0.50	8.2	0.0339	164.9	0.3420
85	225	900	1.32	0.50	7.9	0.0334	169.1	0.3427
66	204	900	1.68	0.61	47.5	0.0541	45.5	0.1697
66	205	900	1.68	0.61	29.0	0.0447	61.7	0.1697
66	206	900	1.68	0.61	29.1	0.0428	58.8	0.1702
60	169	900	1.59	0.64	9.7	0.0322	132.4	0.1213
92	187	1000	0.31	0.52	12.2	0.0482	157.5	0.0869
88	184	1000	0.5	0.53	13.4	0.0515	154.2	0.0660
68	218	1000	0.72	0.57	12.3	0.0364	118.1	0.3490
68	220	1000	0.72	0.57	12.2	0.0306	100.6	0.3485
56	189	1000	0.92	0.60	18.6	0.0522	111.9	0.0751
84	201	1000	1.15	0.64	166.2	0.1203	21.3	0.2239
84	202	1000	1.15	0.64	182.0	0.1272	20.6	0.2232
83	212	1000	1.34	0.61	138.9	0.1041	22.1	0.4753
64	185	1000	1.52	0.67	205.5	0.1427	20.5	0.1337
91	160	1100	0.31	0.60	9.1	0.0465	204.3	0.1931
86	219	1100	0.51	0.55	42.8	0.0521	48.6	0.1680
86	221	1100	0.51	0.55	41.7	0.0521	49.9	0.1672
69	170	1100	0.72	0.58	11.3	0.0313	111.4	0.1467
74	209	1100	0.96	0.66	188.6	0.1224	19.1	0.1308
74	210	1100	0.96	0.66	187.4	0.1256	19.7	0.1308
74	211	1100	0.96	0.66	149.2	0.0928	18.1	0.1317
80	168	1100	1.17	0.70	253.6	0.1600	18.5	0.1371
81	203	1100	1.32	0.72	290.2	0.1701	17.3	0.0490
65	164	1100	1.53	0.80	329.6	0.2094	18.7	0.0637

APPENDIX 4.6

Summary of Char Specifications

Table A.4.6.1. Summary of char specifications.

Run #	T (°C)	Res.time (s)	Xc (%)	C (%)	Na (%)	K (%)	Cl (%)	$S^{=}$ (%)
71	700	0.88	38.5	31.0	19.0	0.05	1.00	0.87
76	700	1.25	38.1	31.7	22.4	0.08	1.00	0.56
61	700	1.71	59.4	28.8	20.3	na	0.84	0.72
93	900	0.39	40.6	31.7	20.4	0.26	1.00	0.77
54	900	0.64	57.0	28.6	18.9	0.06	0.69	1.04
77	900	0.67	43.2	31.7	18.8	0.09	0.69	0.72
75	900	1.12	51.6	31.0	19.8	0.06	0.81	1.80
85	900	1.32	50.1	29.9	20.0	0.07	0.81	1.88
66	900	1.68	64.0	27.3	19.1	0.08	0.83	2.75
60	900	1.59	64.1	27.4	18.4	0.04	0.66	4.66
92	1000	0.31	52.2	30.0	24.4	0.35	0.74	0.77
88	1000	0.50	52.8	30.3	18.0	0.20	0.74	1.79
68	1000	0.72	57.0	30.2	18.8	0.04	0.82	2.19
56	1000	0.92	59.5	27.8	17.4	0.25	0.75	2.33
84	1000	1.15	63.6	29.1	19.8	0.06	0.64	2.52
83	1000	1.34	61.0	28.9	23.9	0.14	0.67	2.90
64	1000	1.52	67.1	26.8	20.9	0.03	0.82	2.24
91	1100	0.31	59.9	29.1	19.8	0.22	0.22	1.49
86	1100	0.51	55.0	29.2	18.1	0.23	0.23	2.81
69	1100	0.72	57.8	29.4	19.9	0.03	0.03	2.84
74	1100	0.96	66.0	30.8	18.5	0.18	0.18	2.80
80	1100	0.96	70.4	30.6	18.5	0.13	0.13	3.22
81	1100	1.32	71.6	31.2	19.2	0.14	0.14	2.46
65	1100	1.53	79.9	28.5	15.6	0.05	0.05	3.92

na = not available

APPENDIX 4.7

Summary of Chemisorption Data

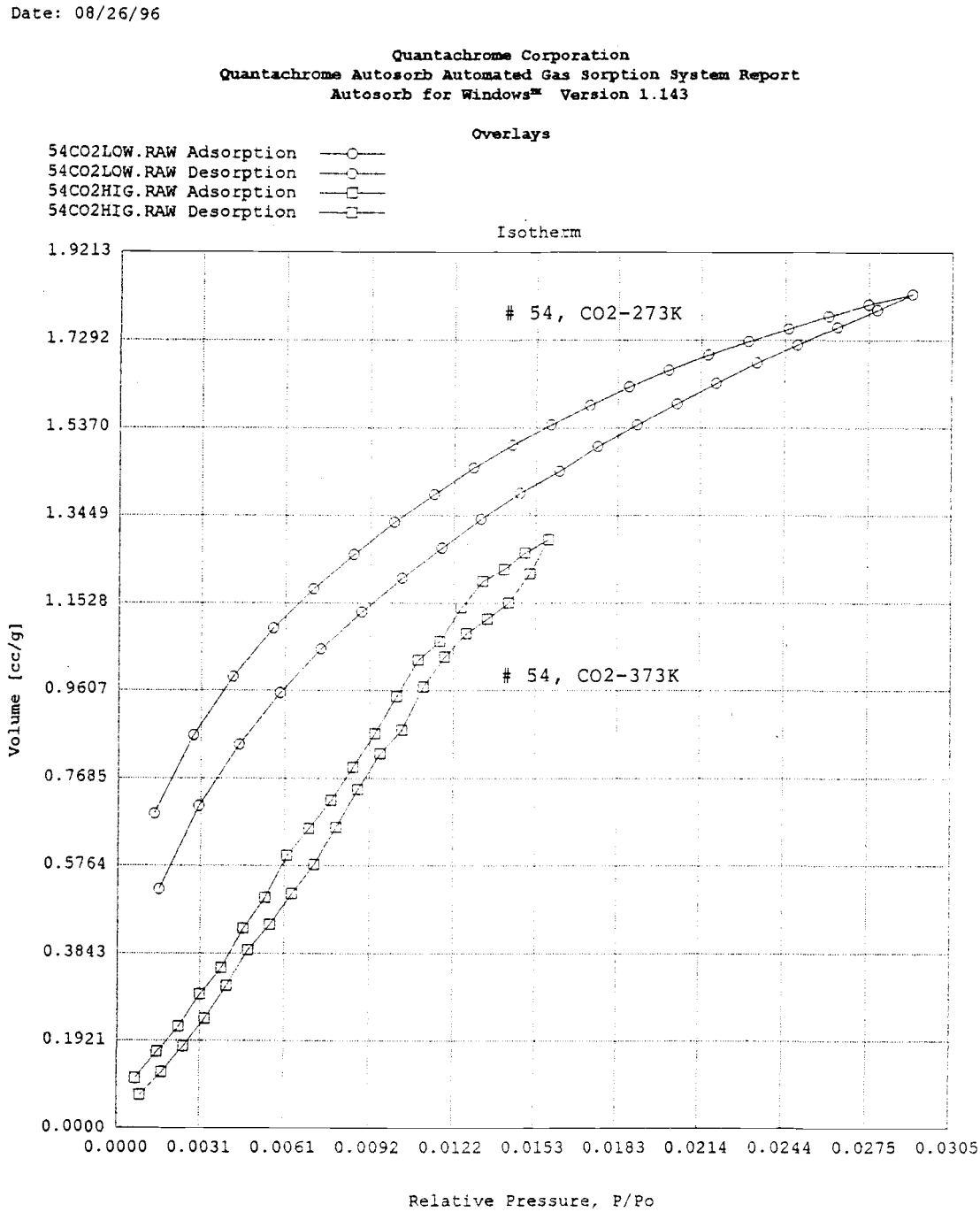

Figure A.4.7.1. CO_2 isotherms at 273 and 373K for char #54.

Date: 08/26/96

Quantachrome Corporation
Quantachrome Autosorb Automated Gas Sorption System Report
Autosorb for Windows™ Version 1.143

Sample ID	Sample # 54				
Description	Biomass Char				
Comments	OREGON STATE UNIVERSITY				
Sample Weight	0.4795 g				
Adsorbate	Carbon Dioxide	**Outgas Temp**	125.0 °C	**Operator**	CAL
Cross-Sec Area	21.0 Å²/molecule	**Outgas Time**	24.0 hrs	**Analysis Time**	205.8 min
NonIdeality	9.100E-06	**P/Po Toler**	1	**End of Run**	05/08/96 23:50
Molecular Wt	44.0100 g/mol	**Equil Time**	3	**File Name**	54CO2LOW.RAW
				Station #	1

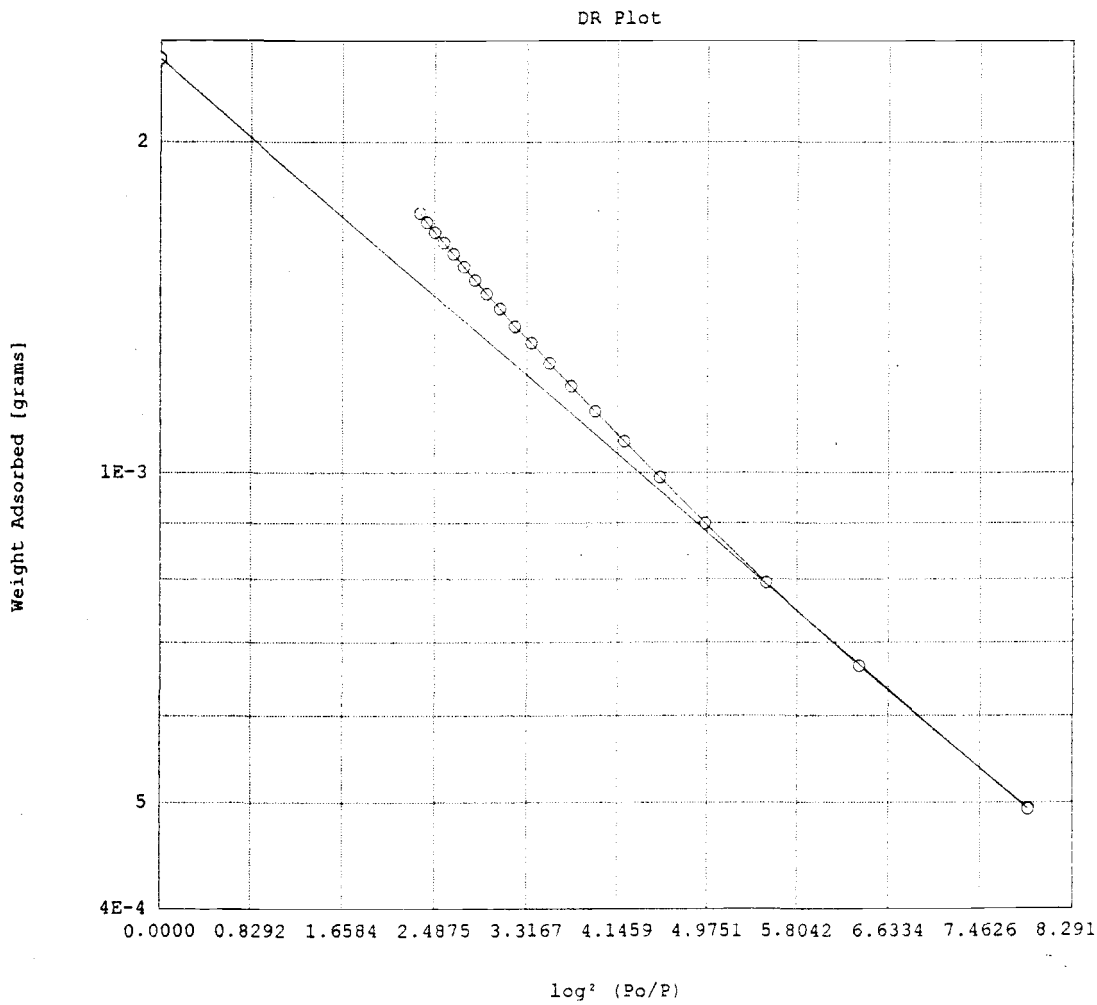

Figure A.4.7.2. Dubinin-Raduschkevich plot for CO_2 for char #54.

Date: 08/26/96 Page 1

Quantachrome Corporation
Quantachrome Autosorb Automated Gas Sorption System Report
Autosorb for Windows™ Version 1.143

Sample ID	Sample # 54				
Description	Biomass Char				
Comments	OREGON STATE UNIVERSITY				
Sample Weight	0.4795 g				
Adsorbate	Carbon Dioxide	Outgas Temp	125.0 °C	Operator	CAL
Cross-Sec Area	21.0 Å²/molecule	Outgas Time	24.0 hrs	Analysis Time	205.8 min
NonIdeality	9.100E-06	P/Po Toler	1	End of Run	05/08/96 23:50
Molecular Wt	44.0100 g/mol	Equil Time	3	File Name	54CO2LOW.RAW
				Station #	1

DR Method Micro-Pore Analysis

log^2.00(Po/P)	Weight Adsorbed [grams]
7.89693E+00	4.935E-04
6.37267E+00	6.655E-04
5.52350E+00	7.929E-04

Slope = -8.658E-02

Y - Intercept (anti-log) = 2.379E-03

Correlation Coefficient = 0.999911

Average Pore Width = 1.062E+00 nm

Adsorption Energy (Eo) = 2.448E+01 kJ/mol

Micro Pore Volume = 4.753E-03 cc/g

Micro Pore Surface Area = 1.426E+01 m²/g

Figure A.4.7.3. Summary of data from Dubinin-Raduschkevich analysis for char #54.

Date: 08/26/96

Quantachrome Corporation
Quantachrome Autosorb Automated Gas Sorption System Report
Autosorb for Windows℠ Version 1.143

Sample ID	Sample # 54				
Description	Biomass Char				
Comments	OREGON STATE UNIVERSITY				
Sample Weight	0.4795 g				
Adsorbate	Carbon Dioxide	**Outgas Temp**	125.0 °C	**Operator**	CAL
Cross-Sec Area	21.0 Å²/molecule	**Outgas Time**	24.0 hrs	**Analysis Time**	205.8 min
NonIdeality	9.100E-06	**P/Po Toler**	1	**End of Run**	05/08/96 23:50
Molecular Wt	44.0100 g/mol	**Equil Time**	3	**File Name**	54CO2LOW.RAW
				Station #	1

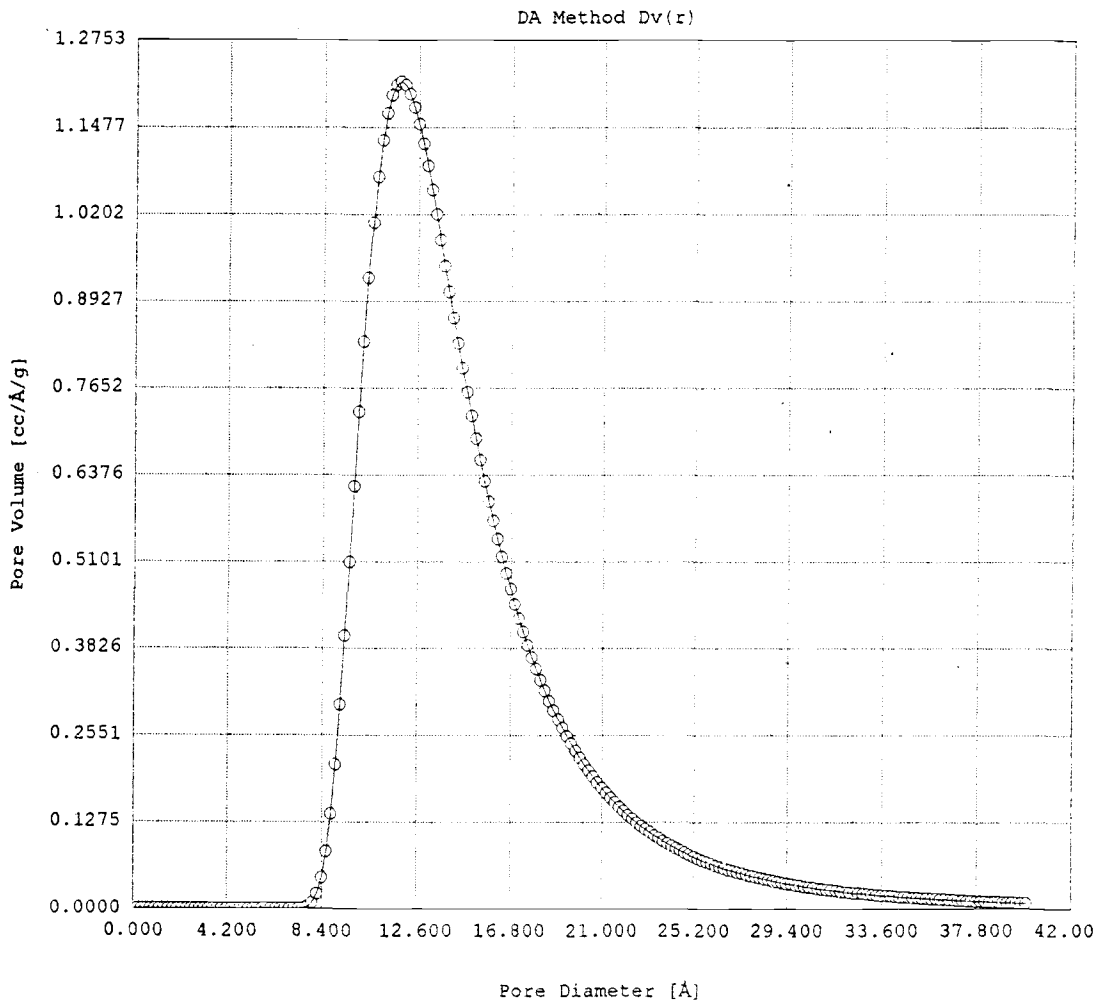

Figure A.4.7.4. Pore distribution plot for char #54 using the Dubinin-Astakhov method.

Date: 08/29/96

Quantachrome Corporation
Quantachrome Autosorb Automated Gas Sorption System Report
Autosorb for Windows® Version 1.142

Sample ID	Sample # 54	File Name	AS682701.CRW
Description	Biomass Char	Comments	OREGON STATE UNIVERSITY
Analysis Temp	100.0 °C	Operator	CAL
Sample Wt	0.2125 g	Treatment Temp	1000.0°C
Metal Loading	100.00 Percent	Treatment Time	0.5 hrs
Metal	Carbon	Gas	Oxygen
Metal Mol. Wt.	12.0000 g/mol	Gas Mol. Wt.	31.9990 g/mol
Cross-Sec. Area	8.3000 Å²	Cross-Sec. Area	14.1000 Å²
Metal Density	2.126 g/cc	Stoichiometry	2.00 Atoms/Molec

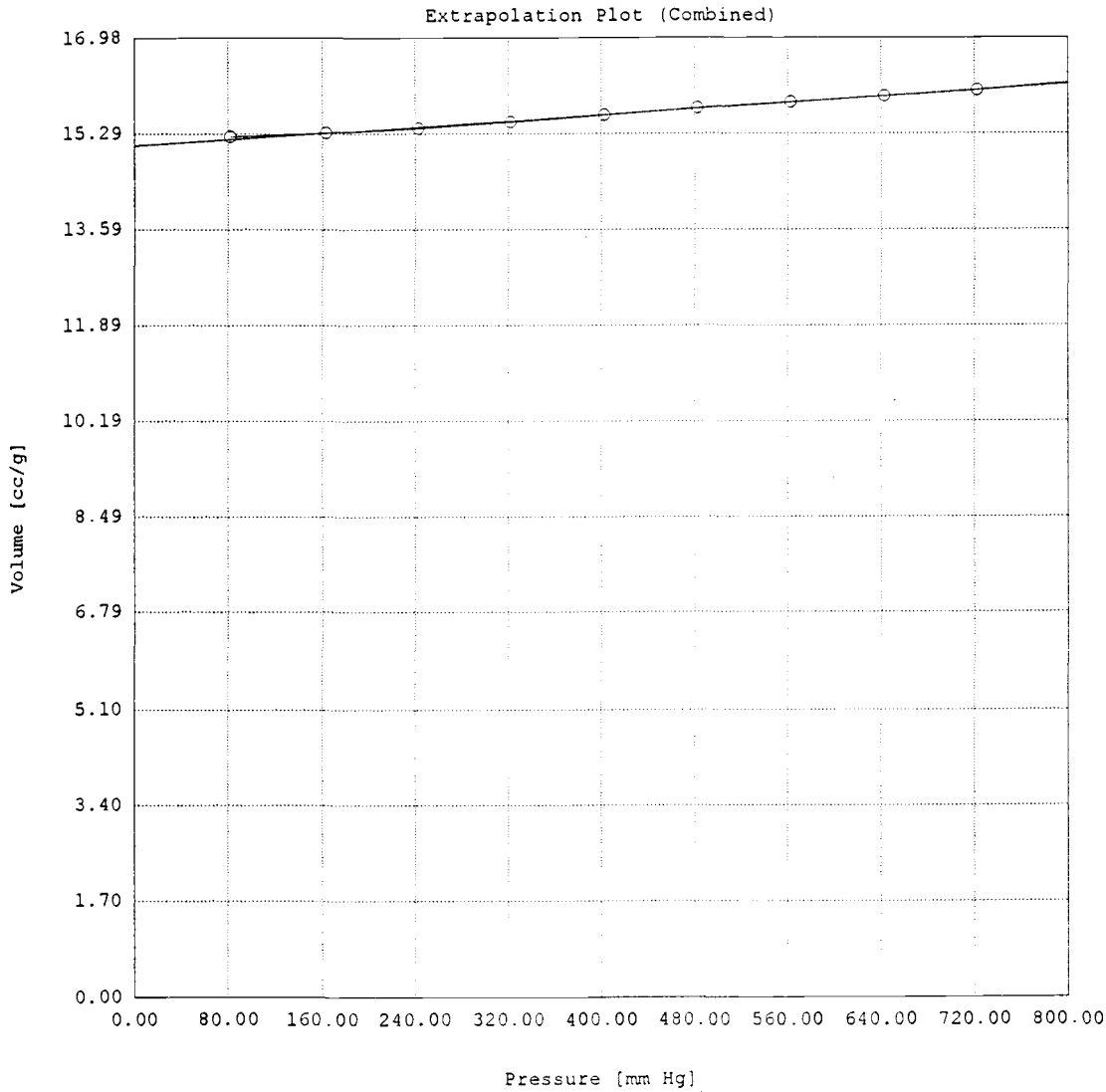

Figure A.4.7.5. Oxygen isotherm at 100°C for char #54.

Date: 08/29/96

Quantachrome Corporation
Quantachrome Autosorb Automated Gas Sorption System Report
Autosorb for Windows® Version 1.142

Sample ID	Sample # 54	File Name	AS682701.CRW
Description	Biomass Char	Comments	OREGON STATE UNIVERSITY
Analysis Temp	100.0 °C	Operator	CAL
Sample Wt	0.2125 g	Treatment Temp	1000.0°C
Metal Loading	100.00 Percent	Treatment Time	0.5 hrs
Metal	Carbon	Gas	Oxygen
Metal Mol. Wt.	12.0000 g/mol	Gas Mol. Wt.	31.9990 g/mol
Cross-Sec. Area	8.3000 Å²	Cross-Sec. Area	14.1000 Å²
Metal Density	2.126 g/cc	Stoichiometry	2.00 Atoms/Molec

Extrapolation Data (Combined)

Active Metal Surface Area = 6.726E+01 m²/g

Percent Metal Dispersion = 1.615E+00 %

Average Crystallite Size = 4.196E+02 Å

Slope = 1.348E-03

Y - Intercept = 1.508E+01 cc/g

Monolayer Uptake (Nm) = 6.727E+02 µmol/g

Correlation Coefficient = 0.998408

Figure A.4.7.6. Summary of data from oxygen isotherm for char #54.

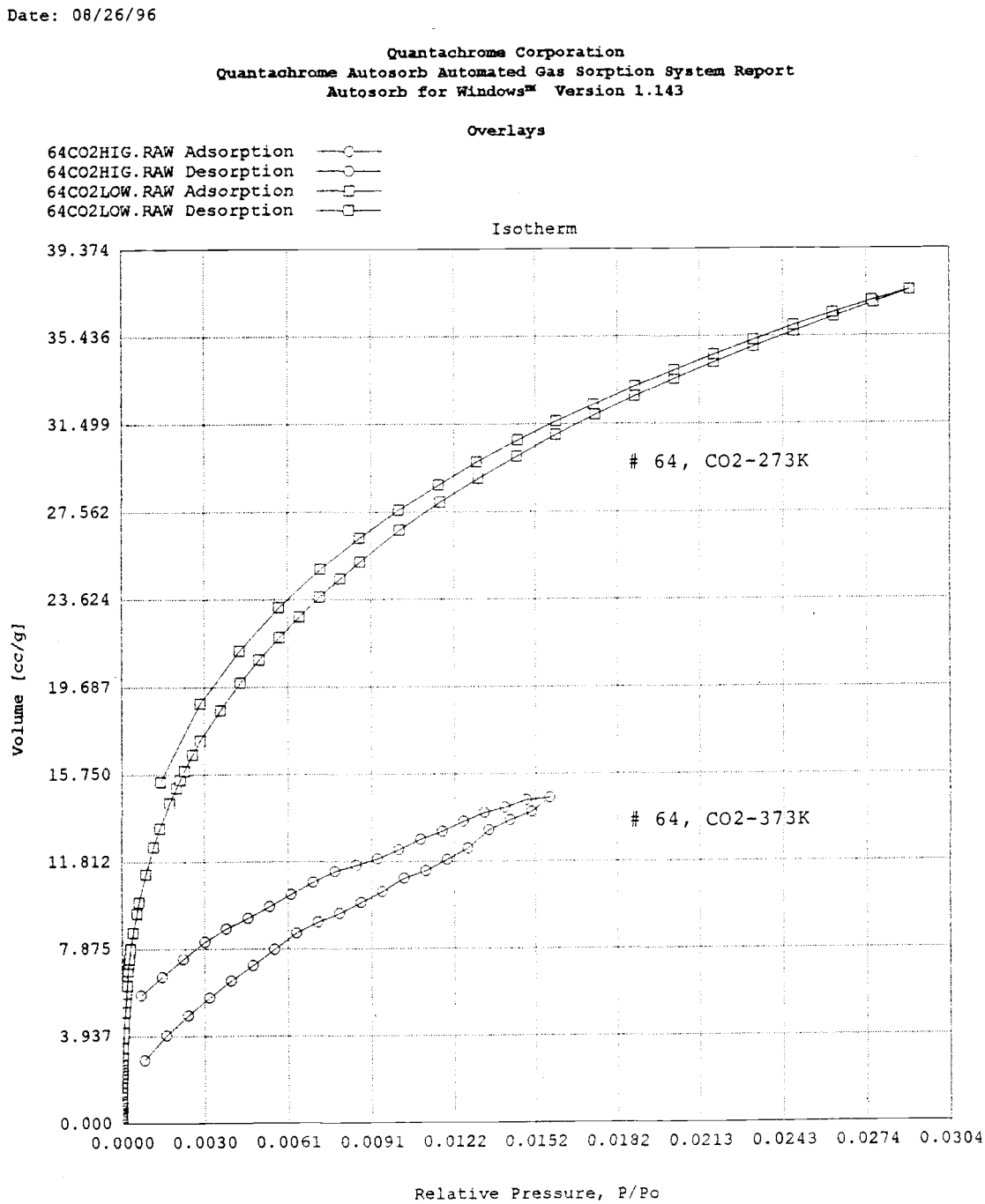

Figure A.4.7.7. CO_2 isotherms at 273 and 373K for char #64.

Date: 08/26/96

Quantachrome Corporation
Quantachrome Autosorb Automated Gas Sorption System Report
Autosorb for Windows™ Version 1.143

Sample ID	Sample # 64				
Description	Biomass Char				
Comments	OREGON STATE UNIVERSITY				
Sample Weight	0.5158 g				
Adsorbate	Carbon Dioxide	**Outgas Temp**	125.0 °C	**Operator**	CAL
Cross-Sec Area	21.0 Å²/molecule	**Outgas Time**	24.0 hrs	**Analysis Time**	1213.0 min
NonIdeality	9.100E-06	**P/Po Toler**	0	**End of Run**	05/31/96 18:18
Molecular Wt	44.0100 g/mol	**Equil Time**	3	**File Name**	64CO2LOW.RAW
				Station #	1

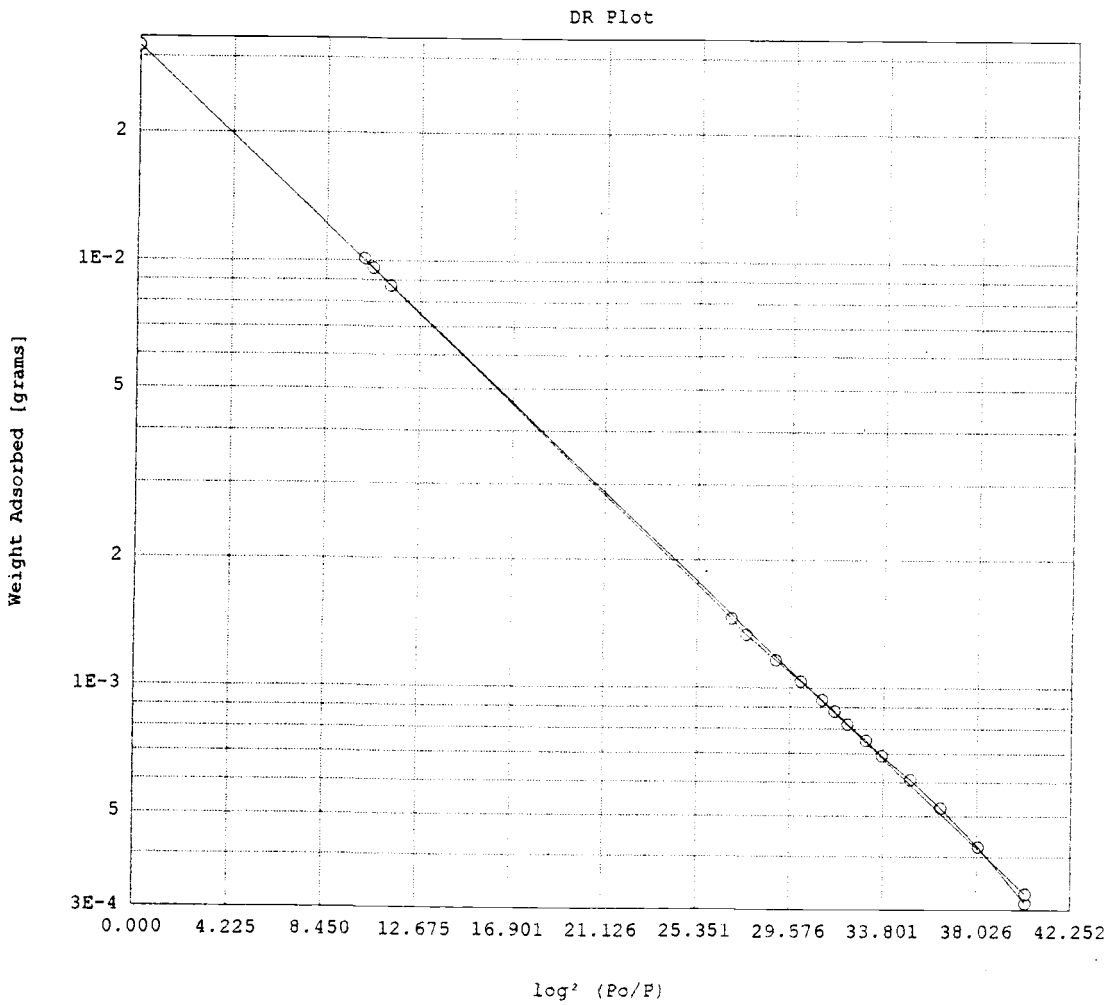

Figure A.4.7.8. Dubinin-Raduschkevich plot for CO_2 for char #64.

Date: 08/26/96 Page 1

Quantachrome Corporation
Quantachrome Autosorb Automated Gas Sorption System Report
Autosorb for Windows™ Version 1.143

Sample ID	Sample # 64				
Description	Biomass Char				
Comments	OREGON STATE UNIVERSITY				
Sample Weight	0.5158 g				
Adsorbate	Carbon Dioxide	Outgas Temp	125.0 °C	Operator	CAL
Cross-Sec Area	21.0 Å²/molecule	Outgas Time	24.0 hrs	Analysis Time	1213.0 min
NonIdeality	9.100E-06	P/Po Toler	0	End of Run	05/31/96 18:18
Molecular Wt	44.0100 g/mol	Equil Time	3	File Name	64CO2LOW.RAW
				Station #	1

DR Method Micro-Pore Analysis

log^2.00(Po/P)	Weight Adsorbed (grams)
4.02396E+01	3.103E-04
3.81032E+01	4.226E-04
3.63972E+01	5.213E-04
3.50258E+01	6.068E-04
3.37413E+01	6.913E-04
3.30333E+01	7.506E-04
3.22076E+01	8.209E-04
3.16032E+01	8.783E-04
3.10487E+01	9.352E-04
3.00767E+01	1.035E-03
2.89449E+01	1.162E-03
2.76029E+01	1.335E-03
2.69245E+01	1.454E-03
1.13571E+01	8.712E-03
1.05847E+01	9.581E-03
1.01881E+01	1.009E-02

Slope = -4.944E-02

Y - Intercept (anti-log) = 3.186E-02

Correlation Coefficient = 0.999812

Average Pore Width = 8.024E-01 nm

Adsorption Energy (Eo) = 3.240E+01 kJ/mol

Micro Pore Volume = 5.917E-02 cc/g

Micro Pore Surface Area = 1.775E+02 m²/g

Figure A.4.7.9. Summary of data from Dubinin-Raduschkevich analysis for char #64.

Date: 08/26/96

Quantachrome Corporation
Quantachrome Autosorb Automated Gas Sorption System Report
Autosorb for Windows™ Version 1.143

Sample ID	Sample # 64				
Description	Biomass Char				
Comments	OREGON STATE UNIVERSITY				
Sample Weight	0.5158 g				
Adsorbate	Carbon Dioxide	**Outgas Temp**	125.0 °C	**Operator**	CAL
Cross-Sec Area	21.0 Å²/molecule	**Outgas Time**	24.0 hrs	**Analysis Time**	1213.0 min
NonIdeality	9.100E-06	**P/Po Toler**	0	**End of Run**	05/31/96 18:18
Molecular Wt	44.0100 g/mol	**Equil Time**	3	**File Name**	64CO2LOW.RAW
				Station #	1

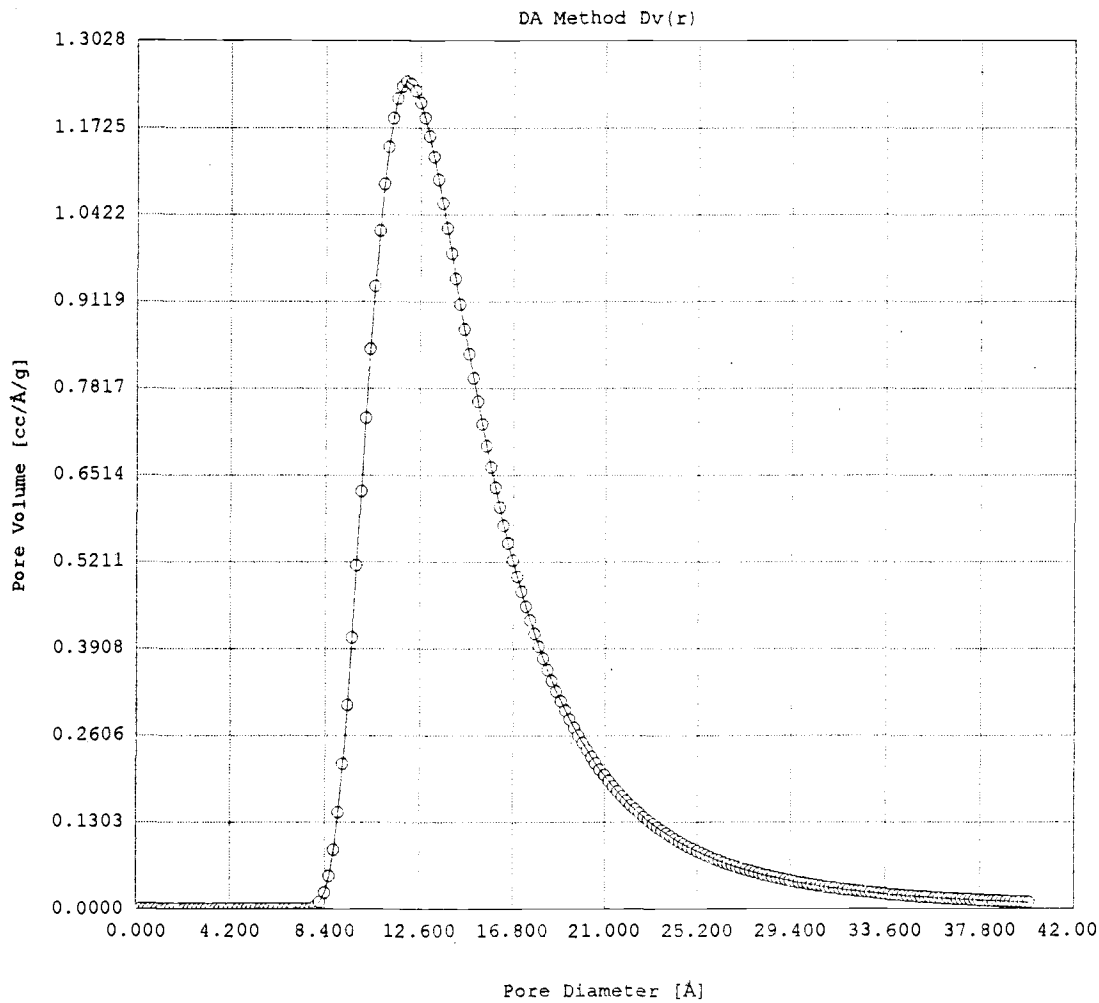

Figure A.4.7.10. Pore distribution plot for char #64 using the Dubinin-Astakhov method.

Date: 08/29/96

Quantachrome Corporation
Quantachrome Autosorb Automated Gas Sorption System Report
Autosorb for Windows® Version 1.142

Sample ID	Sample # 64	File Name	AS682801.CRW
Description	Biomass Char	Comments	OREGON STATE UNIVERSITY
Analysis Temp	100.0 °C	Operator	CAL
Sample Wt	0.1663 g	Treatment Temp	1000.0°C
Metal Loading	100.00 Percent	Treatment Time	0.5 hrs
Metal	Carbon	Gas	Oxygen
Metal Mol. Wt.	12.0000 g/mol	Gas Mol. Wt.	31.9990 g/mol
Cross-Sec. Area	8.3000 Å²	Cross-Sec. Area	14.1000 Å²
Metal Density	2.126 g/cc	Stoichiometry	2.00 Atoms/Molec

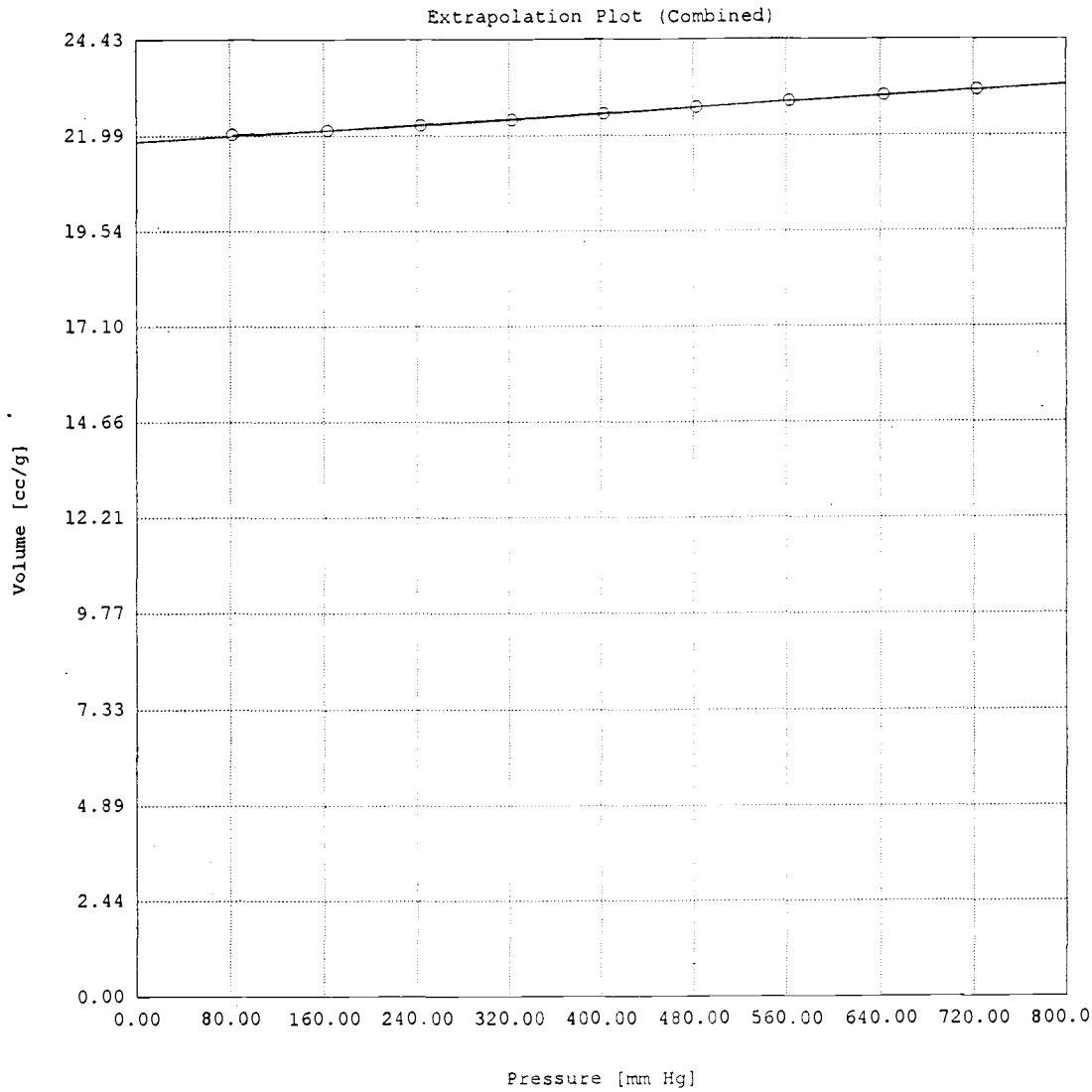

Figure A.4.7.11. Oxygen isotherm at 100°C for char #64.

Date: 08/29/96

Quantachrome Corporation
Quantachrome Autosorb Automated Gas Sorption System Report
Autosorb for Windows® Version 1.142

Sample ID	Sample # 64	File Name	AS682801.CRW
Description	Biomass Char	Comments	OREGON STATE UNIVERSITY
Analysis Temp	100.0 °C	Operator	CAL
Sample Wt	0.1663 g	Treatment Temp	1000.0°C
Metal Loading	100.00 Percent	Treatment Time	0.5 hrs
Metal	Carbon	Gas	Oxygen
Metal Mol. Wt.	12.0000 g/mol	Gas Mol. Wt.	31.9990 g/mol
Cross-Sec. Area	8.3000 Å²	Cross-Sec. Area	14.1000 Å²
Metal Density	2.126 g/cc	Stoichiometry	2.00 Atoms/Molec

Extrapolation Data (Combined)

Active Metal Surface Area =	9.738E+01 m²/g
Percent Metal Dispersion =	2.338E+00 %
Average Crystallite Size =	2.898E+02 Å
Slope =	1.785E-03
Y - Intercept =	2.183E+01 cc/g
Monolayer Uptake (Nm) =	9.739E+02 µmol/g
Correlation Coefficient =	0.998911

Figure A.4.7.12. Summary of data from oxygen isotherm for char #64.

Chapter 5
Application of Molecular Beam Mass Spectrometry to the Study of Black Liquor Char Gasification

INTRODUCTION

Mass spectrometry is an analytical technique that is used to identify unknown compounds, quantify known materials, and to elucidate the structural and chemical properties of molecules. Mass spectrometry can be used as a qualitative tool to identify and characterize different materials of interest. This technique is attractive because of its speed, sensitivity, and reliability. Its development traces back to 1913 when J.J.Thompson first used mass spectrometry to show that neon consisted of two nonradioactive isotopes (1). This was significant because it demonstrated that elements existed as isotopes with different atomic masses. However, the accuracy of the pioneering equipment was not very good. The highest mass numbers that could be detected were around 150. Today, mass spectrometry is one of few methods that can accurately determine molecular weights up to 10000, and approximately up to 100000 and higher (1). Detection of compounds can be accomplished down to one part in 10^{12} at its best.

OBJECTIVES

The objective of this chapter is to gain a general understanding of molecular beam mass spectrometry, and apply it to the study of black liquor char gasification in a convective flow reactor in gas mixtures of CO_2 , O_2, and He at 1100°C. The second objective was to investigate the effect of gas composition by identifying the gas species evolved as a function of time. The third objective was to study the effect on the results of char samples obtained at different temperatures and pyrolysis times. The last objective

was to develop a model for carbon release, and based on the model, find out to what extent the reaction rates of CO_2 and O_2 are additive at 1100°C.

THEORY OF MOLECULAR BEAM MASS SPECTROMETRY

A mass spectrometer measures the masses of individual molecules that have been converted into ions, i.e. molecules that have been electrically charged. In fact, a mass spectrometer does not measure the mass directly, but rather the mass-to-charge ratio of the ions. The unit of mass is the dalton (Da), which is defined as 1/12 of the mass of a single atom of the isotope carbon-12. The electrical charge is a quantized property, which can exist only in integral multiples of the fundamental charge, z. For an electron it is negative and a proton positive. Most ions encountered in mass spectrometry have just one charge (z=1), so the m/z value is numerically equal to the ionic mass in Da.

All mass spectrometers are constructed to separate ions of gas-phase molecules and atoms according to their masses. They are designed to carry out four principal operations: (a) introduction of a sample as a gas, (b) ionization of the gas phase molecules, (c) separation by mass, (d) detection of separated species. Although the principle of mass spectral measurement is simple and easily understood, this simplicity does not extend to the instrumentation. A typical high-resolution mass spectrometer is a complex electronic and mechanical device that is expensive to construct and maintain. Figure 5.1 shows a blockdiagram that illustrates the sequential functions in a mass spectrometer.

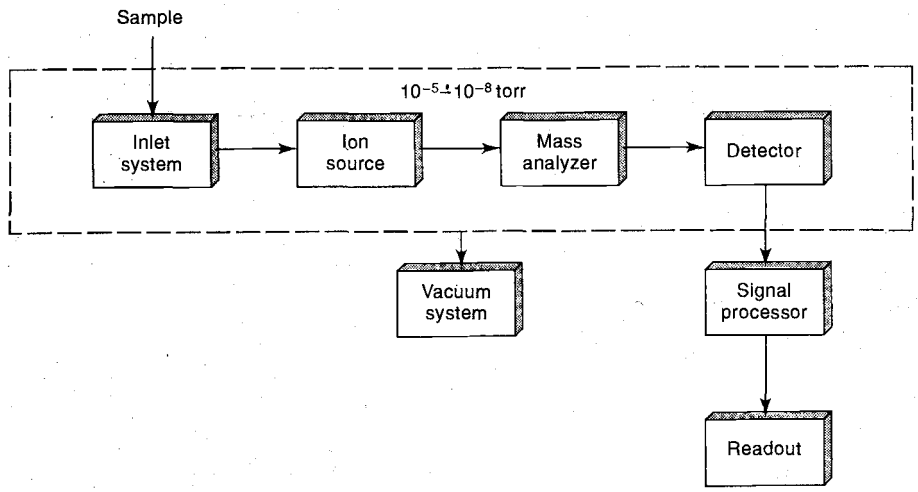

Figure 5.1. A block diagram of the sequential functions in a mass spectrometer (2).

Early mass spectrometers required the samples to be gaseous, but today the applicability has been extended to include solid samples as well. A beam of gas is introduced into a vacuum chamber through an inlet and ionized in the ion source. The ions, which are now all in the gas phase, are sorted in the mass filter according to their mass-to-charge ratios, after which they are collected by a detector. In the detector, the ions generate an electrical signal that is proportional to the number of ions. The data acquisition system records these electrical signals as a function of mass-to-charge ratio.

The characteristics of a mass spectrum

A mass spectrum is a graph of ion abundance versus mass-to-charge ratio. The ions and their abundances serve to establish the molecular weight and structure of the compound being mass analyzed. For example, a mass spectrum of CO_2 is shown in Figure 5.2. Since the ionization process frequently breaks up the molecule (fragmentation), ion intensities appear in the spectrum at lower m/z values than the parent ion.

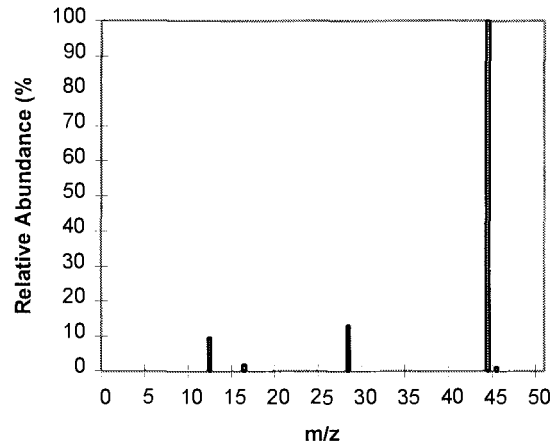

Figure 5.2. Mass spectrum for carbon dioxide showing fragmentation effects.

Figure 5.2 shows that the ionized CO_2 molecule has a mass-to-charge ratio = 44. The cleavage of a carbon-oxygen bond results in the production of ionized CO and atomic oxygen according to the following reactions:

1. $CO_2 + e^- \rightarrow CO^+ + O + 2e^-$
2. $CO_2 + e^- \rightarrow CO + O^+ + 2e^-$

This results in signals in the mass spectrum at m/z = 28 and 16. The loss of two neutral oxygen atoms results in an additional fragment at m/z = 12 for carbon. In Figure 5.2 all the ions are positively charged, but it is possible to generate and detect negative ions as well.

Experimental approach

Since the sample to be investigated is volatile, and contains reactive alkali species, it is evident that regular experimental systems suffer from thermophoresis. A molecular beam mass spectrometer (MBMS) is ideal when the product gases contain highly condensable and reactive vapors. The integrity of the highly reactive molecules present in the product gases can be preserved by free-jet expansion, which effectively quenches chemical reactions and therefore eliminates condensation and thermophoresis.

However, molecular beam generation has undergone an evolution for more than 80 years. The first beams of neutral particles moving in straight lines were produced more than 70 years ago by Dunoyer (3). The beams were formed by allowing a vapor to effuse from a closed chamber through a small hole into an evacuated chamber. The vapor pressure was kept low to maintain molecular flow, which means that the atoms move through the hole and within the beam without undergoing collisions. This simple principle is still the basis for all effusive beams.

The effusion of gases and vapors from a thin-walled circular orifice, a slit, or a short channel was almost the only method for producing molecular beams until between 1950 and 1960. At that time Kantrowitz and Grey suggested the use of gas dynamic expansion through a nozzle for beam formation (3). This suggestion initiated a large number of both theoretical and experimental investigations that led to the development of nozzle beams and finally to a replacement of the conventional effusive sources by nozzle sources.

The free-jet molecular beam

A free-jet molecular beam is a neutral supersonic beam produced by continuum jet expansion through a nozzle. The underexpanded free-jet is formed when a high-pressure gas source expands into a low-pressure ambient environment through a pinhole, also called a nozzle. The term nozzle is commonly used because the same type of expansion

occurs from converging-diverging supersonic rocket nozzles. However, molecular beam researchers have done away with the diverging portion of the nozzle - hence the term "free-jet". The main features of a free-jet are that once the molecules enter the free molecular flow region of the expansioin collisions are minimized and the internal degrees of freedom of the gas are cooled, thus, decreasing molecular rotations and vibrations. Figure 5.3 shows the complicated features of a free jet expansion under continuum conditions.

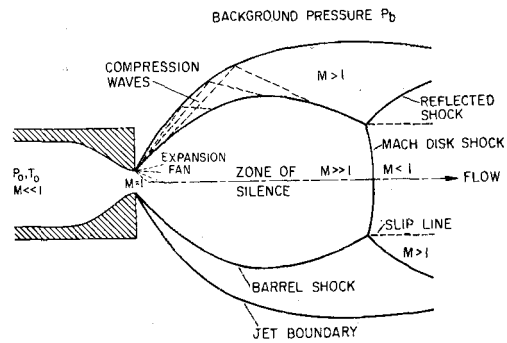

Figure 5.3. Continuum free-jet expansion from a nozzle reduces the internal energy of molecules in the beam so that collisions are absent preserving highly reactive and condensable species (3).

Molecular beam researchers complicate the situation in Figure 5.3 by placing a wall in front of the expansion with a small skimmer aperture to extract the centerline beam. The source in Figure 5.3 is a short converging nozzle for which the accelerating flow can be approximated as an isentropic flow with negligible viscous and heat conduction effects as well as diffusion effects. The reason for this approximation is that the molecular diffusion time is much longer than the characteristic mean flow time. This ratio of times is approximately the Mach number, a flow field property, over the Knudsen number, a transport property. Typically, at the nozzle exit this ratio of times exceeds 100 and diffusion effects are too slow to be important in the core of the supersonic jet. Obviously,

near solid boundaries, where the velocity and Mach number approach zero, transport effects become important - also known as the boundary layer. The Mach number is defined as (4):

$$M = \frac{V}{a} = \text{(velocity of gas)} \div \text{(velocity of sound in the gas)} \quad (5\text{-}1)$$

For an ideal gas, the speed of sound is (3):

$$a = \sqrt{\frac{\gamma R T}{W}} \quad (5\text{-}2)$$

where γ is the heat capacity ratio, W the molecular weight, R the ideal gas constant, and T the absolute temperature. The Knudsen number is given by (4):

$$Kn = \frac{\lambda}{d} = \text{(mean free path of molecules)} \div \text{(diameter of flow channel)} \quad (5\text{-}3)$$

and the mean free path by (5):

$$\lambda = \frac{1}{\sqrt{2}\,\pi\sigma^2 n_0} = \text{(average distance traveled in 1sec)} \div \text{(nr. of collisions per sec)} \quad (5\text{-}4)$$

where σ is the collision diameter and n_0 the atomic population density.

The gas accelerates from a negligibly small velocity, called the stagnation state (P_0, T_0) to a mean velocity around Mach number M equal to 1. This occurs when the imposed pressure difference provides a pressure ratio P_0/P_b that exceeds the critical value of about 2.1, where P_b is the background pressure shown in Figure 5.3. This ratio is a function of γ, a property of the fluid species (5/3 for Helium). If the pressure ratio is less than this value, then the flow will exit subsonically, with an exit pressure nearly equal to P_b without any further expansion. As P_0/P_b increases beyond its critical value, M equals 1 at the nozzle throat, and the exiting flow is known as choked flow. It is called choked because the mass flux out of the aperture will not exceed M=1 regardless of how low the exit chamber pressure has been pumped. The exit pressure is independent of P_b and approximately one half of P_0 ($P_{exit} \sim 0.5$ atm). Since the pressure at the exit exceeds P_b,

the flow is said to be underexpanded and a subsequent expansion occurs as the flow attempts to adjust to the low background pressure, P_b~21 mtorr, in the exit chamber.

Supersonic flow has two characteristics that make the expansion interesting. First, unlike subsonic flow, a supersonic flow increases velocity so that M>>1 as the flow area increases. Second, a supersonic flow cannot sense downstream boundary conditions, such as the presence of a solid surface. The fact that information propagates at the speed of sound whereas the fluid moves faster, results in the occurrence of shock waves, the barrel shock at the sides and the Mach disk shock normal to the centerline. This system of shocks are very thin nonisentropic regions of large density, pressure, temperature, and velocity gradients, that provide a mechanism by which the flow can adjust to downstream boundary conditions. The region between the barrel shock and the jet boundary is a viscous, heat conducting, nonisentropic region. The core of the expansion is isentropic and the properties in this region are independent of P_b because, as earlier mentioned, the supersonic flow is not aware of any external condition. It is from this isentropic core one would like to extract a molecular beam to pass into a mass spectrometer.

Continuum properties of free-jet expansion

The isentropic, compressible flow of a single component ideal gas is characterized by a constant heat capacity ratio. The fluid flow equations to be solved are the equations of mass, momentum, and energy conservation. Neglecting viscosity and heat conduction, and assuming steady state, a complete set of equations are given by equations 5-5 to 5-9 (3):

Mass:	$\nabla \cdot (\rho V) = 0$	(5-5)
Momentum:	$\rho V \cdot \nabla V = -\nabla P$	(5-6)
Energy:	$\rho V \cdot \nabla(h+V^2/2) = \rho V \cdot \nabla(h_0) = 0$	(5-7)
	or h_0 = constant along streamlines	
Equation of state:	$P = \rho RT$ (ideal gas)	(5-8)
Thermal eq. of state:	$dh = \hat{C}_p dT$ (ideal gas)	(5-9)

A rigorous solution is difficult to obtain for the complete fluid flow equations. Since the subsonic flow is contained by the converging nozzle walls, viscous effects are important in the boundary layer near the walls. The isentropic part of the subsonic flow is usually approximated as a quasi one-dimensional compressible flow. This approximation treats the flow properties as constant across any cross section of the nozzle. It can be shown that for isentropic, quasi one-dimensional flow equation 5-5 can be integrated to obtain:

$$\rho VA = \text{constant} = \text{mass flow rate} \qquad (5\text{-}10)$$

where A is the cross-sectional area and V the one-dimensional flow speed. By assuming that M=1 it is possible to obtain a relation for mass flow rate from a nozzle source. This equation as well as the thermodynamic properties of the free jet is well documented in the literature and will not be repeated here (3).

Ion generation

Upon supersonic expansion, the neutral gas beam enters the ionization cell. Here a stream of electrons is accelerated across the molecular beam. The molecules in the beam become ionized according to the reaction:

3. $mol + e^- \rightarrow mol^+ + 2e^-$

If the beam of electrons are accelerated at a low voltage, they move slowly and the molecules tend to remain intact as long as this voltage is below the ionization potential of the molecules of interest. As the voltage is increased, some molecules will become ionized. At a high voltage, the molecules are shattered into well-defined fragments because enough excess energy is impacted into the molecules that bonds are broken. Each fragment is charged and it is possible that the fragments could recombine to form molecules that were not present in the original sample. This is being inhibited by maintaining a high vacuum in the ionization chamber. A compromise is necessary in selecting the ionization voltage to ensure efficient ionization but restricting excessive fragmentation, getting sufficient sensitivity, and obtaining a high signal-to-noise ratio. A typical ionization potential varies below 10 to 40 eV.

Ion sources are sorted out on the basis of the physical method used for producing the ions. These methods consist of surface, hot-filament electron-impact, field emission ionizers, and lasers. Here, special consideration is given only to the ion source used, the electron-impact ion source. Whatever ion source is implemented, a common desired property is stability in ion concentration. If the source is not stable over the time needed to run a spectrum, then the peak abundances cannot be compared.

Electron Impact Ion Sources (EI)

A simple method for ionizing neutral molecules may be obtained by bombarding the molecules with a beam of electrons. When energetic electrons collide with neutral species, a mixture of positive ions, negative ions and neutral species is generated. The most probable reaction is the formation of singly charged positive ions with emission of a secondary electron. More complex reactions may lead to the formation of negatively charged ions. The probability of different processes occurring depends on the electron energy and the nature of the neutral gas. Figure 5.4 shows the salient features and the operating principle of an EI source.

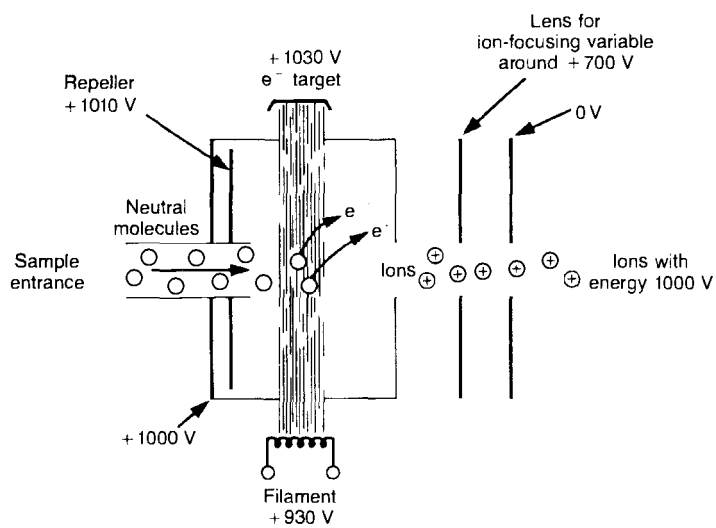

Figure 5.4. Ions are formed by an electron beam colliding with a neutral molecular beam. Positive ions are propelled into the mass analyzer by applying voltages to a lens system, and by maintaining a positive potential between the ion source and the mass analyzer. The role of the repeller is to further assist in focusing the ions into the mass analyzer. Negative ions and electrons are attracted to a positively charged electron collector (target). Neutral species that are not ionized are pumped away. The figure is adapted from (6).

The ionizer consists essentially of three parts: a thermoionic electron emitter (filament), an electron collector (target), and some ion extraction optics. The geometry of the source may be simple or complex depending on the application. In this work the ionizer is in a square configuration. The filament wire is attached to four posts so that it makes a square and the molecular beam passes through the center of this square. The filament is a coiled wire made of either tungsten or thoriated iridium. A set of lenses are used to focus the ions into the mass filter. Although both positive and negative ions are formed in the ion source at the same time, the recorded mass spectrum consists of either positive or negative ions. Neutral particles are not detected. Positive ion mass spectra are the most commonly recorded, since the negative ions generated by this particular technique are much less abundant than positive ions.

Ion filtering

The purpose of the mass analyzer is to limit the accelerated ions that arrive at the detector to a narrow mass range. The instrument is designed in a way that a large fraction of the ions will focus onto the detector. Most mass spectrometers contain one of four types of mass filters: single focusing, double focusing, quadrupole, and time-of-flight. Only the mass filter used is discussed, namely the quadrupole mass filter. It is usually more compact, less expensive, and more rugged than the magnetic counterparts.

Quadrupole mass filters are by far the most common mass analyzers today. They offer the advantage of low scan times (<100 ms). A quadrupole is analogous to a variable, narrow-band filter, because at any set of operating conditions it transmits only ions within a small range of m/z ratios. All other ions are neutralized and carried away as uncharged molecules. By varying the electrical signals to a quadrupole, the DC voltage and the RF power, it is possible to vary the range of m/z values transmitted. Figure 5.5 is a simplified diagram of a quadrupole mass filter. It consists of four parallel cylindrical metal rods that serve as the electrodes of the instrument. Ions from the source are accelerated by a potential of 5 to 15 V and injected into the space between the rods. Opposite rods are

connected electrically, one pair being attached to the positive side of a variable DC source and the other pair to the negative terminal. In addition, variable radio-frequency AC potentials, which are 180 degrees out of phase, are applied to each pair of rods. The cylindrical rods are in the order of 6 mm in diameter, rarely more than 15 cm in length, and are rigidly held in precisely machined ceramic holders. The size of the rods dictates the detectable mass range of the instrument.

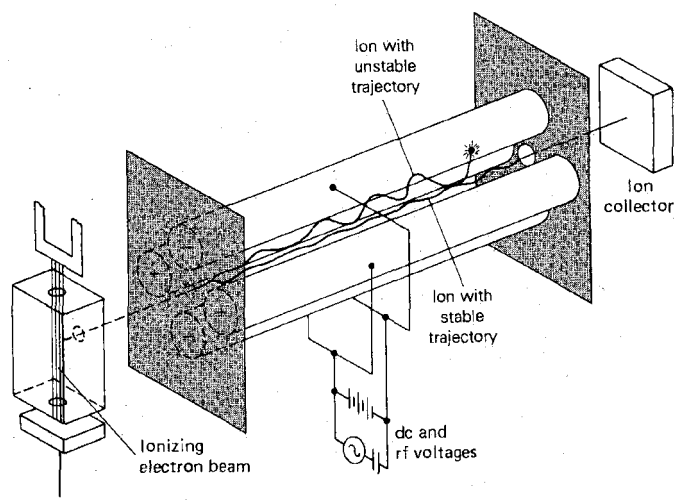

Figure 5.5. A schematic illustration of a quadrupole (2). A triple quadrupole mass filter was used in this work, i.e. quad-gas cell-quad.

To understand the filtering capability of a quadrupole, one needs to consider the effect of the DC and AC potentials on the trajectory of ions as they pass through the channel between the rods. Ions may follow stable trajectories and pass through the filter, if their displacement from the Z-axis is sufficiently low to avoid a collision with the quadrupole rods. The operating principle may be understood by considering the combined effect of a positive X-Z plane and a negative Y-Z plane. In the positive plane, the ions are located at an electron sink, where the ions oscillate due to the radio frequency field. Since the oscillation amplitude increases with ionic mass, the heavy ions are more likely to collide with the conducting rods than the lighter ones. The X-Z plane acts, therefore, like

a low-pass mass filter. With similar arguments the Y-Z plane works like a high-pass mass filter. The combination of the two planes may be considered as a band-pass mass filter.

Ion detection

Neutral beams may be detected in a number of ways, and a variety of beam detectors have been developed. The ideal beam detector should fulfill three main requirements. First, it should give information about all beam properties (intensity, chemical composition, kinetic and internal energy distributions). Second, its detection efficiency should be the same for all species. Third, it should discriminate against beam particles from the residual vacuum background gas. Unfortunately, none of the available detectors fulfills all the requirements of an ideal detector. Real beam detectors may be grouped into three main categories: ionization detectors, laser-based detectors, and accommodation and accumulation detectors. Only the ionization detectors are discussed here.

Ion detection can be accomplished by three principal methods: the Faraday cup, Electron multipliers, and the Scintillation detector. The Scintillation detector is quite complex, but has the advantage of being insensitive to surface contamination. The Faraday cup is the simplest and cheapest method for detecting ion beams. Positive ions are collected by a cylindrical cup, which is partially surrounded by a negatively polarized shield. This method is cheap, stable, and insensitive to air exposure. However, the detection sensitivity is limited by noise and slow response time. An enhancement of sensitivity and response time can be achieved by replacing the Faraday cup with an Electron Multiplier of which there are two types: discrete dynode and continuous dynode. The Electron Multiplier converts the positive ion current into an electron current, which can be further amplified.

The detector employed in this work is the continuous dynode multiplier consisting of a hollow circular glass tube covered by a semiconducting layer from within. This layer has the function to produce secondary electrons, since each collision of electrons with the

multiplier walls releases additional electrons. These electrons are accelerated by the electrostatic field along the axis of the multiplier. The multiplier here is installed offset from the transmission axis of the molecular beam so that X-rays and metastable species generated in the ionizer are not detected. Figure 5.6 illustrates the operation principle.

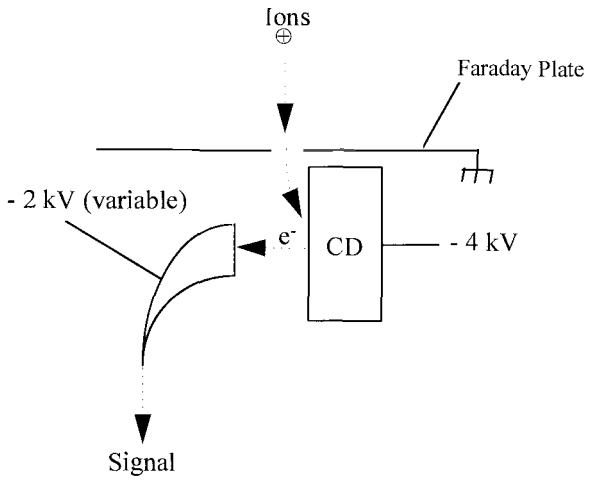

Figure 5.6. A schematic illustration of a continuous dynode electron multiplier (7). Positive ions enter an aperture after which they are drawn to the negatively charged conversion dynode. Electrons are produced that impinge into the funnel of a channeltron producing an electron current that is amplified.

The positive ions in Figure 5.6 enter an aperture in a grounded shield (Faraday plate), after which they are drawn towards a highly negatively charged conversion dynode (-4 kV). There the ions produce secondary electrons which are pushed by an electric field from the conversion dynode to a multiplier funnel. The electron multiplier used was a Galileo 4770E Channeltron. The gain of the multipliers depend primarily on the polarization voltage and the ion flux. Multiplier gain is defined as the electron current out of the multiplier divided by the ion current impinging on its front end.

$$G = \frac{I_{out}}{I_{in}} \tag{5-12}$$

This ratio represents the number of electrons leaving for every ion (or electron) entering.

APPLICATION OF MBMS TO BLACK LIQUOR CHAR GASIFICATION

A black liquor char sample (20 ± 5 mg) was placed in a hemi-capsular quartz boat on the tip of a quartz rod that is inserted into a heated convective gas flow furnace. The gas flowrate was 3.33 slm. The reacting gases were varying mixtures of O_2, CO_2, and He. Argon was used as an internal standard. The experiments in this work were performed at a furnace temperature of 1100°C. The experimental conditions studied are given in Table 5.1.

Table 5.1. Experimental conditions employed in the convective flow reactor.

Set	Gas composition	Total flow rate *	Reactor temperature
1	5% O_2 + He	3.33slm + 1sccm Argon	1100°C
2	10% CO_2 + He	3.33slm + 1sccm Argon	1100°C
3	10% CO_2 + 5% O_2 + He	3.33slm + 1sccm Argon	1100°C

* slm = standard liters per minute, sccm = standard cm^3 per minute

The convective flow reactor is shown in Figure 5.7.

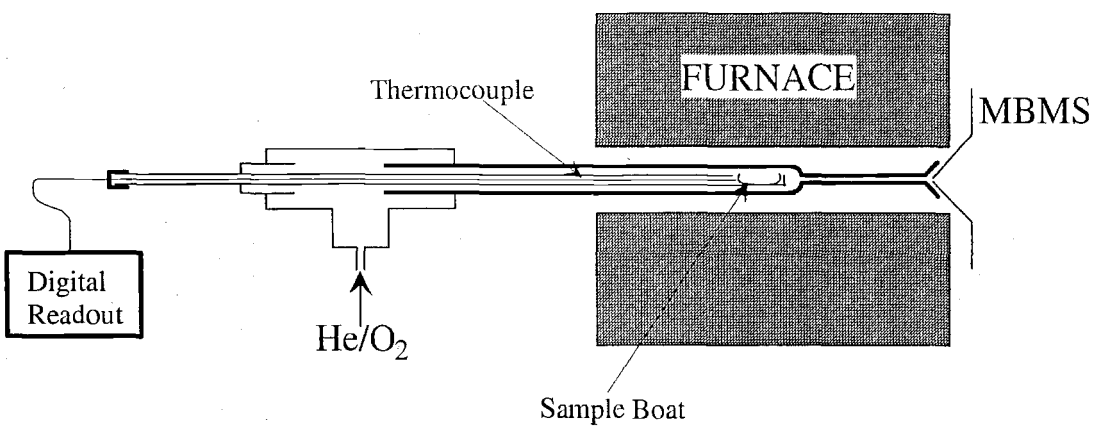

Figure 5.7. Convective flow reactor coupled to the MBMS. The figure is adapted from (8) with permission.

The convective flow reactor was placed in a standard two-zone, electric clam-shell furnace with a 30 cm long heated zone. The outer diameter of the tubular quartz rector was 1 inch and the tube thickness was 2 mm. The end of the furnace was aligned around the tip of the sampling orifice of the mass spectrometer. The sampling orifice was a stainless steel cone 25 mm in length with a 90° interior angle and an orifice diameter of 200 μm. The residence time of the product gases was on the order of 0.1 sec before reaching the sampling orifice. A type-K thermocouple was inserted through a hollow 6 mm quartz rod such that the junction was close to the sample boat. Hence, the temperature of the hot gases surrounding the sample boat could be monitored. The flame temperature and the actual boat temperature were not measured. The quartz rod was inserted through a brass tee that also supplied the inlet gases. The insertion occurred always at 0.2 min, and it was assumed that the sample was in place at 0.3 min for all the experiments, which was taken as time zero.

The product gases from the black liquor char samples inside the combustion reactor were transported by the convective gas flow into the molecular beam mass spectrometer. The objective was to extract samples of the product gases in real time in order to identify molecular compounds released during combustion and gasification of black liquor char. The approach to achieving this goal is to apply free-jet expansion through an extractive sampling orifice with rapid quenching to molecular flow while minimizing wall collisions or condensation of vapors. The gas entering the MBMS orifice at a temperature of 1100°C and exiting at a pressure of ~ 0.5 atm. Here, diffusion effects are too slow to be important in the core of the supersonic jet, as discussed in the section on free-jet molecular beams. The expanded gases were then skimmed through a second conical 1.2 mm orifice (skimmer) at the entrance to the second vacuum stage. The following mean free paths are obtained: 89 cm for O_2 and 55 cm for CO_2 when the pressure is assumed to be ~ 10^{-6} torr and temperature ~ 5 K. Thus, the Knudsen number is 742 for O_2 and 458 for CO_2, i.e. free molecular flow applies. A molecular beam is formed in the second vacuum stage from which the beam is directed into the ionizer continuing through a triple

quadrupole mass filter to the detector. The apparatus to accomplish this is shown in Figure 5.8.

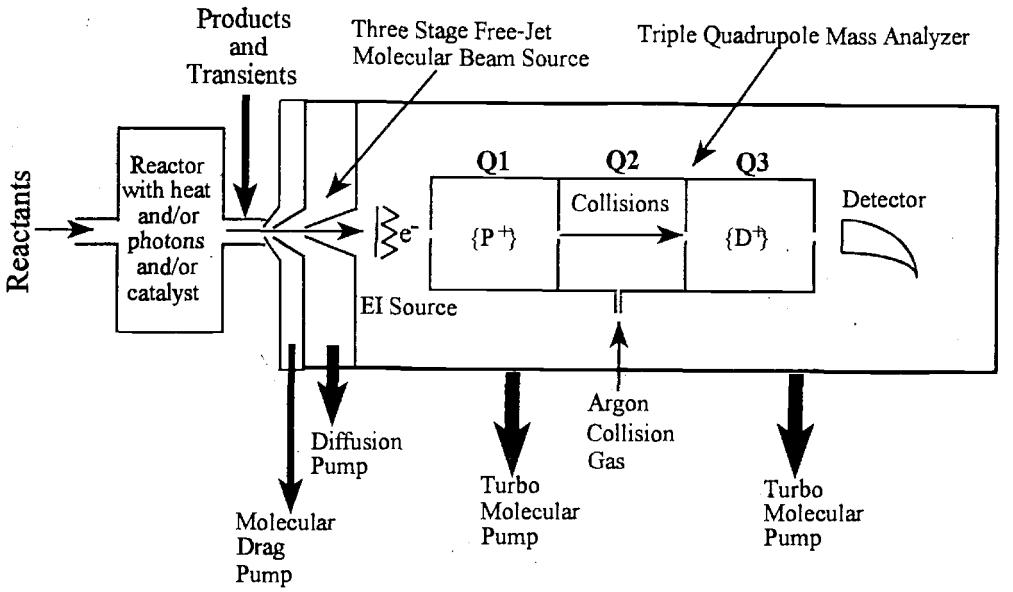

Figure 5.8. The MBMS consists of three vacuum chambers, a sampling orifice, skimmer, electron beam ionizer, a triple quadrupole mass filter and a detector. The figure is adapted from (8) with permission.

With a sufficiently low pressure in the first vacuum stage and a proper placement of the skimmer, a supersonic flow enters the second vacuum stage without shock formation. The intense molecular beam was ionized by electron impact ionization. A low-energy electron beam (20-25 eV) from a hot-filament ionization source was used. In the third vacuum stage, the quadrupole mass filter selects the desired species to be mass analyzed. A computer hardware & software system was utilized to control the scanning parameters and to collect the pre-amplified electron multiplier signal as a function of time and mass-to-charge ratio. The mass spectrometer was scanned continuously at a rate of 100 amu/sec giving a complete mass spectrum approximately every 1.5 sec. Typical settings for the operation of the MBMS are given in Table 5.2.

Table 5.2. Typical operation settings of the MBMS (9).

Electron energy	25 eV
Electron emission current	-1.35 mA
Multiplier	-1.8 kV
Dynode	-4 kV
Pressure in stage 1	21 mtorr
Pressure in stage 2	2.6e-5 torr
Pressure in stage 3	1e-7 torr
Ionization voltage	+8.0V
Extraction voltage	-5.0V
Voltage applied to lens 1 and 3	-72.0V
Voltage applied to lens 2	23.0V
Voltage applied to exit lens	-140.4V
Pole offset applied to quadrupole 1	0.2V
Entrance voltage to quadrupole 2	-107.2V
Voltage applied to quadrupole 2	-51.0 V
Exit voltage from quadrupole 2	-140.4V
Voltage applied to quadrupole 3	-22.8V

A flowrate of argon was maintained in the combustion reactor in order to obtain a stable reference point from the MBMS for normalization purposes during data reduction. The ion intensities were normalized with respect to the argon intensity. The ion currents for the following mass-to-charge ratios were scanned: 10-31, 33-43, 45-150. The following molecular masses were analyzed: 18, 23, 28, 30, 34, 45, 58, 64, 78, and 128; i.e. $H_2O(g)$, Na, CO, NO, H_2S, CO_2 , NaCl, SO_2 , C_6H_6 (benzene), and $C_{10}H_8$ (naphthalene). However, special attention was focused on the permanent gases: CO_2, CO, and $H_2O(g)$. The data for masses 32 and 44 were not collected because that would have overloaded the detector, since oxygen and CO_2 were the reacting gases. CO_2 was calculated from mass 45 as described later. Each sample was analyzed in triplicate if no evident reason existed for discarding data points, i.e. a lowering of the pressure in stage 1 of the mass spectrometer would generally result from a plugged orifice. An oversaturation of the detector (pins) would result from a bad reactor alignment. The success rate was 80-90% for the performed experiments.

Analysis of transport resistances in convective flow reactor

Temperature measurements using a K-type thermocouple by Dayton et al. (10) indicate that the heating of the gas takes place very rapidly. However, the temperature measured by the thermocouple is probably mainly due to black-body radiation effects. Assuming the gas temperature at the sample location was close to the furnace temperature, an analysis was made of the significance of the internal and external transport resistances. Table 5.3 shows the effectiveness factor and the mass transfer Biot number for the conditions studied. The computer program is given in Appendix 5.1. The sample geometry was assumed to be a slab.

Table 5.3. Effectiveness factor and mass transfer Biot number (Bi_m) for mesopores as well as the estimated particle temperature. The results indicate that pore diffusion is important. Calculations were done for a 1100°C furnace with the gas temperature 100°C below the furnace. The computer program with calculation details is given in Appendix 5.1.

O_2 (bar)	CO_2 (bar)	η	Bi_m O_2	Bi_m CO_2	T_{part} (°C)
0.05	0.10	0.22	4.7	4.9	1093
0	0.10	0.22	4.7	4.9	1093
0.05	0.0	*	*	*	1150**

* not calculated because assumed exclusively controlled by external mass transfer
** in 5% O_2 the literature indicates the temp to be 50°C higher than the furnace (11)

Table 5.3 shows that the particle temperature is close to the furnace temperature. The effectiveness factors are clearly below unity indicating that pore diffusion limits strongly the reaction rate with respect to chemical reaction. The mass transfer Biot numbers are ~5 which shows that both external and internal mass transfer are important. When no CO_2 was present in the reacting gases, then the combustion process was assumed to be entirely mass transfer controlled. The particle temperature at these conditions could be significantly higher than the furnace temperature (11).

Sample preparation and data reduction

The black liquor char samples studied were obtained by feeding 90-125 μm diameter dry black liquor particles into the laminar entrained flow-reactor (LEFR) at Oregon State University with a short, medium, and long residence time at temperatures of 700, 900, and 1100°C, producing 9 different char samples. A description of this device and the experimental procedures can be found in Appendix 13. Each char sample was pelletized using a hand operated device, after which the char was crushed into a powder using a spatula. This procedure was necessary to fit a sufficient amount of material into the sample boat (25±5 mg). Table 5.4 shows data for the studied chars.

Table 5.4. Elemental composition and LEFR experimental conditions for chars studied.

Sample no.	LEFR Temp (°C)	LEFR Res.time (s)	Xc (%)	C (%)	Na (%)	K (%)	S (%)	Cl (%)
BLS	-	-	0	35.00	22.70	0.62	2.90	0.67
94	700	0.38	32.0	33.50	16.70	0.22	1.45	0.63
78	700	0.66	31.3	32.30	20.00	0.15	1.03	0.67
62	700	1.49	48.3	29.10	21.60	0.08	0.73	0.84
93	900	0.39	40.6	31.70	21.20	0.27	0.77	1.00
77	900	0.67	43.2	31.70	18.80	0.01	0.72	0.69
85	900	1.32	50.1	29.90	20.00	0.07	1.88	0.81
91	1100	0.31	59.9	29.10	19.80	0.22	1.49	1.50
69	1100	0.72	57.8	29.40	19.90	0.03	2.84	0.75
81	1100	1.32	71.6	31.20	19.20	0.14	2.46	0.76

Since the detection of mass 44 was turned off in the MBMS, it was backcalculated from the isotopic abundances of $^{12}C^{16}O^{16}O$ versus $^{13}C^{16}O^{16}O + {}^{12}C^{16}O^{17}O$ (12,13). These ratios are as follows: 325000 ppm(v) $^{12}C^{16}O^{16}O$, 3600 ppm(v) $^{13}C^{16}O^{16}O$, 260 ppm(v) $^{12}C^{16}O^{17}O$. This means that $^{12}C^{16}O^{16}O$ at m/z=44 accounts for 98.432% of the signal from CO_2, and the contribution from the isotopes at m/z=45 accounts for 1.169% of the CO_2. The ionization cross sections of the two CO_2 isotopes are virtually the same, and therefore, not considered. Hence, mass m/z=44 is estimated as follows:

$$I_{44,estimated} = I_{45,measured} \times \frac{98.432}{1.169} = I_{45,measured} \times 84.2 \quad (5\text{-}13)$$

Furthermore, the CO intensity was corrected by considering that 6% of the CO measured is originating from the fragmentation of CO_2 at 25 eV ionization energy. Hence, the corrected CO intensity is given by equation 5-14.

$$I_{28,corrected} = I_{28,measured} \times 0.94 \quad (5\text{-}14)$$

Comparisons were made for the amount of specific gases produced for different samples using equation 5-15. The area of a species above the baseline was evaluated, and normalized with respect to the argon background and initial sample weight. This equation, however, was not used in the modeling section.

$$\text{Normalized amount of species i} = \frac{\text{Area of species i}}{(\text{Area of Argon}) \times (\text{Initial sample weight})} \times 100 \quad (5\text{-}15)$$

Tables of normalized species amounts are given in Appendix 5.2. The areas and initial sample weights in equation 5-15 are given in Appendix 5.3.

Time evolution profiles and mass spectra

The time evolution profile, ion intensity versus time, was always more or less bell shaped with a small peak just after insertion of the sample inside the reactor. An example of the total ion current (TIC) is shown in Figure 5.10. In 5% O_2 + 10% CO_2 the TIC was similar in shape and intensity increase as in Figure 5.9. In 5% O_2 the TIC intensities increased more than double after sample insertion compared to when CO_2 was present.

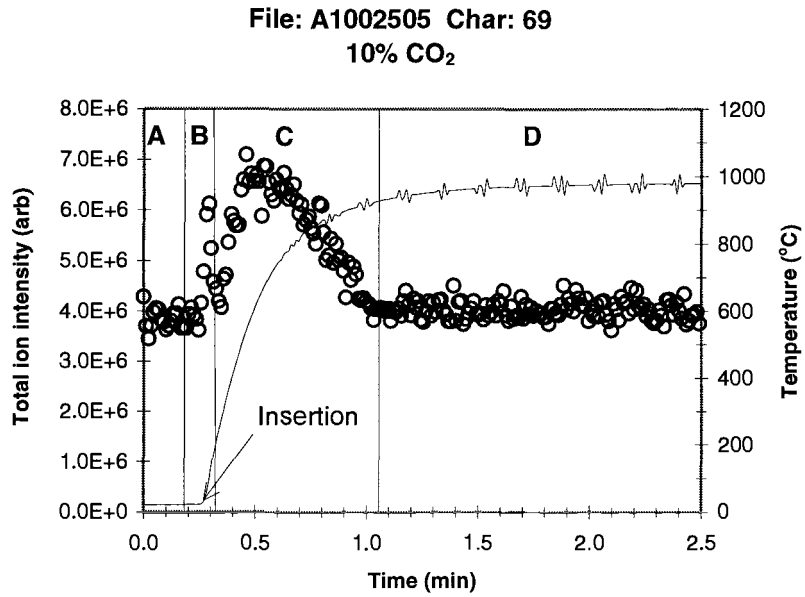

Figure 5.9. A time evolution profile of the total ion current shows the signal obtained from the MBMS detector. The thermocouple temperature is shown in the secondary axis. The time at which the sample is inserted is shown with an arrow. Region A is the background, region B is drying, region C is char burning, and region D is the smelt reaction phase. The experiment was made in 10% CO_2 and 90% He.

Figure 5.9 shows 4 distinguishable regions. Region A is the background with just the reacting gases reaching the detector. Region B shows that there is a small peak at about 0.3 min. This is water from drying of moisture left in the char samples. The temperature increases rapidly when the sample has reached its position inside the hot reactor. Region C is the char burning stage, where the main gasification reactions take place. Region D is where smelt reactions occur. Here, the temperature levels off below 1000°C, because the tip of the thermocouple was shielded by a hollow quartz rod. The particle temperature was close to 1100°C according to calculations shown in Table 5.3. Figure 5.10 shows an average mass spectrum of region C, the char burning stage. Figure 5.11 shows the time evolution profiles of the permanent gases H_2O^+, $^{13}CO_2^+$, and $^{12}CO^+$.

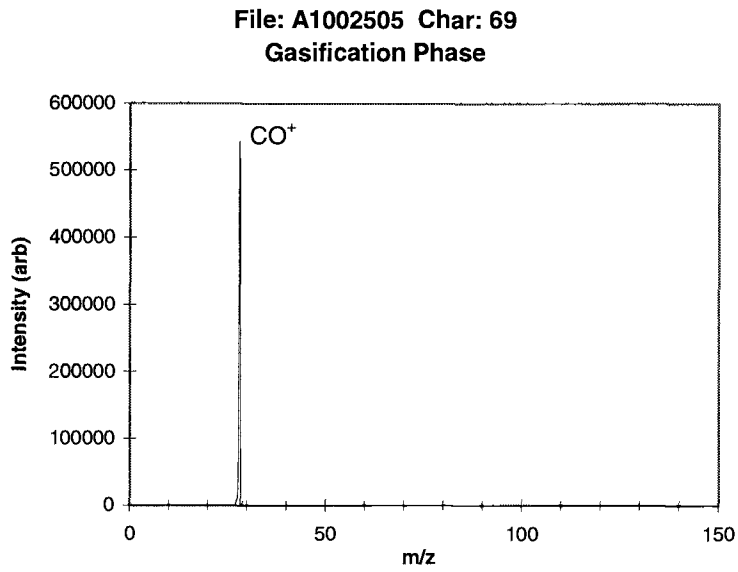

Figure 5.10. An average mass spectrum of the char burning stage (region C) shows that CO^+ was the most abundant species detected.

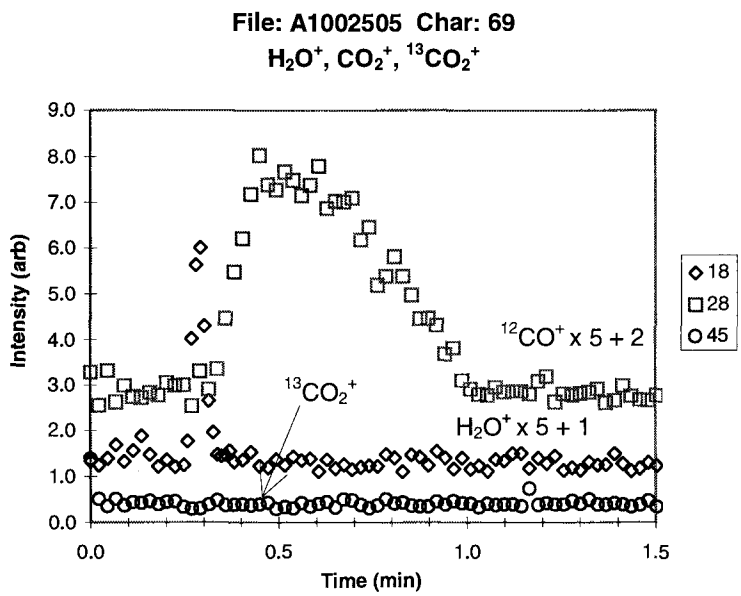

Figure 5.11. The intensity of CO^+ was usually always a bell shaped curve. Water vapor was always released right after insertion. The $^{13}CO_2^+$ isotope was flat due to the high CO_2 content. All signals are given on a scale in which the maximum water ion signal is 1. This experiment was made in 10% CO_2 and 90% He.

Figure 5.11 shows that the intensity of CO^+ follows closely the total ion intensity in Figure 5.9. Water vapor is responsible for the peak right after insertion. The $^{13}CO_2^+$ isotope was flat in 10% CO_2 + 5% O_2, and in 10% CO_2 because the amount of CO_2 in the reactant gases was orders of magnitude greater than the amount of CO_2 released from the sample. However, in 5% O_2 the $^{13}CO_2^+$ intensity followed the bell shape of mass 28. All signals were normalized so that the maximum water ion signal was 1.

DISCUSSION OF RESULTS

Residue obtained

The residues obtained were usually black when no oxygen was present in the gas atmosphere, indicating that some carbon was still left in the sample. However, when oxygen was present, the residues were white and crystalline inorganic material as shown in Figure 5.12.

Figure 5.12. The residue was a gray salt crystal like inorganic material when oxygen was present in the reacting gases. Picture taken with an optical microscope at a magnification of 10×. There appears to be another type of inorganic material that is transparent in the upper left hand corner.

Figure 5.13 shows an overview of the material in the bottom of the sample boat. There appears to be a coating of material with bubbles. This coating may be a solidified mixture of sodium carbonate and sulfate. The crystalline like matter in the upper left hand corner may be sodium chloride.

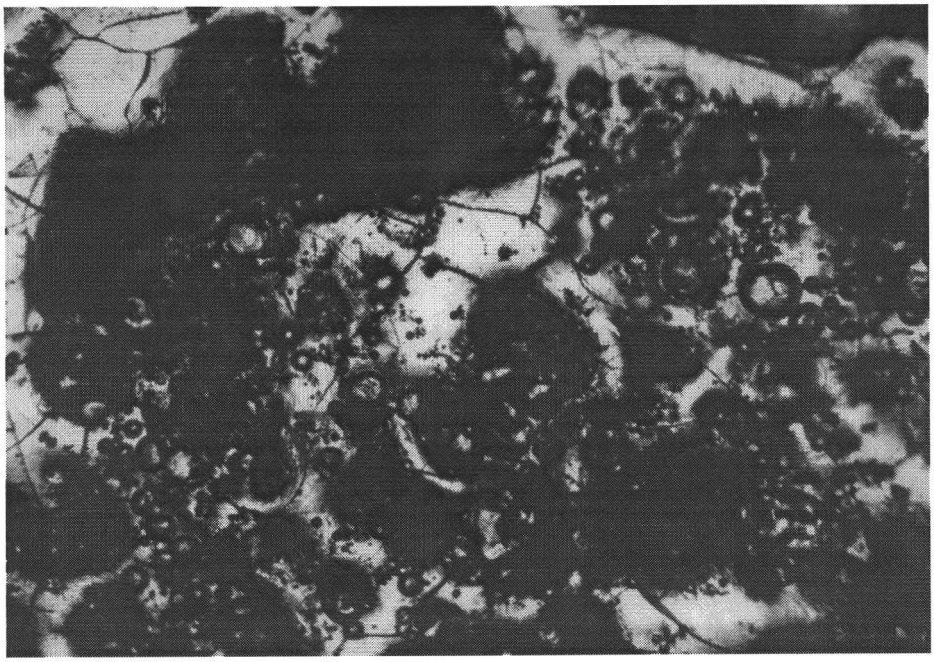

Figure 5.13. The bottom of a sample boat shows an inorganic layer with bubbles and another gray inorganic residue from experiments with oxygen in the reacting gases.

Carbon release

The actual release of CO_2^+ (m/z=44) could not be estimated when CO_2 was present in the reacting gases, because there is no method to distinguish the source of the CO_2^+ detected (from the gas or from the particle). It is possible to do this when CO_2 is absent from the reacting gases using the $^{13}CO_2^+$ (m/z=45) isotope intensity by employing equation 5-14. However, in such a case one could have had the detection of mass 44 activated. Table 5.5 shows that the amount of CO^+ released is about the same when 5% O_2 is present. However, the amount of CO^+ released in 10% CO_2 was on the average about 6.5 times higher compared to when 5% O_2 was present, and 9.9 times higher when both gases were present. This is probably due to the reaction between oxygen and CO, reaction 4, but also from the fragmentation of CO_2.

4. $CO + \frac{1}{2}O_2 \rightarrow CO_2$

Table 5.5 was obtained using Equation 5-15 corrected by subtracting the CO coming from the fragmentation of CO_2, 84.2×{Normalized Area of $^{13}CO_2$}×0.06.

Table 5.5. The normalized and corrected amounts of CO^+ released according to equation 5-15 are shown for the chars studied. The data is approximately for a 95% confidence interval.

LEFR Temp. (°C)	LEFR Res.time (sec)	Amount in 5% O_2	Amount in 5% O_2 + 10% CO_2	Amount in 10% CO_2
700	0.38	2.2	0.6	19.8
700	0.66	1.9	1.7	17.0
700	1.49	2.4	3.7	23.0
900	0.39	1.9	2.5	17.7
900	0.67	2.9	3.0	19.6
900	1.32	3.0	0.2	21.8
1100	0.31	5.4	1.7	14.6
1100	0.72	2.9	2.0	14.9
1100	1.32	3.3	1.6	19.7

The release of $^{12}CO_2^+$ (m/z=44) was monitored by measuring the $^{13}CO_2^+$ (m/z=45) isotope, because mass 44 was shut off for all the experiments. Table 5.6 shows that approximately twice as much $^{13}CO_2^+$ isotope was measured when CO_2 was present compared to when only O_2 was present. This means that twice as much $^{12}CO_2^+$(m/z=44) was present in the reacting gases. How much of this CO_2 was from the gas and how much from the particle was not possible to measure. Equation 5-15 was used to obtain Table 5.6.

Table 5.6. The normalized amounts of $^{12}CO_2^+$ (m/z=45) released are shown for the chars studied. The data is approximately for a 95% confidence interval.

LEFR Temp. (°C)	LEFR Res.time (sec)	Amount in 5% O_2	Amount in 5% O_2 + 10% CO_2	Amount in 10% CO_2
700	0.38	0.8	1.2	0.9
700	0.66	0.8	1.7	1.0
700	1.49	0.7	1.1	1.0
900	0.39	0.7	1.5	1.4
900	0.67	0.7	1.2	1.3
900	1.32	0.7	1.5	1.3
1100	0.31	0.6	2.1	1.3
1100	0.72	0.6	1.3	1.8
1100	1.32	0.6	1.6	1.1

Hydrogen and chloride release

Table 5.7 shows the amount of H_2O^+ generated in 5% O_2, in 5% O_2 + 10% CO_2, and in 10% CO_2. The data for Table 5.7 are given in Appendix 5.3, and this data were obtained using equation 5-15 averaging usually three experiments.

Table 5.7. The normalized amounts of H_2O^+ released are shown for the chars studied. The data is approximately for a 95% confidence interval.

LEFR Temp. (°C)	LEFR Res.time (sec)	Amount in 5% O_2	Amount in 5% O_2 + 10% CO_2	Amount in 10% CO_2
700	0.38	4.2	4.1	2.4
700	0.66	3.7	3.8	2.1
700	1.49	3.2	3.1	1.9
900	0.39	4.2	3.0	2.3
900	0.67	2.4	2.6	1.8
900	1.32	2.1	2.2	2.7
1100	0.31	2.8	2.9	1.9
1100	0.72	2.3	2.0	2.6
1100	1.32	2.3	1.9	1.7

Table 5.7 shows that more water was detected when oxygen was present. This is probably due to the reaction between oxygen and hydrogen. There is a clear effect of increasing LEFR residence time and pyrolysis temperature. One reason could be that a lesser amount of hydrogen is left in the char at higher LEFR residence times and temperatures. However, hydrogen analysis numbers were not available to test this theory. Another reason could be that hydrogen is released through another species, e.g. HCl^+, which was indeed detected. The HCl^+ data are given in Table A.5.2.5 in Appendix 5.2. When CO_2 was present, the amount of HCl^+ released increased with pyrolysis temperature and at the same time the amount of H_2O^+ released decreased. This indicates that HCl^+ and water vapor are part of the same chemical reaction. Reaction 5 could be a possible mechanism if it did not become thermodynamically unfavorable at higher temperatures.

5. $2NaCl(g) + H_2O(g) + CO_2(g) \rightarrow 2HCl(g) + Na_2CO_3$

However, in 5% O_2 a similar correlation between HCl^+ and water vapor did not exist. In fact, the amount of HCl^+ decreased with increasing pyrolysis temperature in oxygen alone. A possible reason could be the following reaction:

6. $2Na_{(v)} + 2HCl(g) + ½O_2 \rightarrow 2NaCl(g) + H_2O(g)$

Equilibrium calculations using HSC Chemistry (23) show that reaction 6 is very favorable from a thermodynamic standpoint, ΔG is negative. More $NaCl^+$ is in fact detected at higher temperatures in 5% O_2 supporting reaction 6. However, the amount of water vapor should also increase which it does not.

Sodium release

$NaCl^+$ and Na^+ were the main sodium containing species released. It appears that $NaCl^+$ is generated somewhat more from the high temperature chars. The effect of LEFR residence time was insignificant. $NaCl^+$ contained most of the chloride relesed. The amounts of elemental sodium released are given in Appendices 5.2 and 5.3. Figure 5.14 shows typical $NaCl^+$ and Na^+ time evolution profiles in 5% O_2.

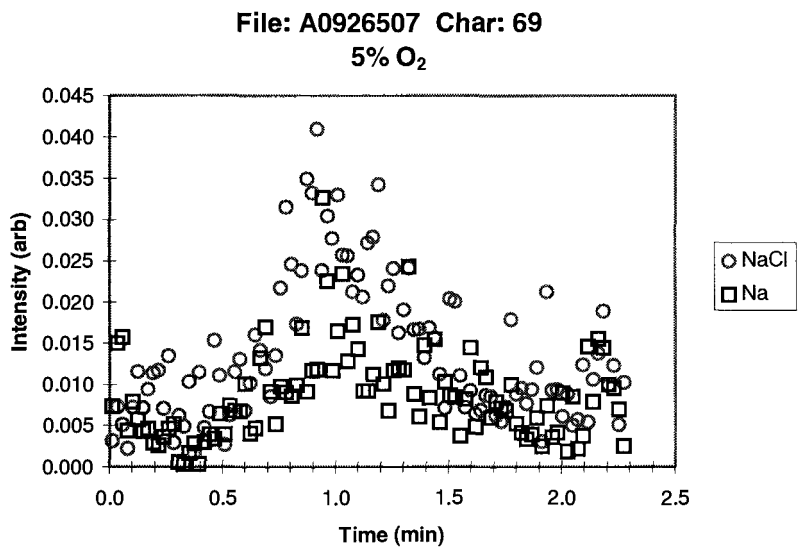

Figure 5.14. Typical $NaCl^+$ and Na^+ spectra in 5% O_2. The signals are given on a scale in which the maximum water ion signal is 1.

Elemental sodium was probably a fragment ion of $NaCl^+$ during ionization (8) as evidence by the fact that the time evolution profiles are almost identical. In CO_2 atmospheres the release of Na^+ and $NaCl^+$ scatter into each other and the spectra are more or less flat. $NaCl^+$ is released the most in 5% O_2. This probably occurs through vaporization according to reaction 7.

7. $NaCl(s,l) \rightarrow NaCl(g)$

Table 5.8 shows the data for $NaCl^+$ release for all chars studied. Appendix 5.2 contains the Na^+ release data.

Table 5.8. The normalized amounts of $NaCl^+$ released are shown for the chars studied. The data is approximately for a 95% confidence interval.

LEFR Temp. (°C)	LEFR Res.time (sec)	Amount in 5% O_2	Amount in 5% O_2 + 10% CO_2	Amount in 10% CO_2
700	0.38	0.7	0.3	0.5
700	0.66	0.5	0.5	0.3
700	1.49	0.6	0.6	0.5
900	0.39	0.7	0.6	0.4
900	0.67	0.7	0.6	0.6
900	1.32	0.6	0.6	0.6
1100	0.31	1.0	0.7	0.6
1100	0.72	0.7	0.6	0.8
1100	1.32	1.1	0.7	0.7

Sulfur release

The sulfur released was mainly SO_2 and H_2S coming from organic and inorganic precursors. Here, the organic sulfur is regarded as pyrolysis residue, and inorganic sulfur as coming from the smelt reactions. The organic sulfur would come out first as SO_2 and H_2S, typically during the drying process. The sulfur release from inorganic sources starts when most of the carbon is gone and when the smelt reactions begin. The release of inorganic SO_2 is usually more abundant than the preceding release of organic SO_2. The amount of H_2S released was more uniform for the different char samples than for SO_2. Figure 5.15 shows a typical H_2S and SO_2 release spectrum. It appears that not much sulfur is released during char burning, between 0.5 and 1 min.

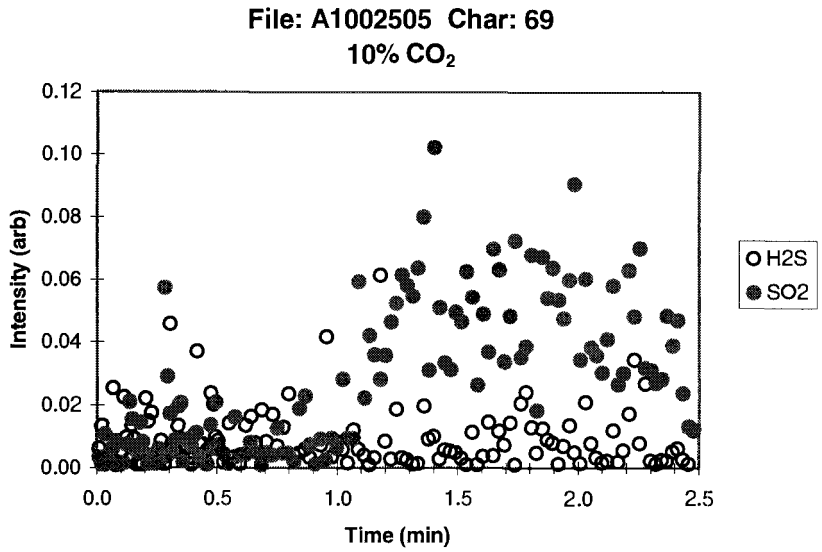

Figure 5.15. Typical SO_2 and H_2S release spectra in 10% CO_2 at 1100°C. All signals are given on a scale in which the maximum water ion signal is 1.

Interesting transitions are observed for the amounts of SO_2 coming from organic precursors with different char samples. The amounts of the release trends for the SO_2 from organic precursors were decreasing with LEFR residence time and temperature as shown in Table 5.9. The raw data for Table 5.9 are given in Appendix 5.3.

Table 5.9. The normalized amounts of SO_2^+ released from organic precursors are shown for the chars studied. The data is approximately for a 95% confidence interval.

T (°C)	Res.time (sec)	5% O_2	5% O_2 + 10% CO_2	10% CO_2
700	0.38	1.4	1.1	0.3
700	0.66	1.0	0.8	0.3
700	1.49	0.3	0.2	0.1
900	0.39	0.5	0.4	0.2
900	0.67	0.1	0.2	0.2
900	1.32	0.0	0.0	0.2
1100	0.31	0.1	0.1	0.1
1100	0.72	0.0	0.0	0.1
1100	1.32	0.0	0.0	0.0

The trends for inorganic SO_2 release appeared to be increasing with LEFR residence time. These trends, shown in Appendix 5.2, are somewhat inconclusive. Generally, more SO_2 was detected from inorganic sources than from organic. A possible thermodynamically favorable release mechanism could be:

8. $Na_2S + O_2 + 2CO_2 \rightarrow SO_2 + CO + Na_2CO_3(s)$

Much less inorganic SO_2 was detected when both CO_2 and O_2 were present compared to when they were present separately. This could indicate that both CO_2 and O_2 are needed to recapture SO_2. Reaction 9 is thermodynamically more favorable than reaction 8, which could explain the lesser amount of SO_2 released at these conditions.

9. $4Na + CO_2 + 1.5O_2 + SO_2 \rightarrow Na_2CO_3 + Na_2SO_4$

The signal for SO_2 from organic sources is more reliable being a clear peak in the beginning of the experiment whereas the inorganic SO_2 data is more noise like, increasing and extending beyond the cut-off time of 1.5 min. The release of H_2S agrees with equilibrium calculations in the literature (14).

Release of other species

More benzene was released than naphthalene. The release of benzene and naphthalene decreased with increasing LEFR residence time and increasing pyrolysis temperature. Char samples obtained at 700°C would yield more benzene and naphthalene than char samples obtained at 900 and 1100°C. Hardly any NO^+(m/z=30) was detected.

Calibration considerations

It is desirable to obtain concentrations of known units instead of intensities of arbitrary units. The problem is that the calibration intensity of CO is not known. If it was known, one would obtain C_i at any time according to equation 5-16 and the rate of reaction could then be obtained using equation 5-17.

$$C_i \propto I_i \tag{5-16}$$

$$\text{rate} = C_i \times \text{Flowrate} \tag{5-17}$$

The corresponding concentrations can be obtained using equations 5-18 and 5-19.

$$F_{i,Ar} = \left[\frac{C_i / C_{Ar}}{I_i / I_{Ar}}\right]_{\text{before insertion}} \tag{5-18}$$

$$F_{i,Ar} = \left[\frac{C_i / C_{Ar}}{I_i / I_{Ar}}\right]_{\text{after insertion}} \tag{5-19}$$

where $F_{i,Ar}$ is a calibration constant. This method can be found in the literature (15). However, no calibration runs were made in this work. An alternative is to operate with the following equation:

$$\text{rate} = k \times I_{\text{normalized}} \tag{5-20}$$

where k is a rate constant with the units mol/s or equivalent. If the assumption is made that the changes in ionization efficiency are negligible, then the exact concentrations are not needed. This alternative method will be employed to determine the carbon release rates in the modeling section to follow. When this assumption is not valid, then the calibration method outlined above should be used. This issue was left as a recommendation for future work.

CHARACTERIZATION AND MODELING OF THE GASIFICATION RATES

One of the objectives was to predict the carbon removal rate and to find out if the sum of the carbon release rate in CO_2 and O_2 equals the rate when both gases are present at the same time as shown in equation 5-21. The data for this analysis is given in Appendix 5.4.

$$\left(\frac{dC}{dt}\right)_{CO_2} + \left(\frac{dC}{dt}\right)_{O_2} = \left(\frac{dC}{dt}\right)_{CO_2+O_2} \tag{5-21}$$

An important note is made in that the following rate models are not based on an attempt to measure the moles of CO or CO_2 from the MBMS intensities, because such an approach would require a calibration procedure. The procedure employed here is based on the known amount of carbon removed during gasification and the fact that the MBMS signal is proportional to the rate of release of the relevant species, i.e.CO and CO_2.

<u>10% CO_2 runs</u>

The assumption is made that only CO is produced according to reaction 10 taking into consideration that 6% of the CO comes from the fragmentation of CO_2 molecules:

10. $C + CO_2 \rightarrow 2CO$

The rate constant for CO generation, k_1, was evaluated using equation 5-22 assuming the total weight loss equals $C_{char,fixed}$ (mol):

$$k_1 = \frac{C_{char,fixed}}{\int_0^{\infty} \frac{[\text{CO intensity after insertion}] - [\text{CO intensity before insertion}]}{[\text{Argon intensity}]} dt} \times \frac{1}{72\,\text{sec}} \tag{5-22}$$

where 72 sec is the actual reaction time inside the reactor, and k_1 was found to be 7.4×10^{-6} mol CO produced/sec (Appendix 5.4).

Since,

$$-\frac{dC}{dt} = \frac{1}{2} \times \frac{dCO}{dt} \tag{5-23}$$

then the rate equation is given as follows:

$$-\left(\frac{dC}{dt}\right)_{CO_2} =$$

$$\frac{1}{2} \times k_1 \times \frac{\{[\text{CO intensity after insertion}] - [\text{CO intensity before insertion}]\}}{[\text{Argon intensity}]} \tag{5-24}$$

The carbon release rate in 10% CO_2 can be obtained from the data using equation 5-24. The result is given in Figure 5.16.

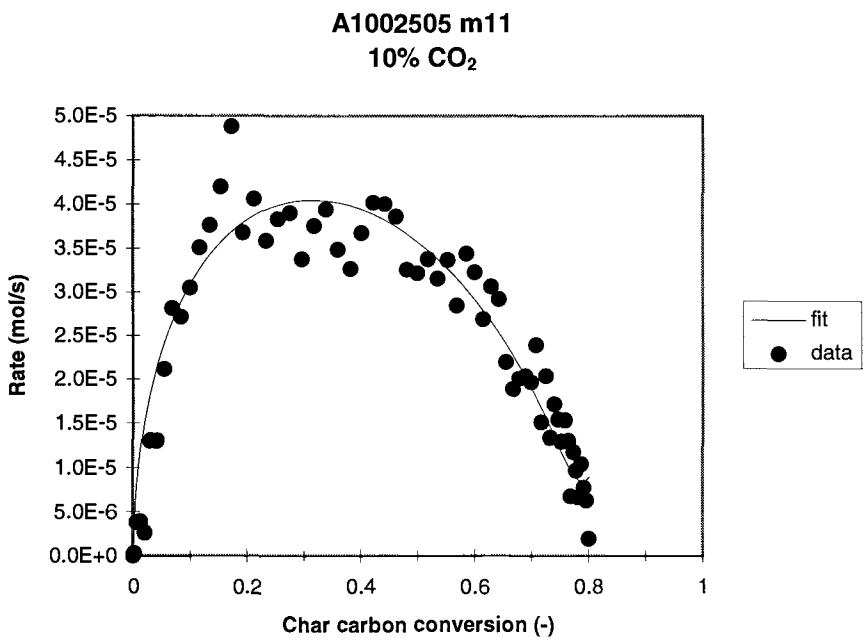

Figure 5.16. Carbon release rate versus char carbon conversion in 10% CO_2 at 1100°C. The solid line is a fit to the experimental data (dots).

The data shown in Figure 5.16 is right after insertion of the sample in the furnace. The bell shape of the rate curves is consistent with what can be found in the literature for black liquor char (16).

5% O_2 runs

The assumption was made that the signal for CO that is detected by the MBMS is independent of the gas atmosphere, i.e. the CO intensity is the same in CO_2 and O_2 if the same amount of CO and O_2 impinge on the detector.

$$\left(\frac{mol\ CO\ produced}{Area\ of\ CO}\right)_{10\%\ CO_2} = \left(\frac{mol\ CO\ produced}{Area\ of\ CO}\right)_{5\%\ O_2} \tag{5-25}$$

The problem is to find the rate constant for CO_2 generation, k_2, assuming that k_1 is valid in 5% O_2. The amount of carbon going to CO_2 is evaluated by equation 5-26.

$$\text{mol C to } CO_2 = C_{char,fixed} - \int_0^\infty \frac{dCO}{dt}dt =$$

$$C_{char,fixed} - k_1 \int_0^\infty \frac{[\text{CO intensity after insertion}] - [\text{CO intensity before insertion}]}{[\text{Argon intensity}]}dt \tag{5-26}$$

k_2 can now be calculated from equation 5-27.

$$k_2 = \frac{\text{C to } CO_2}{\int_0^\infty \frac{[CO_2\ \text{intensity after insertion}] - [CO_2\ \text{intensity before insertion}]}{[\text{Argon intensity}]}dt} \times \frac{1}{72\,\text{sec}} \tag{5-27}$$

Result: $k_2 = 9.0\times10^{-7}$ mol CO_2 produced/sec (Appendix 5.4).

The rate equation for reaction 11 is given by equation 5-28:

11. $C + 1/2\ O_2 \rightarrow CO$

$$\frac{dCO}{dt} = k_1 \times \frac{[CO\ \text{intensity after insertion}] - [CO\ \text{intensity before insertion}]}{[\text{Argon intensity}]} \tag{5-28}$$

The rate equation for reaction 12 is given by equation 5-29:

12. $C + O_2 \rightarrow CO_2$

$$\frac{dCO_2}{dt} = k_2 \times \frac{[CO_2\ \text{intensity after insertion}] - [CO_2\ \text{intensity before insertion}]}{[\text{Argon intensity}]} \tag{5-29}$$

Since,

$$-\frac{dC}{dt} = \frac{dCO}{dt} \tag{5-30}$$

and

$$-\frac{dC}{dt} = \frac{dCO_2}{dt} \tag{5-31}$$

then the total carbon release rate equation for 5% oxygen runs is given by equation 5-32:

$$-\left(\frac{dC}{dt}\right)_{O_2} = k_1 \times \frac{\{[CO\ \text{intensity after insertion}] - [CO\ \text{intensity before insertion}]\}}{[Argon\ \text{intensity}]} + k_2 \times \frac{\{[CO_2\ \text{intensity after insertion}] - [CO_2\ \text{intensity before insertion}]\}}{[Argon\ \text{intensity}]} \tag{5-32}$$

The predicted rate of carbon release in 5% O_2 is shown in Figure 5.17.

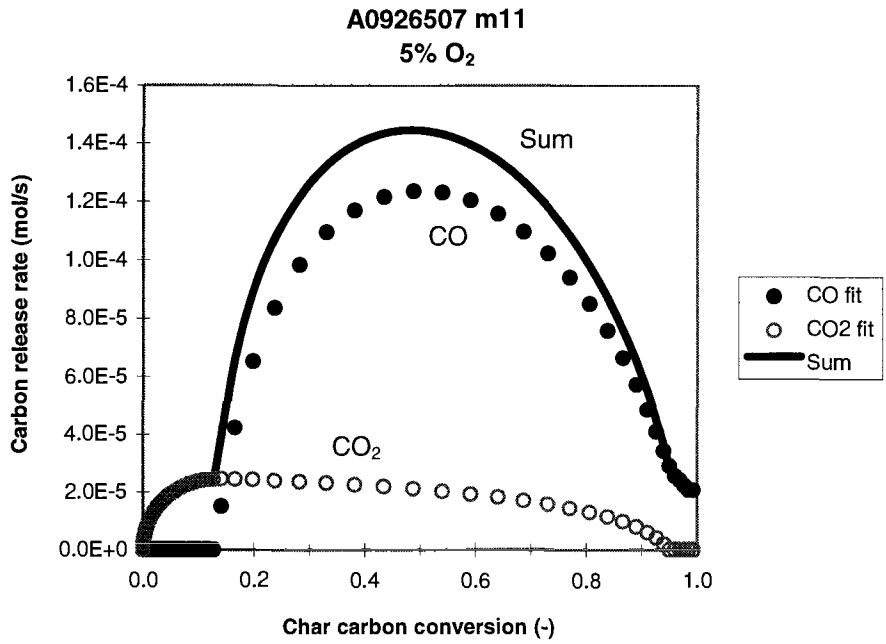

Figure 5.17. The predicted rate versus carbon conversion in 5% O_2 at 1100°C. The solid line is the sum of the CO and CO_2 generation.

Figure 5.17 shows that gasification in oxygen produces a lot more CO than CO_2. Carbon is released as CO 3-4 times as fast compared to CO_2. CO_2 starts to come off immediately after insertion, where as CO comes off at ~15% carbon conversion. The reason for this is under investigation.

5% O_2 + 10% CO_2 runs

The assumption is made that the signal for CO is the same in CO_2 and a mixture of CO_2 and O_2. Hence, the rate constant for CO generation, k_1, applies here, too.

$$\left(\frac{mol\ CO\ produced}{Area\ of\ CO}\right)_{10\%\ CO_2} = \left(\frac{mol\ CO\ produced}{Area\ of\ CO}\right)_{5\%\ O_2+10\%CO_2} \qquad (5\text{-}33)$$

The rate constant for CO_2 generation in gas mixtures of O_2 and CO_2, k_3, can be obtained analogously to k_2:

$$\text{mol C to } CO_2 = C_{char,fixed} - \int_0^{\infty} \frac{dCO}{dt} dt =$$

$$C_{char,fixed} - k_1 \int_0^{\infty} \frac{[\text{CO intensity after insertion}] - [\text{CO intensity before insertion}]}{[\text{Argon intensity}]} dt \quad (5\text{-}34)$$

$$k_3 = \frac{\text{C to } CO_2}{\int_0^{\infty} \frac{[CO_2 \text{ intensity after insertion}] - [CO_2 \text{ intensity before insertion}]}{[\text{Argon intensity}]} dt} \times \frac{1}{72 \text{ sec}} \quad (5\text{-}35)$$

Result: $k_3 = 4.3 \times 10^{-7}$ mol CO_2 produced/sec (Appendix 5.4).

The rate equation for reaction 13 is given by equation 5-36:

13. $2C + CO_2 + 1/2\ O_2 \rightarrow 3CO$

$$\frac{dCO}{dt} = k_1 \times \frac{[\text{CO intensity after insertion}] - [\text{CO intensity before insertion}]}{[\text{Argon intensity}]} \quad (5\text{-}36)$$

The rate equation for reaction 14 is given by equation 5-37:

14. $C + CO_2 + O_2 \rightarrow 2CO_2$

$$\frac{dCO_2}{dt} = k_3 \times \frac{[CO_2 \text{ intensity after insertion}] - [CO_2 \text{ intensity before insertion}]}{[\text{Argon intensity}]} \quad (5\text{-}37)$$

Since,

$$-\frac{dC}{dt} = \frac{2}{3} \times \frac{dCO}{dt} \quad (5\text{-}38)$$

and

$$-\frac{dC}{dt} = \frac{1}{2} \times \frac{dCO_2}{dt} \quad (5\text{-}39)$$

then the total carbon release rate equation for 5% O_2 + 10% CO_2 runs is given by equation 5-40.

$$-\left(\frac{dC}{dt}\right)_{CO_2+O_2} =$$

$$\frac{2}{3}\times k_1 \times \frac{\{[CO\ \text{int}ensity\ after\ insertion]-[CO\ \text{int}ensity\ before\ insertion]\}}{[Argon\ \text{int}ensity]} + \quad (5\text{-}40)$$

$$\frac{1}{2}\times k_3 \times \frac{\{[CO_2\ \text{int}ensity\ after\ insertion]-[CO_2\ \text{int}ensity\ before\ insertion]\}}{[Argon\ \text{int}ensity]}$$

The data for CO release was subtracted from the average baseline intensity of CO, divided by the argon background signal, and corrected by accounting for the CO coming from CO_2 fragmentation. The resulting normalized data is shown in Figure 5.18 along with a fit of the data. This fit was needed to estimate the CO_2 released and the total carbon released.

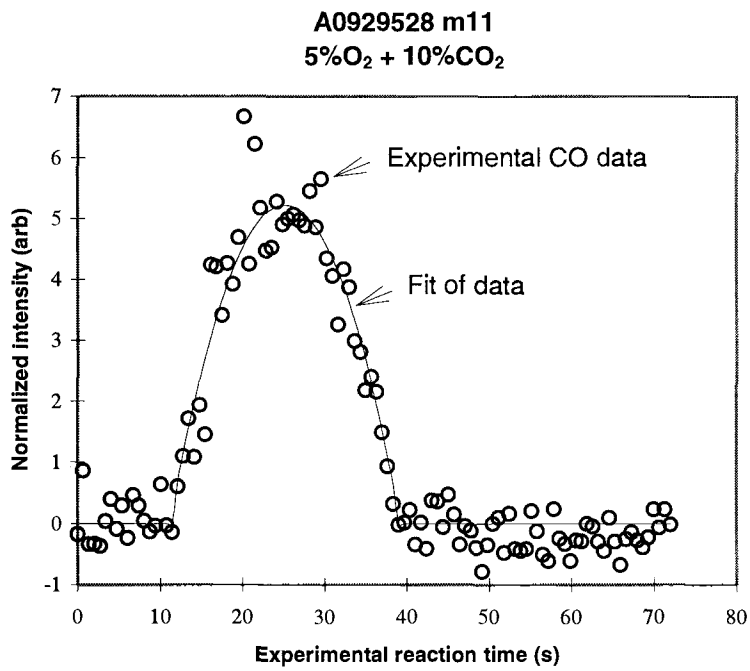

Figure 5.18. Normalized CO intensity versus time in 5% O_2 + 10% CO_2 at 1100°C. The solid line is a fit to the experimental data (circles).

It was not possible to extract information on how much carbon was released as CO_2 from the char carbon due to the presence of 10% CO_2 in the reacting gases causing the signal for $^{13}CO_2^+$ to be constant. The literature, however, indicates that the carbon release rate and the CO/CO_2 ratio increased from 0.50 to 0.64 when both O_2 and CO_2 were present compared to when only oxygen was present (17). Assuming a similar CO/CO_2 ratio, the CO_2 generation rate could be estimated and the carbon release rate in 5% O_2 + 10% CO_2 can be obtained from the data in Figure 5.18 using equations 5-36, 5-38, and 5-39. The predicted carbon removal rates using this method are given in Figure 5.19.

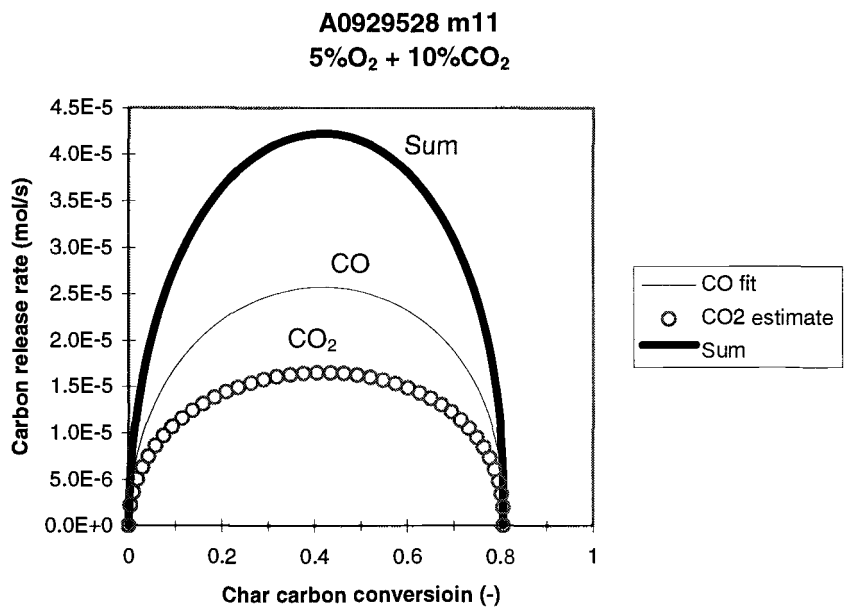

Figure 5.19. Rate versus carbon conversion in 5% O_2 + 10% CO_2 at 1100°C. The CO_2 generation rate is estimated = 0.64 of the CO generation rate according to the literature (17).

Since the rate is strongly limited by both film mass transfer and pore diffusion, the stoichiometric factors used in predicting the rates have little meaning. By assuming that the CO and CO_2 generation rates are directly proportional to the carbon release rates, one

would obtain 81% conversion instead of 49%. The carbon release rates in Figures 5.16 (CO_2), 5.17 (O_2), and 5.19 (CO_2+O_2) are compared in Figure 5.20.

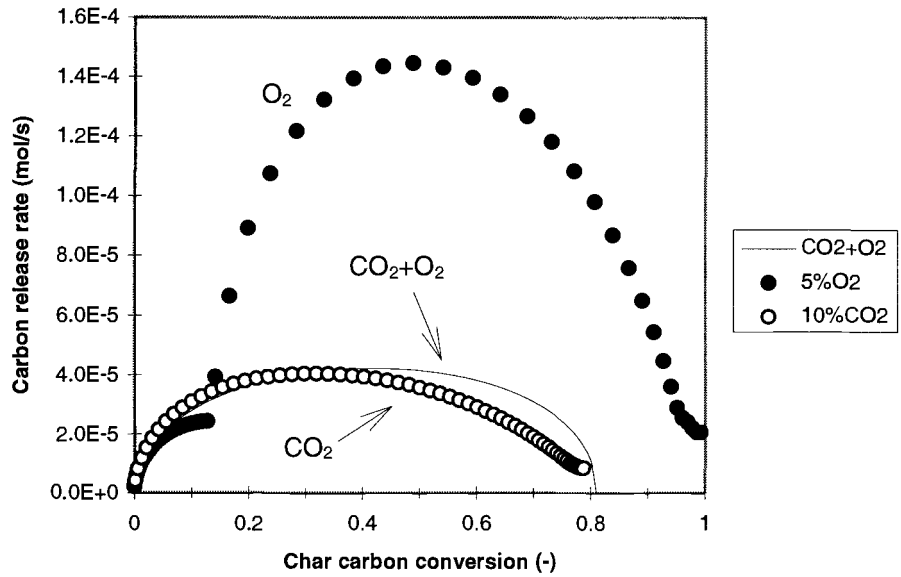

Figure 5.20. A comparison between the carbon release rates in 10% CO_2 + 5% O_2, 5% O_2, and 10% CO_2 in He shows that CO_2 and O_2 are not additive at 1100°C, and that the rate is about 3.5 times faster in oxygen alone than when CO_2 is present.

Figure 5.20 shows that based on this analysis the rates are not additive. If they were, the white dots would be above the black ones. It also shows that the carbon release rate is ~3.5 times faster in oxygen alone compared to when CO_2 was present. For this data the rates are fastest in 5% O_2, and the rates in CO_2 are almost the same regardless whether O_2 is present or not. It is also evident from Figure 5.21 that CO_2 suppresses the rate of carbon release by blocking active sites from the access of oxygen. This is due to strong adsorption of CO_2 onto the char surface as will be explained in Chapter 8.

CONCLUSIONS AND RECOMMENDATIONS

Mass spectrometry is a powerful technique in several fields and it proved to be a useful tool in studying black liquor char gasification as well. To it's strengths can be included that all species are monitored simultaneously and in real time without risk of condensation providing a fingerprint of the complex gasification process. Sampling can occur from an environment that closely represent real world systems such as a recovery boiler or gasifier. It's main weakness may be that it is fairly semiquantitative compared to many other techniques and that it is sensitive to noise and disturbances. E.g. fluctuating vacuum levels and electron beam intensities, different multiplier settings, and background noise may give varying results from day to day. Argon was injected in the reacting gases as a measure to take these uncertainties into consideration.

The results of this work show that:

1. The release of carbon in gas environments of CO_2 and/or O_2 was strongly limited by pore diffusion and film mass transfer at 1100°C.
2. The total ion current was always bell shaped coming mainly from CO.
3. Water vapor is always detected right after insertion of sample. This is a result of drying.
4. More CO was formed (about 6 to 10 times) in 10% CO_2 compared to when oxygen was present.
5. NaCl is the main sodium containing species measured. Elemental sodium from carbonate reduction was probably a deposited on the reactor walls.
6. Less SO_2 from organic sources was detected for chars obtained at higher LEFR residence times and temperatures.
7. Less SO_2 from inorganic sources was detected when both CO_2 and oxygen were present simultaneously.
8. Some H_2S and HCl were detected.
9. Aromatic species such as benzene and naphthalene were detected in trace amounts.

10. Three quantitative models were developed for the rate of carbon removal in CO_2, O_2, and $CO_2 + O_2$.
11. The rate of carbon removal was not additive in CO_2 and O_2 gasification separately compared to when they were both present simultaneously.
12. The rates in CO_2 were almost the same regardless whether O_2 was present or not.
13. The rates were fastest in 5% O_2.
14. There appears to be two inorganic phases in the char residues: salt crystals and a coating of alkali carbonate and sulfate.

It is recommended that in future work one would monitor CO_2 directly in 5% O_2, and using $^{13}CO_2^+$ isotopes when CO_2 is present. Further experiments using calibration methods presented in the literature (15) would further improve the models presented herein.

ACKNOWLEDGMENT

The author acknowledges the National Renewable Energy Laboratory, the Associated Western Universities Inc., and the Niemi Foundation at Oregon State University. The Office of Industrial Technology at the United States Department of Energy is also acknowledged. Dr. David C. Dayton is acknowledged for advice and guidance. Mr. Joe Patrick is acknowledged for technical assistance.

NOMENCLATURE

Symbol	Description, Units
a	speed of sound, m/s
A	cross sectional area, m^2
A*	orifice area, m^2
Bi_m	mass transfer Biot number, dimensionless = $k_m \cdot L / \mathcal{D}_{eff}$
C_i	concentration of species i. mol/L
$\hat{C}_p$	specific heat capacity, J/kg K
$\overline{C}_p$	molar average heat capacity, J/mol K
d	orifice diameter, m
$\mathcal{D}_{eff}$	effective diffusion constant, m^2/s (continuum diffusion assumed)
$F_{i,Ar}$	calibration constant, dimensionless
G	multiplier gain, dimensionless
h	enthalpy per unit mass, J/kg
h_0	stagnation enthalpy, J/kg
I_i	intensity of species i, arbitrary units
I_{out}	electron (ion) current out, milliamps
I_{in}	electron (ion) current in, milliamps
k	Boltzmann constant, J/K = 1.380621×10^{-23}
k'''	1. order rate constant, m^3 gas / m^3 solid · sec
Kn	Knudsen number, dimensionless
l	thickness of slab, m
L	characteristic length, m = l/2 for slab
M	Mach number, dimensionless
n	molar population, mol
n_0	initial molar population, mol = P/kT
P	absolute pressure, Pa
P_0	initial pressure, Pa

P_b	background pressure, Pa
P_{exit}	exit pressure, Pa
R	ideal gas constant, J/mol K
T	absolute temperature, K
T_0	initial temperature, K
V	gas velocity, m/s
W	molecular weight, g/mol
$\overline{W}$	molar avg. molecular weight, g/mol
X	location from orifice, m
X_i	mol fraction, dimensionless
X_q	location of quitting surface, m

Greek Symbols

γ	ideal heat capacity ratio, dimensionless = $\overline{C}_p \div \overline{C}_v$
ρ	density , kg/m^3
ρ_0	initial density, kg/m^3
η	effectiveness factor, dimensionless = $\tanh(\Phi) \div \Phi$
λ	mean free path,
σ	collision diameter, nm
Φ	Thiele modulus, dimensionless = $L\sqrt{k''' / D_{eff}}$
∇	differential operator, not applicable

REFERENCES

1. Robinson, J.W., Undergraduate Instrumental Analysis, 5th ed., Marcel Dekker Inc., 1994

2. Skoog, D.A., Leary, J.J., Principles of Instrumental Analysis, 4th ed., Saunders College Publishing, 1992

3. Scoles, G., editor, Atomic and Molecular Beam Methods, Vol.1, Chapters 2, 4, 6, 7, Oxford University Press, 1988

4. Levenspiel, O., Engineering Flow and Heat Exchange, Plenum Press, 1984

5. McGee, H.A., Molecular Engineering, McGraw-Hill, Inc., 1991

6. Rubinson, K.A., Chemical Analysis, Little, Brown & Company, 1987

7. MBMS manual, Flange Mounted Mass Filter Assembly, p.8-5, Extrel Corp., Pittsburgh, PA, 1996

8. Dayton, D.C., French, R.J., Milne, T.A., The Direct Observation of Alkali Release During Combustion and Gasification. 1. The Application of Molecular Beam/Mass Spectrometry to Switchgrass Combustion, ENERGY & FUELS, Vol. 9, No. 5, p.855-865, 1995

9. Patrick, J., National Renewable Energy Laboratory, Golden, CO, personal communication, March 8, 1996

10. Dayton, D.C., Frederick, W.J., Direct Observation of Alkali Vapor Release during Biomass Combustion and Gasification. 2. Black Liquor Combustion at 1100°C, ENERGY & FUELS, Vol. 9, No. 5, p.855-865, 1995

11. Frederick, W.J., Hupa, M., Stenberg, J., Hernberg, R., Optical Pyrometric Measurements of Surface Temperatures During Black Liquor Char Burning and Gasification, FUEL, Vol.73, No.12, p.1889-1893, 1994

12. Dayton, D.C., National Renewable Energy Laboratory, Golden, CO, E-mail communication, May 6, 1996

13. CRC Handbook of Chemistry and Physics, Weast, R.C., editor, CRC Press, Inc., 1985-1986

14. Wåg, K.J., Reis, V.V., Frederick, W.J., Grace, T.M., Proceedings of the 1995 TAPPI Engineering Conference, Dallas, TX, p.841-852, 1995

15. Pugliese, R.A., Ph.D. dissertation, U. of Massachusetts, February, 1993

16. Frederick, W.J., Wåg, K.J., Hupa, M.M., Ind.Eng.Chem.Res., Vol.32, No.8, p.1747-1753, 1993

17. Grace, T.M., Lien, S.J., Brown, C.A., Proceedings of the International Chemical Recovery Conference, TAPPI, Atlanta, GA, p.539-550, 1992

APPENDICES

APPENDIX 5.1

Computer Program for Estimating the Internal and External Mass Transport Resistances

TK program

VARIABLE SHEET

Input	Name	Output	Unit	Comment
				Program for calculating the external and internal transport resistances in the NREL convective flow reactor Gas properties for 100% He Last modified: 2/7/96 KW
	dT	6.964	K	Temp diff between furnace and particle
300	Tini		K	Initial gas temp
1373	Tfur		K	Furnace wall temp
1273	Tgas		K	Gas temp (3.33slm=200l/h 300K inlet)
	Tp	1366	K	GUESS PARTICLE TEMPERATURE
	Tf	1320	K	Particle film temp (for Sc and DiffCO2
.05	po2		bar	O2 partial pressure
.1	pco2		bar	CO2 partial pressure
0	pco		bar	CO partial pressure
1.04e-3	Carb		mol/part	C init. in particle for 25mg sample 50% of char is carbon: 12.5mg
	rCO2	.0180767	mol/s	CO2 kinetic rate
	Rreduc	.0003675	mol/s	C converted by sulfate reduction
.18	SO4			SO4/Na2 mole ratio
3.141	pi			Archimedes' constant
	dHrtot	1086.449	J/mol	Total heat of reaction
	dHrO2	-255.512	J/mol	O2 heat of reaction
	dHrCO2	-236.785	J/mol	CO2 heat of reaction
	dHrRed	1578.746	J/mol	Sulfate reduction heat of reaction
	HfO2	421.7447	J/mol	O2 heat of formation
	HfCO	302.0646	J/mol	CO heat of formation
	HfCO2	494.2102	J/mol	CO2 heat of formation
	HfC	346.7041	J/mol	C heat of formation
	HfH2	333.6133	J/mol	H2 heat of formation
	HfNa2S	599.8057	J/mol	Na2S heat of formation
	HfNa2SO	-1157.5	J/mol	Na2SO4 heat of formation

	Qg	1.067421	W	Heat generation by reaction
	Qc	6.00905	W	Heat transfer by convection
	Qr	7.07647	W	Heat transfer by radiation
	wini	.154303	m/s	Flow speed at inlet of reactor
	w	4.58332	m/s	Flow speed at particle
	nyini	.000122	m2/s	Viscosity at inlet of reactor
	ny	.001426	m2/s	Viscosity of gas in bulk
	nys	.001516	m2/s	Viscosity of gas in film
	nyratio	.940842		Viscosity ratio
.000055	Vini		m3/s	Volume flow at inlet of reactor 3.33slm
	V	.001648	m3/s	Volume flow at particle
	mini	6.313E-5	kg/s	Gas mass flow
	kgO2	.30425	m/s	O2 mass transfer coefficient
	kgCO2	.25504	m/s	CO2 mass transfer coefficient
	O2byMT	.00025	mol/s	O2 mass transfer rate
	CO2byMT	.00043	mol/s	CO2 mass transfer rate
	CO2	.478641	mol/m3	O2 concentration
	CCO2	.957282	mol/m3	CO2 concentration
.0214	Dia		m	Tube diameter 25.4-4=21.4mm
.000025	m		kg	Initial particle mass
100	dens		kg/m3	
	Dp	.023562	m	Swollen particle diameter
	Vp	6.849E-6	m3	Particle volume
	Aext	.001744	m2	Particle external surface area
	L	.003927	m	Characteristic length
	h	37.0330	W/m2/K	Convective heat transfer coefficient
.5	f			Fraction of saturated smelt
.5	Pore			Porosity (0.5 because char was crushed
2E-8	Prsz		m	Pore diameter 39A Argon (200A in N2)
5.67E-8	SB		W/m2/K4	Stefan-Boltzmann constant
	k	.155003	W/m/K	Local apparent thermal conductivity
	Nu	5.62934		Nusselt number
.67	Pr			Prandtl number
	Reini	26.9802		Reynolds number at inlet
	Re	68.7603		Reynolds number at particle
	ScO2	1.54141		O2 Schmidt number
	ScCO2	1.94986		CO2 Schmidt number
	ROO2	.000254	mol/s	C depletion by O2 gasification
	ROCO2	.000361	mol/s	C depletion by CO2 gasification
	DiffO2	9.254E-4	m2/s	O2 diffusivity
	DkO2	6.338E-8	m2/s	Knudsen diffusivity of O2
	DeffO2	1.584E-8	m2/s	Effective diffusivity of O2

DiffCO2	7.316E-4	m2/s	CO2 diffusivity
DkCO2	5.405E-8	m2/s	Knudsen diffusivity of CO2
DeffCO2	1.351E-8	m2/s	Effective diffusivity of CO2
THCO2	7.624		CO2 Thiele modulus
EFFCO2	.1312		CO2 effectiveness factor
BiO2	75413.715		O2 Biot number (mass transfer)
BiCO2	74128.783		CO2 Biot number (mass transfer)
DmCO2	.00078403		CO2 Damkohler number
DiffO2o	1.6088E-3	m2/s	
DiffCO2	7.1925E-4	m2/s	
OmegaO2	.5956233		
OmegaCO	.6202770		
TsO2	40.23674		
TsCO2	31.03024		
			Lennard-Jones parameters
sigmaO2	3.0045		
sigmaCO	3.286		
10.2 ekHe			
113 ekO2			
190 ekCO2			
			NEUFELDT PARAMETERS
1.06036 A			
.1561 B			
.193 C			
.47635 D			
1.03587 E			
1.52996 F			
1.76474 G			
3.89411 H			

RULE SHEET
S Rule
* dT=Tfur-Tp
* L=Dp/6
* Dp=(m/dens/pi*6)^0.333*3
* Vp=pi*Dp^3/6
* Aext=pi*Dp^2
* Nu=2+(0.4*Re^0.5+0.06*Re^0.667)*Pr^0.4*nyratio^0.25 "Whitaker equation
* k=(1-f)*(0.05+4*Pore*Prsz*SB*Tp^3)+0.26*f "Merriam equation
* h=Nu*k/Dp
* rCO2=63.0e9*pco2/(pco2+3.4*pco)*Carb*exp(-30070/Tp)
* Rreduc=3790*Carb*SO4^1.4*exp(-9400/Tp)
* Qg=(ROO2+ROCO2+Rreduc)*dHrtot
* Qc=h*Aext*(Tp-Tgas)
* Qr=Aext*SB*(Tfur^4-Tp^4)
* Qr=Qg+Qc
* dHrtot=dHrO2+dHrCO2+dHrRed
* dHrO2=HfCO-HfC-HfO2/2
* dHrCO2=2*HfCO-HfCO2-HfC
* dHrRed=HfNa2S+4*HfCO-HfNa2SO4-4*HfC
* HfO2=(-9679.104+29.95744*Tp+.2092*Tp^2+167360/Tp)/1000
* HfH2=(-8110.091+27.27968*Tp+0.163176*Tp^2-50208/Tp)/1000
* HfCO=(-119348.1+28.40936*Tp+0.205016*Tp^2+46024/Tp)/1000
* HfCO2=(-409930.4+44.1412*Tp+0.451872*Tp^2+853536/Tp)/1000
* HfC=(-2106.402+0.108784*Tp+0.1947024*Tp^2-0.579484e5
*Tp^3+148113.6/Tp)/1000
* HfNa2S=(-397616.4+90.02294*Tp+0.468608*Tp^2)/1000
* HfNa2SO4=(-1427155+197.4011*Tp)/1000
* Re=w*Dia/ny
* Reini=wini*Dia/nyini
* w=V/(pi*Dia^2/4)
* wini=Vini/(pi*Dia^2/4)
* mini=Vini*28/(82.06e-6*Tini)/1000
* V=mini*82.06e-6*Tgas/4*1000
* nyini=(7.56775e-5*Tini^1.69906)*1e-4
* ny=(7.56775e-5*Tgas^1.69906)*1e-4
* nys=(7.56775e-5*Tf^1.69906)*1e-4
* nyratio=ny/nys
* Tf=Tgas+abs(Tp-Tgas)/2
* DiffO2o=0.0000961*(Tp/273)^1.75
* DiffCO2o=DiffO2*1.378/1.773
* sigmaO2=(2.576+3.433)/2
* TsO2=Tp/sqrt(ekO2*ekHe)
* OmegaO2=A/TsO2^B+C/exp(D*TsO2)+E/exp(F*TsO2)+G/exp(H*TsO2)
* DiffO2=0.0018583*Tp^1.5*sqrt(1/32+1/4)/sigmaO2^2/OmegaO2/10000

```
* sigmaCO2=(2.576+3.996)/2
* TsCO2=Tp/sqrt(ekCO2*ekHe)
* OmegaCO2=A/TsCO2^B+C/exp(D*TsCO2)+E/exp(F*TsCO2)+G/exp(H*TsCO2)
* DiffCO2=0.0018583*Tp^1.5*sqrt(1/44+1/4)/sigmaCO2^2/OmegaCO2/10000
* kgO2=DiffO2/Dp*(2+0.6*Re^0.5*ScO2^0.333) "Re < 325
* kgCO2=DiffCO2/Dp*(2+0.6*Re^0.5*ScCO2^0.333)
* ScO2=ny/DiffO2
* ScCO2=ny/DiffCO2
* CO2=po2/82.06e-6/Tgas
* CCO2=pco2/82.06e-6/Tgas
* O2byMT=kgO2*pi*Dp^2*CO2
* CO2byMT=kgCO2*pi*Dp^2*CCO2
* THCO2=Dp/6*sqrt(abs(rCO2)/Vp/DiffCO2/CCO2)
* EFFCO2=tanh(THCO2)/THCO2
* ROO2=O2byMT "assumed exclusively mass transfer controlled
* 1/ROCO2=1/CO2byMT+1/(EFFCO2*abs(rCO2))
* BiO2=kgO2*L/DeffO2
* BiCO2=kgCO2*L/DeffCO2
* DeffO2=Pore^2*1/(1/DiffO2+1/DkO2)
* DeffCO2=Pore^2*1/(1/DiffCO2+1/DkCO2)
C DeffO2=Pore^2*DiffO2 "molecular flow had to be assumed
C DeffCO2=Pore^2*DiffCO2 "molecular flow had to be assumed
C DeffO2=Pore^2*1/DkO2
C DeffCO2=Pore^2*1/DkCO2
* DkO2=9700*Prsz/2*sqrt(Tp/32)/10000 "cm2/s /10000 => m2/s
* DkCO2=9700*Prsz/2*sqrt(Tp/44)/10000 "cm2/s /10000 => m2/s
* DmCO2=THCO2^2/BiCO2
```

APPENDIX 5.2

Species Trend Data for Studied Chars

Table A.5.2.1. The normalized amounts of H_2O^+ released are shown for the chars studied. The data is approximately for a 95% confidence interval.

LEFR Temp. (°C)	LEFR Res.time (sec)	Amount in 5% O_2	Amount in 5% O_2 + 10% CO_2	Amount in 10% CO_2
700	0.38	4.2	4.1	2.4
700	0.66	3.7	3.8	2.1
700	1.49	3.2	3.1	1.9
900	0.39	4.2	3.0	2.3
900	0.67	2.4	2.6	1.8
900	1.32	2.1	2.2	2.7
1100	0.31	2.8	2.9	1.9
1100	0.72	2.3	2.0	2.6
1100	1.32	2.3	1.9	1.7

Table A.5.2.2. The normalized amounts of Na^+ released are shown for the chars studied. The data is approximately for a 95% confidence interval.

LEFR Temp. (°C)	LEFR Res.time (sec)	Amount in 5% O_2	Amount in 5% O_2 + 10% CO_2	Amount in 10% CO_2
700	0.38	0.3	0.2	0.3
700	0.66	0.2	0.4	0.4
700	1.49	0.3	0.4	0.4
900	0.39	0.3	0.4	0.3
900	0.67	0.3	0.4	0.4
900	1.32	0.2	0.4	0.4
1100	0.31	0.3	0.4	0.5
1100	0.72	0.3	0.4	0.6
1100	1.32	0.4	0.4	0.4

Table A.5.2.3. The normalized amounts of CO^+ released are shown for the chars studied. The data is approximately for a 95% confidence interval.

LEFR Temp. (°C)	LEFR Res.time (sec)	Amount in 5% O_2	Amount in 5% O_2 + 10% CO_2	Amount in 10% CO_2
700	0.38	6.1	6.0	24.5
700	0.66	5.8	9.1	22.0
700	1.49	6.0	9.1	27.9
900	0.39	4.8	7.4	24.8
900	0.67	6.3	8.3	26.1
900	1.32	6.1	7.4	28.4
1100	0.31	7.9	6.0	21.1
1100	0.72	5.8	6.8	23.8
1100	1.32	6.6	10.1	25.1

Table A.5.2.4. The normalized amounts of H_2S^+ released are shown for the chars studied. The data is approximately for a 95% confidence interval.

LEFR Temp. (°C)	LEFR Res.time (sec)	Amount in 5% O_2	Amount in 5% O_2 + 10% CO_2	Amount in 10% CO_2
700	0.38	0.3	0.3	0.4
700	0.66	0.2	0.4	0.3
700	1.49	0.2	0.4	0.2
900	0.39	0.1	0.4	0.2
900	0.67	0.2	0.4	0.2
900	1.32	0.2	0.3	0.2
1100	0.31	0.2	0.4	0.3
1100	0.72	0.1	0.3	0.3
1100	1.32	0.1	0.4	0.2

Table A.5.2.5. The normalized amounts of HCl^+ released are shown for the chars studied. The data is approximately for a 95% confidence interval.

LEFR Temp. (°C)	LEFR Res.time (sec)	Amount in 5% O_2	Amount in 5% O_2 + 10% CO_2	Amount in 10% CO_2
700	0.38	0.2	0.1	0.2
700	0.66	0.1	0.2	0.2
700	1.49	0.1	0.2	0.2
900	0.39	0.1	0.2	0.2
900	0.67	0.1	0.2	0.3
900	1.32	0.1	0.2	0.2
1100	0.31	0.1	0.2	0.3
1100	0.72	0.1	0.2	0.3
1100	1.32	0.1	0.2	0.2

Table A.5.2.6. The normalized amounts of $^{13}CO_2^+$ released are shown for the chars studied. The data is approximately for a 95% confidence interval.

LEFR Temp. (°C)	LEFR Res.time (sec)	Amount in 5% O_2	Amount in 5% O_2 + 10% CO_2	Amount in 10% CO_2
700	0.38	0.8	1.2	0.9
700	0.66	0.8	1.7	1.0
700	1.49	0.7	1.1	1.0
900	0.39	0.7	1.5	1.4
900	0.67	0.7	1.2	1.3
900	1.32	0.7	1.5	1.3
1100	0.31	0.6	2.1	1.3
1100	0.72	0.6	1.3	1.8
1100	1.32	0.6	1.6	1.1

Table A.5.2.7. The normalized amounts of $NaCl^+$ released are shown for the chars studied. The data is approximately for a 95% confidence interval.

LEFR Temp. (°C)	LEFR Res.time (sec)	Amount in 5% O_2	Amount in 5% O_2 + 10% CO_2	Amount in 10% CO_2
700	0.38	0.7	0.3	0.5
700	0.66	0.5	0.5	0.3
700	1.49	0.6	0.6	0.5
900	0.39	0.7	0.6	0.4
900	0.67	0.7	0.6	0.6
900	1.32	0.6	0.6	0.6
1100	0.31	1.0	0.7	0.6
1100	0.72	0.7	0.6	0.8
1100	1.32	1.1	0.7	0.7

Table A.5.2.8. The normalized amounts of organic SO_2^+ released are shown for the chars studied. The data is approximately for a 95% confidence interval.

LEFR Temp. (°C)	LEFR Res.time (sec)	Amount in 5% O_2	Amount in 5% O_2 + 10% CO_2	Amount in 10% CO_2
700	0.38	1.4	1.1	0.3
700	0.66	1.0	0.8	0.3
700	1.49	0.3	0.2	0.1
900	0.39	0.5	0.4	0.2
900	0.67	0.1	0.2	0.2
900	1.32	0.0	0.0	0.2
1100	0.31	0.1	0.1	0.1
1100	0.72	0.0	0.0	0.1
1100	1.32	0.0	0.0	0.0

Table A.5.2.9. The normalized amounts of inorganic SO_2^+ released are shown for the chars studied. The data is approximately for a 95% confidence interval.

LEFR Temp. (°C)	LEFR Res.time (sec)	Amount in 5% O_2	Amount in 5% O_2 + 10% CO_2	Amount in 10% CO_2
700	0.38	0.0	0.0	1.8
700	0.66	0.0	0.4	1.3
700	1.49	0.4	0.4	2.3
900	0.39	2.4	0.2	1.3
900	0.67	0.2	0.2	1.4
900	1.32	0.5	0.3	2.7
1100	0.31	0.8	0.5	2.4
1100	0.72	2.0	0.6	3.0
1100	1.32	5.6	0.6	4.7

Table A.5.2.10. The normalized amounts of $C_6H_6^+$ released are shown for the chars studied. The data is approximately for a 95% confidence interval.

LEFR Temp. (°C)	LEFR Res.time (sec)	Amount in 5% O_2	Amount in 5% O_2 + 10% CO_2	Amount in 10% CO_2
700	0.38	0.1	0.1	1.7
700	0.66	0.1	0.1	1.3
700	1.49	0.1	0.1	0.5
900	0.39	0.1	0.1	1.0
900	0.67	0.1	0.1	0.3
900	1.32	0.1	0.1	0.2
1100	0.31	0.1	0.2	0.2
1100	0.72	0.1	0.1	0.3
1100	1.32	0.1	0.1	0.4

Table A.5.2.11. The normalized amounts of $C_{10}H_8^+$ released are shown for the chars studied. The data is approximately for a 95% confidence interval.

LEFR Temp. (°C)	LEFR Res.time (sec)	Amount in 5% O_2	Amount in 5% O_2 + 10% CO_2	Amount in 10% CO_2
700	0.38	0.1	0.1	1.4
700	0.66	0.1	0.1	1.2
700	1.49	0.1	0.1	0.3
900	0.39	0.1	0.1	0.9
900	0.67	0.1	0.1	0.2
900	1.32	0.1	0.1	0.1
1100	0.31	0.1	0.2	0.2
1100	0.72	0.1	0.1	0.3
1100	1.32	0.0	0.1	0.5

MBMS repeat data for black liquor char (10/5/95 KW)

Revised April 96

Filename	Char code	Notes	Ar bckgnd	W of smpl	*H2O* A of 18	*Na* A of 23	*CO* A of 28	*H2S* A of 34	*HCl* A of 36	*CO2* A of 45	*NaCl* A of 58	*C6H6* A of 78	*C10H8* A of 128	*SO2o* A of 64	*SO2i* A of 64	*SO2tot* A of 64
A0926503	91s11o5		226209	22.4	133102	14622	413038	6281	8609	35074	43522	2909	3395	3677	34240	37917
A0926504	91s11o5		156459	23.0	118924	16372	418948	11788	6176	37516	46145	4725	3403	6374	42755	49129
A0926505	91s11o5		244983	24.1	140329	16884	450218	5605	3765	30287	43980	4150	3246	3270	31106	34376
A0926506	69m11o5		205515	28.8	131558	10769	178337	5715	4419	36038	29349	3226	3191	5297	33128	38425
A0926507	69m11o5		191273	25.0	104221	16603	240461	7639	4465	27138	36981	3796	2870	8064	81990	90054
A0926508	69m11o5		197529	27.3	139544	12800	353207	6873	3785	30301	42607	3218	2680	6570	113169	119739
A0926511	81h11o5		208415	25.5	127388	17605	328921	5655	3542	31291	45231	3847	861	12847	229237	242084
A0926512	81h11o5		192061	27.8	132215	19845	363973	4037	3236	34982	53894	3793	1632	3906	330036	333942
A0926514	81h11o5		181496	25.2	98400	20932	311183	5120	3635	33504	52503	3605	2387	22187	290847	313034
A0926515	93s9o5		193305	24.0	203029	17880	350260	4635	3567	30314	45068	3850	4115	28506	102720	131226
A0926517	93s9o5		215390	23.1	194420	9973	191163	4153	5029	32980	31664	2491	3484	22466	100991	123457
A0926518	93s9o5		186390	25.0	205136	12279	221600	5223	4865	30422	16842	4300	5879	19340	10350	29690
A0926519	93s9o5		191518	24.4	204959	11538	242846	5605	6695	34940	37559	4873	5638	22528	128524	151052
A0926520	93s9o5		191341	21.2	164141	13485	212524	2899	6583	27411	32677	5910	2961	19386	109085	128471
A0927503	77m9o5		177876	24.9	111812	15642	285338	12031	3579	29698	30704	3576	2888	3938	5616	9554
A0927504	77m9o5		183288	24.0	107064	11635	282289	6432	3682	31167	29578	2614	1833	4307	6923	11230
A0927505	77m9o5		186855	22.7	99711	13687	259372	6567	3587	28964	25367	1885	2328	3555	6671	10226
A0927506	85h9o5		203725	21.6	83043	8270	242248	7231	3446	29419	25579	2331	2706	207	13750	13957
A0927507	85h9o5		206421	23.2	106169	10714	300381	9152	2515	29132	27781	3287	2519	513	21426	21939
A0927508	85h9o5		206555	27.0	123678	11569	368575	7906	4104	33667	34165	2312	3111	544	26780	27324
A0927509	62h7o5		176949	27.7	163284	13110	309468	7236	3042	40627	27563	3860	2097	7767	21471	29238
A0927510	62h7o5		203604	23.4	148257	12349	296109	9504	3554	28360	24002	2642	3195	5425	10054	15479
A0927516	78m7o5		179204	24.5	165288	9472	259822	8979	4102	34567	17050	3819	3452	39607	9830	49437
A0927517	78m7o5		169250	25.0	163973	10277	256328	7232	3200	33843	17955	3552	2720	37946	5355	43301
A0927521	78m7o5		169353	18.8	122981	6852	187873	7989	4360	25531	23084	3053	1885	24233	3353	27586
A0927522	78m7o5		179289	20.6	123758	9990	194473	7286	4973	27013	22112	2732	3183	28753	5281	34034
A0927524	62h7o5		158946	26.2	133490	10875	254685	8165	4832	28381	29648	2423	2522	6596	4033	10629
A0927525	62h7o5		156004	20.3	101691	8617	170091	9986	4290	23697	22247	3081	2595	3288	5320	8608
A0928503	94s7o5		162732	22.9	151043	8935	213270	10308	4251	28465	23923	2600	2368	47289	13644	60933
A0928504	94s7o5	spike	170738	25.3	180155	9904	278758	18626	7255	37564	29851	9518	2334	55887	6051	61938
A0928505	94s7o5	spike	154301	26.1	177748	14802	251581	11174	9826	27614	29518	3865	6281	48551	2626	51177
A0928507	94s7o	spike	106389	22.3	85107	3893	119288	7671	3535	31150	6104	1831	1873	21770	1640	23410
A0928508	94s7o	sm spike	100905	24.7	95999	4424	141981	8908	3121	25420	5186	1565	1826	23367	1478	24845

Filename	Char code	Notes	Ar bckgnd	W of smpl	*H2O* A of 18	*Na* A of 23	*CO* A of 28	*H2S* A of 34	*HCl* A of 36	*CO2* A of 45	*NaCl* A of 58	*C6H6* A of 78	*C10H8* A of 128	*SO2o* A of 64	*SO2i* A of 64	*SO2tot* A of 64
A0928509	94s7o		87072	23.7	101665	5059	146850	6334	2506	26194	10563	1457	1052	19662	7044	26706
A0928510	94s7		122812	25.1	58886	7732	759872	12561	4567	32169	11811	50855	40414	8199	55128	63327
A0928511	94s7		114790	20.8	60783	5864	601536	10138	3501	20425	15512	39467	35804	10098	43078	53176
A0928512	94s7		105868	27.7	82964	7000	693519	11751	4214	26016	11266	53089	41047	7557	49864	57421
A0928513	62h7		104112	23.5	39289	7425	689155	4165	3089	27692	13374	12072	7476	3066	57369	60435
A0928514	62h7		106971	27.6	57513	11957	807812	5329	3682	20929	13830	12154	8070	4270	61360	65630
A0928515	62h7		103395	23.2	48318	10040	674834	3828	4665	24849	13635	11551	5667	3505	62670	66175
A0928516	62h7o		81456	27.4	65259	7279	212284	7115	2594	15227	12815	2879	2525	4070	13811	17881
A0928517	62h7o		96909	26.3	71940	10289	226725	9046	4224	26189	11888	3059	1337	7067	12066	19133
A0928518	62h7o		96032	23.5	74753	7613	206121	6932	4293	31963	11564	3381	1979	3649	7234	10883
A0928519	62h7o		88977	23.6	69835	10684	186763	8300	4375	24432	13654	1857	2131	3699	6840	10539
A0928520	78m7o		86931	22.6	86971	6957	183172	10871	3591	40575	7302	2226	2007	14415	6498	20913
A0928521	78m7o		86293	22.7	67141	7344	170470	5884	2285	24346	11148	2921	2317	15236	8159	23395
A0928522	78m7o		93401	21.1	71738	8018	181660	9188	3624	32349	8981	2136	2844	14765	6027	20792
A0928523	78m7		95792	27.2	60118	8480	596853	8059	5014	18353	8457	30936	29294	6009	25270	31279
A0928524	78m7		89476	20.9	46498	7773	454735	4708	2498	21390	13187	28658	23912	4952	29745	34697
A0928525	78m7		90054	23.7	33346	6106	403592	5732	4402	24846	7114	25952	23293	2625	5476	8101
A0929503	93s9o		62202	27.5	59247	5702	164933	5477	2031	24076	10377	1770	1573	8214	2464	10678
A0929504	93s9o		89582	26.3	69242	8813	152036	8915	3301	33967	9242	1800	1940	7873	6830	14703
A0929505	93s9o		99521	21.1	56563	7103	128836	7493	3970	33466	13460	3307	1660	4853	2441	7294
A0929506	93s9		93847	22.1	43006	8514	538852	3414	3381	28401	6501	20754	18229	4201	9743	13944
A0929507	93s9		84855	24.0	49339	7043	516858	4601	6109	28329	8224	20776	18399	3143	31373	34516
A0929508	93s9		87664	26.7	55803	5876	537556	6669	6106	33868	9210	24262	21839	4229	22808	27037
A0929509	85h9		77455	23.1	49345	6780	589457	4647	3417	27020	12625	2306	1700	6156	46762	52918
A0929510	85h9		86993	22.2	48300	7466	534186	2861	3086	32901	8955	4335	1926	827	54649	55476
A0929511	85h9		100092	22.5	63230	8405	556894	3234	4822	17202	10978	2129	992	1558	62343	63901
A0929512	85h9o		74647	22.8	38580	5573	121621	4105	3553	23486	9370	1801	2188	630	4500	5130
A0929513	85h9o		98069	22.5	46068	8009	149388	6193	3295	30797	12577	1748	1459	298	5731	6029
A0929514	85h9o		78062	23.2	41854	5160	149636	6831	3949	32198	10982	2013	2594	292	7733	8025
A0929515	77m9o		78958	25.8	56385	7613	161040	6764	3292	29574	14068	3096	2117	3067	3742	6809
A0929516	77m9o		84892	27.5	55175	6693	196157	9258	3657	23633	11239	1791	1988	3978	2951	6929
A0929517	77m9o		74918	26.8	51249	9200	173477	6138	3611	23610	10265	1911	1695	3959	3653	7612
A0929518	77m9		81297	22.9	31830	7365	498454	3957	5600	16812	12635	3934	2689	3350	27672	31022
A0929519	77m9		80117	25.9	35742	7175	502133	4112	5466	33891	10960	5153	3312	2792	36324	39116
A0929520	77m9		69198	26.5	38063	7436	501457	4251	5661	24203	12619	5140	2922	4304	18280	22584

Filename	Char code	Notes	Ar bckgnd	W of smpl	*H2O* A of 18	*Na* A of 23	*CO* A of 28	*H2S* A of 34	*HCl* A of 36	*CO2* A of 45	*NaCl* A of 58	*C6H6* A of 78	*C10H8* A of 128	*SO2* A of 64	*SO2* A of 64	*SO2* A of 64
A0929521	81h11		99972	21.3	31123	9732	554799	3706	3054	22305	12666	8422	12265	594	85421	86015
A0929522	81h11		96490	21.0	34553	8009	532618	3257	3547	22145	13399	8918	8986	1288	89598	90886
A0929523	81h11		103336	22.1	42909	9454	526937	2484	5260	25318	15273	9543	9701	1467	103328	104795
A0929524	81h11o		68917	25.5	33869	10273	199317	6644	3158	31056	13199	1997	2090	360	14262	14622
A0929525	81h11o		79826	22.7	36575	6165	179386	7778	3164	32277	13767	1749	1564	967	7497	8464
A0929526	81h11o		78961	20.9	30393	5108	149488	7836	3628	24869	9961	1679	1925	545	6576	7121
A0929527	69m11o		76130	23.7	32181	7793	133301	6742	3614	15557	12028	2072	1782	471	3796	4267
A0929528	69m11o		67745	24.1	35064	5165	128793	6120	4268	22488	8212	1744	1785	176	3831	4007
A0929530	69m11o		67949	25.8	34170	6134	91132	3857	2693	26122	7114	1501	1170	1149	10508	11657
A1002504	69m11		59677	27.1	35017	8877	374638	4456	3921	27818	10699	2916	3479	0	42831	42831
A1002505	69m11		55789	20.4	35562	10800	278552	2665	3834	20817	10617	3549	3604	899	38759	39658
A1002506	91s11		65087	23.2	28695	9316	329719	3540	4562	22440	7284	4360	3065	2575	35212	37787
A1002507	91s11		67813	22.3	29503	5840	306474	4249	5132	16154	9209	2590	3316	1618	38263	39881
A1002508	91s11o		59821	22.5	37699	4519	92465	5740	3497	13817	8372	2471	1443	1516	5481	6997
A1002509	91s11o		59006	20.9	36053	4562	89048	6174	2645	38397	8564	2923	2381	588	7686	8274

MBMS repeat data for black liquor char (5/9/95 KW) revised 5/19/96 revised 9/4/96

CO only from CO2 runs

Filename	Char code	Notes	Ar bckgnd (arb)	W of smpl (mg)	W of boat (g)	B+ash (g)	W of rsd (mg)	Cchar,fixed (mg)	CO (mmol)	CO A of 28	k1 mmol CO/min	Avg
A0928510	94s7	10%CO2	122812	25.1	0.5722	0.5765	4.3	20.8	3.47	759872	**0.25**	
A0928511	94s7	10%CO2	114790	20.8	0.5236	0.5270	3.4	17.4	2.90	601536	**0.25**	0.25
A0928512	94s7	10%CO2	105868	27.7	0.5400	0.5447	4.7	23.0	3.83	693519	**0.26**	
A0928513	62h7	10%CO2	104112	23.5	0.5132	0.5178	4.6	18.9	3.15	689155	**0.21**	
A0928514	62h7	10%CO2	106971	27.6	0.5240	0.5278	3.8	23.8	3.97	807812	**0.23**	0.22
A0928515	62h7	10%CO2	103395	23.2	0.5518	0.5568	5.0	18.2	3.03	674834	**0.21**	
A0928523	78m7	10%CO2	95792	27.2	0.5648	0.5700	5.2	22.0	3.67	596853	**0.26**	
A0928524	78m7	10%CO2	89476	20.9	0.5678	0.5721	4.3	16.6	2.77	454735	**0.24**	0.27
A0928525	78m7	10%CO2	90054	23.7	0.5041	0.5100	5.9	17.8	2.97	403592	**0.29**	
A0929506	93s9	10%CO2	93847	22.1	0.5220	0.5290	7.0	15.1	2.52	538852	**0.19**	
A0929507	93s9	10%CO2	84855	24.0	0.5677	0.5759	8.2	15.8	2.63	516858	**0.19**	0.21
A0929508	93s9	10%CO2	87664	26.7	0.5450	0.5518	6.8	19.9	3.32	537556	**0.24**	
A0929509	85h9	10%CO2	77455	23.1	0.5324	0.5406	8.2	14.9	2.48	589457	**0.14**	
A0929510	85h9	10%CO2	86993	22.2	0.5032	0.5108	7.6	14.6	2.43	534186	**0.18**	0.16
A0929511	85h9	10%CO2	100092	22.5	0.5489	0.5583	9.4	13.1	2.18	556894	**0.17**	
A0929518	77m9	10%CO2	81297	22.9	0.5285	0.5337	5.2	17.7	2.95	498454	**0.21**	
A0929519	77m9	10%CO2	80117	25.9	0.5650	0.5717	6.7	19.2	3.20	502133	**0.23**	0.22
A0929520	77m9	10%CO2	69198	26.5	0.5393	0.5456	6.3	20.2	3.37	501457	**0.21**	
A0929521	81h11	10%CO2	94734	21.3	0.5215	0.5270	5.5	15.8	2.63	554799	**0.20**	
A0929522	81h11	10%CO2	106321	21.0	0.5338	0.5392	5.4	15.6	2.60	532618	**0.23**	0.20
A0929523	81h11	10%CO2	93362	22.1	0.5754	0.5836	8.2	13.9	2.32	526937	**0.18**	
A1002503	69m11	10%CO2	22086	24.8	0.5520	0.5563	4.3	20.5	3.42	333629	**0.10**	
A1002504	69m11	10%CO2	60689	27.1	0.5445	0.5509	6.4	20.7	3.45	361421	**0.26**	0.20
A1002505	69m11	10%CO2	56279	20.4	0.5325	0.5375	5.0	15.4	2.57	269707	**0.24**	
A1002506	91s11	10%CO2	69166	23.2	0.5723	0.5775	5.2	18.0	3.00	319592	**0.29**	
A1002507	91s11	10%CO2	69992	22.3	0.5617	0.5652	3.5	18.8	3.13	314642	**0.31**	0.30

All avg	0.22	mmol C/min
	0.44	mmol CO/min
	7.39E-03	mmol CO/s

CO2 + CO from O2 runs

Filename	Char code	Notes	Ar bckgnd (arb)	W. spl (mg)	W. boat (g)	B+ash (g)	Wgt rsd (mg)	Cchar fixed (mg)	CO A of 28	CO2 A of 45	CO2 A of 44	CO (mmol)	C to CO mg	C to CO2 mg	k2 mmol C to CO2 / min	Avg
A0926503	91s11o5	5%O2	226209	22.4	0.5255	0.5295	4.0	18.4	413038	35073	2953147	0.91	11.0	7.4	0.040	
A0926505	91s11o5	5%O2	244983	24.1	0.5496	0.5507	1.1	23.0	450218	30287	2550165	0.92	11.0	12.0	0.080	0.060
A0926506	69m11o5	5%O2	205515	28.8	0.5366	0.5425	5.9	22.9	178337	36038	3034400	0.43	5.2	17.7	0.083	
A0926507	69m11o5	5%O2	191273	25.0	0.5219	0.5247	2.8	22.2	240461	27138	2285020	0.63	7.5	14.7	0.085	0.076
A0926508	69m11o5	5%O2	197529	27.3	0.5263	0.5316	5.3	22.0	353207	30301	2551344	0.89	10.7	11.3	0.061	
A0926511	81h11o5	5%O2	208415	25.5	0.5678	0.5744	6.6	18.9	328921	31291	2634702	0.79	9.5	9.4	0.052	
A0926512	81h11o5	5%O2	192061	27.8	0.5662	0.5682	2.0	25.8	363973	34982	2945484	0.95	11.4	14.4	0.065	0.053
A0926514	81h11o5	5%O2	181496	25.2	0.5554	0.5612	5.8	19.4	311183	33504	2821037	0.86	10.3	9.1	0.041	
A0926515	93s9o5	5%O2	193305	24.0	0.5327	0.5361	3.4	20.6	350260	30314	2552439	0.91	10.9	9.7	0.051	
A0926518	93s9o5	5%O2	186390	25.0	0.533	0.5392	6.2	18.8	221600	30422	2561532	0.59	7.1	11.7	0.059	
A0926519	93s9o5	5%O2	191518	24.4	0.5444	0.5513	6.9	17.5	242846	34940	2941948	0.63	7.6	9.9	0.045	0.051
A0926520	93s9o5	5%O2	191341	21.2	0.5531	0.5591	6.0	15.2	212524	27411	2308006	0.56	6.7	8.5	0.049	
A0927503	77m9o5	5%O2	177876	24.9	0.5429	0.5466	3.7	21.2	285338	29698	2500572	0.80	9.6	11.6	0.057	
A0927504	77m9o5	5%O2	183288	24.0	0.5426	0.5461	3.5	20.5	282289	31167	2624261	0.77	9.2	11.3	0.055	0.055
A0927505	77m9o5	5%O2	186855	22.7	0.5687	0.5730	4.3	18.4	259372	28964	2438769	0.69	8.3	10.1	0.054	
A0927506	85h9o5	5%O2	203725	21.6	0.5794	0.5846	5.2	16.4	242248	29419	2477080	0.59	7.1	9.3	0.053	
A0927507	85h9o5	5%O2	206421	23.2	0.5177	0.5218	4.1	19.1	300381	29132	2452914	0.73	8.7	10.4	0.061	0.055
A0927508	85h9o5	5%O2	206555	27.0	0.5752	0.5813	6.1	20.9	368575	33667	2834761	0.89	10.7	10.2	0.052	
A0927509	62h7o5	5%O2	176949	27.7	0.5462	0.5495	3.3	24.4	309468	40627	3420793	0.88	10.5	13.9	0.050	
A0927510	62h7o5	5%O2	203604	23.4	0.5481	0.5518	3.7	19.7	296109	28360	2387912	0.73	8.7	11.0	0.065	0.057
A0927516	78m7o5	5%O2	179204	24.5	0.5615	0.5693	7.8	16.7	259822	34567	2910541	0.73	8.7	8.0	0.034	
A0927517	78m7o5	5%O2	169250	25.0	0.5381	0.5400	1.9	23.1	256328	33843	2849581	0.76	9.1	14.0	0.058	
A0927521	78m7o5	5%O2	169353	18.8	0.5345	0.5402	5.7	13.1	187873	25531	2149710	0.56	6.7	6.4	0.035	0.042
A0927522	78m7o5	5%O2	179289	20.6	0.5362	0.5429	6.7	13.9	194473	27013	2274495	0.54	6.5	7.4	0.040	
A0927524	62h7o5	5%O2	158946	26.2	0.5781	0.5848	6.7	19.5	254685	28381	2389680	0.80	9.6	9.9	0.046	
A0927525	62h7o5	5%O2	156004	20.3	0.5496	0.5552	5.6	14.7	170091	23697	1995287	0.55	6.5	8.2	0.044	0.045
A0928503	94s7o5	5%O2	162732	22.9	0.5643	0.5672	2.9	20.0	213270	28465	2396753	0.66	7.9	12.1	0.057	
A0928504	94s7o5	5%O2	170738	25.3	0.5453	0.5501	4.8	20.5	278758	37564	3162889	0.82	9.8	10.7	0.040	0.051
A0928505	94s7o5	5%O2	154301	26.1	0.5051	0.5094	4.3	21.8	251581	27614	2325099	0.82	9.8	12.0	0.055	
														All avg	**0.054**	mmol C to CO2/min
															9.00E-04	mmol C to CO2/s

CO2 + O2 runs

Filename	Char code	Notes	Ar bckgnd (arb)	W. spl (mg)	W. boat (g)	B+ash (g)	W. rsd (mg)	Cchar,fixed (mg)	CO A of 28	CO2 A of 45	CO2 A of 44	CO mmol	C to CO mg	C to CO2 mg	k3 mmol C to CO2 / min	Avg
A0928507	94s7o	10%CO2	106389	22.3	0.5913	0.5970	5.7	16.6	119288	31150	2622830	0.56	4.5	12.1	0.034	
A0928508	94s7o	10%CO2	100905	24.7	0.5563	0.5628	6.5	18.2	141981	25420	2140364	0.70	5.6	12.6	0.041	0.034
A0928509	94s7o	10%CO2	87072	23.7	0.5375	0.5445	7.0	16.7	146850	26194	2205535	0.84	6.8	9.9	0.027	
A0928516	62h7o	10%CO2	81456	27.4	0.5891	0.5945	5.4	22.0	212284	15227	1282113	1.30	10.4	11.6	0.051	
A0928517	62h7o	10%CO2	96909	26.3	0.4964	0.5068	10.4	15.9	226725	26189	2205114	1.17	9.4	6.5	0.020	
A0928518	62h7o	10%CO2	96032	23.5	0.5201	0.5234	3.3	20.2	206121	31963	2691285	1.07	8.6	11.6	0.029	0.033
A0928519	62h7o	10%CO2	88977	23.6	0.5428	0.5468	4.0	19.6	186763	24432	2057174	1.05	8.4	11.2	0.034	
A0928520	78m7o	10%CO2	86931	22.6	0.5247	0.5296	4.9	17.7	183172	40575	3416415	1.05	8.4	9.3	0.016	
A0928521	78m7o	10%CO2	86293	22.7	0.5239	0.5304	6.5	16.2	170470	24346	2049933	0.99	7.9	8.3	0.024	0.020
A0928522	78m7o	10%CO2	93401	21.1	0.5460	0.5508	4.8	16.3	181660	32349	2723786	0.97	7.8	8.5	0.020	
A0929503	93s9o	10%CO2	62202	27.5	0.5490	0.5554	6.4	21.1	164933	24076	2027199	1.33	10.6	10.5	0.022	
A0929504	93s9o	10%CO2	89582	26.3	0.5420	0.5472	5.2	21.1	152036	33967	2860021	0.85	6.8	14.3	0.031	0.025
A0929505	93s9o	10%CO2	99521	21.1	0.5500	0.5567	6.7	14.4	128836	33466	2817837	0.65	5.2	9.2	0.023	
A0929512	85h9o	10%CO2	74647	22.8	0.5178	0.5229	5.1	17.7	121621	23486	1977521	0.82	6.5	11.2	0.029	
A0929513	85h9o	10%CO2	98069	22.5	0.4775	0.4815	4.0	18.5	149388	30797	2593107	0.76	6.1	12.4	0.033	0.027
A0929514	85h9o	10%CO2	78062	23.2	0.5318	0.5380	6.2	17.0	149636	32198	2711072	0.96	7.7	9.3	0.019	
A0929515	77m9o	10%CO2	78958	25.8	0.5214	0.5280	6.6	19.2	161040	29574	2490131	1.02	8.2	11.0	0.024	
A0929516	77m9o	10%CO2	84892	27.5	0.5325	0.5394	6.9	20.6	196157	23633	1989899	1.16	9.2	11.4	0.034	0.029
A0929517	77m9o	10%CO2	74918	26.8	0.5798	0.5867	6.9	19.9	173477	23610	1987962	1.16	9.3	10.6	0.028	
A0929524	81h11o	10%CO2	68917	25.5	0.5676	0.5802	12.6	12.9	199317	31056	2614915	1.45	11.6	1.3	0.002	
A0929525	81h11o	10%CO2	79826	22.7	0.5270	0.5338	6.8	15.9	179386	32277	2717723	1.12	9.0	6.9	0.014	0.011
A0929526	81h11o	10%CO2	78961	20.9	0.5224	0.5290	6.6	14.3	149488	24869	2093970	0.95	7.6	6.7	0.018	
A0929527	69m11o	10%CO2	76130	23.7	0.5332	0.5399	6.7	17.0	133301	15557	1309899	0.88	7.0	10.0	0.040	
A0929528	69m11o	10%CO2	67745	24.1	0.5399	0.5464	6.5	17.6	128793	22488	1893490	0.95	7.6	10.0	0.025	0.025
A0929530	69m11o	10%CO2	67949	25.8	0.5217	0.5369	15.2	10.6	91132	26122	2199472	0.67	5.4	5.2	0.011	
A1002508	91s11o	10%CO2	59821	22.5	0.5386	0.5449	6.3	16.2	92465	13817	1163391	0.77	6.2	10.0	0.036	
A1002509	91s11o	10%CO2	59006	20.9	0.5607	0.5660	5.3	15.6	89048	38397	3233027	0.76	6.0	9.6	0.012	0.024
														All avg	0.026	mmol C to CO2/min
															4.31E-04	mmol C to CO2/s

Chapter 6

Thermal Analysis of Black Liquor Char with CO_2 and CO

To be Presented at the 1996 AIChE Annual Meeting

Chicago, November 10-15, 1996

INTRODUCTION

Thermal analysis is the measurement of changes in chemical and physical properties of substances as a function of temperature. The French scientist Le Chatelier is credited for discovering thermal analysis in 1887, when studying the decomposition of clays using heat (1). However, the study of the effect of heat on materials has a longer history: e.g. mankind attempted to produce pottery, extract metals, and make glass several millennia before the modern era. Only in the 19th century did experiments on the effect of heat on materials become more controlled and more quantitative. From that time on the development of new, sophisticated techniques has been rapid, especially in the last 20 years. Today, thermal analysis is an analytical tool for measuring the following physical and chemical phenomena:

- thermal disintegration of solids and liquids,
- solid-solid and solid-gas chemical reactions,
- material identification, specification, and purity,
- inorganic solid material adsorption,
- phase transitions.

This information can be used to characterize polymers, organic and inorganic compounds, metals, and other materials. At present, thermal analysis consists of techniques that can be divided into six major classes according to the convention of the International Confederation of Thermal Analysis (ICTA) (1). For all these methods, the substance and the reference material are subjected to a controlled temperature program.

1. Thermogravimetry (TG), a dynamic mass change method where the mass of a substance is measured as a function of temperature;

2. Differential Scanning Calorimetry (DSC), an enthalpy change method where the difference in energy flux into a substance and a reference material is measured as a function of temperature;
3. Differential Thermal Analysis (DTA), a temperature change method where the difference in the temperature between a substance and a reference material is measured;
4. Dynamic Mechanical Analysis (DMA), a mechanical characteristics-change method where the dynamic modulus and the damping of a substance is measured under oscillatory load as a function of temperature;
5. Thermomechanical Analysis (TMA), a mechanical characteristics-change method where the deformation of a substance is measured under non-oscillatory load as a function of temperature;
6. Dielectric Analysis (DEA), is an electrical characteristics change method where the electrical properties of a substance are measured to determine the conductive and capacitive nature of the substance.

Mass, temperature, and time experiments are among the oldest measurements in the modern era. Looking into an alchemist's laboratory of the fifteenth century, one could see balances and furnaces, although accurate temperature determinations were difficult. Today, thermogravimetry provides a quantitative method to measure any weight change associated with a transition. For example, it is being used for determining the water content in numerous samples as well as the carbon and ash contents of coal. Using TG one can record directly the loss of weight with time or temperature due to dehydration or decomposition. Thermogravimetric curves (thermograms) are characteristic for a given compound, because of the unique physical transitions and chemical reactions that occur over definite temperature ranges and at rates that are dependent on the molecular structure. Changes in weight are a result of the rupture and formation of various physical and chemical bonds at elevated temperatures that lead to the evolution of volatile products (gases) and the formation of heavier reaction products (fragments). From such data, information is obtained concerning the thermodynamics and kinetics of the various

chemical reactions, reaction mechanisms, and the intermediate and final reaction products. The usual temperature range investigated is from ambient to 1200°C with inert or reactive gases.

When chemical reactions are involved, the most useful information can be obtained when thermogravimetry is complemented by differential scanning calorimetry. They provide accurate quantitative data on reaction enthalpies, phase changes, decomposition, and heat capacities. It is also possible to examine the sample in an atmosphere of a reactive gas, thus studying the reaction between the sample and the gas. Therefore these two methods were used in this study and will be discussed in further detail.

OBJECTIVES

One objective of the work reported in this chapter is to characterize the gasification of black liquor char with CO_2 and CO using thermogravimetry at different concentrations of CO_2 and CO. This includes obtaining the concentration of carbonate in the char at different temperatures, which is closely related to the question of how and to what extent carbonate reduction is suppressed by CO_2 and CO. This is discussed based on equilibrium calculations and experimental TG results. Another objective was to detect elemental sodium and CO, and CO_2 in the gases evolved from the TG using a quadrupole molecular beam mass spectrometer (MBMS) to verify the carbonate reduction mechanism.

The only available model for carbonate reduction of kraft black liquor char does not include carbon dependency. Another key objective is to overcome this apparent deficiency by developing a new rate equation, based on experimental data, for carbonate reduction. The last objective is to characterize black liquor char gasification by identifying the endotherms and exotherms using differential scanning calorimetry and comparing the results with the TG thermograms and MBMS spectra. Such a comparison may be useful in validating a proposed mechanism for the overall gasification process.

INSTRUMENTATION AND METHODOLOGY

The instruments used are Thermogravimetric Analyzer TGA 2950, commonly known as a thermobalance, and Differential Scanning Calorimeter DSC 2910 manufactured by TA Instruments Inc., New Castle, Delaware. Both these equipment are controlled by a special operating system TA version 8.6.

TG

Although thermal analysis has come a long way since the systems developed in the 19th century, this analyzer still contains the same functional components: a specimen holder, measuring system, furnace, temperature programmer, and a recorder. Figure 6.1 shows the different components of TGA 2950.

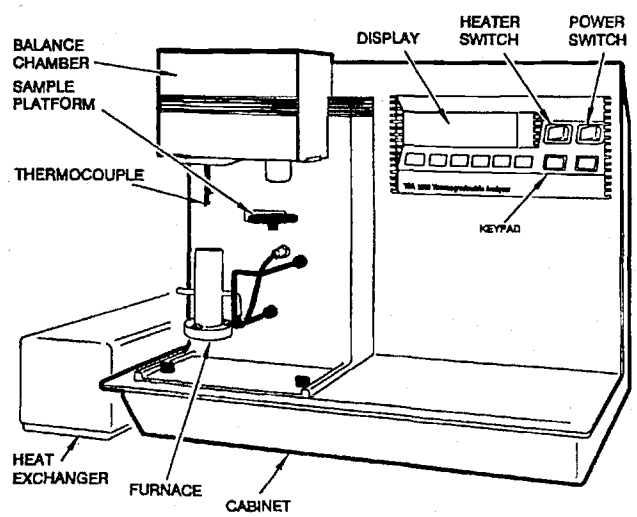

Figure 6.1. The main components in a TGA 2950 are the balance chamber, sample platform, furnace, cabinet, and heat exchanger (1).

Five major components can be distinguished:

1. the balance, which provides the measurement of the sample weight,
2. the sample platform, which loads and unloads the sample,
3. the furnace, which controls the temperature and gas atmosphere,
4. the cabinet, where the system electronics and mechanics are located,
5. the heat exchanger, which dissipates excess heat from the furnace.

Table 6.1 shows the operating parameters of TGA 2950.

Table 6.1. TGA 2950 operating parameters.

Temperature range	25-1000°C
Thermocouple	Platinel II
Heating rate	0.1 to 100°C/min
Sample pan	Platinum 100 μL
Weighing capacity	1.0 g
Balance resolution	0.1 μg
Accuracy	$< \pm 0.1\%$
Purge gas	N_2
Reacting gases	CO_2 and CO
Total flow rate	100 sccm

After taring the circular sample pan, a sample of black liquor char (~20 mg) was poured into it. The pan is placed in the panhole on the sample platform. The wire in the bottom of the pan should align with the groove in the panhole so that the pan can be picked up by the hang down wire. The wire is attached to an automatic recording balance. The sample hook and pan are shown in Figure 6.2.

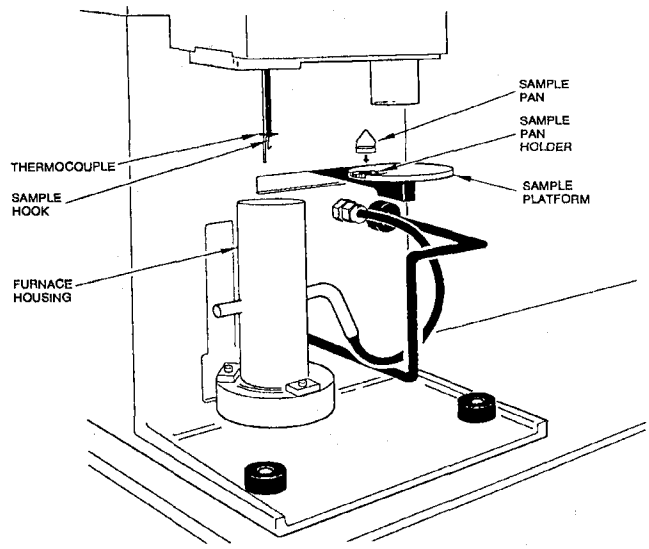

Figure 6.2. Sample pan, thermocouple and furnace of TGA 2950 (1).

The sample is continuously weighed isothermally as a function of time, or non-isothermally as it is heated to higher temperatures at a pre-set constant heating rate. In this study the experiments were done non-isothermally.

DSC

The char is placed on a small aluminum cup covered with an aluminum lid using an encapsulating press. 5 to 10mg of BL char is placed evenly on the bottom of the aluminum cup. A small hole is poked through the lid to allow the contact of the char with the gases. These non-hermetic experiments were the focus of attention. A few hermetic experiments with no poked holes were also made for comparison. A regular cell operating at atmospheric was used in these experiments. Figure 6.3 shows a schematic illustration of the regular DSC setup.

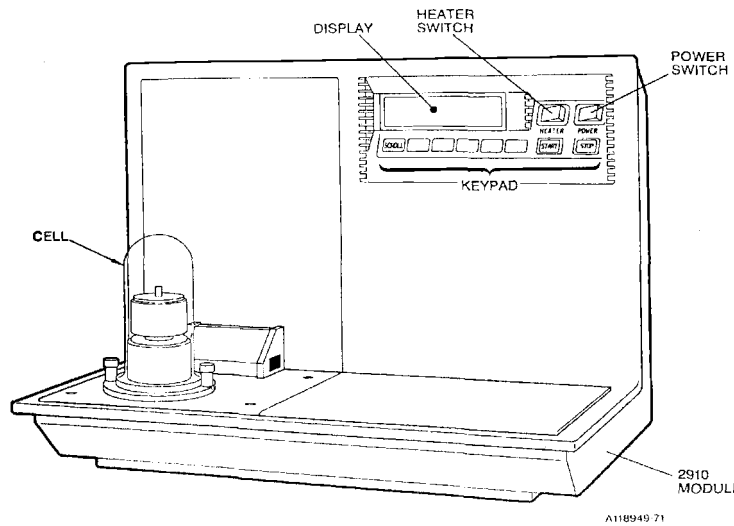

Figure 6.3. Schematic picture of the DSC analyzer used (2).

Table 6.2 shows the specifications of the standard DSC.

Table 6.2. Operating parameters for the standard DSC cell.

Temperature range	-150 to 725°C
Atmosphere	1atm
Control thermocouple	Platinel II
Sample thermocouple	Chromel-alumel
Studied heating rates	10°C/min
Sample cup	aluminum 100 μL
Sample volume	10 mm^3
Calorimetric sensitivity	3 μW
Calorimetric precision	1%
Dynamic gas purge	200 mL/min
Purge gases	N_2, CO_2 and CO
Baseline noise	±30 μW

Figure 6.4 shows the principle of operation of a standard DSC cell. Pure nitrogen or gas mixtures of CO_2, CO, and N_2 were purged through the cell.

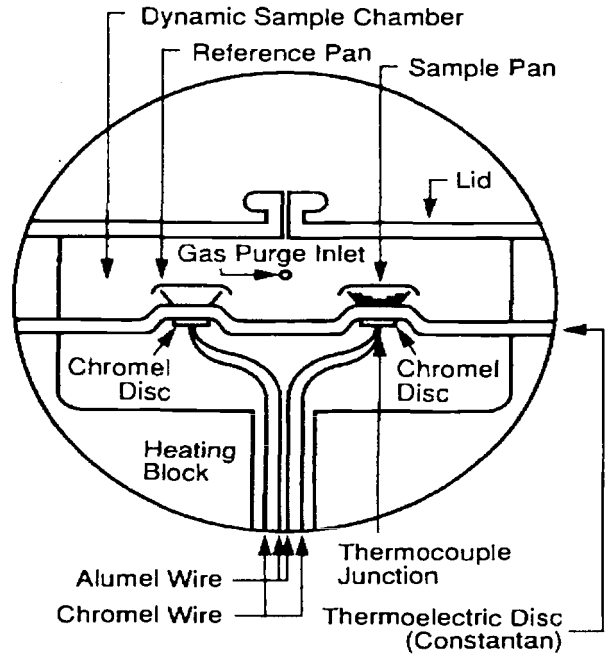

Figure 6.4. Schematic of the operation principle of a DSC (2). It measures the differential heat flow to the sample and the reference using thermocouples.

The raised platform within a thermoelectric disk of constantan serves as the primary means of heat transfer to the sample and the reference pan from the temperature programmed furnace. The temperature of the furnace is raised or lowered in a linear fashion, while the difference in heat flow to the sample and the reference pan are monitored by area thermocouples placed under the raised platforms. The increase in sample and reference temperature will be the same, unless a heat related change occurs in the sample. If a change takes place, the sample temperature either evolves or absorbs heat. The temperature difference between the sample and the reference from such a heat change is directly related to the differential heat flow, which is the measured variable.

The thermocouples are connected in series so that if the sample and the reference temperatures are the same, the resulting electrical potential is zero. The polarity of the electrical potential is reversed depending on if the sample temperature is higher or lower than the reference. The signal is amplified by the ΔT amplifier, which provides a gain of

3000. The amplifier output is applied through the E curve linearizer and monitored so that exotherms are displayed upward and endotherms downward. The E curve is the calibration curve obtained by indium or another metal whose heat of fusion is well known. It acts as an attenuator to shape the gain of the amplified DC output and provides constant calorimetric sensitivity over the studied temperature range. The E curve varies with pressure and thermal conductivity of the gas used. Calibration runs were performed for the relevant gases (N_2, CO_2, CO).

BUOYANCY EFFECTS AND TRANSPORT RESISTANCES

Although the basic principle of thermogravimetry is simple, various tests had to be performed to ensure that precise data were obtained. For the TG, pieces of indium and aluminum were run to check the operation of the thermocouple. For the DSC, tin and indium were used. The calibration runs are given in Appendix 6.1. However, to measure a true sample temperature in the TG is more difficult, since the temperature sensor is not in direct contact with the sample pan as it is in the DSC.

Analysis of buoyancy effects in TG

A blank TG run with the pan only was performed to check the effects of the density change of the reacting gases during heating. The weight increase was 0.06 mg which is approximately 0.5% of the measured maximum weight change of 11.6 mg. Third, the buoyancy effect from the change in sample size was tested. Equation 6-1 gives the mass of the displaced gas resulting in a decrease in weight according to Archimedes' principle (a body in a fluid is buoyed up by a force equal to the weight of the fluid displaced).

$$m = \frac{pM\Delta V}{RT} \qquad (6\text{-}1)$$

Equation 6-1 shows that the mass of the displaced nitrogen was 0.11mg at 300K and 0.27mg at 1273K (max. volume displacement = 100 μL). Considering the offsetting effect of the lighter gas during heat up, the maximum weight change is therefore = 0.27mg (decreased weight due to Archimedes' law) - 0.06mg (increased weight due to less dense gas) = 0.21mg. This is 1.8% of the measured maximum weight change of 11.6mg which was considered negligible.

Analysis of transport resistances in TG

It is a standard procedure to determined to what degree the diffusion of a reacting gas into a porous particle is limited by mass transfer. The analysis was made assuming convective flow above a flat plate, and that the purge and main gas flow were fully mixed above the sample location. The total flow rate was 100 sccm of which 40% was purge flow from above and 60% main gas flow from the side. The diameter of the platinum sample pan was 9 mm and height 1.5 mm, hence the volume of the pan was approximately 100 mm^3, and therefore the bulk density was around 200 kg/m^3. The analysis was made assuming the flow pattern illustrated in Figure 6.5.

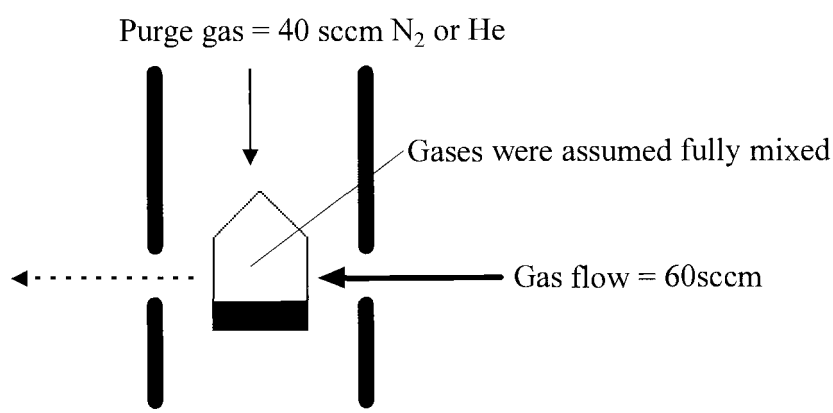

Figure 6.5. Flow pattern of TG sample pan consists of a horizontal flow of reacting gases and a balance purge. It was assumed that the furnace operates as a continuous stirred tank reactor.

No noise was detected in the thermograms, which is an indication that there were no irregular convection currents surrounding the sample pan. Figure 6.6 shows the importance of transport resistances with respect to the mass transfer Biot number and effectiveness factor. The effectiveness factor was based on a crushed char bed inside the sample pan. Two void fractions, 0.1 and 0.5, were used in the calculations because it was difficult to accurately estimate the void fraction of the char bed in the sample pan. The lower fraction is more likely true, because the porosity was altered during sample preparation.

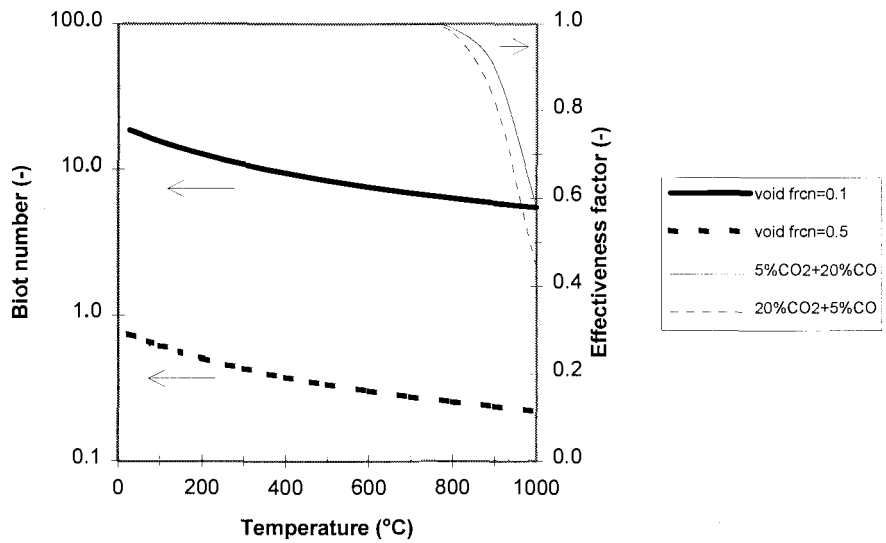

Figure 6.6. Pore diffusion effects are negligible below 800-900°C. The details of the calculations are given in Appendix 6.2.

The importance of the external mass transfer resistance was estimated based on the mass transfer Biot number (Bi_m). It was between 0.2 and 18 depending what porosity was chosen (void fractions of 0.1 and 0.5 were tested). Figure 6.6 shows that the Biot number is most of the time below 10 and above 0.1 meaning that it is in the mixed regime for external and internal mass transfer. However, since the effectiveness factor was unity till 800°C, it was concluded that the gasification rate was kinetically limited at the

temperatures of most interest (600-800°C). Pore diffusion was expected to be negligible since the particle size was so small (~50μm). At temperatures between 900 and 1000°C the diffusion resistance became increasingly important, but these temperatures were of minor importance in this study. Calculation details including a computer program are given in Appendix 6.2.

MATERIAL STUDIED

The black liquor char samples used in this study were obtained by pyrolyzing dry black liquor 90-125 μm diameter particles in nitrogen at 900°C in a laminar entrained-flow reactor (LEFR) with a residence time of 0.8-0.87 s. A detailed description of the device can be found in Appendix 13. The char samples were crushed into small particles ~10-50 microns before placing into the respective sample pans for the TG and DSC analyses. This procedure was necessary to have a sufficient amount of sample in the thermobalance (~20 mg) and the DSC (~5-10 mg). The sample numbers were 70 and 52. The elemental composition for respective char is given in Table 6.3. The valence ratios for the chars were around 1.4 and 2.4 for the BLS.

Table 6.3. The elemental composition of char #77. Carbon data taken from (3) and sulfur from (4). The valence ratio for the BLS was ~2.4 and the char ~1.4. Data is in weight-%.

	C	Na^+	K^+	$SO_4^=$	$S_2O_3^=$	$SO_3^=$	$S^=$	Cl^-	$CO_3^=$
BLS	35.0±0.1	22.7±0.1	0.62±0.1	2.4±0.1	4.45±0.1	0.0	0.0	0.67±0.1	8.1±0.1
char52	28.6±0.1	17.0±0.1	0.25±0.1	1.94±0.1	0.13±0.1	0.75±0.1	1.10±0.1	0.66±0.1	*
char70	31.1±0.1	20.0±0.1	0.43±0.1	1.72±0.1	*	*	*	0.90±0.1	16.5±0.1

* = no data available

The BET surface area for this char was about 10 m^2/g, fairly low but typical for BL chars. The average pore diameter was 210-230Å. The average pore volume was between 0.042 and 0.054 cm^3/g. However, these numbers may have altered during sample preparation.

ASSESSMENT OF RESULTS

TG results

The TG experiments were made at a heating rate of 10°C/min with a varying gas composition of 5-50% CO_2 and CO in helium or nitrogen. The experiments were performed at a total pressure of 1 atm with a temperature increasing from about 50°C to 1000°C. All runs were made in triplicates but some of them had to be discarded due to experimental errors. Figure 6.7 shows a typical experimental thermogram where the weight decreases as the temperature increases at a constant rate.

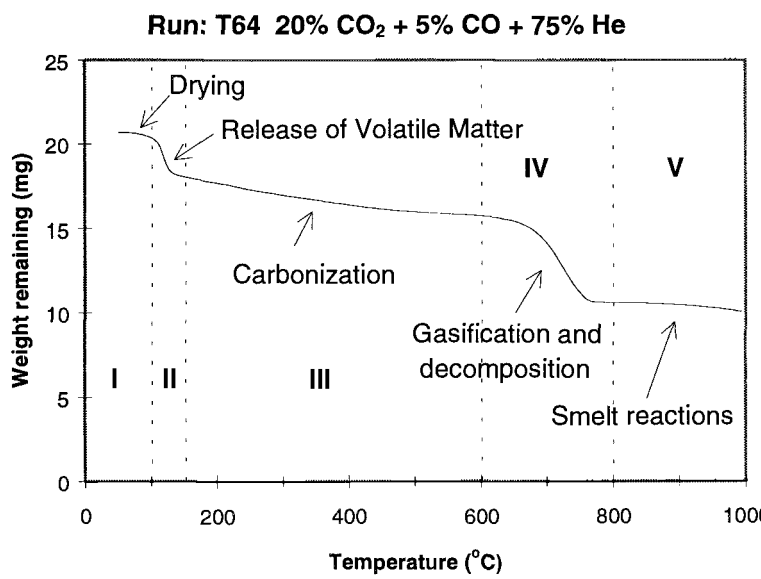

Figure 6.7. An example of a TG thermogram shows five distinguishable mass loss regions. The heating rate = 10°C per min.

In region I of Figure 6.6, the sample weight decreases due to drying. In region II, at about 140°C, there appears to be a shoulder that will be explained when the DSC is discussed. In region III, between 150 and 600°C, there is a weight loss of about 2mg corresponding to about 20% of the total weight change. It is called here carbonization, describing a slow release of volatile matter before reaching temperatures that can overcome the activation energy for reaction of CO_2 with the char. This step can also be examined when the DSC thermogram is discussed. The region between 600 and 800°C is the combined process of gasification with CO_2 and CO, and carbonate decomposition. This temperature region cannot be observed in the DSC data due to the upper limit of its operating temperature. Beyond 800°C, the weight loss has usually leveled off. Step V is discussed in more detail in the suppression effects section.

TG Residue Composition and Valence Balance

The main species found in the char residues were sodium, carbonate, sulfate, potassium, chloride, and thiosulfate in the order of decreasing abundance. Appendix 6.3 lists the concentrations of Na, K, Cl, $SO_4^{=}$, $S_2O_3^{=}$, $CO_3^{=}$, and the cation/anion ratio based on these species. The valence balance was calculated using equation 6-2.

$$\text{Valence balance} = \frac{\frac{\text{ppm Na}}{23} + \frac{\text{ppm K}}{39.1}}{\frac{\text{ppm Cl}}{36.5} + 2 \times \frac{\text{ppm SO}_4}{96} + 2 \times \frac{\text{ppm S}_2\text{O}_3}{112} + 2 \times \frac{\text{ppm CO}_3}{60}} \qquad (6\text{-}2)$$

The average cation/anion ratio was 2.0 with a standard deviation of 0.85. The high standard deviation was caused by a small volume of the residue solution. The reason why the ion mole ratio is ~2 is because it was not possible to measure the carbonate bound to organic alkali species (carboxylic and phenolic groups). This is because these groups would not form $CO_3^{=}$ or $C_2O_3^{=}$ ions in the dissolved solution. In effect, the carbonate measured was exclusively from inorganic precursors, probably the whiskers as discussed

in Chapter 3. No sulfide was detected, because the sample was hot when exposed to the ambient atmosphere which would oxidize the sulfur. Figure 6.8 lists the cation to anion mole ratios in the TG char residues.

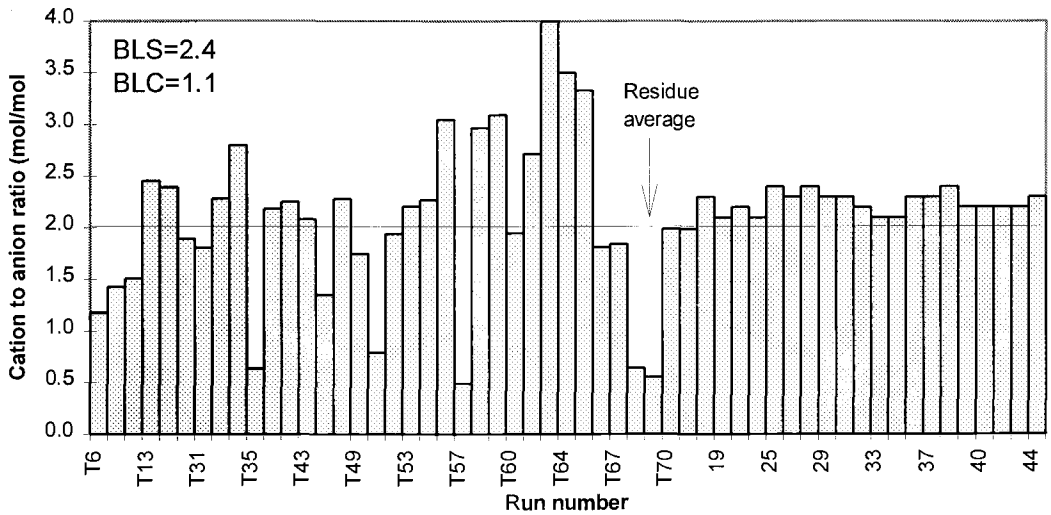

Figure 6.8. The average valence balance ratio for the char residues was 2.1, and the standard deviation 0.85. The valence balance was 1.3 for the studied char and 2.4 for the black liquor solids.

The balance closure was reasonable since it was not possible to account for the organic ions. The corresponding cation to anion ratio was 1.3 for the studied char and 2.4 for the black liquor solids. Appendix 6.3 shows the data and the conditions at which these results were obtained.

Carbonate in Char Residue

It was of interest to measure the variation of carbonate concentration in the char in 100% nitrogen. This would shed light into the carbonate reduction mechanism. The variation in carbonate concentration was obtained by running an experiment at a constant

heating rate till 450, 700, 800, 900, and 1000°C. When respective temperature was reached, the experiment was terminated and the sample residue was dissolved in a test tube into deionized water using an ultrasonic bath. Assuming that the amount of carbonate did not change during cooling to room temperature, and that the ion concentration of carbonate in the solution is representative of that in the solid char residue, the results obtained indicate that the carbonate concentration goes through a maximum at around 700°C as shown in Figure 6.9.

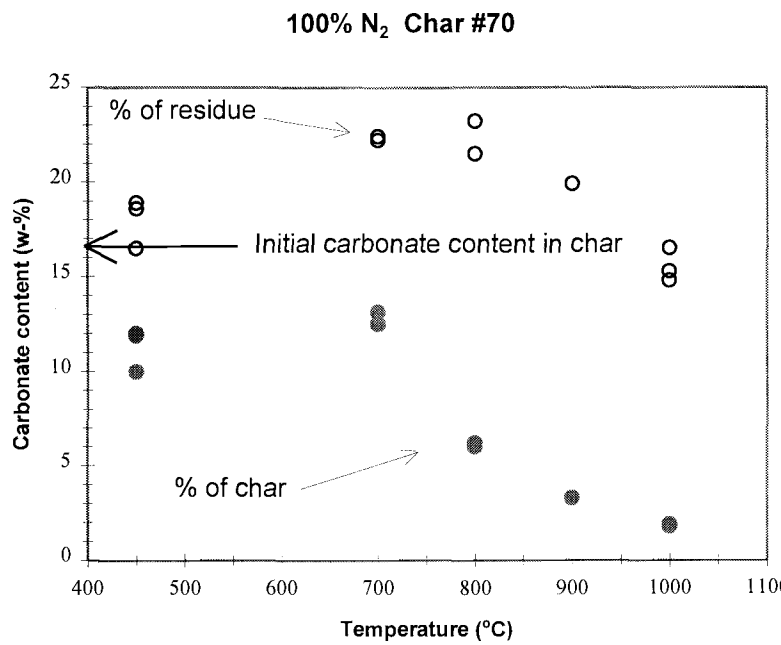

Figure 6.9. The concentration of carbonate goes through a maximum in the char residue.

The initial carbonate content was around 16.5 w-% in the black liquor char (Table 6.3). Thus, the carbonate content decreased between 25 and 450°C with respect to the char. Intuitively one would not expect that the carbonate concentration would decrease to ~11 w-% at 450°C. This phenomenon is under investigation. The subsequent increase in carbonate content can be explained with the overall gasification mechanism. Polysaccharides and lignin are the organic matter in wood that are the precursors of black

liquor char. Constituents from these species decompose to form carbonate during carbonization between 450 and 700°C. This is consistent with the literature where Stewart et al. (6) showed that alkali benzoate decomposes between 400 and 600°C to form condensed ring organic molecules, alkali carbonate, and carbon dioxide.

Mechanism for Carbonate Formation and Depletion

The reaction scheme in Figure 6.10 shows the proposed overall mechanism of carbonate formation and the subsequent reduction of carbonate and sulfate. The carbonate reduction reaction is based on the widely accepted mechanism for catalyzed CO_2 gasification by Sams et al. (5), where the active sites consist of alkali phenolates and carboxylates:)>C-Na,)>C-O-Na, and)>C=O-O-Na. These groups act as important gasification intermediates in carbonate decomposition and in disintegration of lignin and polysaccharinic constituents. The overall scheme also includes the sulfate reduction mechanism which is the second important process in BL char gasification processes. The sulfate-sulfide cycle provides reduced sulfur species that can regenerate carbonate in the presence of CO_2 and H_2O. The major sodium and sulfur release pathways are also indicated. What is not shown in Figure 6.10 is that sodium carbonate is also formed by thermal decomposition of sodium benzoate (6) according to reaction 1.

1. 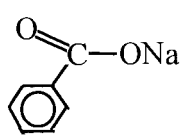 + heat → Na_2CO_3 + organics + C + CO_2

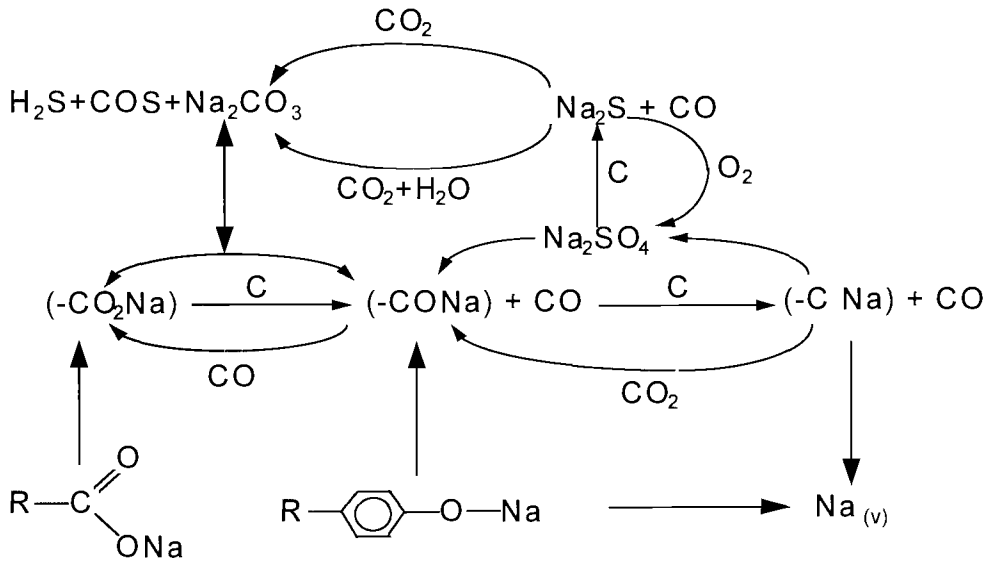

Figure 6.10. In the overall gasification mechanism, CO is formed from carboxylic and phenolic groups. These groups are formed from carbonate, lignin and polysaccharinic precursors.

The reaction mechanism in Figure 6.10 is the same that will be presented in Chapter 8, and it helps explain the data shown in Figure 6.9. When a temperature of around 700°C is reached, the decomposition rate of sodium caronate offsets the formation rate of carbonate from sodium benzoate. At higher temperatures the decomposition rate increases faster than the formation rate. Hence, the carbonate concentration decreases. This can be clearly seen in Figure 6.9. It is also evident that CO_2 and CO are important intermediate species in the reaction scheme in Figure 6.10. In fact, CO is the same product species from catalyzed CO_2 gasification. Therefore, an attempt was made to assess their role as suppression agents during carbonate reduction.

Suppression Effects in CO_2 and CO

One of the objectives was to investigate to what extent the suppression effects of CO_2 and CO were important during carbonate reduction. A first estimation was made by equilibrium calculations. The Gibbs' free energy was minimized using the software HSC Chemistry (7). Two cases were considered. One that had an equivalent amount of moles of compounds corresponding to the stoichiometric constants in reaction 2, and the other case according to reaction 3.

2. $Na_2CO_3 + C \rightarrow 2Na + CO + CO_2$
3. $Na_2CO_3 + 2C \rightarrow 2Na + 3CO$

Details on calculating the results shown in Figure 6.11 are given in Appendix 6.4.

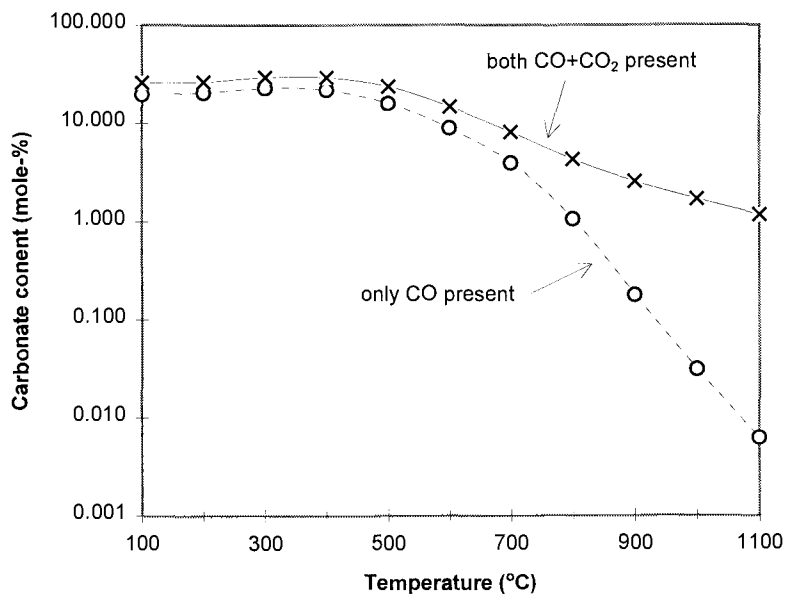

Figure 6.11. When both CO_2 and CO were present, the carbonate content was much higher at chemical equilibrium compared to when only CO was present. Details of the calculations can be found in Appendix 6.4.

The equilibrium calculations showed that carbonate is much more stable when both CO_2 and CO were present according to reaction 2. If reaction 3 applies (no CO_2 present), then the carbonate is much less stable. However, equilibrium calculations do not always represent real systems especially when kinetic limitations are important. Therefore, TG experiments were carried out in an attempt to study whether a real system behaves similarly.

TG experiments were performed at different CO_2/CO ratios at a constant heating rate of 10°C per min till 450, 700, 1000°C, when each run was terminated at the corresponding temperature. The gas concentrations were varied from 5 and 50% CO_2 and CO, respectively. The char residues were dissolved in deionized water and analyzed for carbonate ions. The analyses were done by acid titration in the Central Analytical Laboratory at OSU. At temperatures below 600°C, the experimental carbonate contents as shown in Table 6.4 were in line with the equilibrium calculations that predicted no remarkable difference in carbonate content. However, the experiments that were terminated at 700 and 1000°C did not have a lower carbonate content at low CO_2/CO ratios as would have been expected from equilibrium calculations in Figure 6.10. In fact, the summarized results in Table 6.4 show that the carbonate concentration in BL char is independent of both the CO_2/CO ratio and final temperature. Table 6.4 illustrates the fact that equilibrium calculations do not always predict what the actual experiments show. A complete listing of the carbonate content at 1000°C in different CO_2/CO ratios is given in Appendix 6.5.

Table 6.4. The carbonate content in the char residue is independent of CO_2/CO ratio at 450, 700 and 1000°C. A complete listing at 1000°C is given in Appendix 6.5.

CO_2/CO ratio	0.1	0.25	1	4	10
$CO_3^{=}$ in residue at 450°C (w-%)	21.0±0.2	nm	nm	nm	22.2±0.2
$CO_3^{=}$ in residue at 700°C (w-%)	nm	20.3±0.2	19.3±0.2	24.6±0.2	nm
$CO_3^{=}$ in residue at 1000°C (w-%)	nm	27.0±0.2	22.9±0.2	27.7±0.2	nm

nm = not measured

Another way of studying the suppression effects is to compare the thermograms at different gas compositions: 100% He, 20%CO_2+5%CO, and 5%CO_2+20%CO. This is shown in Figure 6.12.

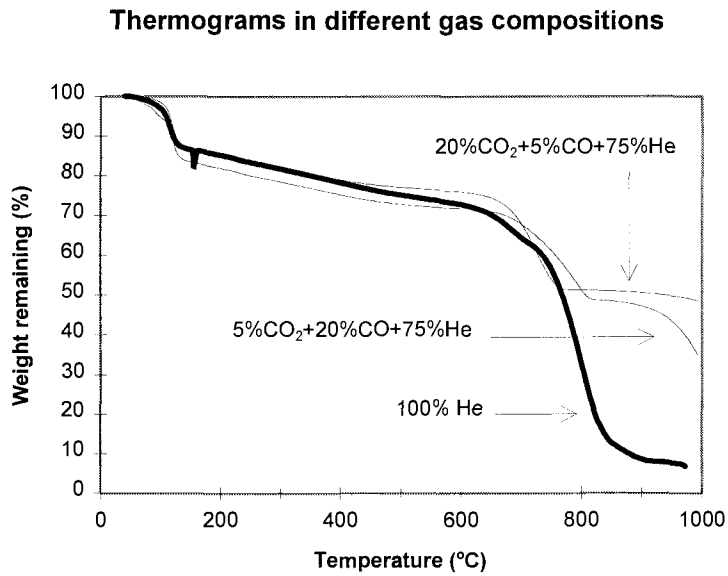

Figure 6.12. The thermograms in different gas compositions show that the total weight loss is much higher in 100% He compared to when CO_2 and CO were present. The reproducibility of these runs is shown in Appendix 6.9.

Figure 6.12 shows that the thermograms are virtually the same till around 750°C after which the thermogram in inert atmosphere continues to lose weight below 10% of its original weight leaving a light gray ash residue. The carbonate remaining in the residue was 11.9 w-%. The high CO_2 run leveled off at 50% weight remaining of the initial mass leaving a gray salt like residue with some pink color that probably is sulfate. The low CO_2 run started to level off at around 45% weight remaining but starting to lose weight rapidly at 925°C. The residue was gray (residual carbon) and salt like but with no pink color. The carbonate remaining in the residue was between 22.9 and 27.7 w-% for the high and low CO_2 experiments as shown in Table 6.4.

Even though Figure 6.12 indicates that CO_2 would inhibit more than CO, it was not entirely clear how significant this difference is. This is because it is likely that more carbon is consumed the higher the CO_2 content. The higher the CO_2 content, the sooner the carbon would be depleted. Thus, there would be more inorganic matter left. In an inert atmosphere there is no driving force to remove the carbon besides carbonate reduction. Therefore, the weight remaining would be the lowest in 100% He.

Therefore, several experiments were made where the CO_2 and CO flows were turned off at 700°C, and then immediately replaced with helium to maintain a constant total flow rate. Since the total carbonate is approximately the same at 700°C in 100% nitrogen as when CO_2 and CO were present (as shown in Figures 6.9 and Table 6.4), then the carbonate in the residue should be the same after turning off the gasification gases at 700°C and allowing the experiment proceed to 1000°C. The result is shown in Figure 6.13.

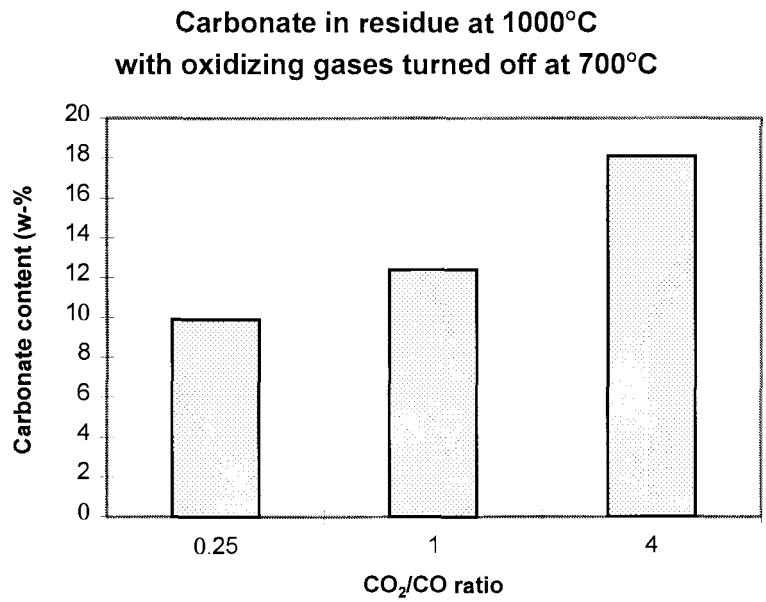

Figure 6.13. The carbonate content in the residue is strongly dependent on CO_2/CO ratio at 1000°C when CO_2 and CO are turned off at 700°C and switched to 100% helium.

Figure 6.13 shows that the carbonate in the residue is vastly different at 1000°C when CO_2 and CO were turned off at 700°C. The first conclusion is that CO_2 suppresses more than CO. Even though the carbonate content was the same when terminating the runs at 700°C for different CO_2/CO ratios (Table 6.4), this does not give any information specificly about the organic carbonate since these species were undetectable as discussed in the valence balance section. As a corollary, the initial carbonate molecular structures have to be different at respective CO_2/CO ratio at 700°C. This means that there has to be a different population distribution of the carboxylic and phenolic groups. A plausible explanation for this is that at high CO_2/CO ratios (-CNa) forms (-CONa), and (-CONa) forms ($-CO_2Na$) which inhibits and suppresses the decomposition of Na_2CO_3 in Figure 6.10. The carboxylic groups have to become phenolic groups before they can decompose to CO and elemental sodium. Therefore, there has to be more carboxylate groups at high CO_2/CO ratios than at low. Figure 6.14 shows the thermograms for the same experiments as in Figure 6.13.

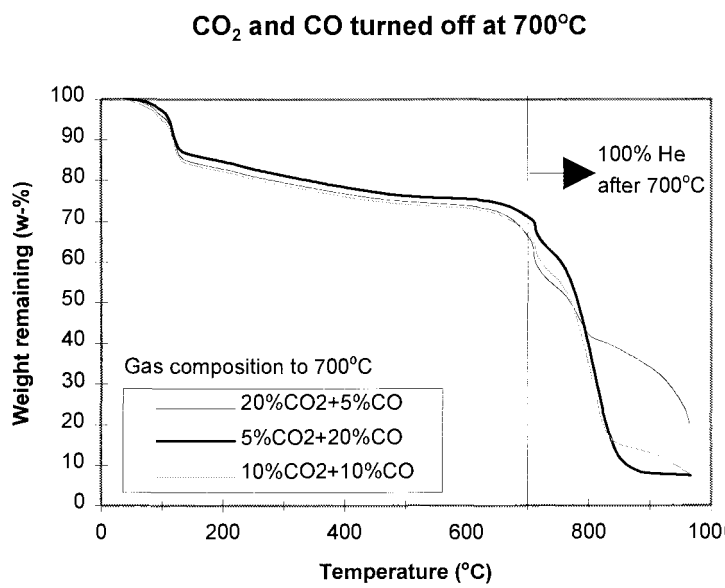

Figure 6.14. When CO_2 and CO were turned off at 700°C, the thermograms were different depending on the CO_2/CO ratio.

Figure 6.14 shows that the thermograms were different depending on the CO_2/CO ratio. At a high CO_2/CO ratio the rate of weight loss was much slower than at a low ratio. The thermograms should all be the same if the carboxylate concentration was independent of CO_2 and CO. In other words, the overall reaction mechanism (Figure 6.10) must be unaffected by CO_2 and CO, if the thermograms in Figure 6.14 were all the same. Since they are not, the only conclusion is that there is a shift in active site distribution of carboxylate and phenolic groups. The effect of carbon depletion can be seen when the gases are turned off at different temperatures in Appendix 6.10.

Boudouard Equilibrium

In order to understand the overall gasification mechanism one has to to consider the Boudouard equilibrium. The Boudouard equilibrium is the equilibrium of reaction 3.

3. $CO_2 + C \leftrightarrow 2CO$

with the equilibrium constant defined by equation 6-3.

$$K_{eq} = \frac{P_{CO}^{\ 2}}{P_{CO_2}} \qquad (6\text{-}3)$$

The calculation procedure for calculating the chemical equilibrium is given in reference (8). The result is given in Figure 6.15, but one has to keep in mind that this plot applies for uncatalyzed gasification.

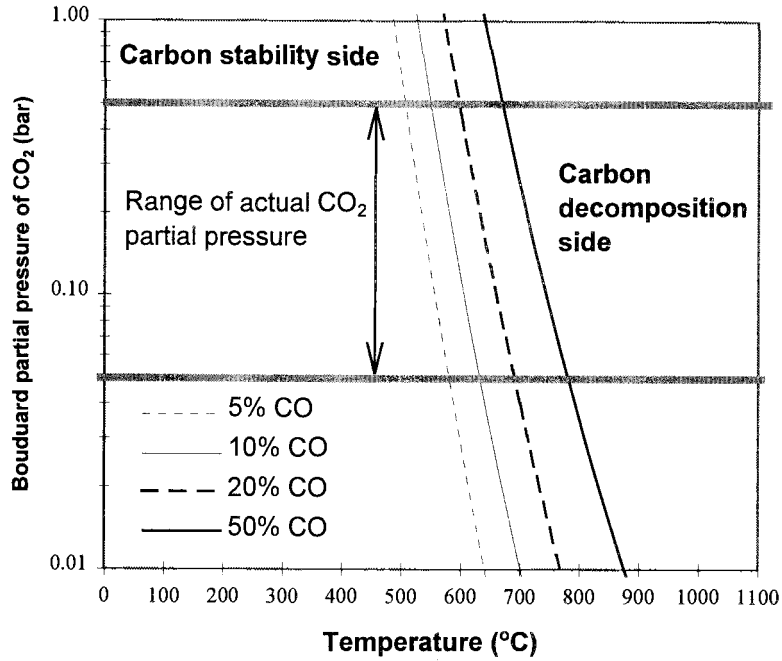

Figure 6.15. The Boudouard equilibrium shows that the cross over point to carbon decomposition occurs between 560 and 750°C depending on CO partial pressure. Calculations apply only for uncatalyzed gasification.

Figure 6.15 shows that the higher the CO partial pressure, the higher the temperature for the onset of carbon decomposition. The carbon decomposition temperatures of 560 and 670°C for 5 and 20 % CO, respectively, agree well with the thermograms in Figure 6.12. At a fixed CO_2 partial pressure, say 0.1 bar, the higher the CO partial pressure, the later does the decomposition of carbon commence.

Summary of suppression effect results

Based on these results, there is least amount of resistance to carbonate decomposition when no CO_2 and CO are present. This is due to the fact that the carbon necessary to decompose the inorganic matter has been depleted faster in high CO_2 atmospheres. This effect shows up as an apparent suppression effect. In fact, the reduction of carbonate is coupled to the overall carbon removal mechanism as shown in Figure 6.10. In this view, the suppression effect of CO_2 is actually a redistribution of catalytic sites from phenolic to carboxylate groups which has an impact on the rate at which carbon is removed. This will have to be verified by experimental methods such as NMR and IR spectroscopy.

MBMS Spectra

A quadrupole molecular beam mass spectrometer (MBMS) was used to monitor the off gases to verify the carbonate reduction mechanism. A free molecular jet beam is especially suitable when condensable gases such as elemental sodium are monitored. The thermobalance was connected with a 1 meter tygon line which was heated to 100°C. However, the highly reactive gases such as elemental sodium condensed before reaching the MBMS orifice. Therefore, only the permanent gases were detected such as CO, CO_2, and water vapor. Figure 6.16 shows a spectrum in 100% helium. The intensity was normalized with respect to background argon (1sccm).

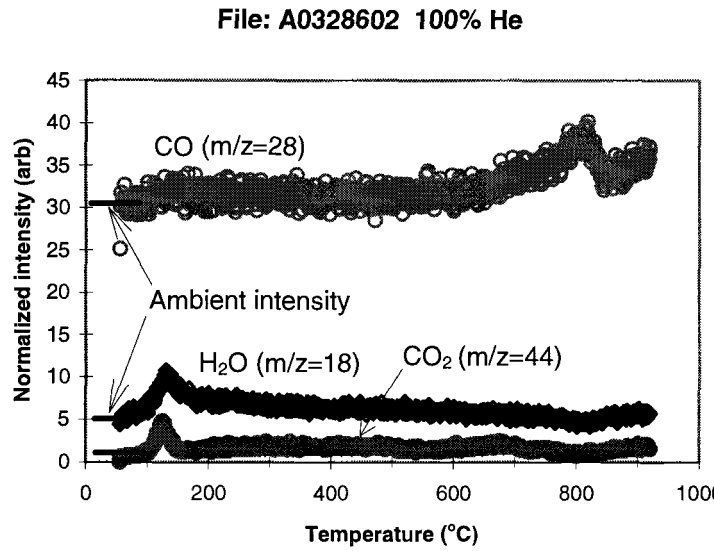

Figure 6.16. The MBMS spectra in 100% He show that humidity and adsorbed CO_2 are all released by 150°C. The CO peak is due to carbonate decomposition.

Figure 6.16 shows that water evaporates right after 100°C and that some CO_2 release coincides. This could be adsorbed CO_2 from the atmosphere. The release of CO is fairly constant until a temperature of around 650°C is reached, increasing steadily at 700 and reaching its peak at 800°C after which it rapidly decreases. The release of CO at 700-800°C verifies that CO is the main product gas during carbonate decomposition. This peak for CO release coincides with the thermogram in Fig. 6.12. It was also examined whether the same was true when CO_2 and CO were present. The result is shown in Fig. 6.17.

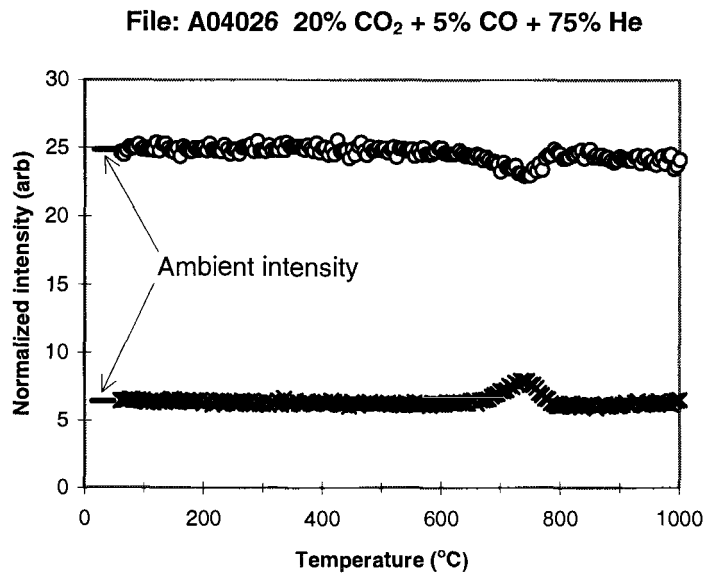

Figure 6.17. MBMS spectra in 20% CO2 + 5% CO + 75% He show that CO is released and CO_2 consumed when carbonate decomposes.

Figure 6.17 shows that CO is generated by the decomposition mechanism and that CO_2 is consumed by the gasification mechanism. The results are the same in 5% CO_2 + 20% CO. The release of water vapor is not shown because it is in such a small scale. It is similar to that in Figure 6.16. The normalized intensities in Figures 6.16 and 6.17 are not directly comparable due to different gas atmospheres, i.e. the intensity of CO_2 in Figure 6.17 is higher than for CO because there is 20% CO_2 in the reacting gases.

DSC results

The DSC results show that there is an endothermic peak at 140-150°C that coincides with the water vapor release as shown in the MBMS spectrum in Figure 6.16. No other peaks were detected in pure nitrogen when heating to 600°C which was the upper limit of this equipment. Figure 6.18 shows the DSC thermogram in 100% nitrogen, heat flow versus temperature.

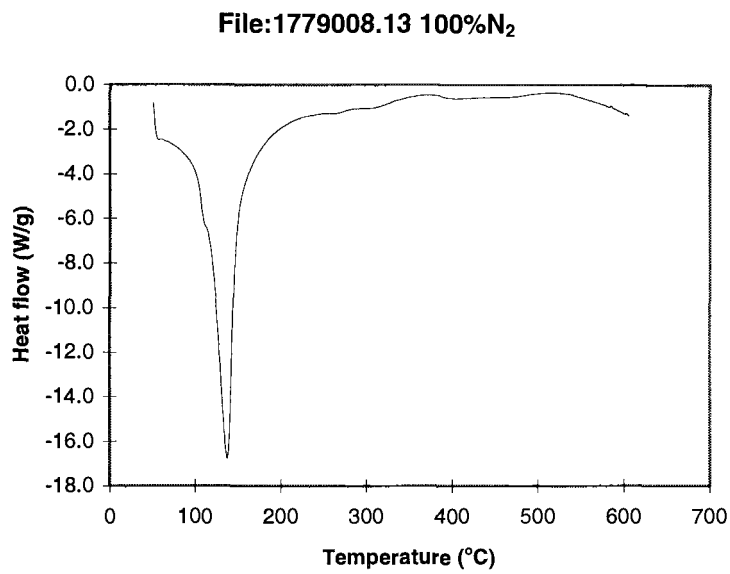

Figure 6.18. DSC thermogram at 100% nitrogen.

The water vapor measured is adsorbed humidity in ambient air. Since only the release of water vapor was detected in the DSC thermogram, the gas atmosphere was changed to include CO_2 and CO. The result is shown in Figure 6.19.

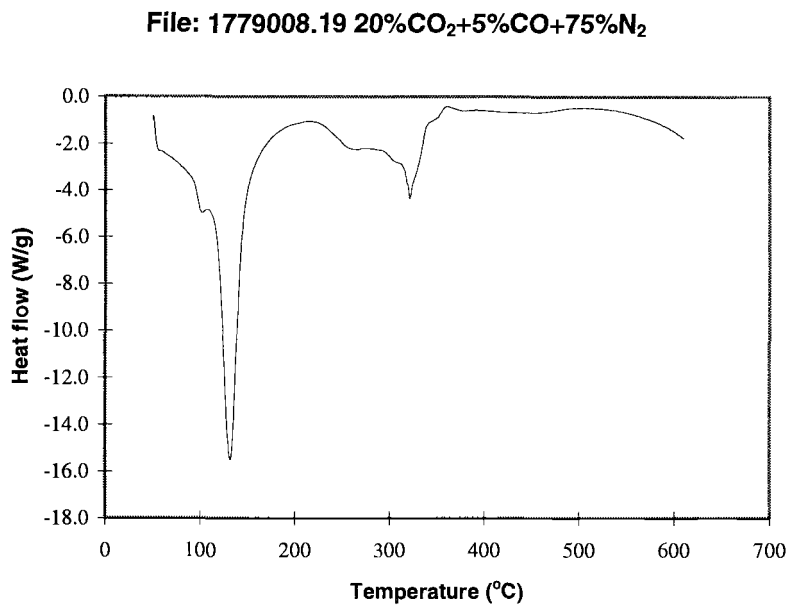

Figure 6.19. DSC thermogram in 20% CO_2 + 5% CO.

Figure 6.19 shows that besides the peak from water vapor there is another much broader but smaller peak around 300°C. Studying the MBMS spectrum it is not clear what the reason for this second peak is. Comparing it to the TG thermogram, one could conclude that it is residual volatilization, but then it should show up in the DSC thermogram in 100% nitrogen as well. This remains to be determined and the apparatus should be designed to reach temperatures up to 1000°C to fully address all issues using DSC.

A MODIFIED RATE MODEL FOR CARBONATE REDUCTION

The current carbonate reduction model is assumed to be zero order in carbon and first order in carbonate. This is a drawback when carbon starts to deplete because there is nothing that would stop the estimated rate when complete carbon conversion is approached. An attempt is made here to evaluate these reaction orders that would correct

this limitation based on data found in the literature (9). The objective was to deduce the pre-exponential factor and the parameters, a and b, in equation 6-4.

$$\frac{d[CO_3]}{dt} = A \times [CO_3]^a [C]^b \times e^{-\frac{29350}{T}} \qquad (6\text{-}4)$$

The decomposition of sodium carbonate according to reaction 3 was assumed to be kinetically limited and the only weight loss reaction.

3. $Na_2CO_3 + 2C \rightarrow 2Na + 3CO$

Table 6.5 shows measured weight loss rate found in the literature (9). A complete data table is given in Appendix 6.6.

Table 6.5. Measured rate of weight loss during carbonate reduction at 800°C (9).

Time (min)	Measured total weight loss rate (mg/min)	Calc weight loss rate from CO (mg/min)	Calc weight loss rate from CO_2 (mg/min)
0	0.72±0.02	na	na
5	0.75±0.02	0.58	0.12
10	0.70±0.02	0.62	0.10
15	0.53±0.02	0.45	0.08
20	0.33±0.02	0.27	0.06
25	0.18±0.02	0.09	0.04

Based on Table 6.5 and the MBMS spectrum in Figure 6.16 it was assumed that CO_2 generation was negligible. It was further assumed that the initial carbon concentration was 30 w-%. The following data was given in the literature: 36.2 mg BLS, 16.5 w-% carbonate left in char based on BLS, 10 w-% sodium left in char based on BLS, around 22 w-% of total weight was lost during pyrolysis. Since the rate of weight loss at 800°C is known at any time, then the change in carbonate and carbon concentrations can be calculated using the following equations 6-5 and 6-6.

$$\Delta CO_3 = \{\text{rate of weight loss}\} \times \frac{60}{130} \quad (6\text{-}5)$$

$$\Delta C = \{\text{rate of weight loss}\} \times \frac{24}{130} \quad (6\text{-}6)$$

The values obtained using equations 6-5 and 6-6 were used as experimental values to compare the calculated concentration profiles during integration of equation 6-4. Plots of these comparisons are given Appendix 6.7. The optimizations were done in a mass and mole basis. The results on a mole basis are given in Table 6.6. The results on a mass basis is given in Table 6.7. A comparison of the two tables shows that the exponentials are the same both ways. Only the pre-exponential factor changes, except for set III. The calculations are given in Appendix 6.8 (Spreadsheet: CO3RED.XLS). The constants obtained may be affected by the presence of CO_2 due to its suppressing effect on carbonate reduction. Equation 6-4 may need to be modified further to take this effect into consideration.

Table 6.6. Optimization results on a mole basis.

MOLE BASIS	I.	II.	III.	IV.
A (mol/min)	7.37e7	1.03e10	4.94e10	7.54e13
a (CO_3)	0.170	0.0535	1.0 (set)	1.0 (set)
b (C)	0.177	1.0 (set)	0.0	1.0 (set)
error	0.0747	0.0781	0.585	0.787

Table 6.7. Optimization results on a mass basis.

MASS BASIS	I.	II.	III.	IV.
A (mg/min)	1.29e11	2.84e10	4.94e10	6.29e9
a (CO_3)	0.169	0.0536	1.0 (set)	1.0 (set)
b (C)	0.179	1.0 (set)	0.0	1.0 (set)
error	0.0747	0.0781	0.585	0.787

Tables 6.6 and 6.7 show that the best fit is obtained when no parameters are fixed, set I. It also shows that the reaction orders are the same on a mole and mass basis. The optimized parameters were constrained to be positive. Newton's search method with forward derivatives and tangential estimates was used in the optimization in MS Excel 5.0a. The tolerance was set to: 10^{-8}.

Test of model

Model I was compared to experimental values and the predictions using the old model as given in equation 6-7.

$$\frac{d[CO_3]}{dt} = A_{old} \times [CO_3] \times e^{-\frac{E_a}{RT}} \qquad (6\text{-}7)$$

where $A_{old} = 10^9$ sec^{-1} and $E_a = 244$ kJ/mol. The goodness of fit of model I comparing with predictions using the old equation is shown in Figure 6.20.

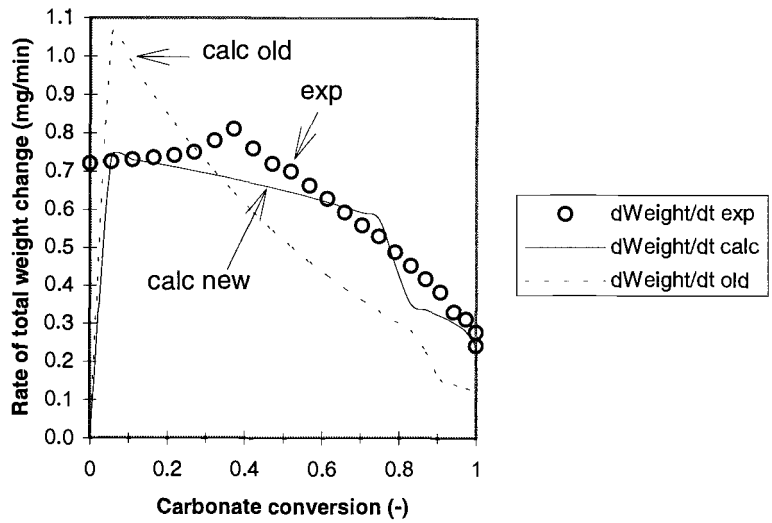

Figure 6.20. The new model (solid line) fits better to the experimental data than the old one (dashed line).

Figure 6.20 shows that the new rate equation is a significant improvement comparing to experimental weight loss rate data. Figure 6.21 shows the predicted concentration profiles for carbonate and carbon comparing with experimental data.

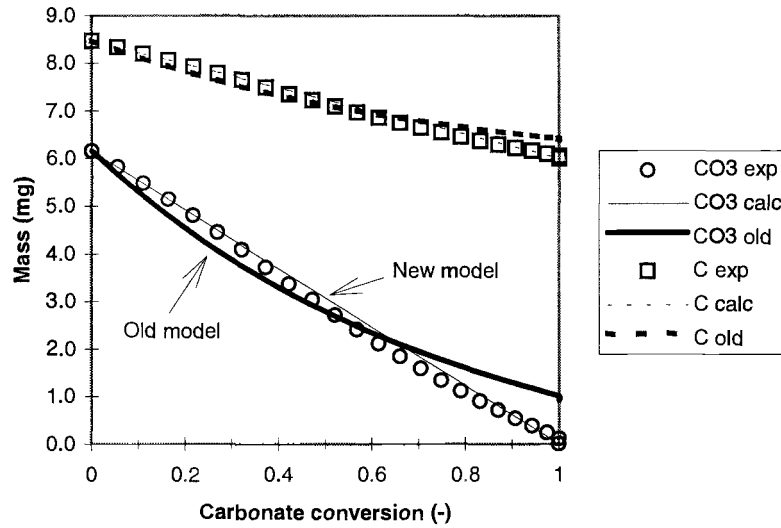

Figure 6.21. Experimental and calculated concentration profiles of carbonate and carbon. The thick lines are predictions using the old model and the thin lines are using the new model.

Figure 6.21 shows that the improvement is less significant with respect to the predicted carbonate and carbon concentration profiles. An important observation is that there is around 70% carbon left when all the carbonate is depleted. However, in typical gasification environments the carbon would be gasified by water vapor and CO_2. In these conditions it is important to consider the dependency on both carbon and carbonate rather than carbonate alone because the carbon would deplete faster. The old rate equation is not valid when the carbon is almost completely gone and there is still carbonate left. This is perhaps the greatest advantage of the new rate equation, not the improved fit to experimental data per se.

CONCLUSIONS AND RECOMMENDATIONS

The data presented herein demonstrates that there are apparent suppression effects present during carbonate reduction as predicted by chemical equilibrium calculations. TG experiments show that the total weight loss is much higher in inert conditions compared to when CO_2 and CO are present. This may be largely due to more rapidly consumed organic carbon that is needed to deplete inorganic carbonate. Even though the weight loss history is nearly the same till 700°C at high and low CO_2/CO ratios (Figure 6.12), further experiments revealed that the chemical structures in the char were probably different (Figures 6.13 and 6.14). At high CO_2/CO ratios the results indicated that there may be a lot more carboxylic groups in the char, and at low ratios more phenolic groups. The carboxylic groups have to become phenolic groups before they can decompose to CO and elemental sodium. This is why CO_2 inhibits the decomposition of organic carbonate more than CO does. The inorganic carbonate is a precursor to organic carbonate, the carboxylate and phenolate groups.

MBMS spectra confirm that CO is the main product during carbonate decomposition. However, the setup was not suitable for detecting condensable species such as elemental sodium unlike other setups in the literature (6,10). DSC thermograms detected an endothermic peak during drying of the char. When CO_2 and CO were present, another smaller and broader endothermic peak was detected around 300°C. This could be residual volatilization.

A new rate equation was obtained that accounted for the dependency on both carbon and carbonate. The best fit was obtained with values of 0.17 for a and b. It is recommended that a rate equation be obtained that would account for CO_2 and CO suppression. It is also recommended that additional experiments be made with a DSC that is designed to reach temperatures up to 1000°C. It would be useful to do TG experiments with pure sodium benzoate and in mixtures of activated carbon and sodium benzoate at the same experimental conditions as were used in this work.

ACKNOWLEDGMENT

The National Renewable Energy Laboratory is acknowledged for providing the facilities and equipment necessary to obtain the data presented. The Associated Western Universities is acknowledged for financial support. Drs. David C. Dayton and Stephen S. Kelley are acknowledged for advice and guidance. Mr. Joe Patrick is acknowledged for technical support.

NOMENCLATURE

Symbol	*Description, Units*
A	pre-exponential factor, mol/min or mg/min
a	reaction order of carbonate, dimensionless
Bi_m	mass transfer Biot number, dimensionless = k_m L ÷ $\mathcal{D}$
b	reaction order of carbon, dimensionless
[C]	carbon concentration, mol per particle
$[CO_3]$	carbonate concentration, mol per particle
$\mathcal{D}$	molecular diffusivity, $m^2\ s^{-1}$
E_a	activation energy, kJ/mol
E	calibration coefficient, dimensionless
K_{eq}	Boudouard equilibrium constant, bar
k_m	mass transfer coefficient, $m\ s^{-1}$
L	characteristic length, m = sample thickness ÷ 2 (slab)
M	molecular weight, g/mol
m	mass of displaced gas, mg
p, P_i	absolute pressure of gas or partial pressure of CO_2 and CO, Pa or atm
R	ideal gas constant, $J\ mol^{-1}\ K^{-1}$
T	particle temperature, K
V	volume of displaced gas by TG sample pan, μL

REFERENCES

1. Thermal Analyst 2100 Operators Manual version 8.6, TA Instruments, New Castle, Delaware, September, 1992

2. Differential Scanning Calorimeter, Operator's Manual, , TA Instruments, New Castle, Delaware, February, 1993

3. Weyerheuser Analytical & Testing Services, Federal Way, WA, September 20, 1994

4. Sricharoenchaikul, V., M.S. thesis, Oregon State University, 1995

5. Sams, D.A., Shadman, F., Mechanism of Potassium Catalyzed Carbon/CO2 Reaction, AIChE J., Vol.37, No.7, p.1132-1137, 1986

6. Stewart, G.W., Chakrabarti, A., Moore, W.R., Reactions of Alkali Containing Species in Combustion Streams, USDOE Proceedings: High-Temperature, High-Pressure Particulate and Alkali Control in Coal Combustion Process Streams. Science Applications Inc., McLean, VA, p.275-300, 1981

7. HSC Chemistry for Windows Version 2.03, Outokumpu Research Ltd., Pori, Finland, 1994

8. Wåg, K., p.453 in Appendix 13 of this thesis, Oregon State University, 1996

9. Li, J., van Heiningen, A.R.P., Sodium Emssion During Pyrolysis and Gasification of Black Liquor Char, TAPPI J., Vol.73, No.12, Fig.6, p.217, December, 1990

10. Behrens, R., Jr., New Simultaneous Thermogravimetriy and Modulated Molecular Beam Mass Spectrometry Apparatus for Quantitative Thermal Decomposition Studies, Rev.Sci.Instrum., 58(3), Am. Inst. of Physics, March, 1987

APPENDICES

APPENDIX 6.1

TG and DSC Calibration Curves

TG calibration curves are shown for 100% He, but a new set was run in 20% CO_2 + 5% CO + 75% He. These curves are not shown in this appendix because the effect of gas composition was negligible. DSC calibration curves are given in 20% CO_2 + 5% CO + 75% N_2 , but another set was run in 100% N_2 eventhough the effect was minimal. The measured and actual melting points (MP) of the calibration samples are given below. The TG MPs are based on the derivative temperature (°C/min). The DSC MPs are based on the uncorrected heat flow (mW).

Summary of calibration results:	TG	Measured	Actual
	MP of Indium (°C):	161.07	156.61
	MP of Aluminum (°C):	641.35	660.37
	DSC		
	MP of Indium (°C):	157.72	156.61
	MP of Tin (°C):	229.86	231.89

DSC Cell constant used:	1.2817
DSC onset slope:	-6.13 mW/°C
DSC baseline slope:	-0.2895
DSC offset:	50118.1
DSC calibration file:	1779008.17

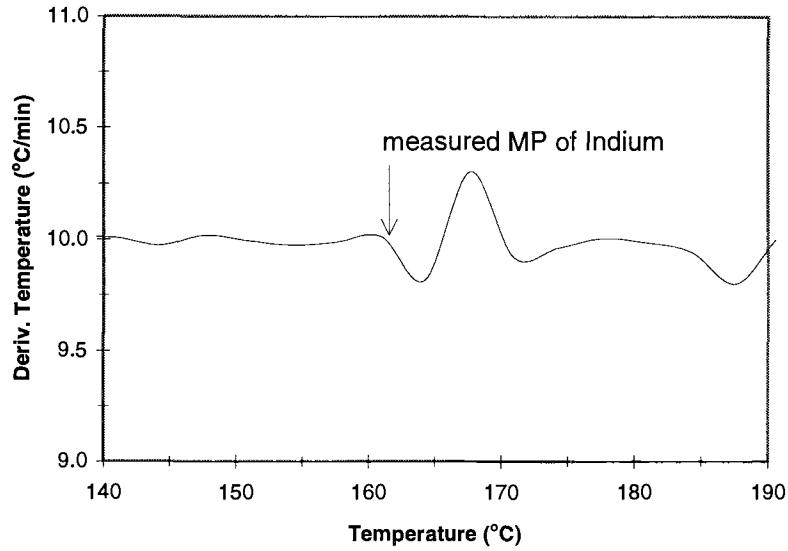

Figure A.6.1.1. TG calibration curve for indium.

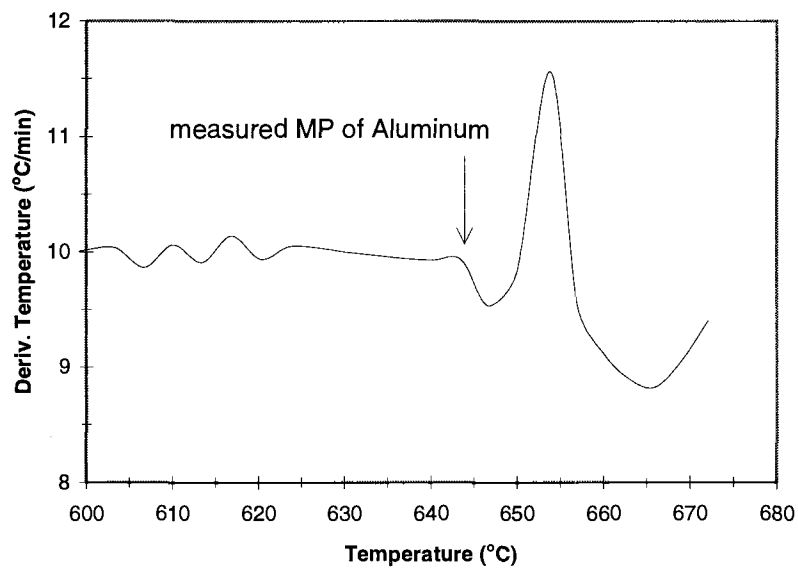

Figure A.6.1.2. TG calibration curve for Aluminum.

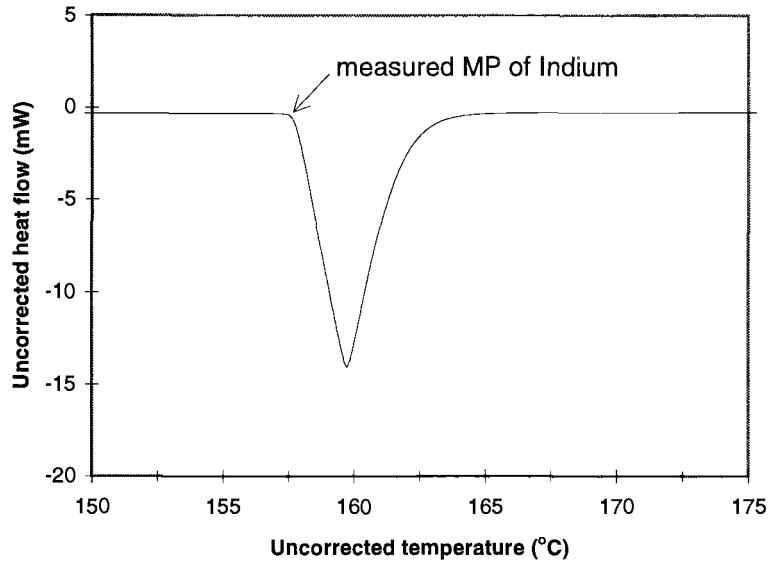

Figure A.6.1.3. DSC calibration curve for indium.

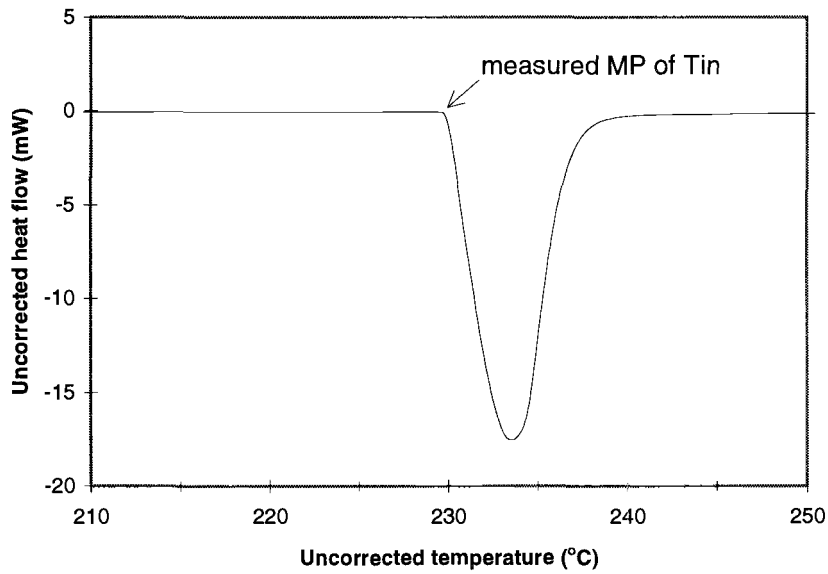

Figure A.6.1.4. DSC calibration curve for tin.

APPENDIX 6.2

Documentation of Computer Program for Assessment of External and Internal Mass Transfer Limitations

The sample geometry was assumed to be a thin cylinder (~slab). Molecular diffusion was assumed to apply (no Knudsen diffusion was considered). A Reynolds number based on the distance from the sample edge to the other edge was used, Re_x. Neufeldt's correlation was used to evaluate the collision integral for estimating the CO_2 diffusivity. A computer program was created using TK-Solver to evaluate the mass transfer Biot number and the effectiveness factor at different temperatures and gas conditions. Calculations were done in the following conditions:

1. Void fraction = 0.1, Gas composition: 100% He
2. Void fraction = 0.5, Gas composition: 100% He
3. Void fraction = 0.1, Gas composition: 20% CO_2 + 5% CO
4. Void fraction = 0.5, Gas composition: 20% CO_2 + 5% CO
5. Void fraction = 0.1, Gas composition: 5% CO_2 + 20% CO
6. Void fraction = 0.5, Gas composition: 5% CO_2 + 20% CO

The results show:

- no effect of void fraction on effectiveness factor,
- big effect of void fraction on Biot number,
- no effect of gas composition on Biot number,
- no effect of gas composition on effectiveness factor.

A more detailed description of the equations used in the TK-Solver program can be found in the appendix of this thesis (documentation of the Black Liquor Combustion Simulator: BLCS). The key equations used are given as follows:

Equations: Volume of cylinder: $V_{cylinder} = \frac{\pi}{4} d^2 h$

Dimensionless mass transfer group: $j_D = 0.664 \times Re_x^{-0.5} = St_D \times Sc^{0.67}$

Schmidt number: $Sc = \frac{\nu}{\mathcal{D}} = \frac{\mu}{\rho \mathcal{D}}$

Stanton number: $St_D = \frac{Sh}{Re_x \times Sc}$

Sherwood number $Sh = \frac{k_{m,CO_2}}{\mathcal{D}}$

Thiele modulus $M_T = L\sqrt{\frac{k'''}{\mathcal{D}}}$

Effectiveness factor $\eta = \frac{\tanh(M_T)}{M_T}$

Biot number: $Bi_m = \frac{k_{m,CO_2} L}{\mathcal{D}}$

Estimated reaction rate: $Rco_2 = 63 \times 10^9 \frac{P_{CO_2}}{P_{CO_2} + 3.4 P_{CO}} [C] e^{-\frac{30070}{T}}$

Data:

Initial char mass = 20 mg

Char bulk density = 200 kg/m^3

Sample disk length = 9 mm

Sample disk thickness = 1.5 mm

Volume flow at particle location = 100 cm^3/min

Pr = 0.67

Void fraction = 0.1 and 0.5 (0.1 more likely true)

Fraction of saturated smelt = 0.25

Average pore diameter = 200 Å

TK program

VARIABLE SHEET

St	Input	Name	Output	Unit	Comment
					Program for calculating the external
					and internal transport resistances
					in the NREL thermobalance TGA 2950
					Gas properties for 100% He
					Last modified: 8/21/96 KW
L	1273	Tp		K	PARTICLE AND FURNACE TEMP
	.00001	pco2		bar	CO2 partial pressure
	0	pco		bar	CO partial pressure
	.000528	Carb		mol/part	C init. in particle for 20mg sample
					31.7% of char is carbon: 6.34mg
		ROCO2	2.78E-10	mol/s	C depletion by CO2 gasification
		rCO2	.0018348	mol/s	CO2 kinetic rate
		Rreduc	.0001127	mol/s	C converted by sulfate reduction
	.18	SO4			SO4/Na2 mole ratio
3.1415927		pi			Archimedes' constant
		w	.0850524	m/s	Flow speed at particle
		ny	.0014265	m2/s	Viscosity of gas in bulk
		nys	.0014265	m2/s	Viscosity of gas in film
	1	nyratio			Viscosity ratio
.00000167		V		m3/s	Volume flow at particle 0.00164854
					100sccm=1.67e-6 m3/s
		kgCO2	.0455748	m/s	CO2 mass transfer coefficient
		CO2byMT	2.78E-10	mol/s	CO2 mass transfer rate
		CO2		mol/m3	O2 concentration
		CCO2	9.573E-5	mol/m3	CO2 concentration
	.005	Dia		m	Tube diameter: 0.5cm=5mm=0.005m
	.00002	m		kg	Initial particle mass
	200	dens		kg/m3	
	.009	Dp		m	Sample diameter
		height	.001572	m	Sample height
		Vp	1E-7	m3	Sample volume
		Aext	6.362E-5	m2	Sample external surface area
		L	.0007860	m	Characteristic length
		h	49.70145	W/m2/K	Convective heat transfer coefficient
	.25	f			Fraction of saturated smelt
	.1	Pore			Porosity = volume of pores/total vol
	2E-8	Prsz		m	Pore diameter = 200A in N2
	5.67E-8	SB		W/m2/K4	Stefan-Boltzmann constant
		k	.1025007	W/m/K	Local apparent thermal conductivity

	4.364	Nu			Nusselt number for constant heat flux
	.67	Pr			Prandtl number 0.67 = He; 0.75 = N2
		ScCO2	2.191476		CO2 Schmidt number
L		Rex	.5366271		Reynolds number at end edge of sample
L		jD	.9064248		Mass transfer dimensionless group
L		StD	.5358438		Stanton number
L		Sh	.6301551		Sherwood number
L		THCO2	426.5		CO2 Thiele modulus
L		EFFCO2	.002345		CO2 effectiveness factor
L		BiCO2	5.503007		CO2 Biot number (mass transfer)
L		DmCO2	33053.85		CO2 Damkohler number
		DiffCO2	6.509E-4	m2/s	CO2 diffusivity
		DkCO2	5.218E-8	m2/s	Knudsen diffusivity of CO2
		DeffCO2	6.509E-6	m2/s	Effective diffusivity of CO2
					Lennard-Jones' parameters
		sigmaCO	3.286		
	10.2	ekHe			
	190	ekCO2			
		TsCO2	28.9169		
					Collision Integral
		OmegaCO	.6271447		
					Neufeldt's Parameters
	1.06036	A			
	.1561	B			
	.193	C			
	.47635	D			
	1.03587	E			
	1.52996	F			
	1.76474	G			
	3.89411	H			

RULE SHEET
S Rule
* L=height/2
* height=4*m/dens/pi/Dp^2
* Vp=pi*Dp^2*height/4
* Aext=pi*Dp^2/4
* k=(1-f)*(0.05+4*Pore*Prsz*SB*Tp^3)+0.26*f "Merriam equation
* h=Nu*k/Dp
* rCO2=63.0e9*pco2/(pco2+3.4*pco)*Carb*exp(-30070/Tp)
* Rreduc=3790*Carb*SO4^1.4*exp(-9400/Tp)
* w=V/(pi*Dia^2/4)
* ny=(7.56775e-5*Tp^1.69906)*1e-4
* nys=ny
* DiffO2=0.0000961*(Tp/273)^1.75
* DiffCO2o=DiffO2*1.378/1.773
* sigmaCO2=(2.576+3.996)/2
* TsCO2=Tp/sqrt(ekCO2*ekHe)
* OmegaCO2=A/TsCO2^B+C/exp(D*TsCO2)+E/exp(F*TsCO2)+G/exp(H*TsCO2)
* DiffCO2=0.0018583*Tp^1.5*sqrt(1/44+1/4)/sigmaCO2^2/OmegaCO2/10000
* Rex=w*Dp/ny
* jD=0.664/sqrt(Rex)
* StD=jD/ScCO2^0.67
* Sh=StD*Rex*ScCO2
* kgCO2=Sh*DiffCO2/Dp
* ScCO2=ny/DiffCO2
* CCO2=pco2/82.06e-6/Tp
* CO2byMT=kgCO2*Aext*CCO2
* THCO2=L*sqrt(abs(rCO2)/Vp/DiffCO2/CCO2)
* EFFCO2=tanh(THCO2)/THCO2 "flat plate
* 1/ROCO2=1/CO2byMT+1/(EFFCO2*abs(rCO2))
* BiCO2=kgCO2*L/DeffCO2
* DeffCO2=Pore^2*DiffCO2
* DkCO2=9700*Prsz/2*sqrt(Tp/44)/10000 "cm2/s /10000 => m2/s
* DmCO2=THCO2^2/BiCO2

APPENDIX 6.3

Valence Balance Data Tables

Table A.6.3.1. Valence balance data for TG 96 experiments.

Spl #	Res.wgt mg	Vol mL	actual Na ppm	actual K ppm	actual Cl ppm	actual SO4= ppm	actual Thio ppm	CO3= ppm	Cations	Anions	Ratio
T6	2.7	13.3	71.0	15.4	2.0	90.9	0.0	30.0	3.5	3.0	1.2
T10	2.5	9.8	89.0	3.7	0.0	71.2	0.0	39.0	4.0	2.8	1.4
T11	2.4	12.0	69.0	0.8	0.1	43.4	0.0	33.0	3.0	2.0	1.5
T13	12.4	5.5	833.0	1.7	6.6	104.6	0.0	372.0	36.3	14.8	2.5
T16	15.8	5.7	687.3	14.7	8.3	68.5	0.0	330.0	30.3	12.7	2.4
T30	1.9	6.3	89.5	0.0	0.0	40.9	0.0	36.0	3.9	2.1	1.9
T31	2.3	7.2	89.2	3.9	0.2	52.5	0.0	33.0	4.0	2.2	1.8
T33	9.2	7.8	610.1	11.9	0.4	34.4	8.4	327.0	26.8	11.8	2.3
T34	7.0	7.4	607.1	8.8	0.4	36.9	13.1	255.0	26.6	9.5	2.8
T35	12.9	8.1	166.8	3.5	4.3	29.3	0.0	324.0	7.3	11.5	0.6
T40	3.4	6.8	169.6	3.9	2.0	12.8	0.0	93.0	7.5	3.4	2.2
T41	2.6	6.2	172.1	3.5	1.5	10.4	0.4	93.0	7.6	3.4	2.2
T43	1.9	8.5	94.6	3.5	1.8	17.6	0.2	48.0	4.2	2.0	2.1
T45	1.1	7.3	40.2	0.5	0.2	14.3	0.0	30.0	1.8	1.3	1.4
T47	2.8	5.5	221.4	4.0	2.0	19.2	0.4	114.0	9.7	4.3	2.3
T49	0.8	6.2	48.6	1.4	1.1	9.2	0.2	30.0	2.1	1.2	1.8
T51	2.1	4.9	49.3	0.6	0.3	1.1	0.0	81.0	2.2	2.7	0.8
T52	4.1	6.2	244.5	5.4	3.0	26.8	0.1	147.0	10.8	5.5	1.9
T53	2.9	7.8	141.9	2.8	1.4	9.2	0.0	78.0	6.2	2.8	2.2
T54	2.4	7.7	147.4	3.4	1.4	10.9	0.0	78.0	6.5	2.9	2.3
T55	2.9	6.6	277.9	6.7	2.0	17.6	0.0	108.0	12.3	4.0	3.0
T57	7.4	6.9	102.4	2.6	0.1	1.4	0.0	276.0	4.5	9.2	0.5
T58	3.7	7.2	334.7	1.9	0.8	86.6	0.0	93.0	14.6	4.9	3.0
T59	4.9	5.7	620.2	10.2	0.0	120.8	0.0	189.0	27.2	8.8	3.1
T60	1.6	6.2	167.0	0.0	0.0	131.0	0.0	30.0	7.3	3.7	1.9
T61	5.4	7.3	493.9	8.1	0.0	90.4	0.0	183.0	21.7	8.0	2.7
T62	6.6	7.2	835.3	14.6	0.7	67.5	3.3	231.0	36.7	9.2	4.0
T64	10.6	5.5	1324.6	25.8	0.7	77.2	0.0	450.0	58.3	16.6	3.5
T65	4.4	6.9	459.8	10.3	3.5	33.0	0.0	159.0	20.3	6.1	3.3
T66	6.5	5.9	402.3	9.0	3.9	26.1	1.3	273.0	17.7	9.8	1.8
T67	8.5	5.9	533.8	11.0	3.5	7.9	10.3	369.0	23.5	12.7	1.8
T68	1.9	4.2	14.0	15.4	0.0	3.3	0.0	45.0	1.0	1.6	0.6
T69	1.7	3.9	23.5	0.0	0.0	2.5	0.0	54.0	1.0	1.9	0.6
T70	7.7	4.7	641.8	12.4	0.4	81.4	0.7	375.0	28.2	14.2	2.0
T71	7.0	6.0	365.4	8.3	2.6	25.2	0.0	225.0	16.1	8.1	2.0

Table A.6.3.2. Experimental conditions for TG 96 data.

Run #	Gases	Char #	Stopped at (°C)	MBMS used
T6	100% N_2	70	1000	
T10	100% N_2	70	1000	
T11	100% N_2	70	1000	
T13	100% N_2	70	450	
T16	100% He	70	450	
T30	100% He	52	970	M
T31	100% He	52	900	M
T33	20%CO_2+5%CO+75%He	52	1000	M
T34	5%CO_2+20%CO+75%He	52	1000	M
T35	5%CO_2+20%CO+75%He	52	700	M
T40	100% N_2	70	450	
T41	100% N_2	70	700	
T43	100% N_2	70	800	
T45	100% N_2	70	900	
T47	100% N_2	70	700	
T49	100% N_2	70	800	
T51	100% N_2	70	450	
T52	50%CO_2+5%CO+45%N_2	70	450	
T53	5%CO_2+50%CO+45%N_2	70	450	
T54	20%CO_2+5%CO+75%N_2	70	650	
T55	20%CO_2+5%CO+75%N_2	70	700	
T57	20%CO_2+5%CO+75%He	52	1000	M
T58	20%CO_2+5%CO+75%He	52	CO_2 off 700	M
T59	20%CO_2+5%CO+75%He	52	CO_2 off 730	M
T60	20%CO_2+5%CO+75%He	52	CO_2 off 650	M
T61	20%CO_2+5%CO+75%He	52	CO_2 off 760	M
T62	20%CO_2+5%CO+75%He	52	CO_2 off 800	M
T64	20%CO_2+5%CO+75%He	52	1000	M
T65	20%CO_2+5%CO+75%He	52	730	
T66	20%CO_2+5%CO+75%He	52	760	
T67	20%CO_2+5%CO+75%He	52	800	
T68	5%CO_2+20%CO+75%He	52	CO_2 off 700	M
T69	10%CO_2+10%CO+80%He	52	CO_2 off 700	M
T70	10%CO_2+10%CO+80%He	52	1000	M
T71	10%CO_2+10%CO+80%He	52	700	M

Table A.6.3.3. Valance balance data for TG 95 data.

Spl #	Res.wgt mg	Vol. mL	actual Na ppm	actual K ppm	actual Cl ppm	actual SO4= ppm	actual Thio ppm	CO3= ppm	Cations	Anions	Ratio
44	12.0	5.1	843	25	26.8	90	0	405	37.3	16.1	2.3
39	9.9	6.3	670	18	5.1	83.1	3.7	339	29.6	13.2	2.2
40	10.2	5.0	817	15	5.4	95	3.8	420	35.9	16.2	2.2
41	10.4	5.4	795	13	5.3	91	4.1	414	34.9	15.9	2.2
42	10.1	5.5	769	18	5.7	96.3	2.7	405	33.9	15.7	2.2
19	9.8	6.4	667	15.6	5.8	83.2	3.6	354	29.4	13.8	2.1
20	10.4	5.2	872	20.3	6.4	84.5	4.3	468	38.4	17.6	2.2
21	10.0	6.1	711	18.4	6	78.2	4.2	393	31.4	15.0	2.1
36	9.7	6.2	677	16	5	73.2	7.5	339	29.8	13.1	2.3
37	9.8	6.2	687	19	5.3	79.3	6.2	339	30.4	13.2	2.3
38	9.4	7.6	564	13	5.3	61.8	7	270	24.9	10.6	2.4
33	9.2	7.4	566	7	5.6	54.6	12.8	312	24.8	11.9	2.1
34	9.7	6.9	656.3	10	3.2	53.5	16.1	360	28.8	13.5	2.1
15	9.0	6.2	629	9	6.5	23.4	29.7	330	27.6	12.2	2.3
29	9.9	7.2	618	8	5.8	27.3	23	315	27.1	11.6	2.3
30	10.3	6.5	688	12	6.3	33.1	22.7	360	30.2	13.3	2.3
31	9.8	4.6	875	18	6.7	34.7	23.1	489	38.5	17.6	2.2
25	9.5	6.4	671	11	5.7	24.2	17.3	345	29.5	12.5	2.4
26	10.1	5.5	801	14	6.7	28.5	17.9	435	35.2	15.6	2.3
27	9.1	7.0	611	9	6	27.9	14.4	309	26.8	11.3	2.4

Table A.6.3.4. Experimental conditions for TG 95 data

Run #	Gases	Char #
44	50%CO_2+5%CO+45%N_2	70
39	5%CO_2+5%CO+90%N_2	70
40	5%CO_2+5%CO+90%N_2	70
41	5%CO_2+5%CO+90%N_2	70
42	5%CO_2+5%CO+90%N_2	70
19	5%CO_2+10%CO+85%N_2	70
20	5%CO_2+10%CO+85%N_2	70
21	5%CO_2+10%CO+85%N_2	70
36	5%CO_2+20%CO+75%N_2	70
37	5%CO_2+20%CO+75%N_2	70
38	5%CO_2+20%CO+75%N_2	70
33	5%CO_2+30%CO+65%N_2	70
34	5%CO_2+30%CO+65%N_2	70
15	5%CO_2+50%CO+45%N_2	70
29	10%CO_2+50%CO+40%N_2	70
30	10%CO_2+50%CO+40%N_2	70
31	10%CO_2+50%CO+40%N_2	70
25	20%CO_2+50%CO+30%N_2	70
26	20%CO_2+50%CO+30%N_2	70
27	20%CO_2+50%CO+30%N_2	70

APPENDIX 6.4

Initial Conditions for Equilibrium Calculations

Total pressure: 1 bar

Reaction 1: $Na_2CO_3 + C \leftrightarrow 2Na + CO + CO_2$

Reaction 2: $Na_2CO_3 + 2C \leftrightarrow 2Na + 3CO$

Raw materials:

Reaction 1	Reaction 2
1.0 mol CO(g)	3.0 mol CO(g)
1.0 mol CO_2(g)	0.1 mol Cl_2(g)
0.1 mol C_{l2}(g)	0.1 mol H_2(g)
0.1 mol H_2(g)	0.1 mol K(g)
0.1 mol K(g)	1.0 mol N_2(g)
1.0 mol N_2(g)	2.0 mol Na(g)
2.0 mol Na(g)	1.0 mol S
1.0 mol S	

Table A.6.4.1. Equilibrium composition of solid phase.

Temp (°C)	Rxn. 1 Na_2CO_3 mol-%	Rxn. 2 Na_2CO_3 mol-%
100	25.78	19.51
200	26.15	20.28
300	29.26	22.71
400	29.22	21.72
500	23.61	15.85
600	14.57	8.91
700	8.09	4.01
800	4.31	1.07
900	2.56	0.18
1000	1.72	0.03
1100	1.18	0.01

The following table is a list of all possible product species at chemical equilibrium. The column for phase 1 lists all gases and phase 2 all solid compounds. The input amounts are given as moles in the "Amount" columns. These amounts were varied depending on the reaction studied.

Table A.6.4.2. All product gases accounted for in equilibrium calculation.

PHASE	**1**	**PHASE**	**2**
Input	Amount	Input	Amount
COS(g)	0.00	C	0.00
CH_4(g)	0.00	K	0.00
CO(g)	1.00	K_2CO_3	0.00
CO_2(g)	1.00	KCl	0.00
Cl_2(g)	0.10	KOH	0.00
HCl(g)	0.00	K_2S	0.00
H_2O(g)	0.00	K_2SO_4	0.00
H_2(g)	0.10	Na	0.00
H_2S(g)	0.00	Na_2CO_3	0.00
K(g)	0.10	NaCl	0.00
KCl(g)	0.00	NaOH	0.00
KOH(g)	0.00	Na_2S	0.00
K_2S(g)	0.00	Na_2SO_4	0.00
K_2SO_4(g)	0.00	S	1.00
He(g)	1.00		
N_2(g)	0.00		
NO(g)	0.00		
NO_2(g)	0.00		
NO_3(g)	0.00		
Na(g)	2.00		
NaCl(g)	0.00		
NaOH(g)	0.00		
Na_2SO_4(g)	0.00		
O_2(g)	0.00		
S(g)	0.00		
SO(g)	0.00		
SO_2(g)	0.00		
SO_3(g)	0.00		

APPENDIX 6.5

Carbonate Content in Char Residue in Varying CO_2/CO Ratios at 1000°C

Figure A.6.5.1 shows the carbonate concentration in all the char residues for the experiments in CO_2 and CO and terminated at 1000°C.

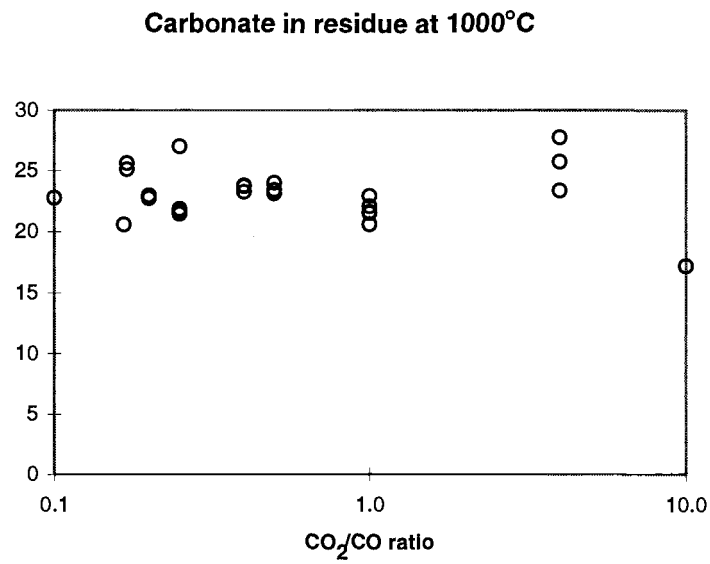

Figure A.6.5.1. The carbonate content remaining as percent of char at 1000°C is independent of CO_2/CO ratio.

APPENDIX 6.6

Source of Li's Carbonate Reduction Data

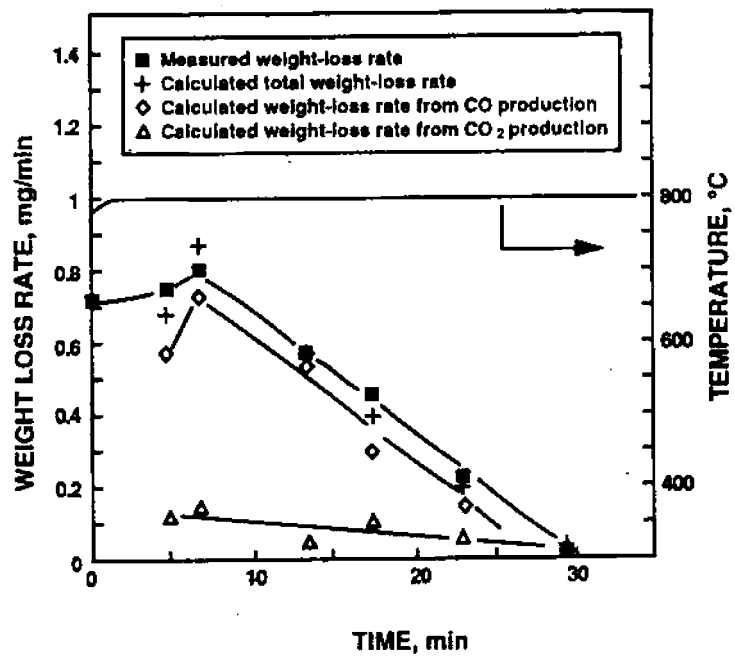

Figure A.6.6.1. The experimental weight loss data is based on this plot in Li and van Heiningen's paper, TAPPI J., Vol.73, No.12, figure 6, p. 217, December 1990.

APPENDIX 6.7

Comparison of Predictions by New Models with Experimental Data

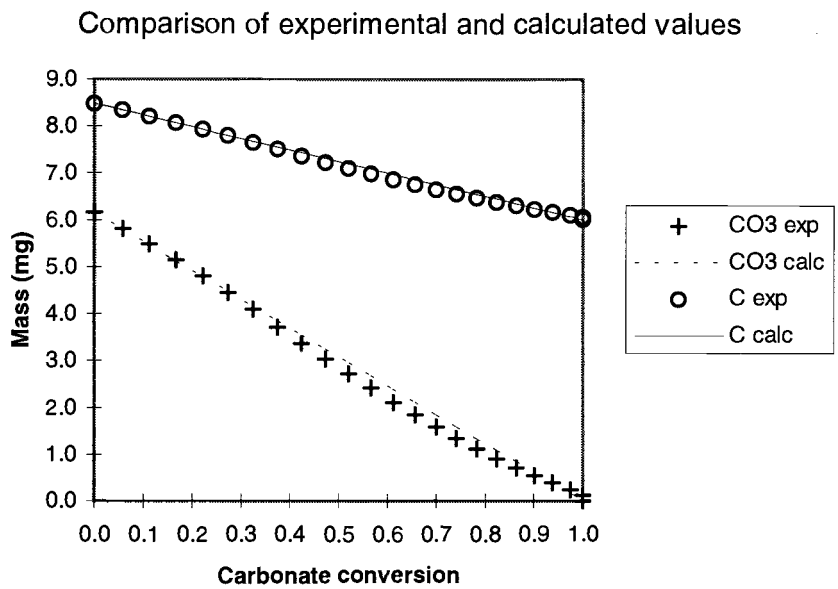

Figure A.6.7.1. Model II gives the second best fit of predicted and experimental carbonate and carbon concentration profiles. A = 1.03e10 mol/min, a = 0.0535, b = 1.0 (set), error = 0.0781.

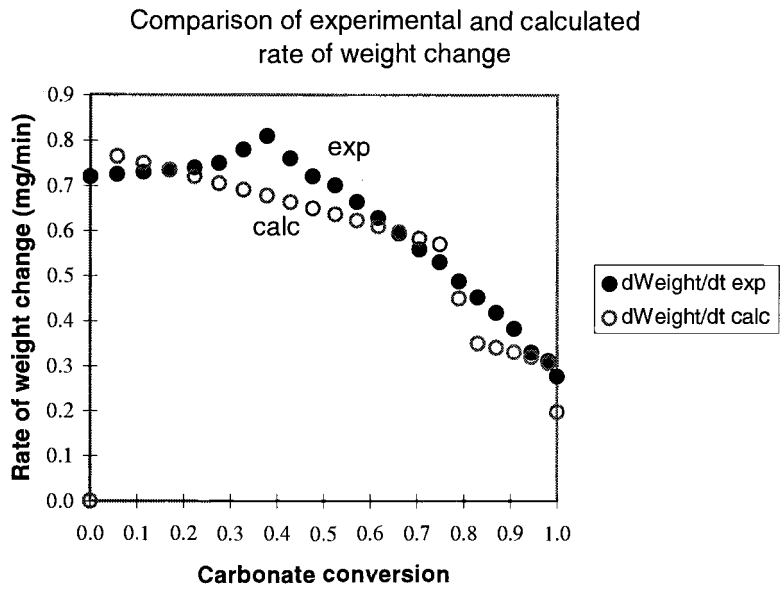

Figure A.6.7.2. Model II gives the second best fit between calculated and experimental rate of weight loss.

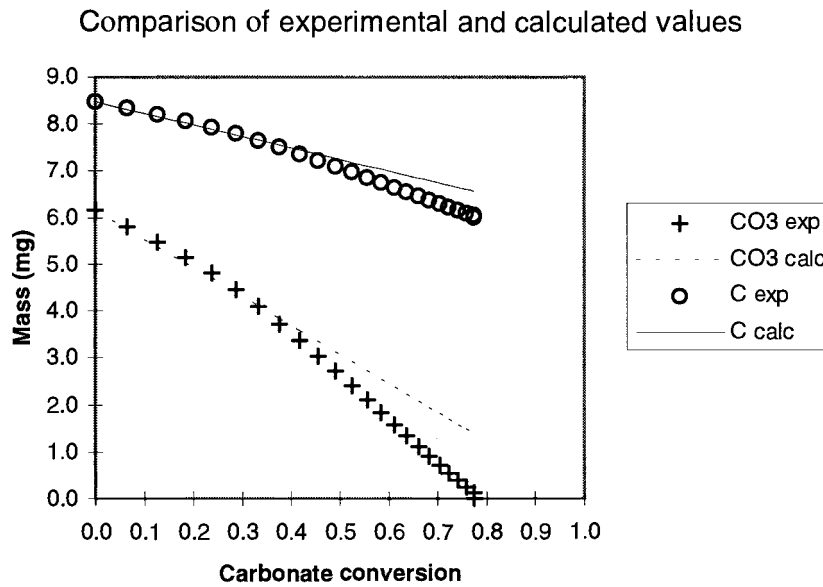

Figure A.6.7.3. Model III gives the second worst fit of predicted and experimental carbonate and carbon concentration profiles. A = 4.94e10 mol/min, a = 1.0 (set), b = 0.0, error = 0.585.

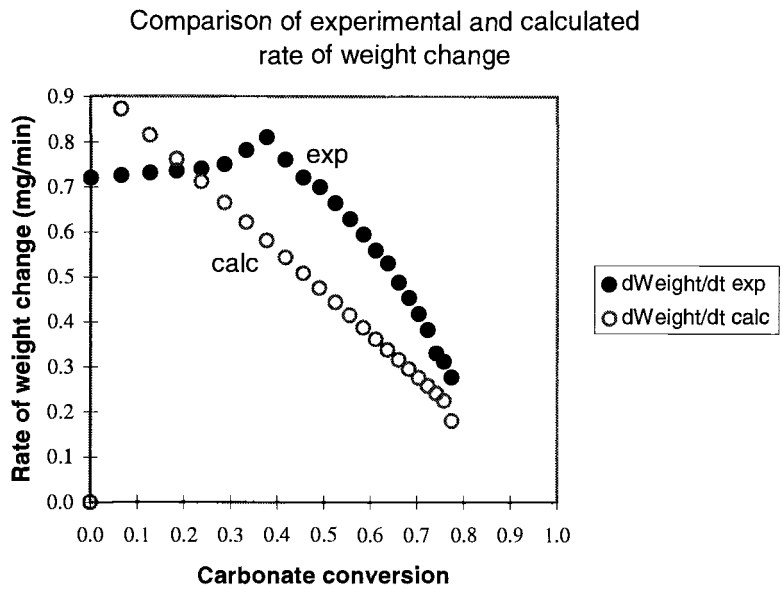

Figure A.6.7.4. Model III gives the second best fit between calculated and experimental rate of weight loss.

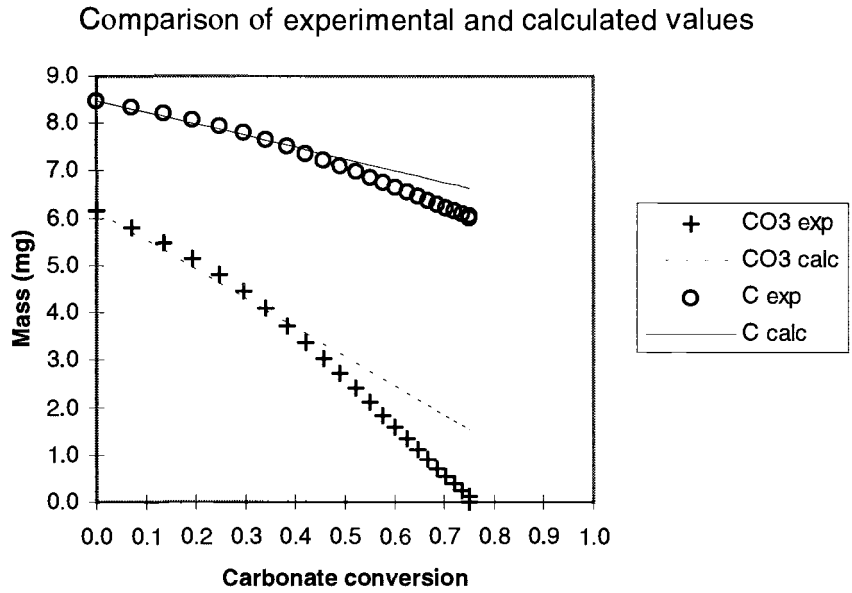

Figure A.6.7.5. Model IV gives the worst fit of predicted and experimental carbonate and carbon concentration profiles. A = 7.54e13 mol/min, a = 1.0, b = 1.0, error = 0.787.

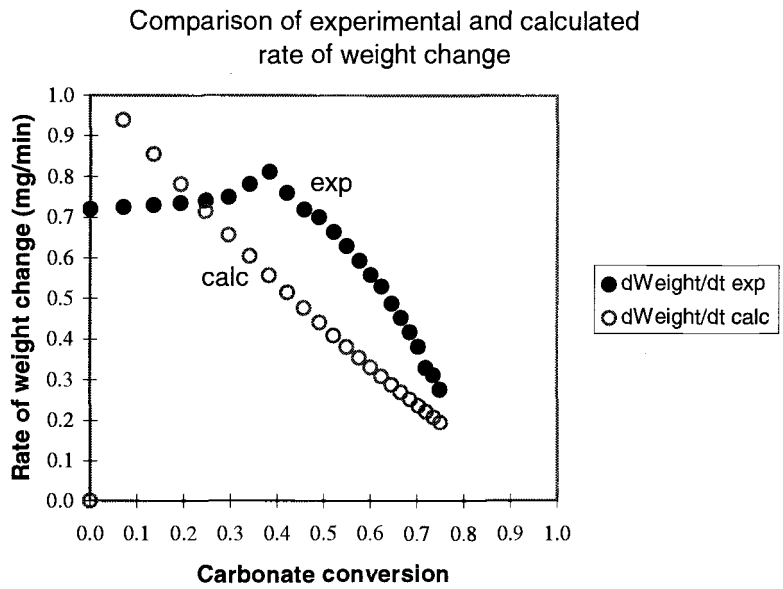

Figure A.6.7.6. Model IV gives the second best fit between calculated and experimental rate of weight loss.

APPENDIX 6.8

Spreadsheet for Optimizing Pre-exponential Factor and Reaction Orders

The spreadsheet for obtaining the best fit is given in this appendix. The other four cases were obtained by using the same spreadsheet but with either "a: or "b", or both set to 1. To calculate the values on a mass basis, the same spreadsheet was converted to a mass basis. This spreadsheet is not given here because it is virtually the same as the one on a mole basis.

Carbonate reduction rate equation from Li's data at 800C (8/13/96 KW)

BLS	36.2 mg	
BLC	28.2 mg	22% lost during heat up and stabilization at 800C
Sodium	3.6 mg	
Carbonate	6.2 mg	17% CO3= based on 36.2mg BLS
C in BLC	8.5 mg	30% C in char
gamma	-27.3514 dimensionless	
Initial char mass	28.2 mg	

RESULT

	A	7.37E+07	mol/min
[CO3]	a	1.70E-01	
[C]	b	1.77E-01	
	error	7.47E-02	

	exp	exp	exp	exp	exp	exp	exp	exp	exp	exp	exp	exp	exp
Time	dWeight/dt	dChar	Char left	dCO3=	dCO3=	CO3 left	CO3 left	dNa2	Na2 left	dCfixed	Cfixed left	Cfixed lef	dCO3/dt
min	mg/min	mg	mg	mg	mol	mg	mol	mg	mg	mg	mg	mol	mol/min
0	0.72	0.72	28.2	0.33	5.54E-06	6.2	1.03E-04	0.25	3.6	0.13	8.5	7.06E-04	0.00
1	0.73	0.73	27.5	0.33	5.58E-06	5.8	9.70E-05	0.26	3.4	0.13	8.3	6.95E-04	5.58E-06
2	0.73	0.73	26.7	0.34	5.62E-06	5.5	9.14E-05	0.26	3.1	0.13	8.2	6.84E-04	5.62E-06
3	0.74	0.74	26.0	0.34	5.65E-06	5.1	8.57E-05	0.26	2.8	0.14	8.1	6.72E-04	5.65E-06
4	0.74	0.74	25.3	0.34	5.69E-06	4.8	8.00E-05	0.26	2.6	0.14	7.9	6.61E-04	5.69E-06
5	0.75	0.75	27.5	0.35	5.77E-06	4.5	7.43E-05	0.27	2.3	0.14	7.8	6.49E-04	5.77E-06
6	0.78	0.78	26.7	0.36	6.00E-06	4.1	6.83E-05	0.28	2.0	0.14	7.6	6.37E-04	6.00E-06
7	0.81	0.81	25.9	0.37	6.23E-06	3.7	6.20E-05	0.29	1.8	0.15	7.5	6.25E-04	6.23E-06
8	0.76	0.76	25.3	0.35	5.85E-06	3.4	5.62E-05	0.27	1.5	0.14	7.4	6.13E-04	5.85E-06
9	0.72	0.72	24.6	0.33	5.54E-06	3.0	5.06E-05	0.25	1.2	0.13	7.2	6.02E-04	5.54E-06
10	0.70	0.70	26.8	0.32	5.38E-06	2.7	4.53E-05	0.25	1.0	0.13	7.1	5.91E-04	5.38E-06
11	0.66	0.66	26.0	0.31	5.11E-06	2.4	4.02E-05	0.23	0.7	0.12	7.0	5.81E-04	5.11E-06
12	0.63	0.63	25.3	0.29	4.84E-06	2.1	3.53E-05	0.22	0.5	0.12	6.9	5.71E-04	4.84E-06
13	0.59	0.59	24.7	0.27	4.56E-06	1.8	3.08E-05	0.21	0.3	0.11	6.7	5.62E-04	4.56E-06
14	0.56	0.56	24.0	0.26	4.29E-06	1.6	2.65E-05	0.20	0.1	0.10	6.6	5.54E-04	4.29E-06
15	0.53	0.53	26.2	0.24	4.08E-06	1.3	2.24E-05	0.19	0.0	0.10	6.5	5.46E-04	4.08E-06
16	0.49	0.49	25.5	0.23	3.75E-06	1.1	1.86E-05	0.17	0.0	0.09	6.5	5.38E-04	3.75E-06
17	0.45	0.45	24.9	0.21	3.48E-06	0.9	1.51E-05	0.16	0.0	0.08	6.4	5.31E-04	3.48E-06
18	0.42	0.42	24.2	0.19	3.21E-06	0.7	1.19E-05	0.15	0.0	0.08	6.3	5.25E-04	3.21E-06
19	0.38	0.38	23.6	0.18	2.94E-06	0.5	9.00E-06	0.14	0.0	0.07	6.2	5.19E-04	2.94E-06
20	0.33	0.33	25.9	0.15	2.54E-06	0.4	6.46E-06	0.12	0.0	0.06	6.2	5.14E-04	2.54E-06
21	0.31	0.31	25.2	0.14	2.40E-06	0.2	4.06E-06	0.11	0.0	0.06	6.1	5.09E-04	2.40E-06
22	0.28	0.28	24.6	0.13	2.13E-06	0.1	1.93E-06	0.10	0.0	0.05	6.1	5.05E-04	2.13E-06
23	0.24	0.24	24.0	0.11	1.86E-06	0.0	7.59E-08	0.09	0.0	0.04	6.0	5.01E-04	1.86E-06
24	0.21	0.21	23.4	0.10		-0.1				0.04	6.0		0.00E+00

OLD: old carbonate reduction equation with no carbon dependency
NEW: new carbonate reduction equation being optimized with carbon dependency

NEW calc dCO3/dt mol/min	NEW calc CO3 left mol	NEW calc CO3 left mg	OLD calc dCO3/dt mol/min	OLD calc CO3 left mol	OLD calc CO3 left mg	OLD calc dCf/dt mol/min	OLD calc Cfix left mol	OLD calc Cfix left mg	OLD calc dNa2/dt mg/min	OLD calc Na left mg	OLD calc Char left mg	OLD calc dWeight/dt mg/min	NEW calc dCf/dt mol/min
0	1.03E-04	6.15	0.00E+00	1.03E-04	6.15	0	7.06E-04	8.47	0.00	3.62	28.2	0.00	0
5.68E-06	9.69E-05	5.81	8.14E-06	9.44E-05	5.67	1.63E-05	6.90E-04	8.28	0.37	3.25	27.2	1.06E+00	1.1E-05
5.61E-06	9.13E-05	5.48	7.49E-06	8.69E-05	5.22	1.50E-05	6.75E-04	8.10	0.34	2.90	26.2	9.74E-01	1.1E-05
5.54E-06	8.57E-05	5.14	6.90E-06	8.00E-05	4.80	1.38E-05	6.61E-04	7.93	0.32	2.58	25.3	8.97E-01	1.1E-05
5.46E-06	8.03E-05	4.82	6.35E-06	7.37E-05	4.42	1.27E-05	6.48E-04	7.78	0.29	2.29	24.5	8.26E-01	1.1E-05
5.39E-06	7.49E-05	4.49	5.85E-06	6.78E-05	4.07	1.17E-05	6.36E-04	7.64	0.27	2.02	23.7	7.60E-01	1.1E-05
5.31E-06	6.96E-05	4.17	5.38E-06	6.25E-05	3.75	1.08E-05	6.26E-04	7.51	0.25	1.77	23.0	7.00E-01	1.1E-05
5.23E-06	6.43E-05	3.86	4.96E-06	5.75E-05	3.45	9.91E-06	6.16E-04	7.39	0.23	1.55	22.4	6.44E-01	1E-05
5.14E-06	5.92E-05	3.55	4.56E-06	5.29E-05	3.18	9.13E-06	6.07E-04	7.28	0.21	1.34	21.8	5.93E-01	1E-05
5.06E-06	5.41E-05	3.25	4.20E-06	4.87E-05	2.92	8.40E-06	5.98E-04	7.18	0.19	1.14	21.2	5.46E-01	1E-05
4.97E-06	4.92E-05	2.95	3.87E-06	4.49E-05	2.69	7.73E-06	5.91E-04	7.09	0.18	0.97	20.7	5.03E-01	9.9E-06
4.87E-06	4.43E-05	2.66	3.56E-06	4.13E-05	2.48	7.12E-06	5.83E-04	7.00	0.16	0.80	20.3	4.63E-01	9.7E-06
4.77E-06	3.95E-05	2.37	3.28E-06	3.80E-05	2.28	6.56E-06	5.77E-04	6.92	0.15	0.65	19.9	4.26E-01	9.5E-06
4.67E-06	3.49E-05	2.09	3.02E-06	3.50E-05	2.10	6.04E-06	5.71E-04	6.85	0.14	0.51	19.5	3.92E-01	9.3E-06
4.56E-06	3.03E-05	1.82	2.78E-06	3.22E-05	1.93	5.56E-06	5.65E-04	6.78	0.13	0.38	19.1	3.61E-01	9.1E-06
4.44E-06	2.59E-05	1.55	2.56E-06	2.97E-05	1.78	5.12E-06	5.60E-04	6.72	0.12	0.27	18.8	3.33E-01	8.9E-06
4.31E-06	2.16E-05	1.29	2.35E-06	2.73E-05	1.64	4.71E-06	5.55E-04	6.66	0.11	0.16	18.5	3.06E-01	8.6E-06
4.16E-06	1.74E-05	1.04	2.17E-06	2.52E-05	1.51	4.34E-06	5.51E-04	6.61	0.10	0.06	18.2	2.82E-01	8.3E-06
4.00E-06	1.34E-05	0.80	2.00E-06	2.32E-05	1.39	3.99E-06	5.47E-04	6.56	0.09	0.00	18.0	2.27E-01	8E-06
3.82E-06	9.57E-06	0.57	1.84E-06	2.13E-05	1.28	3.68E-06	5.43E-04	6.52	0.08	0.00	17.8	1.54E-01	7.6E-06
3.60E-06	5.97E-06	0.36	1.69E-06	1.96E-05	1.18	3.38E-06	5.40E-04	6.48	0.08	0.00	17.7	1.42E-01	7.2E-06
3.31E-06	2.65E-06	0.16	1.56E-06	1.81E-05	1.08	3.11E-06	5.37E-04	6.44	0.07	0.00	17.5	1.31E-01	6.6E-06
2.88E-06	0.00E+00	0.00	1.43E-06	1.66E-05	1.00	2.87E-06	5.34E-04	6.41	0.07	0.00	17.4	1.20E-01	5.8E-06
0.00E+00	0.00E+00	0.00	1.32E-06	1.53E-05	0.92	2.64E-06	5.31E-04	6.38	0.06	0.00	17.3	1.11E-01	0

Sheet: new eq. (mol)

RESULT

	A	7.37E+07	mol/min
[CO3]	a	1.70E-01	
[C]	b	1.77E-01	
	error	0.00E+00	

NEW calc fixed lef	NEW calc fixed lef	NEW calc dNa2/dt	NEW calc Na left	NEW calc Inert	NEW calc Char left	NEW calc dWeight/dt	NEW Squares of diff.	NEW calc Xco3	NEW calc CO3 left	NEW calc fixed left
mol	mg	mg/min	mg	mg	mg	mg/min	(exp-cal)^2	(-)	mg	mg
7.06E-04	8.47	0.000	3.62	10.0	28.2	0.00		0.00	6.15	8.47
6.95E-04	8.33	0.261	3.36	10.0	27.5	7.39E-01	1.89E-04	0.06	5.81	8.33
6.83E-04	8.20	0.258	3.10	10.0	26.8	7.30E-01	2.25E-07	0.11	5.48	8.20
6.72E-04	8.07	0.255	2.85	10.0	26.0	7.20E-01	2.22E-04	0.16	5.14	8.07
6.61E-04	7.94	0.251	2.59	10.0	25.3	7.10E-01	8.74E-04	0.22	4.82	7.94
6.51E-04	7.81	0.248	2.35	10.0	24.6	7.01E-01	2.45E-03	0.27	4.49	7.81
6.40E-04	7.68	0.244	2.10	10.0	23.9	6.90E-01	8.05E-03	0.32	4.17	7.68
6.29E-04	7.55	0.241	1.86	10.0	23.3	6.80E-01	1.70E-02	0.37	3.86	7.55
6.19E-04	7.43	0.237	1.62	10.0	22.6	6.69E-01	8.31E-03	0.42	3.55	7.43
6.09E-04	7.31	0.233	1.39	10.0	21.9	6.58E-01	3.90E-03	0.47	3.25	7.31
5.99E-04	7.19	0.228	1.16	10.0	21.3	6.46E-01	2.94E-03	0.52	2.95	7.19
5.89E-04	7.07	0.224	0.94	10.0	20.7	6.33E-01	9.21E-04	0.57	2.66	7.07
5.80E-04	6.96	0.220	0.72	10.0	20.0	6.21E-01	6.50E-05	0.61	2.37	6.96
5.70E-04	6.85	0.215	0.51	10.0	19.4	6.07E-01	1.82E-04	0.66	2.09	6.85
5.61E-04	6.74	0.210	0.30	10.0	18.8	5.92E-01	1.17E-03	0.70	1.82	6.74
5.52E-04	6.63	0.204	0.09	10.0	18.3	5.77E-01	2.19E-03	0.75	1.55	6.63
5.44E-04	6.53	0.198	0.00	10.0	17.8	4.53E-01	1.18E-03	0.79	1.29	6.53
5.36E-04	6.43	0.192	0.00	10.0	17.5	3.50E-01	1.06E-02	0.83	1.04	6.43
5.28E-04	6.33	0.184	0.00	10.0	17.1	3.36E-01	6.56E-03	0.87	0.80	6.33
5.20E-04	6.24	0.176	0.00	10.0	16.8	3.21E-01	3.75E-03	0.91	0.57	6.24
5.13E-04	6.15	0.166	0.00	10.0	16.5	3.02E-01	7.64E-04	0.94	0.36	6.15
5.06E-04	6.07	0.152	0.00	10.0	16.2	2.78E-01	1.12E-03	0.97	0.16	6.07
5.00E-04	6.00	0.133	0.00	10.0	16.0	2.28E-01	2.34E-03	1.00	0.00	6.00
5.00E-04	6.00	0.000	0.00	10.0	16.0	0.00E+00	5.83E-02	1.00	0.00	6.00
					Sum of squares		**7.47E-02**			

Summary of results, also shown in plots

Xco3 (-)	CO3 exp	CO3 calc	CO3 old	C exp	C calc	C old	Xco3 (-)	dWeight/dt exp	dWeight/dt calc	dWeight/dt old
0.00	6.15	6.15	6.15	8.47	8.47	8.47	0.00	0.72	0.00	0.000
0.06	5.82	5.81	5.67	8.34	8.33	8.28	0.06	0.73	0.74	1.058
0.11	5.48	5.48	5.22	8.20	8.20	8.10	0.11	0.73	0.73	0.974
0.16	5.14	5.14	4.80	8.07	8.07	7.93	0.16	0.74	0.72	0.897
0.22	4.80	4.82	4.42	7.93	7.94	7.78	0.22	0.74	0.71	0.826
0.27	4.46	4.49	4.07	7.79	7.81	7.64	0.27	0.75	0.70	0.760
0.32	4.10	4.17	3.75	7.65	7.68	7.51	0.32	0.78	0.69	0.700
0.37	3.72	3.86	3.45	7.50	7.55	7.39	0.37	0.81	0.68	0.644
0.42	3.37	3.55	3.18	7.36	7.43	7.28	0.42	0.76	0.67	0.593
0.47	3.04	3.25	2.92	7.22	7.31	7.18	0.47	0.72	0.66	0.546
0.52	2.72	2.95	2.69	7.10	7.19	7.09	0.52	0.70	0.65	0.503
0.57	2.41	2.66	2.48	6.97	7.07	7.00	0.57	0.66	0.63	0.463
0.61	2.12	2.37	2.28	6.86	6.96	6.92	0.61	0.63	0.62	0.426
0.66	1.85	2.09	2.10	6.75	6.85	6.85	0.66	0.59	0.61	0.392
0.70	1.59	1.82	1.93	6.64	6.74	6.78	0.70	0.56	0.59	0.361
0.75	1.34	1.55	1.78	6.55	6.63	6.72	0.75	0.53	0.58	0.333
0.79	1.12	1.29	1.64	6.46	6.53	6.66	0.79	0.49	0.45	0.306
0.83	0.91	1.04	1.51	6.37	6.43	6.61	0.83	0.45	0.35	0.282
0.87	0.72	0.80	1.39	6.30	6.33	6.56	0.87	0.42	0.34	0.227
0.91	0.54	0.57	1.28	6.23	6.24	6.52	0.91	0.38	0.32	0.154
0.94	0.39	0.36	1.18	6.16	6.15	6.48	0.94	0.33	0.30	0.142
0.97	0.24	0.16	1.08	6.11	6.07	6.44	0.97	0.31	0.28	0.131
1.00	0.12	0.00	1.00	6.06	6.00	6.41	1.00	0.28	0.23	0.120
1.00	0.00	0.00	0.92	6.01	6.00	6.38	1.00	0.24	0.00	0.111

APPENDIX 6.9

TG Reproducibility Runs

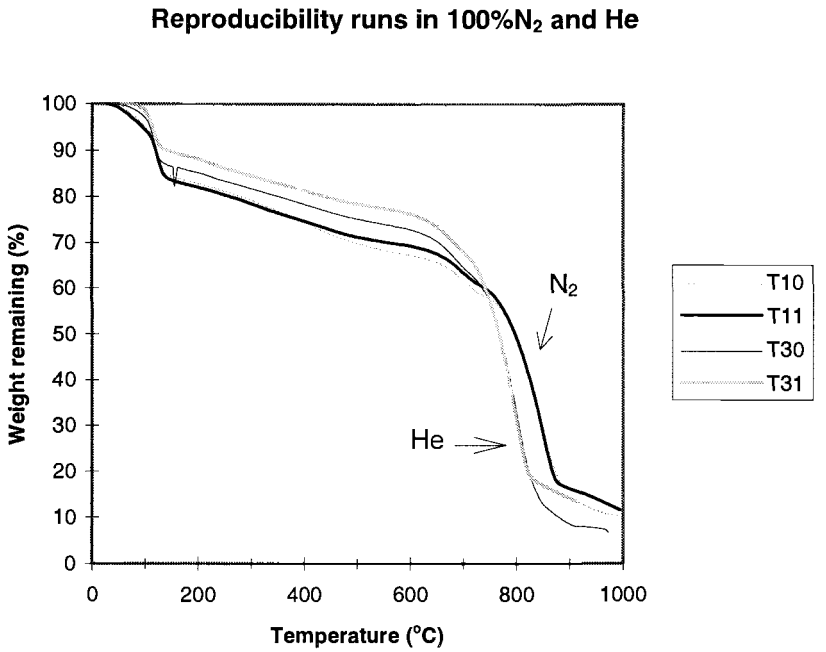

Figure A.6.9.1. The reproducibility is almost the same in nitrogen as in helium. Gas composition: T10 and T11: 100% N_2, T30 and T31: 100% He.

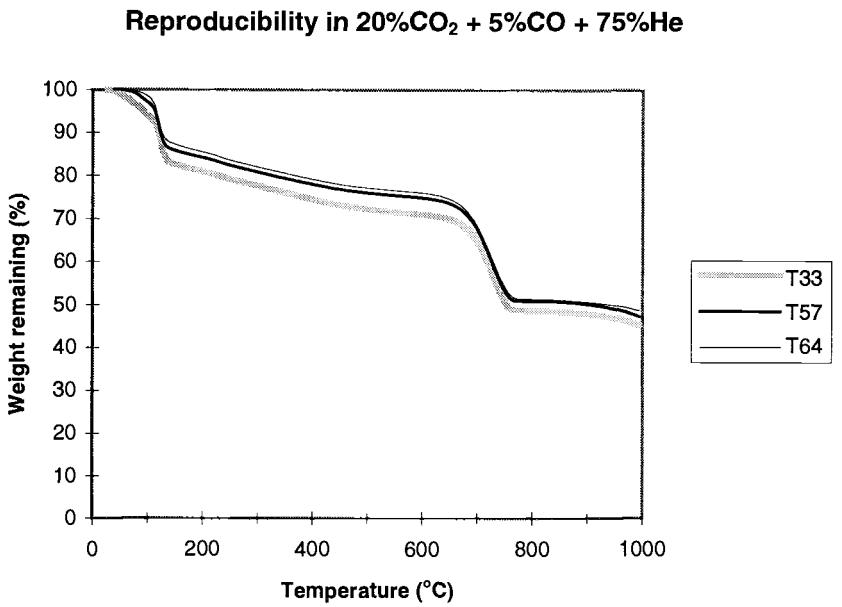

Figure A.6.9.2. The reproducibility in 20% CO_2 was very good.

APPENDIX 6.10

Effect of Carbon Depletion

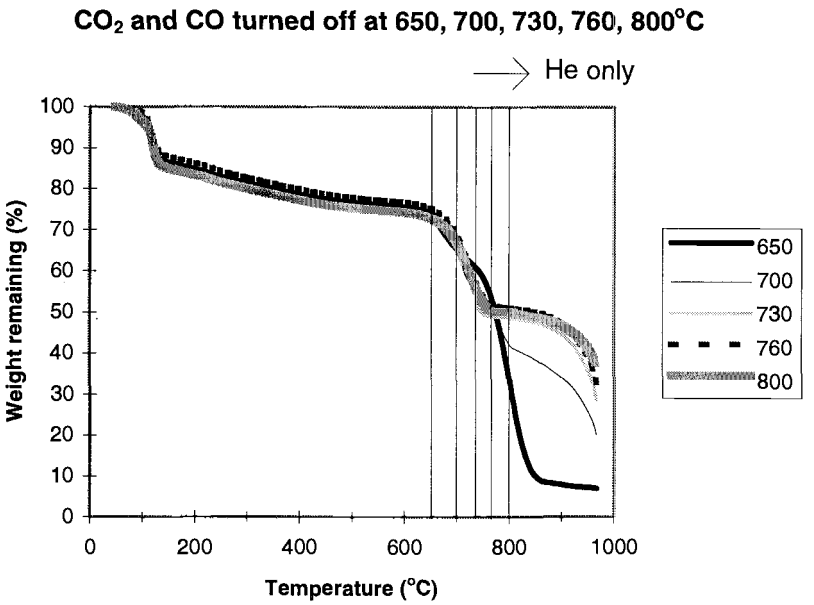

Figure A.6.10.1. The thermograms fall in a nice sequential order when CO_2 is turned off at 650, 700, 730, 760, and 800°C.

Chapter 7
Estimation of Element Distribution and Heat of Pyrolysis During Black Liquor Devolatilization

INTRODUCTION

A FORTRAN computer program was created for calculating the split of elements during devolatilization of black liquor solids (BLS) and estimating to what extent this process is endothermic or exothermic at typical recovery boiler conditions. The computer program accounts for elements typically present in black liquor such as carbon, sodium, and sulfur. The program is composed of a main program and five subroutines each part having its purpose. The main program contains mainly the in- and output operations. The gas phase partial pressures were calculated in one subroutine and the water gas shift equilibrium composition in another. The heat of pyrolysis was calculated in a third, and the inorganic species mole fractions in a fourth. The fifth subroutine was used in the printing operation. The executable file is no more than 53 kB large and can easily be used in any portable or desktop computer. Sensitivity analyses were carried out for an exothermic and an endothermic process that corresponded to two different black liquor solids compositions. The program has a built-in trouble shooting capability.

OBJECTIVES

The objective of this chapter is to present a method for estimating the distribution of mass and the heat of pyrolysis during devolatilization of black liquor solids. The other objective is to provide a simple tool for a first validation of comprehensive computational fluid-dynamic models for recovery boilers. This validation is important before any operational and design changes be made on a large scale recovery boiler.

ASSUMPTIONS AND LIMITATIONS

The following key assumptions were made:

1. The amount of sodium sulfate in BLS remains constant during devolatilization.
2. When the mole of oxygen is less than carbon in BLS, then CO, CH_4, H_2S, and H_2 are formed (no CO_2 is formed).
3. When the mole of oxygen is higher than carbon in BLS, then CO, CO_2, H_2S, and H_2 are formed.
4. Soot is formed when not enough hydrogen is present for CH_4 formation.

The program is not designed for calculations with unrealistic compositions, e.g. zero or very small hydrogen concentrations. Such a composition would violate one of the initial assumptions, e.g. H_2S formation might not be complete due to too little hydrogen in the original material.

INPUT AND OUTPUT DATA

The following input data is required by the user either by default or as new input values:

- Sample weight of black liquor solids in grams
- Mass fraction of the species: C, H, O, Na, S, K, Cl
- X weight-% of Na+K goes to volatiles during devolatilization

The following data can be used to estimate the sodium released during devolatilization (1):

700°C: 13% ; 900°C: 16% ; 1000°C: 20%

- Y weight-% of S goes to volatiles during devolatilization

The following data can be used to estimate the sulfur released during devolatilization (2):

700°C: 60% ; 900°C: 40% ; 1100°C: 26%

- Z weight-% of C goes to volatiles during devolatilization

The following data can be used to estimate the carbon released during devolatilization (2):

700°C: 47% ; 900°C: 56% ; 1100°C: 69%

- R weight-% of S in BLS is as Na_2SO_4 after devolatilization

The following data can be used to estimate the sulfate initially in BLS (2):

700°C: 18% ; 900°C: 10% ; 1100°C: 5%

- The temperature at which the water gas shift equilibrium is to be calculated

All output data are calculated in grams except for the gas species that are given in partial pressures. Appendices 7.2 and 7.3 contain examples of the following output data.

- Elemental solids composition
- Elemental volatiles composition
- Elemental char composition
- Volatiles species composition
- Char species composition

Error control numbers are printed next to the sums of the calculated species. When the estimated values are equal to the sum of the elements, then a complete mass balance is maintained and the program works as intended.

CHEMICAL REACTIONS

The following reactions are accounted for. These reactions are assumed to go to completion.

Gas phase reactions

1. $H_2S(g) + Na_2CO_3(s,l) + 2O_2(g) \rightarrow Na_2SO_4(s,l) + H_2O(g) + CO_2(g)$
2. $2Na(g) + CO_2(g) + \frac{1}{2}O_2(g) \rightarrow Na_2CO_3(s,l)$
3. $2K(g) + CO_2(g) + \frac{1}{2}O_2(g) \rightarrow K_2CO_3(s,l)$

4. $CO(g) + \frac{1}{2}O_2(g) \rightarrow CO_2(g)$
5. $CH_4(g) + 2O_2(g) \rightarrow CO_2 + 2H_2O(g)$
6. $H_2(g) + \frac{1}{2}O_2(g) \rightarrow H_2O(g)$

Char reactions

7. $Na_2S(s,l) + 2O_2(g) \rightarrow Na_2SO_4(s,l)$
8. $C(s) + O_2(g) \rightarrow CO_2(g)$
9. $C(s) + \frac{1}{2}O_2(g) \rightarrow CO(g)$

STOICHIOMETRY

From the input assumption that Y weight-% of sulfur goes to volatiles and R % sulfur is as Na_2SO_4 in BLS, the amount of Na associated to Na_2S and Na_2SO_4 in char can be calculated. The amount of Na_2SO_4 is assumed to remain unchanged during devolatilization. All Cl goes to NaCl which gives all Na associated to this compound. By difference Na associated with Na_2CO_3 can be calculated as well as C and O associated to the same compound. This is assuming there are no Na containing species except Na_2S, Na_2SO_4, Na_2CO_3. All K goes to K_2CO_3, and the C and O associated to this compound can be calculated. This gives the char species composition. From the char elemental composition, by difference the volatiles elemental composition can be calculated. Depending on the input assumptions there are two cases, one where mol C > mol O and only CO is formed. In the other case when mol C < mol O, both CO and CO_2 are formed. If mol C > mol O then calculate how much H is associated with CH_4, H_2S, H_2, and how much C is associated with CO. If mol C < mol O then calculate H associated with H_2S, H_2, and how much C is associated with CO and CO_2. However, if there is not enough hydrogen for CH_4 formation soot is formed. If there is too little hydrogen, some H_2S is formed and no CH_4 or H_2 is released. This situation, however, is rare and is omitted in this analysis. The equations are given in Appendix 7.1.

WATER GAS SHIFT EQUILIBRIUM CALCULATION

The program determines automatically when the water gas shift equilibrium is feasible in the gas phase. This will be calculated when CO_2 is formed. However, when no CO_2 is formed, it was not possible to calculate the water gas shift equilibrium composition. This is typical when the carbon content is high and the oxygen content low. The user can determine the theoretical equilibrium state by giving the desired temperature. The water gas shift reaction is given by reaction 10:

10. $H_2O + CO = CO_2 + H_2$

The equilibrium constant is given by equation 7-1:

$$K_p = (pCO_2 \times pH_2) \div (pH_2O \times pCO) \quad (7\text{-}1)$$

The numerical value of the equilibrium constant is given by equation 7-2 (3):

$$K_p = e^{(-3.49+3563/T+0.313\,(1000/T)^2)} \quad (7\text{-}2)$$

The following equations apply:

Carbon balance:

$$pCO_2 + pCO = C_1 \quad (7\text{-}3)$$

Hydrogen balance:

$$pH_2 + pH_2O = C_2 \quad (7\text{-}4)$$

Oxygen balance:

$$2 \times pCO_2 + pCO + pH_2O = C_3 \quad (7\text{-}5)$$

By elimination the following equation is obtained:

$$a\,pCO_2 + b\,pCO + c = 0 \quad (7\text{-}6)$$

where

$$a = K_p - 1 \quad (7\text{-}7)$$

$$b = K_p C_3 - 2 K_p C_1 + C_2 - C_3 + 3 C_1 \quad (7\text{-}8)$$

$$c = C_1 C_3 - C_1 C_2 - 2 C_1^2 \quad (7\text{-}9)$$

Hence,

$$pCO_{sh} = \left(-b + \sqrt{b^2 - 4ac}\right) \div 2a \quad (7\text{-}10)$$

$$pCO_{2,sh} = C_1 - pCO_{sh} \quad (7\text{-}11)$$

$$pH_2O_{sh} = C_3 - 2 \times pCO_{2,sh} - pCO_{sh} \quad (7\text{-}12)$$

$$pH_{2,sh} = K_p \, pCO_{sh} \, pH_2O_{sh} \div pCO_{2,sh} \quad (7\text{-}13)$$

PROCEDURE FOR ESTIMATING HEAT OF PYROLYSIS

The heat of reaction for the overall pyrolysis process (heat of pyrolysis) is calculated from the standard heats of combustion of the individual chemical reactions at 298 K (see chemical reactions). The following species are considered as the fuel compounds that undergo complete conversion to combustion products: H_2S, Na, K, CO, CH_4, Na_2S, C, and H_2. The amounts of these species come from the outputs of the mass balance. The heat balance is given by equation 7-14:

(heat generated) = (heat in) - (heat out) (7-14)

(Heat of Pyrolysis) =

(HHV of BLS) - (Heat of comb of char) - (Heat of comb of volatiles) (7-15)

HHV is the higher heating value in MJ/kg and the heat of pyrolysis is defined as exothermic when positive. The percentage of the heat of pyrolysis with respect to the higher heating value of black liquor solids is defined as follows.

$$\frac{(\text{Heat of pyrolysis})}{(\text{HHV BLS})} = \left[1 - \frac{\Delta H_{comb}(\text{volatiles} + \text{char})}{(\text{HHV BLS})}\right] \times 100\% \qquad (7\text{-}16)$$

Thus, a negative sign would indicate an endothermic and a positive sign an exothermic reaction. Two examples are shown; one for an endothermic and another for an exothermic reaction. These examples are also the two sensitivity studies shown in tables 7.1 and 7.2.

The heat of combustion of the volatiles is given by equation 7-17:

$$\Delta H_{comb}(\text{volatiles}) = \sum \Delta H_{rxn,1\text{-}6} \qquad (7\text{-}17)$$

The heat of combustion of the char is given by equation 7-18:

$$\Delta H_{comb}(\text{char}) = \sum \Delta H_{rxn,7\text{-}9} \qquad (7\text{-}18)$$

SENSITIVITY STUDY I (endothermic)

A case study was made for the following solids composition which is high in carbon content: 39 % C, 3.8 % H, 33% O, 18.6 % Na, 3.6 % S, 1.2 % K, 0.8 % Cl. The following parameters were investigated with the base case values in the brackets: X % of Na+K to volatiles (20), Y % of S to volatiles (35), Z % of C to volatiles (50), R % of S as Na_2SO_4 (50). The higher heating value (HHV) of the solids is assumed 15.4 MJ/kg which is a typical measured value. Table 7.1 lists the results. HHVs are given in MJ/kg. The shaded cells indicate the base case.

Table 7.1. Sensitivity study for a low oxygen content black liquor.

X, Na+K vol	HHV vol	HHV char	HHV vol+char	% Heat of pyro
0.1	10.0	5.6	15.6	-1.5
0.2	10.3	5.8	16.1	-4.6
0.3	10.7	5.9	16.6	-7.8
Y, S vol				
0.2	10.2	5.9	16.2	-4.9
0.35	10.3	5.8	16.1	-4.6
0.5	10.5	5.6	16.1	-4.4
Z, C vol				
0.3	7.9	8.3	16.2	-5.0
0.5	10.3	5.77	16.1	-4.6
0.7	11.8	3.2	15.0	2.3
R, S as Na_2SO_4				
0.1	10.3	6.1	16.4	-6.3
0.5	10.3	5.8	16.1	-4.6
0.9	10.4	5.5	15.9	-3.0

For this particular black liquor solids composition, the heat of pyrolysis is always endothermic except when 70% of the carbon goes to volatiles. The percentage of the heat of pyrolysis with respect to the higher heating value of black liquor solids ranges from 1.5 % to 7.8 % for this particular solids composition. By reading the table one can see that increasing the carbon fraction to volatiles from 30% to 50% makes the process less endothermic. At 70% carbon volatility soot is formed, and the process becomes exothermic. Increasing Na+K to volatiles makes the process more endothermic. A larger fraction of sulfur to volatiles and a larger fraction of sulfur as sulfate will both make the process less endothermic. Only CO is formed except when only 30% of the carbon goes to volatiles. Here, both CO and CO_2 are formed.

SENSITIVITY STUDY II (exothermic)

For higher oxygen compositions an exothermic reaction is predicted. A case study was made for the following solids composition which is low in carbon content: 30 % C, 3.8 % H, 42 % O, 18.6 % Na, 3.6 % S, 1.2 % K, 0.8 % Cl. The following parameters were investigated with the base case values in the brackets: X % of Na+K to volatiles (20%), Y % of S to volatiles (35%), Z % of C to volatiles (50%), R % of S as Na_2SO_4 (50%). The higher heating value of the solids was again assumed 15.4 MJ/kg. Table 6.2 lists the results. HHV are given in MJ/kg. The shaded cells indicate the base case.

Table 7.2. Sensitivity study for a high oxygen content black liquor.

X, Na+K vol	HHV vol	HHV char	HHV vol+char	% Heat of pyro
0.1	7.8	4.1	12.0	22.3
0.2	7.9	4.3	12.2	21.0
0.3	7.9	4.5	12.4	19.7
Y, S vol				
0.2	7.7	4.5	12.2	21.0
0.35	7.9	4.3	12.2	21.0
0.5	8.0	4.1	12.2	21.0
Z, C vol				
0.3	5.1	6.3	11.4	25.9
0.5	7.9	4.3	12.2	21.0
0.7	10.5	2.3	12.9	16.5
R, S as Na_2SO_4				
0.1	7.6	4.6	12.2	21.1
0.5	7.9	4.3	12.2	21.0
0.9	8.2	4.0	12.2	20.9

For this black liquor solids composition, the heat of pyrolysis is always exothermic. The water gas shift equilibrium is calculated at 750°C. CO and CO_2 are always formed except when 70% of carbon goes to volatiles. Here only CO is formed. The percentage of the heat of pyrolysis with respect to the higher heating value of black liquor solids ranges

from 16.5 % to 25.9 % for this particular solids composition. By reading the table one can see that increasing Na+K to volatiles the heat of pyrolysis decreases. Increasing the fraction sulfur to volatiles and sulfur as sulfate have virtually no effect. The heat of pyrolysis is strongly dependent on how much carbon goes to volatiles.

CONCLUSIONS AND RECOMMENDATIONS

This study shows that the elemental composition has an important impact on whether the devolatilization process is endothermic or exothermic. When the oxygen to carbon ratio was 0.85, the process was endothermic. When this ratio was 1.4, the process was exothermic. The role of the empirical split factors was small for the heat of pyrolysis. The only exceptions was that the devolatilization process would become slightly exothermic at an oxygen to carbon ratio of 0.85 when 70% of the carbon in the BLS would volatilize.

It is recommended that a new method is developed for estimating the element distribution that is based on the energy required to devolatilize black liquor solids rather than empirical split factors. However, due to its simplicity and compactness, this empirical method may fulfill a need in validating and developing comprehensive combustion models for real systems such as a recovery boiler.

ACKNOWLEDGMENT

The Office of Industrial Technology at the U.S. Department of Energy is acknowledged for financial support. Drs. W.J.Frederick and T.M. Grace are acknowledged for guidance.

NOMENCLATURE

Symbol	description, dimension
K_p	equilibrium constant, dimensionless
C_1, C_2, C_3	constant, dimensionless
a,b,c	parameters in 2nd order equation, dimensionless
p_i	non-shifted partial pressure of species i, bar
$p_{i,sh}$	shifted partial pressure of species i, bar
i	CO_2, H_2O, CO, H_2
HHV	higher heating value, MJ/kg
ΔH_{comb}	heat of combustion, MJ/kg
ΔH_{rxn}	heat of reaction, MJ/kg

REFERENCES

1. Frederick, W.J., Iisa, K., Wåg. K.J., Reis, V.V., Boonsongsup, L., Forssén, M., Hupa, M., Report to the U.S. Department of Energy, DOE/CE/40936-T2, August, 1995

2. Sricharoenchaikul, V., M.S. thesis, Oregon State U., 1995

3. Meijer, R., Sibeijn, M., van Dillen, M.R.B., Kapteijn, F., Moulijn, J.A., Ind. Eng. Chem. Res., Vol. 30, 1991

APPENDICES

APPENDIX 7.1

Stoichiometric Equations for Char and Volatile Formation

Char formed as elements (by weight):

(C in char) = (C in BLS) - (C to volatiles)

(H in char) = 0

(O in char) = (O in Na2SO4) + (O in K2CO3) + (O in Na2CO3)

(Na in char) = (1-X)×(Na in BLS)

(S in char) = (1-Y)×(S in BLS)

(K in char) = (1-X)×(K in BLS)

(Cl in char) = (Weight of sample)×(Fraction Cl in Sample)

Volatiles formed as elements (by weight):

C = (C in BLS) × Z

H = (H in BLS)

O = (O in BLS) - (O in char)

Na = (Na in BLS) - (Na in char)

S = (S in BLS) - (S in char)

K = (K in BLS) - (K in char)

Cl = 0

(S in Na2SO4) = R × (S in char)

(Na in Na2SO4) = (S in Na2SO4) ÷ 32 × 46

(O in Na2SO4) = (S in Na2SO4) ÷ 32 × 4 × 16

(S in Na2S) = (1 - R) × (S in char)

(Na in Na2S) = (S in Na2S) ÷ 32 × 46

(Cl in NaCl) = (CL in char)

(Na in NaCl) = (Cl in NaCl) ÷ 35.5 × 23

(K in K2CO3) = (K in char)

(O in K2CO3) = (K in K2CO3) ÷ 39.1 × 16 × 3 ÷ 2

(C in K2CO3) = (K in K2CO3) ÷ 39.1 × 12 ÷ 2

(Na in Na2CO3) =(Na in char) - (Na in Na2SO4) - (Na in Na2S) - (Na in NaCl)

(O in Na2CO3) = (Na in Na2CO3) ÷ 46 × 16 × 3

(C in Na2CO3) = (Na in Na2CO3) ÷ 46 × 12

Volatiles formed as species (by weight: no CO_2 formed):

H2S = (S as volatiles) + (H to H2S)

CO = (mol CO formed) × (12+16)

CO2 = 0

soot = 0

CH4 = [(mol C as volatiles) - (mol CO formed)] × (12+4)

H = (H as volatiles) - (H to CH4) × 4 ÷ (12+4) - (H to H2S)

if H < 0 then too little H2 for CH4 (Calculation of H to CH4 needed)

H = (H as volatiles) - (H to H2S)

if H < 0 then there is not enough H2 for H2S formation (program terminates)

(If there is enough H2 for H2S formation):

mol CH4 = H2 ÷ 4

CH4 = (mol CH4) × (12+4)

soot = (mol C - mol CO - mol CH4) × 12

H = (H as volatiles) - (H to H2S) - (H to CH4) × 4 ÷ (12+4)

Na-vapor = (Na as volatiles)

K-vapor = (K as volatiles)

(Subroutine call for calculation of the partial pressures)

Volatiles formed as species (by weight: CO and CO_2 formed):

H2S = (S as volatiles) + (H as H2S)

mol CO2 = (mol O - mol C) ÷ 2

CO2 = (mol CO2) × (12+32)

mol CO = (mol C) - (mol CO2)

CO = (mol CO) × (12+16)

mol O = (mol O initially) - (mol CO) - 2 × (mol CO2)

CH4 = 0

H = (H as volatiles) - (H to H2S)

if H < 0 then there is not enough H2 for H2S formation (program terminates)

(H2O formation from O and H):

if mol O > H then

mol H2O = H ÷ 2

mol O = (mol O initially) - (mol CO) - 2 × (mol CO2) - (mol H2O)

H = 0

else

mol H2O = mol O

mol O = 0

H = (H as volatiles) - (H to H2S) - 2 × (mol H2O)

(H2O is also calculated from the water gas shift equilibrium in subroutine SHIFT)

O2 = (mol O) × 32

mol H2 = H ÷ 2

H2O = (mol H2O) × 18

Na-vapor = (Na as volatiles)

K-vapor = (K as volatiles)

Char formed as species (by weight) :

Na2S = (Na as Na2S) + (S as Na2S)

Na2SO4 = (S as Na2SO4) + (O as Na2SO4) + (Na as Na2SO4)

Na2CO3 = (C as Na2CO3) + (O as Na2CO3) + (Na as Na2CO3)

C(fixed) = (C in char) - (C in K2CO3) - (C in Na2CO3)

O(fixed) = (O in char)-(O in Na2SO4)-(O in K2CO3)-(O in Na2CO3)

K2CO3 = (C in K2CO3) + (O in K2CO3) + (K in K2CO3)

NaCl = (Na in NaCL) + (Cl in NaCl)

APPENDIX 7.2

Sensitivity Study I (Endothermic Process)

Give the dry sample weight (grams)
1.000000

Carbon	=	39.0000 %
Hydrogen	=	3.8000 %
Oxygen	=	33.0000 %
Sodium	=	18.6000 %
Sulfur	=	3.6000 %
Potassium	=	1.2000 %
Chloride	=	.8000 %
Total	=	100.0000 %

X % of Na+K to volatiles	20.000000
Y % of S to volatiles	35.000000
Z % of C to volatiles	50.000000
R % of S as Na2S	50.000000
Water gas shift temp (C)	750.000000

BLS in grams

Carbon	=	.3900000
Hydrogen	=	.0380000
Oxygen	=	.3300000
Sodium	=	.1860000
Sulfur	=	.0360000
Potassium	=	.0120000
Chloride	=	.0080000
Total	=	1.0000000

	Vol. formed (g)	Char formed (g)		
Carbon:	.1950000000	.1950000000		
Hydrogen:	.0380000000	.0000000000		
Oxygen:	.1859463000	.1440537000		
Sodium:	.0372000000	.1488000000		
Sulfur:	.0126000000	.0234000000		
Potassium:	.0024000000	.0096000000		
Chloride:	.0000000000	.0080000000		
Total:	.4711463000	.5288537000	1.0000000000	combined

Only CO formed !

pCO2 : .0000000000
pCO : .4331154000
pH2 : .3484386000
pH2S : .0146742700
pCH4 : .1724895000
psoot: .0000000000
pNa2 : .0301384700
pK2 : .0011437750
Total: 1.0000000000

Volatiles formed by species (grams)

CO	=	.3254060000	
CO2	=	.0000000000	
H2	=	.0186990800	
H2O	=	.0000000000	
H2S	=	.0133875000	
CH4	=	.0740536700	
Soot	=	.0000000000	
Excess O2	=	.0000000000	
Na2-vapor	=	.0372000000	
K2-vapor	=	.0024000000	
Total	=	.4711463000	.4711463000

Char formed (grams)

Na2S	=	.0285187500	
Na2SO4	=	.0519187500	
Na2CO3	=	.2534308000	
Cfixed	=	.1648366000	
Ofixed	=	-.0000000070	
K2CO3	=	.0169657300	
NaCl	=	.0131831000	
Total	=	.5288537000	.5288537000

HEATING VALUE CALCULATION (kJ) at 273 K
HHVvol = 10.3408500000
HHVchar = 5.7713300000
HHV(vol+char) = 16.1121800000 MJ/kg

APPENDIX 7.3

Sensitivity Study II (Exothermic Process)

Give the dry sample weight (grams)
1.000000

Carbon	=	30.0000 %
Hydrogen	=	3.8000 %
Oxygen	=	42.0000 %
Sodium	=	18.6000 %
Sulfur	=	3.6000 %
Potassium	=	1.2000 %
Chloride	=	.8000 %
Total	=	100.0000 %

X % of Na+K to volatiles	20.000000
Y % of S to volatiles	35.000000
Z % of C to volatiles	50.000000
R % of S as Na2S	50.000000
Water gas shift temp (C)	750.000000

BLS in grams

Carbon	=	.3000000
Hydrogen	=	.0380000
Oxygen	=	.4200000
Sodium	=	.1860000
Sulfur	=	.0360000
Potassium	=	.0120000
Chloride	=	.0080000
Total	=	1.0000000

	Vol. formed (g)	Char formed (g)		
Carbon:	.1500000000	.1500000000		
Hydrogen:	.0380000000	.0000000000		
Oxygen:	.2759463000	.1440537000		
Sodium:	.0372000000	.1488000000		
Sulfur:	.0126000000	.0234000000		
Potassium:	.0024000000	.0096000000		
Chloride:	.0000000000	.0080000000		
Total:	.5161463000	.4838537000	1.0000000000	combined

Both CO+CO2 formed

pCO2 : .0678482900
pCO : .3186773000
pH2O : .0789276100
pH2 : .4964154000
pH2S : .0121755500
pCH4 : .0000000000
psoot: .0000000000
pO2 : .0000000000
pNa2 : .0250065300
pK2 : .0009490142
Total: .9999997000

Volatiles formed by species (grams)
CO = .2835470000
CO2 = .1044261000
H2 = .0324658600
H2O = .0427198000
H2S = .0133875000
CH4 = .0000000000
Soot = .0000000000
Excess O2 = .0000000000
Na2-vapor = .0372000000
K2-vapor = .0024000000
Total = .5161463000 .5161463000

Char formed (grams)
Na2S = .0285187500
Na2SO4 = .0519187500
Na2CO3 = .2534308000
Cfixed = .1198366000
Ofixed = -.0000000070
K2CO3 = .0169657300
NaCl = .0131831000
Total = .4838537000 .4838537000

HEATING VALUE CALCULATION (kJ) at 273 K
HHVvol = 7.8688540000
HHVchar = 4.2957050000
HHV(vol+char) = 12.1645600000 MJ/kg

APPENDIX 7.4

Computer Code

```
C     MASSPLIT.FOR
C     Last modified 5/30/94 Kaj Wag
C     Program for mass balance calculations
C     Volatiles and char split from BL solids
C     See documentation for details
      real RS,SC,ClC,NaC,KC,Nana,Sna,Sso4,Naso4,Cnco3,Naco3,Ckco3,
     & Kco3,Nacl,Clna,pco2,pco,ph2o,ph2,Temp,pco2s,pcos,ph2os,ph2s,
     & molH2S,molNa2,molK2,molCO,molCH4,molH2,molNa2S,molCC,soot,
     & HHVvol,HHVchar,H2S,CO,CO2,CH4,H1,NAV,KV,Oso4,Okco3,Onco3,
     & C,H,O,Na,S,K,Cl,W,CS,HS,OS,NaS,SS,KS,ClS,tot,CV,CC,HV,HC,
     & OV,OC,SV,ClV,tot1,tot2,XN,YS,ZC,molC,molO,molHH2S,molCO2,
     & HH2S,CF,OF,Na2S,Na2SO4,K2CO3,NaCll,HHVAL,Na2CO3,H2O,nO,Ox,
     & molH2O,check
      integer flag
      COMMON/kaj/RS,SC,ClC,NaC,KC,Nana,Sna,Sso4,Naso4,Cnco3,
     & Naco3,Ckco3,Kco3,Nacl,Clna
      common/P/pco2,pco,ph2o,ph2,Temp
      common/Ps/pco2s,pcos,ph2os,ph2s
c*******INPUTS*****************************************
      open(1,file='massplit.out',status='unknown')
      write(*,*) 'Give the dry sample weight (grams)'
      write(1,*) 'Give the dry sample weight (grams)'
      read(*,*) W
      write(1,*) W
      write(*,*) 'Give default elemental composition (1)'
      write(*,*) 'Give new elemental composition (2)'
      read(*,*) flag
      if (flag.eq.1) then
       C=0.35
       H=0.038
       O=0.35
       Na=0.206
       S=0.036
       K=0.012
       Cl=0.008
      else
       write(*,*) 'Give C H O Na S K Cl in mass fractions'
       read(*,*) C,H,O,Na,S,K,Cl
```

```
      endif
      write(*,9) 'Carbon   = ',C*100,' %'
      write(1,9) 'Carbon   = ',C*100,' %'
      write(*,9) 'Hydrogen = ',H*100,' %'
      write(1,9) 'Hydrogen = ',H*100,' %'
      write(*,9) 'Oxygen   = ',O*100,' %'
      write(1,9) 'Oxygen   = ',O*100,' %'
      write(*,9) 'Sodium   = ',Na*100,' %'
      write(1,9) 'Sodium   = ',Na*100,' %'
      write(*,9) 'Sulfur   = ',S*100,' %'
      write(1,9) 'Sulfur   = ',S*100,' %'
      write(*,9) 'Potassium = ',K*100,' %'
      write(1,9) 'Potassium = ',K*100,' %'
      write(*,9) 'Chloride = ',Cl*100,' %'
      write(1,9) 'Chloride = ',Cl*100,' %'
      tot=(C+H+O+Na+S+K+Cl)*100
      write(*,9) 'Total    = ',tot,' %'
      write(1,9) 'Total    = ',tot,' %'
9     format(A14,F10.4,A5)
      write(1,*)
      write(*,*) 'Input parameters (1) for default (2) for new'
      read(*,*) flag
      if (flag.eq.1) then
       XN=0.2
       YS=0.35
       ZC=0.5
       RS=0.5
       Temp=750.0
      else
       write(*,*) 'Give X Y Z and R in mole fractions'
       read(*,*) XN,YS,ZC,RS
      write(*,*)
     & 'Give T at which water gas shift equilibrium applies (C)'
      read(*,*) Temp
      endif
      write(*,*) 'X % of Na+K to volatiles ',XN*100
      write(1,*) 'X % of Na+K to volatiles ',XN*100
      write(*,*) 'Y % of S to volatiles   ',YS*100
      write(1,*) 'Y % of S to volatiles   ',YS*100
      write(*,*) 'Z % of C to volatiles   ',ZC*100
      write(1,*) 'Z % of C to volatiles   ',ZC*100
      write(*,*) 'R % of S as Na2S        ',RS*100
      write(1,*) 'R % of S as Na2S        ',RS*100
      write(*,*) 'Water gas shift temp (C) ',Temp
      write(1,*) 'Water gas shift temp (C) ',Temp
```

```
      write(1,*)
      write(*,*) 'Push <CR>'
      read(*,*)
C*******End of Input**********************************
      CS=C*W
      HS=H*W
      OS=O*W
      NaS=Na*W
      SS=S*W
      KS=K*W
      ClS=Cl*W
      WRITE(*,*) 'BLS in grams'
      write(*,11) 'Carbon    = ',CS
      write(*,11) 'Hydrogen  = ',HS
      write(*,11) 'Oxygen    = ',OS
      write(*,11) 'Sodium    = ',NaS
      write(*,11) 'Sulfur    = ',SS
      write(*,11) 'Potassium = ',KS
      write(*,11) 'Chloride  = ',ClS
      WRITE(1,*) 'BLS in grams'
      write(1,11) 'Carbon    = ',CS
      write(1,11) 'Hydrogen  = ',HS
      write(1,11) 'Oxygen    = ',OS
      write(1,11) 'Sodium    = ',NaS
      write(1,11) 'Sulfur    = ',SS
      write(1,11) 'Potassium = ',KS
      write(1,11) 'Chloride  = ',ClS
      tot=CS+HS+OS+NaS+SS+KS+ClS
      write(*,11) 'Total     = ',tot
      write(*,*)
      write(1,11) 'Total     = ',tot
      write(1,*)
11    format(A16,f13.7)
C*******Volatiles formed******************************
      CV=CS*ZC
      CC=CS-CV
      HV=HS
      HC=0
      NaC=(1-XN)*NaS
      NaV=NaS-NaC
      SC=(1-YS)*SS
      SV=SS-SC
      KC=(1-XN)*KS
      KV=KS-KC
      ClC=ClS
```

```
      ClV=0
      call POT(Oso4,Okco3,Onco3)
      OC=Oso4+Okco3+Onco3
      OV=OS-OC
      write(*,10) '          ','Vol. formed (g)','Char formed (g)'
      write(*,110) ' Carbon:   ',CV,CC
      write(*,110) ' Hydrogen: ',HV,HC
      write(*,110) ' Oxygen:   ',OV,OC
      write(*,110) ' Sodium:   ',NaV,NaC
      write(*,110) ' Sulfur:   ',SV,SC
      write(*,110) ' Potassium: ',KV,KC
      write(*,110) ' Chloride: ',ClV,ClC
      write(1,10) '          ','Vol. formed (g)','Char formed (g)'
      write(1,110) ' Carbon:   ',CV,CC
      write(1,110) ' Hydrogen: ',HV,HC
      write(1,110) ' Oxygen:   ',OV,OC
      write(1,110) ' Sodium:   ',NaV,NaC
      write(1,110) ' Sulfur:   ',SV,SC
      write(1,110) ' Potassium: ',KV,KC
      write(1,110) ' Chloride: ',ClV,ClC
      tot1=CV+HV+OV+NaV+SV+KV+ClV
      tot2=CC+HC+OC+NaC+SC+KC+ClC
      write(*,110) ' Total:    ',tot1,tot2,tot1+tot2,' combined'
      write(1,110) ' Total:    ',tot1,tot2,tot1+tot2,' combined'
      write(1,*)
10     FORMAT(A12,2A16)
110    FORMAT(A12,3F16.10,a12)
      WRITE(*,*) 'Push <cr>'
      READ(*,*)
C*******Volatiles formed by species*****************
C     Two cases: 1 no CO2 formed 2 CO+CO2 formed
      molC=CV/12
      molO=OV/16
      molHh2s=SV/32*2
      Hh2s=molHh2s
      H2S=SV+Hh2s
      molH2S=H2S/(2+32)
C**************
      if (molC.gt.molO) then
       write(*,*) 'Only CO formed !'
       write(1,*) 'Only CO formed !'
       molCO=molO
       CO=molCO*(12+16)
       CO2=0
       molCO2=0
```

```
      CH4=(molC-molCO)*(12+4)
      molCH4=CH4/(12+4)
C      moles free hydrogen = grams free hydrogen
      H1=HV-Hh2s-4*CH4/(12+4)
      soot=0.0
      if (H1.lt.0) then
      write(*,*) 'Too little hydrogen for CH4'
      write(1,*) 'Too little hydrogen for CH4'
C      grams of Hydrogen left over for CH4
       H1=HV-Hh2s
C      H1/4 is the moles of carbon needed for CH4
       molCH4=H1/4
       CH4=molCH4*(12+4)
       soot=(molC-molCO-molCH4)*12
       H1=HV-Hh2s-4*CH4/(12+4)
       if (H1.lt.0) then
        write(*,*) 'Too little hydrogen for H2S'
        write(1,*) 'Too little hydrogen for H2S'
        stop
       endif
      endif
      call print(H2S,CO,CO2,CH4,soot,H1,NAV,KV)
     else
      check=3*molC
      if (check.lt.molO) then
       write(*,*) 'Too much oxygen in BLS'
       write(1,*) 'Too much oxygen in BLS'
       stop
      endif
      write(*,*) 'Both CO+CO2 formed'
      write(1,*) 'Both CO+CO2 formed'
      molCO2=(molO-molC)/2
      CO2=molCO2*44
      molCO=molC-molCO2
      CO=molCO*28
      nO=molO-molCO-2*molCO2
C     No CH4 formation
      molCH4=0
      CH4=0
      H1=HV-Hh2s
      if (H1.lt.0) then
       write(*,*) 'Too little hydrogen for H2S'
       write(1,*) 'Too little hydrogen for H2S'
       stop
      endif
```

```
C     H2O formation from O and H
      if (nO.gt.H1) then
       molH2O=H1/2
       nO=molO-molCO-2*molCO2-molH2O
       H1=0
      else
       molH2O=nO
       nO=0
       H1=HV-Hh2s-2*molH2O
      endif
      call molFr(H2S,molH2O,nO,CO,CO2,CH4,soot,H1,NAV,KV)
      endif
      molH2=H1/2
      H2O=molH2O*18
      Ox=nO*32
      write(*,*)
      write(*,*) 'Volatiles formed by species (grams)'
      write(*,12) 'CO       = ',CO
      write(*,12) 'CO2      = ',CO2
      write(*,12) 'H2       = ',H1
      write(*,12) 'H2O      = ',H2O
      write(*,12) 'H2S      = ',H2S
      write(*,12) 'CH4      = ',CH4
      write(*,12) 'Soot     = ',soot
      write(*,12) 'Excess O2 = ',Ox
      write(*,12) 'Na2-vapor = ',NaV
      write(*,12) 'K2-vapor  = ',KV
      write(*,16) 'Total = ',H2O+H2S+CO+CO2+Ox+CH4+H1+NaV+KV+soot,
     & tot1
      write(1,*)
      write(1,*) 'Volatiles formed by species (grams)'
      write(1,12) 'CO       = ',CO
      write(1,12) 'CO2      = ',CO2
      write(1,12) 'H2       = ',H1
      write(1,12) 'H2O      = ',H2O
      write(1,12) 'H2S      = ',H2S
      write(1,12) 'CH4      = ',CH4
      write(1,12) 'Soot     = ',soot
      write(1,12) 'Excess O2 = ',Ox
      write(1,12) 'Na2-vapor = ',NaV
      write(1,12) 'K2-vapor  = ',KV
      write(1,16) 'Total = ',H2O+H2S+CO+CO2+Ox+CH4+H1+NaV+KV+soot,
     & tot1
12    format(A15,f15.10)
16    format(A15,2f15.10)
```

```
      write(*,*)
      write(1,*)
C*******Char composition*************************************
      Na2S=Nana+Sna
      molNa2S=Na2S/(46+32)
      Na2SO4=Sso4+Oso4+Naso4
      Na2CO3=Cnco3+Onco3+Naco3
      Cf=CC-Ckco3-Cnco3
      Of=OC-Onco3-Okco3-Oso4
      K2CO3=Ckco3+Okco3+Kco3
      NaCll=Nacl+Clna
      write(*,*) 'Char formed (grams)'
      write(*,13) 'Na2S   = ',Na2S
      write(*,13) 'Na2SO4 = ',Na2SO4
      write(*,13) 'Na2CO3 = ',Na2CO3
      write(*,13) 'Cfixed = ',Cf
      write(*,13) 'Ofixed = ',Of
      write(*,13) 'K2CO3  = ',K2CO3
      write(*,13) 'NaCl   = ',NaCll
      tot=Na2S+Na2SO4+Na2CO3+Cf+Of+K2CO3+NaCll
      write(*,17) 'Total  = ',tot,tot2
      write(1,*) 'Char formed (grams)'
      write(1,13) 'Na2S   = ',Na2S
      write(1,13) 'Na2SO4 = ',Na2SO4
      write(1,13) 'Na2CO3 = ',Na2CO3
      write(1,13) 'Cfixed = ',Cf
      write(1,13) 'Ofixed = ',Of
      write(1,13) 'K2CO3  = ',K2CO3
      write(1,13) 'NaCl   = ',NaCll
      write(1,17) 'Total  = ',tot,tot2
13     format(A15,f15.10)
17     format(A15,2f15.10)
      write(1,*)
C*******Heating value calculation*****************************
      molNa2=NaV/23/2
      molK2=KV/39.1/2
      molCC=Cf/12
      call HHV(molH2S,molNa2,molK2,molCO,molCH4,molH2,molNa2S,
     &  molCC,HHVvol,HHVchar)
      write(*,*)
      write(*,*) 'HEATING VALUE CALCULATION (kJ) at 273 K'
      write(*,14) 'HHVvol  = ',HHVvol
      write(*,14) 'HHVchar = ',HHVchar
      HHval=(HHVvol+HHVchar)/W
      write(*,15) 'HHV(vol+char) = ',HHval,' MJ/kg'
```

```
      write(1,*) 'HEATING VALUE CALCULATION (kJ) at 273 K'
      write(1,14) 'HHVvol  = ',HHVvol
      write(1,14) 'HHVchar = ',HHVchar
      write(1,14) 'HHV(vol+char) = ',HHval,' MJ/kg'
14     format(A15,f15.10,A10)
15     format(A20,F15.10,A8)
      END

      subroutine HHV(molH2S,molNa2,molK2,molCO,molCH4,molH2,
     &  molNa2S,molCC,HHVvol,HHVchar)
      real molH2S,molNa2,molK2,molCO,molCH4,molH2,molNa2S,molCC,
     &  HHVvol,HHVchar,R1,R2,R3,R4,R5,R6,R7,R8
      parameter(R1=871.9,R2=874.8,R3=883.8,R4=283,R5=802.3,
     &  R6=241.8,R7=1001.2,R8=393.5)
      HHVvol=R1*molH2S+R2*molNa2+R3*molK2+R4*molCO+R5*molCH4+
     &  R6*molH2
      HHVchar=R7*molNa2S+R8*molCC
      return
      END

      subroutine molFr(H2S,molH2O,nO,CO,CO2,CH4,soot,H1,NAV,KV)
      real H2S,CO,CO2,CH4,soot,H1,NAV,KV,pco2,pco,ph2o,ph2,Temp,
     &  pco2s,pcos,ph2os,ph2s,nH2S,nCO,nCO2,nCH4,nsoot,nH2,nNAV,pO2,
     &  nKV,ntot,ph22s,ptot,ptot2,pk2,pna2,psoot,pch4,H2O,nH2O,nO,
     &  molH2O
      common/P/pco2,pco,ph2o,ph2,Temp
      common/Ps/pco2s,pcos,ph2os,ph2s
      nH2S=H2S/(2+32)
      nH2O=molH2O
      nCO=CO/28
      nCO2=CO2/44
      nCH4=CH4/16
      nsoot=soot/12
      nH2=H1/2
      nNAV=NAV/46
      nKV=KV/39.1/2
      ntot=nH2S+nCO+nCO2+nCH4+nsoot+nH2+nNAV+nKV+nO/2+nH2O
      pco2=nCO2/ntot
      pco=nCO/ntot
      ph2=nH2/ntot
      ph2o=nH2O/ntot
      call SHIFT
      ph22s=nH2S/ntot
      pch4=nCH4/ntot
      psoot=nsoot/ntot
```

```
      pna2=nNAV/ntot
      pk2=nKV/ntot
      pO2=nO/2/ntot
      ptot=pco2s+pcos+ph2os+ph2s+ph22s+pch4+psoot+pna2+pk2+pO2
      ptot2=pco2+pco+ph2o+ph2+ph22s+pch4+psoot+pna2+pk2+pO2
      write(*,*)
      write(*,111) 'pCO2 : ',pco2s
      write(*,111) 'pCO  : ',pcos
      write(*,111) 'pH2O : ',ph2os
      write(*,111) 'pH2  : ',ph2s
      write(*,111) 'pH2S : ',ph22s
      write(*,111) 'pCH4 : ',pch4
      write(*,111) 'psoot: ',psoot
      write(*,111) 'pO2  : ',pO2
      write(*,111) 'pNa2 : ',pna2
      write(*,111) 'pK2  : ',pk2
      write(*,111) 'Total: ',ptot
      write(1,*)
      write(1,111) 'pCO2 : ',pco2s
      write(1,111) 'pCO  : ',pcos
      write(1,111) 'pH2O : ',ph2os
      write(1,111) 'pH2  : ',ph2s
      write(1,111) 'pH2S : ',ph22s
      write(1,111) 'pCH4 : ',pch4
      write(1,111) 'psoot: ',psoot
      write(1,111) 'pO2  : ',pO2
      write(1,111) 'pNa2 : ',pna2
      write(1,111) 'pK2  : ',pk2
      write(1,111) 'Total: ',ptot
111     format(A10,F15.10)
      write(*,*) 'Push <CR>'
      read(*,*)
      return
      end

      subroutine SHIFT
      real Keq,pco2,pco,ph2o,ph2,Temp,pco2s,pcos,ph2os,ph2s,
     & A,B,C,const,ph,pc,test,pcov
      common/P/pco2,pco,ph2o,ph2,Temp
      common/Ps/pco2s,pcos,ph2os,ph2s
      Keq=exp(-3.49+3563.0/(Temp+273)+0.313*(1000.0/(Temp+273))**2.)
      pc=pco2+pco
      ph=ph2o+ph2
      const=2*pco2+pco+ph2o
      A=Keq-1
```

```
      B=Keq*const-2*Keq*pc+pc+ph-const+2*pc
      C=pc*const-pc*ph-2*pc*pc
      test=B*B-4*A*C
      if (test.lt.0) then
       stop
      endif
      pcov=(-B+sqrt(B*B-4*A*C))/2/A
      if (pcov.gt.0) then
       pcos=pcov
      else
       pcov=(-B-sqrt(B*B-4*A*C))/2/A
       pcos=pcov
      endif
      pco2s=pc-pcos
      ph2os=const-2*pco2s-pcos
      ph2s=Keq*pcos*ph2os/pco2s
      return
      end

      subroutine POT(Oso4,Okco3,Onco3)
      REAL Oso4,Okco3,Onco3,RS,SC,ClC,NaC,KC,Nana,Sna,Sso4,
     &  Naso4,Cnco3,Naco3,Ckco3,Kco3,Nacl,Clna
      common/kaj/RS,SC,ClC,NaC,KC,Nana,Sna,Sso4,Naso4,Cnco3,
     &  Naco3,Ckco3,Kco3,Nacl,Clna
      Sso4=(1-RS)*SC
      Naso4=Sso4*46/32
      Oso4=Sso4*4*16/32
      Sna=RS*SC
      Nana=Sna*46/32
      Clna=ClC
      Nacl=Clna*23/35.5
      Kco3=KC
      Okco3=Kco3*16*3/39.1/2
      Ckco3=Kco3*12/39.1/2
      Naco3=NaC-Naso4-Nana-Nacl
      Onco3=Naco3*16*3/46
      Cnco3=Naco3*12/46
      return
      END

      subroutine print(H2S,CO,CO2,CH4,soot,H1,NAV,KV)
      real H2S,CO,CO2,CH4,soot,H1,NAV,KV,pco2,pco,ph2o,ph2,Temp,
     &  nH2S,nCO,nCO2,nCH4,nsoot,nH2,nNAV,nKV,ntot,H2O,nH2O,
     &  ph22s,ptot,pk2,pna2,psoot,pch4
      nH2S=H2S/(2+32)
```

```
      nH2O=H2O/18
      nCO=CO/28
      nCO2=CO2/44
      nCH4=CH4/16
      nsoot=soot/12
      nH2=H1/2
      nNAV=NAV/46
      nKV=KV/39.1/2
      ntot=nH2S+nCO+nCO2+nCH4+nsoot+nH2+nNAV+nKV
      pco2=nCO2/ntot
      pco=nCO/ntot
      ph2=nH2/ntot
      ph2o=nH2O/ntot
      ph22s=nH2S/ntot
      pch4=nCH4/ntot
      psoot=nsoot/ntot
      pna2=nNAV/ntot
      pk2=nKV/ntot
      ptot=pco2+pco+ph2o+ph2+ph22s+pch4+psoot+pna2+pk2
      write(*,*)
      write(*,111) 'pCO2 : ',pco2
      write(*,111) 'pCO  : ',pco
      write(*,111) 'pH2  : ',ph2
      write(*,111) 'pH2S : ',ph22s
      write(*,111) 'pCH4 : ',pch4
      write(*,111) 'psoot: ',psoot
      write(*,111) 'pNa2 : ',pna2
      write(*,111) 'pK2  : ',pk2
      write(*,111) 'Total: ',ptot
      write(1,*)
      write(1,111) 'pCO2 : ',pco2
      write(1,111) 'pCO  : ',pco
      write(1,111) 'pH2  : ',ph2
      write(1,111) 'pH2S : ',ph22s
      write(1,111) 'pCH4 : ',pch4
      write(1,111) 'psoot: ',psoot
      write(1,111) 'pNa2 : ',pna2
      write(1,111) 'pK2  : ',pk2
      write(1,111) 'Total: ',ptot
111     format(A10,2F15.10)
      write(*,*) 'Push <CR>'
      read(*,*)
      return
      end
```

Chapter 8

Carbon Burn-Off During Black Liquor Char Gasification with CO_2 and Water Vapor: Assessment of the Mechanism and Rate

Presented at the 1994 AIChE annual meeting
San Francisco, November 13-18, 1994
Revised October 1996

INTRODUCTION

A lot of research effort has been put in studying the gasification of carbonaceous materials catalyzed by alkali carbonates. Various techniques have been used to describe gasification and explain the role and structure of the catalyst. These experimental methods include e.g. mass loss curves from thermogravimetric (TG) analyses, steady state and transient kinetic studies, temperature programmed desorption (TPD) and chemisorption, combined with the use of labeled molecules, $^{13}CO_2$ and $C^{18}O_2$ (1,2).

The accelerating effects of impurities on the combustion of carbonaceous materials have been known for a long period of time. The major contributing factors are: the concentration of active sites, the crystallinity and structure of the carbonaceous material, the presence of inorganic impurities, and the diffusion of reactive gases to the active catalytic sites. A characteristic of black liquor char gasification is that the overall reaction rate is several orders of magnitude faster than for alkali-impregnated chars and alkali-impregnated activated carbon. Black liquor char is unique with respect to other carbons due to differences in structure and chemical behavior. Graphite related chars, e.g. coal chars, are crystalline whereas black liquor char is amorphous by nature due to the presence of a substantial inorganic phase within the molecular structure. The reactivity of black liquor char increases with increasing alkali content. Alkali-metal oxygen surface species of phenolic and carboxylic type are presumed to be the active intermediate groups that are responsible for the higher reactivity of black liquor char (BLC). For alkali-impregnated chars the reactivity goes through a maximum at relatively low alkali concentrations. This may be a result of the catalyst being deposited on the char surfaces without chemical bonding (no electron transfer). BLC is more porous due to high swelling characteristics absent for manually impregnated chars, which may be the key reason for the higher reactivity. BLC may have more surface area covered with catalyst than regularly impregnated chars, because this occurs during devolatilization at a high temperature allowing electron transfer to occur. Table 8.1 shows a typical composition of organic material in black liquor prior to devolatilization.

Table 8.1. Typical composition of organic material in black liquor (3).

Component	Content (%)
Lignin	47
Hydroxy acids	28
Formic acid	7
Acetic acid	4
Extractives	5
Other compounds	9

Black liquor char gasification has been studied for CO_2 and water vapor separately both under atmospheric and pressurized conditions (4,5,6,7). Li et al. (5) studied the CO_2 gasification rate of black liquor char in a thermogravimetric system at temperatures between 600°C and 800°C and at atmospheric pressure. They assumed that black liquor char gasification with CO_2 can be described by Langmuir-Hinshelwood type reaction kinetics assuming that all the adsorption sites are equivalent, interactions between the molecules bonded to these sites are negligible, and that only one adsorbing molecule can be bonded to each site on the solid. Langmuir type reaction kinetics may not be entirely valid for black liquor char as will be shown later. The rate data and kinetic models that have been reported for black liquor char gasification are summarized in Table 8.2.

Table 8.2. Kinetic data and models reported for gasification of black liquor.

Gasifying agent	Other gases present	Temp. °C	Pressure bar	References
CO_2	CO	600-800	1	Li et al., 1990
CO_2	CO	600-800 700	1-30	Frederick et al.,1991; 1993
H_2O	H_2	600-700	1	Li et al., 1991
H_2O	H_2 or CO	600-675	1-30	Whitty et al., 1992
$H_2O + CO_2$	$H_2 + CO$	750	2-30	Whitty et al., 1993

Frederick et al. (4) have found for pressurized CO_2 gasification of black liquor char that the gasification mechanism can be derived from a two step oxidation reduction cycle similar to what has been reported for alkali impregnated carbon (8). Frederick et al. observed a variation in the rate constants and a maximum in reaction rate occurring typically between 20% and 60% carbon conversion. This was explained by the variation of the active number of catalyst and carbon sites. Similar results had been observed in all of the studies listed in Table 8.2. Many earlier investigators have observed, in both uncatalyzed and alkali-catalyzed steam gasification of carbonaceous materials, that a maximum in gasification rate occurs followed by a subsequent decline in rate with increasing carbon conversion. Frederick et al. (4) explained this with pore plugging and the loss of catalyst.

OBJECTIVES

The objective of this chapter is to review available data on black liquor char gasification in water vapor and carbon dioxide, present a kinetic rate equation based on a unified reaction mechanism, and to determine the rate constants. The new rate equation should predict accurately the rate of gasification of black liquor char in the presence of CO_2, water vapor, CO, and H_2, and account for product gas inhibition and the change in rate with carbon conversion. The issue is addressed to what extent water vapor and CO_2 gasification are additive with respect to reaction rate. The question of the extent to which the gases approach equilibrium with respect to the water gas shift reaction is also discussed.

ASSESSMENT OF AVAILABLE DATA

$H_2O(g) + CO_2$ data when both H_2 and CO are present

The data discussed here have been published in the literature (9). The experiments were performed in a pressurized thermobalance at 750°C and 2-30 bar total pressure for a North American Kraft char with 31.47% carbon by weight. The procedure for obtaining this char is described by Clay et al. (10). The sodium and sulfur contents were 21.7% and 4.85%, respectively. A detailed description of the thermobalance and the experimental procedure is provided by Whitty et al. (7). The gasification experiments were designed to minimize the degree of correlation of the partial pressures to obtain representative data. The CO_2 concentration was varied between 20% and 60%, H_2 and CO between 3% and 15%, and $H_2O(g)$ between 10% and 74% on a molar basis. Since no partial pressure was constant for any set of runs, it was difficult to look at the effect of one variable, e.g. the effect of CO_2/H_2O ratio. However, this was overcome by comparing individual experiments that were approximately similar. Table 8.3 shows the effect of increasing CO_2 partial pressure. All reaction rates are normalized with respect initial weight (mg reacted per mg initial weight per sec).

Table 8.3. Increasing CO_2 partial pressure decreases the rate of reaction. Data is from (9).

Run #	Total pressure (bar)	H_2O (%)	CO_2 (%)	H_2 (%)	CO (%)	Max. rate (1/s)
5200	2	74	20	3	3	16.2
5192	2	41	50	3	6	11.2
5189	3	68	20	3	9	9.3
5205	3	22	60	3	15	2.2
5217	12	59	20	12	9	6.0
5208	12	32	50	12	6	3.5

Table 8.3 shows that at a given total pressure, a higher CO_2 partial pressure decreases the maximum rate of reaction. This conclusion is not directly apparent from the complete data set available due to highly different concentrations of CO and H_2. However, this conclusion is supported by findings of Meijer et al. (11). They obtained data for potassium impregnated peat char using a fixed-bed reactor, which showed that an addition of 10% CO_2 to a water vapor containing mixture decreased the rate of reaction by about 40%. The high sensitivity to the inhibition gases suggests that there are no independent parallel processes in simultaneous water vapor, CO_2, CO, and H_2 gasification. A complex interaction prevails between these gases and the active sites on the char surface. In addition, the apparent gas concentrations are skewed by the water gas shift reaction which is catalyzed by the alkali compounds in the char. In addition to the whole data set of Whitty et al. (9), the data in Table 8.3 were not shifted at the inlet.

$H_2O(g)$ data with either H_2 or CO present

There is published data, with no CO_2 present (7), which shows that gasification in water vapor is roughly 3-4 times faster than CO_2 gasification at equivalent gas partial pressures and 650°C, which is consistent with Table 8.3, which indicated that water vapor gasification is strongly dependent on the presence of CO_2. Figure 8.1 indicates that $H_2O(g)$ gasification is suppressed by CO_2 at a total pressure below 5 bar, where the gasification rate is much lower with CO_2 present than for water vapor alone. The solid line is a theoretical prediction using a rate equation presented later in this paper.

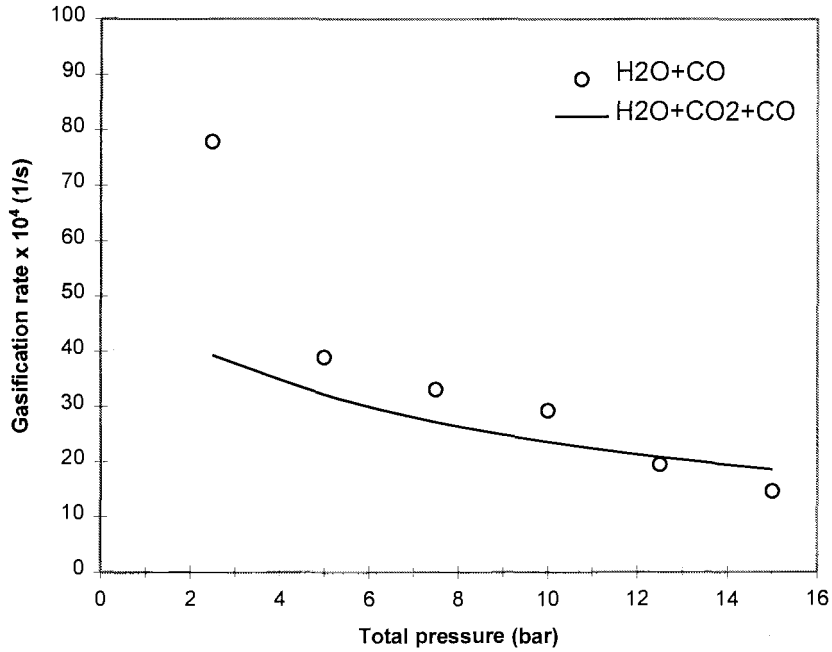

Figure 8.1. Reaction rate data in 20% $H_2O(g)$ and 4% CO at 750°C. The data are for black liquor char (7). The solid line is a theoretical prediction assuming an arbitrary amount of CO_2, because CO_2 is intrinsically accounted for.

Figure 8.2 shows that there is a significant difference in the reaction rate when H_2 is present. Here, the presence of hydrogen clearly enhances the gasification rate, and the presence of CO_2 appears to suppress the gasification rate. The solid line represents the predicted reaction rate using a rate model presented later in this chapter.

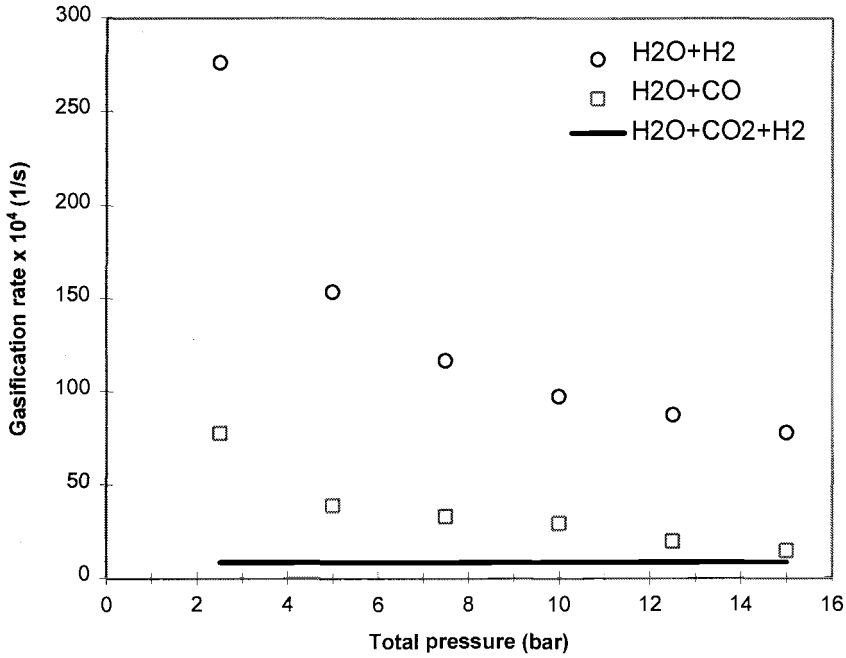

Figure 8.2. Reaction rate data in 20% $H_2O(g)$ and 4% H_2 at 750°C. The data are for black liquor char (7). The solid line is a theoretical prediction assuming an arbitrary amount of CO_2, because CO_2 is intrinsically accounted for.

CO_2 data when only CO present

Results reported by Frederick et al. (4) show that at low CO_2 partial pressures carbon burn-off ceased below 60% conversion when only CO_2 and CO were present. This is probably due to increasing pore diffusion resistance and catalyst depletion through carbonate reduction and alkali catalyst vaporization. Structural changes such as decreasing surface area in conjunction with pore combination could block the access of the gasifying agent at low partial pressures. At higher CO_2 partial pressures the fixed carbon was consumed more rapidly. When the CO_2 partial pressure exceeded approximately 15 bar, there was no increase in reaction rate as can be seen in Figure 8.3.

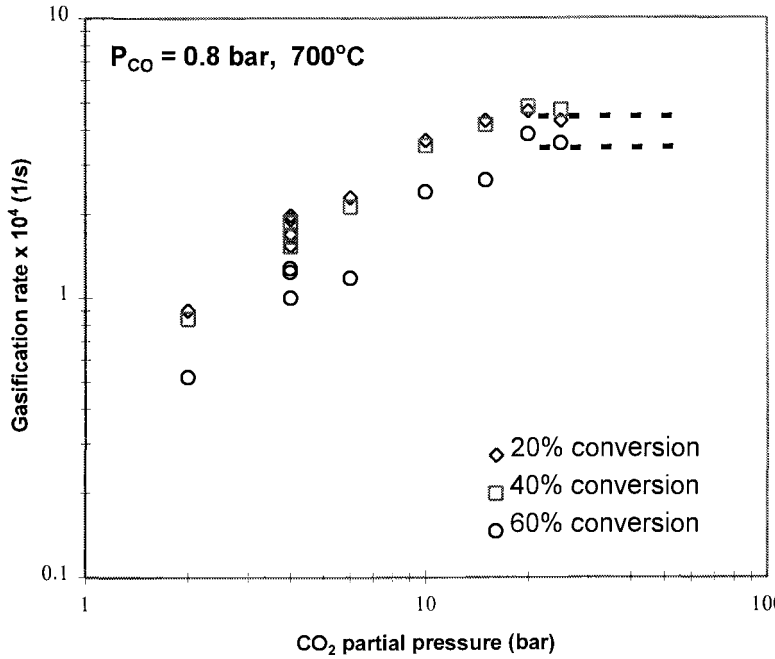

Figure 8.3. Reaction rate as a function of CO_2 partial pressure. Data are for black liquor char by Frederick et al. (4).

Figure 8.6 shows that the reaction rate levels off at sufficiently high CO_2 partial pressures. An important implication is that when the CO_2 partial pressure is sufficiently high, the catalytic sites may be fully blocked from access to $H_2O(g)$ molecules. CO_2 is known to adsorb strongly (12) on the catalyst sites while water vapor is not (13). Depending on the degree of conversion of the char carbon the rate of gasification levels off at different rates. At low carbon conversions the data appears to have a lower saturation pressure than at high carbon conversions. This indicates that at low conversions the gasification process is less inhibited. This could be caused by the fact that less CO is available to be adsorbed by the free carbon sites at low carbon conversions, the opposite being true at high carbon conversions. The chemisorbed CO compound could form a relatively stable moiety causing an inhibition effect by reducing the amount of active carbon sites available for gasification at low carbon conversions.

Comparison of gasification data

Further testing was performed with a rate equation available in the literature (4). It is based on a mechanism where no $H_2O(g)$ and H_2 are present and it takes into account CO suppression. The rate constants for this equation were evaluated at 700°C, but the overall rate was adjusted to 750°C by multiplying by a factor of 3.45 corresponding to an activation energy of 205 kJ/mol. This would allow a comparison with Whitty's data taken at 750°C. The rate constants obtained for CO_2 gasification were for a similar char as the rate data taken by Whitty et al. (9). The equation applies for black liquor char gasification with 0.1-15 bar CO_2 partial pressures and 0-6 bar CO partial pressures. The purpose was to see how much slower the predicted rates would be at the same conditions as when both CO_2 and $H_2O(g)$ were present. This could verify to what extent CO_2 and $H_2O(g)$ gasification are additive processes. Figure 8.4 shows how this data compares with data for $H_2O(g)$ and CO_2 only for a practically similar char.

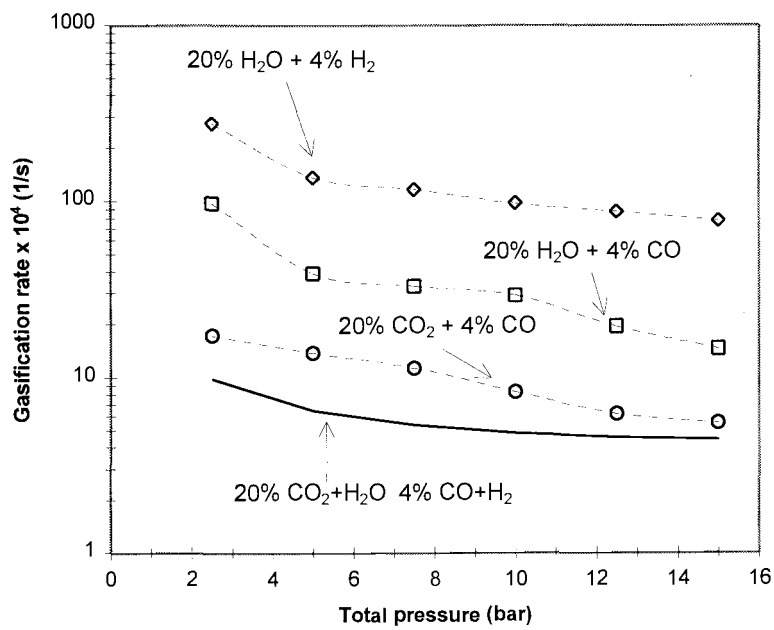

Figure 8.4. Gasification rate of black liquor char in $H_2O(g)$ only, and CO_2 only, and $H_2O(g)+CO_2$. Data are from (9), (4), and (7), respectively. $CO_2+H_2O(g)$ curve is predicted using an empirical equation (7).

Figure 8.4 shows that the overall gasification rate in the presence of both water vapor and CO_2 is much lower than for the data with either water vapor or CO_2 independently, even when product gas suppression is accounted for.

Figure 8.5 shows that the predicted rates by the CO_2 gasification rate equation at 20% conversion were of the same order of magnitude as the experimental rates. A similar trend was found at 60% conversion. More than half of the rates of the experiments were overpredicted. Most of the underpredicted data points were at lower total pressures and most of the overpredicted rates were at higher total pressures. At the same total pressure one would underpredict the combined rate of gasification, when the CO_2 partial pressure was lower than the $H_2O(g)$ partial pressure. The opposite was true when the CO_2 partial pressure was higher than the $H_2O(g)$ partial pressure. This can be seen in Figure 8.5.

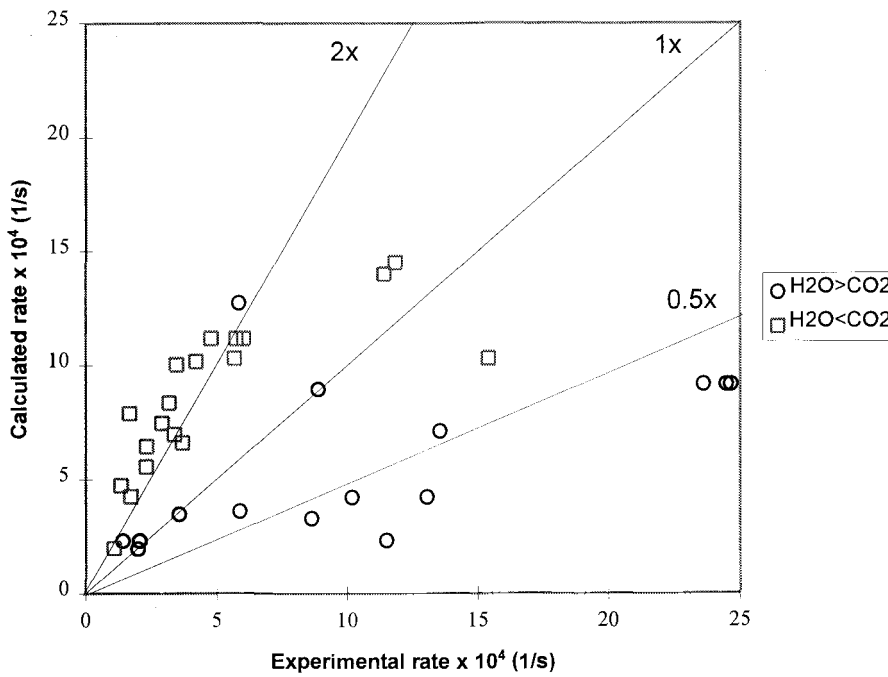

Figure 8.5. Predictions of $H_2O(g)$ and CO_2 rates at 20% carbon conversion with CO_2 equation reported by Frederick et al. (4). Data are for black liquor char from (9).

Figure 8.6 indicates strong CO_2 adsorption on the catalyst sites, thus, blocking access to water vapor molecules. The question rises whether there is a correlation between CO_2 partial pressure and how strongly it is adsorbed.

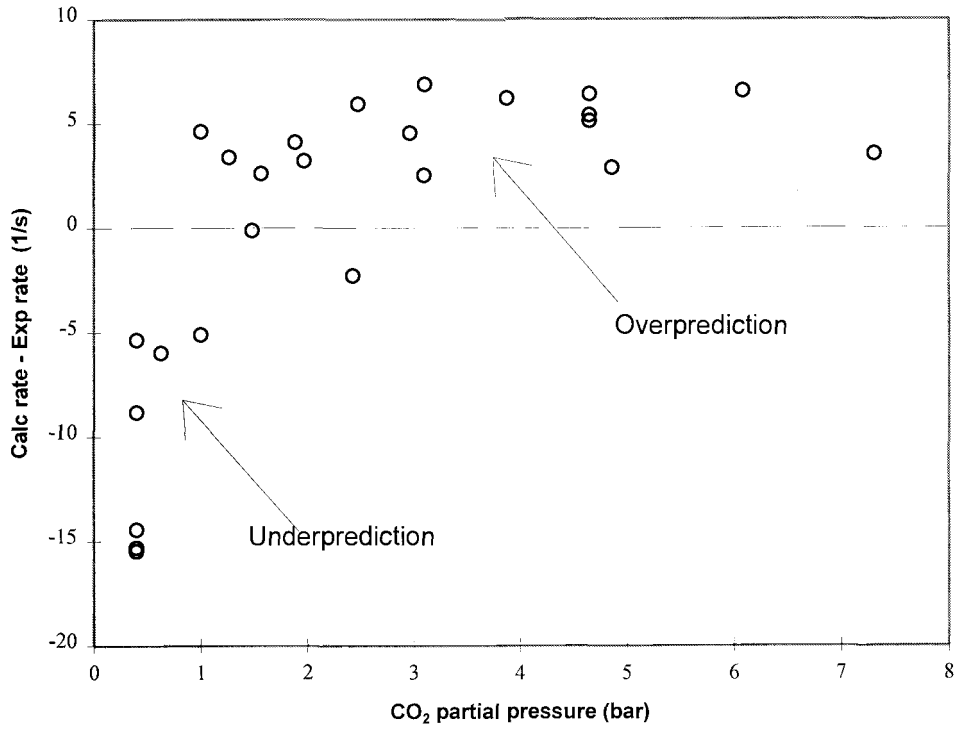

Figure 8.6. Experimental minus calculated rate as a function of CO_2 partial pressure.

Figure 8.6 shows for which CO_2 partial pressures the rates are over- and underpredicted. This infers that simultaneous CO_2 and $H_2O(g)$ gasification may be an additive process at atmospheric pressure, but not at higher pressures.

Inhibition effects

For potassium impregnated peat char Meijer et al. (11) have shown that addition of H_2 and CO to the reactant gases reduces the rate of gasification, where the inhibiting effect of CO is stronger than for H_2 . For pCO/pH_2O ratios above 0.05 no gasification was detected at 1000K (11). CO may inhibit the rate by reducing the amount of free carbon sites available for gasification through the following reaction.

$$CO + C_f = C(CO)$$

H_2 is probably capable of blocking free carbon sites in a similar manner (14). It is likely that in simultaneous $H_2O(g)$ and CO_2 for black liquor char, that a similar effect will be discovered. For separate gasification with CO_2 and $H_2O(g)$ with black liquor char, the inhibiting effects of the product gases have been reported in the literature (4,7).

MECHANISM OF SIMULTANEOUS GASIFICATION WITH CO_2 AND $H_2O(g)$

The classic mechanism for noncatalytic oxidation of solid carbons has been proposed to proceed according to the following mechanism (15):

a) $H_2O(g) + \_ \rightarrow H_2 + \underline{O}$

b) $CO_2 + \_ \rightarrow CO + \underline{O}$

c) $\underline{O} \rightarrow CO$

Here, _ represents a carbon surface site and $\underline{O}$ represents an oxidized form of the site. For alkali catalyzed gasification a similar mechanism has been proposed with the addition of catalytically active species. Such species include empty catalyst sites (*) and oxygen containing catalyst sites (O-*). Alkali phenolates,)>C-O-M, where M designates an alkali metal atom, oxygen deficient alkali compounds,)>C-M, as well as alkali carboxylates,)>C=O-O-M, have been proposed to constitute these chemically active structures (16,17).

A third significant type of catalyst intermediate present in alkali catalyzed char gasification are the sites containing chemisorbed carbon dioxide (CO_2 -*),)>C-M-CO_2, from which CO_2 can be desorbed, or that can decompose yielding CO and an alkali phenolate.

The following sequence of elementary reactions can be extracted from an overall reaction scheme that includes the $H_2O(g)$ gasification reaction as well as the Boudouard and the water gas shift reactions. The literature shows that water vapor decomposes to yield an oxidized site rather than a physisorbed $H_2O(g)$ molecule (13). The measured concentrations of CO_2 and CO after partial gasification of alkali-impregnated peat char in CO_2 indicates that 3-5 alkali atoms form a cluster that is involved in chemisorption of one CO_2 gas molecule (2,16).

1. $H_2O(g) + * \leftrightarrow H_2 + O\text{-}*$
2. $CO + O\text{-}* \leftrightarrow CO_2\text{-}*$
3. $CO_2\text{-}* \leftrightarrow CO_2 + *$
4. $O\text{-}* + C_f \rightarrow C(O) + *$
5. $C(O) \rightarrow CO$

Li et al. (6) speculate that the phenolic groups are oxidized by $H_2O(g)$ into carboxylic groups (reaction 6), followed by the reduction of the carboxylic group to CO and a phenolic group (reaction 7).

6.)>C-O-M + $H_2O(g)$ ↔)>C=O-O-M + H_2
7.)>C=O-O-M + C →)>C-O-M + CO

Alternatively the carboxylic groups are reduced with water vapor to form CO_2 (reaction 8).

8.)>C=O-O-M + $H_2O(g)$ + C →)>C-O-M + CO_2 + H_2

DERIVATION OF RATE EQUATION FOR CO_2 AND $H_2O(g)$

Reactions 4 and 5 are considered as one single step. Hence, the transfer of an oxygen atom from a catalytic site to a free carbon site and the subsequent desorption of the formed CO molecule are assumed to proceed at the same rate. Assuming that this process is the rate limiting step, then the overall reaction rate is given by equation 8-1.

$$\text{Rate } (1/s) = k_4 [O\text{-}*][C_f] \tag{8-1}$$

If reactions 1 and 2 are assumed to be at equilibrium, then the following equations apply.

$$K_1 = \frac{P_{H_2}[O\text{-}*]}{P_{H_2O}[*]} \tag{8-2}$$

$$K_2 = \frac{[CO_2\text{-}*]}{P_{CO}[O\text{-}*]} \tag{8-3}$$

The total amount of active catalyst sites, N_{ox}, is given by equation 8-4.

$$N_{ox} = [*] + [O\text{-}*] + [CO_2\text{-}*] \tag{8-4}$$

Solving equations 8-2 and 8-3 for [*] and $[CO_2\text{-}*]$ and substituting into the N_{ox} equation gives equation 8-5:

$$[O\text{-}*] = \frac{N_{ox}}{1 + \frac{P_{H_2}}{K_i P_{H_2O}} + K_{ii} P_{CO}} \tag{8-5}$$

Assuming that the number of free carbon sites is proportional to the total number of carbon sites, N_t, according to equation 8-6:

$$N_t \sim [C_f] \tag{8-6}$$

then equation 8-7 can be obtained.

$$\frac{\text{Rate}}{1/s} = \frac{k_4 N_{ox} N_t}{1 + \frac{P_{H_2}}{K_1 P_{H_2O}} + K_2 P_{CO}} \tag{8-7}$$

This equation accounts for product gas inhibition by CO and H_2 as previous researchers have observed earlier (4,7,18). It accounts intrinsically for the rate lowering effect of CO_2.

EVALUATION OF MECHANISTIC RATE EQUATION

Rearranging equation 8-8 with $k' = k_4 N_{ox} N_t$, $k'' = K_1$, $k''' = K_2$ yields equation 8-8.

$$\frac{\text{Rate}}{1/s} = \frac{k' P_{H2O}}{P_{H2O} + \frac{P_{H_2}}{k''} + k''' P_{CO} P_{H2O}} \tag{8-8}$$

This equation was fitted to the data of Whitty et al. (9) with a least squares minimization method for rates with 10% increments in carbon conversion. The rate versus carbon conversion data was extracted from mass versus time data from the pressurized thermobalance. The mass versus time data was converted to rate versus conversion data by fitting a straight line to the data points nearest a particular conversion to get an average slope from the raw data. The slopes were then normalized with the amount of initial carbon to achieve the desired definition of the reaction rate. The rate versus conversion data was further smoothed to get a uniform curve suitable for optimization purposes. This procedure is described in detail by Overacker et al. (19). Figure 8.7 shows a typical rate versus conversion plot.

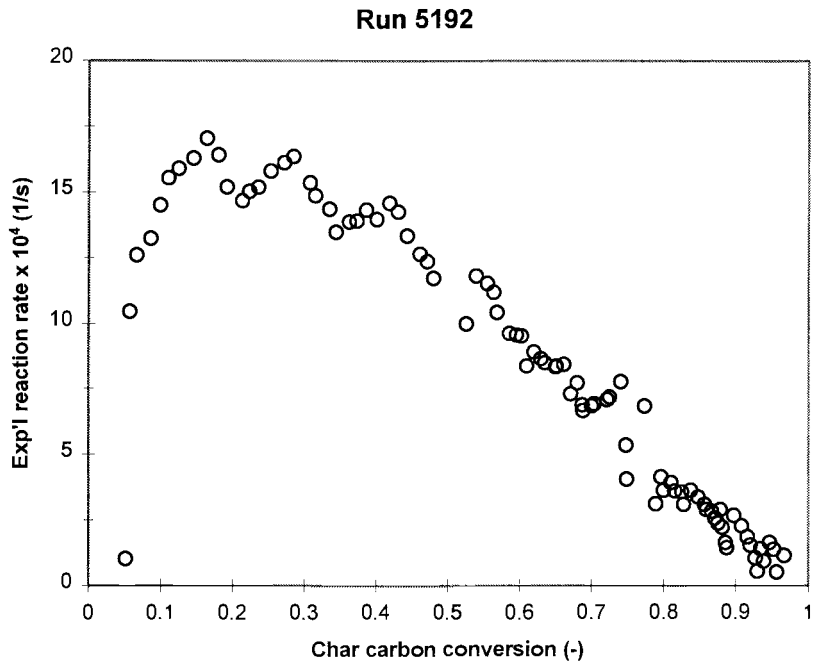

Figure 8.7. Rate versus carbon conversion in 41% H_2O(g), 50% CO_2, 3% H_2, 6% CO, 750°C, P_{tot}=2 bar.

The mean sum of squares is defined by equation 8-9.

$$\text{Mean sum of squares (MSS)} = \sum(\text{exp-calc})^2 \div (\text{number of experiments}) \qquad (8\text{-}9)$$

Table 8.4 summarizes the mean sum of squares for the entire carbon conversion range.

Table 8.4. Mean sum of squares at different carbon conversions.

Conv. (%)	0	10	20	30	40	50	60	70	80	90
MSS	9.05	6.70	8.37	9.49	9.14	7.76	5.94	4.02	2.19	0.68
R^2	0.63	0.81	0.80	0.78	0.75	0.71	0.66	0.55	0.43	0.32

The correlation coefficient, R^2, varies typically between 0.6 and 0.8 at conversions less than 70%. The goodness of fit is conversion dependent and it goes through a maximum as does the numerator rate constant. The goodness of fit based on equation 8-9 is illustrated by Figure 8.8. It shows that the predicted rates with the extracted rate constants fall satisfactorily on the 45 degree line when plotted against the experimental rates.

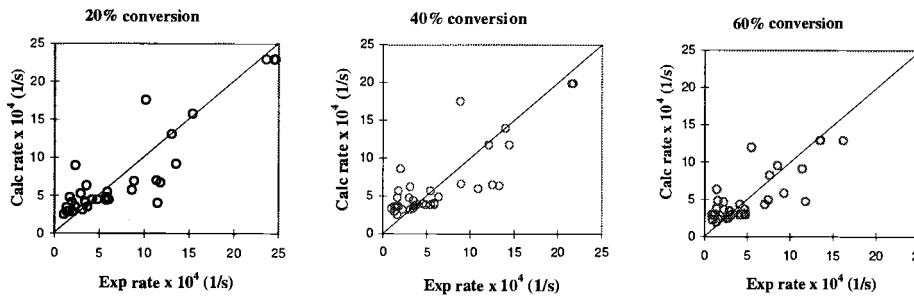

Figure 8.8. Closeness of fit for the mechanistic model at 20, 40, and 60% carbon conversions.

The number of active catalyst sites and free carbon sites are not known, and they may vary with conversion similarly as for alkali-impregnated chars. The rate constant itself is constant, but the number of active catalyst and carbon sites is not. A loss of catalyst activity, depletion of catalytic sites and free carbon sites, or pore plugging may occur at high carbon conversions. This could be a reason for why the model fits better at low carbon conversions. Sams et al. (20) reported that the completely reduced active site (-CNa) is readily decomposed to free alkali metal, which is easily vaporized at gasification temperatures. This could be one mechanism that could explain the decrease in k' at higher carbon conversions. k" remains fairly constant indicating that reaction 1 remains at quasi equilibrium. k'", however, decreases with carbon burn-off, indicating that reaction 2 is shifted to the left favoring carbon deficient catalyst moieties. The rate constants vary with carbon burn-off as illustrated in Figure 8.9.

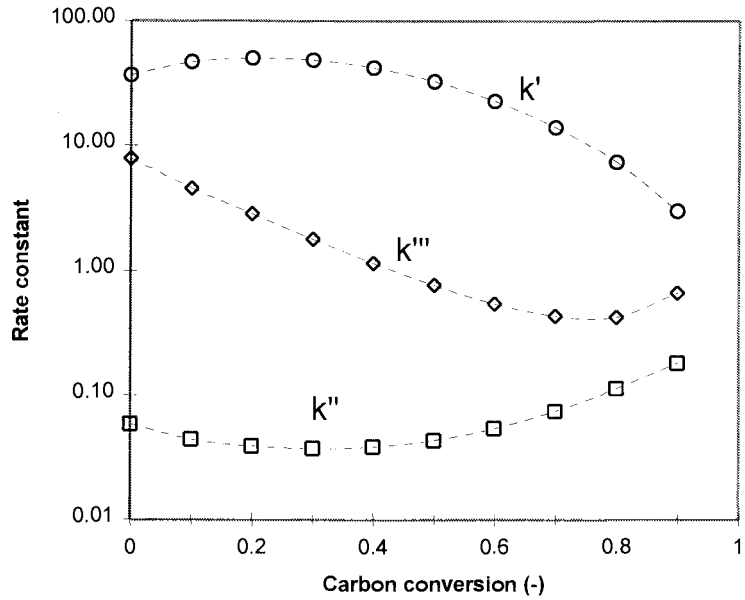

Figure 8.9. Rate constants k', k'', and k''' as a function of carbon conversion at 750°C.

Figure 8.9 shows that physically feasible rate constants are obtained over the entire range of carbon conversion.

WATER GAS SHIFT EQUILIBRIUM

The equilibrium constant for the water gas shift reaction is defined by reaction 8.

8. $H_2O(g) + CO = CO_2 + H_2$

The equilibrium constant is given by equation 8-11.

$$K_{WGS,eq} = \frac{P_{CO_2} P_{H_2}}{P_{H_2O} P_{CO}} \qquad (8\text{-}10)$$

Meijer et al. (13) have investigated the water gas shift reaction catalyzed by the alkali-metal species in activated carbon. They measured the kinetics of both forward ($H_2O(g)$ + CO) and backward (CO_2 + H_2) oxygen exchange rates over a broad range of partial pressures. On the basis of these measurements a three step mechanism was proposed, where the water gas shift oxygen exchange proceeds through the CO_2-* intermediate according to the same mechanism as for the proposed overall gasification scheme.

a) $H_2O(g) + * = H_2 + O\text{-}*$

b) $CO + O\text{-}* = CO_2\text{-}*$

c) $CO_2\text{-}* = CO_2 + *$

d) $H_2O(g) + CO = CO_2 + H_2$

Kinetic models were fitted to different assumptions, but the mechanism was found to fit the experimental data the best when reaction step 1 was considered to be at quasi-equilibrium. The estimated parameters for the selected model obeyed the thermodynamic constraints which gave additional support for the proposed mechanism. Meijer's data for alkali-impregnated peat char shows that water gas shift equilibrium does apply at 750°C, Figure 8.10.

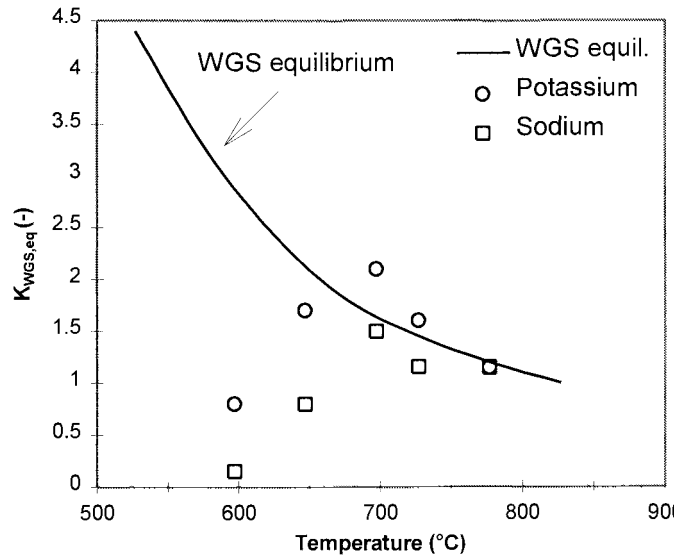

Figure 8.10. Theoretical and measured water gas ratio at different catalyst to carbon ratios. Data are for alkali-impregnated peat char by Meijer (11). circles: K/C = 0.019; squares: Na/C = 0.019.

For black liquor char it was also to be studied to what degree the inlet gases would reach water gas shift equilibrium prior to reaching the sample. Whitty et al. (9) have conducted experiments with entry gases on either side of the water gas shift equilibrium. The rate of gasification was generally the fastest when the inlet gases were at water gas shift equilibrium compared to when they were shifted to the CO_2 or $H_2O(g)$ side. They also found that the gasification rate was always lower when the inlet gases were on the CO_2 side compared with the $H_2O(g)$ side. This result indicates that the water gas shift reaction would not reach equilibrium, because the rates should be the same for all three cases (CO_2 side, $H_2O(g)$ side, and equilibrium). However, this data is fairly limited to be conclusive.

Using the new mechanistic rate equation this issue was further investigated. The bulk gas partial pressures for the data discussed herein were not at equilibrium with respect to the water gas shift reaction. Therefore, the partial pressures were recalculated to their corresponding values at water gas shift equilibrium to see what effect it had on the re-

evaluated rate constants. One of the constants, K_2, was small when the other two were large, indicating that the rate would become independent of $H_2O(g)$ partial pressure at these conditions. When the water vapor term was assumed negligible, optimization yielded a better fit than for equation 8-8. However, a physically feasible solution was not obtained at conversions above 50% carbon conversion. This may imply that the gases appear not to be equilibrated at higher carbon conversions. When K_2 approaches zero indicates that reaction 2 is completely shifted to the left meaning that the active catalyst sites are mainly occupied with oxygen atoms. This compares well with Meijer et al.s finding (13) where the (O-*) sites increase and the (CO_2-*) sites decrease rapidly with conversion. The fact that reaction 2 is shifted to the left with conversion can be readily rationalized by a decrease in active surface area as reflected by the decreasing rate in Figure 8.7. When the catalyst is depleted to the extent that the gasification rate starts to decrease, gasification is becoming increasingly an intrinsic process where carboxylic and phenolic groups deplete the remaining carbonaceous structure with a lessening importance of the gas phase. Here, the distribution of CO_2, $H_2O(g)$, CO, and H_2 is different at the catalyst surface than could be the reason why feasible solutions were not obtained above 50% conversion.

Another attempt was made to find the extent the gases had shifted towards equilibrium by introducing a new variable, α, in order to obtain an apparent equilibrium constant, $K_{apparent}$.

$$\alpha = \frac{K_{apparent} - K_{bulk}}{K_{WGS,\,eq} - K_{bulk}} \qquad (8\text{-}12)$$

The variable, α, is allowed to vary between 0 and 1 indicating that the apparent gas composition is somewhere between that of the bulk gases and that at equilibrium. When all four variables, α, k', k'', and k''' are optimized, the result is that depending on the initial guess used for the variables, the final values were different. It is evident that this is caused by the fact that multiple solutions exist for this many parameters. This approach was therefore not considered further.

CONCLUSIONS AND RECOMMENDATIONS

Strong competition has been observed between $H_2O(g)$ and CO_2 for oxidation of the catalytic sites in BLC and that relatively little chemisorption of $H_2O(g)$ occurs. This is in line with the finding that most of the gasification rate is attributed to CO_2. Experimental data appears to support the additivity of CO_2 and $H_2O(g)$ at typical gasification environments in atmospheric pressure. The sodium catalyzed gasification of black liquor char proceeds via an oxidation-reduction cycle of the catalyst in which oxygen is transferred to the carbon surface from the active catalyst present. The transfer of oxygen atoms from the catalytic sites to the free carbon sites is probably the rate determining step. The fact that the rate is slower in simultaneous gasification can be ascribed to chemisorption of gas phase CO_2 into the active alkali cluster. Hence, CO_2 forms relatively stable intermediate moieties, CO_2-*, with the catalyst sites, making fewer catalyst sites available for water vapor to react and subsequently lowering the rate of gasification. CO may inhibit the gasification rate through the reverse of reaction 5.

The presented mechanism-based rate equation provides a reasonable estimator of gasification rates, that will likely provide an improved basis for designing gasification based pressurized black liquor recovery processes. The rate constants obtained account for the active site distribution during conversion of char carbon. An assessment of the currently available data infers that CO_2 and $H_2O(g)$ gasification is not an additive process above atmospheric pressure. At atmospheric pressure it may indeed be additive. More data is needed at atmospheric pressure to fully address this question. The rate of water vapor gasification is inhibited by addition of CO_2 , CO, and H_2 into the system. In simultaneous CO_2 and $H_2O(g)$ gasification the data indicates that the reaction pathway through CO_2 constitutes the major source of precursors to the rate limiting step.

Water gas shift equilibrium is probably approached rapidly due the fact that alkali metals catalyze this reaction. Water gas shift equilibrium is probably attained in real reactors with significant gas residence times and typical gasification temperatures. However, further experimental work is needed to conclusively establish to what extent water gas shift equilibrium is reached.

ACKNOWLEDGMENT

This work was supported by the U.S. Department of Energy through the Office of Industrial Technology and Oregon State University through the Niemi foundation.

NOMENCLATURE

Symbol	description, dimension
α	parameter indicating the degree of water gas shift reaction, dimensionless
[ ]	number concentration, dimensionless
_	carbon surface site, dimensionless
O	oxidized carbon surface site, dimensionless
*	catalytic surface site, dimensionless
*-O	oxidized catalytic surface site, dimensionless
*-CO2	catalytic site with chemisorbed CO_2, dimensions
C_f	free carbon surface site, dimensionless
C(O)	chemisorbed oxygen at occupied carbon surface site, dimensionless
)>C-O-M	phenolic group, dimensionless
)>C=O-O-M	carboxylic group, dimensionless
k_4	reaction rate constant for reaction 4, 1/s
k', k'', k'''	overall rate constants, 1/sec, dimensionless, and 1/ bar, respectively
$K_{apparent}$	apparent water gas shift equilibrium constant, dimensionless
K_{bulk}	bulk water gas shift equilibrium constant , dimensionless
$K_{WGS,eq}$	equilibrium constant for water gas shift reaction, dimensionless
K_1 , K_2	equilibrium constants, dimensionless for rxn. 1 and bar^{-1} for rxn. 2
MSS	mean sum of squares, dimensionless
N_{ox}	number of active carbon sites, dimensionless
N_t	number of active catalyst sites, dimensionless

REFERENCES

1. Cerfontain, M.B., Kapteijn, F., Moulijn, J.A., Characterization of Alkali Carbonate Catalysts for Carbon Gasification with ^{18}O Labeled CO_2, CARBON, 26(1), p,41-48, 1988

2. Kapteijn, F., Meijer, R., Moulijn, J.A., Kinetics and Mechanism of the Alkali Catalyzed Gasification of Carbon, 1991 International Conference on Coal Science Proceedings, 16-20 September 1991, U. of Newcastle-upon-Tyne, Butterworth, Oxford, United Kingdom, 1991

3. Sjöström, E., Wood Chemistry Fundamentals and Applications, Academic Press, Inc., New York, NY, 1981

4. Frederick, W.J., Wåg, K., Hupa, M., Rate and Mechanism of Black Liquor Gasification with CO_2 at Elevated Pressures, Ind.Eng.Chem.Res., 32, 8, 1747-1753, 1993

5. Li, J., van Heiningen, A.R.P., Kinetics of CO_2 Gasification of Fast Pyrolysis Black Liquor Char, Ind.Eng.Chem.Res., 29(9), p.1776-1785, 1990

6. Li, J., van Heiningen, A.R.P., Kinetics of Gasification of Black Liquor Char by Steam, Ind.Eng.Chem.Res., 30(7), p.1594-1601, 1991

7. Whitty, K.J., Gasification of Black Liquor Char with H_2O under Pressurized Conditions, M.S.thesis, Åbo Akademi U., 1993

8. Cerfontain, M.B., Meijer, R., Kapteijn, F., Moulijn, J.A., Alkali-Catalyzed Carbon Gasification in CO/CO_2 Mixtures: An Extended Model for the Oxygen Exchange and Gasification Reaction, J. Catalysis, 107, p.173-180, 1987

9. Whitty, K.J., Backman, R., Hupa, M., An Empirical Rate Model for Black Liquor Char Gasification as a Function of Gas Composition and Pressure, Proc. 1993 AIChE Conf., St.Louis, MO, 1993

10. Clay, D.T., Lien, S.J., Grace, T.M., Macek, A., Semerjian, H.C., Amin, N., Charagundla, S.R, "Fundamental Studies of Black Liquor Combustion", Report No.2, U.S. DOE Report DE88005756, January, 1987

11. Meijer, R., Kinetics and Mechanism of the Alkali-Catalyzed Gasification of Carbon, Ph.D. thesis, U. of Amsterdam, Holland, 1992

12. Meijer, R., van der Linden, B., Kapteijn, F., Moulijn, J.A., FUEL, Vol.70, 1991

13. Meijer, R., Sibeijn, M., van Dillen, M.R.B., Kapteijn, F., Moulijn, J.A., Ind.Eng.Chem.Res., 30(8), p.1760-1770, 1991

14. Hüttinger, K.J., CARBON, 26(1), p.79-87, 1988

15. Mims, C.A., Pabst, J.K., Role of Surface Salt Complexes in Alkali-Catalyzed Carbon Gasification, Fuel, 62(2), p.179-179, 1983

16. Meijer, R., Weeda, M., Kapteijn, F., Moulijn, J.A., Carbon, 29(7), p.929-941, 1991

17. Meijer, R., Mühlen, H.-J., Kapteijn, F., Moulijn, J.A., Fuel Processing Technology, Vol.29, p.5-17, 1991

18. Frederick, W.J., Hupa, M., Gasification of Black Liquor Char with CO_2 at Elevated Pressures, TAPPI J., 74(7), p.177-184, 1991

19. Overacker, N.L., Wåg, K.J., Frederick, W.J., Whitty, K.J., Application of a Mechanism-Based Rate Equation to Black Liquor Gasification Rate Data, Åbo Akademi U., 1994

20. Sams, D.A., Shadman, F., Mechanism of Potassium Catalyzed Carbon/CO_2 Reaction, AIChE J., 32(7), p,1132-1137, 1986

Chapter 9

Sulfate Reduction and Carbon Removal During Kraft Char Burning

Presented at the 1995 International Chemical Recovery Conference
Toronto, April 24-27, 1995

INTRODUCTION

Black liquor combustion is usually considered to take place in four stages; drying, volatiles burning, char burning, and smelt reoxidation; Hupa (1). Char burning is a very critical step. It is a relatively slow process and takes place when the liquor particle is in a highly swollen state, typically 20-90 cm^3/g char at the onset of char burning. Thus the rate of char burning has a large effect on the trajectories followed by the burning black liquor particles in the furnace. Slow rates of char burning can cause increased physical carryover of particles out of the furnace into the convective heat transfer sections and this can cause boiler plugging.

A substantial amount of sulfate reduction also occurs during char burning. This is desirable because sodium sulfide is an active pulping chemical. The effectiveness of the furnace operation in producing sulfide is characterized by the reduction efficiency. One of the most important factors affecting reduction efficiency is the black liquor spray characteristics. Furnace temperature and the oxygen concentration in the lower furnace are also very important.

OBJECTIVES

The objective of this chapter is to develop an improved mathematical model for the char burning step based on extensive experimental studies. An effort is made to gain insight into sulfate reduction and sulfide reoxidation processes during black liquor droplet combustion. The effects of drop size, furnace temperature, and gas concentrations on reduction efficiency and burn times are calculated. An interpretation is made of the simulation results to provide guidelines for achieving high reduction during black liquor combustion in a recovery furnace.

BACKGROUND

Many of the available models of char oxidation have focused on coal chars (2,3). Black liquor char combustion involves two features not seen in coal chars; the extremely high reactivity of the chars and the importance of reducing Na_2SO_4 to Na_2S. Black liquor char carbon is several orders of magnitude more reactive than other carbons because of the catalytic effect of sodium inherent in the char (4,5,6). Because of this higher reactivity, the rate of carbon oxidation with oxygen is film mass transfer controlled at temperatures above 1000°C for char particles of typical size (3-20mm). At typical gas concentrations and temperatures that exist in recovery boilers, the rates of carbon oxidation with carbon dioxide and water vapor are quite high and all three oxidants are important in black liquor char burning.

An accurate model of char burning must deal with three process items:

1. conversion of char carbon to the gases CO and CO_2,
2. the state of reduction of the sulfur in the burning particle,
3. the decrease in the size of the swollen char particle as the carbon is burned away.

None of the previous models of char burning have properly dealt with all of these issues. Models which have been used for black liquor drop trajectory calculations (7,8) have focused on carbon removal. Char burning was modeled as an oxygen mass transfer limited process. Chemical kinetic limitations and gasification of carbon with $H_2O(g)$ and CO_2 have not been handled in a rigorous manner. None of the models have dealt with sulfate reduction.

This paper describes an improved model of char burning that is capable of predicting reduction changes as well as the rate of carbon removal. This model includes the following:

1. gasification of carbon by $H_2O(g)$ and CO_2
2. direct carbon oxidation with O_2

3. reactions between O_2 and combustibles in the boundary layer which reduce the transfer of O_2 to the particle surface
4. simultaneous sulfate reduction with carbon and sulfide reoxidation with oxygen
5. volatilization of sulfur and sodium from the burning char particle
6. reduction computed by a sulfur balance

By treating both the char gasification and sulfur oxidation/reduction reactions simultaneously, the model allows a gradual transition between char carbon removal and net sulfide reoxidation as the char carbon is depleted. Thus this new model is applicable to both the char burning and smelt reoxidation stages and, in fact, eliminates the need to make a distinction between them.

CHEMICAL DESCRIPTION OF CHAR BURNING MODEL

Char burning involves the reactions occurring in a smelt/char particle. Each particle is considered as a mini chemical reactor interacting with the surrounding gases. The smelt/char particle is considered to contain carbon and three inorganic compounds, Na_2CO_3, Na_2S, and Na_2SO_4. The model described herein includes sodium vaporization reactions as well as sulfur release as COS and H_2S, both of which occur during char burning. Thus, the amount of sodium and the total moles of inorganic decrease with time during char burning.

The following eight reactions involving the constituents in the smelt/char are considered:

1. $C(s) + O_2(g) \rightarrow CO_2(g)$
2. $C(s) + CO_2(g) \rightarrow 2\ CO$
3. $C(s) + H_2O(g) \rightarrow CO(g) + H_2(g)$
4. $2\ C(s) + Na_2CO_3(s,l) \rightarrow 2\ Na(g) + 3CO(g)$
5. $C(s) + (2\text{-}f)/4\ Na_2SO_4(s,l) \rightarrow (2\text{-}f)/4\ Na_2S(s,l) + f\ CO(g) + (1\text{-}f)\ CO_2(g)$
6. $Na_2S(s,l) + 2\ O_2(g) \rightarrow Na_2SO_4(s,l)$

7. $Na_2S(s,l) + 2CO_2(g) \rightarrow Na_2CO_3(s,l) + COS(g)$

8. $Na_2S(s,l) + H_2O(g) + CO_2(g) \rightarrow Na_2CO_3(s,l) + H_2S(g)$

Reactions 1, 2, and 3 are heterogeneous reactions between furnace gases and char carbon. Reactions 4 and 5, the reduction reactions, are treated as a homogeneous reactions occurring in the condensed smelt/char phase. The variable stoichiometry indicated by the use of the parameter "f" is a reflection of the fact that both CO and CO_2 can be products of the sulfate-carbon reaction. Reaction 5, sulfide reoxidation, is treated as a heterogeneous reaction between gas phase oxygen and sulfide. Reactions 1 and 5 are assumed to be totally mass transfer controlled. Data supporting this assumption are contained in references (10) and (11). Reactions 2 and 3 are treated as controlled by external mass transfer, intraparticle diffusion and chemical kinetics in series. Reaction 4 is assumed to be completely controlled by chemical kinetics. Reactions 6 and 7 are film mass transfer limited assuming that the vapor partial pressures are at chemical equilibrium.

Reduction reactions between sulfate and reducing gases such as CO or H_2 are not included in this treatment. Experimental work (12) has shown that the rates of these reactions are several orders of magnitude less than those between carbon and sulfate.

In addition to reactions occurring with smelt/char components, there are also gaseous reactions occurring in the boundary layer adjacent to the smelt/char phase. These gaseous reactions are:

9. $CO(g) + 1/2\ O_2(g) \rightarrow CO_2(g)$

10. $H_2(g) + 1/2\ O_2(g) \rightarrow H_2O(g)$

The CO and H_2 are produced through gasification of carbon by CO_2 and $H_2O(g)$ and by the sulfate-carbon reaction.

MATHEMATICAL DESCRIPTION OF CHAR BURNING MODEL

The net rate of mass transfer of O_2 to the particle surface is determined by calculating the O_2 mass transfer rate in the absence of gas phase reactions and then subtracting the rate of O_2 consumption in the boundary layer. The following considerations apply.

- Each CO_2 that reacts in the particle produces 2 CO which then react with one O_2 in the boundary layer. Thus each CO_2 that reacts consumes one O_2 in the boundary layer.
- Each H_2O that reacts in the particle produces one H_2 and one CO which subsequently react with one O_2 in the boundary layer. Thus each $H_2O(g)$ that reacts consumes one O_2 in the boundary layer.
- Each CO produced by sulfate reduction consumes 1/2 O_2. The amount of O_2 consumed is then $2f/(2-f) \times R_{SO4}$.
- Each CO produced by carbonate reduction consumes 1/2 O_2. The amount of O_2 consumed is then $3/2 \times R_{Na2CO3}$.

These considerations are valid as long as there is sufficient O_2 to consume all of the combustibles produced. If there is insufficient O_2, the net oxygen flux at the surface will be zero and there will be some net production of combustibles. The net O_2 rate to the smelt/char particle is then given by equation 9-1:

$$R'_{O2} = R_{O2} - R_{CO2} - R_{H2O} - 2f/(2-f) \times R_{SO4} - 3/2 \times R_{Na2CO3} \quad \text{where } R'_{O2} \geq 0 \qquad (9\text{-}1)$$

The O_2 reaching the surface can react with either Na_2S or C. The relative amount of oxygen reacting with each is specified by a partition parameter, "p", the fraction of O_2 reaching the surface that reacts with C. The use of an arbitrary partition parameter is necessary because there are no kinetic data on carbon burnup and sulfide oxidation

occurring in parallel on which to base an estimate of the partition parameter. It was set equal to the mole fraction carbon in the particle, i.e. p = C/(C + I). This approach has the advantage that all of the O_2 will react with sulfide as the carbon becomes depleted.

The parameter "f" is the fraction of CO in the gas produced by the sulfate reduction reaction. Cameron's data (13) indicates that CO_2 is the major product of this reaction, and therefore f was assumed to be 0. The rate of carbon burnup is then given by:

$$R_C = 4/(2\text{-}f) \times R_{SO4} + R_{CO2} + R_{H2O} + p \times R'_{O2} = -\, d[C]/dt \qquad (9\text{-}2)$$

The reduction efficiency, E, is defined as the smelt reduction, the fraction of the sulfur in the smelt that is sulfide.

$$E = [Na_2S] / [\, Na_2S + Na_2SO_4] \text{ where } 0 < E < 1 \qquad (9\text{-}3)$$

The smelt reduction efficiency in the particle is calculated from a sulfide balance. Sulfur is assumed to be present as sulfide, sulfate, COS and H_2S.

Change of overall reduction efficiency =

[sulfide formed - sulfide consumed] / [total sulfur present] (9-4a)

$$S \times I \times dE/dt = R_{SO4} - R_S - R_{COS} - R_{H2S} = R_{SO4} - (1\text{-}p)/2 \times R'_{O2} - R_{COS} - R_{H2S} \qquad (9\text{-}4b)$$

where "S" is the total sulfur in the inorganics, and the inorganics, "I", is the sum of sulfide, sulfate, and carbonate.

If all oxygen is depleted in the boundary layer ($R'_{O2} = 0$), the rate of carbon consumption then becomes through substitution of equation 9-4b into equation 9-2:

$$R_C = R_{CO2} + R_{H2O} + 4/(2\text{-}f) \times \{\, S \times I \times dE/dt + R_{COS} + R_{H2S} \,\} \qquad (9\text{-}5)$$

However, if there is an abundance of oxygen, all CO will be consumed in the boundary layer and, hence, the rate of carbon consumption reduces to:

$$R_C = R_{O2} + 2 \times \{ S \times I \times dE/dt + R_{COS} + R_{H2S} \} \quad (9\text{-}6)$$

If there is no change in the reduction state of the particle and the formation of COS and H_2S is neglected,

$$R_C = R_{O2} \text{ or } R_{CO2} + R_{H2O} \text{ whichever is greater.} \quad (9\text{-}7)$$

This is the same result as that which had been obtained earlier by Grace (14) in the treatment of bed burning when reduction state changes were neglected. The key expressions for the char burning model are equations 9-1, 9-3, and 9-4. To solve them, rate equations for R_{O2}, R_{CO2}, R_{H2O}, and R_{SO4} and values for the parameters "f" and "p" are needed.

The overall rates of consumption of CO_2 and $H_2O(g)$ were calculated as:

$$1/R_i = 1/R_{m,i} + 1/(\eta_i R_{c,i}) \quad (9\text{-}8)$$

where i designates CO_2 and $H_2O(g)$. The rates of consumption of gas species CO_2 and $H_2O(g)$ under film mass transfer limited conditions were calculated as:

$$R_{m,i} = k_{m,i} A_p (C_{i,bulk} - C_{i,surface}) \quad (9\text{-}9)$$

where the mass transfer constant is evaluated at the film temperature.

The bulk concentration is evaluated at the bulk temperature and the surface concentration at the film temperature. The fact that the reactant concentration is lower within the pores than at the surface is taken into consideration by a Thiele modulus-based effectiveness factor, η_i. It applies for first-order reactions with spherical geometry (22):

$$\eta_i = \frac{1}{\Phi_i}\left(\frac{1}{\tanh 3\Phi} - \frac{1}{3\Phi_i}\right) \tag{9-10}$$

where

$$M_{Ti} = D_p/6\ (k_{r,i}/\mathcal{D}_i)^{0.5} \tag{9-11}$$

and

$$k_{r,i} = R_{c,i}/(V_p C_i) \tag{9-12}$$

The surface partial pressures are calculated assuming steady-state between film mass transfer and chemical reaction taking into consideration pore diffusion effects.

$$k_{m,i}\, A_p\, (P_{i,bulk} - P_{i,surface}) = \eta_i\, k_{r,i}\, P_{i,surface} \tag{9-13}$$

where $P_i = C_i\, RT$ (9-14)

Solving equation 9-11 for $P_{i,surface}$ gives:

$$P_{i,interface} = \frac{k_{m,i} P_{i,bulk} A_p}{k_{m,i} A_p + \eta_i k_{r,i} V_p} \tag{9-15}$$

The mass transfer coefficient was estimated from (15):

$$Sh = k_{m,i}\, D_p / \mathcal{D}_i = 2 + 0.569\ (Gr\ Sc)^{0.25} + 0.347\ (Re\ Sc^{0.5})^{0.62} \tag{9-16}$$

Diffusion coefficients for the reacting gas species were estimated by the Chapman-Enskog equation (8).

$$\mathcal{D}_i = 0.0018583 \frac{T^{1.5} \sqrt{\left(\frac{1}{M_A} + \frac{1}{M_B}\right)}}{P \sigma_{AB}^{\ 2} \Omega_{AB}(T^*)} \tag{9-17}$$

Note that equation 9-17 requires the following units: (P in atm, σ in Å, T in K, and M in kg/kmol). Neufeldt's correlation was used to estimate the diffusion collision integral (16).

$$\Omega_{AB} = \frac{1.06036}{(T^*)^{0.15610}} + \frac{0.193000}{e^{0.47635T^*}} + \frac{1.03587}{e^{1.52996T^*}} + \frac{1.76474}{e^{3.89411T^*}} \qquad (9\text{-}18)$$

The Lennard-Jones parameters, σ_{AB} and ε_{AB} , including the dimensionless temperature, T*, can be evaluated according to standard chemical engineering procedures. Table 9.1 lists the most relevant parameters.

Table 9.1. Lennard-Jones parameters most often needed in modeling of BL char gasification are listed below (22). The values are valid in the temperature range: 330-1000K.

Gas	ε/k_B (K)	σ (Å)
N_2	79.8	3.749
O_2	88	3.541
CO_2	213	3.897
$H_2O(g)$	356	2.649
$Na_{(v)}$	2171	4.924

The rates equations applicable under chemical kinetic controlled conditions have been derived based on data obtained by Li and van Heiningen (4,5).

$$R_{CO2} = 6.3\times10^{10}\,[C]\,P_{CO2}/(P_{CO2} + 3.4\,P_{CO})\exp(-30070/T) \qquad (9\text{-}19)$$

$$R_{H2O} = 2.56\times10^{9}\,[C]\,P_{H2O}/(P_{H2O} + 1.42\,P_{H2})\exp(-25300/T) \qquad (9\text{-}20)$$

The overall rate of consumption of O_2 was assumed to be limited by the rate of film mass transfer and was calculated from equation 9-9. The reduction rate equation is developed in Appendix 9.1:

$$R_{SO4} = 3790\,[C]\,[SO_4]^{1.4}\,e^{-9400/T} \quad (9\text{-}21)$$

The rate of formation of COS is assumed by Li (17) to be film mass transfer controlled, and the concentration of COS is assumed to be at thermodynamic equilibrium at the particle surface.

$$R_{COS} = k_{m,COS} \times A_p \times [COS]_{eq} \times (1 - X_s) \quad (9\text{-}22)$$

$$\text{where } [COS]_{eq} = K_{C,COS}\,[CO_2]^2 \text{ and } K_{C,COS} = e^{-13.9+7273/T} \quad (9\text{-}23)$$

Likewise in H_2S formation, it is assumed that there are no internal diffusion resistances, and that the rate is limited by film mass transfer and the equilibrium partial pressure of H_2S.

$$R_{H2S} = k_{m,H2S} \times A_p \times [H_2S]_{eq} \times (1 - X_s) \quad (9\text{-}24)$$

$$\text{where } [H_2S]_{eq} = K_{C,H2S}\,[CO_2]\,[H_2O] \text{ and } K_{C,H2S} = e^{-14.2+11351/T} \quad (9\text{-}25)$$

X_s is the fraction of sulfide that has reacted away. $[CO_2]$ and $[H_2O]$ are partial pressures evaluated in the particle boundary layer. The equations for $K_{C,COS}$ and $K_{C,H2S}$ were evaluated for the temperature range 900-1100°C based on data from the software HSC Chemistry (18).

SENSITIVITY TESTS OF MODEL

The model was used for a series of simulations to illustrate the effect of process variables on char burning. A base case set of model parameters was chosen to reflect typical conditions in a recovery boiler. They are shown as follows along with the changes for the sensitivity analysis:

Initial droplet diameter = 2 (4, 6, 8, 10) mm

Temperature = 1000 ± 100°C

O_2 = 5 ± 3%

$H_2O(g)$ = 15 ± 5%, CO_2 = 10 ± 5%,

H_2 = 2 ± 2%, CO = 2 ± 2%,

The initial droplet was assumed to swell 30 times by volume corresponding to a particle diameter approximately three times the initial diameter. The sulfate reduction reaction was assumed to produce only CO_2.

The gas mass transfer coefficients depend on the Reynolds number, Re, which is proportional to the product of the particle diameter and the relative velocity of the gas past the particle. Black liquor drops swell greatly during pyrolysis and then contract as the carbon is burnt away during char burning. The changing diameter, particle density and relative velocity must be accounted for in determining the Reynolds number.

The change in diameter is calculated using the following equation developed by Frederick (19, 20):

$$(D^3 - D_{max}^3) / (D_{max}^3 - D_s^3) = (1 - X_{cb})^m \qquad (9\text{-}24)$$

where "D_p" is the particle diameter at any conversion, "D_{max}" the diameter at maximum swelling, "D_s" the smelt bead diameter, "m" an experimental power law exponent (=1), and "X_{cb}" the fraction of oxidizing agent that has been provided for complete burnup of fixed carbon.

In a complete computational fluid dynamics based recovery furnace model the trajectories of individual particles are calculated as they respond to fluid drag and gravity. Reynolds number calculations are an inherent part of such models. For this paper, Re was estimated by assuming that the particles are entrained in the gas and the relative velocity will be close to the terminal velocity of the particle. The terminal settling velocity was estimated by equation 9-25 (11):

$$\frac{U}{cm/s} = 1164 \cdot 10^3 \times SG^{0.714} \left(\frac{D}{m} \right)^{1.143} \tag{9-25}$$

Since decreasing diameter and increasing terminal velocity offset each other, Re decreases by about 15-20% as char burning proceeds.

Figure 9.1 shows a typical reduction history during char burning. The reduction efficiency, which characterizes the state of the sulfur in the particle rises during char burning, reaches a maximum at about the point of carbon depletion, and then falls off at a constant rate because of sulfide reoxidation. The particle diameter decreases greatly as burning proceeds and reaches the diameter of a smelt drop as the carbon is depleted.The mass of char carbon decreases with time as the carbon is converted to gases. The total mass of the char particle drops off and goes through a minimum as the carbon is depleted and then increases slightly as sulfide is reoxidized to sulfate.

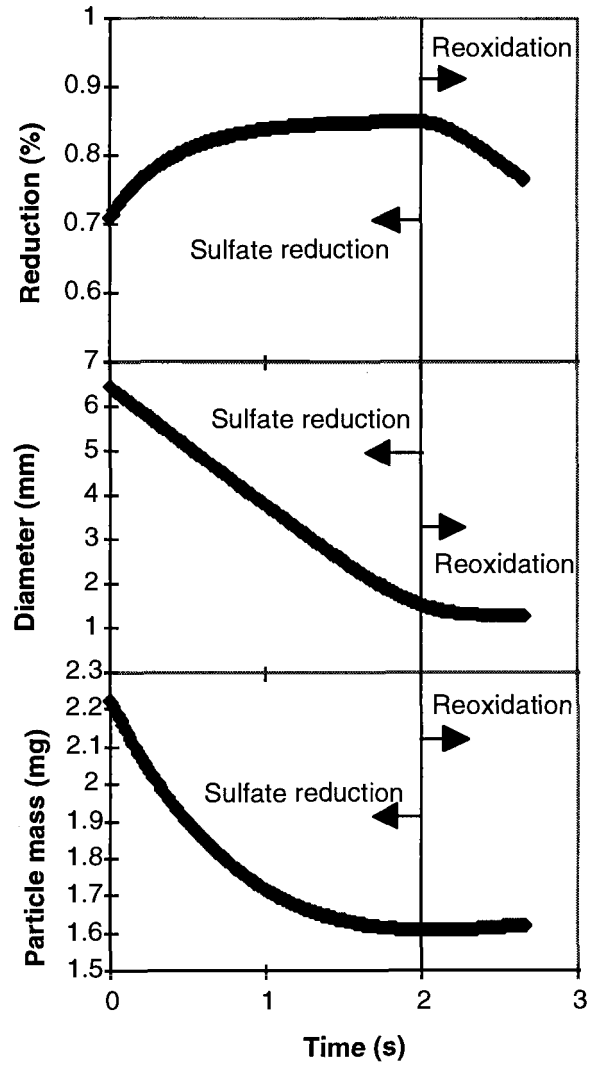

Figure 9.1. Typical behavior during char burning. The degree of reduction goes through a maximum, the diameter decreases, and the particle mass starts to slowly gain weight during reoxidation of the inorganic smelt.

Effect of drop diameter and temperature

Char burning is here characterized by four parameters: the time for 95% char carbon burnup, t_{95}, the degree of reduction at 95% carbon conversion, E_{95}, the maximum increase in reduction efficiency achieved at any point during char burning, ΔE, and the time to reach maximum reduction, t_{max}. The effect of process variables on these quantities

can provide considerable insight into the nature of black liquor combustion in a recovery boiler. The two most important process variables are the initial black liquor drop diameter and the furnace temperature. Figure 9.2 shows the effect of drop diameter and temperature on t_{95} and ΔE. The spacing between points indicates that at a given temperature, both t_{95} and ΔE increase monotonically with increasing drop diameter. As temperature increases, the gain in reduction increases in an exponential manner, while the time for carbon burnout shortens at a slower rate. It is evident that bigger drops contribute much more to reduction than do smaller drops. It is also apparent that high temperature is more important than drop size in achieving high reduction.

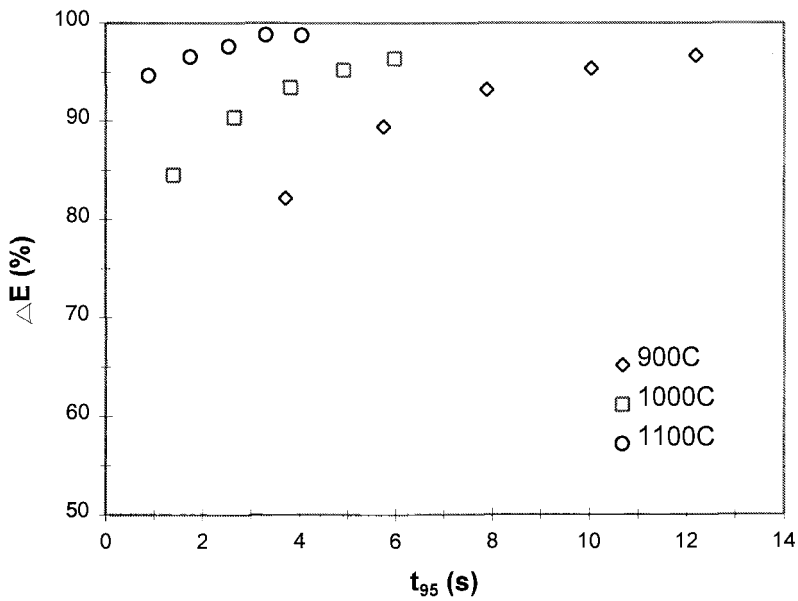

Figure 9.2. Points are for increasing drop diameter in order from 2 to 10 mm, with 2 mm increments.

Figure 9.2 also shows that, at a given temperature, the reduction gain increases monotonically with char burnout, which is to be expected. The reduction reaction takes place homogeneously throughout the particle at a rate dependent on carbon concentration

but independent of the external gas environment. The longer the time allowed for this to occur, the more reduction takes place. At a given temperature, any variable that shortens the char burnout time will result in less reduction. The effect of temperature on the sulfate reduction kinetics is so great that higher temperature results in more reduction even though it also shortens char burnout times.

Effect of gas composition

The effect of gas composition on char burning was examined by making changes in gas concentrations around the base case conditions and determining the effects on t_{95} and ΔE. $H_2O(g)$ and CO_2 were varied by ±5%, and O_2 by ±3% on an absolute basis. Plots of the effects on reduction over these ranges are given in Appendix 9.2 (Figures A.9.1.1 to A.9.1.3. For the base case, reduction increased with increasing temperature. An increased partial pressure of any gas tended to decrease reduction only slightly, and vice versa. Oxygen behaved similarly with respect to the maximum reduction achieved. However, at 95% conversion and 900°C, a significant decrease in reduction occurred for an oxygen concentration of 8%. This is an indication of that the degree of reduction is not dependent on the oxygen concentration as long as sufficient H_2 and CO is present in the boundary layer to consume O_2. The deviation at 900°C implies that some O_2 has reached the char surface, where it reacts with sulfide and consequently lowers the reduction. This is when the single film model applies. Figure 9.3 shows the calculation result that this conclusion is based on.

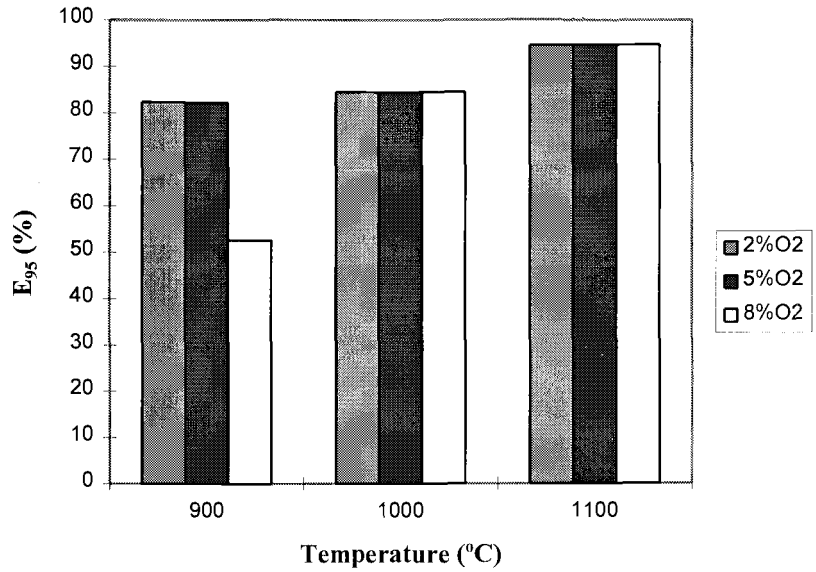

Figure 9.3. At 8% oxygen concentration and a temperature of 900°C, there is too little CO and H_2 in the boundary layer to prevent oxygen molecules from reaching the char surface, thus, reoxidatioin of the sulfide decreases the degree of reduction.

Increasing $H_2O(g)$ and CO_2 concentrations increases carbon gasification rates which shorten burning times as shown in Appendix 9.2 (Figures A.9.2.4 and A.9.2.5). $H_2O(g)$ has a larger effect than CO_2. The char burning time is much shorter at 1000 and 1100°C, because at higher temperatures film mass transfer is the rate controlling process, whereas at 900°C pore diffusion dominates. Another reason is that the char yield decreases at higher temperatures, hence, lowering the amount of fixed carbon. Other carbon consuming reactions such as sulfate and carbonate reduction increase rapidly at higher temperatures, which affects the char burning times as well. This is shown in Figure 9.4.

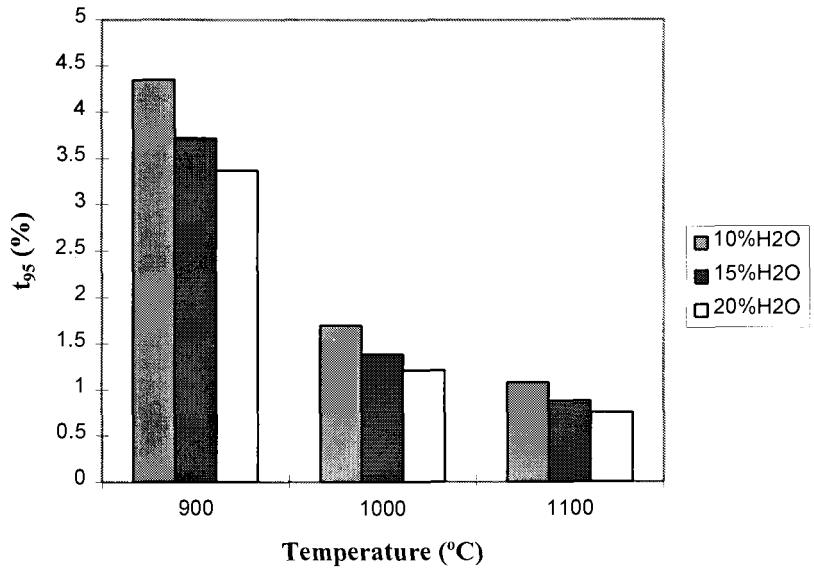

Figure 9.4. Increasing water vapor concentration decreases the char burning time.

The O_2 concentration, over the range from 2 to 8%, has virtually no effect on char burning times at Xc=95% (Figure 9.2.7 in Appendix 9.2). However, at 900°C and 2% O_2 the time to maximum reduction is higher than for t_{95} (Figure 9.2.8 in Appendix 9.2). The opposite is true for 8% O_2. This apparently surprising result can be readily explained. At low oxygen concentrations and temperatures, maximum reduction is reached at higher conversions than at 95%. The oxygen controlled process is calculated to start at 99% conversion, which is where maximum reduction is obtained. For 8% O_2, oxygen reaches the particle surface at a much earlier stage. Maximum reduction is achieved at Xc= 77%. This behavior is a result of the fact that the combustible CO and H_2 coming from the particle, consume the O_2 in the boundary layer, and effectively prevent it from reaching the particle itself until the carbon is nearly depleted. This is when the double film model applies. At low O_2 concentrations, the oxygen is prevented from reaching the particle surface for a longer time. At high O_2 concentrations, the oxygen reaches the particle surface much earlier. Hence, sulfate reoxidation occurs at a higher/lower extent of carbon

conversions at low/high oxygen concentrations, and, thus, the higher/lower time to maximum reduction is quite plausible. This is shown in Figure 9.5.

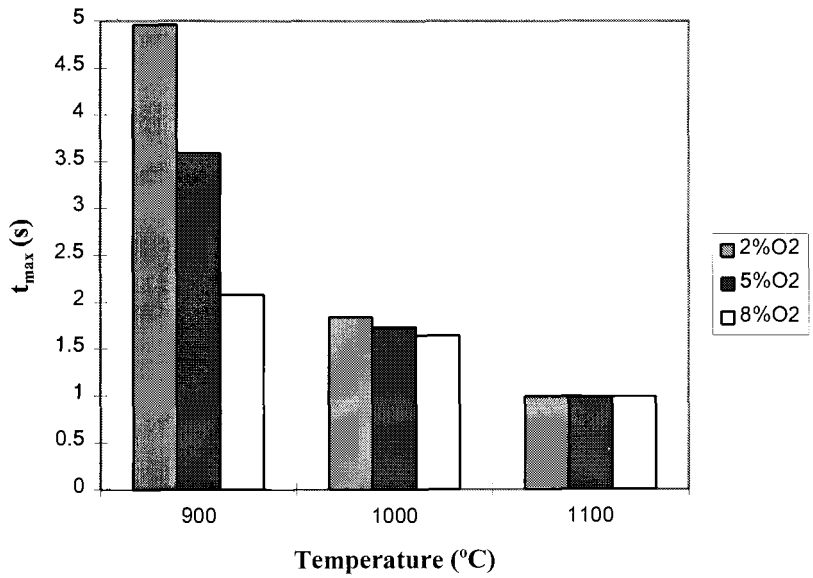

Figure 9.5. The effect of oxygen concentration on time to maximum reduction is minor at the same temperature.

Both H_2 and CO suppress the rates of gasification slightly, so that higher H_2 and CO concentrations increase char burning times and give only slightly higher reduction. The effects are not very large at atmospheric pressure. The effect of the inhibition gases on reduction and char burning time is given in Appendix 9.2 (Figures A.9.2.7 to A.9.2.10)

CONCLUSIONS

The following conclusions can be made based on this chapter:

1. A substantial amount of sulfate reduction can occur within black liquor particles burning in suspension even in an oxygen-containing atmosphere.
2. Reduction increases with increasing drop size and with increasing temperature. Temperature is more important than drop size. The composition of the gas has generally only a minor effect on reduction.
3. Reoxidation after char carbon is depleted is the most important factor affecting reduction efficiency in the recovery furnace. When reoxidation occurs the single film model applies in the boundary layer.
4. At a given temperature, any variable that increases char burnout times will also increase reduction efficiency.
5. Gasification of char carbon by reaction with $H_2O(g)$ and CO_2 is the most important means for carbon release under typical recovery furnace conditions. Sulfate reduction is responsible for only a minor part of the carbon release. Direct carbon oxidation by reaction with O_2 is insignificant until the carbon is nearly depleted, because O_2 is prevented from reaching the particle surface due to reaction with H_2 and CO coming from the particle.
6. Under the normal range of recovery furnace conditions, the rate of carbon burnup is not enhanced by increased O_2 concentrations. Consumption of O_2 by combustible products of gasification reactions prevents direct oxidation of the char carbon. This is when the double film model applies in the boundary layer.
7. The H_2 and CO from char carbon gasification by $H_2O(g)$ and CO_2 preserve reduction, since they prevent O_2 from reaching the char surface where it could oxidize sulfide. This is significant in obtaining high degrees of reduction.

ACKNOWLEDGMENT

This work was supported by the U.S. Department of Energy through the Office of Industrial Technology and by the Niemi Foundation at Oregon State University. Support for one of the authors (TMG) was provided by the American Forest and Paper Association's Recovery Boiler Committee and the Institute of Paper Science and Technology.

NOMENCLATURE

Symbol	description, dimension
[ ]	symbol for concentration, mol (unless otherwise indicated)
A	pre-exponential factor, 1/s
A_p	external surface area of char particle, cm^2
C_i	concentration of species i in bulk gas, mol/m^3
[C]	moles of fixed carbon in the particle at any time, mol/particle
$[COS]_{eq}$	equilibrium concentration of COS, mol/m^3
D_{max}	diameter at maximum swelling, cm
D_p	char particle diameter, cm
D_s	smelt bead diameter, cm
$\mathcal{D}_i$	diffusivity of gases, cm^2/sec
E	reduction efficiency at any time = $[Na_2S] / [Na_2S + Na_2SO_4]$, dimensionless
f	fraction of CO in the gas produced by the sulfate-carbon reaction, dimensionless
g	acceleration due to gravity, m/s^2
Gr	Grashof number = $g L^3 \Delta T \beta \div \nu^2$, dimensionless
$[H_2S]_{eq}$	equilibrium concentration of H_2S, mol/m^3
I	mole inorganic in the particle, mol ($Na_2S + Na_2SO_4 + Na_2CO_3$)
$K_{C,COS}$	equilibrium constant for COS formation, $(mol/m^3)^{-1}$
$K_{C,H2S}$	equilibrium constant for H_2S formation, $(mol/m^3)^{-1}$

$k_{m,i}$ film mass transfer coefficients for reacting gases, cm/sec

$k_{r,i}$ apparent first order rate constant for carbon gasification reaction, s^{-1}

M_{Ti} Thiele modulus, dimensionless

m experimental power law exponent, dimensionless

n reaction order with respect to sulfate, dimensionless

P_i partial pressure of gases, bar

p fraction of the O_2 reaching the surface that reacts with fixed carbon, dimensionless

R_{O2} rate of mass transfer of O_2 to the particle that would occur if there were no gas phase reactions in the boundary layer, mol O_2/sec

R'_{O2} net rate of O_2 transfer to the particle after reactions with combustibles in the boundary layer, mol O_2/sec

R_{CO2} rate of CO_2 reaction with fixed carbon in the particle, mol CO_2/sec

R_{H2O} rate of H_2O(g) reaction with char carbon in the particle, mol H_2O(g)/sec

R_{SO4} rate of reaction of C and Na_2SO_4 to Na_2S, (mol Na_2SO_4 consumed or Na_2S formed)/sec

R_S rate of oxidation of Na_2S to Na_2SO_4, mol Na_2S/sec

R_{COS} rate of reaction of Na_2S to COS, mol Na_2S/sec

R_{H2S} rate of reaction of Na_2S to H_2S, mol Na_2S/sec

$R_{c,i}$ kinetic rate of reaction of species i, mol/sec

$R_{m,i}$ rate of gas transport, mol/sec

Re Reynolds number, UD_p/ν, dimensionless

S sulfidity of the inorganic = moles sulfur per mole inorganic, dimensionless

Sc Schmidt number, $\upsilon/\mathcal{D}_i$, dimensionless

SG Specific gravity, dimensionless

Sh Sherwood number = $k_{m,i}D_p/\mathcal{D}_i$, dimensionless

$[SO_4]$ sulfate concentration, mol/mol Na_2

t time, sec

t_{95} time at 95% carbon conversion, sec

T	temperature, °K
T^*	reduced temperature, dimensionless
ΔT	temperature difference between particle and furnace temperature, K
U	relative velocity between gas and char particle, cm/sec
X_c	fraction of carbon that has reacted away, dimensionless
X_{cb}	fraction of oxidizing agent needed for complete burnup of fixed carbon, dimensionless
X_s	fraction of sulfide that has reacted away, dimensionless

Greek Symbols

β	coefficient of volumetric expansion, K^{-1} $\approx 1/T$
η_i	effectiveness factor to account for the effects of intraparticle diffusion, dimensionless
ε_{AB}	Lennard-Jones parameter, J/K
σ_{AB}	Lennard-Jones parameter, Å
ν	kinematic viscosity of gas, m^2/s
Φ_i	Thiele modulus, dimensionless
Ω_{AB}	collision integral, dimensionless

REFERENCES

1. Hupa, M., Solin, P., Hyöty, P., J. of Pulp & Paper Sci., 13(2):J67-72, 1987

2. Smoot, L.D. and Smith, P.J., Coal Combustion and Gasification, Plenum, New York, 1985

3. Bartok, W. and Sarofim, A.F. Fossil Fuel Combustion, John Wiley & Sons, New York, 1991

4. Li, J. and van Heiningen, A.R.P., Ind. Eng. Chem. Res. 29(9):1776-1785, 1990

5. Li, J. and van Heiningen, A.R.P., Ind. Eng. Chem. Res. 30(7):1594-1601, 1991

6. Frederick, W.J., Wåg, K.J., Hupa, M.M., Ind. Eng. Chem. Res. 32(8):1747-1753, 1993

7. Walsh, A.R. and Grace, T.M., J. of Pulp & Paper Science 15(3):J84-J89, 1989

8. Jones, A.K. and Chapman, P.J., TAPPI J., 76(7):195-202, 1993

9. Grace, T.M., Cameron, J.H., Clay, D.T., TAPPI J. 69(10):108-113, 1986

10. Frederick, W.J., Hupa, M., U.S. DOE Report DOE/CE/40936-T1 (DE94007502), 1993

11. Adams. T.N., Frederick, W.J., Kraft Recovery Boiler Physical and Chemical Processes, American Forestry and Paper Institute, New York, NY, 1988

12. Sjoberg, M., Cameron, J.H., AIChE Symposium Series, 239(80):35-40, 1984

13. Cameron, J.H., Grace, T.M., Ind. Eng. Chem. Fundam. 24(4):443-449, 1985

14. Grace, T.M., Lien, S.J. and Brown, C.A., Proceedings of 1992 International Chemical Recovery Conference, TAPPI, Atlanta, GA p.539-550, 1992

15. Treybal, R.E., Mass Transfer Operations, Third Edition, McGraw-Hill Book Company, New York, NY, p.75, 1981

16. Reid, R.C., Prausnitz, J.M., Poling, B.E., The Properties of Gases and Liquids, 4th ed., McGraw-Hill Book Company, New York, 1987

17. Li, J., Rate Processes During Gasification and Reduction of Black Liquor Char, Ph.D. thesis, McGill U., Montreal, Canada, October, 1989

18. HSC Chemistry for Windows Ver. 2.0, Outokumpu Research Ltd., Finland, 1994

19. Frederick, W.J., U.S. DOE Report DOE/CE/40637-T8 (DE90012712), 1990

20. Kymäläinen, M., Janka, K., Frederick, W.J., Sricharoenchaikul, V., Jivakanun, N., Wåg, K.J., Littau, M., 1995 TAPPI-CPPA Int'l Chemical Recovery Conference, April 24-27, Toronto, Canada, Paper 7b6, 1995

21. Sricharoenchaikul, V., Frederick, W. J., Kymäläinen, M., Grace, T. M., 1995 TAPPI-CPPA Int'l Chemical Recovery Conference, April 24-27, Toronto, Canada, Paper 3b4, 1995

22. Wåg, K., this thesis, Appendix 13, "Documentation of computer program", 1996

APPENDICES

APPENDIX 9.1

A Rate Equation for Sulfate Reduction in Black Liquor Char

The only rate equation available for predicting sulfate reduction in black liquor char is that of Cameron and Grace (13). However, data reported recently by Kymäläinen et al. (20) shows that the Cameron and Grace rate equation can underestimate the rate of sulfate reduction by an order of magnitude as shown in Figure A.9.1.1.

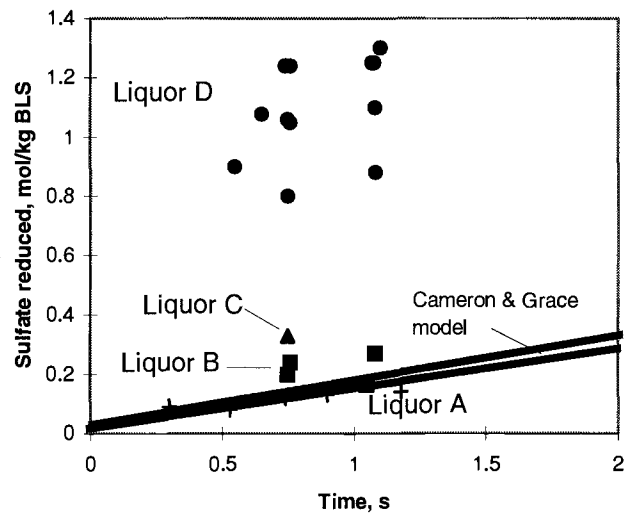

Figure A.9.1.1. Moles of sulfate reduced per gram of black liquor solids versus time at 1000°C for four kraft black liquors, comparing LEFR results and predicted conversions based on Cameron and Grace's model. The band marked "model" indicates the range of predictions for the four liquors.

The experimental data in Figure A.9.1.1 were obtained in experiments in a laminar entrained-flow reactor (LEFR) as described in Appendix 13. The data for liquor A was from (21), and for liquor D from (20). The initial sulfate contents for the four liquors are given in Table A.9.1.1.

Table A.9.1.1. Composition of black liquor chars used in the model calculations.

Liquor	A	B	C	D
Carbon in char, g/g BLS	0.164	0.166	0.158	0.134
Na in char, g/g BLS	0.226	0.192	0.213	0.234
SO_4 in char, g/g BLS	0.0158	0.0321	0.0504	0.136
Initial [C], mole/mole Na_2	2.77	3.30	2.84	2.19
Initial [SO_4], mole/mole Na_2	$3.36x10^{-2}$	$8.01x10^{-2}$	$1.13x10^{-1}$	$2.78x10^{-1}$

Comparing Figure A.9.1.1 and Table A.9.1.1 one can conclude that the rate of reduction apparently varies by an order of magnitude and increases with increasing sulfate content of the black liquor solids. The moles of sulfate reduced versus time as estimated with Cameron and Grace's equation is also plotted in Figure A.9.1.1. Their model predicts that sulfate reduction is essentially zero order in sulfate and occurs more slowly than the data for three of the four liquors. This is the driving force for obtaining an improved sulfate reduction model that would fit the experimental data better. A rate equation could be of the form of equation A.9.1-1.

$$\frac{d[SO_4]}{dt} = A \times [C][SO_4]^n e^{-E_a/RT} \qquad \text{(A.9.1-1)}$$

An apparent activation energy of 78.1 kJ/mole was obtained from the time to 50% conversion of sulfate for liquor A (Table A.9.1.2).

Table A.9.1.2. Time to 50% conversion of sulfate versus reaction temperature for liquor A. Data are from Sricharoenchaikul et al. (21).

Temperature, °C	Time, s
900	1.37
1000	0.80
1100	0.43

An optimization procedure was applied to equation A.9.1-1 and the data in Figure A.9.1.1 to obtain values of A = 3790 and N = 1.40. In the parameter estimation, the rate of sulfate reduction and the rate of carbon conversion were accounted for by integrating equation A.9.1-1 using a stoichiometric ratio of 3 moles carbon consumed/mole sulfate reduced. The initial carbon and sulfate concentrations in the char ([C] and [SO_4]) are given in Table A.9.1.1 expressed as moles per mole total inorganic (Na_2). Four of the lowest experimental values of sulfate conversion in Figure A.9.1.1 for several of the liquors (one for liquors A and B, two for liquor D) were not included in the optimization. The justification for this is that reoxidation of sulfide is expected to be the greatest source of error and would result in low experimental values of reduction, while nothing other than random experimental error would result in too high values.

Figure A.9.1.2 shows that the new model fits the experimental data much better.

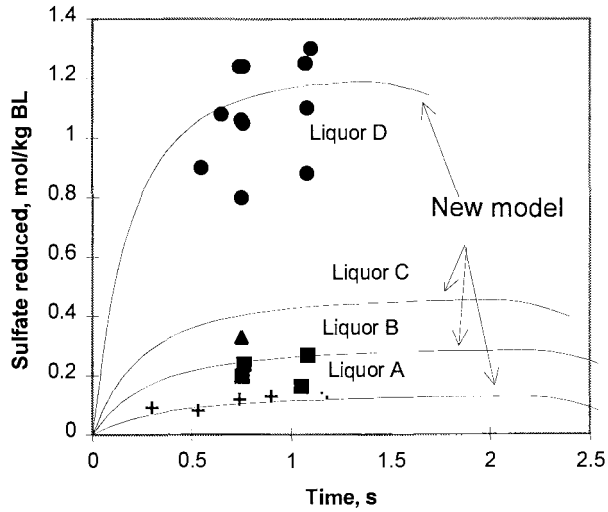

Figure A.9.1.2. Moles of sulfate reduced per gram of black liquor solids versus time at 1000°C for four kraft black liquors. The solid curves are predictions using the new model and the points are results from the LEFR.

APPENDIX 9.2

The Effect of Gas Composition and Temperature on the Degree of Reduction and Char Burning Time

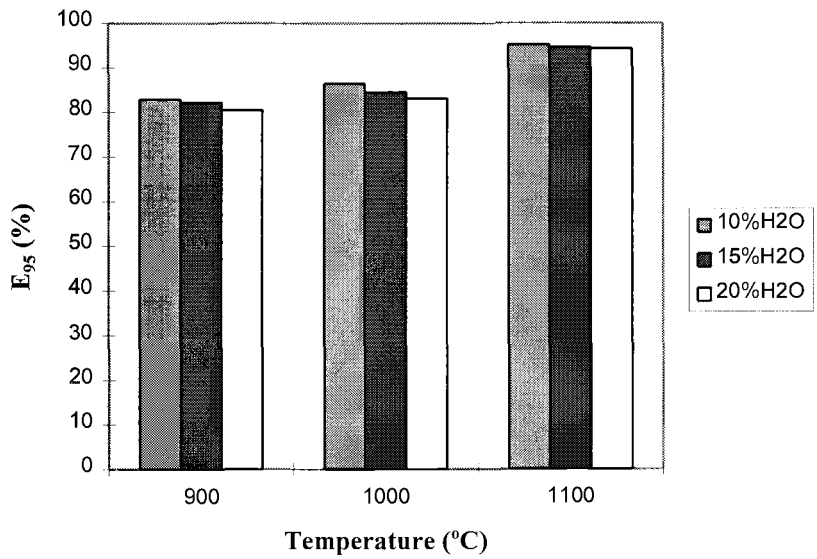

Figure A.9.2.1. A higher water vapor concentration decreases reduction, but a higher temperature increases reduction.

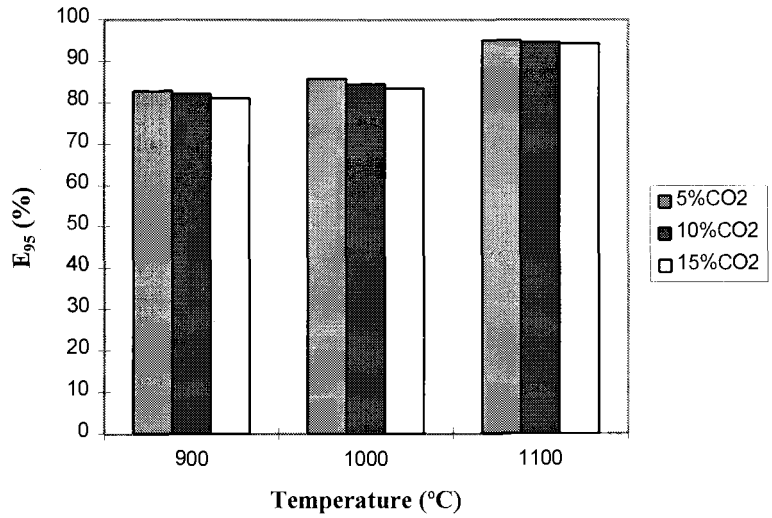

Figure A.9.2.2. A higher CO_2 concentration decreases reduction, and a higher temperature increases reduction.

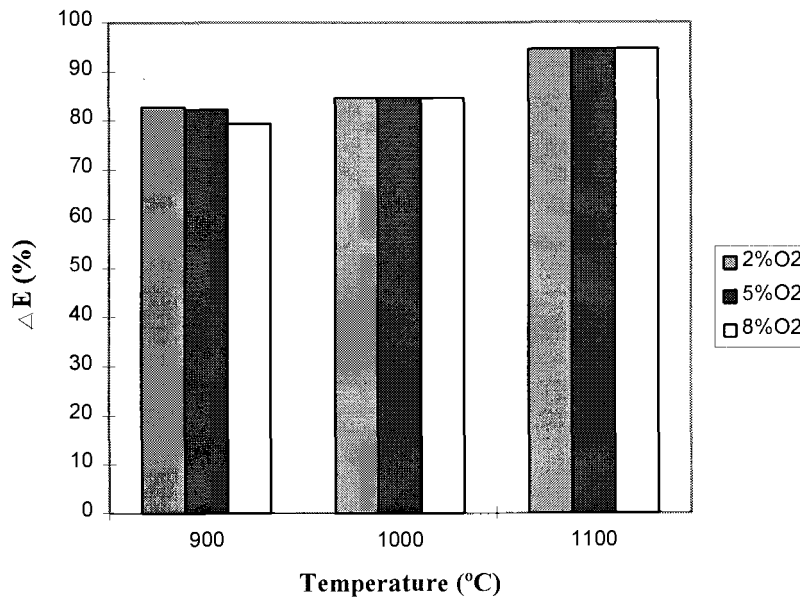

Figure A.9.2.3. There is no effect of O_2 concentration on maximum reduction at 1000 and 1100°C.

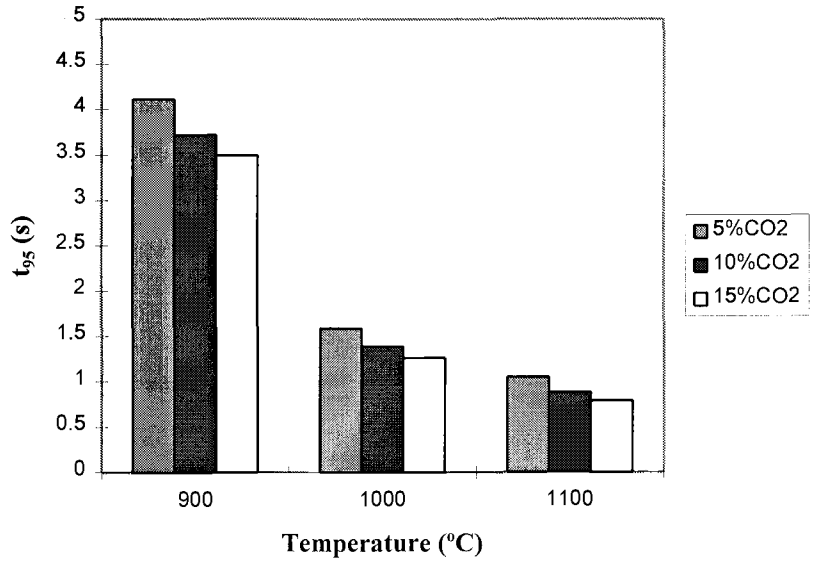

Figure A.9.2.4. Higher CO_2 concentrations and temperatures decrease char burning times.

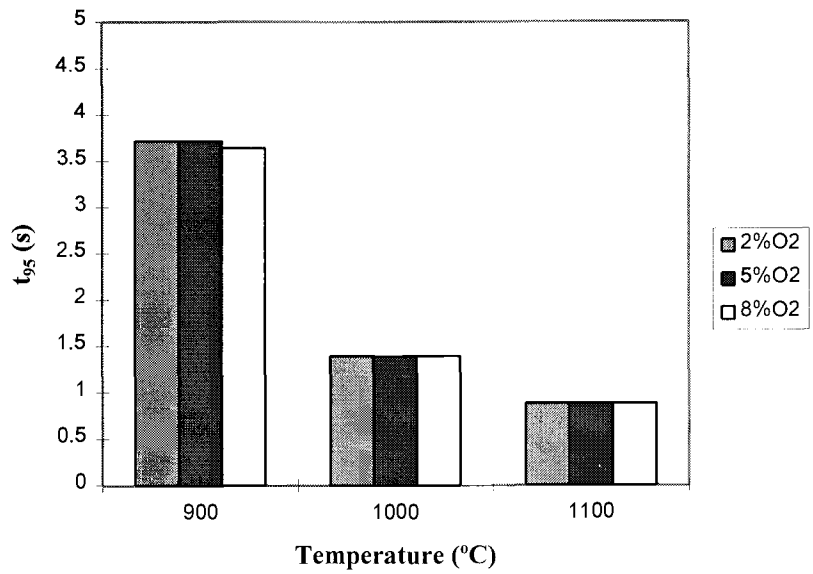

Figure A.9.2.5. Effect of O_2 on char burning time.

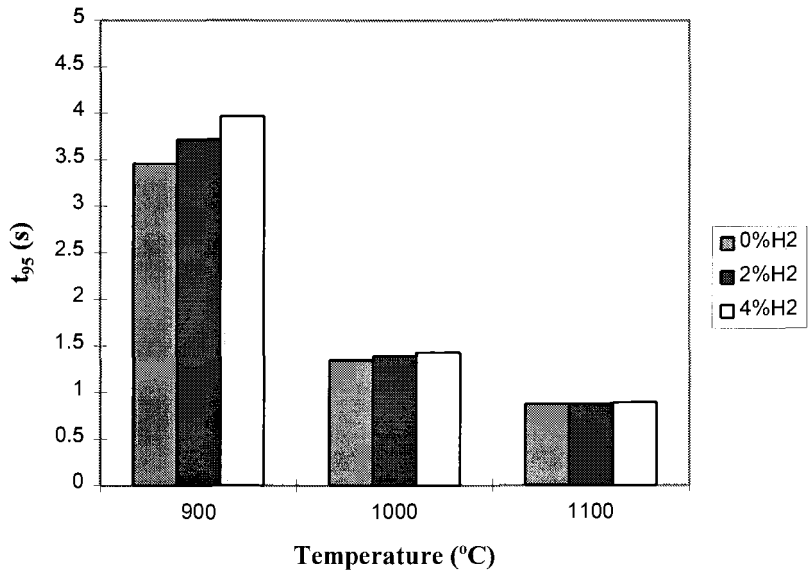

Figure A.9.2.6. Increasing H_2 partial pressure increases the char burning time at a given temperature.

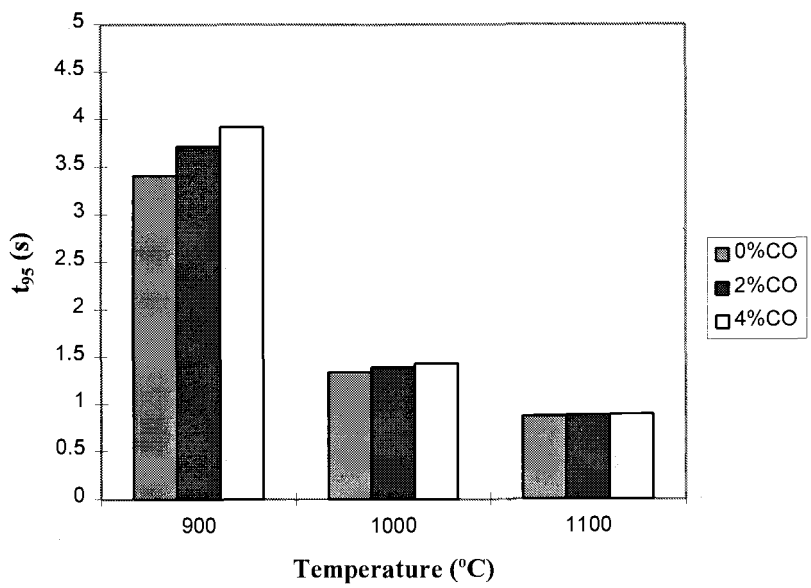

Figure A.9.2.7. Increasing CO partial pressure increases the char burning time at a given temperature.

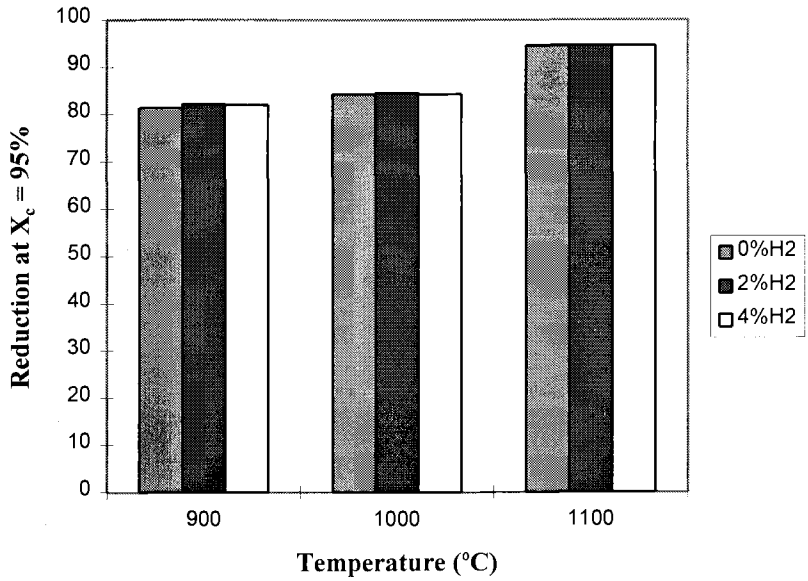

Figure A.9.2.8. Increasing H_2 partial pressure increases the degree of reduction at a given temperature.

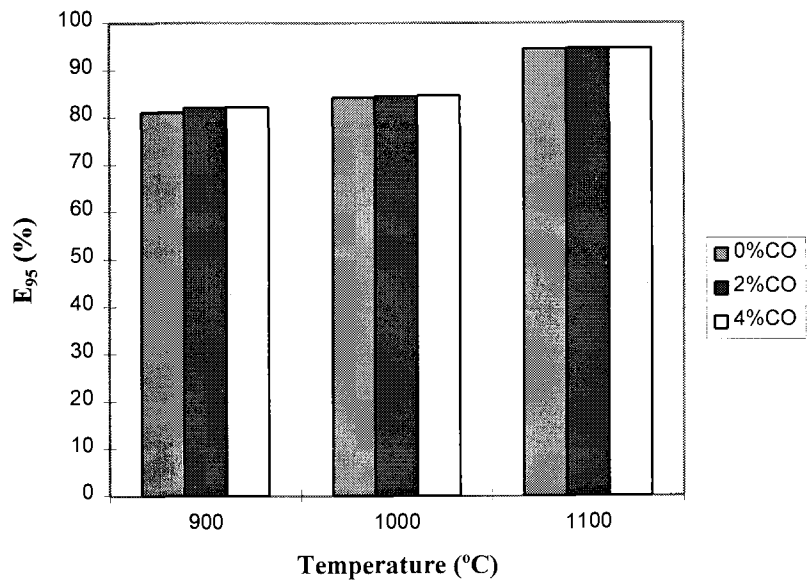

Figure A.9.2.9. Increasing CO partial pressure increases the degree of reduction at a given temperature.

Chapter 10

Release of Inorganic Emissions During Black Liquor Char Combustion: A Predictive Model

Presented at the 1995 TAPPI Engineering Conference
Dallas, September 11-14, 1995
To be published in the March 1997 issue of TAPPI Journal

INTRODUCTION

A validated computational combustion model is essential in improving the design and operation of modern recovery boilers. The objective of this paper is to present in a unified manner black liquor char combustion sub-models that describe the chemical species transitions of importance in recovery boilers. The development of accurate but numerically efficient sub-models are necessary in large scale computational combustion models. To accomplish this objective two tasks were defined: firstly, to develop an overall chemical element-based model which can predict the fate of all chemical species of interest (C, H, O, S, Na, K, and Cl) during black liquor char combustion and gasification, and, secondly, to obtain relevant experimental data as a basis for modeling key processes during black liquor char burning at typical furnace conditions.

The key processes involved in black liquor char combustion are:

1. conversion of carbon-containing solid species to carbon-containing gases,
2. release of sulfur gases and their recapture by fume,
3. reduction of sulfur species,
4. release of sodium, potassium, and chloride,
5. temperature history of the burning particle,
6. decrease in the size of the swollen char particles.

None of the previous models have properly dealt with all of these processes. Earlier models which have been used for black liquor droplet calculations focused on carbon removal (1, 2) and a more recent model included sulfate reduction as well (3). None of the models have dealt with sulfur, sodium, potassium, and chloride release in a comprehensive manner. The model presented here treats the char gasification, sulfur reactions, and fume formation processes simultaneously.

OBJECTIVES

The objective of this chapter is to present an improved char burning model that can accurately predict the following phenomena in typical gas environments and temperatures of a recovery boiler:

1. the differential and integral release of sodium, sulfur, potassium, and chloride during black liquor char combustion,
2. the effect of initial particle size on inorganic emissions during char combustion,
3. the effect of temperature on fume formation.

CHEMICAL DESCRIPTION OF MODEL

Char burning involves the reactions occurring in a char/smelt particle. Each particle is considered as a mini chemical reactor interacting with the surrounding gases. The char/smelt particle is considered to contain carbon and the following inorganic compounds: Na_2CO_3, K_2CO_3, Na_2S, and Na_2SO_4, NaCl, and KCl. The model described here includes sodium, potassium, and chloride vaporization reactions as well as sulfur release as COS and H_2S, both of which occur during char burning (4). Thus, the total moles of inorganic material in the char decrease with time during char burning.

The following reactions involving the constituents in the smelt/char are considered:

1. $C(s) + O_2(g) \rightarrow CO_2(g)$
2. $C(s) + CO_2(g) \rightarrow 2\,CO(g)$
3. $C(s) + H_2O(g) \rightarrow CO(g) + H_2(g)$
4. $2\,C(s) + Na_2CO_3(s,l) \leftrightarrow 2\,Na(g) + 3CO(g)$
5. $2\,C(s) + K_2CO_3(s,l) \leftrightarrow 2\,K(g) + 3CO(g)$
6. $C(s) + (2\text{-}f)/4\,Na_2SO_4(s,l) \rightarrow (2\text{-}f)/4\,Na_2S(s,l) + f\,CO(g) + (1\text{-}f)\,CO_2(g)$

7. $Na_2S(s,l) + 2\ O_2(g) \rightarrow Na_2SO_4(s,l)$
8. $Na_2S(s,l) + 2CO_2(g) \leftrightarrow Na_2CO_3(s,l) + COS(g)$
9. $Na_2S(s,l) + H_2O(g) + CO_2(g) \leftrightarrow Na_2CO_3(s,l) + H_2S(g)$
10. $NaCl(s,l) \leftrightarrow NaCl(g)$
11. $KCl(s,l) \leftrightarrow KCl(g)$

Reactions 1, 2, and 3 are heterogeneous reactions between furnace gases and char carbon. Reactions 4, 5 and 6, the reduction reactions, are treated as a homogeneous reactions occurring in the condensed smelt/char phase. The variable stoichiometry indicated by the use of the parameter "f" is a reflection of the fact that both CO and CO_2 can be products of the sulfate-carbon reaction. Reaction 7, sulfide reoxidation, is treated as a heterogeneous reaction between gas phase oxygen and sulfide. Reactions 1 and 7 are assumed to be totally mass transfer controlled. Data supporting this assumption are contained in references (5) and (6). Reactions 2 and 3 are treated as controlled by external mass transfer, intraparticle diffusion and chemical kinetics in series. Reactions 4 and 5 are assumed to be reversible reactions the forward rate being controlled by chemical kinetics. Reactions 8 and 9 are film mass transfer limited, assuming that the vapor partial pressures in the particle boundary layer are at chemical equilibrium with the solid phase. Reactions 10 and 11 are assumed to be at chemical equilibrium according to Raoult's law.

In addition to reactions occurring with smelt/char components, there are also gaseous reactions that may occur in the boundary layer adjacent to the char/smelt phase. These gaseous reactions are:

12. $CO(g) + 1/2\ O_2(g) \rightarrow CO_2(g)$
13. $H_2(g) + 1/2\ O_2(g) \rightarrow H_2O(g)$
14. $2\ Na(g) + 1/2\ O_2(g) \rightarrow 2\ Na_2O(g)$
15. $2\ K(g) + 1/2\ O_2(g) \rightarrow 2\ K_2O(g)$
16. $Na_2O(g) + CO_2(g) \rightarrow Na_2CO_3(s,l)$
17. $K_2O(g) + CO_2(g) \rightarrow K_2CO_3(s,l)$

18. $2\ Na_2O(g) + 2\ SO_2(g) + O_2(g) \rightarrow 2\ Na_2SO_4(s,l)$

19. $2\ K_2O(g) + 2\ SO_2(g) + O_2(g) \rightarrow 2\ K_2SO_4(s,l)$

CO and H_2 are produced through gasification of carbon by CO_2 and $H_2O(g)$ and by the sulfate/carbonate-carbon reaction. These species are consumed by oxygen through reactions 12 and 13. The elemental alkali species generated from carbonate reduction reacts with oxygen according to reactions 14 and 15. The oxidized alkali species are recaptured by reaction with SO_2 and CO_2 to reform carbonate and sulfate; reactions 16-19. Reduction reactions between sulfate and reducing gases such as CO or H_2 are not included in this treatment. Experimental work (7) has shown that the rates of these reactions are several orders of magnitude less than those between carbon and sulfate.

CARBON BURN-OFF AND SULFATE REDUCTION MODELS

The rate of carbon removal from the char particle proceeds through either combustion or gasification at typical recovery boiler conditions. Under conditions where the partial pressures of CO_2 and water vapor are normally higher than that of O_2, reactions 2 and 3 are responsible for conversion of char carbon to CO. The CO and H_2 produced react with O_2 in the boundary layer, and all oxygen is prevented from reaching the particle surface when sufficient amounts of combustible volatiles are generated from the gasification reactions. When oxygen does reach the surface, it reacts much more readily with active carbon sites than do CO_2 and $H_2O(g)$. This is discussed in more detail in reference (3).

The overall consumption rate of carbon is determined by gasification with CO_2 and $H_2O(g)$ or by oxidation with O_2, whichever is greater (8). The access of the reacting gaseous species to the pore surfaces of the char particle is limited by film mass transfer and pore diffusion in series. A detailed mathematical description of carbon release calculations is given in reference (3).

The change of sulfide concentration in the particle is calculated from a sulfur balance:

$$\frac{d[Na_2S]}{dt} = \frac{d[Na_2S]_{formed}}{dt} - \frac{d[Na_2S]_{consumed}}{dt} \qquad (10\text{-}1)$$

The reduction efficiency, E, is defined as the fraction of the sulfur in the smelt that is sulfide.

$$E = \frac{[Na_2S]}{[Na_2S + Na_2SO_4]} \qquad \text{where } 0<E<1 \qquad (10\text{-}2)$$

By differentiating equation 10-2 with respect to the sulfide concentration one obtains the overall rate of change in reduction efficiency. The sum of the concentrations of sulfide and sulfate was assumed constant. A detailed mathematical description of the reduction efficiency calculation procedure is given in reference (3).

SODIUM, POTASSIUM, AND CHLORIDE RELEASE MODELS

Sodium, potassium, and chloride release from black liquor char proceeds by the parallel reaction paths of formation of elemental sodium and potassium vapor via reduction of their carbonates, and evaporation of NaCl and KCl. Atomic sodium quickly reacts with the species present in the complex chemical environment surrounding the reacting char surface to yield bound molecular states especially when $H_2O(g)$, H_2, and O_2 are present (23). Hence, carbonate reduction was treated essentially as an irreversible chemical reaction. The existence of NaCl in the vapor phase has been confirmed for coal fuels in 10 and 20% oxygen at 1200K (24). At these conditions it was shown through kinetic calculations that steady state would be achieved rapidly for a sodium/chlorine/oxygen/hydrogen system.

The overall generation rate of sodium vapor through carbonate reduction was assumed to be limited by chemical kinetics, pore diffusion, and film mass transfer resistances in series according to equation 10-3.

$$1/R_i = 1/R_{m,i} + 1/\eta_i R_{c,i} \quad \text{where i = Na or K vapor} \tag{10-3}$$

The rate of mass transfer of sodium vapor was calculated by equation 10-4.

$$R_{m,i} = k_{m,i} A_p C_i \quad \text{where i = leaving gas species} \tag{10-4}$$

The mass transfer coefficient, $k_{m,i}$, was evaluated from a Sherwood number equation (3). The equilibrium partial pressure in the particle gas film, C_{Na} was calculated using the software Chemsage (12). The rate limiting effect of intraparticle diffusion was accounted for with a Thiele modulus-based effectiveness factor (11).

$$\eta_i = \tanh(M_{Ti})/M_{Ti} \tag{10-5}$$

where

$$M_{Ti} = D_p/6\,(k_{r,i}/\mathcal{D}_i)^{0.5} \tag{10-6}$$

and

$$k_{r,i} = R_{c,i}/(V_p C_i) \tag{10-7}$$

The kinetic rate of Na_2CO_3 reduction in black liquor char reported by Li and van Heiningen (13) is described by equation 10-8.

$$R_{c,i} = \frac{d[Na_2CO_3]}{dt} = 10^9 [Na_2CO_3]\, e^{-\frac{244000}{RT}} \tag{10-8}$$

A rate equation analogous to equation 10-8, but adjusted by the ratio of K/Na in the particle was used for the rate of production of potassium vapor from reduction of K_2CO_3.

Inhibition of carbonate reduction by CO or CO_2 was neglected because much of the experimental data (14) shows no evidence of suppression at 1000°C in a typical recovery boiler environment (20% CO_2 and H_2O(g), 10% CO and H_2). However, experimental data with CO_2 being the only major gaseous species (15-20% CO_2) does show that the reduction process is inhibited at 800 and 900°C (14, 15). Reduction of Na_2CO_3 may also proceed by reduction with sulfide, i.e.:

20. $Na_2CO_3(s,l) + 1/4\ Na_2S(s,l) \iff 2\ Na(g) + CO_2(g) + 1/4\ Na_2SO_4(s,l)$

However, the equilibrium sodium vapor partial pressure from the reduction of Na_2CO_3 with carbon is much greater than that obtained by reduction with Na_2S. Therefore Na_2CO_3 will be reduced by Na_2S only after the fixed carbon has been consumed, i.e. not during char burning.

Since black liquor is a Na, K, and Cl containing fuel, fuming processes involve vaporization of NaCl and KCl. Experimental work with molten salt pools (16) indicates that sodium chloride vaporization is a mass transfer controlled process, where the smelt is an ideal system and the gas film is saturated with sodium chloride. During these conditions Raoult's law applies:

$$y_a P_{tot} = x_a P_a^{sat} \text{ where } a = NaCl(g,l) \text{ or } KCl(g,l) \qquad (10\text{-}9)$$

The rates of NaCl and KCl vaporization were calculated by equation 10-4 assuming that mass transfer across the gas film adjacent to the burning particles was the rate-limiting step and that the vapor pressures of NaCl and KCl were negligibly small in the bulk gas beyond the gas film.

The partial pressures of NaCl(g) and KCl(g) at the particle interface were assumed to be in chemical equilibrium with an inorganic phase consisting of Na^+, K^+, Cl^-, CO_3^{2-}, S^{2-}, and SO_4^{2-} in the particle. In the results presented here, P_{NaCl} and P_{KCl} should be calculated using a chemical equilibrium program. There are several available such as

HSC Chemistry (10) that was used here, and Chemsage (12). Perhaps the best software is ChemApp (27) which would eliminate the manual stepwise integration procedure necessary with HSC Chemistry and Chemsage. However, ChemApp has not yet been released (September 1996).

The rate of sodium release, dNa/dt, was calculated as the sum of the rate of sodium loss from reduction of Na_2CO_3 and from evaporation of NaCl, equations 10-9 and 10-10.

$$dNa/dt = dNaCl/dt + dNa_2CO_3/dt \qquad (10\text{-}10)$$

The rate of potassium release, dK/dt, is obtained analogously by equation 10-11.

$$dK/dt = dKCl/dt + dK_2CO_3/dt \qquad (10\text{-}11)$$

The overall Cl release rate is given by the sum of NaCl and KCl vaporization, equation 10-12:

$$dCl/dt = dNaCl/dt + dKCl/dt = k_{m,NaCl}\, A_p\, (P_{NaCl} + P_{KCl}) \qquad (10\text{-}12)$$

SULFUR RELEASE MODELS

The rate of formation of COS was assumed by Li (9) to be film mass transfer controlled, and the concentration of COS was assumed to be at thermodynamic equilibrium at the particle surface.

$$R_{COS} = k_{m,COS} \times A_p \times [COS]_{eq} \times (1 - X_s) \qquad (10\text{-}13)$$

$$\text{where } [COS]_{eq} = K_{C,COS}\, [CO_2]^2 \text{ and } K_{C,COS} = e^{-A+B/T} \qquad (10\text{-}14)$$

$$R_{H2S} = k_{m,H2S} \times A_p \times [H_2S]_{eq} \times (1 - X_s) \quad (10\text{-}15)$$

where $[H_2S]_{eq} = K_{C,H2S}\,[CO_2]\,[H_2O]$ and $K_{C,H2S} = e^{-C+D/T}$ (10-16)

X_s is the fraction of sulfide that has reacted away. $[CO_2]$ and $[H_2O]$ are partial pressures evaluated in the particle boundary layer. The equations for $K_{C,COS}$ and $K_{C,H2S}$ were evaluated for the temperature range 900-1100°C based on data from the software HSC Chemistry (10). The parameters A,B,C,D were evaluated through optimization to fit the equilibrium constants for equations 10-14 and 10-16. Table 10.1 shows the values for these parameters for two temperature ranges.

Table 10.1. The following values apply to the constants A, B, C, and D.

Temp (°C)	A	B	C	D
700-899	16.1	12307	16.5	16507
900-1100	12.6	8514	12.9	12585

MODEL PREDICTIONS AND COMPARISONS WITH EXPERIMENTAL DATA

The experimental data for carbon, sodium, and sulfur were obtained in two sets of experiments. At Oregon State University (OSU) a laminar entrained-flow reactor (LEFR) was used for ~100 μm particles, and single droplet reactors were used at Åbo Akademi University (ÅAU) for 2-3 mm droplets. A detailed description of these reactors can be found in Appendix 13.

Experimental data for sodium, potassium, and chloride release for were obtained from LEFR experiments at OSU. Dry black liquor solids particles of the diameter size range of 90-125 μm were pyrolyzed in 100% N_2, 4% O_2, and 21% O_2 at 700-1100°C. The

elemental composition of the OSU liquor is as follows: 35% C, 22.7% Na, 0.62% K, 0.67% Cl, 2.9% S. The particle heating rate was on the order of 10^4 °C/s and the residence time 0.6 - 0.8 sec. The samples were quenched with nitrogen in a water-cooled probe to stop the chemical reactions. The solid products of combustion were collected as char (> 3 μm) and fine particles (< 3 μm), and analyzed for Na, K, and Cl content. The experimental sodium, potassium, and chloride release data at OSU was measured from the fume collected.

At ÅAU two different reactor types were used: a stagnant gas reactor and a convective flow reactor. Black liquor droplets, typically 2-3 mm in diameter, were pyrolyzed at 800 or 900°C in different gas mixtures. The dry solids contents of the droplets were 76.1% and 82.3%, and they had the following elemental composition: 31.4% C, 19.1% Na, 6.4% S. The experimental sodium loss data at ÅAU was measured from the char residue. Table 10.4 shows the amount of sodium released during char burning as percent of that in the black liquor solids.

For the convective flow reactor the particle surface temperature was calculated to be approximately 40 degrees below the furnace temperature. This is due to the fact that the gas stream entered at a lower temperature than that of the furnace, and the gas flow did not attain the temperature of the furnace before it reached the particle. The temperatures of the particles were therefore determined by the net rate of heat input by radiation from the furnace and removal by convection to the gas. A detailed description of the particle temperature estimation can be found in reference (14).

Carbon release

The validity of the carbon release model was established by comparing char burning times measured in a stagnant gas reactor and a single droplet reactor at ÅAU (14,17) with the corresponding times calculated with the model (Tables 10.2 and 10.3). The predicted times are given at 99% carbon conversion for the cases when the parameter "f" is 1 and 0, i.e. when only CO and only CO_2 is produced by sulfate reduction, respectively. Table 10.2 gives the char burning times when assuming steady state for the interface concentration. The char burning times are given when assuming that all reactant gas is at equilibrium with the particle interior. The droplets in Table 10.2 had a dry solids content of 65%, and the initial weight varied between 3 and 10 mg. The experiments were made at 800°C (14).

Table 10.2. Experimental and calculated char burning times for stagnant gas experiments. Sulfur in BLS = 4%, g Na in char / g BLS = 0.2, g SO_4 / g BLS = 0.05, g C in char / g BLS = 0.18. When f = 1, the mean square difference is 42.2. When f = 0, the mean square difference is 48.7.

Weight and Gas Composition	T (°C)	C.B. time exp (s)	C.B. time calc (s) f = 1	C.B. time calc (s) f = 0
3.5mg 20% H_2O 4%CO	900	10 ± 2	8.5	8.7
10mg 20% H_2O 4%CO	900	13 ± 3	9.7	10.0
3mg 20% CO_2 4%CO	900	15 ± 2	23.1	24.4
10mg 20% CO_2 4%CO	900	20 ± 3	25.8	27.1

The droplets in Table 10.3 are assumed to have a droplet weight of 6 mg with a dry solids content of 60% at a furnace temperature of 800°C. $C_{CO2,surface}$ is assumed = 0.

Table 10.3. Experimental and calculated char burning times for single droplet experiments. Sulfur in BLS = 4%, g Na in char / g BLS = 0.2, g SO_4 / g BLS = 0.05, g C in char / g char initially = 0.32. When f = 1, the mean square difference is 14.4. When f = 0, the mean square difference is 13.0.

Gases	T (°C)	C.B. time exp (s)	C.B. time calc (s) f = 1	C.B. time calc (s) f = 0
20% CO_2	800	88.1±5	90.0	92.5
2% O_2 +20% CO_2	800	24±2	18.5	20.5
5% O_2 +20% CO_2	800	13.7±1	8.9	9.8
10% O_2 +20% CO_2	800	6.4±1	4.7	5.2
16.8% O_2 +20% CO_2	800	4±1	2.6	2.7

Table 10.3 was obtained assuming that $C_{CO2,surface} = 0$. The theoretical char burning times are somewhat higher when only CO_2 is generated from sulfate reduction (f = 0). If only CO is produced from sulfate reduction, then the char burning times are somewhat lower (f = 1). The data in Tables 10.2 and 10.3 show that the predicted char burning times agree well with experimental data. For sulfite liquors, the char burning times are satisfactorily predicted. The swelling characteristics are modeled empirically.

The mean square difference is given by equation 10-17. It is an indication of the overall agreement with the model, and it is expressed as the percentage of the average of the experimental data.

$$\text{Mean square difference (\%)} = \left(\Sigma(\text{exp-calc})^2 \div \text{n-1} \right)^{0.5} \div (\text{exp avg}) \times 100 \qquad (10\text{-}17)$$

where n is the number of experimental data points.

Limitations of Model

This char burning model can be used to predict carbon release for liquors of other types as well, say sulfite, but the degree of sulfate reduction only for kraft liquors since the sulfate reduction model is derived for a system where the sulfur species present are as

sulfide and sulfate. The model cannot take into consideration other sulfur species in the inorganic phase.

Another limitation is that the rate equation for CO_2 gasification was obtained from experimental data taken at 600-800°C (11). The rate equation for $H_2O(g)$ gasification was obtained from experimental data taken at 600-700°C (12). At temperatures above these limits, the predicted reaction rates are extrapolations

Sodium release

2-3 mm Droplets

The experimental sodium release data as well as the model predictions for the single droplet experiments are summarized in Table 10.4. The experiments were carried out for particle diameters of 2-3 mm. One data point represents an average of 8 droplet experiments with a particle weight ranging between 10 and 20 mg. The theoretical calculations were performed for an average droplet weight of 18 mg. The data shows a greater loss of sodium at a higher temperature. It also indicates that there is no increase in sodium loss when oxygen, water vapor, or CO_2 are present when compared with droplets heated in a CO or nitrogen environment. The data in CO_2 at 900°C suggests that CO_2 may be suppressing sodium volatilization at 900°C, but there is no indication that CO suppresses sodium volatilization at this temperature. The experimental char burning times listed in Table 10.4 are in most cases longer than the actual burnout times for fixed carbon. It is assumed that the loss of sodium is negligible after carbon is completely converted. In these instances our model predictions agree well with the measured sodium losses.

Table 10.4. Experimental and predicted sodium release for single droplet experiments. The mean square difference is 28.3 for the bold face numbers. The experimental data were obtained in the ÅAU reactor (14).

Gas	Mole %	T (°C)	C.B. time (s)	Na exp (%)	Na calc (%) mass transfer	Na calc (%) kinetics only	Na calc (%) η × kinetics	Na calc (%) overall
H_2O	15	800	15	-3±1.4		0.47	0.47	**0.46**
	15	900	15	4±7.1		5.0	4.9	**4.8**
CO_2	1	900	85	17.4±5.7		21.2	20.7	**19.9**
	2	800	85	4.0±1.8		2.6	2.6	**2.6**
	2	900	85	7.6±5.8		15.3	14.9	**14.3**
	4	900	100	14.5±13.4		11.8	11.5	**11.0**
O_2	1	800	115	1.3±2.2	59.8	6.1	5.6	**5.1**
	1	900	115	24.8±8.9	100.0	30.2	28.5	**25.4**
	4	800	200	0.3±4.2	17.8	3.2	2.8	**2.4**
	4	900	20	67.4±15.6	**77.8**	16.4	14.4	12.0
	7	800	20	23±na	**10.1**	3.0	2.5	2.0
	7	900	20	60.1±27.6	**47.5**	16.9	13.8	10.4
N_2	100	800	165	8±na		5.0	5.0	**4.9**
	100	900	165	36.5±19.3		37.0	36.6	**35.9**
CO	4	900	165	37.9±5.0		37.0	36.6	**35.9**
	12	800	20	0±na		0.63	0.62	**0.62**
	12	900	20	5.7±3.8		6.6	6.4	**6.3**
	12	900	100	25.3±3.4		26.4	26.1	**25.5**
	12	900	165	32.2±8.0		37.0	36.6	**35.9**

na = not available

The sodium lost during devolatilization has been accounted for. The experimental amount of sodium released during char burning was calculated as the amount of sodium in the black liquor solids minus that released during devolatilization minus that remaining in the char after the indicated char burning time. The sodium released during devolatilization was taken to be 13% at 900°C and 18% at 800°C. For water vapor the experiments showed that 19% of the sodium was released during devolatilization at 900°C and 12% at 800°C. The predicted fraction sodium lost for the data in Table 10.5 is plotted in Figure 10.1. No empiricism was needed to obtain a good fit of data.

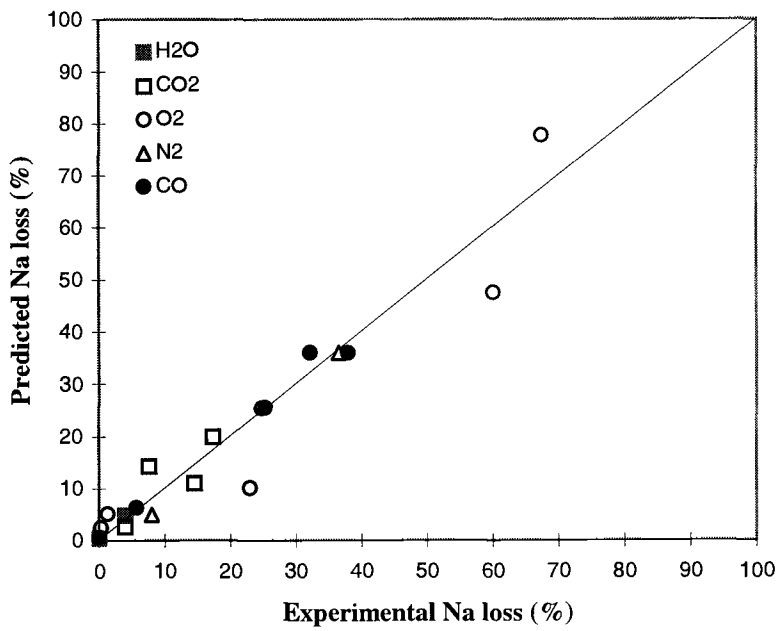

Figure 10.1. Sodium retained in char residue versus reaction time for black liquor droplets burned, pyrolyzed, or gasified at 800°C and 900°C.

Three of the circles in Figure 10.1 appear to have a large difference between experimental and predicted sodium loss. The difference would be even higher, if chemical kinetics would limit the overall rate. However, if the sodium release at these conditions is essentially film mass transfer controlled, then, one can obtain a reasonable agreement between experimental and predicted sodium loss. This could take place if a

significant temperature gradient existed within the particle. The literature indicates that there is a temperature difference of 100 degrees or more between the core of the particle and the surface for 2-3 mm black liquor droplets burned in air at 800°C (18). Verrill et al. have shown that the release of sodium may indeed be enhanced by to the presence of oxygen (24). Therefore, the predicted sodium losses for the indicated experiments were calculated based on the assumption that they are controlled by film mass transfer only.

The effect of gas composition is of minor importance as does the form of the sodium released rate equation indicates. It does not include any dependence on gas composition even though it is known that the presence of CO and CO_2 does inhibit the release of sodium. Figure 10.2 shows data with corresponding model predictions for 15% $H_2O(g)$, 1% CO2, 12% CO, 1% O_2, and 100% N_2 for large droplets burning at 900°C. The agreement is good for all data points regardless of the gas composition. This indicates that the current form of the carbonate reduction rate equation provides a reasonable estimator of sodium release rates.

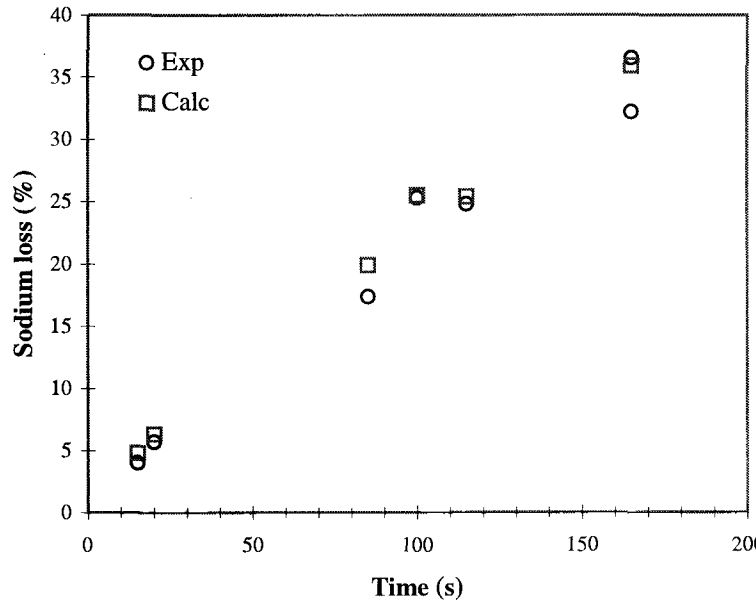

Figure 10.2. The effect of gas composition is negligible for large droplets burning at 900°C in different gas compositions: 15% H_2O(g), 1% CO2, 12% CO, 1% O_2, and 100% N_2.

100 μm Particles

The experimental sodium release data as well as the model predictions for the LEFR experiments are summarized in Table 10.5.

Table 10.5. Experimental and predicted sodium release for LEFR experiments. Mean square difference: 58.1.

Gas	Mole %	T_{fur} (°C)	T_{par} (°C)	time (s)	Na exp (%)	Na calc (%)
N_2	100	700	700	0.79	0.2	< 0.1
	100	900	900	0.7	4.1	0.5
	100	1100	1100	0.63	9.6	10.4
O_2	4	700	799	0.79	0.4	< 0.1
	4	900	986	0.7	2.8	2.1
	4	1100	1175	0.63	15.0	22.0
	21	700	1149	0.79	25.3	17.1
	21	900	1297	0.7	36.8	42.6
	21	1100	1448	0.63	27.7	45.9

Table 10.5 shows that the agreement between experimental and theoretical sodium loss is generally good except at high oxygen concentrations. This was also the case for the 2-3 mm droplets. Figure 10.3 shows the experimental sodium loss as a function of the actual particle temperature for the 100 μm particles. The particle temperature increases with increasing oxygen concentration. The experimental and predicted loss of sodium increases rapidly at oxygen concentrations above 4%. The particle temperature estimation is based on the method of Reis (19).

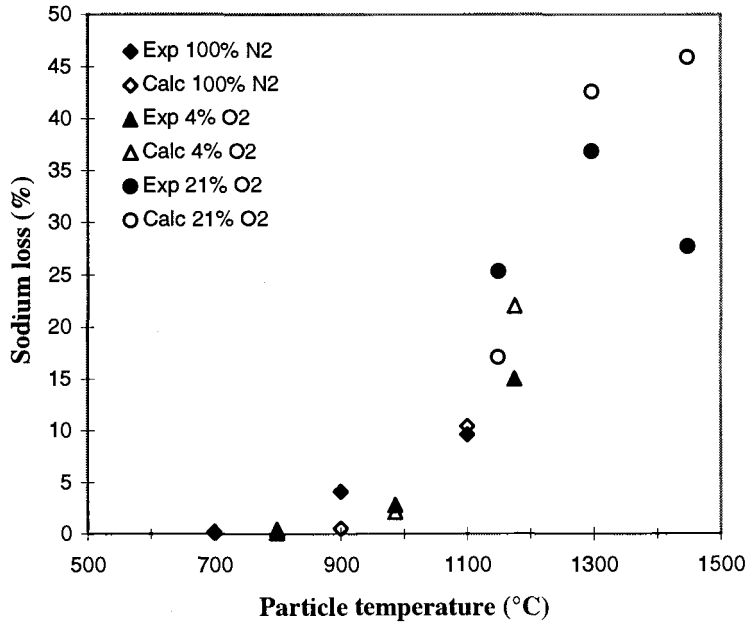

Figure 10.3. Experimental sodium loss versus actual particle temperature. Residence time: 0.6-0.8s.

One should avoid comparing LEFR data directly with single droplet data, because of a significant difference in reactor residence time. Experimental sodium loss in the LEFR with 100 μm particles at similar conditions were less than with the 2-3 m droplets. Table 10.6 shows a sodium loss of 2.8% in 4% O_2 at 900°C in the LEFR, whereas the single droplet furnace yields a sodium loss of 67% at similar conditions. If the residence times were the same one would actually obtain a higher sodium loss for the smaller particles. The effect of particle size is illustrated by Figure 10.4. It shows that small particles yield more sodium than large do for the same char burning time. Calculations are based on the assumption that the particle temperature is the same as the indicated furnace temperature.

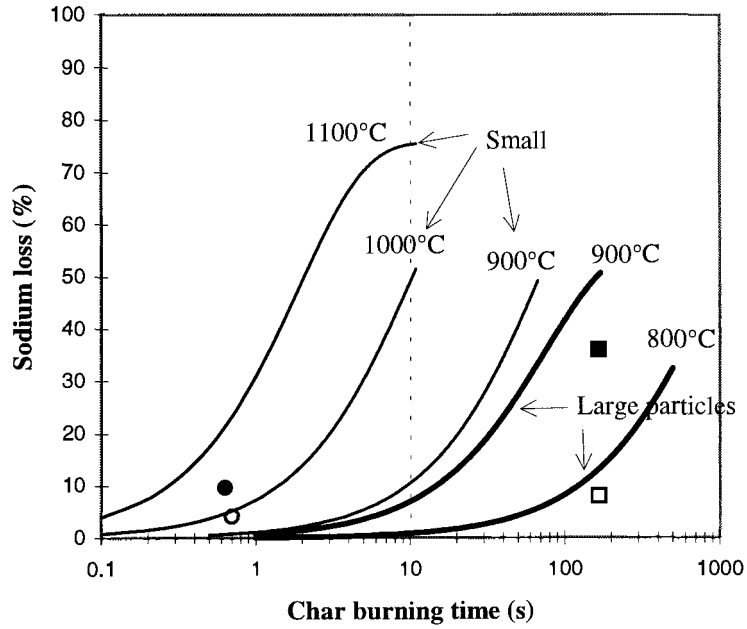

Figure 10.4. Sodium loss as a function of particle size and char burning time in 100% N_2. Solid lines are generated by the model. The thin lines are for 100 μm particles and the thick lines for 2.9 mm droplets. Experimental data points: •, 100 μm particle at 1100°C; O, 100 μm particle at 900°C; ■, 2.9 mm droplet at 900°C; □, 2.9 mm droplet at 800°C.

Potassium and chloride release

The release of potassium and chloride was modeled as the competing processes of evaporation of alkali metal chlorides, and sodium and potassium vaporization via reduction of Na_2CO_3 and K_2CO_3. Table 10.6 summarizes the data for potassium and chloride release during char burning. The predicted values are based on the method of Reis (19).

Table 10.6. Experimental and predicted potassium and chloride release for LEFR experiments. The mean square differences for K and Cl are, 79.6 and 30.7, respectively.

Gas	Mole %	T (°C)	time (s)	K exp (%)	K calc (%)	Cl exp (%)	Cl calc (%)
N_2	100	700	0.79	3.4	0.1	16.2	0.2
	100	900	0.7	7.2	1.0	36.7	15.0
	100	1100	0.63	9.8	16.9	75.1	54.5
O_2	4	700	0.79	2.4	1.2	17.5	8.0
	4	900	0.7	3.5	2.8	26.1	37.7
	4	1100	0.63	15.9	39.1	57.8	56.5
	21	700	0.79	23.1	10.7	60.7	50.2
	21	900	0.7	29.2	21.4	55.5	62.6
	21	1100	0.63	33.6	46.7	83.7	70.5

Table 10.6 shows that the agreement between experimental and calculated values is generally reasonable, however, not as good as for sodium. The potassium release predictions are always low at low temperatures and high at high temperatures. The poor agreement at 1100°C is probably due to an overprediction of the rate of potassium carbonate reduction, and at 700°C possibly due to an underprediction of the reduction rate. This is caused by the modified sodium carbonate reduction rate equation being used, because no experimental data is yet available for potassium carbonate reduction. Consequently, the rate of potassium carbonate reduction is predicted to be more important at 1100°C than it really is, and vice versa at 700°C. Figure 10.5 shows how much potassium is released experimentally and theoretically at the actual particle temperature.

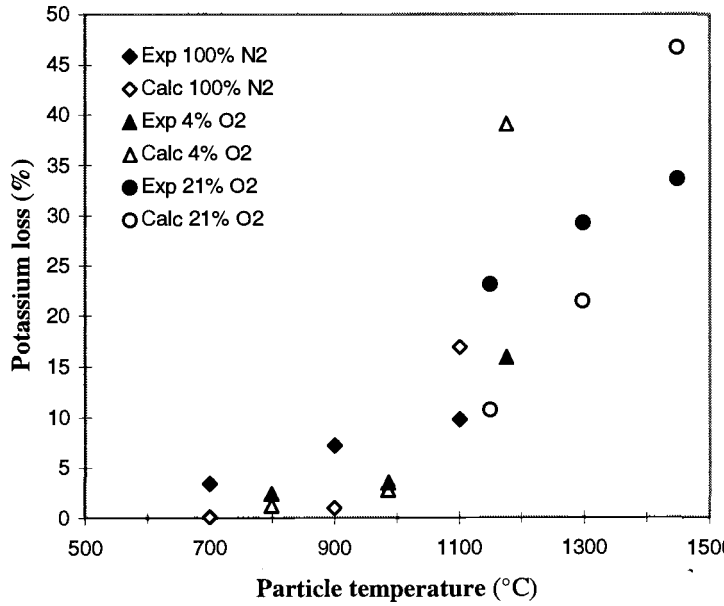

Figure 10.5. Experimental and calculated potassium loss at actual particle temperature.

For chloride, the agreement is generally reasonable except when only nitrogen is present. The reason may be due to experimental error. Figure 10.6 shows the theoretical and experimental chloride release values as a function of actual particle temperature.

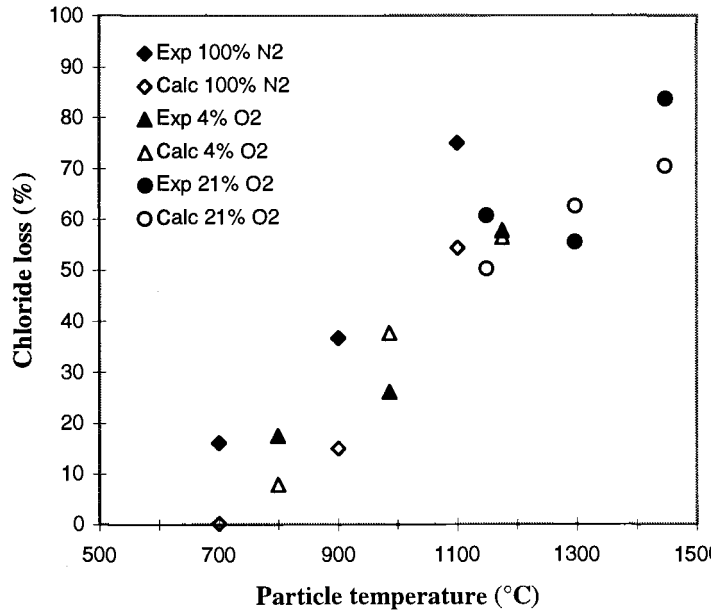

Figure 10.6. Experimental and calculated chloride loss at actual particle temperature.

Sulfur release

The sulfur release models give fair predictions of the rates of H_2S and COS formation from char particles when compared with the data when both $H_2O(g)$ and CO_2 are present. H_2S and COS formation can account for all the sulfur released at these conditions. However, these models do not apply if no CO_2 or $H_2O(g)$ is present. Table 10.7 summarizes the data for sulfur release during char burning. The droplet temperature is 900°C.

Table 10.7. Experimental and predicted sulfur release from single droplet experiments. The mean square difference is 66.9.

Gases	Mole %	S exp (%)	S calc (%)
CO_2+H_2O	10+5	14	16.1
CO_2+H_2O	10+15	16	33.6
CO_2+H_2O+CO	10+10+10	28	33
CO_2+H_2O+CO	5+5+5	37	12.1
CO_2+H_2O+CO	5+10+5	36	19.6

The scatter in the agreement between experimental and predicted values may be attributed to the fact that the gas composition within the particle may be different from the external, bulk concentration. This is particularly true for the larger particles (2-3 mm droplet). This remains to be tested with small particles in LEFR experiments at similar conditions as in Table 10.7.

The models predict that the rates of H_2S and COS release decrease with increasing temperature due to a decrease in the equilibrium partial pressures of H_2S and COS. This probably accounts for the higher sulfur release observed in colder lower furnaces in recovery boilers. However, at high H_2O(g) concentrations sulfur loss is overpredicted, and at low CO_2 concentrations it is underpredicted. This could indicate that all sulfur release mechanisms are not considered. E.g. direct vaporization of SO, SO_2, and SO_3 has been found in mass spectrometry studies for black liquor (25). Thermodynamic equilibrium calculations predict that the concentration of SO_2 becomes increasingly important at higher temperatures, Figure 10.7. Thus, SO_2 may further enhance the release of sodium and potassium by depleting Na_2O and K_2O through reactions 18 and 19 in the gas film surrounding the particle.

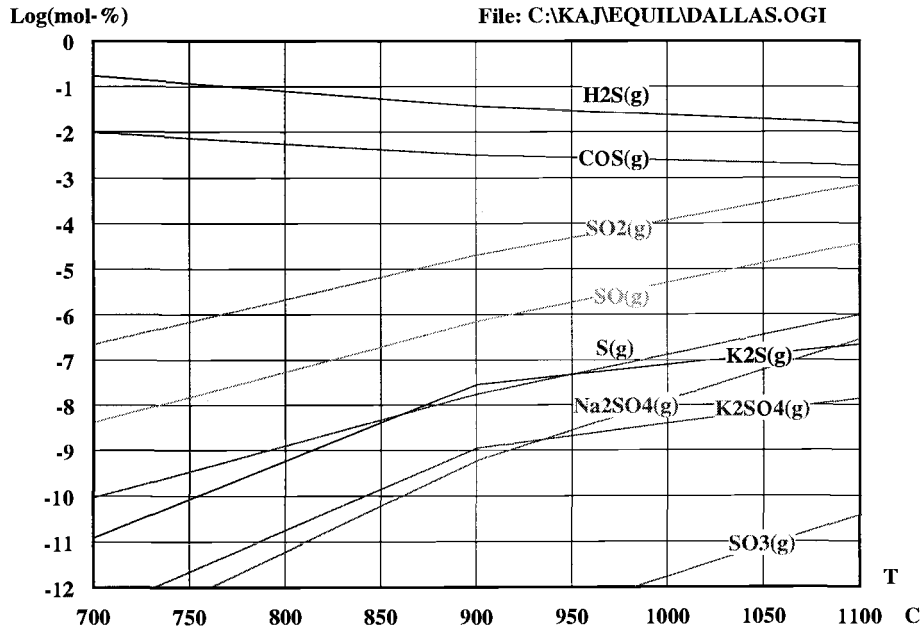

Figure 10.7. Thermodynamic equilibrium mole fractions of main sulfur gas species in 5% H_2O, CO_2 and CO. Calculations were performed with HSC Chemistry (10). The following particle smelt composition is assumed: 66.31% C, 0.43% NaCl, 0.01% KCl, 10.26% Na_2CO_3, 0.18% K_2CO_3, 11.23% Na_2S and Na_2SO_4, 0.18% K_2S and K_2SO_4.

DISCUSSION

The unified model presented for the release of inorganic emissions during black liquor char burning is the first model developed to date. The ability to predict is best for sodium, for large as well as for small particles (Tables 10.5 and 10.6). Carbonate reduction, the main sodium and potassium release mechanism, is essentially an irreversible reaction at typical recovery boiler conditions, because elemental sodium and potassium react rapidly in the gas phase with oxygen, CO_2, and SO_2. For potassium the agreement is reasonable but not as good as for sodium. One reason is that the potassium release model lacks an experimental data-based reduction rate equation. Another reason could be that the experimental data available has not been reproduced rigorously. Experimental difficulties are caused by the fact that there are relatively small amounts of

potassium in the black liquor initially. This may result in poor accuracy in the quantitative measurements.

The calculated chloride release when oxygen is present is quite good, but in an inert atmosphere the predicted values are much lower than the experimental values. The explanation for the difference at lower oxygen concentrations remains to be determined. The sulfur release model overpredicts sulfur loss with high $H_2O(g)$ concentrations and underpredicts at low CO_2 concentrations. This question may need the most attention in future modeling efforts.

Greater inorganic emissions are expected from smaller particles at a similar reaction time. This is a result from a lesser influence of pore diffusion and film mass transfer effects. The Thiele modulus number (equation 10-6) becomes smaller with decreasing particle diameter. Thus, the effectiveness factor approaches unity (equation 10-5). The mass transfer coefficient increases as the diameter decreases according to the definition of the Sherwood number.

Table 10.8 summarizes the mean square differences for all the different elements accounted for. It shows that chloride and sodium have the best agreements of the inorganic elements. Potassium and sulfur have the poorest agreements.

Table 10.8. The mean square differences for the different element models.

Element	Mean Square Difference
Carbon (O_2+CO_2) f=1	14.4
Carbon (O_2+CO_2) f=0	13.0
Carbon (H_2O+CO) f=1	42.2
Carbon (H_2O+CO) f=0	48.7
Chloride	30.7
Sodium (large particles)	28.3
Sodium (small particles)	58.1
Sulfur	66.9
Potassium	79.9

Potassium and chloride release can also be expressed in terms of enrichment factors. Increasing K or Cl release increases enrichment if the loss of sodium is assumed constant. Reis et al. (20) have found that both potassium and chloride enrichment decrease as particle temperature increases. Vakkilainen et al. (21) discovered that SO_2 can increase Cl volatilization, but this has not yet been taken into account in the current Cl release model.

CONCLUSIONS

The unified model presented herein contains sub-models that can accurately predict the release of sodium, sulfur, potassium, and chloride during char combustion of black liquor. The burning times for black liquor char combustion agree well with experimental data. Single particle data (2-3 mm) shows on a per unit mass basis less fume formation than do 100 μm particles. This apparently surprising result is due to the difference in residence time and the fact that smaller particles have a smaller resistance to pore diffusion and film mass transfer.

With respect to black liquor char burning, the following general conclusions can be assessed from the model predictions and presented experimental data:

1. The release of sodium, potassium, and chloride increases with increasing particle temperature.
2. Sulfur release decreases with increasing particle temperature.
3. Fume generation increases with decreasing particle size.
4. Carbonate reduction is more important in sodium and potassium volatilization than is vaporization of the chlorides at elevated temperatures, because the kinetics of carbonate reduction is more temperature sensitive than are the vapor pressures of NaCl and KCl.

5. At high oxygen concentrations and furnace temperatures, the internal particle temperatures may be higher than measured particle surface temperatures. Hence, fume formation is essentially film mass transfer limited at high oxygen concentrations.

The implications are to recovery boiler operation that higher operational temperatures in the lower furnace and increased air supplied there may decrease sulfur release, and increase fume generation by increasing vaporization of Na(g), K(g), NaCl(g), and KCl(g). This leads to lower enrichment because Na vaporization increases faster with increasing temperature than does NaCl or KCl. Conversely, lower temperatures and oxygen concentrations, as sometimes is used to combat NO_x, will decrease the rate of fume formation but will increase K and Cl enrichment.

ACKNOWLEDGMENT

This work was supported by the U.S. Department of Energy through the Office of Industrial Technology and by the Niemi Foundation at Oregon State University. Support for one of the authors (TMG) was provided by the American Forest and Paper Association's Recovery Boiler Committee and the Institute of Paper Science and Technology.

NOMENCLATURE

Symbol	**description, dimension**
[ ]	symbol for concentration, mol (unless otherwise indicated)
A,B,C,D	fitted parameters for sulfur release equilibrium constants, dimensionless
A_p	external surface area of char particle, cm^2
C_i	concentration of species i in gas film, mol/m^3
$[COS]_{eq}$	equilibrium concentration of COS, mol/m^3

D_p	diameter of particle, m
$\mathcal{D}_i$	diffusivity of gas species i, cm^2/sec
E	reduction efficiency at any time, dimensionless
$[H_2S]_{eq}$	equilibrium concentration of H_2S, mol/m^3
$K_{C,COS}$	equilibrium constant for COS formation, $(mol/m^3)^{-1}$
$K_{C,H2S}$	equilibrium constant for H2S formation, $(mol/m^3)^{-1}$
$k_{m,i}$	film mass transfer coefficient of species i, cm/sec
$k_{r,i}$	apparent first order rate constant for carbon gasification reaction, 1/s
M_{Ti}	Thiele modulus, dimensionless
n	number of experimental data points, dimensionless
η_i	effectiveness factor to account for the effects of intraparticle diffusion, dimensionless
P_i	partial pressure of gases, bar
P_{tot}	atmospheric pressure, bar
R	gas constant, J / mol K
R_{COS}	rate of reaction of Na_2S to COS, mol Na_2S/sec
R_{H2S}	rate of reaction of Na_2S to H_2S, mol Na_2S/sec
$R_{c,i}$	kinetic rate of reaction of species i, mol/sec
$R_{m,i}$	rate of gas transport of species i, mol/sec
Sh	Sherwood number, dimensionless = $k_{m,i} D_p / \mathcal{D}_i$
t	time, sec
T	temperature, K
x_a	mole fraction of species a in the liquid phase, dimensionless
y_a	mole fraction of species a in the vapor phase, dimensionless
V_p	particle volume, m^3
X_s	fraction of sulfide that has reacted away, dimensionless

REFERENCES

1. Frederick, W.J., Combustion Processes in Black Liquor Recovery: Analysis and Interpretation of Combustion Rate Data and an Engineering Design Model, U.S. DOE Report DOE/CE/40637-T8 (DE90012712), March, 1990

2. Kulas, K.A., An Overall Model of the Combustion of a Single Droplet of Kraft Black Liquor, Ph.D. thesis, The Institute of Paper Science and Technology, Atlanta, GA, January, 1990

3. Wåg, K.J., Frederick, W.J., Sricharoenchaikul, V., Grace, T.M., Kymäläinen, M., Proc. TAPPI-CPPA Int'l Chemical Recovery Conference, April 24-27, Toronto, Canada, 1995

4. Li, J., van Heiningen, A.R.P., Chem.Eng.Sci., Vol.49, No.24, p.4143-4151, 1994

5. Frederick, W.J., Hupa, M., Combustion Properties of Kraft Black Liquors, U.S. DOE Report DOE/CE/40936-T1 (DE94007502), April, 1993

6. Grace, T.M., Cameron, J.H., Clay, D.T., Char Burning, Project 3473-6, Summary Technical Report, The Institute of Paper Chemistry, February 22, 1985

7. Sjöberg, M. and Cameron, J.H., AIChE Symposium Series, 239(80):35-40, 1984

8. Grace, T.M., Lien, S.J., Brown, C.A., Proc. TAPPI Int'l Chemical Recovery Conference, Seattle, WA, p.539-550, 1992

9. Li, J., Rate Processes During Gasification and Reduction of Black Liquor Char, Ph.D. thesis, McGill U., Montreal, Canada, October, 1989

10. HSC Chemistry for Windows Ver. 2.0, Outokumpu Research Ltd., Finland, 1994

11. Levenspiel, O., The Chemical Reactor Omnibook, OSU Book Stores Inc., January, 1989

12. Chemsage Ver. 3.0, GTT-Technologies, Germany, January, 1994

13. Li, J., van Heiningen, A.R.P., TAPPI J., Vol.73, No.12, p.213-219, 1990

14. Frederick, W. J. Iisa, K. Wåg, K. J. Reis. V. V. Boonsongsup, L. Hupa, M. Forssén, M., Sodium and Sulfur Release and Recapture During Black Liquor Burning, U.S. Department of Energy Report DOE/CE/40936-T2, August, 1995

15. Gairns, S.A., Kubes, G.J., van Heiningen, A.R.P, Proc. TAPPI-CPPA Int'l Chemical Recovery Conference, April 24-27, Toronto, Canada, 1995

16. Cameron, J.H., J. Pulp & Paper Science, Vol.14, No.4, p.J76-J81, July, 1988

17. Frederick, W.J., Hupa, M., Gasification of Black Liquor at Elevated Pressures, Åbo Akademi U., Combustion Chemistry Research Group Report 90-12, 1990

18. Frederick, W.J., Hupa, M., Stenberg, J., Hernberg, R., FUEL, Vol.73, No.12, p.1889-1893, 1994

19. Reis, V.V., Potassium and Chloride Release During Black Liquor Combustion, M.S. thesis, Oregon State U., July, 1994

20. Reis, V.V., Frederick, W.J., Wåg, K.J., Iisa, M.K., Sinquefield, S.A., Effects of Temperature and Oxygen Concentration on Potassium and Chloride Enrichment During Black Liquor Combustion, TAPPI J., Vol.78, No. 12, p.67-76, 1995

21. Vakkilainen, E.K., Frederick, W.J., Reis, V.V., Wåg, K.J., Proc. TAPPI-CPPA Int'l Chemical Recovery Conference, April 24-27, Toronto, Canada, 1995

22. Srinivasachar, S., Helble, J.J., Ham, D.O., Domazetis, G., Prog.Energy Combust.Sci., Vol.16, p.303-309, 1990

23. Helble, J.J., Srinivasachar, S., Boni, A.A., Charon, O., Modestino, A., Combust.Sci. and Tech., Vol.81, p.193-205, 1992

24. Verrill, C.L., Wessel, R.A., Sodium Loss During Black Liquor Drying and Devolatilization - Application of Modeling Results to Understanding Laboratory Data, Proc. TAPPI-CPPA Int'l Chemical Recovery Conference, April 24-27, Toronto, Canada, 1995

25. Dayton, D.C., Frederick, W.J., Direct Observation of Alkali Vapor Release During Biomass Combustion and Gasification. 2. Black Liquor Combustion at 1100°C, ENERGY & FUELS, Vol.10, No.2, p.284-292, 1996

26. ChemApp, GTT-Technologies, Germany, 1996

Chapter 11
Conclusions and Recommendations

In order to improve the design and operation of black liquor recovery furnaces, it is necessary to constantly improve the basic understanding of black liquor combustion. This thesis was an attempt to characterize black liquor char as a fuel and its burning behavior in typical recovery boiler environments by experimental and modeling methods. The contributions to achieving this goal are summarized in this chapter.

Black liquor char is an isotropic material consisting of non-graphitizable carbon and inorganic matter. It is comprised of two phases, amorphous being the major and crystalline being the minor. For the chars prepared in this study, the inorganic matter is found in whiskers and in a coating on the char surfaces. The whiskers and the coating probably consist of sodium carbonate and sulfate. The amount of whiskers decreased at higher pyrolysis temperatures and devolatilization times. This indicates that the inorganic matter is not simply dispersed uniformly within the char matrix. The reason why black liquor char is more reactive than alkali impregnated chars could be that there are less catalytic sites and active free carbon sites present in alkali impregnated chars.

The physisorption isotherms for nitrogen on char were of type V with strong hysteresis. The chemisorption isotherms measured with CO_2 were of type I with weak hysteresis. The pores are a mixture of tapered and wedge shaped pores with either open ends or narrow necks at one or both ends with meso- and micropores being the dominating pore types. The total surface area increased by one order of magnitude at about 60% carbon conversion, and the average pore size decreased correspondingly by an order of magnitude. The active surface area increased with temperature and carbon conversion. The reactivity increased at higher carbon conversions, apparently because the high pyrolysis temperature chars contained more edge atom structures particularly zig-zag edges.

In combustion experiments carried out at 1100°C using a convective flow reactor coupled to a Molecular Beam Mass Spectrometer to monitor the combustion products

evolved. The reaction of carbon with CO_2 and O_2 was strongly limited by pore diffusion and film mass transfer. The results from the MBMS showed that more CO was formed in gas environments with 10% carbon dioxide compared to when oxygen was present. NaCl was the main sodium-containing species measured. SO_2 and H_2S were the main sulfur-containing species released. Models were developed for predicting the rate of carbon release in CO_2, O_2, and CO_2 + O_2 containing gas environments. Using these models it was found that the rate of carbon removal was not additive in CO_2 and O_2 separately compared to when they were present simultaneously. The carbon removal rate in CO_2 was essentially the same regardless if O_2 was present or not. The carbon removal rate in O_2 was the fastest.

Thermobalance experiments showed that the amount of inorganic carbonate in the char residue was higher at high CO_2/CO ratios than at low, when the gasification gases were turned off at 700°C. This indicated that there were a lot more carboxylic groups in the char at high CO_2/CO ratios than at low, and more phenolate groups in the char at low CO_2/CO ratios. This is apparently the suppression mechanism during decomposition of sodium carbonate. However, the decomposition seized when all carbon was depleted which occurred more rapidly the higher the CO_2 partial pressure. According to MBMS spectra, CO was the only gas produced during carbonate decomposition, sulfate reduction, and CO_2 gasification .

A unified chemical reaction mechanism and a kinetic model for carbon removal were presented for a gas environment containing CO_2, water vapor, CO, and H_2. The transfer of oxygen atoms from a catalyst site to a free carbon site and the subsequent desorption of CO is the rate limiting step. An assessment of available data indicated that the addition of CO_2 suppresses the rate of water vapor gasification, and that CO may inhibit the transfer of oxygen by occupying free carbon sites. Simultaneous CO_2 and water vapor gasification was found to be additive under atmospheric pressure but not at higher pressures. The water gas shift reaction is known to be catalyzed by the presence of alkali species, and equilibrium is therefore probably approached rapidly in typical black liquor combustion conditions.

Relevance

The knowledge of black liquor char combustion develop in this work is an improved combustion model to predict the release of key elements and the degree of reduction which is needed to improve the operation and design of recovery boilers. Improved sulfate and carbonate reduction rate equations were obtained that fit new experimental data much better. Using these improved rate equations, it was possible to determine that a high degree of sulfate reduction can be obtained even in oxygen containing atmospheres. This is in part because the carbon in the char provides a source for CO that will prevent oxygen from reaching the char surface, thereby preserving a high degree of reduction. Reduction increases with droplet size and with increasing temperature, with the latter being more important in determining the extent of reduction. The gas composition had a minor effect on reduction. At a given temperature, any variable that increases the char burnout time increases reduction. After the char carbon is nearly depleted, reoxidation is the most important factor affecting reduction efficiency.

Further modeling of the combustion process showed that CO_2 and water vapor are the principal pathways for carbon removal in a typical recovery furnace, and that oxygen plays a secondary role for carbon removal by increasing the amount of CO_2 and $H_2O(g)$. The release of inorganic emissions (except for sulfur) increases with temperature. Fume generation increases with decreasing particle size. Carbonate reduction is more important for sodium release than alkali chloride vaporization. At high oxygen concentrations and furnace temperature, the internal particle temperatures may be higher than measured surface temperatures. Hence, fume formation becomes essentially film mass transfer controlled. Higher operational temperatures in the lower recovery furnace and increased air supplied there may decrease sulfur release, but increase fume generation.

Recommendations

A list of recommendations is given as follows:

1. NMR experiments would improve the understanding of the molecular structure of black liquor char by identifying the key building blocks and complementing the SEM and TEM data already obtained.
2. Scanning tunneling microscopy and Auger spectroscopy is recommended for structural studies in verifying the pore shapes of black liquor char.
3. Immersion calorimetry is recommended for studying the micropores in black liquor char and to complement the Dubinin-Radushkevich approach of gas adsorption.
4. Experiments using Small-angle scattering of X-rays and neutrons could give useful structural information of the char surface and the pores.
5. In-situ Fourier transformed infrared spectroscopy is recommended in studying the chemical transformations of catalyst moieties during black liquor char burning.
6. It is recommended that black liquor char gasification be studied with CO_2 isotopes so that the release of regular CO_2 molecules can be monitored in the MBMS.
7. The thermobalance should be close-coupled to the MBMS so that condensable species are preserved to validate the release of elemental sodium from carbonate reduction.
8. A DSC apparatus that can reach temperatures above 1000°C should be used for identifying exo- and endotherms above 600°C.
9. A method based on the amount of heat released is suggested to estimate the element distribution during devolatilization.
10. There is no published thermobalance data at atmospheric pressure in mixtures of water vapor and CO_2.
11. More data on the water gas shift equilibrium issue is needed for black liquor char.
12. State-of-the-art equilibrium software (e.g. ChemApp) should be implemented to improve the procedure for predicting the release of inorganic emissions.

Lastly, the novel field of ab initio simulation and application of molecular orbital calculations would improve the understanding of the heterogeneous combustion process. Much work is needed in collaboration with surface chemists to identify the appropriate structures needed as initial conditions for these operations.

12. Bibliography

BIBLIOGRAPHY

Adams. T.N., Frederick, W.J. 1988. *Kraft Recovery Boiler Physical and Chemical Processes*, New York, NY: American Paper Institute.

Aggarwal, R., Zaccharia, T. 1994. Parallel Computing, *Yosemite Colloquium on Recovery Boiler Modeling*, Yosemite Marriot, California, September 25-28 1994.

Backman, R. 1989. *Sodium and Sulfur Chemistry in Combustion Gases*, Åbo Akademi University, paper VI, p.8: Academic Dissertation, May 12 1989.

Bartok, W., Sarofim, A.F. 1991. *Fossil Fuel Combustion*, New York, NY: John Wiley & Sons.

Behrens, R., Jr. 1987. New Simultaneous Thermogravimetriy and Modulated Molecular Beam Mass Spectrometry Apparatus for Quantitative Thermal Decomposition Studies, *Rev.Sci.Instrum.*, 58(3): American Inst. Physics, March 1987.

Cameron, J.H., Grace, T.M. 1983. Kinetic Study of Sulfate Reduction With Carbon, *Ind.Eng.Chem.Fundam.*, 22(4):486-494.

Cameron, J.H., Grace, T.M. 1985, Kinetic Study of Sulfate Reduction With Kraft Black Liquor Char, *Ind. Eng. Chem. Fundam.*, 24(4):443-449.

Cameron, J.H. 1988. *J. Pulp & Paper Science*, 14(4): J76-J81.

Carangal, A. 1995, *Release of NO During Black Liquor Pyrolysis*, M.S. thesis, Oregon State University.

Cerfontain, M.B., Meijer, R., Kapteijn, F., Moulijn, J.A. 1987, Alkali-Catalyzed Carbon Gasification in CO/CO_2 Mixtures: An Extended Model for the Oxygen Exchange and Gasification Reaction, *J. Catalysis*, Vol.107, p.173-180.

Cerfontain, M.B., Kapteijn, F., Moulijn, J.A. 1988. Characterization of Alkali Carbonate Catalysts for Carbon Gasification with ^{18}O Labeled CO_2, *CARBON*, 26(1), 41-48.

ChemApp 1996. not released at time of printing, GTT-Technologies, Herzogenrath, Germany.

ChemSage Ver. 3.01 1994. GTT-Technologies, Herzogenrath, Germany.

Clay, D.T., Lien, S.J., Grace, T.M., Macek, A., Semerjian, H.C., Amin, N., Charagundla, S.R. 1987. *Fundamental Studies of Black Liquor Combustion, Report No.2*, U.S. Department of Energy Report DE88005756, January 1987.

Clay, D.T., Lien, S.J., Grace, T.M., Brown, C.A., Empie, H.L., Macek, A., Amin, N., Rao Charangundla, S. 1990. *Fundamental Studies of Black Liquor Combustion, Report No.4*, U.S. Department of Energy Report DOE/CE/40637-T9 (DE91018580), March 1990.

CRC Handbook of Chemistry and Physics 1985-1986. ed. Weast, R.C.: CRC Press, Inc..

Davis, M., Wåg, K. 1996. *unpublished results*, National Renewable Energy Laboratory, Golden, CO, April 1996.

Dayton, D.C. 1996. *personal correspondence*, National Renewable Energy Laboratory, Golden, CO, May 6 1996.

Dayton, D.C., French, R.J., Milne, T.A. 1995. The Direct Observation of Alkali Release During Combustion and Gasification. 1. Application of Molecular Beam/Mass Spectrometry to Switchgrass Combustion, *ENERGY & FUELS*, 9(5): 855-865.

Dayton, D.C., Frederick, W.J. 1996. Direct Observation of Alkali Vapor Release During Biomass Combustion and Gasification. 2. Black Liquor Combustion at 1100°C, *ENERGY & FUELS*, 10(2): 284-292.

Delannay, F. 1984. *Characterization of Heterogeneous Catalysts*, Chemical Industries Vol.15, New York, NY: Marcel Dekker, Inc..

Differential Scanning Calorimeter, Operator's Manual 1993. TA Instruments, New Castle, Delaware.

Dogan, C. 1996, *personal correspondence*, U.S. Bureau of Mines, Albany, OR, April 30 1996.

Energy-Dispersive X-ray Microanalysis An Introduction 1996., Kevex Corporation, Foster City, CA, handout from Dr. Cindy Dogan, U.S. Bureau of Mines, Albany, OR, Spring 1996.

Frederick, W.J., Hupa, M. 1990. Gasification of Black Liquor at Elevated Pressures, Åbo Akademi University, *Combustion Chemistry Research Group Report 90-12*.

Frederick, W.J. 1990. *Combustion Processes in Black Liquor Recovery: Analysis and Interpretation of Combustion Rate Data and an Engineering Design Model*, U.S. Department of Energy Report DOE/CE/40637-T8 (DE90012712), March 1990.

Frederick, W.J., Hupa, M. 1991. Gasification of Black Liquor Char with CO_2 at Elevated Pressures, *TAPPI J.*, 74(7), 177-184.

Frederick, W.J., Hupa, M. 1993. *Combustion Properties of Kraft Black Liquors*, U.S. Department of Energy Report DOE/CE/40936-T1 (DE94007502), April 1993.

Frederick, W.J., Wåg, K.J., Hupa, M.M. 1993. Rate and mechanism of Black Liquor Char gasification With CO_2 at Elevated pressures, *Ind.Eng.Chem.Res.*, 32(8): 1747-1753.

Frederick, W.J., Hupa, M., Stenberg, J., Hernberg, R. 1994. Optical Pyrometric Measurements of Surface Temperatures During Black Liquor Char Burning and Gasification, *FUEL*, 73(12): 1889-1893.

Frederick, W.J., Iisa, K., Wåg. K.J., Reis, V.V., Boonsongsup, L., Forssén, M., Hupa, M. 1995. *Sodium and Sulfur Release and Recapture During Black Liquor Burning*, U.S. Department of Energy Report DOE/CE/40936-T2 (DE96006558), August 1995.

Forssén, M. 1991. *Sulfur Release During Pyrolysis of Single Black Liquor Droplets* (in Swedish), M.Sc. thesis, Åbo Akademi University.

Gairns, S.A., Kubes, G.J., van Heiningen, A.R.P 1995. *Sodium Loss Mechanisms and the Formation of Reduced Sodium During the Fast Pyrolysis of Kraft Black Liquor*, Proc. TAPPI-CPPA International Chemical Recovery Conference, Toronto, Canada.

Goerg, K.A., Cameron, J.H. 1986. *A Kinetic Study of Kraft Char Gasification with CO_2*, Proc. AIChE Summer National Meeting, Boston, MA, p.E7-E12, August 1986.

Goerg, K.A. 1989. *A Study of Fume Particle Deposition*, Ph.D. thesis, The Institute of Paper Science and Technology.

Grace, T.M., Cameron, J.H., Clay, D.T. 1985. *Char Burning, Project 3473-6, Summary Technical Report*, The Institute of Paper Chemistry, February 22 1985.

Grace, T.M., Cameron, J.H., Clay, D.T. 1986. Role of the sulfate-sulfide Cycle in Char Burning: Experimental Results and Implications, *TAPPI J.*, 69(10): 108-113.

Grace, T.M., Lien, S.J., Brown, C.A. 1992. *Char Bed Burning - Laboratory Studies*, Proc. TAPPI International Chemical Recovery Conference, Seattle, WA.

Harper, F.D. 1989. *Sulfur Release During the Pyrolysis of Kraft Black Liquor*, Ph.D. thesis, The Institute of Paper Science and Technology.

Helble, J.J., Srinivasachar, S., Boni, A.A., Charon, O., Modestino, A. 1992. Measurement and Modeling of Vapor-Phase Sodium Chloride Formed During Pulverized Coal Combustion, *Comb.Sci.Tech.*, Vol.81, p.193-205.

HSC Chemistry for Windows Ver. 2.03 1994. Outokumpu Research Ltd., Pori, Finland.

Hupa, M., Solin, Hyöty, P. 1987. Combustion Behavior of Black Liquor Droplets, *J. Pulp & Paper Science*, 13(2): J67-72.

Hylton, J.O. 1994. Information for Validation of Combustion Models, *Yosemite Colloquium on Recovery Boiler Modeling*, Yosemite Marriot, California, September 25-28 1994.

Hüttinger, K.J. 1988. Mechanism of Water Vapor Gasification at High Hydrogen Levels, *CARBON*, 26(1): 79-87.

IMSL MATH/LIBRARY User's Manual 1989. FORTRAN Subroutines for Mathematical Applications, Vol. 2, Chapter 5, p.640-652, IMSL, Inc., Houston, TX, August 1989.

Jones, A.K. 1989. *A Model of the Kraft Recovery Furnace*, Ph.D. thesis, The Institute of Paper Science and Technology.

Jones, A.K., Chapman, P.J. 1993. Computation Fluid Dynamics Combustion Modelling - A Comparison of Secondary Air System Designs, *TAPPI J.*, 76(7): 195-202.

Karvinen, R. 1994. Recovery Boiler Modeling, *Yosemite Colloquium on Recovery Boiler Modeling*, Yosemite Marriot, California, September 25-28 1994.

Kapteijn, F., Meijer, R., Moulijn, J.A. 1991. *Kinetics and Mechanism of the Alkali Catalyzed Gasification of Carbon*, Proc. International Conference on Coal Science, U. of Newcastle-upon-Tyne, Butterworth, Oxford, United Kingdom, 16-20 September 1991.

Kimura, S. 1993. *Mass Transfer Class Notes*, Oregon State University, Winter, 1993.

Kulas, K.A. 1990. *An Overall Model of the Combustion of a Single Droplet of Kraft Black Liquor*, Ph.D. thesis, The Institute of Paper Science and Technology.

Kymäläinen, M., Janka, K., Frederick, W.J., Sricharoenchaikul, V., Jivakanun, N., Wåg, K.J., Littau, M. 1995. *Sulfate Reduction in an Entrained-Flow Black Liquor Gasifier*, Proc. TAPPI-CPPA International Chemical Recovery Conference, Toronto, Canada.

Lee, S.R. 1993. *The Role of Carbon Dioxide in the Combustion of Kraft Black Liquor Char*, Ph.D. thesis, The Institute of Paper Science and Technology.

Levenspiel, O. 1972. *Chemical Reaction Engineering*, 2nd ed.: John Wiley & Sons.

Levenspiel, O. 1984. *Engineering Flow and Heat Exchange*: Plenum Press.

Levenspiel, O. 1989. *The Chemical Reactor Omnibook*: OSU Book Stores Inc..

Li, J. 1986. *Pyrolysis and CO_2 Gasification of Black Liquor*, M.S. thesis, McGill U., Montreal, Canada, February 1986.

Li, J., van Heiningen, A.R.P. 1986. Mass Transfer Limitations in the Gasification of Black Liquor Char by CO_2, *J. Pulp & Paper Science*, 12(5): J146-J151.

Li, J. 1989. *Rate Processes During Gasification and Reduction of Black Liquor Char*, Ph.D. thesis, McGill U., Montreal, Canada, October 1989.

Li, J., van Heiningen, A.R.P. 1989. Reaction Kinetics of Gasification of Black Liquor Char, *Canadian J. Chem. Eng.*, Vol.67, p.693-697, August 1989.

Li, J., van Heiningen, A.R.P. 1990. Kinetics of CO_2 Gasification of Fast Pyrolysis Black Liquor Char, *Ind.Eng.Chem.Res.*, 29(9): 1776-1785.

Li, J., van Heiningen, A.R.P. 1990. Sodium Emission During Pyrolysis and Gasification of Black Liquor Char, *TAPPI J.*, 73(12): 213-219.

Li, J., van Heiningen, A.R.P. 1991. Sulfur Emission During Slow Pyrolysis of Kraft Black Liquor, *TAPPI J.*, p.237, March 1991.

Li, J., van Heiningen, A.R.P. 1991. Kinetics of Gasification of Black Liquor Char by Steam, *Ind.Eng.Chem.Res.*, 30(7): 1594-1601.

Li, J., van Heiningen, A.R.P. 1994. The Rate Process of H_2S Emission During Steam Gasification of Black Liquor Char, *Chem.Eng.Sci.*, 49(24): 4143-4151.

Lourvanij, K. 1995. *Partial Dehydration of Glucose to Oxygenated Hydrocarbons in Molecular-Sieving Catalysts*, Ph.D. thesis, Appendix B, Oregon State University.

Lowell, S., Shields, J.E. 1991. *Powder Surface Area and Porosity*, 3rd ed.: Chapman & Hall.

Marsh, H. editor 1989. *Introduction to Carbon Science*, Butterworth & Co., Chapter 4 by H. Marsh and K. Kuo.

Martin, D.M. 1995. *The Pyrolysis of Fuel Nitrogen from Black Liquor*, Ph.D. thesis, The Institute of Paper Science and Technology.

MBMS manual 1996. *Flange Mounted Mass Filter Assembly*, p.8-5, Extrel Corp., Pittsburgh, PA.

McGee, H.A. 1991. *Molecular Engineering*, McGraw-Hill, Inc..

McKeough, P.J., Kurkela, M., Arpiainen, V., Mikkanen, P., Kauppinen, E., Jokiniemi, J. 1995. *The Release of Carbon, Sodium and Sulfur During Rapid Pyrolysis of Black Liquor*, Proc. TAPPI-CPPA International Chemical Recovery Conference, Toronto, Canada.

Medvecz, P. 1991. *Spectroscopic Evaluation of the Gas Phase Above a Burning Black Liquor Char Bed*, Ph.D. thesis, The Institute of Paper Science and Technology.

Meijer, R., Sibeijn, M., van Dillen, M.R.B., Kapteijn, F., Moulijn, J.A. 1991. Kinetics of the Alkali-Metal-Carbonate-Catalyzed Gasificatiion of Carbon. 2. The Water-Gas-Shift Reaction, *Ind. Eng. Chem. Res.*, 30(8): 1760-1770.

Meijer, R., van der Linden, B., Kapteijn, F., Moulijn, J.A. 1991. The Interaction of H_2O, CO_2, H_2, and CO With the Alkali-Carbonate/Carbon System: A Thermogravimetric Study, *FUEL*, Vol.70, p.205-214.

Meijer, R., Weeda, M., Kapteijn, F., Moulijn, J.A. 1991. Catalyst Loss and Retention During Alkali-Catalysed Carbon Gasification in CO_2, *CARBON*, 29(7): 929-941.

Meijer, R., Mühlen, H.-J., Kapteijn, F., Moulijn, J.A. 1991. Burn-off Behaviour in Alkali-Catalysed CO_2 Gasification of Bituminous Coal Char: A Comparison of TGA and Fixed-Bed Reactor, *Fuel Processing Technology*, Vol.28, p.5-17.

Meijer, R. 1992. *Kinetics and Mechanism of the Alkali-Catalyzed Gasification of Carbon*, Ph.D. thesis, U. of Amsterdam, Holland.

Miller, P.T. 1986. *Swelling of Kraft Black Liquor*, Ph.D. thesis, The Institute of Paper Science and Technology.

Mims, C.A., Pabst, J.K. 1983. Role of Surface Salt Complexes in Alkali-Catalyzed Carbon Gasification, *FUEL*, 62(2): 179-179.

Noopila, T.Hupa, M., *Measuring the Combustion Properties of Black Liquors by Different Techniques*, Åbo Akademi University, Combustion Chemistry Research Group Report 88-5, 1988

Nowak, P., Matys, P., Sabhapathy, P., Abdullah, Z., Salcudean, M. 1995. *Numerical Study of a Kraft Recovery Furnace*, Proc. TAPPI-CPPA International Chemical Recovery Conference, Toronto, Canada.

Overacker, N.L., Wåg, K.J., Frederick, W.J., Whitty, K.J. 1994. *Application of a Mechanism-Based Rate Equation to Black Liquor Gasification Rate Data*, Oregon State University.

Patrick, J. 1996. *personal correspondence*, National Renewable Energy Laboratory, Golden, CO, March 8 1996.

Patrick, J.W. editor 1995. *Porosity in Carbons, Characterization and Applications*: Halsted Press.

Perry's Chemical Engineers' Handbook, edited by R.H.Perry and D.W.Green, 6th ed., p.3-112, McGraw-Hill Book Company, 1984

Pianpucktr, R. 1996. *Formation of NO During Pyrolysis and Combustion of Kraft Black Liquor*, M.S. thesis, Oregon State University.

Pugliese, R.A. 1993. *Microprobe and Molecular-Beam Mass Spectrometry in Plasma-Enhanced Chemical Vapor Deposition*, Ph.D. thesis, U. of Massachusetts.

Quantachrome Corp. 1996. Report 8-29-96 from Dr. Carlos A. Leon y Leon D., Boynton Beach, FL.

Reed, S.J.B. 1993. *Electron Microprobe Analysis*, 2nd ed.: Cambridge U. Press.

Reeve, D.W. 1992. *The Kraft Recovery Cycle*, Kraft Recovery Operations Short Course.

Reid, R.C., Prausnitz, J.M. and Poling, B.E. 1987. *The Properties of Gases and Liquids*, 4th ed., New York, NY: McGraw-Hill Book Company.

Reis, V. 1994. *Potassium and Chloride Release During Black Liquor Combustion*, M.S. thesis, Oregon State University.

Reis, V.V., Frederick, W.J., Wåg, K.J., Iisa, M.K., Sinquefield, S.A. 1995. Effects of Temperature and Oxygen Concentration on Potassium and Chloride Enrichment During Black Liquor Combustion, *TAPPI J.*, 78(12): 67-76.

Robinson, M.L. 1987. *Characterization of Black Liquor Drop Drying in Air and Superheated Steam*, Ph.D. thesis, The Institute of Paper Science and Technology.

Robinson, J.W. 1994. *Undergraduate Instrumental Analysis*, 5th ed.: Marcel Dekker, Inc..

Rubinson, K.A. 1987. *Chemical Analysis*: Little, Brown & Company.

Rompho, N. 1996. M.S. thesis, Oregon State University, in progress.

Saastamoinen, J. 1988. *Modeling of Coal Pyrolysis and Combustion*, Am.Flame Res.Comm., Fall International Symposium, Pittsburgh, PA.

Samretvanich, A. 1996. M.S. thesis, Oregon State University, in progress.

Sams, D.A., Shadman, F. 1986. Mechanism of Potassium Catalyzed Carbon/CO_2 Reaction, *AIChE J.*, 32(7): 1132-1137.

Saviharju, K., Moilanen, A., van Heiningen, A.R.P. 1995. *New High Pressure Gasification Rate Data on Fast Pyrolysis of Black Liquor Char*, Proc. TAPPI-CPPA International Chemical Recovery Conference, Toronto, Canada.

Scoles, G. editor 1988. *Atomic and Molecular Beam Methods*, Vol.1, Chapters 2, 4, 6, 7: Oxford U. Press.

Sinquefield, S. 1996. Ph.D. thesis, Sandia National Laboratories, in progress.

Sjöberg, M., Cameron, J.H. 1984. A Kinetic Study of Sodium Sulfate Reduction by Carbon Monoxide Gas, *AIChE Symposium Series*, 239(80): 35-40.

Sjöström, E. 1981. *Wood Chemistry Fundamentals and Applications*, New York, NY: Academic Press, Inc..

Skoog, D.A., Leary, J.J. 1992. *Principles of Instrumental Analysis*, 4th ed.: Saunders College Publishing.

Smoot, L.D., Smith, P.J. 1985. *Coal Combustion and Gasification*, New York, NY: Plenum Press.

Somorjai, G. 1994. *Introduction to Surface Chemistry and Catalysis*: John Wiley & Sons.

Sricharoenchaikul, V. 1995. *Sulfur Species Transformations and Sulfate Reduction During Pyrolysis of Kraft Black Liquor*, M.S. thesis, Oregon State University.

Sricharoenchaikul, V., Frederick, W. J., Kymäläinen, M., Grace, T. M. 1995. *Sulfur Species Transformations and Sulfate Reduction During Pyrolysis of Kraft Black Liquor,* Proc. TAPPI-CPPA International Chemical Recovery Conference, Toronto, Canada.

Srinivasachar, S., Helble, J.J., Ham, D.O., Domazetis, G. 1990. A Kinetic Desription of Vapor Phase Alkali Transformations in Combustion Systems, *Prog.Energy and Comb.Sci.*, Vol.16, p.303-309.

Stewart, G.W., Chakrabarti, A., Moore, W.R. 1981. Reactions of Alkali Containing Species in Combustion Streams, *U.S. Department of Energy Proceedings: High-Temperature, High-Pressure Particulate and Alkali Control in Coal Combustion Process Streams*. p.275-300, Science Applications Inc., McLean, VA.

Sumnicht, D.W. 1989. *A Computer Model of a Kraft Char Bed*, Ph.D. thesis, The Institute of Paper Science and Technology.

Tavares, A., Tran, H., Barham, D., Rouilard, P., Adams, B. 1995. *Fume Chemistry, Morphology and Deposition in a Kraft Recovery Boiler*, Proc. TAPPI-CPPA International Chemical Recovery Conference, Toronto, Canada.

Tanganpanyapinit, V. 1996. M.S. thesis, Oregon State University.

Techakijkajorn, U. 1996. *Sintering of Fume Deposits in Kraft Recovery Boilers*, M.S. thesis, Oregon State University.

Thermal Analyst 2100 Operators Manual Ver. 8.6 1992. TA Instruments, New Castle, Delaware, September 1992.

Thompson, L. 1995. *The Depletion of Nitric Oxide by Reaction With Molten Sodium Carbonate and Sodium Carbonate/Sodium Sulfide Mixtures*, Ph.D. thesis, The Institute of Paper Science and Technology.

Thunman, H. 1994. *Combustion of Black Liquor Drops in A Kraft Recovery Furnace* (in Swedish), M.Sc. thesis, Chalmers University of Technology, Sweden.

Treybal, R.E. 1981. *Mass Transfer Operations*, 3rd ed., p.75, New York, NY: McGraw-Hill Book Company.

Turkdogan, E.T., Grieveson, P., Darken, L.S. 1963. Enhancement of Diffusion-Limited Rates of Vaporization of Metals, J. Phys. Chem., Vol.67, p.1647-1654

Vakkilainen, E.K., Frederick, W.J., Reis, V.V., Wåg, K.J. 1995. *Potassium and Chloride Enrichment During Black Liquor Combustion. Laboratory and Mill Measurements and A Mechanistic Model*, Proc. TAPPI-CPPA International Chemical Recovery Conference, Toronto, Canada.

van Heiningen, A.R.P., Arpiainen, V.T., Alén, R. 1992. *Effect of Liquor Type and Pyrolysis Rate on the Steam Gasification Reactivities of Black Liquors*, Proc. TAPPI International Chemical Recovery Conference, Seattle, WA.

Verrill, C.L. 1994. *Inorganic Aerosol Formation During Black Liquor Drop Combustion*, Ph.D. thesis, The Institute of Paper Science and Technology.

Verrill, C.L., Wessel, R.A. 1995. *Sodium Loss During Black Liquor Drying and Devolatilization - Application of Modeling Results to Understanding Laboratory Data*, Proc. TAPPI-CPPA International Chemical Recovery Conference, Toronto, Canada.

Walsh, A.R., Grace, T.M. 1989. TRAC: A Computer Model to Analyze the Trajectories and Combustion Behaviour of Black Liquor Droplets, *J. Pulp & Paper Science*, 15(3): J84-J89.

Walsh, A.R. 1989. *A Computer Model for In-Flight Black Liquor Combustion in A Kraft Recovery Furnace*, Ph.D. thesis, The Institute of Paper Science and Technology.

Welty, J.R., Wicks, C.E., Wilson, R.E. 1983. *Fundamentals of Momentum, Heat and Mass Transfer*, 3rd ed., John Wiley & Sons, p.487.

Wendt, J.O, *Lecture on Heterogenous Solid Phase Combustion*, Seminar on Advanced Combustion Technology for Protection of Environment, Sjökulla, Finland, April 15-17, 1991, Sponsored by Helsinki University of Technology, Laboratory of Energy Economics and Power Plants.

Weyerheuser Analytical & Testing Services 1994. Federal Way, WA, September 20 1994.

Whitty, K.J. 1993. *Gasification of Black Liquor Char With H_2O Under Pressurized Conditions*, M.S. thesis, Åbo Akademi University.

Whitty, K.J., Backman, R., Hupa, M. 1993. *An Empirical Rate Model for Black Liquor Char Gasification as a Function of Gas Composition and Pressure*, Proc. AIChE Conference, St.Louis, MO.

Whitty, K.J., Backman, R., Forssén, M., Hupa, M., Rainio, J., Sorvari, V. 1995. *Liquor to liquor Differences in Combustion and Gasification Processes: Pyrolysis Behavior and Char Reactivity*, Proc. TAPPI-CPPA International Chemical Recovery Conference, Toronto, Canada.

Wu, S.-L. 1995. *Kinetics of NO Reduction by Black Liquor Char*, M.S. thesis, Oregon State University.

Wåg, K.J. 1991. *A Rate Model for Gasification of Black Liquor Char with CO_2 Under Pressurized Conditions* (in Swedish), M.Sc. thesis, Åbo Akademi University.

Wåg, K.J., Frederick, W.J., Sricharoenchaikul, V., Grace, T.M., Kymäläinen, M. 1995. *Sulfate Reduction and Carbon Removal During Kraft Char Burning*, Proc. TAPPI-CPPA International Chemical Recovery Conference, Toronto, Canada.

Wåg, K.J., Reis, V.V., Frederick, W.J., Grace, T.M. 1995. *Release of Inorganic Emissions During Black Liquor Char Combustion: A Predictive Model*, Proc. TAPPI Engineering Conference, Dallas, TX.

13. APPENDICES

Documentation of Computer Code

INTRODUCTION

This computer program is designed to calculate the following phenomena during char burning of a black liquor droplet:

1. char burning times for combustion and gasification of a black liquor droplet
   - CO_2 and H_2O gasification
   - combustion with O_2
   - suppression by CO and H_2
2. overall gasification rate with any combination of gases present
3. degree of sulfate reduction in char
4. Na release and C depletion through carbonate reduction
5. S release and Na_2S depletion through COS and H_2S formation
6. K and Cl enrichment (to be implemented soon)
7. swelling and char diameter changes
8. char particle density changes
9. terminal velocity changes
10. particle temperature estimation (currently empirical)

The overall reaction rate is calculated taking into account the resistances from mass transfer, pore diffusion, and chemical kinetics in series. In oxidizing conditions the particle surface temperature profile is calculated with a parabolic equation with adjustable parameters dependable on the O_2 mole fraction. In reducing conditions the particle temperature is assumed to be at a user specified constant value. Typically the particle temperature is 40-50°C below the furnace temperature in reducing conditions.

PROGRAM STRUCTURE

The program name is BLCS.FOR (Black Liquor Combustion Simulator). It consists of a main program and six subroutines (FCN, MASSTR, DIFFU, TEMPER, CARBON, and FCNJ). Figure A.13.1 illustrates the organization of the computer program.

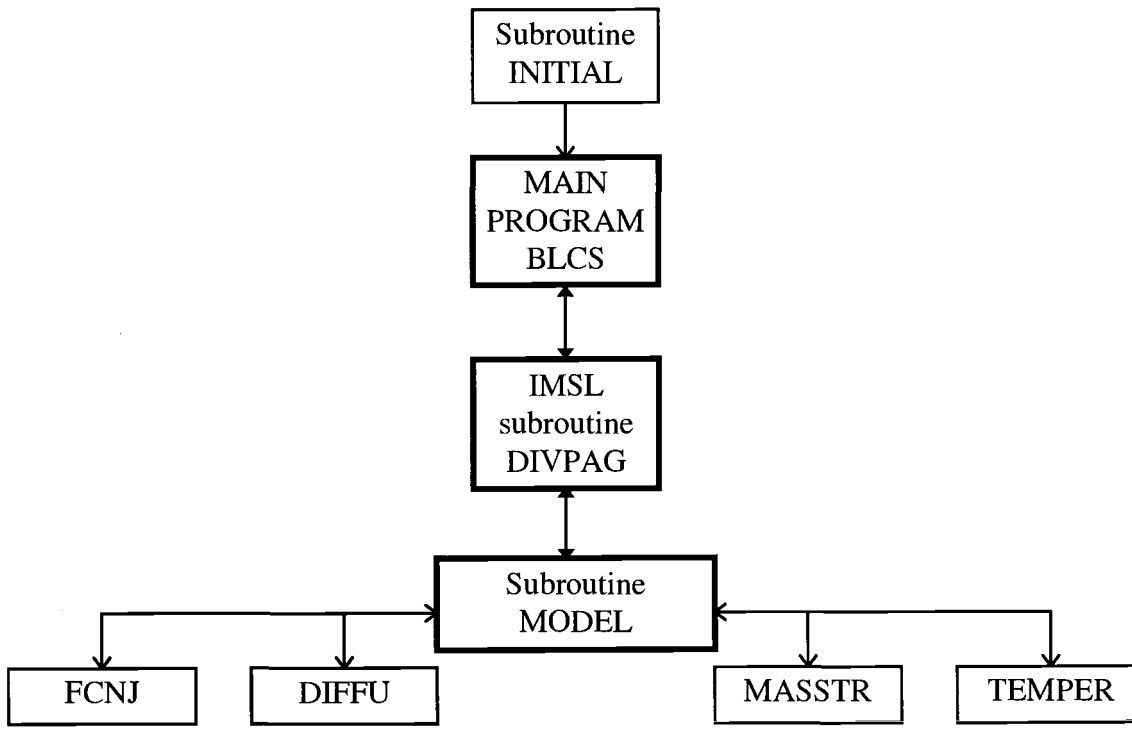

Figure A.13.1. The black liquor combustion simulator operates using 7 subroutines.

The main program calls only the subroutine CARBON. From this subroutine the main program retrieves experimentally obtained information for the necessary initial conditions of carbon and sulfur. Based on the interactive input data given by the user, the main program then calls the IMSL subroutine DIVPAG that solves the combustion and gasification model (19 ordinary differential equations). It then writes the calculated values in the following output files (BLCS10.dat, ..., BLCS99.DAT).

The subroutine FCN is called by IMSL and it contains the kinetic models for the different combustion and gasification processes (O_2, CO_2, H_2O, sulfate reduction, carbonate reduction kinetics and the diameter shrinkage model, plus the COS and H_2S release models). FCN calculates the effectiveness factors, but it calls another subroutine MASSTR to obtain the mass transfer rates for respective species.

The subroutine MASSTR calculates the mass transfer rates based on the gas partial pressures, particle temperature and diameter. MASSTR calls another subroutine DIFFU to obtain the diffusion constants for respective species.

The subroutine DIFFU calculates the binary diffusivity of the gas species in nitrogen. It is assumed that the active gas species interact only with nitrogen molecules and therefore the diffusivity in mixtures is neglected.

The subroutine TEMPER calculates the particle temperature for exothermic reactions. It also calculates the sodium vapor equilibrium partial pressure at respective temperature.

The subroutine CARBON sets the desired furnace temperature and it also calculates the fraction char, the amounts of carbon and sulfur left after pyrolysis.

The subroutine FCNJ is required by IMSL and it has no other purpose.

DESCRIPTION OF INITIAL CONDITION CALCULATIONS

The amount of carbon left after pyrolysis Cchar is obtained from the following equation:

$$C_{char} = \frac{g\,C\,char}{g\,C\,BLS} = 1.50851 \times e^{-0.00143954 \times \frac{T}{C}} \qquad (12\text{-}1)$$

This equation is based on the data by Sricharoenchaikul (1):

Table A.13.1. Experimental data for carbon yields (1).

	700°C	800°C	900°C	1000°C	1100°C
g C ap / g C BLS	0.534	0.487	0.439	0.336	0.313

The amount of sulfur left after pyrolysis S_{char} is obtained from the following equation (2):

$$S_{char} = \frac{g\,S\,char}{g\,S\,BLS} = \frac{\left(-163.27 + 0.9175 \times T - 0.0011504 \times T^2 + 4.2827 \times 10^{-7} \times T^3\right)}{1} \quad (12\text{-}2)$$

Fraction char left after pyrolysis is an input value obtained from the following equation valid between 700 and 900°C:

$$X_{mc} = \frac{g\,char\,ap}{g\,BLS} = 1.48434 \times e^{-0.001055 \times \frac{T}{C}} \quad (12\text{-}3)$$

This equation is based on the following data (1):

Table A.13.2. Experimental data on char yields (1).

	700°C	800°C	900°C	1000°C	1100°C
g char ap / g BLS	0.718	0.623	0.581	0.583	0.582

If char burning times are calculated for prepyrolized char, it would be necessary to set $X_{mc} = 1$.

There is an option to give the amount of C before or after pyrolysis. If C is given before pyrolysis, then the parameter C_{init} must be given:

$$C_{init} = \frac{g\,C\,BLS}{g\,BLS} \tag{12-4}$$

Then C after pyrolysis, C_{comp}, is calculated:

$$\frac{g\,C\,char}{g\,char\,ap} = \frac{g\,C\,char}{g\,C\,BLS} \times \frac{g\,C\,BLS}{g\,BLS} \times \frac{g\,BLS}{g\,char\,ap} \tag{12-5}$$

In terms of parameters:

$$C_{comp} = C_{char} \times C_{init} \times \frac{1}{X_{mc}} \tag{12-6}$$

If C is given after pyrolysis, then the parameter C_{comp} must be given:

$$C_{comp} = \frac{g\,C\,ap}{g\,char\,ap} \tag{12-7}$$

Then C before pyrolysis, C_{init}, is calculated:

$$C_{init} = C_{comp} \times X_{mc} \times \frac{1}{C_{char}} = \frac{g\,C\,BLS}{g\,BLS} \tag{12-8}$$

The carbon left for char burning can now be evaluated from:

$$C_{burn}(g) = M_0 \times S_0 \times C_{init} \times C_{char} \tag{12-9}$$

The following parameter can be defined:

$$X_c = \frac{C_{burn}}{S_0 \times M_0} = \frac{g\,C\,ap}{g\,BLS} \tag{12-10}$$

where S0 is the fractional dry solids content and M0 the initial wet droplet weight in grams.

The volume of a black liquor droplet is:

$$V_{part}\left(m^3\right)=\frac{\pi \times D_0{}^3}{6} \tag{12-11}$$

Using this equation the initial droplet diameter before drying can be written:

$$D_0(m)=\sqrt[3]{\left(\frac{M_0 \times 6}{dens \times \pi}\right)} \tag{12-12}$$

The maximum droplet diameter ratio is:

$$DR_{max}=\sqrt[3]{SV_{max} \times dens \times S_0} \tag{12-13}$$

The diameter at the end of devolatilization is calculated by:

$$D_{max}(m)=DR_{max} \times D_0 \tag{12-14}$$

The particle diameter during char burning:

$$D_p(m)=DR_c \times D_0 \tag{12-15}$$

DR_C is the diameter ratio of the char particle and it is defined later.

The specific gravity of the char particle is obtained by:

$$SG=\frac{dens \times X_{mc} \times S_0}{DR_{max}{}^3} \tag{12-16}$$

Black liquor droplet density:

$$dens\left(\frac{g}{cm^3}\right)=0.997+0.649 \times S_0 \tag{12-17}$$

If a predicted swelling factor is calculated, one experimental data point is needed for one specific liquor. This information is sufficient to get swelling factors at other temperatures and oxygen concentrations for the same liquor. SV_{max} is the specific volume of the swollen droplet at the end of devolatilization and is referred to as the maximum swollen volume.

$$SV_{max}\left(\frac{cm^3}{g}\right)=\frac{1}{S_0 \times dens}\left[\frac{D_{max}}{D_0}\right]^3 \qquad (12\text{-}18)$$

where S_0 is the solids content, dens is the black liquor droplet density, D_{max} is the diameter at the end of swelling which always occurs at the end of the devolatilization stage, D_0 is the initial diameter of the unswollen black liquor droplet.

Data in the literature show that liquor droplets swell less both at higher temperatures and oxygen concentrations. A higher oxygen concentration may mean that the volatiles leaving the particle will burn more intensely near the particle surface, increasing the droplet temperature. This is the basis for the assumption that it is the gas temperature surrounding the particle that determines how much the droplet swells. A nonadiabatic flame temperature is used to estimate it, reference (3).

$$T_g^* = T_g + \frac{0.232 k_f f_g \Delta H_c Y_{O2}}{0.21 C_p} \qquad (12\text{-}19)$$

where T_g* is the gas temperature surrounding the particle surface, T_g is the ambient gas temperature, k_f is the flame efficiency factor (=0.12 for BL droplets in oxygen), f_g is the stoichiometric CO/O_2 mass ratio (=1.75), ΔH_c is the heat of combustion for pyrolized gases (=10e4 J/g), Y_{O2} is the mole fraction of oxygen in the bulk gas, and C_p is the heat capacity of the gas (=1.17 J/g/C). After substitution the equation reduces to:

$$T_g^* = T_g + 1980 \times Y_{O2} \qquad (12\text{-}20)$$

It is necessary to begin with experimentally measured SV_{max} data for a specific liquor, because it is not yet possible to estimate SV_{max} based on the composition of a given liquor. To obtain SV_{max} at other temperatures and gas compositions, the following equation can be derived from the procedure of Noopila et al. (4):

$$SV_{max\,2} = SV_{max\,1} \times e^{-0.0021\left(T_{g2} - T_{g1}\right)} \tag{12-21}$$

where SV_{max1}, T_{g1} and SV_{max2}, T_{g2} are the maximum swollen volume and the surface gas temperature for the experimental data point and the predicted data point respectively.

The char diameter shrinks during char burning independently of temperature, gas composition, liquor composition and initial dry solids content. An empirical power law equation for describing the particle shrinkage is:

$$\frac{DR_c^{\,3} - DR_{max}^{\,3}}{DR_s^{\,3} - DR_{max}^{\,3}} = \left(1 - X_{cb}\right)^{n_c} \tag{12-22}$$

where DR_c is the diameter ratio of the char, DR_{max} is the diameter ratio at maximum swollen volume, and DR_s is the diameter ratio of the smelt bead remaining after completion of char burning divided by the initial droplet diameter. The smelt bead ratio, DR_s, is needed for calculating the char particle diameter as a function of time. Assuming a smelt density of 2 g/cm^3 the smelt bead ratio is approximately 0.63 for S_0 in the range 60-80% (5). n_c has been experimentally found to be approximately 1 (6). X_{cb} is the degree of completion of the char burning stage (fraction carbon that has reacted away):

$$X_{cb} = \frac{m_{C,reacted}}{m_{C,0}} \tag{12-23}$$

Initial carbonate concentration

The initial Na_2CO_3 content is calculated by specifying the fraction Na_2 in char (22.6% by default). By subtracting the sodium that is bound as sulfate or sulfide one obtains the initial carbonate concentration.

$$\text{mmol}\,Na_2CO_3 = \frac{C_{burn}}{12.01 \times CNa_2} - \text{mmol}[Na_2S + Na_2SO_4] \tag{12-24}$$

CNa_2 is given by:

$$CNa_2 = \frac{C_{comp}}{0.226 \times \frac{45.98}{12.01}} \tag{12-25}$$

Initial sulfate concentration

The sulfate concentration after pyrolysis is user specified through the parameter "num" which is typically less than 0.4. The sulfur in BLS is by default 3.6%.

$$\text{mmol}\,SO_4\ \text{char} = \text{num} \times 0.036 \times M_0 \times \frac{S_0}{32.07} \times 1000 \tag{12-26}$$

where M_0 is the initial BL droplet weight in grams and S_0 the initial dry solids content. Subtracting the sulfate from the total sulfur one obtains the sulfide concentration assuming all sulfur is as sulfide and sulfate and the release of COS and H_2S have negligible effect with respect to reduction. Hence, the following definition of sulfate reduction can be defined:

$$\text{Reduction} = \frac{Na_2S}{Na_2S + Na_2SO_4} \tag{12-27}$$

COMBUSTION AND GASIFICATION MODELS

A key question in modeling the char combustion of black liquor is the rate controlling step in the combustion process. This question can be addressed by considering the relative importance of film mass transfer and pore diffusion compared with the chemical kinetic rate. The following experimentally based rate equations were derived when chemical kinetics was the rate limiting process.

Carbon loss due to direct oxidation, $C + O_2 = CO_2$, reference (7):

$$\text{Rate}_{O2}\left(\frac{\text{mmol}}{\text{s}}\right) = 9.5\times10^{6} \times \frac{A_{int}}{m^2} \times \frac{P_{O2}}{\text{bar}} \times \frac{n_{C,left}}{\text{mmol}} \times e^{\frac{17086}{T}} \tag{12-28}$$

where T is in Kelvin.

The specific area of carbon in char is an experimental input value, A_{sp} = 122 m^2/g. It is assumed that A_{sp} decreases with carbon conversion. The internal surface area then becomes:

$$A_{int}\left(m^2\right) = \frac{\pi}{6} \times A_{sp} \times D_0{}^3 \times \text{dens} \times C_{char} \times S_0 \tag{12-29}$$

At each time step it is adjusted as follows:

$$A_{int,new} = A_{int,old} \times \left(1 - X_{cb}\right) \tag{12-30}$$

Carbon loss due to CO_2 gasification, $C + CO_2 = 2CO$, reference (8):

$$\text{Rate}_{CO2}\left(\frac{\text{mmol}}{\text{s}}\right) = 63\times10^{9} \times \left[\frac{C}{\text{mmol}}\right] \times \frac{\frac{P_{CO2}}{\text{bar}}}{\frac{P_{CO2}}{\text{bar}} + 3.4 \times \frac{P_{CO}}{\text{bar}}} \times e^{-\frac{30070}{T}} \tag{12-31}$$

Carbon loss due to water vapor gasification, $C + H_2O = CO + H_2$, reference (9):

$$\text{Rate}_{H2O}\left(\frac{\text{mmol}}{\text{s}}\right) = 2.56\times10^{9} \times \left[\frac{C}{\text{mmol}}\right] \times \frac{\frac{P_{H2O}}{\text{bar}}}{\frac{P_{H2O}}{\text{bar}} + 1.42 \times \frac{P_{H2}}{\text{bar}}} \times e^{-\frac{25300}{T}} \tag{12-32}$$

Carbon loss due to the sulfate-sulfide cycle,

$C + (2\text{-}f)/4\ Na_2SO_4 = (2\text{-}f)/4\ Na_2S + fCO + (1\text{-}f)\ CO_2$

and

$Na_2S + 2O_2 = Na_2SO_4$

where "f" is the fraction of CO in the gas produced by the sulfate-carbon reaction. See chapter 9 for derivation

$$Rate_{SS}\left(\frac{mmol}{s}\right) = 3790 \times \frac{[SO_4]^{1.4}}{\frac{mol\ SO_4}{mol\ Na_2}} \times \frac{n_{carb}}{\frac{mmol}{particle}} \times e^{-\frac{9400}{T}} \quad (12\text{-}33)$$

Carbon loss due to carbonate reduction, $2C + Na_2CO_3 = 2Na + 3CO$, reference (10):

$$Rate_{Na2CO3,reduction}\left(\frac{mmol}{s}\right) = 2 \times 10^9 \frac{[Na_2CO_3]}{mmol} e^{-\frac{29335}{T}} \quad (12\text{-}34)$$

For film mass transfer limited conditions the rate of carbon consumption by O_2, CO_2, and H_2O was calculated according to:

$$Rate_{mass\,transfer,i} = k_{m,i} \times A_p \times \left(C_{bulk,i} - C_{interface,i}\right) \quad (12\text{-}35)$$

where $Rate_{mass\ transfer,i}$ is the mole of gas i transferred per second, A_p is the external surface area of the particle, $C_{bulk,i}$ is the concentration of the gas species of interest in the bulk gas, and $C_{interface,i}$ is the boundary layer partial pressure. $C_{bulk,i}$ and $C_{interface,i}$ are given by equation 12-36:

$$C_i\left(\frac{mmol}{m^3}\right) = \frac{\frac{P_i}{bar} \times 10^3}{R_{gas} \times Temp_g} \quad (12\text{-}36)$$

where $Temp_g$ is the furnace temperature in degrees Kelvin. $C_{bulk,Na}$ was assumed to be 0.

Gas constant:

$$Rgas\left(\frac{bar \times m^3}{mol \times K}\right) = 82.06 \times 10^{-6} \quad (12\text{-}37)$$

To get the gas concentration of sodium, the equilibrium vapor pressure has been evaluated with the software Chemsage (11).

Table A.13.3. Sodium equilibrium partial pressure.

T (°C)	700	800	900	1000	1100
$P_{Na,eq}$ (bar)	0.00047142	0.0044532	0.027354	0.12074	0.38354

Overall rate of reaction

The overall reaction rates are given by equation 12-38:

$$\frac{1}{\text{Overall rate}} = \frac{1}{\text{Mass transfer rate}} + \frac{1}{\text{kinetic rate with pore diffusion effect}} \qquad (12\text{-}38)$$

The oxygen process can be chosen to be either limited by all resistances (low temp) or by mass transfer only (high temp).

$$\frac{1}{RO_{O2}} = \frac{1}{O_2 byMT} + \frac{1}{eff_{O2} \times \left(\frac{dO_2}{dt} + \frac{dSS}{dt}\right)} \qquad (12\text{-}39)$$

For CO_2 and H_2O the following equations apply:

$$\frac{1}{RO_{CO2}} = \frac{1}{CO_2 byMT} + \frac{1}{eff_{CO2} \times \frac{dCO_2}{dt}} \qquad (12\text{-}40)$$

$$\frac{1}{RO_{H2O}} = \frac{1}{H_2 ObyMT} + \frac{1}{eff_{H2O} \times \frac{dH_2O}{dt}} \qquad (12\text{-}41)$$

The sodium release process can be chosen to be kinetically limited or limited by all resistances.

$$\frac{1}{RO_{Na}} = \frac{1}{NabyMT} + \frac{1}{eff_{Na} \times \frac{dNa}{dt}} \tag{12-42}$$

"eff_i" (or η) is the effectiveness factor taking into account the pore diffusion effects, which is needed to calculate the overall reaction rates. The effectiveness factor for gas species i (O_2, CO_2, H_2O, Na) is defined by equation 12-43:

$$eff_i = \frac{\tanh\left(M_{Th,i}\right)}{M_{Th,i}} \tag{12-43}$$

The effectiveness factors can be calculated using the Thiele modulus (12):

$$M_{Th,i} = L\sqrt{\frac{k_{i,gas}'''}{Diff_i}} \tag{12-44}$$

The rate constant:

$$k_{i,gas}'''\left(\frac{m^3\ gas}{m^3\ solid \times s}\right) = \frac{\frac{dConc_{gas}}{dt}}{V_{part} \times Conc_{gas}} \tag{12-45}$$

Note: the rate constants are defined on the basis of gaseous species.

For O_2:

$$M_{Th,O2} = \frac{D_p}{6}\sqrt{\frac{\frac{dO_2}{dt} + \frac{dSS}{dt}}{V_{part} \times Diff_{O2} \times Conc_{O2}}} \tag{12-46}$$

For CO_2:

$$M_{Th,CO2} = \frac{D_p}{6}\sqrt{\frac{\frac{dCO_2}{dt} + \frac{dSS}{dt}}{V_{part} \times DiffC_{O2} \times Conc_{CO2}}} \tag{12-47}$$

For H_2O:

$$M_{Th,H2O} = \frac{D_p}{6}\sqrt{\frac{\frac{dH_2O}{dt}}{V_{part} \times DiffC_{H2O} \times Conc_{H2O}}} \tag{12-48}$$

For Na:

$$M_{Th,Na} = \frac{D_p}{6}\sqrt{\frac{\frac{dNa}{dt}}{V_{part} \times DiffC_{Na} \times Conc_{Na}}} \quad (12\text{-}49)$$

Mass transfer coefficients

The mass transfer coefficient, $k_{m,i}$, was estimated from a Sherwood number correlation which accounts for both free and forced convection effects.

Sherwood number (13):

$$Sh = \frac{k_{m,i} D_p}{Diff_i} = 2 + 0.569 \times (Gr \times Sc)^{0.25} + 0.347 \times \left(Re \times Sc^{0.5}\right)^{0.62} \quad (12\text{-}50)$$

The swelling effect on mass transfer coefficients is obtained by rearranging equation (12-22):

$$DR_c = \left[DR_{max}^{\ 3} - \left(DR_{max}^{\ 3} - DR_s^{\ 3}\right) \times \left(1 - X_{cb}\right)\right]^{\frac{1}{3}} \quad (12\text{-}51)$$

This equation gives the particle diameter change as a function of char burning time.

Schmidt number:

$$Sc = \frac{\nu}{Diff_i} \quad (12\text{-}52)$$

Reynolds number:

$$Re = \frac{D_p \times vt}{\nu} \quad (12\text{-}53)$$

where n is the kinematic viscosity and vt the terminal settling velocity (14):

$$vt = 11640 \times SG^{0.714} \times D_p^{\ 1.143} \quad (12\text{-}54)$$

where SG is the specific gravity of the char particle relative to water and D_p is the particle diameter.

The change in SG is obtained from:

$$SG\left(\frac{\frac{\text{density of particle}}{\text{g/cm}^3}}{\frac{\text{density of water}}{\text{g/cm}^3}}\right)=\frac{\text{mass of particle}}{V_{part}}\div 1 \qquad (12\text{-}55)$$

Grashof number (15):

$$Gr=\frac{g\times L^3\times\Delta T\times\beta}{\nu^2} \qquad (12\text{-}56)$$

where g is the acceleration due to gravity, ΔT is the temperature difference between the surface and the bulk, n is the kinematic viscosity, and the coefficient of volumetric expansion comes from:

$$\beta=\frac{1}{V}\frac{\partial V}{\partial t}=\frac{1}{T}\ \text{for ideal gases} \qquad (12\text{-}57)$$

The characteristic length is given by:

$$L=\frac{R}{3}=\frac{D_p}{6}\ \text{for spheres} \qquad (12\text{-}58)$$

Now the Grashof number becomes:

$$Gr=\frac{9.82}{\nu^2}\times\left(\frac{D_p}{6}\right)^3\times\left(\frac{\Delta T}{T_f}\right) \qquad (12\text{-}59)$$

For oxidation reactions T_f is estimated by:

$$T_f=\frac{dT}{2}+Temp_g \qquad (12\text{-}60)$$

where $Temp_g$ is the furnace temperature and dT is the difference between the maximum surface temperature during char burning and the furnace temperature (16):

$$dT = 13 + 664 \times \frac{P_{O2}}{bar} + 0.357 \times \left(100 \times \frac{P_{O2}}{bar}\right)^2 \quad (12\text{-}61)$$

Diffusion constants

The intermolecular energy y between two molecules to the distance of separation r, is given by:

$$\Psi = 4\varepsilon_{ij}\left[\left(\frac{\sigma_{ij}}{r}\right)^{12} - \left(\frac{\sigma_{ij}}{r}\right)^{6}\right] \quad (12\text{-}62)$$

where σ_{ij}, and ε_{ij} are the characteristic Lennard-Jones length and energy. They are evaluated as follows:

$$\sigma_{ij} = \frac{\sigma_i + \sigma_j}{2} \quad (12\text{-}63)$$

$$\varepsilon_{ij} = \sqrt{\varepsilon_i \varepsilon_j} \quad (12\text{-}64)$$

The diffusion coefficient for a binary system can be derived from the Chapman-Enskog equation in SI units:

$$Diff_{ij}\left(\frac{m^2}{s}\right) = 2.6629 \times 10^{-22} \frac{\sqrt{T^3\left(\frac{M_i + M_j}{2M_iM_j}\right)}}{P\sigma_{ij}{}^2\Omega_{ij}{}^{(1,1)*}(T^*)} \quad (12\text{-}65)$$

The dimensionless temperature T^* is related to ε by

$$T^* = \frac{k_B T}{\varepsilon_{ij}} \quad (12\text{-}66)$$

W_D is evaluated from the relation of Neufield et al. (17):

$$\Omega_{ij} = \frac{A}{(T^*)^B} + \frac{C}{e^{DT^*}} + \frac{E}{e^{FT^*}} + \frac{G}{e^{HT^*}} \quad (12\text{-}67)$$

where A = 1.06036, B = 0.15610, C = 0.193000, D = 0.47635, E = 1.03587, F = 1.52996, G 1.76474, H = 3.89411.

The Lennard-Jones parameters, σ and ε, for the species of interest are given in Table A.13.4:

Table A.13.4. The values for Lennard-Jones parameters are given in reference (18).

Gas	ε/k (K) 330-1000 K	σ (Å)330-1000 K
Air	84	3.689
O_2	88	3.541
CO_2	213	3.897
H_2O	356	2.649
Na_v	2171	4.924

The values for sodium vapor was estimated making use of the critical temperature and pressure for Na_v found in the literature (19): $T_C = 2819\,K$, $P_C = 343\,bar$.

The Lennard-Jones parameters for sodium vapor was then estimated using the following empirical relations found in the literature (20):

$$\sigma = 2.44 \times \left(\frac{T_C}{P_C}\right)^{\frac{1}{3}} \tag{12-68}$$

$$\frac{\varepsilon}{k} = 0.77 \times T_C \tag{12-69}$$

The Chapman-Enskog equation is then used to calculate the binary diffusivities for sodium vapor.

Sodium release during char burning

Sodium release during char burning is accounted for mainly by the following reaction:

Reduction of sodium carbonate in char carbon: $Na_2CO_3 + 2C = 2Na + 3CO$

The following reactions are of minor importance:

CO_2 formation: $Na_2CO_3 + C = 2Na + CO + CO_2$ (mainly at low temps)

Sulfation in the char smelt: $Na_2CO_3 + 0.25\ Na_2S = 2Na + CO_2 + 0.25\ Na_2SO_4$

A chemical kinetic rate equation can be derived according to the following mechanism of Sams et al. (21):

$M_2CO_3 + C \leftrightarrow -CO_2M + -COM$

$-CO_2M + C \leftrightarrow -CM + CO_2$

$-CO_2M + C \leftrightarrow -COM + CO$

$-COM + C \leftrightarrow -CM + CO$

$-CM_s \leftrightarrow M_v$

where M designates an alkali metal. Assuming that the fourth reaction is the rate limiting step the following equation can be obtained:

$$\frac{d[Na_2CO_3]}{dt} = \frac{k_1[Na_2CO_3]}{1 + k_2P_{CO2} + k_3P_{CO}} \qquad (12\text{-}70)$$

For pCO_2=pCO=0, k_1 has been determined from the data provided by van Heiningen et al. to be 10^9 and first order in carbon. No data is yet available to determine the suppressing effects of CO and CO_2. Pore diffusion and mass transfer effects are taken into consideration the same way as for O_2, CO_2, and H_2O.

Stoichiometry gives the change of Na_2CO_3 concentration with respect to carbon and Na(vapor).

$$-\frac{1}{2}\frac{d[C]}{dt} = -\frac{d[Na_2CO_3]}{dt} = \frac{1}{2}\frac{d[Na_v]}{dt} \tag{12-71}$$

The temperature dependence is given by:

$$k_1 = A \times e^{-\frac{E_a}{RT}} \tag{12-72}$$

where A is the pre-exponential factor (=10^9 s^{-1}), E_a the activation energy (=244kJ/mol), R the gas constant, and T the absolute temperature in Kelvin. From this information the engineering equation could be obtained given in the "Model" section.

Sulfur release during char burning

Sulfur release during char burning occurs in three ways:

a) COS formation: $Na_2S + 2CO_2 = Na_2CO_3 + COS$

b) H_2S formation: $Na_2S + H_2O + CO_2 = Na_2CO_3 + H_2S$

c) decomposition of sodium thiosulfate (not important above 600°C):

The rate of COS release is film mass transfer limited at temperatures of interest (700-1100°C). At these temperatures COS exists within the char at an equilibrium partial pressure determined by the local CO_2 partial pressure. The rate of COS release for film mass transfer conditions is given by:

$$\frac{dCOS}{dt}\left(\frac{mmol}{s}\right) = k_{m,COS} \times A_p \times [COS]_{eq}(1 - X_s) \tag{12-73}$$

where X_S is the fraction sulfide that has reacted away and

$$K_{p,COS} = \frac{P_{COS,eq}}{P_{CO2,interface}} = e^{-A+\frac{B}{T}}$$

where A = 16.1 and B = 12307 (700-900°C) and A = 12.6 and B = 8514 (900-1100°C)

$$[COS]_{eq}\left(\frac{mol}{m^3}\right)=\frac{P_{COS,eq}}{RT} \tag{12-74}$$

Likewise for H_2S formation it is assumed that there are no internal resistances, and that the rate is limited by film mass transfer and the equilibrium partial pressure of H_2S.

$$\frac{dH_2S}{dt}\left(\frac{mmol}{s}\right)=k_{m,H2S}\times A_p\times[H_2S]_{eq}(1-X_s) \tag{12-75}$$

where X_S is the degree if sulfide conversion and

$$K_{p,H2S}=\frac{P_{H2S,eq}}{P_{CO2,interface}P_{H2O,interfac}e}=e^{-C+\frac{D}{T}} \tag{12-76}$$

where C = 16.5 and D = 16507 (700-900°C) and C = 12.9 and D = 12585 (900-1100°C)

$$[H_2S]_{eq}\left(\frac{mol}{m^3}\right)=\frac{P_{H2S,eq}}{RT} \tag{12-77}$$

The partial pressures at the interface are evaluated just before the entering the pores. Therefore, the concentrations are not calculated from an equilibrium in the bulk and not within the particle either. By assuming steady state between equations 12-78 and 12-79, one can obtain an equation for $P_{i,interface}$. The interface here is the concentration of i (CO_2 or H_2O) at the bottom of the boundary layer.

$$Rate_i=k_{m,i}\times(P_{bulk,i}-P_{interface,i}) \tag{12-78}$$

$$Rate_i=k_{r,i}\times h\times P_{interface,i} \tag{12-79}$$

where i = CO_2 or H_2O

Thus,

$$P_{interface,i}=k_{m,i}\times P_{bulk,i}\times A_p\times[A_p\times k_{m,i}+V_p\times h\times k_{r,i}] \tag{12-80}$$

Temperature profile prediction

The temperature profile is estimated from experimental data of the maximum droplet temperature during char burning. The following empirical equation is a function of conversion:

$$Temp = T_{furnace} + A + B \times Conv - C \times Conv^2 \quad (12\text{-}81)$$

The constants A, B, and C are dependent of oxygen content:

$$A = 5.19 + 2.48 \times O_2 + 0.137 \times O_2^2 \quad (12\text{-}82)$$

$$B = 24.66 + 13.06 \times O_2 + 0.693 \times O_2^2 \quad (12\text{-}83)$$

$$C = 19.08 + 10.25 \times O_2 + 0.537 \times O_2^2 \quad (12\text{-}84)$$

where O_2 is the oxygen content in percent (%).

METHOD OF SOLUTION

The following differential equations are solved simultaneously. IMSL subroutine DIVPAG in double precision is used to solve the set of differential equations. It uses Gear's integration method for stiff equations with internal step size adjustment.

Rate of carbon burn-off due to direct oxidation (mmol/s):

$$Y_1' = \frac{dO_2}{dt} \quad (12\text{-}85)$$

Rate of carbon burn-off due to CO_2 gasification (mmol/s):

$$Y_2' = \frac{dCO_2}{dt} \quad (12\text{-}86)$$

Rate of carbon burn-off due to H_2O gasification (mmol/s):

$$Y_3' = \frac{dH_2O}{dt} \tag{12-87}$$

Rate of carbon burn-off due to the sulfate-sulfide cycle (mmol/s):

$$Y_4' = \frac{4}{2-f} \times Rate_{ss} \tag{12-88}$$

where f is the fraction of CO produced by the sulfate-carbon reaction. The rate of carbon burn-off due to Na_2CO_3 reduction considering all resistances in series (mmol/s):

$$Y_5' = RONa \tag{12-89}$$

Rate of Na_2CO_3 concentration change (mmol/s):

$$Y_6' = -\frac{1}{2}\frac{dNa}{dt} \tag{12-90}$$

Rate of total carbon burn-off (mmol/s):

$$Y_7' = -RO - RONa \tag{12-91}$$

Rate of sulfur release due to COS formation (mmol/s):

$$Y_8' = \frac{dCOS}{dt} \tag{12-92}$$

Rate of sulfur release due to H_2S formation (mmol/s):

$$Y_9' = \frac{dH_2S}{dt} \tag{12-93}$$

Rate of sulfur depletion from char (mmol/s):

$$Y_{10}' = -Y_8' - Y_9' \tag{12-94}$$

Rate of change of sulfate reduction (mmol/s):

$$Y_{11}' = dR \tag{12-95}$$

Rate of change of total particle mass (mg/s):

$$Y_{12}' = -Y_7' \times 12.01 + Y_{14}' \times 78.05 + Y_{15}' \times 142.05 + Y_6' \times 105.99 \tag{12-96}$$

Rate of change of amount inorganics left (mmol/s):

$$Y_{13}' = Y_{14}' + Y_{15}' + Y_6' \tag{12-97}$$

Rate of change of sulfide concentration (mmol/s):

$$Y_{14}' = -Y_8' - Y_9' - RS \tag{12-98}$$

Rate of change of sulfate concentration (mmol/s):

$$Y_{15}' = RS - Rate_{SS} \tag{12-99}$$

Rate of sodium release limited by kinetics only (mmol/s):

$$Y_{16}' = dNa \tag{12-100}$$

Rate of sodium release limited by pore diffusion and kinetics (mmol/s):

$$Y_{17}' = EFFNa \times dNa \tag{12-101}$$

Rate of sodium release limited by mass transfer only (mmol/s):

$$Y_{18}' = NabyMT \tag{12-102}$$

Experimental results show that gasification and oxidation are mutually exclusive (22). The overall reaction rate is equivalent to which reaction process is greater, the overall gasification or oxidation rate.

$$RO = RO_{O2} + 2 \times \left(Y_{10}' \times dR + Y_8' + Y_9'\right) \tag{12-103}$$

or

$$RO = RO_{CO2} + RO_{H2O} + \tfrac{4}{2-f} \times \left(Y_{10}' \times dR + Y_8' + Y_9'\right) \tag{12-104}$$

whichever is greater.

"dR" is given by:

$$dR = \frac{Rate_{SS} - RS}{Y_{10}'} \tag{12-105}$$

RS is given by:

$$RS = \frac{1 - pf}{2} \times R_{O2}' \tag{12-106}$$

The partition factor "pf" is given by:

$$pf = \frac{\text{mol C}}{\text{mol C} + \text{mol inorganics}} \tag{12-107}$$

RPRIMEO2 is given by:

$$R_{O2}' = RO_{O2} - RO_{CO2} - RO_{H2O} - 2 \times \tfrac{f}{2-f} \times Rate_{SS} \tag{12-108}$$

EXAMPLE RUN OF THE COMBUSTION AND GASIFICATION PROGRAM

1. The program asks if O_2 is limited by all resistances or by mass transfer only.
2. The program asks if it is an endothermic or exothermic reaction. If endothermic it asks for the deltaT, the temperature difference between the furnace and the particle.
3. The program asks for the furnace temperature. The temperature code for the furnace is given from the keyboard: 6=600°, 7=700°C, 8=800°C, 9=900°C, 10=1000°C, 11=1100°C.
4. The partial pressures of the following gases are set: O_2, CO, CO_2, H_2O, H_2 .
5. The program asks for "f" or the ffactor, the fraction of CO produced from the sulfate-carbon reaction.
6. The program asks for the dry solids content of the droplet.
7. The program asks for the initial droplet mass or initial droplet diameter.
8. The program asks if a default swelling factor is used or if either a predicted swelling factor is calculated internally from an experimental data point, or an experimental swelling factor is given from the keyboard.
9. The calculations appear on screen as follows:

t(s) Xc C(mg) I(mmol) Mtot(mg) Red(-) Mode(Ox or Gf) T(K)

0.0 .. ..

All the other outputs are accessible in the following output files:

BLSC10.DAT: output of all initial conditions

BLSC11.DAT: t(s), Xc, pCO2i, pH2Oi, krCO2, kgCO2, pCOS

BLSC20.DAT: t(s), Xc, C/mg, Inorg/mmol, Mtot/mg, Red, Mode(Ox or Gf), T(K)

BLSC30.DAT: t(s), Xc, ROCO2, ROH2O, ROO2, S=/mmol, SO4=/mmol, RS/mmol, dSS/mmol

BLSC40.DAT: t(s), Xc, Xstot, COS/S, COS/Stot, H2S/S, H2S/Stot, Red

BLSC50.DAT: t(s), Xc, C/mg, Mtot/mg, D/mm, pf

BLSC60.DAT: t(s), Xc, Na2CO3/mmol, Nakin/mmol, Na overall/%

BLSC65.DAT: t(s), Xc, dNa/%, EFFNa x dNa/%, Na mass.tr./%, Na overall/%

BLSC70.DAT: t(s), Xc, EFFO2, EFFCO2, EFFH2O, EFFNa

BLSC80.DAT: t(s), Xc, O2byMT, CO2byMT, H2ObyMT, NabyMT

BLSC90.DAT: t(s), Xc, dCO2, dH2O, dO2, dNa, dSS

BLSC99.DAT: t(s), Xc, Mtot/mg, D0/mm, DRc/mm, D/mm, dens, vt(m/s)

Parameter list

The following 6 variables are necessary input parameters to IMSL (23):

INIT = internal step length (typically 10^{-8})

INORM = error norm switch (=2; see IMSL manual for details)

IMETH = method indicator (1 for Adams' or 2 for Gear's method)

PARAM(4) = maximum number of allowed iterations (typically 2500)

TOL = error tolerance (typically 10^{-7})

IDO = entry flag

The initial conditions for the differential equations are given as follows:

Y(1) = carbon depletion by O_2 kinetics (mmol)

Y(2) = carbon depletion by CO_2 kinetics (mmol)

Y(3) = carbon depletion by H_2O kinetics (mmol)

Y(4) = carbon depletion by sulfate reduction kinetics (mmol)

Y(5) = overall sodium vapor release (mmol)

Y(6) = Na_2CO_3 depletion (mmol)

Y(7) = carbon in particle (mmol)

Y(8) = COS release (mmol)

Y(9) = H_2S release (mmol)

Y(10) = total sulfur in particle (mmol)

Y(11) = sulfate reduction (dimensionless)

Y(12) = total particle mass (mg)

Y(13) = inorganics (mmol)

Y(14) = sulfide concentration (mmol)

Y(15) = sulfate concentration (mmol)

Y(16) = sodium released by kinetics only (mmol)

Y(17) = sodium released by pore diffusion and kinetics (mmol)

Y(18) = sodium released by mass transfer only (mmol)

Y(19) = sodium released by Turkdogan's oxygen enhanced mass transfer equation (mmol)

Turkdogan's oxygen enhanced mass transfer equation (24) has been developed for systems where the release of alkali is enhanced at high oxygen concentrations. This equation was not considered further because the agreement was poor with experimental data for black liquor char.

REFERENCES

1. Sricharoenchaikul, V., M.S. thesis, Oregon State University, 1995

2. Frederick, W.J., Iisa, K., Wåg, K., Reis, V.V., Boonsongsup, L., Forssen, M., Hupa, M., U.S. DOE Report DOE/CE/40936-T2, August, 1995

3. Saastamoinen, J., Modeling of Coal Pyrolysis and Combustion, Am.Flame Res.Comm., Fall Int'l Symp., Pittsburgh, PA, October 4-6, 1988

4. Noopila, T., Hupa, M., Åbo Akademi U., Combustion Chemistry Research Group Report 88-5, 1988

5. Wåg, K., Smelt bead calculation on a spreadsheet with MS-EXCEL Ver. 4.0, 1993

6. Frederick, W.J., U.S. DOE Report DOE/CE/40637-T8, March, 1990

7. J.Wendt's derivation from Smith's data, Lecture on Heterogenous Solid Phase Combustion, Seminar on Advanced Combustion Technology for Protection of Environment, Sjökulla, Finland, April 15-17, 1991

8. T.M.Grace's derivation from Li & van Heiningen's data, Ind. Eng. Chem. Res., Vol.29, No.9, 1990

9. Frederick's derivation from Li & van Heiningen's data, Ind.Eng.Res., Vol.30, No.7, 1991

10. K.Wåg's derivation from Li's data, M.S. thesis, McGill U., 1986

11. R.Backman's and K.Wåg's simulation using ChemSage, A computer program for calculation of complex chemical equilibria, Åbo Akademi U., Summer, 1993

12. Levenspiel, O., The Chemical Reactor Omnibook, OSU Book Stores Inc., 1989

13. Treybal, R.E., Mass Transfer Operations, 3rd ed., McGraw-Hill Book Company, New York, NY, p.75, 1981

14. Adams, T.N., Frederick, W.J., Kraft Recovery Boiler - Physical and Chemical Processes, American Paper Institute, New York, NY, 1988

15. Levenspiel, O., Engineering Flow and Heat Exchange, Plenum Press, 1984

16. Frederick, W.J., Hupa, M., U.S. DOE Report DOE/CE/40936-T1 (DE94007502), Fig.5.12 (note that 813 should be 13), April, 1993

17. Reid, R.C., Prausnitz, J.M., Poling, B.E., The Properties of Gases and Liquids, 4th ed., p.583, 1987

18. Kimura, S., Force constants from viscosity data, Mass transfer class notes, Oregon State University, Winter, 1993

19. Perry's Chemical Engineers' Handbook, edited by R.H.Perry and D.W.Green, 6th ed., p.3-112, 1984

20. Welty, J.R., Wicks, C.E., Wilson, R.E., Fundamentals of Momentum, Heat and Mass Transfer, 3rd ed., p.487, June, 1983

21. Sams, D.A., Shadman, F., AIChE J., Vol.32, No.7, July, 1986

22. Grace, T.M., Lien, S.J., Brown, C.A., Char Bed Burning - Laboratory Studies, Proc. 1992 International Chemical Recovery Conference, Seattle, WA, June 7-11, 1992

23. IMSL MATH/LIBRARY User's Manual, FORTRAN Subroutines for Mathematical Applications, Solution of Initial Value Problem for ODEs, Vol. 2, Chapter 5, p.640-652, IMSL, Inc., Houston, TX, August, 1989

24. Turkdogan, E.T., Grieveson, P., Darken, L.S., Enhancement of Diffusion-Limited Rates of Vaporization of Metals, J. Phys. Chem., Vol.67, p.1647-1654, 1963

APPENDICES

Computer code

```
C     BLCS.FOR
C*****************************************************************
C     Black Liquor Combustion Simulator (BLCS) for C, Na, and S
C     release and sulfate reduction during char burning
C     Oregon State University, Chemical Engineering Department
C     Corvallis, OR 97331, USA
C     Last modified 3/10/96
C     Created by Kaj Wag
C*****************************************************************
C     Carbon removal through CO2, H2O, O2 gasification
C     Oxygen can be chosen to be either mass transfer limited
C     or limited by all resistances
C     Carbonate reduction can be chosen to be either kinetically
C     limited or limited by all resistances
C     Sulfate reduction and reoxidation included
C     COS and H2S release included
C     Swelling prediction and char diameter changes included
C     Density and terminal velocity changes included
C     Initial carbon, carbonate, sulfur and sulfide in char predicted
C     Particle temp estimated with O2 dependent equation
C     Temperature range: 700-1100C
C-----------------------------------------------------------------
C     IMSL program library used: routine DIVPAG
C     Uses Adams' and Gear's stiff methods
C     Subroutines:
C     FCN: contains C, Na, S release  models
C     MASSTR: mass transfer coefficient calculation
C     DIFFU: diffusivity calculation
C     TEMPER: particle temperature prediction
C     CARBON: estimation of initial C and S in char
C     FCNJ: IMSL required subroutine
C     Output files stored in BLCS1-99.DAT
C*****************************************************************
C     MAIN PROGRAM
C
      integer NEQ,NPARAM,im,flag,flagt,flago,flag4
      parameter (NPARAM=50,NEQ=19)
      INTEGER IDO,IMETH,INORM,NOUT,count,COUNTER
      character mark*2
      double precision FCN,PARAM(50),t,TEND,TOL,Y(NEQ),Asp,Ccomp
      double precision Temp,Tempe,A(1,1),FCNJ,HINIT,end,D0,step
      double precision Sodium,Schar,pi,unacc,num,tol2,pf,Yini
```

```
      double precision Na2CO3,SO4,Aint,pco2,pco,ph2,ph2o,po2
      double precision D,DiffO2,DiffCO2,DiffH2O,DiffNa,dummy
      double precision Vpart,DIA,Conv,delta,DI,Xmc,SG,Temp1
      double precision M0,S0,dens,Cburn,Cchar,Cinit,Xc
      double precision Naratio,Nachar,Na2mol,SO4char
      double precision Sulfur,Sulfide,Sulfate,SO4bls,Sbls,SO4Na2
      double precision Tg1,Tg2,SVmax1,SVmax2,DRs,DRmax,DRc
      double precision ROO2,ROCO2,ROH2O,ROgf,RONa,RO,RS
      double precision Sini,ffactor,CNa2,dSpyr,krCO2,kgCO2
      double precision EFFO2,EFFCO2,EFFH2O,EFFNao,EFFNan
      double precision O2byMT,CO2byMT,H2ObyMT,NabyMT
      double precision dCO2,dH2O,dO2,dNa,dSS,vt,pco2i,ph2oi,pCOS
      double precision irrk,revk,mt,Turkd,Keq
      parameter(pi=3.1415927)
      common/kaj1/count
      common/kaj1a/Yini,Sini,dSpyr,RS,unacc,tol2,pco2i,ph2oi
      common/kaj2/Na2CO3,SO4,Aint,pco2,pco,ph2,ph2o,po2,SG,vt
      common/kaj3/TEMPE,DIA,krCO2,kgCO2,pCOS
      common/kaj4/Cburn,D0,DRmax,DRs,DRc,dens,pf
      common/kaj5/ffactor,M0,S0
      common/kaj7/mark
      common/kaj9/RO,ROO2,ROCO2,ROH2O,RONa
      common/kaj10/Conv,Sulfur
      common/kaj11/delta,flagt
      common/kaj12/EFFO2,EFFCO2,EFFH2O,EFFNao,EFFNan
      common/kaj13/O2byMT,CO2byMT,H2ObyMT,NabyMT
      common/kaj14/dCO2,dH2O,dO2,dNa,dSS
      common/kaj15/flago
      common/kaj16/irrk,revk,mt,Turkd,Keq
      external FCN,DIVPAG,SSET
      EXTERNAL iwkin
      real rwksp(45000)
      common/worksp/rwksp
      call IWKIN(45000)
C*******Sample case to demonstrate logic*****************************
C     Diameter based on non-pyrolized droplet = appr 17 mg wet part
C     dry solids content = 76%
C     17*0.76 = 12.92 mg dry bls
C     31.41% Carbon in initial bls
C     17*0.76*0.3141 = 4.06 mg carbon in initial dry bls
C     At 800C 43% of initial Carbon is pyrolyzed
C     or 57% Carbon left after pyrolysis
C     800C: 17*0.76*0.3141*0.57 = 2.313 mg carbon for char burning
C     Initial conditions  2.28 mg fixed carbon
C     M0 = 17mg = 0.017g
```

```
C     dens=0.997+0.649*0.76
C     D0=0.01*(M0/dens*6/pi)^0.333 = 0.002793 m
C     Fraction C left of the original is given by equation obtained
C     from LEFR data
C     furnace temperature (700-1100C)
C*****************************************************************
      open(10,file='BLCS10.DAT',status='unknown')
      write(*,*) '-----------------------------------------------'
      write(*,*) ' BLACK LIQUOR COMBUSTION SIMULATOR  '
      write(*,*) ' Created by Kaj Wag 7/30/93        '
      write(*,*) ' Last modified: 3/10/96            '
      write(*,*) ' Oregon State University           '
      write(*,*) ' Chemical Engineering Department   '
      write(*,*) ' Corvallis OR 97331 USA            '
      write(*,*) '-----------------------------------------------'
      write(10,*) '-----------------------------------------------'
      write(10,*) 'BLACK LIQUOR COMBUSTION SIMULATOR '
      write(10,*) 'Created by Kaj Wag 7/30/93        '
      write(10,*) 'Date last modified: 3/10/96       '
      write(10,*) 'Oregon State U. / Chemical Engineering Department'
      write(10,*) 'Corvallis OR 97331 USA            '
      write(10,*) '-----------------------------------------------'
      write(*,*)
900   write(*,*)
     & 'This program can treat oxygen as mass transfer limited'
      write(*,*) 'or limited by all resistances'
      write(*,*) 'At higher temp mass transfer dominates'
      write(*,*) 'At lower temp all resistances may be included'
      write(*,*)
      write(*,*) 'Give 1 for all resistances (low temp)'
      write(*,*) 'Give 0 for mass transfer resistance (high temp)'
      read(*,*) flago
      if (flag.lt.0.or.flag.gt.1) then
       write(*,*) 'Wrong input try again'
       goto 900
      endif
910   write(*,*)
      write(*,*)
991   write(*,*)
     & 'Give 1 if it is an endothermic reaction (constant part temp)'
      write(*,*)
     & 'Give 0 if it is an exothermic reaction (temp profile)'
      read(*,*) flagt
      if (flagt.eq.1) then
       write(*,*) 'Give deltaT = Tfurnace - Tparticle'
```

```
        read(*,*) delta
       elseif (flagt.eq.0) then
        delta=0
       elseif (flagt.gt.1.or.flagt.lt.0) then
        write(*,*) 'Wrong input try again'
        goto 991
       endif
77     continue
       WRITE(*,*) 'Give code for furnace temperature'
       write(*,*) '6, 7, 8, 9, 10, or 11 (600 to 1100C)'
       read(*,*) count
       if (count.lt.6.or.count.gt.11) then
        WRITE(*,*) 'WRONG INPUT TRY AGAIN'
        goto 77
       endif
       write(*,*) 'Give pCO2 (bar)'
       read(*,*) pco2
       if (pco2.eq.0) then
        pco2=1e-10
       endif
       write(*,*) 'Give pCO (bar)'
       read(*,*) pco
       write(*,*) 'Give pH2O (bar)'
       read(*,*) ph2o
       if (ph2o.eq.0) then
        ph2o=1e-10
       endif
       write(*,*) 'Give pH2 (bar)'
       read(*,*) ph2
       write(*,*) 'Give pO2 (bar)'
       read(*,*) po2
       if (po2.eq.0) then
        po2=1e-10
       endif
       pco2i=0
       ph2oi=0
       EFFCO2=1.0
       EFFH2O=1.0
       WRITE(*,*) 'GAS COMPOSITION '
       WRITE(*,65) 'CO2','CO','H2O','H2','O2'
       WRITE(*,66) pco2,pco,ph2o,ph2,po2
       WRITE(10,*) 'GAS COMPOSITION '
       WRITE(10,65) 'CO2','CO','H2O','H2','O2'
       WRITE(10,66) pco2,pco,ph2o,ph2,po2
65     format(5A7)
```

```
66    format(5F7.3)
78    write(*,*) 'Give f factor: fCO+(1-f)CO2'
      read(*,*) ffactor
      write(10,400) 'f factor ',ffactor
      if (ffactor.lt.0.or.ffactor.gt.1) then
       write(*,*) 'Wrong input try again'
       goto 78
      endif
C*******Swelling section*********************************************
334   write(*,*) 'Give 1 for default swelling (30x by volume)'
      write(*,*) 'Give 2 for predicted swelling data'
      write(*,*) 'Give 3 for experimental swelling data'
      read(*,*) flag
      if (flag.eq.1) then
       SVmax2=30.
      elseif (flag.eq.2) then
       write(*,*) 'Datapoint for swelling prediction'
       write(*,*) 'Give temperature for datapoint in Celsius'
       read(*,*) Temp1
       write(*,*) 'Give swelling at this datapoint (cm3/g wBL)'
       read(*,*) SVmax1
       Tg1=Temp1+1980.0*po2
       Tg2=Temp+1980.0*po2
       SVmax2=SVmax1*exp(-0.0021*(Tg2-Tg1))
       write(10,*) 'Temp for swelling datapoint (C) ',Temp1
       write(10,*) 'Swelling at this data point (cm3/g wBL) ',SVmax1
       write(10,*) 'SVmax2 (cm3/g wBL)',SVmax2
       write(*,*) 'Predicted SVmax (cm3/g wBL)',SVmax2
      elseif (flag.eq.3) then
       write(*,*) 'Give experimental swelling point'
       read(*,*) SVmax2
       write(10,400) 'SVmax2 (cm3/g wBL)',SVmax2
      else
       write(*,*) 'Wrong input try again'
       goto 334
      endif
C  Calculate fraction carbon left for char burning after pyrolysis
      call CARBON(count,Xmc,Cchar,Schar,Temp)
      write(10,400) 'Temperature (C)',Temp-delta
      write(*,*) 'Give initial solids content (0.0-1.0)'
      read(*,*) S0
      write(10,400) 'S0',S0
      dens=0.997+0.649*S0
      write(*,400) 'BL dens (g/cm3)',dens
      write(10,400) 'BL dens (g/cm3)',dens
```

```
333    write(*,*) 'Give (1) for diameter or (2) for mass'
       read(*,*) im
       if (im.eq.1) then
        write(*,*) 'Give droplet diameter in mm'
        read(*,*) D0
        M0=dens*pi*(D0/10)**3./6.
        write(*,400) 'Droplet wet mass (mg)',M0*1000.
        write(10,400) 'Droplet wet mass (mg)',M0*1000.
       elseif (im.eq.2) then
        write(*,*) 'Give droplet wet mass in (mg)'
        read(*,*) M0
        M0=M0/1000.
        write(*,400) 'Droplet wet mass (mg)',M0*1000.
        write(10,400) 'Droplet wet mass (mg)',M0*1000.
       else
        write(*,*) 'Wrong input try again'
        goto 333
       endif
       write(*,400) 'Droplet dry mass (mg)',S0*M0*1000.
       write(10,400) 'Droplet dry mass (mg)',S0*M0*1000.
C*******Diameter section*********************************************
c      D0=0.002793 typical value
C      Smelt bead ratio = 0.63329
       DRs=0.63329
       write(10,400) 'DRs ',DRs
       DRmax=(SVmax2*dens*S0)**0.333
       write(*,400) 'DRmax ',DRmax
       write(10,400) 'DRmax ',DRmax
       D0=0.01*(M0/dens*6/pi)**0.333
       write(*,400) 'D0 (mm)',D0*1000.
       write(10,400) 'D0 (mm)',D0*1000.
       D=DRmax*D0
       write(*,400) 'Dmax (mm)',D*1000.
       write(10,400) 'Dmax (mm)',D*1000.
       Vpart=pi/6.*D0**3.
       write(*,401) 'Vpart (m3)',Vpart
       write(10,401) 'Vpart (m3)',Vpart
C*******Xc Xmc Cchar Ccomp and Cburn ****************************
C      Cchar and Xmc come from subroutine CARBON
       write(*,*) 'Give Xc (g C ap / g BLS) typically 0.1-0.2'
       read(*,*) Xc
       write(*,400) 'Xc (g C ap / g BLS)',Xc
       write(10,400) 'Xc (g C ap / g BLS)',Xc
       write(*,400) 'Xmc (g char after pyro / g bls)',Xmc
       write(10,400) 'Xmc (g char after pyro / g bls)',Xmc
```

```
        write(*,400) 'Char particle dry mass (mg)',Xmc*S0*M0*1000.
        write(10,400) 'Char particle dry mass (mg)',Xmc*S0*M0*1000.
        Cburn=Xc*M0*S0*1000.
        write(*,400) 'Carbon left in char (mg)',Cburn
        write(10,400) 'Carbon left in char (mg)',Cburn
        Cinit=Xc/Cchar
        write(*,400) 'C in BLS (g C BLS / g BLS)',Cinit
        write(10,400) 'C in BLS (g C BLS / g BLS)',Cinit
        Ccomp=Cchar*Cinit/Xmc
        write(*,400) 'Ccomp (g C ap / g char ap)',Ccomp
        write(10,400) 'Ccomp (g C ap / g char ap)',Ccomp
C     Specific gravity of particle relative to water
C     SG=0.02333333 typical value
        SG=dens/DRmax**3.*Xmc*S0
        write(10,400) 'Initial spec gravity of char particle (-)',SG
C*******C/Na2 mol ratio*****************
        write(*,*) 'Give fraction Na left in char (g Na / g BLS)'
        read(*,*) Naratio
        write(10,400) 'Na left in char (g Na char / g BLS)',Naratio
        write(*,*) 'Fraction Na in char is more than in BLS'
C     Nachar is initial Na2 in char
        Nachar=M0*S0*Naratio*1000.
        write(*,400) 'Na left in char (mg) =',Nachar
        write(10,400) 'Na left in char (mg) =',Nachar
        Na2mol=Nachar/45.98
        CNa2=Cburn/Na2mol/12.01
        write(*,400) 'mol C / mol Na2 =',CNa2
        write(10,400) 'mol C / mol Na2 =',CNa2
C******* Sulfur **********************
C mmol S ap = (g S ap/g S BLS)*(g S BLS/g BLS)*M0*S0/32.07*1e3
992   write(*,*) 'Give S in bls (%) typically 3.6-6.4%'
        read(*,*) Sbls
        Sbls=Sbls/100.
        write(*,400) 'S in BLS (%)',Sbls*100.
        write(10,400) 'S in BLS (%)',Sbls*100.
C     Schar comes from subroutine CARBON
        write(*,400) '(g S ap/g S in BLS)',Schar
        write(10,400) '(g S ap/g S in BLS)',Schar
        Sulfur=Schar*Sbls*M0*S0/32.07*1000.
        write(*,400) 'Sulfur in char (mmol)',Sulfur
        write(10,400) 'Sulfur in char (mmol)',Sulfur
        write(*,*) 'Give g SO4= / g BLS '
        write(*,*) 'This is typically >0.01 and <0.15'
        read(*,*) num
        write(10,400) '(g SO4 / g BLS)',num
```

```
C       SO4bls=num*Sbls*M0*S0/32.07*1000.
C       Sulfate=SO4bls
C      SO4char is here mg SO4 in char
        SO4char=M0*S0*1000.*num
C      Sulfate is in mmol
        Sulfate=SO4char/96.07
cc      Sulfate=Sulfur
cc      Sulfide=0.001
C      Sulfate Na2 ratio
        SO4Na2=Sulfate/Na2mol
        write(*,400) 'SO4 / Na2 ratio =',SO4Na2
        write(10,400) 'SO4 / Na2 ratio =',SO4Na2
        Sulfide=Sulfur-Sulfate
        if (Sulfate.lt.0.or.Sulfide.lt.0) then
         write(*,*) 'Too much sulfate; try again'
         goto 992
        endif
C mmol Na2CO3 = mmol C/CNa2 - (Na2S+Na2SO4)
        Na2CO3=Cburn/12.01/CNa2-Sulfur
        write(*,400) 'Na2CO3 (mmol)',Na2CO3
        Asp=122.
        write(10,400) 'Specific area of carbon in char (m2/g)',Asp
        Aint=Asp*pi/6.*D0**3.*dens*1e6*S0*Cchar
        write(*,400) 'Aint (m2) ',Aint
        write(10,400) 'Aint (m2) ',Aint
C  Depletion of Aint WAS accounted for by mC(momentaneous)/mC(init)
C*******End of general input**************************************
C*******Section for initial conditions*****************************
C ALL INITIAL CONDITIONS ARE IN (mmol)
C Initial condition for C by O2 kinetics
        Y(1)=0.0
C Initial condition for C by CO2 kinetics
        Y(2)=0.0
C Initial condition for C by H2O kinetics
        Y(3)=0.0
C Initial condition for C by SS kinetics
        Y(4)=0.0
C Initial condition for C by Na2CO3 reduction kinetics
        Y(5)=0.0
C Initial condition for Na2CO3 depletion
        Y(6)=Na2CO3
C Initial condition for total carbon burn off including
C mass transfer and pore diffusion effects (mmol)
        Yini=Cburn/12.01
        Y(7)=Yini
```

```
C Initial condition for COS release
      Y(8)=0
C Initial condition for H2S release
      Y(9)=0
C Y(10) is the total sulfur initially
      Y(10)=Sulfur
C Initial condition for sulfate reduction
C Definition: Na2S/(Na2S+Na2SO4)
      Y(11)=Sulfide/Sulfur
      write(*,400) 'Initial reduction ',Y(11)
      write(10,400) 'Initial reduction ',Y(11)
C Initial condition for total particle mass (mg)
      Y(12)=Y(7)*12.01+Y(6)*105.99+Sulfide*78.05+Sulfate*142.05
C Initial condition for inorganics
C Unit: mmol (Sulfide+Sulfate+Carbonate+unaccounted)
      unacc=(Xmc*S0*M0*1000.-Y(12))/105.99
      Y(13)=Sulfur+NA2CO3+unacc
C Initial sulfide concentration
      Y(14)=Sulfide
C     Sini is for the COS and H2S conversion term
      Sini=Y(14)
      Y(15)=Sulfate
      RS=0
      Y(16)=0.0
      Y(17)=0.0
      Y(18)=0.0
      Y(19)=0.0
C     Sodium is the initial Na in char
C     Sodium is in 2*mmol Na2S+Na2SO4+Na2CO3+unacc=mmol Na
      Sodium=2.*(Y(13)-unacc)
      write(*,*)
      write(*,*) 'INITIAL CONDITIONS'
      write(*,400) 'Total mass (mg) ',Y(12)
      write(10,400) 'Total mass (mg) ',Y(12)
      write(*,400) 'Carbon (mmol)',Y(7)
      write(*,400) 'Carbon (mg)',Y(7)*12.
      write(10,400) 'Carbon (mmol)',Y(7)
      write(10,400) 'Carbon (mg)',Y(7)*12.
      write(*,400) 'Na2CO3 (mmol)',Na2CO3
      write(*,400) 'Na2CO3 (mmol)',Na2CO3*106.
      write(10,400) 'Na2CO3 (mmol)',Na2CO3
      write(10,400) 'Na2CO3 (mg)',Na2CO3*106.
      write(*,401) 'Sulfide (mmol)',Y(14)
      write(*,400) 'Sulfide (mg)',Y(14)*78.05
      write(10,401) 'Sulfide (mmol)',Y(14)
```

```
      write(10,400) 'Sulfide (mg)',Y(14)*78.05
      write(*,401) 'Sulfate (mmol)',Y(15)
      write(*,400) 'Sulfate (mg)',Y(15)*142.05
      write(10,401) 'Sulfate (mmol)',Y(15)
      write(10,400) 'Sulfate (mg)',Y(15)*142.05
      write(*,400) 'Unaccounted (mmol)',unacc
      write(10,400) 'Unaccounted (mmol)',unacc
400   format(A45,F12.6)
401   format(A45,E12.3)
      write(*,*) '==========END OF INPUT============'
      write(*,*) 'Output stored in files: BLCS10-99.dat'
      write(*,*)
C*******IMSL specification section**********************************
C     SET parameters before integration loop
C     Internal steplength
cc     write(*,*) 'Give internal step length (typically 1e-8)'
cc     read(*,*) HINIT
       HINIT=1e-8
C     Switch determining error norm
       INORM=2
C     Method indicator (Gear's backward difference method)
cc     write(*,*)
cc    &  'Give method: 1 for Adams or 2 for Gears (recommend 2)'
cc     read(*,*) IMETH
       IMETH=1
C                    Set PARAM to default
       call SSET(NPARAM,0.0,PARAM,1)
C                    Set internal IMSL parameters
       PARAM(1)=HINIT
       write(*,*) 'Give max nr of iterations (typically 2500)'
       read(*,*) PARAM(4)
cc     PARAM(4)=3000
       PARAM(10)=INORM
       PARAM(12)=IMETH
C                    Set error tolerance
cc     write(*,*) 'Give IMSL error tolerance (typically 1e-7)'
cc     read(*,*) TOL
       TOL=1e-7
cc     write(*,*)
cc    & 'Give tolerance for full conversion (typically 1e-10)'
cc     read(*,*) tol2
       tol2=1.e-10
C
C         IDO=1 is for the initial entry
C
```

```
      IDO=1
      t=0.0
C*****************************************************************
      write(*,*) 'Give end time for integration'
      read(*,*) end
      write(*,*) 'Give time step'
      read(*,*) step
      step=step/10.
      write(*,*) 'Push <CR> to execute calculations'
      read(*,*)
      open(11,file='BLCS11.dat',status='unknown')
      open(20,file='BLCS20.dat',status='unknown')
      open(30,file='BLCS30.dat',status='unknown')
      open(31,file='BLCS31.dat',status='unknown')
      open(40,file='BLCS40.dat',status='unknown')
      open(50,file='BLCS50.dat',status='unknown')
      open(60,file='BLCS60.dat',status='unknown')
      open(65,file='BLCS65.dat',status='unknown')
      open(70,file='BLCS70.dat',status='unknown')
      open(80,file='BLCS80.dat',status='unknown')
      open(90,file='BLCS90.dat',status='unknown')
      open(99,file='BLCS99.dat',status='unknown')
      write(11,12) 't','Xc','pco2i','ph2oi','krCO2','kgCO2','pCOS'
      write(*,778) 't(s)','Xc','C/mg','I/mmol','Mtot/mg','Red',
     & 'Mode','T/K'
      write(20,778) 't(s)','Xc','C/mg','I/mmol','Mtot/mg','Red',
     & 'Mode','T/K'
      write(30,778) 't(s)','Xc','Na2S/mmol','Na2SO4/mmol',
     & 'Stot/mmol','RS/mmol/s','dSS/mmol/s','Red'
      write(31,781) 't(s)','Xc','ROCO2','ROH2O','ROO2','SG'
      write(40,786) 't(s)','Xc','Xstot','COS/S','COS/St',
     & 'H2S/S','H2S/St','Red'
      write(50,782) 't(s)','Xc','C/mg','Mtot/mg','D/mm','pf'
      write(60,784) 't(s)','Xc','Na2CO3/mmol','Na/mmol','allres/%'
      write(65,800) 't(s)','Xc','kin/%','effkin/%','mt/%','Turkd/%',
     & 'all_res'
      write(70,782) 't(s)','Xc','EFFO2','EFFCO2','EFFH2O','EFFNao'
      write(80,782) 't(s)','Xc','O2byMT','CO2byMT','H2ObyMT','NabyMT'
      write(90,12)  't(s)','Xc','dCO2','dH2O','dO2','dNa','dSS'
      write(99,789) 't(s)','Xc','Mtot.mg','D0/mm','DRc','D/mm',
     & 'dens','vt(m/s)'
      COUNTER=9
C     ***************************************************
C     **********LOOP*************************************
C     ***************************************************
```

```
      do 10 TEND=0,end,step
       call DIVPAG(IDO,NEQ,FCN,FCNJ,A,t,TEND,TOL,PARAM,Y)
      COUNTER=COUNTER+1
       IF (COUNTER.EQ.10) THEN
      write(11,13) t,conv,pco2i,ph2oi,krCO2,kgCO2,pCOS
      write(*,779) t,Conv,Y(7)*12.01,Y(13),Y(12),Y(11),mark,TEMPE
      write(20,779) t,Conv,Y(7)*12.01,Y(13),Y(12),Y(11),mark,TEMPE
      write(30,830) t,Conv,Y(14),Y(15),Y(10),RS,dSS,Y(11)
      write(31,780) t,Conv,ROCO2,ROH2O,ROO2,SG
      write(40,790) t,Conv,1-Y(10)/Sulfur,100.*Y(8)/Sulfide,
     & 100.*Y(8)/Sulfur,100.*Y(9)/Sulfide,100.*Y(9)/Sulfur,Y(11)
      write(50,785) t,Conv,Y(7)*12.01,Y(12),DIA*1e3,pf
      write(60,785) t,Conv,Y(6),Y(5),100.*Y(5)/Sodium
      write(65,783) t,Conv,100.*Y(16)/Sodium,100.*Y(17)/Sodium,
     & 100.*Y(18)/Sodium,100.*Y(19)/Sodium,100.*Y(5)/Sodium
      write(70,780) t,Conv,EFFO2,EFFCO2,EFFH2O,EFFNao
      write(80,780) t,Conv,O2byMT,CO2byMT,H2ObyMT,NabyMT
      write(90,13)  t,Conv,dCO2,dH2O,dO2,dNa,dSS
      write(99,788) t,Conv,Y(12),D0*1000,DRc,DIA*1000,dens,vt
      COUNTER=0
      ENDIF
C Terminate integration when conversion > 0.999
      if (conv.gt.0.999) then
       goto 99
      endif
10    continue
12    FORMAT(A7,',',6(A10,','))
776   FORMAT(A7,',',9(A12,','))
778   FORMAT(A8,',',7(A8,','))
781   FORMAT(A7,',',6(A15,','))
782   FORMAT(A8,',',5(A10,','))
784   FORMAT(A8,',',5(A10,','))
786   FORMAT(A8,',',7(A15,','))
787   FORMAT(A7,',',7(A10,','))
789   FORMAT(A7,',',7(A9,','))
800   FORMAT(A8,',',6(A10,','))
13    format(F7.2,',',6(E10.4,','))
777   format(F7.2,',',9(E12.4,','))
779   format(F8.2,',',5(F8.4,','),A8,',',F8.0,',')
780   format(F8.3,',',6(E15.5,','))
790   format(F8.3,',',7(E15.5,','))
783   format(F8.3,',',4(F10.3,','),E10.3,',',F10.3,',')
785   format(F8.3,',',5(F10.5,','))
788   format(F6.3,',',7(F9.5,','))
830   format(F6.3,',',6(E15.5,','),F10.3,',')
```

```
C
C     End of integration loop #2
C
C     Release workspace for next integration
C
99    IDO=3
      call DIVPAG(IDO,NEQ,FCN,FCNJ,A,t,TEND,TOL,PARAM,Y)
C*********************************************************
C     End of integration loop
C*********************************************************
999   continue
      END

C  This subroutine is called from the IMSL code
C  Rgas gasconstant in atm m3 / mol K
C
      subroutine FCN(NEQ,t,Y,YPRIME)
      integer NEQ,count,flago
      character mark*2
      double precision t,Y(NEQ),YPRIME(NEQ),Temp,PNA,Rgas,Sulfur
      double precision TEMPE,Cburn,r,DRmax,DRs,SG,Tempg,COS,Aext
      double precision XSO4,const,rc,tol2,ConcCO2i,ConcH2Oi
      double precision THO2,THCO2,THH2O,THNa
      double precision O2byMT,CO2byMT,H2ObyMT,NabyMT
      double precision EFFO2,EFFCO2,EFFH2O,EFFNao,EFFNan
      double precision Na2CO3,SO4,Aint,pco2,pco,ph2,ph2o,po2,pCOS
      double precision D,D0,DRc,DiffO2,DiffCO2,DiffH2O,DiffNa,dummy
      double precision Vpart,Vp,DIA,Yini,Conv,kgCOS,kgH2S,H2S,pH2S
      double precision dCO2,dH2O,dO2,dNa,dSS,dCOS,dH2S,kgCO2,kgH2O
      double precision ROO2,ROCO2,ROH2O,ROgf,RONa,RO,ROox,RS
      double precision ConcO2,ConcCO2,ConcH2O,ConcNa,ch2o,ch2
      double precision krO2,krCO2,krH2O,krNa,DI,pco2i,ph2oi,Sini
      double precision Rold,Sulfid,pf,RPRIMEO2,dR,CSMLT,dens,vt
      double precision Kcos,Kh2s,ffactor,M0,S0,pi,dSpyr,unacc
      double precision irrk,revk,mt,Turkd,Keq,PNApa,XSO4old
      parameter(Rgas=82.06e-6,pi=3.1415927)
      common/kaj1/count
      common/kaj1a/Yini,Sini,dSpyr,RS,unacc,tol2,pco2i,ph2oi
      common/kaj2/Na2CO3,SO4,Aint,pco2,pco,ph2,ph2o,po2,SG,vt
      common/kaj3/TEMPE,DIA,krCO2,kgCO2,pCOS
      common/kaj4/Cburn,D0,DRmax,DRs,DRc,dens,pf
      common/kaj5/ffactor,M0,S0
      common/kaj7/mark
      common/kaj9/RO,ROO2,ROCO2,ROH2O,RONa
      common/kaj10/Conv,Sulfur
```

```
      common/kaj12/EFFO2,EFFCO2,EFFH2O,EFFNao,EFFNan
      common/kaj13/O2byMT,CO2byMT,H2ObyMT,NabyMT
      common/kaj14/dCO2,dH2O,dO2,dNa,dSS
      common/kaj15/flago
      common/kaj16/irrk,revk,mt,Turkd,Keq
C     This line is to prevent IMSL to print warning on screen
      t=t
C     Rates in mmoles/sec
C     Y(7) =  mmoles  carbon
      if (Y(7).lt.tol2) then
       Y(7)=tol2
C     All carbon is gone
       Conv=1.0
      else
C     Fraction carbon that has left
       Conv=1.0-Y(7)/Yini
      endif
C     if mmol Sulfate > mmol Sulfur then Sulfate = Sulfur
      if (Y(15).gt.Y(10)) then
       Y(15)=Y(10)
      endif
      if (Y(15).lt.0) then
       Y(15)=0
      endif
      call TEMPER(count,Temp,Tempg,PNA,Conv,po2)
      TEMPE=Temp+273.15
C******* mmol Ox consumed / sec = mmol C consumed / sec *********
C     Effect of Na catalysis with a rate multiplier of 10-100
C  Depletion of Aint WAS accounted for by mCleft(momentan)/mC(init)
      Aint=Aint*(1-Conv)
      if (po2.gt.1e-3) then
       dO2=9.5E6*Aint*po2*Y(7)*exp(-33950./1.987/TEMPE)
      else
       dO2=0.0
      endif
      if (dO2.lt.1e-10) then
       dO2=0
      endif
C******* mmol CO2 consumed / sec = mmol C consumed / sec *******
      if (pco2.gt.1e-3) then
       dCO2=63.0e9*pco2/(pco2+3.4*pco)*Y(7)*exp(-30070./TEMPE)
      else
       dCO2=0.0
      endif
C******* mmol H2O consumed / sec = mmol C consumed / sec *******
```

```
        if (pH2O.gt.1e-3) then
         dH2O=2.56e9*ph2o/(ph2o+1.42*ph2)*Y(7)*exp(-25300./TEMPE)
        else
         dH2O=0.0
        endif
C******* mmol SO4 consumed / sec = 2 mmol C consumed / sec ********
C     New sulfate reduction equation
C     Sulfate concentration is dimensionless
        XSO4=(1.-Y(11))*Y(10)/Y(13)
cc      dSS=2.44e5*Y(7)*XSO4**1.4*exp(-29200/1.987/TEMPE)*M0*S0*1e3
        dSS=3800.0*Y(7)*XSO4**1.4*exp(-9420/TEMPE)
C******* mmol Na produced / sec = mmol C consumed / sec *******
C******* Na2CO3 + 2C = 2Na + 3CO (high T) **********************
C******* -0.5 dC/dt = -dNa2CO3/dt ******************************
C******* dNa(v)/dt = -dC/dt; -dNa2CO3/dt = 0.5 dNa(v) *********
        if (Y(7).gt.1.e-10) then
         dNa=2.*1e9*Y(6)*exp(-29335./TEMPE)
        else
         dNa=0.0
        endif
C******* Na2CO3 + C = 2Na + CO2 + CO (low T) ******************
C     Boudouard equilibrium (CO2+C=2CO)
C     CO/CO2 = 1.6 3.5 7.3 at 700 750 800C respectively
C     HSC calcs show that CO and Na dominate
C*************************************************************
C     Swelling effect on masstransfer coefficients
C     r = mC(instantaneous)/mCtot
C*************************************************************
        r=Y(7)/Cburn*12.
        if (r.lt.0) then
         r=0.0
        endif
        if (r.gt.1) then
         r=1.0
        endif
        DRc=(DRmax**3.-(DRmax**3.-DRs**3.)*abs(1.-r))**.333
        if (DRc.lt.0.0) then
         write(*,*) 'WARNING swelling factor below zero !'
         D=0.0
        elseif (DRc.gt.7.5) then
         write(*,*) 'WARNING swelling factor > 7.5 !'
         write(*,*) ' DRc = ',DRc
         D=6.0
        endif
        D=DRc*D0
```

```
      DIA=D
C Density of particle dens=Mass(mg)/Vol (mg/m3)*1e-9=(g/cm3)
      dens=(Y(12)+unacc*105.99)/(4./3.*pi*(D/2.)**3.)*1e-9
C Specific gravity of particle (-)
      SG=dens/1.
C******* Mass transfer subroutine uses a new diameter ********
      CALL
MASSTR(PNA,TEMPE,Tempg,O2byMT,CO2byMT,H2ObyMT,NabyMT,D,
     & DiffO2,DiffCO2,DiffH2O,DiffNa,ConcO2,ConcCO2,ConcH2O,ConcNa,
     & kgCOS,kgH2S,kgCO2,kgH2O)
C******* interface concentration ******************************
C     Mass transfer coefficient in m/s
      Aext=pi*D**2.
      Vp=pi*D*D*D/6.0
C     Interface partial pressures
      pco2i=kgCO2*pco2*Aext/(Aext*kgCO2+Vp*EFFCO2*krCO2)
c     write(*,*) 'pCO2i eq =',pco2i
      ConcCO2i=pco2i/Rgas/TEMPE
      ph2oi=kgH2O*pH2O*Aext/(Aext*kgH2O+Vp*EFFH2O*krH2O)
      ConcH2Oi=ph2oi/Rgas/TEMPE
c     write(*,*) 'pH2Oi =',pH2Oi
C******* mmol COS produced ************************************
C     Use TEMPE (K) which is the particle temp
C     Eguilibrium equations are based on Kp
      if (TEMPE.lt.1101) then
       Kcos=exp(-16.0739+12306.9/TEMPE)
      else
       Kcos=exp(-12.63778+8514.329/TEMPE)
      endif
      pCOS=pco2i**2.*Kcos
      COS=pCOS/Rgas/TEMPE
      if (Y(14).lt.0) then
       Y(14)=0
      endif
      if (pco2.gt.0.005) then
       dCOS=kgCOS*Aext*COS*1.e3*(Y(14)/Sini)
      else
       dCOS=0.0
      endif
C******* mmol H2S produced ************************************
C     Temp range for 900-1100K and 900-100C
C     Eguilibrium equations are based on Kp
      if (TEMPE.lt.1101) then
       Kh2s=exp(-16.4674+16506.6/TEMPE)
      else
```

```
          Kh2s=exp(-12.91285+12585.43/TEMPE)
         endif
         if (Y(10).lt.0) then
          Y(10)=0.0
         endif
         pH2S=ph2oi*pco2i*Kh2s
         H2S=pH2S/Rgas/TEMPE
         if (ph2o.gt.0.005.and.pco2.gt.0.005) then
          dH2S=kgH2S*Aext*H2S*1.e3*(Y(14)/Sini)
         else
          dH2S=0.0
         endif
C*******Thiele modulus part*****************************************
C      Overall rates in mmoles/sec
C      Thiele modulii are in terms of GAS consumed
C**************************************************
C****** Rate constant kr in 1/s ********************
         krO2=(abs(dO2)+abs(dSS))/Vp/ConcO2
         if (krO2.gt.0) then
          THO2=D/6.*sqrt(krO2/DiffO2)
          if (po2.lt.1e-3) then
           EFFO2=1.0
          else
           EFFO2=tanh(THO2)/THO2
          endif
         endif
         krCO2=dCO2/Vp/ConcCO2
         if (krCO2.gt.0) then
          THCO2=D/6.*sqrt(krCO2/DiffCO2)
          if (pco2.lt.1e-3) then
           EFFCO2=1.0
          else
           EFFCO2=1/THCO2*(1/tanh(3*THCO2)-1/(3*THCO2))
          endif
         endif
         krH2O=dH2O/Vp/ConcH2O
         if (krH2O.gt.0) then
          THH2O=D/6.*sqrt(krH2O/DiffH2O)
          if (ph2o.lt.1e-3) then
           EFFH2O=1.0
          else
           EFFH2O=1/THH2O*(1/tanh(3*THH2O)-1/(3*THH2O))
          endif
         endif
         krNa=dNa/Vp/ConcNa
```

```
        if (krNa.gt.0) then
         THNa=D/6.*sqrt(krNa/DiffNa)
         EFFNao=tanh(THNa)/THNa
         if (count.gt.8) then
          Keq=5.52126e-43*exp(6.88507e-2*TEMPE)
          THNa=D/6.*sqrt(krNa*(Keq+1)/(Keq*DiffNa))
         else
          THNa=1
         endif
         EFFNan=tanh(THNa)/THNa
        else
C       dNa has to be set to 0 here; otherwise RONa crashes
         dNa=0
        endif
C*******************************************************
C       Overall rates are in mmol Carbon consumed
C       = mmol gases consumed
C*******************************************************
        if (flago.eq.1) then
         if (EFFO2.gt.0.and.dO2.gt.0) then
          ROO2=1./(1./O2byMT+1./(dO2+2*RS)/EFFO2)
         else
          ROO2=O2byMT
         endif
        else
         ROO2=O2byMT
        endif
        if (dCO2.gt.0) then
         ROCO2=1./(1./CO2byMT+1./dCO2/EFFCO2)
        else
         ROCO2=0.0
        endif
        if (dH2O.gt.0) then
         ROH2O=1./(1./H2ObyMT+1./dH2O/EFFH2O)
        else
         ROH2O=0.0
        endif
        if (dNa.gt.0.and.EFFNao.gt.0) then
         RONa=1./(1./NabyMT+1./dNa/EFFNao)
        else
         RONa=0
        endif
C*******************************************************
C       Partition factor
C*******************************************************
```

```
      pf=Y(7)/(Y(7)+Y(13))
      if (pf.lt.0) then
       pf=0.0
      endif
      if (pf.gt.1) then
       pf=1.0
      endif
C*****************************************************
C     Sufate reduction
C*****************************************************
C     This section considers reduction state changes
      RPRIMEO2=ROO2-ROCO2-ROH2O-2.*ffactor/(2.-ffactor)*dSS
      if (RPRIMEO2.lt.0) then
       RPRIMEO2=0.0
      endif
      if (pf.lt.0) then
       pf=0
      endif
C     Sulfide reoxidation
      RS=(1-pf)/2.*RPRIMEO2
      if (Y(10).gt.0) then
       if (Y(14).gt.0) then
        dR=(dSS-RS)/Y(10)
       else
        dR=0
       endif
      else
       dR=0.0
      endif
      if (Y(11).lt.1.e-6) then
       Y(11)=0.0
c      dR=0.0
      endif
      if (Y(11).gt.1) then
       Y(11)=1.0
c      dR=0.0
      endif
C*****************************************************
C     This section for overall gasification
      ROgf=ROCO2+ROH2O+4./(2.-ffactor)*(Y(10)*dR+dCOS+dH2S)
      ROox=ROO2+2.*(Y(10)*dR+dCOS+dH2S)
      if (ROox.lt.ROgf) then
       RO=ROgf
       mark='GF'
      elseif (ROO2.lt.1e-10) then
```

```
C If in 100% N2
          RO=ROgf
          mark='GF'
         else
          RO=ROox
          mark='OX'
         endif
         if (Y(7).lt.tol2) then
          RO=0
          RONa=0
         endif
C*************************************************
C This section for IMSL inputs
         YPRIME(1)=dO2
         YPRIME(2)=dCO2
         YPRIME(3)=dH2O
         YPRIME(4)=4./(2.-ffactor)*dSS
         YPRIME(5)=RONa
C Carbonate concentration
         YPRIME(6)=-dNa/2.
         if (Y(7).lt.1.0e-10) then
          YPRIME(6)=0.0
         endif
C Carbon left
         YPRIME(7)=-RO-RONa
C Sulfur release
         YPRIME(8)=dCOS
         YPRIME(9)=dH2S
         YPRIME(10)=-dCOS-dH2S
C Sulfate reduction
         if (Y(11).gt.0.1) then
          YPRIME(11)=dR
         else
          YPRIME(11)=0.0
         endif
C Total particle mass in mg (excluding unacc which is handled in main)
         YPRIME(12)=YPRIME(7)*12.01+YPRIME(14)*78.05
     &  +YPRIME(15)*142.05+YPRIME(6)*105.99
C Amount of inorganics left (mmol)
         YPRIME(13)=YPRIME(14)+YPRIME(15)+YPRIME(6)
c        YPRIME(13)=YPRIME(10)+YPRIME(6)
C Amount of sulfide left mmol
         YPRIME(14)=-dCOS-dH2S-RS
C Amount of sulfate left = sulfate formed - sulfate consumed (mmol)
         YPRIME(15)=RS-dSS
```

```
C-----------------------------------------------------------------
C This part is for investigating the sodium release concept
C irreversible reaction
      YPRIME(16)=dNa
C suppression of irreversible reaction
      YPRIME(17)=EFFNao*dNa
C Standard mass transfer equation w/ ChemSage Na partial pressures
      YPRIME(18)=NabyMT
C Turkdogan oxygen enhanced mass transfer equation
C PNApa is in mmHg from Turkdogans paper
      PNApa=PNA*760.
C Units in mmol/sec
      YPRIME(19)=PNApa/sqrt(2.*pi*8.314*TEMPE*23.)/3.6e4*Aext
      RETURN
      END

C  In this subroutine the mass transfer rates are calculated.
C  ASSUMPTION:  film temp average of surface and bulk
C            surface temp estimated from pyrometer measurements
C  VARIABLES:
C  Tempg = furnace temperature
C  Tfilm is the average of the furnace and surface temperature
C  TEMPE and Tempg are in Kelvin
C  Rgas gasconstant in atm m3 / mol K
C
      SUBROUTINE MASSTR(PNA,TEMPE,Tempg,O2byMT,CO2byMT,H2ObyMT,
     & NabyMT,D,DiffO2,DiffCO2,DiffH2O,DiffNa,ConcO2,ConcCO2,
     & ConcH2O,ConcNa,kgCOS,kgH2S,kgCO2,kgH2O)
      integer count
      double precision PNA,Rgas,TEMPE,Gr,kvis,vt,SG,dT,Tf,Re
      double precision ConcO2,ConcCO2,ConcH2O,ConcNa,Tempg,Temp
      double precision ScO2,ScCO2,ScH2O,ScNa,ScCOS,ScH2S
      double precision kgO2,kgCO2,kgH2O,kgNa,kgCOS,kgH2S
      double precision THO2,THCO2,THH2O,THNa,DiffH2S
      double precision O2byMT,CO2byMT,H2ObyMT,NabyMT
      double precision EFFO2,EFFCO2,EFFH2O,EFFNao,EFFNan,pi
      double precision Na2CO3,SO4,Aint,pco2,pco,ph2,ph2o,po2
      double precision D,DiffO2,DiffCO2,DiffH2O,DiffNa,DiffCOS
      double precision Yini,Sini,dSpyr,RS,unacc,tol2
      double precision pco2i,ph2oi,ConcCO2i,ConcH2Oi
      parameter(Rgas=82.06e-6,pi=3.1415927)
      common/kaj1/count
      common/kaj1a/Yini,Sini,dSpyr,RS,unacc,tol2,pco2i,ph2oi
      common/kaj2/Na2CO3,SO4,Aint,pco2,pco,ph2,ph2o,po2,SG,vt
      dT=abs(TEMPE-Tempg)
```

```
      Tf=dT/2.0+Tempg
C     Gasconcentration are in mmoles/m3 evaluated at film temp
      ConcO2=po2/Rgas/Tf*1000.
      ConcCO2=pco2/Rgas/Tf*1000.
c     write(*,*) 'pco2i MT =',pco2i
      ConcCO2i=pco2i/Rgas/Tf*1000.
      ConcH2O=ph2o/Rgas/Tf*1000.
      ConcH2Oi=ph2oi/Rgas/Tf*1000.
c     write(*,*) 'ConcH2Oi MT =',ConcH2Oi
      if (ConcCO2.lt.ConcCO2i) then
       write(*,*) 'WARNING: CO2 < CO2i'
       stop
      endif
      if (ConcH2O.lt.ConcH2Oi) then
       write(*,*) 'WARNING: H2O < H2Oi'
       stop
      endif
      ConcNa=PNA/Rgas/Tf*1000.
      call DIFFU(Tf,DiffO2,DiffCO2,DiffH2O,DiffNa,DiffCOS,DiffH2S)
C     This eq is for N2
      kvis=-8.7664e-5+2.0989e-7*Tf
      Gr=9.81*dT*D**3./Tf/kvis/kvis/6**3.0
      ScO2=kvis/DiffO2
      ScCO2=kvis/DiffCO2
      ScH2O=kvis/DiffH2O
      ScNa=kvis/DiffNa
      ScCOS=kvis/DiffCOS
      ScH2S=kvis/DiffH2S
C     Terminal settling velocity from a force balance
C     Weight of particle = drag force yields following equation
      vt=11640*SG**.714*D**1.143
      Re=D*vt/kvis
C Units in m/s
      kgO2=DiffO2/D*(2.0+0.569*(Gr*ScO2)**0.25+
     & 0.347*(Re*ScO2**0.5)**0.62)
      kgCO2=DiffCO2/D*(2.0+0.569*(Gr*ScCO2)**0.25+
     & 0.347*(Re*ScCO2**0.5)**0.62)
      kgH2O=DiffH2O/D*(2.0+0.569*(Gr*ScH2O)**0.25+
     & 0.347*(Re*ScH2O**0.5)**0.62)
      kgNa=1*DiffNa/D*(2.0+0.569*(Gr*ScNa)**0.25+
     & 0.347*(Re*ScNa**0.5)**0.62)
      kgCOS=DiffCOS/D*(2.0+0.569*(Gr*ScCOS)**0.25+
     & 0.347*(Re*ScCOS**0.5)**0.62)
      kgH2S=DiffH2S/D*(2.0+0.569*(Gr*ScH2S)**0.25+
     & 0.347*(Re*ScH2S**0.5)**0.62)
```

```
C Units in mmoles/s
      O2byMT=kgO2*pi*D**2*ConcO2
      if (ConcCO2.eq.ConcCO2i) then
       ConcCO2i=0.0
      endif
      if (ConcH2O.eq.ConcH2Oi) then
       ConcH2Oi=0.0
      endif
      CO2byMT=kgCO2*pi*D**2*(ConcCO2-ConcCO2i)
      H2ObyMT=kgH2O*pi*D**2*(ConcH2O-ConcH2Oi)
      NabyMT=kgNa*pi*D**2*ConcNa
      RETURN
      END

C     Binary diffusivities estimated
C     Mixture diffusivities not accounted for
      subroutine DIFFU(Tf,DiffO2,DiffCO2,DiffH2O,DiffNa,DiffCOS,
     & DiffH2S)
      double precision A,B,C,D,E,F,G,H,sgmO2,sgmCO2,sgmH2O,sgmNa,
     & sgmair,Tf,TsO2,TsCO2,TsH2O,TsNa,ekO2,ekCO2,ekH2O,ekNa,
     & OmegaO2,OmegaCO2,OmegaH2O,OmegaNa,sO2air,sCO2air,sH2Oair,
     & sNaair,DiffO2,DiffCO2,DiffH2O,DiffNa,Mair,MO2,MCO2,MH2O,MNa,
     & MCOS,MH2S,OmegaCOS,OmegaH2S,sCOSair,sH2Sair,ekCOS,ekH2S,
     & TsCOS,TsH2S,sgmCOS,sgmH2S,DiffCOS,DiffH2S,ekair
      data A/1.06036/,B/0.1561/,C/0.193/,D/0.47635/,E/1.03587/,
     & F/1.52996/,G/1.76474/,H/3.89411/
      data ekO2/113./,ekCO2/190./,ekH2O/356./,ekNa/2172./,
     & ekCOS/335./,ekH2S/301./,ekair/97./
      data sgmair/3.689/,Mair/28./,MO2/32./,MCO2/44./,MH2O/18./
      data MNa/23./,MCOS/60.1/,MH2S/34.8/,sgmCOS/4.13/,sgmH2S/3.62/
      data sgmO2/3.433/,sgmCO2/3.996/,sgmH2O/2.649/,sgmNa/4.924/
      TsO2=Tf/sqrt(ekO2*ekair)
      TsCO2=Tf/sqrt(ekCO2*ekair)
      TsH2O=Tf/sqrt(ekH2O*ekair)
      TsNa=Tf/sqrt(ekNa*ekair)
      TsCOS=Tf/sqrt(ekCOS*ekair)
      TsH2S=Tf/sqrt(ekH2S*ekair)
      OmegaO2=A/TsO2**B+C/exp(D*TsO2)+E/exp(F*TsO2)+G/exp(H*TsO2)
     OmegaCO2=A/TsCO2**B+C/exp(D*TsCO2)+E/exp(F*TsCO2)+G/exp(H*TsCO2)
     OmegaH2O=A/TsH2O**B+C/exp(D*TsH2O)+E/exp(F*TsH2O)+G/exp(H*TsH2O)
     OmegaNa=A/TsNa**B+C/exp(D*TsNa)+E/exp(F*TsNa)+G/exp(H*TsNa)
     OmegaCOS=A/TsCOS**B+C/exp(D*TsCOS)+E/exp(F*TsCOS)+G/exp(H*TsCOS)
     OmegaH2S=A/TsH2S**B+C/exp(D*TsH2S)+E/exp(F*TsH2S)+G/exp(H*TsH2S)
C     These are in Angstroms
      sO2air=(sgmO2+sgmair)/2.*1e-10
```

```
      sCO2air=(sgmCO2+sgmair)/2.*1e-10
      sH2Oair=(sgmH2O+sgmair)/2.*1e-10
      sNaair=(sgmNa+sgmair)/2.*1e-10
      sCOSair=(sgmCOS+sgmair)/2.*1e-10
      sH2Sair=(sgmH2S+sgmair)/2.*1e-10
      DiffO2=2.6629e-22*sqrt(Tf**3*(MO2+Mair)/2/MO2/Mair)/101325./
     & sO2air**2/OmegaO2
      DiffCO2=2.6629e-22*sqrt(Tf**3*(MCO2+Mair)/2/MCO2/Mair)/101325.
     & /sCO2air**2/OmegaCO2
      DiffH2O=2.6629e-22*sqrt(Tf**3*(MH2O+Mair)/2/MH2O/Mair)/101325.
     & /sH2Oair**2/OmegaH2O
      DiffNa=2.6629e-22*sqrt(Tf**3*(MNa+Mair)/2/MNa/Mair)/101325./
     & sNaair**2/OmegaNa
      DiffCOS=2.6629e-22*sqrt(Tf**3*(MCOS+Mair)/2/MCOS/Mair)/101325.
     & /sCOSair**2/OmegaCOS
      DiffH2S=2.6629e-22*sqrt(Tf**3*(MH2S+Mair)/2/MH2S/Mair)/101325.
     & /sH2Sair**2/OmegaH2S
      return
      end

C     This subroutine contains the equilibrium partial pressures
C     of sodium vapor and the approximate temperature profiles
C     for the particle surface (calculated from Tainas thesis)
C     Variable Conv is used only for exothermic reactions
C
      subroutine TEMPER(count,Temp,Tempg,PNA,Conv,po2)
      integer count,flagt
      double precision Temp,PNA,t,Tempg,Conv,A,B,C,O2,po2,delta
      common/kaj11/delta,flagt
      O2=po2*100.
      A=5.19+2.48*O2+0.137*O2**2.
      B=24.66+13.06*O2+0.693*O2**2.
      C=19.08+10.25*O2+0.537*O2**2.
c     Temperature profile in a 600 C furnace
      if (count.lt.7.and.count.gt.5) then
       PNA=2.9126E-5
       Temp=600.+A+B*Conv-C*Conv**2.
       Tempg=600.+273.15
       if (Temp.gt.900) then
        Temp=900.
       endif
      endif
c     Temperature profile in a 700 C furnace
      if (count.lt.8.and.count.gt.6) then
       PNA=4.7142E-4
```

```
          Temp=700.+A+B*Conv-C*Conv**2.
          Tempg=700.+273.15
          if (Temp.gt.1000) then
           Temp=1000.
          endif
         endif
c     Temperature profile in a 800 C furnace
         if (count.lt.9.and.count.gt.7) then
          PNA=4.4532E-3
          Temp=800.+A+B*Conv-C*Conv**2.
          Tempg=800.+273.15
          if (Temp.gt.1100) then
           Temp=1100.
          endif
         endif
c     Temperature profile in a 900 C furnace
         if (count.lt.10.and.count.gt.8) then
          PNA=2.7354E-2
          Temp=900.+A+B*Conv-C*Conv**2.
          Tempg=900.+273.15
          if (Temp.gt.1200) then
           Temp=1200.
          endif
         endif
c     Temperature profile in a 1000 C furnace
         if (count.lt.11.and.count.gt.9) then
          PNA=1.2074E-1
          Temp=1000.+A+B*Conv-C*Conv**2.
          Tempg=1000.+273.15
          if (Temp.gt.1300) then
           Temp=1300.
          endif
         endif
c     Temperature profile in 1092 C furnace
c     TEMPERATURE APPROXIMATION 1100C
         if (count.lt.12.and.count.gt.10) then
          PNA=3.8354E-1
          Temp=1100.+A+B*Conv-C*Conv**2.
          Tempg=1100.+273.15
          if (Temp.gt.1400) then
           Temp=1400.
          endif
         endif
C     The following line is needed for endothermic reactions
         if (flagt.lt.2.and.flagt.gt.0) then
```

```
        Temp=Tempg-delta-273.15
       endif
       return
       end

C      This subroutine contains the furnace temperatures
C      as well as fractions carbon remaining after pyrolysis
C      Units: g C ap/g C in BLS
C           g S ap/g C in BLS
C
       SUBROUTINE CARBON(count,Xmc,Cchar,Schar,Temp)
       INTEGER count
       DOUBLE PRECISION Xmc,Cchar,Schar,Temp
c      Temperature in a 600 C furnace
       if (count.eq.6) then
        Temp=600.
       endif
c      Temperature in a 700 C furnace
       if (count.eq.7) then
        Temp=700.
       endif
c      Temperature in a 800 C furnace
       if (count.eq.8) then
        Temp=800.
       endif
c      Temperature in a 900 C furnace
       if (count.eq.9) then
        Temp=900.
       endif
c      Temperature in a 1000 C furnace
       if (count.eq.10) then
        Temp=1000.
       endif
c      Temperature in a 1100 C furnace
       if (count.eq.11) then
        Temp=1100.
       endif
       if (Temp.lt.901) then
        Xmc=1.48434*exp(-0.00105515*Temp)
       else
        Xmc=0.582
       endif
       Cchar=1.50851*exp(-0.00143954*Temp)
       Schar=1.-(-163.27+0.91705*Temp-1.1504e-3*Temp**2+
     &  4.2827e-7*Temp**3)*1e-2
```

```
      RETURN
      END

C  THIS SUBROUTINE IS NEVER CALLED BUT REQUIRED BY IMSL!
      SUBROUTINE FCNJ(NEQ,t,Y,DYPDY)
      INTEGER NEQ
      DOUBLE PRECISION t,Y(NEQ),DYPDY(*)
      t=t
      Y(1)=Y(1)
      DYPDY(1)=DYPDY(1)
      RETURN
      END
```

Description of LEFR and experimental procedures

The black liquor char samples studied in this thesis were obtained with a laminar entrained-flow reactor (LEFR). A schematic of the apparatus is shown in Figure A.13.3. Black liquor solids are carried in the primary gas flow (typically at 15 L/min NTP) from the particle feeder to the injector. The primary flow enters the reactor at the center, coaxially with the preheated secondary gas flow (typically 20 L/min). The particles and gases flow downward through the hot zone of the reactor in a narrow laminar column. When they reach the collector, they are quenched with cooled nitrogen to stop the devolatilization process. Most of the quench gas (15 L/min) is fed into the first 2 cm of the collector, while the rest flows through the remaining porous wall (5 L/min). This is done to avoid deposition of aerosols on the cooled collector walls. The gas residence time is controlled by moving the collector up or down and by changing the gas flow rates. After the quench the products are separated in a cyclone. Particles larger than 3 μm in diameter are collected and the smaller than 3 μm particles are deposited on a filter located before the exhaust. A schematic of the cyclone assembly is shown in Figure A.13.2.

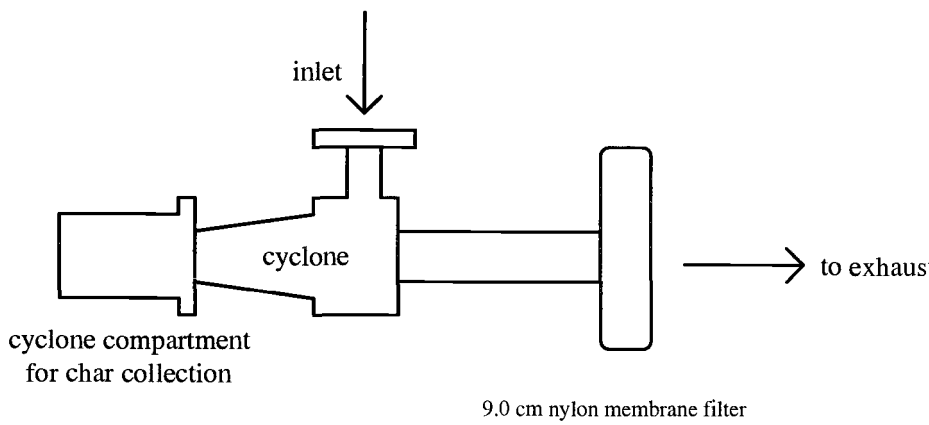

Figure A.13.2. Schematic of cyclone/filter set-up for the LEFR.

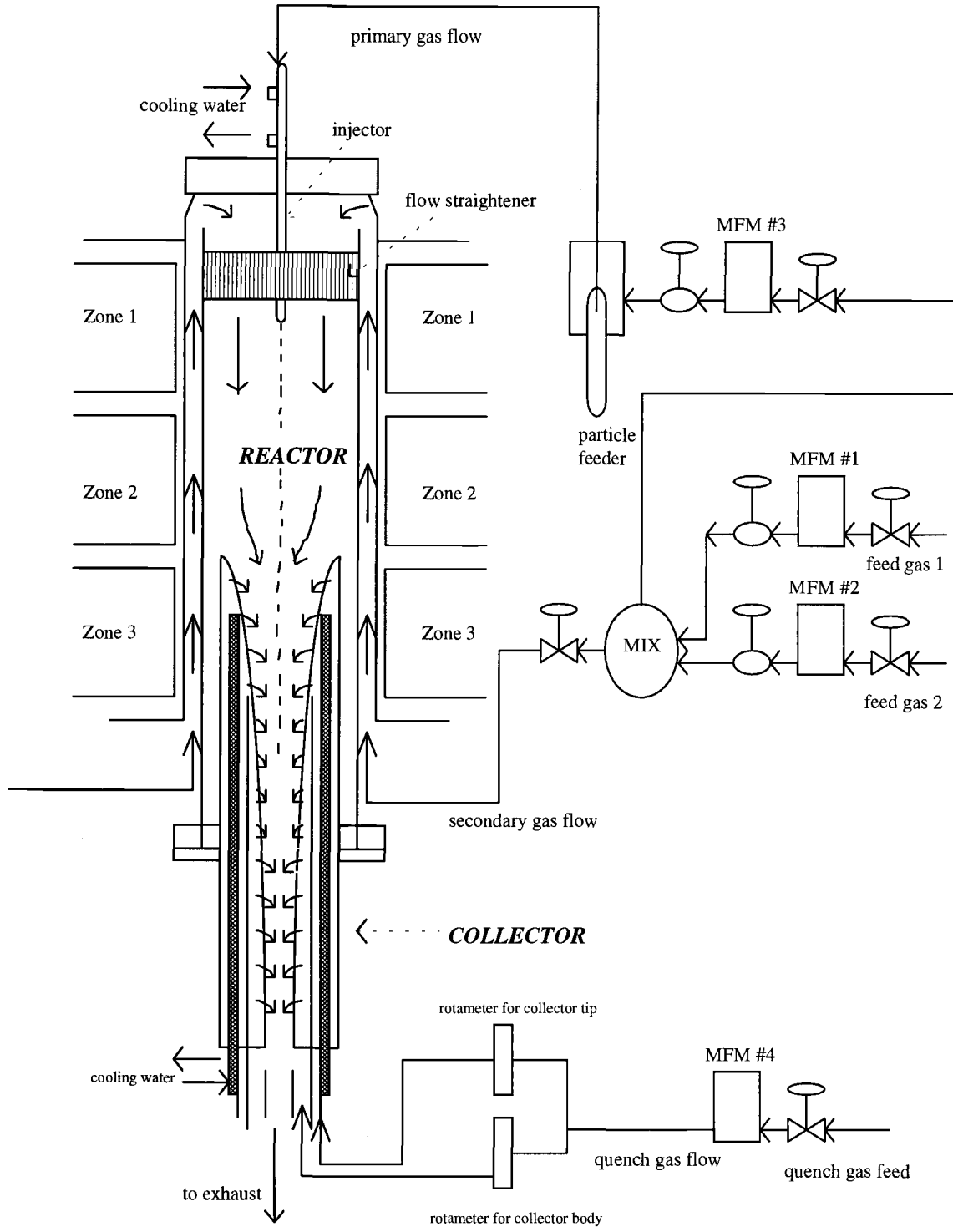

Figure A.13.3. Schematic of the laminar entrained-flow reactor (LEFR).

TK program for calculating the Boudouard-equilibrium

VARIABLE SHEET

St	Input	Name	Output	Unit	Comment
L		CO2	1.00911	bar	
	.2	CO		bar	
		dG	-73.353	J/mol C	
	8.314	R		J/mol K	
L	973	T		K	
		Ke	1.00911	1/bar	
		Gc	-12043.71	J/mol	
		Gco2	-622218.7	J/mol	
		Gco	-317094.5	J/mol	
		Kw	1.4749771		
		H2			
		Kapp		1/bar	
		H2O			
		Ptot			
.8		RH2			
.25		RH2O			
		Gh2	-140917.4	J/mol	
		Gh2o	-442897.6	J/mol	
		dGw	-3143.932	J/mol	

RULE SHEET

S Rule

* dG = -R*T*ln(Ke)
* dG = Gc + Gco2 - 2*Gco
* Gco2 = -409930.4 + 89.47522*T - 44.1412*T*ln(T) - 0.00451872*T^2 + 426768/T
* Gco = -119348.1 - 5.795926*T - 28.40936*T*ln(T) - 0.00205016*T^2 + 23012/T
* Gc = -2106.402 + 6.658662*T -.108784*T*ln(T) - 0.01947024*T^2 + 0.289742e-5*T
* Ke = CO2/CO^2
* Kw = CO2*H2/CO/H2O

C Kapp = CO2/CO^2

C Ptot = CO2 + CO + H2 + H2O

* H2 = RH2*Ptot
* H2O = RH2O*Ptot
* Gh2 = -8110.091 + 52.81627*T -27.27968*T*ln(T) - 0.00163176*T^2 -25104/T
* Gh2o = -251770.9 + 15.2048*T - 29.99928*T*ln(T) - 0.00535552*T^2 - 16736/T
* dGw = -R*T*ln(Kw)
* dGw = Gco2 + Gh2 - Gco - Gh2o